

**A Methodology to Study Cell Deformation Behaviour within Native  
and Tissue Engineered Cartilage Subjected to Incremental  
Compression Using Confocal Microscopy**

Kwan Choi Kwan

Submitted in accordance with the requirements for the degree of  
Doctor of Philosophy

The University of Leeds  
School of Mechanical Engineering

**June, 2020**

The candidate confirms that the work submitted is his own and that appropriate credit has been given where reference has been made to the work of others.

This copy has been supplied on the understanding that it is copyright material and that no quotation from the thesis may be published without proper acknowledgement.

© 2020 The University of Leeds and Kwan Choi Kwan

## Acknowledgements

Firstly, I would like to thank my supervisors Professor Jennifer Kirkham, Dr Scott Finlay, Dr Bahaa Seedom and Professor David Wood for providing me with their tremendous academic guidance and support throughout the years. I have really enjoyed working with all of you and I can't believe I have got here in the end. I wouldn't have got here without all of your help, especially during the last eight months!

I would like to thank the colleagues from Xiros Ltd, the Department of Oral Biology, the institute of Mechanical and Biological Engineering (iMBE), the St James's Flow Cytometry and Imaging Facility, Nikon Instruments and the Henry Moseley X-ray Imaging Facility, University of Manchester for giving me their time and support over the years. I would like to specially thank the numerous individuals that have provided me with their expertise and advice within this thesis. Thanks to Dr Martin Stanley for his advice and assistance on the designs of the compression device. Thanks to Mrs Jackie Hudson for the specialised training and support on confocal microscopy and histology techniques. Thanks to Dr Sarah Myers and Mr Matty Percival for their help and support in the lab. Thanks to Dr Adam Davidson for his expertise and invaluable advice on confocal microscopy. Thanks to Mr Philip Wood and Mr Irvin Homan for their help with tissue ordering. Thanks to Dr Ruikang Xue for introducing me to the software, Amira.

I would like to thank Xiros Ltd for providing the scaffolds used throughout the study. Thanks to Kirkstall Precision for fabricating the compression device. Thanks also Covance Ltd for the embedding and sectioning of produced cartilage constructs and harvested osteochondral plugs.

Thank you to the Centre of Doctoral Training for Tissue Engineering and Regenerative Medicine (CDT TERM) and Xiros Ltd for funding my study and providing me the opportunity to broaden my knowledge in the field that I feel very passionate about.

Finally, I would like to give special acknowledgment to my family and friends. I am grateful to my family for always being there for me and supporting me throughout this journey. I would not be where I am without my mum, dad and brother. The biggest thank you to my partner Mary for always believing in me, especially during some tough times in the last eight months. I am very grateful that you are always there for me and thank you for your help with the figures. A big thank you to Cathie and Mark for putting me up over the last month. Special mention to Jonah, Harry, Mike, Damien, Matt and Katie for being brilliant friends and provided me with great memories in Leeds that I will cherish forever.

## Abstract

In cartilage tissue engineering, it is vital that an appropriate amount of stress is received by the cells to favour for the promotion of a chondrocyte-like phenotype and induction of deposition of an appropriate matrix for tissue maturation. The aim of this thesis was to determine the effects of incremental tissue compression on cell deformation in native and tissue engineered cartilage, in an attempt to better understand Finlay's hypothesised mechanism in developing cartilage-like constructs [1].

A novel compression device was developed to apply compressive tissue strains and simultaneously allow visualisation of cells within native and tissue engineered cartilage disks in real time. A dual staining method of Hoechst 33342 and CellMask Green plasma membrane stains with superior retention of fluorescence signal following the capture of sequential images was developed and used to visualise, track and image cell morphology in native and tissue engineered cartilage. Both were used to address the aim of this thesis.

Significant changes in deformation of superficial zone chondrocytes within cartilage disks were observed under 10 % and 15 % compressive strains and it is believed that these changes were largely influenced by the local ECM environment as well as the pericellular matrix.

For engineered constructs, limited amount of cartilage-like matrix was seen in contrast to Finlay *et al.* (2016) [1]. The reason for the differences could be related to the starting scaffold porosity used in the constructs, emphasising the need to understand the relationships between scaffold porosity, cell seeding density and time to cell differentiation. Limited change in synoviocyte morphology was observed within loaded constructs under the estimated strain experienced by the construct during mechanical loading and under 28 % compressive strain. The observed effects were likely be influenced by the microenvironment around the measured synoviocytes.

It is concluded that a novel methodology capable to visualise, track, image and quantify changes in cell morphology within native cartilage disks and tissue engineered cartilage constructs under static compressive tissue strains has been achieved. This provides a platform upon which to build for future cell deformation experimental studies.

## Table of Contents

<b>Chapter 1 - General Introduction.....</b>	<b>1</b>
1.1 Composition of Articular Cartilage.....	1
1.1.1 Chondrocytes .....	2
1.1.2 Collagen.....	2
1.1.3 Proteoglycans and Water .....	3
1.2 Structure of Articular Cartilage.....	6
1.2.1 Superficial Zone .....	6
1.2.2 Middle Zone.....	6
1.2.3 Deep Zone.....	7
1.2.4 Calcified Zone.....	7
1.3 Articular Cartilage Functions.....	9
1.3.1 Near Frictionless and Wear Resistance Characteristics.....	9
1.3.2 Distribution of Joint Loads .....	10
1.4 Structure-Function Relationships of Articular Cartilage .....	10
1.5 Mechanical Environment of Articular Cartilage .....	10
1.5.1 Joint Forces and Stresses Imposed on Cartilage in Load Bearing Joints ...	11
1.6 Effect of Mechanical Loading on Cartilage.....	11
1.6.1 Effect of Mechanical Loading on Extracellular Matrix.....	11
1.6.2 Effect of Mechanical Loading on Chondrocytes .....	12
1.6.2.1 Previous Studies on Chondrocyte Deformation and Metabolic Activity under Mechanical Loading .....	16
1.7 Articular Cartilage Damage .....	18
1.7.1 Molecular Factors Responsible for Cartilage Damage .....	19
1.7.2 Mechanical Factors Responsible for Cartilage Damage.....	19
1.8 Repair of Articular Cartilage Damage.....	20
1.8.1 Surgical Treatments for Cartilage Lesions.....	21
1.8.1.1 Debridement and Lavage .....	21
1.8.1.2 Microfracture.....	21
1.8.1.3 Osteochondral autograft transplantation system (OATS) .....	22
1.8.1.4 Autologous chondrocytes implantation (ACI) .....	22
1.8.2 Future Repair Strategies.....	23
1.9 Tissue engineering.....	24
1.9.1 Cells.....	24
1.9.2 Scaffolds .....	25

1.9.3	Bioactive factors.....	26
1.9.3.1	Biochemical stimuli .....	26
1.9.3.2	Physical stimuli .....	26
1.9.4	Cartilage Tissue Engineering .....	28
1.10	Thesis Aims and Objectives.....	33
1.10.1	Overall Aim .....	33
1.10.2	Objectives .....	35
<b>Chapter 2 - Development of A Compression Device for the Application of Tissue Strain</b> .....		<b>36</b>
2.1	Introduction.....	36
2.2	Device design specification .....	39
2.3	Compression Device Designs .....	40
2.3.1	Loading configurations .....	40
2.3.2	Compression Device Design Based on Loading Configuration Perpendicular to the Axis of the Light Path .....	41
2.3.3	Compression Device Design Based on Loading Configuration Parallel to the Axis of the Light Path .....	42
2.3.4	Final Design of Compression Device Based on Loading Configuration Parallel to the Axis of the Light Path .....	43
2.3.5	Compression Device Fabrication .....	44
2.4	Validation of Compression Device Final design.....	45
2.4.1	Introduction.....	45
2.4.2	Experimental Methodologies .....	48
2.4.2.1	Application of 5 N Static Load to Coverslips of Different Thicknesses .....	48
2.4.2.2	Coverslip Flexion under Applied Load.....	49
2.4.2.3	Validation of Micrometer Accuracy .....	50
2.4.3	Results .....	51
2.4.3.1	Ability of Coverslip to Withstand 5 N Static Load .....	51
2.4.3.2	Coverslip Flexion under Applied Load.....	51
2.4.3.3	Validation of Micrometer Accuracy .....	52
2.4.4	Discussion.....	53
2.4.4.1	Ability of Coverslip to Withstand 5 N Static Load .....	53
2.4.4.2	Coverslip Flexion under Applied Load.....	53
2.4.4.3	Validation of Micrometer Accuracy .....	54
2.4.5	Conclusion .....	55
2.5	Discussion.....	55

2.6	Conclusion .....	57
<b>Chapter 3 - Development of Methodology to Visualise Live Cells within Native and Tissue Engineered Cartilage .....</b>		
<b>59</b>		
3.1	Introduction.....	59
3.1.1	Confocal Microscopy .....	60
3.1.2	Challenges in Live Cell Imaging in Tissue .....	62
3.1.3	Actin Staining .....	64
3.1.4	Plasma Membrane Staining .....	66
3.2	Objectives .....	66
3.3	Experimental Methodologies .....	71
3.3.1	Cell Isolation and Monolayer Expansion.....	71
3.3.2	Synoviocyte Monolayer Culture for Staining with SiR-actin .....	72
3.3.3	Harvesting of Osteochondral Plugs for Cartilage Disks .....	72
3.3.4	Production of Synoviocyte/PET Immature Constructs.....	72
3.3.4.1	Preparation of Non-Woven PET Fibre Scaffolds .....	72
3.3.4.2	Cell Isolation, Monolayer Expansion and Dynamic Cell Seeding ...	73
3.3.4.3	Chondrogenic Culture of Synoviocytes on PET Scaffolds .....	74
3.4	Analytical Methods .....	75
3.4.1	Live Cell Staining for Cell Nuclei and Actin Filaments with Acridine Orange and SiR-actin Stains .....	75
3.4.2	Alexa Fluor® 488 Phalloidin Staining for F-actin Visualisation.....	76
3.4.3	Live Cell Staining for Cell Nuclei and Plasma Membrane using Hoechst 33342 and CellMask Green Plasma Membrane Stains.....	76
3.4.4	Live Cell Staining with the Addition of ProLong® Live Antifade Reagent76	
3.4.5	Confocal Microscopy Imaging.....	77
3.4.5.1	Confocal Imaging of Synoviocyte Monolayers Following Staining with SiR-actin, Alexa Fluor® 488 Phalloidin or Combined Acridine Orange and SiR-actin Stains .....	77
3.4.5.2	Confocal Imaging of Native Cartilage and Synoviocyte/PET Immature Constructs Following Staining with Combined Acridine Orange and SiR-actin Stains .....	78
3.4.5.3	Confocal Imaging of Synoviocyte Monolayers, Native Cartilage and Synoviocyte/PET Immature Constructs Following Staining with Combined Hoechst 33342 and CellMask Green Plasma Membrane Stains .....	78
3.4.5.4	Determination of Staining Penetration using Cross-Sections of Native Cartilage.....	79
3.4.5.5	Sequential Imaging of Selected Chondrocytes in Native Cartilage Following Staining of Acridine orange and SiR-actin.....	79

3.4.5.6	Comparison in Sequential Imaging of Selected Chondrocytes in Native Cartilage Between Staining of SiR-actin and CellMask Green Plasma Membrane with the addition of ProLong® Live Antifade Reagent .....	80
3.4.5.7	Sequential Imaging of Selected Chondrocytes in Native Cartilage using Galvo and Resonant Scanning Systems Following Staining of Hoechst 33342 and CellMask Green Plasma Membrane with the Addition of ProLong® Live Antifade Reagent .....	81
3.5	Results .....	82
3.5.1	Characterisation and Optimisation of SiR-actin Stain on Synoviocyte Monolayers .....	82
3.5.1.1	Confocal Microscopy of Synoviocyte Monolayers Stained with Different Concentrations of SiR-actin .....	82
3.5.1.2	Comparison of SiR-actin and Alexa Fluor® 488 Phalloidin Stains for F-actin visualisation.....	83
3.5.2	Characterisation of the Dual Staining Method of Acridine Orange and SiR-actin Stains on Synoviocyte Monolayers, Native Cartilage and Synoviocyte/PET Immature Constructs.....	84
3.5.2.1	Confocal Microscopy of Synoviocyte Monolayers Stained with Acridine Orange and SiR-actin .....	84
3.5.2.2	Confocal Microscopy of Cells Stained with Acridine Orange and SiR-actin within Native Cartilage and Synoviocyte/PET Immature Constructs .....	86
3.5.2.3	Retention of Fluorescence Signal after Sequential Imaging of Selected Chondrocytes in Native Cartilage.....	89
3.5.3	Characterisation of the Dual Staining Method of Hoechst 33342 and CellMask Green Plasma Membrane Stains on Synoviocyte Monolayers, Native Cartilage and Synoviocyte/PET Immature Constructs .....	92
3.5.3.1	Confocal Microscopy of Synoviocyte Monolayers Stained with Hoechst 33342 and CellMask Green Plasma Membrane Stains .....	92
3.5.3.2	Confocal Microscopy of Cells within Native Cartilage and Synoviocyte/PET Immature Constructs Stained with Hoechst 33342 and CellMask Green Plasma Membrane Stains .....	92
3.5.3.3	Tissue Penetration of Hoechst 33342 and CellMask Green Plasma Membrane in Native Cartilage .....	96
3.5.4	Effect of Addition of ProLong® Live Antifade Reagent on Retention of Fluorescence Signal after Sequential Imaging of Selected Chondrocytes in Native Cartilage .....	96
3.5.5	Retention of Fluorescence Signal after Sequential Imaging of Selected Chondrocytes in Native cartilage using Galvo and Resonant Scanning with the Addition of ProLong® Live Antifade Reagent .....	99
3.6	Discussion.....	99

3.6.1	Characterisation and Optimisation of SiR-actin Stain on Synoviocyte Monolayers .....	100
3.6.2	Characterisation of the Dual Staining Method of Acridine Orange and SiR-actin Stains on Synoviocyte Monolayers, Native Cartilage and Synoviocyte/PET Immature Constructs.....	102
3.6.3	Characterisation of the Dual Staining Method of Hoechst 33342 and CellMask Green Plasma Membrane Stains on Synoviocyte Monolayers, Native Cartilage and Synoviocyte/PET Immature Constructs .....	107
3.6.4	Effect of Addition of ProLong <sup>®</sup> Live Antifade Reagent on Retention of Fluorescence Signal after Sequential Imaging of Selected Chondrocytes in Native Cartilage .....	108
3.6.5	Retention of Fluorescence Signal after Sequential Imaging of Selected Chondrocytes in Native cartilage using Galvo and Resonant Scanning ..	110
3.6.6	Conclusion .....	113
<b>Chapter 4 - Effect of Compressive Strains on Cell Deformation in Native Cartilage .115</b>		
4.1	Introduction.....	115
4.2	Experimental Methodologies .....	120
4.2.1	Harvest of Osteochondral Plugs for Cartilage Disks .....	120
4.3	Analytical methods.....	120
4.3.1	Metabolic Activity Quantification on Native Cartilage Disks After Harvest of Osteochondral Plugs Using XTT Assay .....	120
4.3.2	Cell Viability Determination on Cross-Sections of Native Cartilage Disks After Harvest of Osteochondral Plugs: Confocal Microscopy and Live/Dead <sup>®</sup> Staining .....	121
4.3.3	Live Cell Staining of Native Cartilage Disks for Cell Nuclei and Plasma Membrane using Hoechst 33342 and CellMask Green Plasma Membrane Stains .....	122
4.3.4	Confocal Image acquisition .....	122
4.3.4.1	Live/Dead <sup>®</sup> imaging of Cross-Sections of Native Cartilage Disks	122
4.3.4.2	Sequential Imaging of Selected Chondrocytes in Native Cartilage Disks under Non-loaded Conditions Following Staining with Hoechst 33342 and CellMask Green Plasma Membrane after the Addition of ProLong <sup>®</sup> Live Antifade Reagent .....	123
4.3.5	Cartilage Compressive Strain Application.....	124
4.3.6	Confocal Image Analysis .....	126
4.3.6.1	Volume Measurements of Chondrocytes in Uncompressed Cartilage using Repeated Confocal Scans.....	126
4.3.6.2	Quantification of Chondrocyte Deformation .....	126
4.4	Results .....	139
4.4.1	The Effect of Culture Duration on Chondrocyte Metabolism and Viability within Native Cartilage.....	139

4.4.2	Chondrocyte Volume Changes in Uncompressed Native Cartilage with Repeated Confocal Scans.....	143
4.4.3	Quantification of Chondrocyte Deformation under Incremental Compressive Tissue Strains In Native Cartilage Disks via Amira: Morphometric Measurements .....	144
4.4.3.1	Absolute Morphometric Measurements for Each Chondrocyte at Each Strain Level in Each of the Four Cartilage Disks .....	145
4.4.3.2	Mean values $\pm$ SD of and Percentage (%) Change in Morphometric Measurements Compared to Baseline (Zero Strain) for All Chondrocytes in Each of the Four Cartilage Disks Following Application of Compressive Strains .....	148
4.4.3.3	Morphometric Measurements Presented as Mean values $\pm$ SD and Percentage (%) Change Compared to Baseline (Zero Strain) for All Chondrocytes Combined in Each Cartilage Disk Following Application of Compressive Strains .....	155
4.5	Discussion.....	159
4.5.1	The Effect of Culture Duration on Chondrocyte Metabolism and Viability within Native Cartilage.....	159
4.5.2	Volume Changes of Chondrocytes in Uncompressed Native Cartilage Following Repeated Confocal Scans .....	161
4.5.3	The Effect of Incremental Compressive Tissue Strains on Chondrocyte Deformation in Native Cartilage .....	162
4.5.3.1	Morphometric Measurements Comparisons with Previous Chondrocyte Deformation Studies .....	169
4.6	Conclusion .....	172
<b>Chapter 5 - Effect of Compressive Strains on Cell Deformation in Cartilage Constructs</b> .....		<b>173</b>
5.1	Introduction.....	174
5.2	Experimental Methodologies .....	179
5.2.1	Cell isolation, Monolayer Culture, Dynamic Seeding and Chondrogenic Culture of Synoviocytes on PET Scaffolds.....	179
5.2.2	Mechanical Loading of Synoviocyte/PET Constructs.....	179
5.2.3	Silicone Ring Fabrication .....	185
5.3	Analytical Methods .....	187
5.3.1	Papain Digestion and Collagen, Sulphated Glycosaminoglycan and DNA Quantification.....	187
5.3.1.1	Papain Digestion.....	187
5.3.1.2	Collagen Quantification .....	188
5.3.1.3	Sulphated Glycosaminoglycan Quantification .....	188
5.3.1.4	DNA Quantification.....	189
5.3.2	Dynamic Mechanical Testing .....	190

5.3.3	Fixation, Embedding and Sectioning of Constructs .....	193
5.3.4	Histological Staining and Light Microscopy of Sectioned Constructs ....	194
5.3.4.1	Alcian Blue/Sirius Red Staining Methodology .....	194
5.3.4.2	Immunohistochemistry and Light Microscopy of Sectioned Constructs .....	194
5.3.5	Live Cell Staining of Cell Nuclei and Plasma Membrane for Synoviocytes within Constructs using Hoechst 33342 and CellMask Green Plasma Membrane .....	196
5.3.6	Confocal Imaging Acquisition of Selected Synoviocytes in Constructs Following Staining after the Addition of ProLong™ Live Antifade Reagent .....	196
5.3.7	Application of Compressive Strain to Synoviocyte/PET Scaffold Constructs .....	196
5.3.8	Confocal Image Analysis .....	200
5.3.8.1	Quantification of Synoviocyte Deformation .....	200
5.4	Results .....	202
5.4.1	Collagen, Sulphated Glycosaminoglycan and DNA Content of Synoviocyte/PET Constructs Subjected to Compressive Mechanical Loading .....	202
5.4.2	Compressive Moduli of Pre-Cultured Synoviocyte/PET Constructs Subjected to Compressive Mechanical Loading .....	206
5.4.3	Histology of Pre-Cultured Synoviocyte/PET Constructs Subjected to Compressive Mechanical Loading .....	208
5.4.4	Confocal Microscopy of Synoviocytes within Compressed and Uncompressed Constructs under Incremental Compressive Strains .....	226
5.4.5	Quantification of Synoviocyte Deformation under Incremental Compressive Tissue Strains In Constructs via Amira: Morphometric Measurements .....	233
5.5	Discussion.....	238
5.5.1	The Effect of Compressive Mechanical Loading on the Collagen and Sulphated Glycosaminoglycan Content of Pre-Cultured Synoviocyte/PET Constructs .....	238
5.5.2	The Effect of Compressive Mechanical Loading on the DNA Content of Pre-Cultured Synoviocyte/PET Constructs.....	240
5.5.3	Histological Appearance of Pre-Cultured Synoviocyte/PET Constructs Subjected to Compressive Mechanical Loading .....	241
5.5.4	The Effect of Compressive Mechanical Loading on the Compressive Moduli of Pre-Cultured Synoviocyte/PET Constructs .....	242
5.5.5	Morphometric Appearance and Distribution of Synoviocytes in Constructs under Incremental Compressive Tissue Strains .....	249

5.5.6	The Effect of Incremental Compressive Tissue Strains on Synoviocyte Deformation in Constructs: Morphometric Measurements.....	253
5.6	Conclusion .....	257
<b>Chapter 6 - General Discussion .....</b>		<b>258</b>
6.1	Introduction.....	258
6.2	Development of a Novel Device for Application of Compressive Loads with Simultaneous Live Cell Imaging .....	259
6.3	Live Cell Staining and Imaging Methodology .....	265
6.4	Quantification of Cell Deformation via Amira Software .....	271
6.5	Chondrocyte Deformation within Native Cartilage .....	276
6.6	Synoviocyte Deformation within Cartilage Constructs .....	277
<b>Chapter 7 - Conclusion .....</b>		<b>281</b>
<b>Chapter 8 - Future work.....</b>		<b>283</b>
<b>Chapter 9 - References.....</b>		<b>285</b>

## Tables

**Table 1: Thickness measurements of an acrylic disk and bovine cartilage disks obtained using the compression device and a Bose Electroforce 3200 mechanical testing machine. There were no statistical significances found in thickness measurements of an acrylic disk (6 repeats) and bovine cartilage disks (n=6) between the two measurement methods. Data represented as mean  $\pm$  SD (n=6). Statistical analysis was determined by t-test for the acrylic disk and paired t-test for bovine cartilage disks. ....53**

**Table 2: Tangential compressive modulus measured at 18 % strain of non-loaded and loaded synoviocyte/PET constructs following pre-culture in chondrogenic medium for 4 weeks and then subjected to a mechanical loading regime for either 28 and 56 days. 208**

**Table 3: Mean values  $\pm$  SD of morphometric measurements for 10 different synoviocytes in the uncompressed state from two constructs in each of the loaded and non-loaded group at Day 56; cell volume, sphericity, height, length and width. ....234**

## Figures

<b>Figure 1: Schematic diagram of a proteoglycan (PG) macromolecule. In the matrix, aggrecans non-covalently bind to Hyaluronan (HA) to form a PG macromolecule and further stabilised by small link proteins. Figure adapted from [5].</b>	<b>4</b>
<b>Figure 2: Schematic depiction of aggrecan, which consists of keratan sulphate and chondroitin sulphate chains attached covalently to a protein core. Figure adapted from [5].</b>	<b>5</b>
<b>Figure 3: Schematic diagram of chondrocyte and collagen fibres organisation within the four histologically distinct zones of articular cartilage. Figure adapted from [5].</b>	<b>8</b>
<b>Figure 4: The cell-matrix interactions are mediated by transmembrane integrins (which consist of <math>\alpha</math> and <math>\beta</math> subunits). Focal adhesion complexes (made up of various structural and regulatory proteins including vinculin, talin, paxilin and FAK) serve as a structural and signalling link between the ECM and the actin cytoskeleton. Figure adapted from [98].</b>	<b>14</b>
<b>Figure 5: Schematic diagram of the mechanotransduction process utilising focal adhesions to transmit mechanical forces from the ECM to a single cell. Figure adapted from [101].</b>	<b>15</b>
<b>Figure 6: General components used in cartilage tissue engineering. [166].</b>	<b>24</b>
<b>Figure 7: Schematic of the mechanical loading regime used to create mechanically competent tissue engineered constructs. Figure adapted from [1].</b>	<b>31</b>
<b>Figure 8: Finlay's hypothesised mechanism explaining the stages in the development of cartilage-like constructs with the application of compressive loading. Adapted from [1].</b>	<b>33</b>
<b>Figure 9: Schematic of immature and mature constructs after application of different magnitudes of compressive load in order to maintain sufficient amount of cell deformation to stimulate ECM production. A greater applied load would be required for a more mature construct (with different matrix composition compared to immature construct) in order to sustain cell stimulation for further ECM deposition.</b>	<b>34</b>
<b>Figure 10: Diagram showing the two potential loading configurations for the compression device; application of compression on a cartilage tissue/construct disk (A) perpendicular and (B) parallel to the axis of the light path of the confocal microscope.</b>	<b>41</b>
<b>Figure 11: Schematic of compression device design based on perpendicular loading configurations to the axis of the light path for use in a upright confocal microscope. The design features include a chamber, front, middle and back walls, a sample holder, a compression platen, rods and a M3 screw/micrometer. The compression device is presented in 3D and top views.</b>	<b>42</b>

**Figure 12: (A) Schematic of the compression device design based on perpendicular loading configurations to the axis of the light path without the micrometer in a 3D view and (B) a sketch of the components (a well with an opening at the bottom, a coverslip, a platen, a magnetic disk, a brace, metal screws and a micrometer) which assemble to form the device in a side view. The compression device can be used to apply compressive tissue strains on native cartilage and tissue engineered cartilage construct disks. ....43**

**Figure 13: A sketch of the compression device which shows the inner ledge required to provide support for the coverslip that is sealed on top of an opening at the bottom of the device to withstand the load applied parallel to the coverslip surface. ....46**

**Figure 14: A sketch of the compression device showing that when load is directly applied onto the coverslip, it would cause bending to the coverslip. ....47**

**Figure 15: Experimental set up for investigating coverslip ability to withstand 5 N applied load for protracted periods of time: (A) support plastic blocks, (B) coverslip, (C) the platen of the prototype device, (D), 5 N of applied load. ....49**

**Figure 16: Bose mechanical testing machine set up for coverslip deflection testing under compression: (A) connection to the actuator, (B, C) platens, (D) compression device and (E) connection to 10 N load transducer. ....50**

**Figure 17: Glass flexion profile of  $0.14 \pm 0.01$  mm and  $0.17 \pm 0.01$  mm-thick coverslips under load of 700 g. ....52**

**Figure 18: Standard curve of displacement vs load for  $0.17 \text{ mm} \pm 0.01$  mm-thick coverslip. Data represented as mean  $\pm$  SD at each 50 g interval (n=6). ....54**

**Figure 19: Schematic of the confocal laser scanning microscopy (CLSM) principle, showing the main components and the excitation and emission light paths. Excitation light (blue lines) is focused to a spot at a desired focal plane (i.e. focal point) in the fluorescently labelled sample. Fluorescent light (green lines) is collected by the objective lens and focused by a second lens through a pinhole onto a detector. Any out of focus emission generated along the light path that is outside the objective focal point (e.g. above and below the focal plane - grey dashed lines) is blocked. Figure adapted from [213]. ....61**

**Figure 20: Overview of experimental plan for optimising SiR-actin stain and comparing with Alexa Fluor<sup>®</sup> Phalloidin stain on bovine synoviocyte monolayers. ....68**

**Figure 21: Overview of experimental plan for characterising a dual staining method of Acridine orange and SiR-actin stains on bovine synoviocyte monolayers, native cartilage and synoviocyte-polyethylene terephthalate (PET) immature constructs to determine the ability to penetrate tissue samples, label cell nuclei and the F-actin structures and image selected cells multiple times without significant signal loss. ....68**

**Figure 22: Overview of experimental plan for characterising a dual staining method of Hoechst 33342 and CellMask Green plasma membrane stains on bovine synoviocyte monolayers, native cartilage and synoviocyte-polyethylene terephthalate (PET) immature constructs to determine the ability to penetrate tissue samples, label cell nuclei and the F-actin structures. ....69**

**Figure 23: Overview of experimental plan for examining the effects of photobleaching with the use of ProLong<sup>®</sup> Live Antifade Reagent in both staining methods. ....70**

**Figure 24: Overview of experimental plan for comparing image acquisition in the confocal microscope using a traditional galvo scanner and a high speed resonant scanner to potentially retain fluorescence signal. ....70**

**Figure 25: (A) Components of two steel disks with twelve 10 mm holes (connected by four shafts) and two steel plates (attachable with screws to the steel disks) combine together and (B) place on a pair of rollers (one of which is connected to a DC electrical motor) to form the assembled dynamic cell seeding device to allow the inserted tubes filled with cells/PET scaffold suspension to rotate at a rate of approximately 0.25 Hz.....74**

**Figure 26: A confocal imaging protocol consisting of a sequential series of four 3D volume images was used to determine the ability of SiR-actin to retain fluorescence signal after tracking and imaging selected cells multiple times. This protocol was applied to chondrocytes located in the superficial surface and the deep zone of native cartilage.....80**

**Figure 27: Confocal images of bovine synoviocytes stained with different concentrations of SiR-actin (red) for F-actin; (A) 2  $\mu$ M, (B) 1  $\mu$ M, (C) 0.5  $\mu$ M and (D) 0.1  $\mu$ M SiR-actin.....83**

**Figure 28: Parallel staining of bovine synoviocyte monolayers using (A) Alexa Fluor<sup>®</sup> 488 phalloidin and (B) SiR-actin (pseudo coloured to green). ....84**

**Figure 29: Confocal images of live bovine synoviocyte monolayers labelled with Acridine orange (pseudo coloured to blue) and SiR-actin stains (pseudo coloured to green) for staining of nuclei and actin filaments, respectively, were visualised using (A-F) various magnifications and digital zooms.....85**

**Figure 30: Maximum projected confocal images of (A) native articular cartilage, (C) synoviocyte/PET immature cartilage construct and (E) a PET scaffold stained with Acridine orange (pseudo coloured to blue) and SiR actin (pseudo coloured to green) for nuclei and actin filaments, respectively; and non-stained samples, (B) native articular cartilage, (D) synoviocyte/PET immature cartilage construct and (F) a PET scaffold. ....87**

**Figure 31: 3D volume images of (A) native articular cartilage, (B) synoviocyte/PET immature cartilage construct and (C) a PET scaffold stained with Acridine orange (pseudo coloured to blue) and SiR-actin (pseudo coloured to green) for nuclei and actin filaments, respectively. Images are presented in the XYZ-plane. ....88**

**Figure 32: A sequential series of four 3D volume images of selected chondrocytes on the superficial surface of bovine cartilage, images 1-4 (left to right) displayed in the SiR-actin (Red) channel in various planes: (A-D) XZY-plane, (E-H) XZ-plane and (J-M) Z-plane. ....90**

**Figure 33: A sequential series of four 3D volume images of selected chondrocytes at the deep zone of bovine cartilage, images 1-4 (left to right) displayed in the SiR-actin (Red) channel in various planes: (A-D) XYZ-plane, (E-H) XZ-plane and (J-M) Z-plane. ....91**

**Figure 34: 3D volume images of live bovine synoviocyte in monolayer cultures stained with Hoechst 33342 (blue) and CellMask green plasma membrane stains (green) for nuclei and plasma membrane, respectively. Cells were visualised by (A) a 20x air and (B) a 40x oil-immersion objectives. Images are presented in the Z-plane. ....92**

**Figure 35: 3D volume images of (A) superficial surface, (B) the deep zone of native articular cartilage, (C) synoviocyte/PET immature cartilage construct and (D) a PET scaffold stained with Hoechst 33342 (blue) and CellMask green plasma membrane stains (green) for nuclei and plasma membrane, respectively. Images are presented in the XYZ-plane. ....94**

**Figure 36: 3D volume images of (A) superficial surface, (B) the deep zone of native articular cartilage, (C) synoviocyte/PET immature cartilage construct and (D) a PET scaffold stained with Hoechst 33342 (blue) and CellMask green plasma membrane stains (green) for nuclei and plasma membrane, respectively. Images are presented in the Z-plane. ....95**

**Figure 37: Confocal image of cross section of native articular cartilage stained with Hoechst 33342 and CellMask green plasma membrane revealed both stains penetrated through the full thickness of the tissue from the superficial layer down to the deep zone.....96**

**Figure 38: A sequential series of three 3D volume images of selected chondrocytes on the superficial surface of bovine cartilage, images 1-3 (left to right) displayed in the CellMask green plasma membrane (Green) channel in various planes: (A-C) XYZ-plane, (D-F) XZ-plane and (G-J) Z-plane. ....97**

**Figure 39: A sequential series of three 3D volume images of selected chondrocytes in the deep zone of bovine cartilage, images 1-3 (left to right) displayed in the SiR-actin (Red) channel in various planes: (A-C) XYZ-plane, (D-F) XZ-plane and (G-J) Z-plane.....98**

**Figure 40: Change in mean fluorescence intensity after selected chondrocytes were sequentially imaged three times under non-loaded conditions using traditional galvo and high speed resonant scanning in the confocal microscope.99**

**Figure 41: A sequential series of three 3D volume images of selected chondrocytes on the articular surface of bovine cartilage captured using the C2-DUVB GaAsP detector on a Nikon C2 confocal microscope, displayed in the CellMask Green plasma membrane (Green) channel in Z-plane: (A-C) image 1 to 3. ....113**

**Figure 42: Overview of experimental plan for determining the effects of incremental compressive strains on chondrocyte deformation behaviour within the superficial zone of native cartilage. ....119**

**Figure 43: (A) All the components of the device (a well with an opening at the bottom, a coverslip, a platen, a magnetic disk, a brace, metal screws and a micrometer) assembled to form the compression device. (B) The compression device mounted on the stage of an Nikon A1R invert confocal microscope system enabling precise compressive tissue strain application while visualising cell deformation behaviour under confocal microscopy. ....125**

**Figure 44: Flow diagram of the experimental procedure used to sequentially image selected chondrocytes in the articular zone of native cartilage disk in the uncompressed state and during applied static compressive strains of 10 % and 15 %.....126**

**Figure 45: The control panel of Amira software displaying the custom workflow used to process the confocal volume images of cells and perform 3D rendering and cell morphometric measurements. ....127**

**Figure 46: XY-orthoslices of the plasma membrane of chondrocytes from (A) ‘raw’ and (B) ‘filtered’ image data and the cell nuclei from (C) ‘raw’ and (D) ‘filtered’ image data, showing before and after the application of ‘*Gaussian filter*’ module used to smooth the raw data in order to reduce noise and preserve cell edges. ....128**

**Figure 47: XY-orthoslices of the plasma membrane of chondrocytes from (A) ‘filtered’ and (B) ‘segmented’ image data and the cell nuclei from (C) ‘filtered’ and (D) ‘segmented’ image data, showing before and after the application of ‘*Interactive Thresholding*’ module used to determine the location and geometry of the plasma membrane and nuclei of chondrocytes. ....130**

**Figure 48: XY-orthoslices of the plasma membrane of chondrocytes from (A) ‘segmented’ and (B) ‘filled holes’ image data and the cell nuclei from (C) ‘segmented’ and (D) ‘filled holes’ image data, showing before and after the application of ‘*Fill Holes*’ module used to fill incompletely labelled objects. ....131**

**Figure 49: XY-orthoslices of the plasma membrane of chondrocytes from (A) ‘filled holes’, (B) ‘removed small spots’ and (C) ‘border killed’ image data and the cell nuclei from (D) ‘filled holes’, (E) ‘removed small spots’ and (F) ‘border killed’ image data, showing before and after the application of the ‘*Remove Small Spots*’ module and the ‘*Border Kill*’ module.....132**

**Figure 50: XY-orthoslice of the image data after merging together both the processed image stacks of the nuclei and plasma membrane of chondrocytes using the ‘*Arithmetic*’ module prior to the cells identification step. ....133**

**Figure 51: The interface of Amira’s Image Segmentation Editor displaying an XY-orthoslice from the processed, merged image stack which highlights the boundaries of the potential nuclei (blue) and plasma membrane (green). ....134**

**Figure 52: An example of cells identification using the Image Segmentation Editor in the case of clear cell boundaries; (A) a nucleus (blue boundary selected in red) and its corresponding plasma membrane (green boundary selected in red) were selected and register the two parts as (B) an individual chondrocyte (red boundary).....134**

**Figure 53: An example of cells identification using the lasso tool from the Image Segmentation Editor in the case of ill-defined cell boundaries; (A) two chondrocytes were in close contact which made it hard to distinguish cell boundaries, (B) a diving line (white arrow) was manually defined by the lasso tool in every 2D image that made up the 3D data, (C) two separated chondrocytes as a result of the extra step taken with the lasso tool to refine cell boundaries, allowing the two chondrocytes to be identified for 3D rendering and cell morphometric measurements. ....135**

**Figure 54: XY-orthoslices of (A) the ‘cellstoanalyse’ image stack following the cell identification step which highlights the chondrocytes (yellow boundaries) selected for 3D rendering and cell morphometric measurements and (B) the processed, merged image stack of the nuclei and plasma membrane showing the corresponding selected chondrocytes (red). .....136**

**Figure 55: The measure port was used to select cell morphometric parameters including cell length, width, height, volume and sphericity (which was manually inserted specific equation) and create a new measure group for cell morphometric quantification. ....137**

**Figure 56: Definition of cell morphology parameters. Cell length and width were defined along the major and minor axes of the cell cross-section perpendicular to its height. Height was defined as the maximum distance between the vertical coordinates of all the vertices on the Z-axis. ....137**

**Figure 57: An example analysis spreadsheet displaying the cell morphometric measurements performed on selected chondrocytes.....138**

**Figure 58: 3D rendering of selected chondrocytes from the label (‘cellstoanalyse’) image for 3D shape visualisation purpose. ....138**

**Figure 59: Viability assessment of cartilage disks harvested from osteochondral plugs after up to 3 days in culture. Chondrocyte metabolic activity was assessed by XTT assay. ....140**

**Figure 60: Live/Dead<sup>®</sup> confocal volume images of chondrocytes in cartilage slices obtained from bovine cartilage disks cultured in different periods of time from Day 0 to 3; (A, E) Day 0, (B, F) Day 1, (C, G) Day 2 and (D, H) Day 3. Images revealed chondrocytes through the depth of the cartilage slices from the superficial zone down to the deep zone labelled with (A-D) both live and dead staining and (E-H) dead staining only. Images are presented in the Z-plane. ...141**

**Figure 61: Live/Dead<sup>®</sup> confocal volume images of chondrocytes in cartilage slices obtained from bovine cartilage disks cultured in different periods of time from Day 0 to 3; (A, E) Day 0, (B, F) Day 1, (C, G) Day 2 and (D, H) Day 3. Images show (A-D) live and (E-H) dead. Images are presented in the XZ-plane. ....142**

**Figure 62: Changes in the volume of chondrocytes in uncompressed cartilage disks with three repeated confocal scans. There was a slight decrease in normalised chondrocyte volume following capture of repeated confocal images and the changes were significant. ....144**

**Figure 63: Absolute morphometric measurements for each individual chondrocyte (n=37) in the superficial zone of each of the four bovine cartilage disks (1-4 = left to right columns) at the selected compressive strain levels of 0 %, 10 % and 15 %; (A, B, C, D) Chondrocyte length, (E, F, G, H) width and (J, K, L, M) height. There was no clear trend for changes in individual chondrocyte width and length with the application of compressive tissue strain. Chondrocyte height appeared to decrease with application of compressive tissue strain. ....146**

**Figure 64: Absolute morphometric measurements for each individual chondrocyte (n=37) in the superficial zone of each of the four bovine cartilage disks (1-4 = left to right columns) at the selected compressive strain levels of 0 %, 10 % and 15 %; (A, B, C, D) chondrocyte volume and (E, F, G, H) sphericity. Dotted line in (E, F, G, H) indicates the value of a perfect sphere. Chondrocyte volume appeared to decrease with application of compressive tissue strain. Sphericity remained consistent in all cartilage disks, apart from chondrocytes in Cartilage Disk 2 where sphericity appeared to increase with application of compressive tissue strain. ....147**

**Figure 65: Mean values  $\pm$  SD of morphometric measurements for all chondrocytes (n=37) in the superficial zone of each of the four bovine cartilage disks (1-4 = left to right columns) at the selected compressive tissue strain levels of 0 %, 10 % and 15 %; (A, B, C, D) chondrocyte width and length and (E, F, G, H) height. Mean values of chondrocyte width decreased with applied tissue strain, with the decrease being statistically significant in Cartilage Disk 1, 3 and 4. Mean values of chondrocyte length decreased with applied tissue strain and a significant difference was seen in Cartilage Disk 1, 2 and 4. Significant decrease in mean values of chondrocyte height was observed in all cartilage disks at each tissue strain level. ....151**

**Figure 66: Mean values  $\pm$  SD of morphometric measurements for all chondrocytes (n=37) in the superficial zone of each of the four bovine cartilage disks (1-4 = left to right columns) at the selected compressive tissue strain levels of 0 %, 10 % and 15 %; (A, B, C, D) chondrocyte volume and (E, F, G, H) sphericity. Dotted line in (E, F, G, H) indicates the cell shape for a perfect sphere. Significant decrease in mean values of chondrocyte volume was observed with application of 10 % and 15 % compressive tissue strains except between 10 % and 15 % strains in Cartilage Disk 1. Mean values of chondrocyte sphericity remained largely consistent irrespective of applied tissue strain, apart from a significant increase in Cartilage Disk 1 at 15 % applied tissue strain and in Cartilage Disk 2 at each tissue strain level. ....152**

**Figure 67: Percentage (%) change in morphometric measurements from baseline (zero strain) for all chondrocytes (n=37) in the superficial zone of each of the four bovine cartilage disks (1-4 = left to right columns) following application of 10 % and 15 % compressive tissue strains; (A, B, C, D) chondrocyte width and length and (E, F, G, H) height. Percentage change in chondrocyte width decreased with applied tissue strain, with the decrease being statistically significant in Cartilage Disk 1, 3 and 4. Percentage change in chondrocyte length decreased with applied tissue strain and this was significant in Cartilage Disk 1, 2 and 4. Percentage change in chondrocyte height also significantly decreased at each tissue strain level. ....153**

**Figure 68: Percentage (%) change in morphometric measurements from baseline (zero strain) for all chondrocytes (n=37) in the superficial zone of each of the four bovine cartilage disks (1-4 = left to right columns) following application of 10 % and 15 % compressive tissue strains; (A, B, C, D) chondrocyte volume and (E, F, G, H) sphericity. Percentage change in chondrocyte volume significantly decreased with applied tissue strain. Significant increase in percentage change in chondrocyte sphericity was only observed in Cartilage Disk 1 at 15 % applied tissue strain and in Cartilage Disk 2 at each tissue strain level. ....154**

**Figure 69: Morphometric measurements for all chondrocytes (n=37) in the superficial zone combined from all bovine cartilage disks (n=4) following application of 10 % and 15 % compressive tissue strains; (A, D) chondrocyte length, (B, E) width and (C, F) height. The data is presented in (A, B, C) mean values and (D, E, F) percentage change from baseline (zero strain). The chondrocytes combined in each cartilage disk showed chondrocyte length, width and height significantly decreased at each tissue strain level. ....157**

**Figure 70: Morphometric measurements for all chondrocytes (n=37) in the superficial zone combined from all bovine cartilage disks (n=4) following application of 10 % and 15 % compressive tissue strains; (A, C) chondrocyte volume and (B, D) sphericity. The data is presented in (A, B) mean values and (C, D) percentage change from baseline (zero strain). Dotted line in (B) indicates the cell shape as a perfect sphere. The chondrocytes combined in each cartilage disk showed chondrocyte volume significantly decreased and sphericity significantly increased at each tissue strain level. ....158**

**Figure 71: Comparison of data (% strain/volume change) obtained in the current study for chondrocyte height strain and volume (black bars) and previous studies using cartilage explants(light grey bars) and intact cartilage (dark grey bars). In all cases, results are presented for an applied tissue compressive strain of 15 %. ....170**

**Figure 72: Overview of experimental plan for determining the effect of incremental compressive strains on cell deformation behaviour in cartilage constructs. ....178**

**Figure 73:Internal assembly of the in-house built cyclic compressive bioreactor; (A) 12 volt DC motor, (B) gear box, (C) timing belt and pulley system, (D) cam shaft, (E) C-shaped follower with roller in contact with cam and connected to (F) transmission shaft and (G) pre-compressed spring and (H) the end of transmission shaft where the plunger and culture apparatus joined by connector (illustrated in Figure 74I). ....182**

**Figure 74:Components of culture apparatus for in-house built cyclic compressive bioreactor; (I) connector to the bioreactor (illustrated in Figure 73H) and (J) plungers, (K) culture lid, (L) culture chamber and (M) assembly of these components. ....183**

**Figure 75: Assembly of the apparatus used to fabricate cured silicone sheets for silicone rings; (A) liquid silicone injected in between two glass plates where (B) a U-shaped spacer is held by (C) clamps to ensure correct spacing. ....186**

**Figure 76: Example of a modified silicone ring. Silicone rings (internal diameter 6 mm and external diameter 14 mm) were further modified by removing 1 mm of the external diameter from four sides (white arrows) to create four edges perpendicular to each other to ensure the rings fitted in to the wells within the culture chambers of the bioreactor, allowing fluid movement but avoiding displacement of constructs occurring during loading.....187**

**Figure 77: Dynamic mechanical testing rig set up; (A) actuator, (B, F) mechanical actin wedge grips, (C,E) platens, (D) space where top platen lowered to form PBS column with suspended construct and (G) 250 N load transducer.....191**

**Figure 78: Example of 10 cycles of 20 % strain triangular waveform at 1Hz applied to constructs for the means of dynamic mechanical testing. ....192**

<b>Figure 79: Example of typical engineering stress vs strain curve acquired from dynamic mechanical testing. Exponential fit (blue line) made between 0.0 and 0.2 strain. ....</b>	<b>193</b>
<b>Figure 80: Flow diagram of the experimental procedure used to sequentially image synoviocytes in the tissue engineered constructs in the uncompressed state and during estimated compressive strain subjected to the construct during mechanical loading and 28 % compressive tissue strain. ....</b>	<b>200</b>
<b>Figure 81: XY-orthoslices of the processed, merged image stack which highlights the boundaries of the potential nuclei (blue) and plasma membrane (green). Synoviocytes segmented from other touching synoviocytes with the use of the lasso tool and registered as synoviocytes (yellow boundaries) for 3D rendering and cell morphometric measurements. ....</b>	<b>201</b>
<b>Figure 82: 3D rendering of selected synoviocytes from the label image for 3D shape visualisation purpose. ....</b>	<b>202</b>
<b>Figure 83: Collagen content of synoviocyte/PET constructs following pre-culture in chondrogenic medium for 4 weeks and then subjected to a mechanical loading regime for either 28 or 56 days. L ≡ Loaded (dark grey), NL ≡ Non-loaded constructs (light grey) and Cartilage ≡ Native cartilage (black). ....</b>	<b>204</b>
<b>Figure 84: sGAG content of synoviocyte/PET constructs following pre-culture in chondrogenic medium for 4 weeks and then subjected to a mechanical loading regime for either 28 and 56 days. L ≡ Loaded (dark grey), NL ≡ Non-loaded constructs (light grey) and Cartilage ≡ Native cartilage (black). ....</b>	<b>205</b>
<b>Figure 85: DNA content of synoviocyte/PET constructs following pre-culture in chondrogenic medium for 4 weeks and then subjected to a mechanical loading regime for either 28 and 56 days. L ≡ Loaded (dark grey), NL ≡ Non-loaded constructs (light grey) and Cartilage ≡ Native cartilage (black). ....</b>	<b>206</b>
<b>Figure 86: Compressive moduli measured at 18 % strain for synoviocyte/PET constructs under 1 Hz 20 % cyclic strain following pre-culture in chondrogenic medium for 4 weeks and then subjected to a mechanical loading regime for either 28 and 56 days. L ≡ Loaded (dark grey) , NL ≡ Non-loaded constructs (light grey). ....</b>	<b>207</b>
<b>Figure 87: Histological appearance of sections of decalcified bovine osteochondral plugs. Sections stained with (A) antibodies to Collagen type II, (C) antibodies to Collagen type I, (E) Alcian blue/Sirius red and without the inclusion of either (B) Collagen type II or (D) Collagen type I primary antibody. ....</b>	<b>210</b>
<b>Figure 88: Negative controls for immunochemistry. Histological appearance of sections from two constructs at Day 56 of mechanical loading stained without the inclusion of either Collagen type I or Collagen type II primary antibodies. Two images captured from each end of the constructs are collaged and shown in each case, representing the entire construct. ....</b>	<b>211</b>
<b>Figure 89: Histological appearance of sections from a construct at Day 0 (Sample 1) after 4 weeks of pre-culture in chondrogenic medium (prior to application of mechanical loading). Sections stained with (A) antibodies to Collagen type I, (B) antibodies to Collagen type II and (C) Alcian blue/Sirius red. Two images captured from each end of the constructs are shown collaged in each case, representing the entire construct. ....</b>	<b>212</b>

**Figure 90: Histological appearance of sections from a construct at Day 0 (Sample 2) after 4 weeks of pre-culture in chondrogenic medium (prior to application of mechanical loading). Sections stained with (A) antibodies to Collagen type I, (B) antibodies to Collagen type II and (C) Alcian blue/Sirius red. Two images captured from each end of the constructs are shown in each case, representing the entire construct. ....213**

**Figure 91: Histological appearance of sections from a construct at Day 0 (Sample 3) after 4 weeks of pre-culture in chondrogenic medium (prior to application of mechanical loading). Sections stained with (A) antibodies to Collagen type I, (B) antibodies to Collagen type II and (C) Alcian blue / Sirius red. Two images captured from each end of the constructs are shown collaged in each case, representing the entire construct. ....214**

**Figure 92: Histological appearance of sections from a non-loaded construct at Day 28 (Sample 1) of culture without the presence of mechanical loading. Sections stained with (A) antibodies to Collagen type I, (B) antibodies to Collagen type II and (C) Alcian blue / Sirius red. Two images captured from each end of the constructs are shown collaged in each case, representing the entire construct. ....215**

**Figure 93: Histological appearance of sections from a non-loaded construct at Day 28 (Sample 2) of culture without the presence of mechanical loading. Sections stained with (A) antibodies to Collagen type I, (B) antibodies to Collagen type II and (C) Alcian blue / Sirius red. Two images captured from each end of the constructs are shown collaged in each case, representing the entire construct. ....216**

**Figure 94: Histological appearance of sections from a non-loaded construct at Day 28 (Sample 3) of culture without the presence of mechanical loading. Sections stained with (A) antibodies to Collagen type I, (B) antibodies to Collagen type II and (C) Alcian blue / Sirius red. Two images captured from each end of the constructs are shown collaged in each case, representing the entire construct. ....217**

**Figure 95: Histological appearance of sections from a loaded construct at Day 28 (Sample 1) of culture with the presence of mechanical loading. Sections stained with (A) antibodies to Collagen type I, (B) antibodies to Collagen type II and (C) Alcian blue / Sirius red. Two images captured from each end of the constructs are shown collaged in each case, representing the entire construct.....218**

**Figure 96: Histological appearance of sections from a loaded construct at Day 28 (Sample 2) of culture with the presence of mechanical loading. Sections stained with (A) antibodies to Collagen type I, (B) antibodies to Collagen type II and (C) Alcian blue / Sirius red. Two images captured from each end of the constructs are shown in each case, representing the entire construct.....219**

**Figure 97: Histological appearance of sections from a loaded construct at Day 28 (Sample 3) of culture with the presence of mechanical loading. Sections stained with (A) antibodies to Collagen type I, (B) antibodies to Collagen type II and (C) Alcian blue / Sirius red. Two images captured from each end of the constructs are shown collaged in each case, representing the entire construct.....220**

**Figure 98: Histological appearance of sections from a non-loaded construct at Day 56 (Sample 1) of culture without the presence of mechanical loading. Sections stained with (A) antibodies to Collagen type I, (B) antibodies to Collagen type II and (C) Alcian blue / Sirius red. Two images captured from each end of the constructs are shown collaged in each case, representing the entire construct. ....221**

**Figure 99: Histological appearance of sections from a non-loaded construct at Day 56 (Sample 2) of culture without the presence of mechanical loading. Sections stained with (A) antibodies to Collagen type I, (B) antibodies to Collagen type II and (C) Alcian blue / Sirius red. Two images captured from each end of the constructs are shown in each case, representing the entire construct. ....222**

**Figure 100: Histological appearance of sections from a loaded construct at Day 56 (Sample 1) of culture with the presence of mechanical loading. Sections stained with (A) antibodies to Collagen type I, (B) antibodies to Collagen type II and (C) Alcian blue / Sirius red. Two images captured from each end of the constructs are shown collaged in each case, representing the entire construct. ....223**

**Figure 101: Histological appearance of sections from a loaded construct at Day 56 (Sample 2) of culture with the presence of mechanical loading. Sections stained with (A) antibodies to Collagen type I, (B) antibodies to Collagen type II and (C) Alcian blue / Sirius red. Two images captured from each end of the constructs are shown collaged in each case, representing the entire construct. ....224**

**Figure 102: Histological appearance of sections from a loaded construct at Day 56 (Sample 3) of culture with the presence of mechanical loading. Sections stained with (A) antibodies to Collagen type I, (B) antibodies to Collagen type II and (C) Alcian blue / Sirius red. Two images captured from each end of the constructs are shown collaged in each case, representing the entire construct. ....225**

**Figure 103: 3D volume images of synoviocytes in both uncompressed and compressed state within two construct samples (1,2) at Day 0 stained with Hoechst 33342 (blue) and CellMask green plasma membrane stains (green) for nuclei and plasma membrane respectively; images of synoviocytes captured during 0 %, estimated strain applied during mechanical loading (23 % for both samples) and 28 % compressive tissue strain in Sample 1 (A, B, C) and Sample 2 (D, E, F). Images are presented in the Z-plane. ....228**

**Figure 104: 3D volume images of synoviocytes in both uncompressed and compressed state within two non-loaded construct samples (1,2) at Day 28 stained with Hoechst 33342 (blue) and CellMask green plasma membrane stains (green) for nuclei and plasma membrane respectively; images of synoviocytes captured during 0 %, estimated strain applied during mechanical loading (23 % for Sample 1 and 22.4 % for Sample 2) and 28 % compressive tissue strain in Sample 1 (A, B, C) and Sample 2 (D, E, F). Images are presented in the Z-plane. ....229**

**Figure 105: 3D volume images of synoviocytes in both uncompressed and compressed state within two loaded construct samples (1,2) at Day 28 stained with Hoechst 33342 (blue) and CellMask green plasma membrane stains (green) for nuclei and plasma membrane respectively; images of synoviocytes captured during 0 %, estimated strain applied during mechanical loading (13.2 % for Sample 1 and 13.5 % for Sample 2) and 28 % compressive tissue strain in Sample 1 (A, B, C) and Sample 2 (D, E, F). Images are presented in the Z-plane. ....230**

**Figure 106: 3D volume images of synoviocytes in both uncompressed and compressed state within two non-loaded construct samples (1,2) at Day 56 stained with Hoechst 33342 (blue) and CellMask green plasma membrane stains (green) for nuclei and plasma membrane respectively; images of synoviocytes captured during 0 %, estimated strain applied during mechanical loading (23.1 % for Sample 1 and 21 % for Sample 2) and 28 % compressive tissue strain in Sample 1 (A, B, C) and Sample 2 (D, E, F). Images are presented in the Z-plane.....231**

**Figure 107: 3D volume images of synoviocytes in both uncompressed and compressed state within two loaded construct samples (1,2) at Day 56 stained with Hoechst 33342 (blue) and CellMask green plasma membrane stains (green) for nuclei and plasma membrane respectively; images of synoviocytes captured during 0 %, estimated strain applied during mechanical loading (14.7 % for Sample 1 and 12.4 % for Sample 2) and 28 % compressive tissue strain in Sample 1 (A, B, C) and Sample 2 (D, E, F). Images are presented in the Z-plane.....232**

**Figure 108: Mean values  $\pm$  SD of morphometric measurements for 10 different synoviocytes from two non-loaded construct samples at Day 56 (Sample 1 and Sample 2 = top and bottom rows) under different experimental conditions (uncompressed state, estimated strain experienced by the constructs during mechanical loading in the bioreactor (23.1 % for Sample 1 and 21 % for Sample 2, respectively) and 28 % compressive tissue strain); cell volume, sphericity, height, width and length for sample 1 (A, B, C, D) and sample 2 (E, F, G, H). Dotted line in (B, F) indicates the value for a perfect sphere. A significant decrease in cell volume was only observed in Sample 2 between synoviocytes in the uncompressed state and those at 28 % strain. Sphericity remained largely consistent irrespective of applied tissue strain in both samples. Significant decrease in cell height was only observed for synoviocytes in Sample 1 with application of 23.1 % and 28 % compressive tissue strains. No significant differences in cell length and width with applied tissue strain were observed in both samples, apart from significant decreases in cell width in Sample 1 at 23.1 % and 28 % strain.....236**

**Figure 109: Mean values  $\pm$  SD of morphometric measurements for 10 different synoviocytes from two loaded construct samples at Day 56 (Sample 1 and Sample 2 = top and bottom rows) under different experimental conditions (uncompressed state, estimated strain experienced by the constructs during mechanical loading in the bioreactor (14.7 % for Sample 1 and 12.4 % for Sample 2, respectively) and 28 % compressive tissue strain); cell volume, sphericity, height, width and length for Sample 1 (A, B, C, D) and Sample 2 (E, F, G, H). Dotted line in (B, F) indicates the value for a perfect sphere. No significant change in cell volume, height, length and width were observed for all samples with applications of estimated strain applied during mechanical loading in the bioreactor and 28 % compressive tissue strain. Sphericity also remained largely consistent irrespective of applied tissue strain in both samples, apart from a significant decrease in sphericity in Sample 1 between synoviocytes in the uncompressed state and those at 28 % strain.....237**

## Abbreviations

2D	Two dimensional
3D	Three dimensional
AB	Antibiotic
ACI	Autologous Chondrocyte Implantation
APO	Apochromatic aberration correction
Au	Airy units
BM-MSC	Bone marrow mesenchymal stem cell
BMP	Bone morphogenetic protein
BW	Body weight
Calcein AM	Calcein-acetoxymethyl ester
CLSM	Confocal laser scanning microscopy
DMEM	Dulbecco's Modified Eagles Medium
DMMB	Dimethylmethylene Blue
DMSO	Dimethyl sulfoxide
DNA	Deoxyribonucleic acid
EDTA	Ethylenediaminetetracetic acid
ECM	Extracellular matrix
EH	Ethidium homodimer-1
F12	Ham's F12 medium
F-actin	Filamentous actin
FACIT	Fibril-associated collagens with interrupted triple helices
FAK	Focal adhesion kinase
FBS	Foetal bovine serum
FCD	Fixed charge density
G-actin	Actin monomer
GaAsP	Gallium arsenide phosphide
GAG	glycosaminoglycan

GelMA	Gelatin methacryloyl
GFP	Green fluorescent protein
HA	Hyaluronan or hyaluronic acid
HD	High definition
HEPES	4-(2-hydroxyethyl)-1-piperazineethanesulfonic acid
hFOB	Human foetal osteoblastic cell line
hMSC	Human mesenchymal stem cell
HRP	Horseradish peroxidase
HYP	Hydroxproline
IM	Interterritorial matrix
ITS	Insulin-transferrin-selenium
MSC	Mesenchymal stem cell
NA	Numerical aperture
NBF	Neutral buffered formalin
OA	Osteoarthritis
OATS	Osteochondral graft transplantation
PBS	Phosphate buffered saline
PCL	Poly(caprolactone)
PCM	Pericellular matrix
PET	Polyethylene terephthalate
PG	Proteoglycan
PGA	Poly(glycolic acid)
PMT	Photomultiplier tube
PL	Flat Field correction
PLA	Poly(lactic acid)
PLGA	Poly(lactic-co-glycolic acid)
Fluor	Fluorite aberration correction
SD	Standard deviation
SEM	scanning electron microscopy

sGAG	Sulphated glycosaminoglycan
SiR	Silicon-rhodamine
TGF	Transforming growth factor
TM	Territorial matrix
TIFF	Tagged Image Format File
ROI	Region of interest
UK	United Kingdom
USA	United States of America
UV	Ultra violet
WD	Working distance
XTT	2,3-bis-[2-methoxy-4-nitro-5-sulfohenyl]-2H-tetrazolium-5-carboxanilide

## Chapter 1 - General Introduction

*This chapter outlines the scope of the thesis and reviews the literature relevant to its subject. It first discusses articular cartilage composition and structure and how these relate to the tissue's unique mechanical properties, which enable its main functions of load bearing and near frictionless articulation. The effect of mechanical loading on cartilage and chondrocyte response are then reviewed. Cartilage damage and current repair strategies are then considered, along with discussion of a promising strategy of tissue engineering for cartilage regeneration. Cartilage tissue engineering is then addressed, describing its key elements and discussing the recent approaches used to create constructs that could be used for cartilage repair.*

### 1.1 Composition of Articular Cartilage

Articular cartilage (also called hyaline cartilage) is a specialised connective tissue that covers the ends of articulating bone in diarthrodial joints, such as the hip and knee [2], [3] and is an essential component for the normal function of synovial joints. Articular cartilage is typically glassy smooth, glistening and bluish-white in appearance with a thickness ranging from 0.5 to 5 mm in human joints [3], [4]. It is an anisotropic tissue of many components [5]. It consists of a dense functional extracellular matrix (ECM), with a relatively small number of specialised cells called chondrocytes that are sparsely distributed within the matrix [6]. Chondrocytes usually constitute around 1-5 % of the total volume of articular cartilage [5], [7], [8]. Chondrocytes synthesise, secrete, organise and maintain matrix components [5], [8]. Although the chondrocyte number per volume unit varies from tissue to tissue, the chondrocyte density within hyaline cartilage is approximately  $15 \times 10^3 \text{ cells/mm}^3$  [9], [10]. The ECM is mainly composed of collagen, proteoglycans (PGs) and glycosaminoglycans (GAGs) [11]. GAGs are highly hydrophilic which attracts water molecules and favours tissue hydration [10], [12]. These components contribute approximately 20-35% of the total cartilage weight [5]–[7], [12], [13]. The remaining weight is represented by water (65-80 % wet weight). Within the ECM, an extensive network of dense collagen fibrils (15-25 % wet weight of cartilage) are enmeshed in a concentrated gel of PGs (5-10 % wet weight) and GAGs [5]–[7], [9], [12], [13].

Unlike the majority of tissues in the body, cartilage is an aneural and avascular connective tissue and therefore nutrient and waste transfer doesn't rely on the circulatory system [7], [8], [13]–[15]. Instead, both nutrient transportation and waste removal occur by diffusion through the synovial fluid [16]–[18]. The interstitial fluid flows through the cartilage matrix to transport and distribute nutrients to the embedded chondrocytes [8]. The absence of vascularisation

contributes to the limited capacity for spontaneous repair and remodelling which may result in progressive damage and degeneration following tissue damage [14].

### **1.1.1 Chondrocytes**

Despite the sparse distribution and low number of chondrocytes in articular cartilage, they play a critical role in the development, maintenance and repair of the tissue's ECM infrastructure [5], [7], [8], [19]. Chondrocytes synthesise all of the matrix components, including type II collagen and PGs and regulate matrix metabolism [7], [20]. The cells vary in shape, number and size throughout the depth of the tissue (as discussed in Section 1.2) [8]. Chondrocytes present near the articular surface are usually flatter and smaller and have a greater density than those located deeper in the matrix [19].

Each chondrocyte is associated with its own specialised microenvironment and determines the turnover of its own local ECM [8]. The microenvironment basically traps individual chondrocytes each within their own matrix, restricting any migration to adjacent areas of the tissue [8]. In articular cartilage, chondrocytes respond to a variety of stimuli, such as growth factors, mechanical loads and hydrostatic pressures, to regulate their metabolic and biosynthesis activities [8], [21], [22]. In addition to low cellularity, they have limited capacity to divide and proliferate, a factor that contributes to the intrinsic inability to repair in response to injury, which in turn, makes cartilage defects very difficult to heal [8], [23], [24].

### **1.1.2 Collagen**

The main structural component of articular cartilage ECM is collagen [25], [26]. The collagen fibrillar network formed within the ECM acts as a framework to provide sufficient resistance to tensile and shear stresses, thus supporting the tissue structure [8]. A typical fibrillar collagen molecule comprises three polypeptide  $\alpha$  strands coiling around each other to form a right-handed triple helical structure [5], [9], [12], [27]. Each polypeptide  $\alpha$  chain is composed of a basic repeating amino acid sequence of [glycine-X-Y]  $n$ , where X is often proline and Y is often hydroxproline [9], [12].

The primary collagen type found in the ECM of articular cartilage is type II collagen, accounting for 90-95% of the tissue's collagen content [6], [28]. This type of collagen is composed of three identical  $\alpha$  polypeptides wound into a triple helical structure [28]. The network of collagen fibrils is formed by assembling type II collagen molecules laterally and longitudinally and through intramolecular and intermolecular cross-linking between lysine residues in adjacent molecules [28]. The triple helical structure and the cross-linking between adjacent chains contribute to articular cartilage's excellent tensile stiffness and strength [8], [12]. Collagen type II content is often used as a marker for hyaline cartilage because it is one of the major components of hyaline cartilage [25].

Apart from type II collagen, a minor proportion of different collagens, such as type III, VI, IX, X, XI, XII and XIV, can also be found within the cartilage ECM [8], [28]. Collagens IX and XI both interact with collagen type II through covalent cross-links on the surface of the collagen type II fibrils to form a network of heteromeric fibrils [29]–[32]. These interactions help to form and stabilise the organisation of the collagen network and therefore provide increase stability and mechanical integrity to articular cartilage [12], [29], [31]. In addition to interfibrillar cross-linking, this allows the collagen fibril network to resist the swelling pressure from PGs and the tensile and shear stresses developed within the matrix when the tissue is loaded *in situ*, along with restraints fibrils to entrap PGs [28], [33].

Collagen III is usually found to be co-polymerised and linked to collagen II as a regular but a minor component in the matrix [34]. A large concentration of collagen III tends to be found in the superficial and upper middle zones of osteoarthritic cartilage [34]. It has been speculated that collagen III is involved in a wound healing role as it is produced by chondrocytes in response to matrix damage [34]. Type X collagen is found in the calcified zone of articular cartilage and thought to be responsible for matrix calcification [9], [35]. It is also found in osteoarthritic cartilage [9].

Type VI collagen is primarily presented in the pericellular region of articular cartilage to form a highly branched filamentous network around the chondrocytes [36]. It also exists throughout the matrix for binding to hyaluronans (GAG) and decorins (small PG) [36]. Both collagen type XII and XIV are members of the fibril-associated collagens with interrupted triple helices (FACIT) collagen subfamily [37]. Collagen XII is found mainly on the articular surface and collagen XIV exists throughout the matrix [38]. These two types of collagen are not covalently polymerised in the matrix and their functions are unknown [37].

### **1.1.3 Proteoglycans and Water**

Proteoglycans are the other major components in articular cartilage. The second largest group of macromolecules in the ECM accounts for 5-10 % of total cartilage wet weight [5]–[9], [12], [13]. They are vital for matrix assembly and structure of articular cartilage. Their primary function is to maintain high water capacity in cartilage which endows the tissue with the required mechanical properties (compressive strength) to carry out the function of load bearing [39]. Proteoglycans are formed with a core protein and one or more covalently attached GAGs chains [9]. The most abundant PG found in articular cartilage is the large aggregating PG, aggrecan [7], [12], [40]. Other PGs also exist in the ECM including the smaller PGs decorin, biglycan and fibromodulin [7], [12], [40]. Aggrecan is the largest PG in size ( $1-4 \times 10^6$  kDa) but even the smaller PGs present in articular cartilage are quite large (approximately  $1 \times 10^4$  kDa) [5]. The common types of GAGs present in cartilage include chondroitin sulphate, keratan sulphate, dermatan sulphate and hyaluronan [7], [12].

Aggrecan is characterised by the ability to form large aggregates and contributes as much as 80 % to 90% of the overall PG content in articular cartilage [6], [8], [9]. Aggrecan in cartilage is found as large PG aggregates of many aggrecan monomers bound non-covalently to a long central core of hyaluronan which is further stabilised by the facilitation of small link proteins (Figure 1) [5], [39]. Hyaluronan, also known as hyaluronic acid (HA), is not sulphated like the other GAGs found in articular cartilage [12]. It is often considered as a PG but it doesn't have a core protein [12]. It consists only of disaccharide repeat units of N-acetylglucosamine linked to glucuronic acid. Its main function is to interact with aggrecan and link protein to form large PG aggregates that are immobilised within the interfibrillar space of the ECM [41]–[43]. In addition, HA has the capacity to link ECM to chondrocytes via interaction with their cell surface hyaluronan receptor CD44 [12].

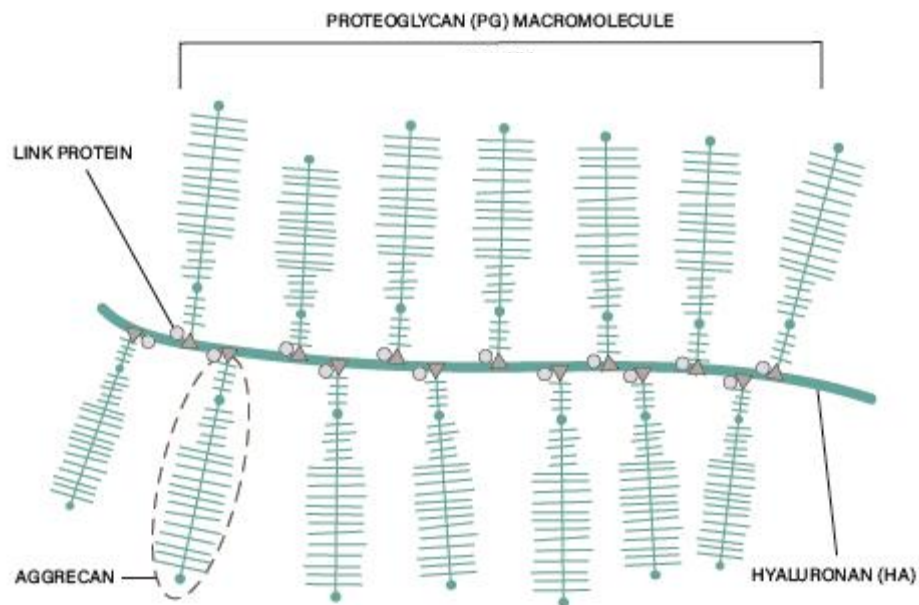


**Figure 1: Schematic diagram of a proteoglycan (PG) macromolecule. In the matrix, aggrecans non-covalently bind to Hyaluronan (HA) to form a PG macromolecule and further stabilised by small link proteins. Figure adapted from [5].**

Aggrecan occupies the interterritorial region of the ECM and provides the cartilage with the osmotic properties that are critical for its ability to withstand compressive loading [8]. Each aggrecan consists of a protein core and as many as 100 chondroitin sulphate and 50 keratan sulphate GAG chains covalently attached (Figure 2) [12]. These subunit side chains of PGs are linear unbranched polysaccharides with disaccharide repeat units that consist of large numbers of negatively charged sulphate and carboxyl groups.

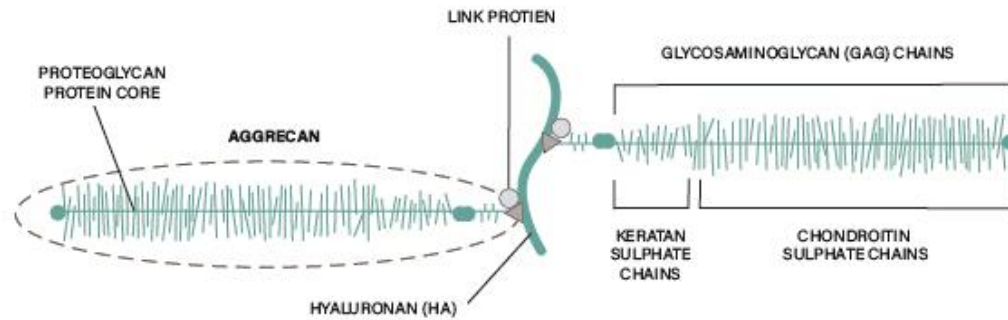


**Figure 2: Schematic depiction of aggrecan, which consists of keratan sulphate and chondroitin sulphate chains attached covalently to a protein core. Figure adapted from [5].**

Due to the high concentration of fixed negative charges, it gives rise to an ion concentration gradient between cartilage and the surrounding synovial fluid, thus creating a fixed charge density (FCD) within the tissue and yielding a Donnan osmotic pressure that favours tissue hydration [6], [39], [44], [45]. In order to maintain the osmotic equilibrium and electrolyte balance inside the matrix, this excess of densely concentrated ions in the matrix attracts counterions and co-ions (i.e. free mobile inorganic ions in water such as sodium, potassium, chloride and calcium). The concentration of these ions in the matrix would thus depend on the local concentration of PGs and their FCD [6], [46]. As a result, water is drawn into the cartilage and held within the collagen fibril network, causing the tissue to swell and expand [6]. As PGs are entrapped in the collagen meshwork, the concentration of fixed negative charges surrounding the PGs remains high and swelling is constrained in the matrix which results in high osmolarity and a high degree of hydration. The resulting hydrated ECM provides the tissue with the osmotic properties to resist significant compressive loads during joint loading and carry out the function of load bearing [39].

The water content of cartilage contributes between 65-80 % of cartilage's wet weight [5], [8]. The water concentration is greatest near the articular surface and decreases in a near linear fashion towards the deep zone of the matrix [5]. Approximately 30 % of water is associated with the intrafibrillar space within the collagen while a small percentage of water resides in the intracellular space [5], [8]. The remaining percentage occupies the interfibrillar (pore) space of the matrix (not held by PG), is free to move and can be exuded out of the ECM when a pressure gradient or load are applied to the tissue [5], [8]. However, a high frictional resistance is generated against the flow of water through the ECM as the permeability of cartilage is very low [5], [8]. Together with the frictional resistance to interstitial fluid (water) movement and the swelling pressure created within the matrix, these two mechanisms are important in controlling cartilage mechanical behaviour and joint lubrication [5], [8].

Besides large PGs (aggrecan), other smaller PGs include decorin, biglycan and fibromodulin, present as less than 10 % of all the PGs in the cartilage tissue [8], [9]. These PGs are

characterised as a small group of leucine rich PGs (because their core proteins are rich in leucine residues) with the ability to interact with collagen [8], [47]. Although they are similar in protein structure, their composition and functions are different [8]. Decorin has one chondroitin/dermatan sulphate chain attached to its core protein and is mainly found bonding directly to collagen type II fibrils in the superficial zone of articular cartilage [9], [48], [49]. Decorin is believed to be responsible for the distribution of collagen type II fibrils in matrix organisation along with involvement in cell adhesion, migration and proliferation as a result of binding to TGF- $\beta$  [48], [50]. Biglycan, which consists of two chondroitin/dermatan sulphate chains linked to a core protein, is localised in the pericellular space of articular cartilage as well as on the surface of chondrocytes, suggesting its involvement in modulating morphogenesis and differentiation [48], [49]. Fibromodulin interacts with collagen fibres and is involved in the structural formation of the matrix by aiding the assembly of collagen network [9].

## **1.2 Structure of Articular Cartilage**

The organisation and composition of ECM components and the morphology and distribution of chondrocytes are inhomogeneous within articular cartilage and vary with depth from the articular surface [12]. Articular cartilage is characterised into four histologically distinct zones: the superficial, middle, deep and calcified zones as illustrated in Figure 3 [51]. Each zone has its specific organisation and distribution of constituent components which directly influence its mechanical properties changing throughout tissue depth and consequently the functions of articular cartilage (see Section 1.4).

### **1.2.1 Superficial Zone**

This zone is situated at the top of the articular cartilage (i.e. the surface furthest away from the underlying bone), and is the narrowest layer representing 10% to 20 % of total cartilage thickness [5], [8], [12]. Chondrocytes in this zone have a flattened morphology and are arranged parallel to the articular surface [8]. Here, the superficial zone has the lowest level of PGs (aggrecan) and the highest water content in articular cartilage [7], [51]. This zone contains the highest level of collagen [8]. These fine, densely packed collagen fibres are aligned parallel to each other and the articular surface, providing tensile and shear strength sufficient to resist to the large tensile, shear and compressive forces encountered during articulation [7], [8].

### **1.2.2 Middle Zone**

Directly underneath the superficial zone is the middle zone which provides an anatomic and functional bridge between the superficial zone and the deep zone [8], [28]. This zone, also known as the transitional zone, forms 40-60% of the total cartilage thickness [5], [8], [12]. Here, the chondrocytes are spherical in shape and evenly distributed. The cell density is lower

compared to the superficial zone but higher than the deep zone [28]. The ECM has a higher PG (aggrecan) content compared with the superficial zone but lower than the deep zone [7]. In addition, the amount of collagen fibrils is lower in this zone compared with the superficial zone but higher than in the deep zone [12]. The fibrils are thicker and less tightly packed with more random arrangement [7].

### **1.2.3 Deep Zone**

In between the middle and calcified zone is the deep zone, occupying approximately 30% of the total cartilage thickness [5], [8], [12]. The cell density in this zone is the lowest of all of the zones with chondrocytes arranged in columns orientated perpendicular with respect to the articular surface and parallel to the collagen fibres [7], [8]. The deep zone also contains the highest PG content and the lowest water concentration [7], [8], [28] of all of the cartilage zones, as well as the thickest collagen fibres which are organised perpendicular to the articular surface [8], [28].

### **1.2.4 Calcified Zone**

This mineralised zone lies in between the uncalcified portion of cartilage and the subchondral bone, providing intermediate mechanical properties between the two tissues [28]. Slow metabolic activity is typical of this zone as a small population of chondrocytes exists which express hypertrophic phenotypes [7], [28]. Hypertrophic chondrocytes are specialised cells that are at the end state of the chondrocyte differentiation process [52]. These cells are characterised by synthesis of type X collagen and are responsible for matrix calcification [28], [52], [53]. This zone plays an integral role in providing an interface for structural integration with the subchondral bone [7], [28]. The collagen fibrils of the deep zone are anchored to the subchondral bone forming an interlocking 'root' system in order to secure cartilage to bone, [5], [8]. The presence of a layer called 'tidemark' distinguishes between the deep and calcified cartilage [7], [8].

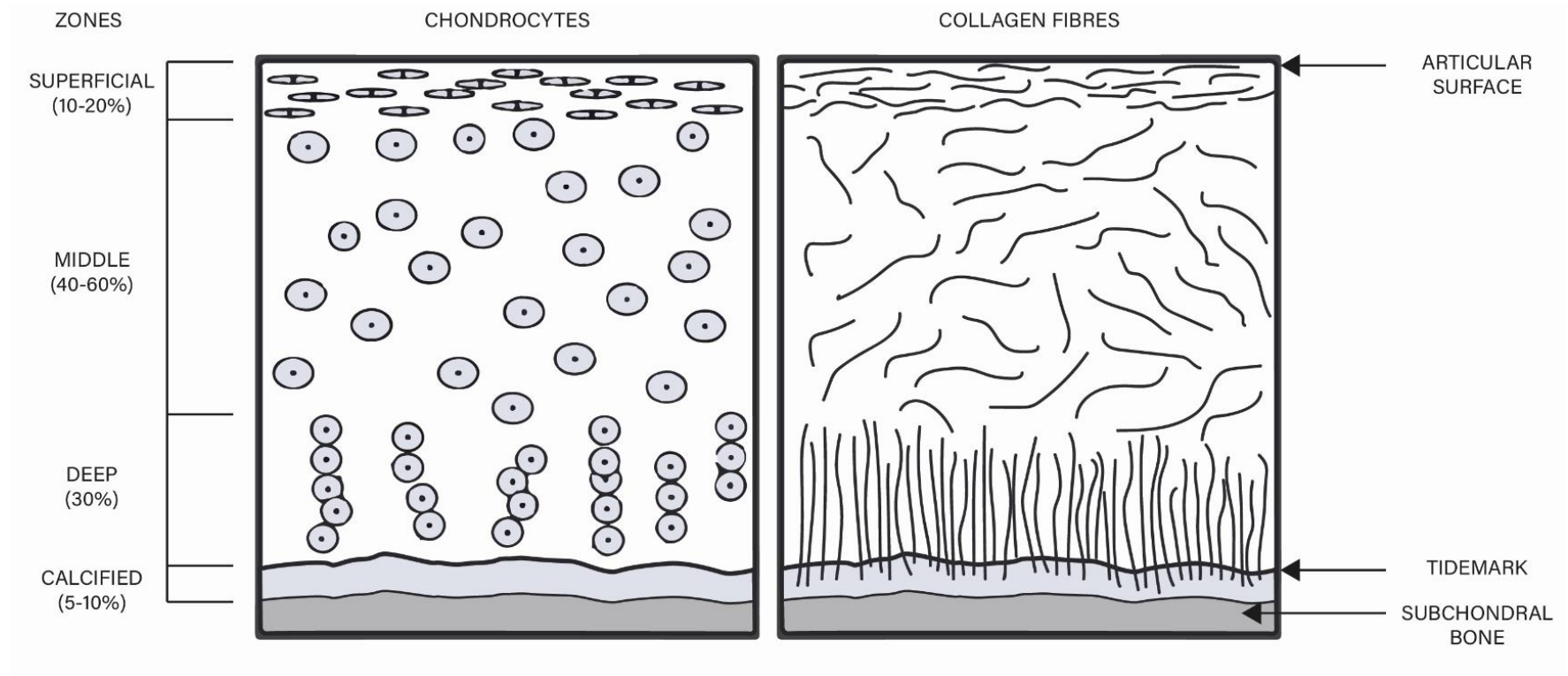


**Figure 3: Schematic diagram of chondrocyte and collagen fibres organisation within the four histologically distinct zones of articular cartilage. Figure adapted from [5].**

### **1.3 Articular Cartilage Functions**

Its main functions are to provide a smooth surface for articulation between bone ends to allow freedom of movement to occur with minimal friction and wear, while facilitating the transmission of load across the joint by distributing applied load over a wider contact area, thus keeping contact stresses to a minimum [2], [5], [8], [54], [55]. These functions of articular cartilage are related to its biomechanical properties, as dictated by its unique composition and structure [5], [22]. To date, its remarkable characteristics are still yet to be matched by anything man made.

#### **1.3.1 Near Frictionless and Wear Resistance Characteristics**

Synovial joints are subjected to a variable range of loading conditions during physiological loading and articulation occurs under very low friction in the presence of synovial fluid in the joint cavity, with minimal wear [5]. Synovial joints have an extremely low coefficient of friction ( $\mu$ ), of approximately 0.02 during static measurement [56] but the value of  $\mu$  measured under dynamic conditions is as low as 0.0057 [5], [57]. The minimal friction and wear characteristics of cartilage associated with such varied loads demonstrates not only its excellent wear resistance properties but also that lubrication processes occur within the joint and within and on the bearing surfaces of cartilage [5]. Numerous theories have been developed depending on the applied load and on the sliding velocity (speed and direction of motion) between two articular surfaces to describe the lubrication mechanism in the diarthrodial joint [5]. There are two fundamental types of lubrication. One is boundary lubrication, which is most effective in describing low articulating speed or high load conditions in which both articular surfaces come in contact with one another [5], [12], [58]. In the diarthrodial joint, lubricin (a glycoprotein) within synovial fluid is absorbed as a monolayer on the bearing surfaces of articular cartilage during motion and loading which prevents direct, surface-to-surface contact and minimise surface wear [5], [12], [58]. The other is fluid-film lubrication, which best describes lubrication with high articulating speed [5], [12]. In this type of lubrication, a thin film of synovial fluid forms between the articular cartilage surface to create a bearing surface separation. The frictional properties are dependent on the viscosity of the fluid, the relative articulating speed between the two surfaces and the magnitude of the applied load [5], [12]. However, no single theory has been able to describe the lubrication mechanism for articular cartilage under all loading circumstances. Thus, it is quite possible that a combination of both lubrication types is responsible for the lubrication of cartilage under varying loading scenarios and that synovial joints would adapt to the mechanism that will most effectively provide lubrication at a given loading condition [5], [12].

### **1.3.2 Distribution of Joint Loads**

The joint is exposed to repetitive mechanical loading during daily activities [59]. Without the layer of cartilage, the underlying bone would experience extremely high contact stresses that would lead to bone destruction and cause a lot of pain [60]. Articular cartilage is a highly hydrated tissue which is significantly less stiff than bone and has the ability to deform under load which allows high forces to be transmitted over a wider contact area across the joint [54], [60], [61]. Thus, this reduces contact stress being transferred to the bone and allows for normal load transmission without damage or pain [60]–[63].

### **1.4 Structure-Function Relationships of Articular Cartilage**

The heterogeneous composition and ultrastructural organisation of matrix components in articular cartilage are key to its unique functional properties, allowing the performance of its functions of load bearing and near frictionless articulation [5], [12]. As described before in Section 1.2, the constituent components of articular cartilage are inhomogeneously distributed throughout the matrix.

The highest water content, lowest amount of PGs and highest content of collagen are found in the superficial zone in comparison to other zones [61]. The collagen fibrils are orientated parallel to articular surface. It is known that this zone experiences the highest tensile and compressive stresses [8], [64]. Given the unique organisation and composition of components in this zone, it provides high tensile and shear strength that endows the cartilage with the ability to resist the large tensile, shear and compressive forces encountered during articulation [7], [8], [64]. Given that this zone is the most hydrated part of the tissue, relatively large deformation occurs with fluid exuding out of the tissue in response to provide resistance to compressive strain.

In contrast, the content of collagen and water decreases with cartilage depth. Thicker collagen fibrils are aligned perpendicular to the articular surface and a large quantity of PGs (and also GAGs) are found in the deep zone [8]. Given the rich PG content and the specific collagen orientation (perpendicular to the articular surface) that is able to entrap the water laden GAGs within the matrix, this zone spreads the applied load across the tissue and provides greatest resilience to compressive forces, endowing the articular cartilage with load bearing properties [8]. These constituent components are distributed and organised in such a way to accommodate the complex mechanical environment that is placed upon cartilage.

### **1.5 Mechanical Environment of Articular Cartilage**

Appropriate physiological mechanical loading is known to be essential for the development, maintenance and repair of healthy and functional articular cartilage [65]. Cartilage responds to

mechanical stimuli and remodels accordingly [12]. Understanding the mechanical environment and its effect(s) on cartilage provides insight into the tissue's homeostasis and the regulatory pathways associated with it. In addition, the response of matrix and chondrocytes to mechanical forces needs to be understood as these contribute greatly to the overall tissue response to loading.

### **1.5.1 Joint Forces and Stresses Imposed on Cartilage in Load Bearing**

#### **Joints**

Articular cartilage, located within the load bearing joint space, is constantly subjected to mechanical loading during normal activities [59], [66]. Depending on the activity (e.g. walking or running), the forces acting on the joints will vary. The forces measured across the hip joint range from 2.5 to 5.8 times body weight (BW) and the tibio-femoral joint experiences an average load of 3.9 times BW during level walking [67], [68]. However, the load can exceed to 8 times BW in the knee during downhill walking [68].

Previous studies reported that during level walking, the mean contact stresses associated with these loads are estimated between 1.5 to 5.5 MPa in the hip, 1.2 to 2.6 MPa in the tibio-femoral joint and 0.6 to 2.4 MPa in patella-femoral joint [63], [69]–[74]. Contact stresses in the human hip joint have been measured to be as high 20 MPa while standing up from a chair or jumping [75]. The frequency of loading during normal walking ranges between 0.8 and 1.1 Hz [76], [77], with each loading duration lasting between 620 and 720 ms [78], [79]. For running motion, the loading durations are shorter and the peak forces and frequencies increase [76], [78].

## **1.6 Effect of Mechanical Loading on Cartilage**

### **1.6.1 Effect of Mechanical Loading on Extracellular Matrix**

The biomechanical response of cartilage to applied loading is largely determined by the interaction between the collagen meshwork, the PGs (entrapped in the collagen meshwork) and the water (held by the PGs). Articular cartilage can be considered as a biphasic material consisting of two distinct phases; an interstitial fluid phase and a porous-permeable solid phase [5], [6], [8], [12]. The fluid phase is composed of mostly water with dissolved solutes and free mobile ions. The solid phase consists primarily of collagen (mainly type II), PGs and GAGs [5], [6], [8], [12]. The primary determinants of the biomechanical behaviour of cartilage are the Donnan osmotic swelling pressure induced by PG molecules in the matrix and the constraining tensile stress developed within the collagen fibrillar network [5], [80]. Thus, it is key to understand how interstitial water flows through and is exuded from the tissue [80].

When cartilage is at the resting state, water flows through the pores of the proteoglycan-collagen matrix by attraction due to the high fixed charge density (FCD) within the matrix,

thereby endowing a high swelling pressure [80]. Water continues to be drawn into the tissue causing it to swell and expand until the swelling pressure and the constraining tensile forces exerted by the collagen network reach equilibrium [80].

Under static compressive loading, cartilage initially undergoes elastic deformation as the applied stress causes the pressure within the tissue to exceed the swelling pressure [5]. This causes interstitial water to be excluded from the tissue. Due to the water loss within the tissue, the effective PG (and in turn the FCD) concentration increases, which in turn, initiates water to be drawn back into the tissue to restore equilibrium [5]. Upon removal of loading, water imbibes back into the tissue to restore the balance between the osmotic swelling pressure and the tension developed by the collagen network [5]. As a result, cartilage returns to its originally 'non-loaded' shape [5].

When the joint is subjected to consistent (i.e. high frequency) loading during physiological activities, there isn't enough time for cartilage to fully recover from the deformation caused by previous loading cycles. With a continual applied cyclic loading, a progressive consolidation of the matrix occurs causing more water to be exuded than is imbibed [35]. This results in successive deformation of tissue which causes a reduction in overall thickness [35]. The thinning of cartilage continues with each cycle until the water exuded is equal to that imbibed. If the loading magnitude or frequency reduces, the tissue will begin to imbibe water and recover from deformation. This eventually leads to full restoration of cartilage thickness obtained in a non-loaded state.

It is well known that the loss of function of osteoarthritic cartilage is due to disruption to the macromolecular matrix network [80]. Disruption to the matrix would reduce the constraining tension developed in the collagen network, allowing entrapped PGs to be depleted which makes it vulnerable to microdamage and hinder its capability to support load [80]. As PG content decreases in the osteoarthritic cartilage, this leads to a reduced ability to bear load and microcracks may begin to develop and grow propagate within the cartilage, further compromising the matrix structural integrity [6], [80]. Should the rate and accumulation of microdamage exceed the rate of matrix repair, it will eventually lead to bulk material failure [6]. In addition to PG depletion from the matrix, the FCD required to maintain tissue hydration (the ability to retain water) is lost. Hence the superficial layer is absent in osteoarthritic cartilage [80], [81].

### **1.6.2 Effect of Mechanical Loading on Chondrocytes**

Articular cartilage homeostasis is maintained through a process of consistent but slow ECM turnover [82]–[84]. Chondrocytes are responsible for the synthesis and organisation of the ECM components through their metabolic activity in order to maintain tissue structural integrity and

functionality [22]. The metabolism of chondrocytes involves both anabolic and catabolic activities and a balance between the two processes maintains the homeostasis of cartilage [12]. Anabolic activity is considered to be the synthesis, assembly and organisation of matrix, while catabolic activity refers to the breakdown and degradation of matrix [12], [85]. Chondrocytes are sensitive to environmental changes and respond through metabolic changes [12], [86]. It is well established that chondrocyte activity is regulated by not only genetic and environmental factors (e.g. growth factors, cytokines, hormones) but also by mechanical factors (e.g. tensile, compressive, shear stresses and strains, fluid pressure and associated electrokinetic effects) [12], [21], [22], [66], [82], [83], [86]. This capability enables articular cartilage to alter its matrix composition and structure to accommodate changes in physiological joint loading during normal activities [21], [66], [87].

Mechanotransduction is a process that chondrocytes detect and respond to changes in their local mechanical environment (e.g. mechanical signals imposed by the ECM) and convert them into intracellular biochemical and molecular signals that subsequently affect gene expression and regulate cell behaviour (e.g. biosynthetic activity) [83], [86], [88]–[92]. Mechanotransduction allows chondrocytes to regulate the rates of matrix synthesis and degradation and therefore adjust the composition of the surrounding matrix that give cartilage its strength and the load-bearing function [22] to better suit its current mechanical environment [93].

When mechanical forces impact on articular cartilage, chondrocytes may detect alterations in their mechanical environment through cell deformation (change in cell shape) induced by the forces acting upon the cell itself and through force transmission from the deformation of ECM in conjunction with changes in fluid shear, hydrostatic pressure, electrical streaming potentials and osmotic pressure [59], [65], [87], [94], [95]. These are considered to be the primary extracellular signalling events of mechanotransduction [59], [65] serving as mechanical signals (forces), in which chondrocytes recognise and respond by triggering intracellular mechanisms that can alter cellular activity for maintaining healthy and functional articular cartilage [94]. As chondrocytes are responsible for matrix turnover and homeostasis of cartilage, understanding how the chondrocytes react to mechanical loading within articular cartilage could aid the understanding of how cartilage maintains a healthy and functional state [96]. In addition, whilst the mechanisms of mechanotransduction are beyond the scope of this thesis, knowledge of the cellular response to deformation or strain caused by applied mechanical loading could provide insight on how best to utilise mechanical loading to promote the a desired cellular behaviour in cartilage tissue engineering.

There are 3 specific intracellular mechanisms that are thought to be activated by these extracellular events including integrin-mediated signalling, stretch-activated ion channels and distortion of intracellular structures and organelles [65].

Integrin is a transmembrane receptor that mediates cell-matrix interactions [89], [91]. It has two main functions: 1) attachment of the cell to the ECM and 2) signal transduction from the ECM to the cell [22], [97] as shown in Figure 4. This type of mechanoreceptor contains  $\alpha$  and  $\beta$  subunits [98]. The  $\beta$  domain is responsible for linking to the external ECM and the  $\alpha$  domain (the cytoplasmic tail) interacts with the intracellular actin cytoskeleton and various associated proteins including vinculin, paxillin, talin and intracellular signalling proteins, such as focal adhesion kinase (FAK) [22], [98], [99]. By assembling various cytoskeletal proteins, associated proteins and protein kinases together at one site, this forms a large protein complex called “focal adhesion” which acts as a physical structural link between the ECM and the actin cytoskeleton [22], [99]. Focal adhesion is known to control the regulation of chondrocyte gene expression and ECM remodelling [100].

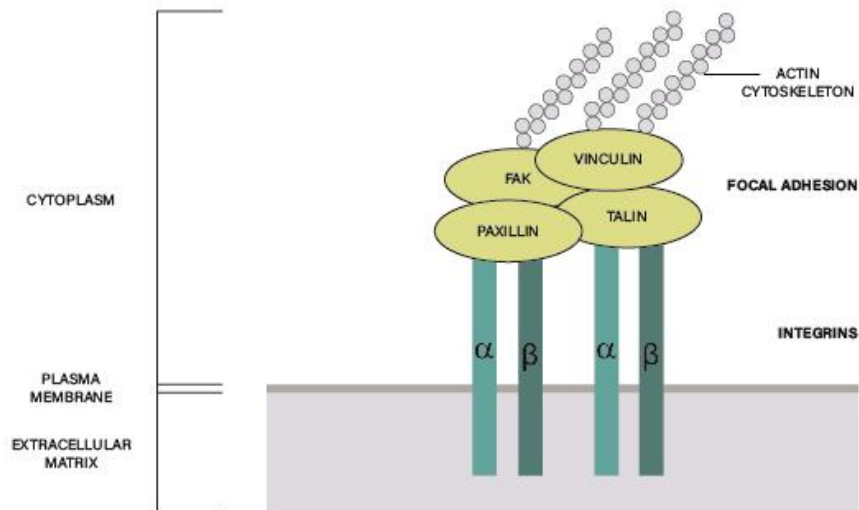


**Figure 4: The cell-matrix interactions are mediated by transmembrane integrins (which consist of  $\alpha$  and  $\beta$  subunits). Focal adhesion complexes (made up of various structural and regulatory proteins including vinculin, talin, paxilin and FAK) serve as a structural and signalling link between the ECM and the actin cytoskeleton. Figure adapted from [98].**

Upon loading of the ECM, chondrocytes can “sense” the changes in their local mechanical environment. Mechanical forces generated internally within and externally from the tissue can be transmitted through integrin receptors to the cell cytoskeleton, where an intracellular signalling cascade occurs to transduce extracellular mechanical signals into intracellular biochemical responses as shown in Figure 5 [98], [101].

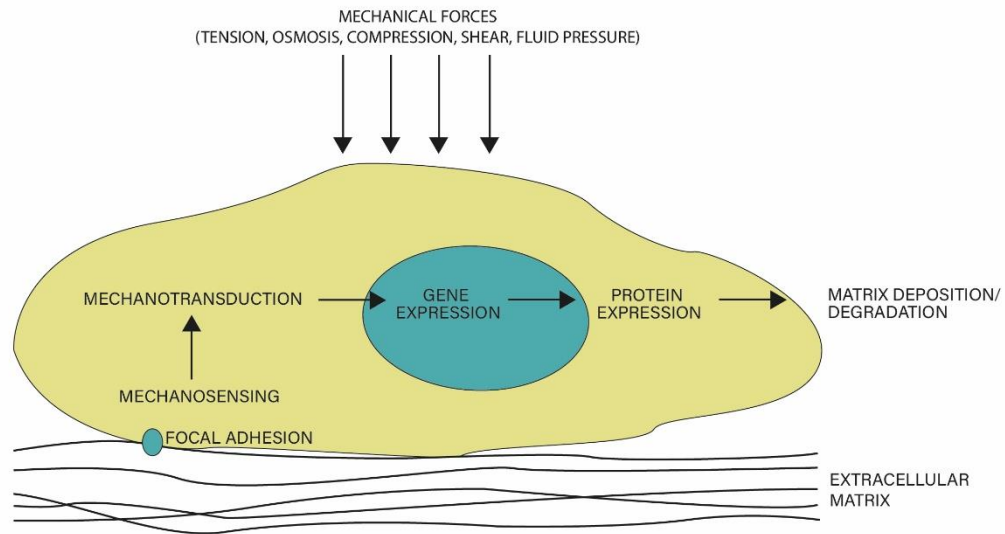


**Figure 5: Schematic diagram of the mechanotransduction process utilising focal adhesions to transmit mechanical forces from the ECM to a single cell. Figure adapted from [101].**

Cell activity is influenced by the activation of stretch-activated ion channels [102]. Upon loading of cartilage, cell deformation induces tension across the plasma membrane which can cause the membrane to deform and distort the lipid bilayer structure [100], [103]. This can lead to changes to the conformation of the stretch-activated ion channels causing an alteration in their opening and closing rates [100], [103]. The load-induced changes to the plasma membrane trigger ion channels to open which allows an influx/efflux of ions (e.g.  $\text{Ca}^{2+}$ ,  $\text{Na}^+$ ,  $\text{K}^+$ ) to occur [22]. Changes in ion concentrations, mainly  $\text{Na}^+$  and  $\text{Ca}^{2+}$ , can initiate biochemical signalling cascades [22], [100]. An alteration to chondrocyte gene expression and translation may be caused by these signalling pathways in response to load-induced deformation of the membrane [100]. These ion channels can also be activated by hydrostatic pressure, shear and fluid flow [100].

In addition, cell deformation can lead to deformation of organelles, such as the nucleus, endoplasmic reticulum and mitochondria [94]. This is because most intracellular structures within the cytoplasm are interconnected by the cytoskeleton [65]. Studies have illustrated that distortion of these organelles can trigger mechanotransduction signalling pathways that alter gene expression and therefore matrix synthesis [65].

The cell cytoskeleton is a 3D interconnected filamentous polymer network which is composed of actin microfilaments, microtubules and intermediate filaments [104], [105]. Together, these cytoskeletal components are responsible for the regulation of cell shape and mechanics [105].

The cytoskeletal network in chondrocytes consists of actin filaments, tubulin microtubules and vimentin intermediate filaments [106]. Several studies have revealed the organisation of the three cytoskeletal networks within chondrocytes in many different preparations; chondrocytes in articular cartilage explants [107], [108], primary chondrocytes cultured in agarose [109]–[111]

and chondrocyte monolayers [112]. In these studies, actin filaments were seen to be mostly distributed at the periphery of the chondrocytes [108]–[112]. The tubulin microtubules were observed to form a loose meshwork that is uniformly distributed across the cytoplasm of chondrocytes [108], [111]–[113]. Vimentin intermediate filaments formed a highly organised network which was distributed between the cell periphery and the nuclear membrane [108], [109], [111], [112].

Actin forms a dynamic network that is able to assemble and disassemble in response to mechanical load. It is responsible for the alteration of cell shape [114], cell-cell and cell-matrix adhesion [115], organelle transport [116], cellular stiffness and signal transduction [115]. The actin cytoskeleton is also involved in maintaining the expression of chondrocyte phenotype and ECM synthesis required for cartilage to resist highly repetitive stresses [104]. These functions are known to be regulated by cell deformation [104], [115]. In response to mechanical forces, actin monomers (G-actin) can assemble (polymerise) into long and highly ordered filaments (F-actin) and organise into functional networks to provide chondrocytes with the mechanical integrity to resist applied forces [104]. Although the function of vimentin intermediate filaments is less known, it is suggested that vimentin is involved in mechanotransduction, particularly in conveying mechanical signals into downstream biochemical signals responsible for ECM production [117]–[119].

#### **1.6.2.1 Previous Studies on Chondrocyte Deformation and Metabolic Activity under Mechanical Loading**

The cellular response to mechanical loading is of particular interest to researchers because the mechanical forces impacting upon chondrocytes strongly influence their deformation behaviour and metabolic activity which are responsible for the biosynthesis and turnover of the ECM (discussed in Section 1.6.2) [82], [120]. Thus, understanding how chondrocytes react to applied mechanical stimulation is essential to understanding the homeostasis of healthy cartilage. In addition, a knowledge of the cellular response to mechanical loading can have important implications in the field of tissue engineering and regenerative medicine.

Previous studies have demonstrated that mechanical loading regulates the biosynthetic response of chondrocytes *in vivo* [121], [122] and *in vitro* [123]–[128], indicating the importance of mechanical loading on normal maintenance of articular cartilage. *In vitro* studies of chondrocyte metabolism showed biosynthetic inhibition ensues when cartilage explants were subjected to static compression. In contrast, cyclic compression applied to cartilage explants can either stimulate or inhibit biosynthetic response of chondrocytes, depending on the frequency, amplitude and the duration of the applied load [12], [123], [128]–[131]. Static compression and loading below a frequency of 0.001 Hz have been shown to decrease chondrocyte PG and GAG synthesis [12], [123], [128], [131], whilst dynamic loading has been shown to promote tissue

synthesis [12], [124], [127], [128], [131]. In immobilisation studies, a decrease of matrix synthesis and content were observed in the immobilised limbs and the weight-bearing limbs showed an increase in matrix components and synthesis [12].

These studies have illustrated that the magnitude, frequency and the duration of mechanical forces strongly affect the biosynthetic response of chondrocytes [12], [132]. Hence, cartilage conditions to changes in mechanical loading during normal activities by adaptive matrix remodelling. It is proposed that cartilage becomes mechanically conditioned to regularly applied stress [93]. Damage to cartilage could result if an increase of prevalent stress was much greater than the stress that was previously routinely applied to the cartilage [93]. In response to an increased prevalent stress, cartilage will only remodel its ECM to cope with such stress if the change is large enough to trigger the anabolic effects of matrix synthesis and yet small enough to not trigger the catabolic activities [93]. In addition, a high magnitude of prevalent stress would favour catabolic effects and cause chondrocytes to breakdown the ECM, making cartilage more likely to sustain damage [12], [93]. The predominant stress to which a cartilage site is subjected will vary for each individual because of their weight, age (state of degeneration) and physical lifestyles and therefore the stress threshold responsible for anabolic and catabolic effects will also vary [93].

The deformation behaviour of chondrocytes has been extensively investigated under static compression using either confocal microscopy or histological evaluation in cartilage explants [21], [51], [87], [133]–[139] and for chondrocytes within other scaffold materials (e.g. isolated chondrocytes seeded in agarose) [88], [140]–[144].

Studies of cartilage explants showed that static loading had significant impact on the shape and volume of chondrocytes [21], [85], [87], [137], [145]. Choi *et al.* (2007) [137] demonstrated that chondrocyte height and volume significantly decreased in porcine cartilage explants subjected to different magnitudes of compressive tissue strains (10 %, 30 % and 50 %). The magnitude of decreased height and volume were dependent on the zone and magnitude of compression. In addition, the measured local tissue strain in each zone showed to be highly inhomogeneous throughout the tissue depth. Guilak *et al.* (1995) [87] found that chondrocyte height and volume significantly reduced, along with significant lateral expansion in explants of canine cartilage subjected to physiological levels of compressive loading (15 % applied strain). The results also showed that a greater magnitude of local tissue deformation was observed in the superficial zone compared to the other zones at 15 % applied tissue strain, suggesting the compressive stiffness of the superficial zone is significantly low. In a study by Madden *et al.* (2013) [85], in which superficial zone chondrocyte deformation was examined in intact cartilage attached to its native bone specimens from two regions of the rabbit knee joint (femoral condyles and patellae) subjected to physiological and extreme compressive loads (0 % - 80 %

applied tissue strains), significant differences in deformation behaviour between chondrocytes from different regions under compression were observed.

Previous studies have provided evidence of the complex and depth-dependent inhomogeneous mechanical environment surrounding chondrocytes within native articular cartilage and suggested the chondrocyte response (i.e. morphological change) is largely related to the local changes in the cell's biophysical environment, in particular the ECM environment [21], [85], [87], [137], [145]. The previous findings suggested that pericellular matrix (PCM) may also greatly influence the mechanical environment of the chondrocyte by serving as a non-linear mechanical transducer in a zone-dependent manner in articular cartilage [85], [87], [137], [145]. PCM is a narrow tissue region that completely surrounds chondrocytes [85], [137]. For studies of isolated chondrocytes seeded in agarose gels, it has been shown that the extent of cell deformation was determined by the matrix previously elaborated from the chondrocytes [142].

In attempts to provide insight into the complex mechanical environment around the chondrocyte within cartilage, theoretical models have been developed to help study the deformation behaviour of chondrocytes [95], [146]–[148]. These models indicated that the relative mechanical properties of the chondrocyte, ECM, and the PCM significantly influence cell deformation behaviour [95], [146]–[148]. However, the deformation of chondrocytes under dynamic loading has not been widely investigated. This is due to the practical difficulties of loading in a controlled, physiological, dynamic manner while simultaneously capturing 3D morphological changes. Nevertheless, these previous works have provided a better insight into cartilage and chondrocyte mechanobiology and served as an important foundation for the current study in this thesis. Knowledge of how native articular cartilage is damaged by applied mechanical loads and corresponding changes in matrix structure and cell function, is also necessary to provide insight into the response of chondrocyte to different loading scenarios that could induce damage to cartilage.

## **1.7 Articular Cartilage Damage**

The many factors that contribute to cartilage damage can be grouped in to two main categories; molecular and mechanical. Molecular factors refer to age related changes. Mechanical factors involve abnormal loading (e.g. temporary increase in applied stress to cartilage) in trauma and fatigue due to repetitive use. Cartilage defects are very common and have the potential to progress to the development of osteoarthritis (OA) [14], [64], [149]. OA is a degenerative joint disease that causes pain and inflammation in a joint due to the degeneration of articular cartilage [150]. Patients with OA often suffer from joint pain, stiffness, swelling and reduced joint movement and function which impact on their quality of life [151], [152].

### **1.7.1 Molecular Factors Responsible for Cartilage Damage**

Articular cartilage undergoes structural, matrix compositional and mechanical changes with age [150]. These changes are believed to be related to progressive changes in cell function that are also associated with aging [150]. As the chondrocytes age, their ability to maintain cartilage homeostasis is reduced as a consequence of senescence through telomere shortening (which occurs with the majority of cells in all other tissues) [150], [153]. This consequently leads to abnormal protein synthesis. Alteration in aggrecan size is one of the matrix compositional changes observed in older cartilage [150], [154]. The number of aggrecan molecules and the length of each aggrecan molecule within the matrix are significantly reduced [150]. This leads to reduced water content held in the matrix, thereby decreasing cartilage stiffness and resilience to compression [150]. As a result of alteration to matrix structure and composition, the mechanical properties of cartilage deteriorate with age [155]. Under physiological loading, the resulting reduced water content in the matrix would substantially hinder the cartilage's ability to withstand compression and therefore the collagen network would experience higher levels of strain than usual. This could cause disruption to the collagen organisation and eventually lead to mechanical failure. In addition, fibrillation forms in the surface zone of cartilage with age. Age-related changes therefore also increase the risk of injury and progressive degeneration of articular cartilage [150].

### **1.7.2 Mechanical Factors Responsible for Cartilage Damage**

Cartilage can sustain damage when subjected to a large single load (i.e. such as might be experienced in trauma) over short intervals of time, where the load might increase from zero to peak value within 1 ms [156]. The single large stresses imparted on the cartilage can lead to creation of fissures in the collagen network which consequently weaken the matrix structure, thereby reducing cartilage stiffness. With changes in the matrix structure, the ability to sustain mechanical loading would be hindered, altering the stress distributions across the joint and making cartilage more susceptible to further damage and development of degeneration [155], [156]. If the rate of damage is greater than the rate of repair, accumulation of damage would progressively lead to OA [93]. Damage to cartilage caused by a single impact will be dependent upon the magnitude and rate of the applied load.

In contrast, fatigue failure can also cause cartilage injury [93]. This is when low magnitude cyclic loads (such as might be experienced in daily activities) impact upon cartilage over long periods of time. It is possible that fatigue failure within cartilage is likely to occur due to the application of repetitive tension to the collagen network within the superficial zone, as this is the region where the collagen network is exposed to the highest amount of strain [93], [157]. Fibrillation of the surface layer of cartilage is believed to initiate this fatigue process which is seen in early OA [157], [158]. Although cartilage is susceptible to fatigue failure, it is difficult

to determine if and when the cartilage will fail due to fatigue because it is not under continuous cyclic loading during normal daily activities and it has an inability to repair itself.

Between the extreme of large trauma load and immobilisation, it is difficult to determine whether a particular load could cause damaging effects to the cartilage. Whilst it might not damage the matrix, it may alter cellular function. Altered cellular function could lead to changes in matrix composition and thereby the cartilage stiffness. As discussed in Section 1.6.2.1, it has been previously hypothesised that cartilage conditions its stiffness to cope with the changes in applied prevalent stress by ECM remodelling [93]; cartilage that is exposed to a high level of prevalent stress will be stiffer than those subjected to a low level of prevalent stress. Previous studies have shown that immobilisation and static loading favour catabolic effects and cause chondrocytes to decrease PG and GAG synthesis in cartilage, with consequent reduction in cartilage stiffness [12], [123], [128], [131]. If normal activities are resumed (i.e. increase applied load) to joints that received minimal loading due to immobilisation, the less stiff cartilage will be susceptible to large strains and subsequent damage.

Articular cartilage has a limited intrinsic repair capacity due to the lack of blood supply supporting waste and nutrient transfer that is required for effective repair and remodelling, which in turn, makes cartilage very difficult to heal once damaged [14]. The primary route for cartilage to receive nutrients and remove waste is through diffusion from the synovial fluid [16]. In addition, low chondrocyte density within the matrix restricts formation of neo-tissue at the damaged site. As a result, minor injury to articular cartilage can lead to progressive damage and development of OA [14]. Degenerative changes in osteoarthritic cartilage are mainly due to an imbalance between anabolic and catabolic activities of chondrocytes favouring net degenerative (catabolic) effects [150]. This consequently leads to progressive thinning and loss of articular cartilage [150].

## **1.8 Repair of Articular Cartilage Damage**

As the general population continue to age and become more obese, OA, primarily developed by progressive damage to cartilage, is a common clinical condition worldwide which affects a large proportion of people. Young and healthy individuals are also prone to a high incidence of cartilage damage from sports injuries, given the limited spontaneous repair of cartilage [23].

There is a major clinical need to address the healthcare challenge presented by cartilage defects. The Arthritis Research UK report (Osteoarthritis in General Practice, [151]) estimated that approximately 8.75 million people (13% of the total population) in the UK are affected by OA to some degree which presents a massive burden to the NHS [152]. OA has a significant negative effect on the UK economy because a large number of the population are affected by the condition, with their reduced quality of life, inability to work and their need for health, social care and welfare benefits [152]. According to the Global Burden of Disease 2010 study, OA

was reported to be the eleventh leading cause of global disability [159]. As life expectancy, ageing populations and levels of obesity continue to rise worldwide, OA was predicted to be the fourth highest contributor of disability by 2020 and to become a significant problem for health care systems globally [159].

### **1.8.1 Surgical Treatments for Cartilage Lesions**

There is currently no cure for OA but surgical treatments are available to treat patients with severe cartilage lesions [14]. These treatments hope to delay the need for total joint replacements (known as the standard treatment for end-stage degenerative diseases [160]) especially in young and active patients [14]. The primary aim of these treatments is to relieve symptoms such as pain, swelling and joint instability, improve joint congruency, restore joint movement and function and prevent further cartilage degeneration [161]. Surgical interventions commonly used to repair cartilage include debridement, lavage, bone marrow stimulation techniques (drilling and microfracture), direct tissue graft replacement (osteochondral autograft transplantation and mosaicplasty) and cell culture-based treatment (autologous chondrocyte implantation) [24], [162]–[166].

#### **1.8.1.1 Debridement and Lavage**

Debridement and lavage are used to remove loose cartilage and fibrin debris from the joint and tissue surface in order to provide relief from symptoms and manage pain [165]. Debridement shaves off tissue fragments that can cause reactive synovitis and joint effusions [165]. Lavage rinses the damaged site with physiologically compatible solutions to remove loose cartilage and fibrin debris and reduce inflammatory mediators [165]. However, both treatments can only provide short term improvement to the symptoms and do not repair the defect itself [165].

#### **1.8.1.2 Microfracture**

Microfracture is an arthroscopic surgery that involves shaving off tissue debris and punching/drilling small holes into the defect area [24], [167]. This technique is effective in treating lesions up to 4 cm<sup>2</sup>. Multiple small holes penetrate through the vascularised subchondral bone inducing bleeding and resulting in fibrin clot formation [24]. Bone marrow also migrates into the defect area along with mesenchymal stem cells that are pluripotent and able to be induced to differentiate into bone or cartilage when subjected to the appropriate chemical or mechanical stimuli [24]. A resulting fibrocartilage is formed as a replacement for the damaged cartilage [24], [168]. However, fibrocartilage has inferior mechanical properties in comparison to healthy articular cartilage due to its low compressive stiffness and consequently lacks the required weight bearing and wear resistance characteristics [168], [169]. Previous studies showed microfracture to be effective in short-term improvement on knee function [170]. However, a high degree of deformation is seen in the repair cartilage when loaded (low

compressive stiffness), which possibly led to the observed variable repair cartilage volume in different studies [170]. This suggests fibrocartilage might not be able to sustain physiological loading in the long term, making it susceptible to further degeneration and possible functional deterioration [168]–[170]. This also highlights the importance of post-operative care and physical therapy, in particular with a gradual weight bearing approach, to prevent mechanical breakdown of fibrocartilage which could lead to denudation of the repair tissue [171]. In addition, removal of tissue debris prior to the drilling process can cause apoptosis, thermal necrosis and trauma to the surrounding healthy tissues [167].

### **1.8.1.3 Osteochondral autograft transplantation system (OATS)**

OATS is a surgical procedure that involves harvesting of healthy autologous cartilage-bone plugs from a less weight bearing site in the joint, such as the retropatellar facet of the femoral condyles or the dorsal part of the condyles, and their implantation in to the defect area [165]. Upon the removal of residual cartilage and debris, osteochondral plugs with the same height and diameter as the defect size are harvested for the procedure [165]. For a large defect site (up to 8 cm<sup>2</sup>), multiple small autologous tissue plugs are used to fill the defect and this process is known as mosaicplasty [167]. One advantage of OATS is that the graft is harvested from and re-implanted in the same individual and therefore it is immunologically compatible [167], [172]. In addition, the graft already has all of the essential components required for a good repair, such as the presence of hyaline cartilage, intact tidemark (as described in Section 1.2.2) and firm native bone which ensures that the graft can also be securely fixed in place aided by bone healing [165], [172]. However, major drawbacks of this procedure are donor site morbidity, limited graft availability and lack of lateral integration between the chondral surface and the surrounding tissue [172]. The donor site would also be damaged from harvesting the graft, therefore creating ever more damage to the patient's joint. In addition, there are limited areas where the graft can be harvest from, thus the number and sizes of defects that can be treated are relatively small.

Allogenic and synthetic materials can also be used as a graft tissue with this procedure [24]. Allografts are often obtained from cadavers, therefore there is no donor site morbidity associated with this type of graft [167]. In addition, medium to large sized defects (up to 3 cm<sup>2</sup>) can be treated [167]. However, the major drawbacks of using allografts are disease transmission and the potential triggering of an immune response [167]. Chondral grafts have been investigated to some extent [171]. However, due to the few cartilage donor sites and the difficulty in fixing the graft in place, a high probability of failure is associated with chondral grafts [171].

### **1.8.1.4 Autologous chondrocytes implantation (ACI)**

ACI is a two-stage procedure [167]. The first stage involves debriding the defect site and harvesting chondrocytes from the patient, generally from the healthy cartilage located in a low-weight bearing area [165]. Once harvested, the cells are cultured and expanded *in vitro* [165]. The second stage comprises chondrocyte implantation into the defect site [167]. Once a sufficient number of cells has been achieved that is suitable to fill the defect volume, the cultured chondrocytes are introduced into the defect site by injection and either a periosteal flap or a collagen membrane is used to cover the defect [167], [171]. The cover over the defect is sutured to the surrounding articular cartilage and may be secured by additional fibrin glue [167], [171]. Over time, transplanted chondrocytes proliferate and lay down cartilaginous matrix which subsequently produces a 'hyaline-like' repair tissue to fill the damaged site [167], [173]. This surgical technique has been demonstrated to have a better clinical outcome than those previously described [174]. However, there are limitations. ACI is associated with prolonged treatment duration as it is a complex procedure involving two surgeries in multiple sites. This could potentially result in increased morbidity and create additional scars in those sites. Other major disadvantages of ACI include potential formation of fibrocartilage at the edges of the flap and inferior fixation if the cartilage is softened/degenerative [167]. Furthermore, ACI might be accessible to only a relative small proportion of patients because of the associated high treatment costs as it is a patient specific and requires two surgeries together with a large amount of expensive laboratory time.

### **1.8.2 Future Repair Strategies**

All of the surgical techniques described in Section 1.8.1 present advantages and disadvantages. However, surgical interventions currently available to treat cartilage defects only provide short term benefits and are not effective enough to restore the normal function of cartilage for the long term. They also present a high probability of failure due to defect recurrence [166], [175]–[178]. For example, studies have shown that significant decline of clinical improvement and increase of failure rate were associated with microfracture after 2 years [166], [170]. Thus, there is a need for novel strategies to improve on the current treatments in order to repair cartilage defects that could progressively lead to development of OA. Ideally, any new strategies would need to be a single stage surgical procedure and be easily implemented. The repair tissue generated should have similar biochemical and biomechanical properties to those of native cartilage so it can function as articular cartilage. It should also be able to restore long term normal joint function and improvement on the symptoms. In addition, it requires to be not patient specific (not use recipient's own cells/tissues), be cost effective and economically viable. Since there is no effective treatment clinically available that can provide restoration of normal cartilage functions [160], [176], there has been much research conducted to find novel strategies for cartilage repair. This has led to the development of an appealing and promising approach

based on tissue engineering for cartilage regeneration [160], [166], [175], [176], [179]. The engineered cartilage is aimed at repairing the defects in order to restore the joint's normal functions of load bearing and articulation and to relieve pain.

## 1.9 Tissue engineering

The general principle of tissue engineering involves three key components: cells, scaffolds and appropriate bioactive factors (i.e. biochemical and physical stimulations) and can be used to create new functional tissue for cartilage defects (Figure 6) [14], [75]. The resulting engineered tissue is intended to replace the damaged tissue and should ideally have similar biochemical and biomechanical properties to those of the original healthy native tissue and the capability to perform normal functions for the long term [14], [75].

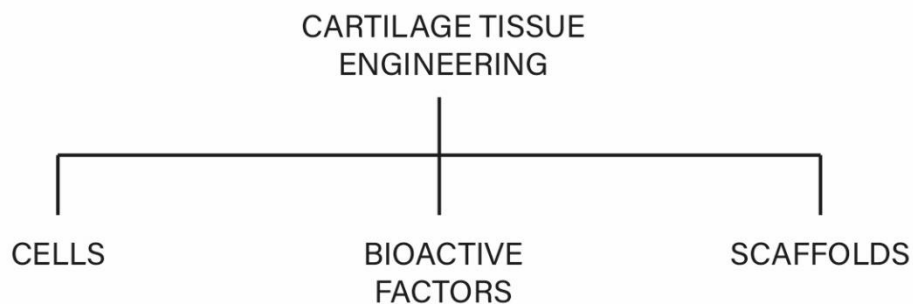


**Figure 6: General components used in cartilage tissue engineering.** [166].

### 1.9.1 Cells

In tissue engineering, cells must be able to provide a specific ECM for new tissue formation. Multipotent/pluripotent stem cells are often used in tissue engineering because of their ability to proliferate and differentiate into a variety of cell types including chondrocytes, adipocytes, osteoblasts and myogenic and neuronal cells [176], [178]. In addition, primary cells (e.g. chondrocytes) that are already differentiated are also utilised due to their existing desired phenotype [178]. Both chondrocytes and multipotent stem cells, in particular mesenchymal stem cells (MSCs), have been the most investigated sources of chondrogenic cells for engineering cartilage tissue (see Section 1.9.4) [175], [176], [180]. Synoviocytes found within the synovial fluid have also shown the ability to differentiate into chondrocytes [180], demonstrating its potential application in cartilage tissue engineering. However, major concerns such as de-differentiation (loss of phenotype) during culture expansion, limited sources and donor site morbidity associated with the use of chondrocytes have restricted their application in cartilage tissue engineering [175], [176], [180]. More recently, the use of MSCs has become the focus of many studies because they are easily accessible from different donor tissue types and their

chondrogenic differentiation ability [175], [176], [180]. The most studied MSC for this purpose is the bone marrow-derived MSC but MSCs can also be isolated from adipose tissue, perisosteum, synovial membrane, dermis and blood [176], [178]. The cell sources for tissue engineering can be autogenic, allogenic or xenogenic but autologous cells are preferred to minimise adverse immunological reactions and cross infection. However, using MSCs as a cell source also presents several limitations such as low cell numbers of MSCs in the bone marrow or other donor tissue, the necessity of careful characterisation, the presence of several cell subpopulations, the time-consuming differentiation procedure and the instability of the chondrogenic phenotype [175].

### **1.9.2 Scaffolds**

The use of a scaffold is to provide a favourable environment for three dimensional (3D) maintenance of a desired phenotype and as well as a structural support to retain the cells and promote cellular attachment, proliferation and differentiation for new specific matrix deposition [14], [176]. Ultimately, it acts as a template for tissue formation, guiding the growth of new tissue [179]. Three dimensional scaffolds such as 3D sponges, nonwoven fibrous constructs, gradient fibrous constructs and woven structures are common scaffold architectures used in cartilage tissue engineering [160]. Scaffolds should also be porous to enable inward migration of seeded cells or infiltration of native cells from the host [14]. Scaffold parameters (i.e. pore size, geometry, distribution, accessibility and porosity), that are dependent on the scaffold's physical architecture play a major role in determining cellular functions [160]. These parameters also affect the structural mechanical properties of the scaffold [160]. For example, a scaffold with high porosity would be expected to have weaker mechanical properties compared to the same scaffold with a lower porosity. Thus, there needs to be a balance between scaffold parameters, mechanical properties and cellular functions in order to create a functional replacement tissue [160]. An ideal scaffold must be biocompatible in order to minimise adverse inflammatory and immunological reactions [14], [176]. The scaffold can be designed to biodegrade, allowing the secreted new ECM to eventually take over the support for the neo-tissues and the cells and leaving a scaffold-free repair tissue [14], [176]. However, the degradation rate needs to be carefully controlled as it is desirable for degradation to occur proportional to new ECM production and deposition, therefore sufficient ECM must be laid down to allow support for the neo-tissue and the cells and to be able to transmit external forces [160]. Furthermore, the scaffold degradation products need to have minimal undesirable effects such as cytotoxicity, tumorigenicity and nephrotoxicity [14]. There are numerous different types of biomaterials developed as scaffolds for cartilage tissue engineering including synthetic and natural materials [14], [160], [175], [179]. Synthetic polymers such as poly(glycolic acid) (PGA), poly(lactic acid) (PLA), their copolymer poly(lactic-co-glycolic acid) (PLGA) and

poly(caprolactone) (PCL) have been frequently used as scaffold materials due to their FDA approval in medical applications [160], [179], [181], [182]. PLA and PGA are used in the clinics in applications including sutures, screws and pins [179]. Naturally derived polymers including collagen, fibrin, agarose, alginate, chitosan and hyaluronan are commonly used in 3D cultures, in the form of hydrogels and solid scaffolds, for cartilage regeneration and have shown promising results in supporting the growth of chondrocytes [14], [160], [179]. Composite scaffolds comprising of both synthetic and natural biopolymers have also been created to closely mimic the natural structural properties of cartilage [160]. Most recently, 3D printing technology has emerged as a new manufacturing technique to allow researchers to bioprint designed scaffolds with biomaterials and cells [160], [166]. Due to its ability to print with speed, reproducibility, accuracy and precision, scaffolds with complex shapes and structures can be created in an efficient and customised approach in an attempt to treat unique defect patterns [160], [166].

### **1.9.3 Bioactive factors**

Appropriate bioactive factors are essential to promote new tissue formation and induce tissue functionality because cells can sense and respond to many types of stimuli that are then transduced into biochemical responses and consequently affect cell behaviour such as matrix synthesis. There are two main types of stimuli; biochemical and physical.

#### **1.9.3.1 Biochemical stimuli**

Biochemical stimuli such as cytokines and growth factors are able to promote and maintain cellular phenotypes during *in vitro* culture of cells and tissues. The ability of biochemical molecules to stimulate cells towards a specific cellular phenotype is dependent on the concentration used [183], the cell type and the state of cells when the biochemical cue is applied; this includes the cell-seeded density [184] and the stiffness of the attached substrate [185]. For cartilage tissue engineering, growth factors such as transforming growth factor-beta proteins (e.g. TGF- $\beta$ 1 and TGF- $\beta$ 3) and bone morphogenetic proteins (BMPs) or a cocktail of these growth factors are commonly used to induce and maintain chondrogenic differentiation of adult MSCs [176], [178], [179]. In addition, the classic *in vitro* culture condition used to modulate chondrogenesis is a combination of TGF- $\beta$ 3, dexamethasone and ascorbic acid in serum free medium [186].

#### **1.9.3.2 Physical stimuli**

Physical stimuli are essential for the development and maintenance of functional tissues as every tissue is exposed to mechanical forces *in vivo* in some way. Physical stimuli used in tissue engineering are focused on four types of mechanical forces; tension, compression, shear and/or hydrostatic pressure [75]. It is typical that only one type of physical stimulation is used for

construct (i.e. engineered tissue) development in tissue engineering. The magnitude and frequency of physical stimuli should closely resemble the physiological parameters to which native tissue is subjected [187]. Application of physiological levels of mechanical stimulation can be achieved by using a bioreactor in which the physical stimuli can be carefully controlled along with other environmental parameters (e.g. pH, temperature, nutrient levels and gas concentration) and subsequently promote functional tissue formation [12], [187]. Thus, a bioreactor is basically used to support the formation of functional tissue through applying *in vivo* mechanical conditions.

Mechanical stimulation used in cartilage tissue engineering has included compression, shear and hydrostatic pressure as these are known to impact upon articular cartilage *in situ* during normal joint activity [75], [140], [188]–[191]. Compression is predominantly the type of mechanical stimulation used in cartilage tissue engineering approaches because the primary function of cartilage is to withstand compressive loading during normal activities. However, studies have also attempted to investigate the potential use of both compression and shear (multi axial stimulation) for cartilage construct development in order to mimic more closely the complex conditions associated with mechanical loading *in vivo* [75], [121], [140], [192], [193]. The cellular response to loading depends on the magnitude, frequency, rate and type of mechanical stimuli, the surrounding ECM and the cells attached to ECM [75]. Cells might proliferate then differentiate and synthesise cartilage matrix if the appropriate type and amount of mechanical loading is applied. In contrast, cell apoptosis might occur as a result of unfavourable applied mechanical loading [187], [189].

As discussed in Section 1.6.2.1, it is well known that under conditions of sufficient dynamic compression, chondrocyte viability, gene expression and biosynthesis of ECM components are modulated in cartilage explants [75]. Based on this knowledge, numerous studies have used the application of unconfined dynamic compression with a range of frequencies (0.001 to 1 Hz), strains (3-15 %) and stresses (0.5-2.5 MPa), on various tissue engineering systems, and differentiated, undifferentiated or de-differentiated cells to promote cell proliferation, differentiation biosynthetic activity and the deposition of a cartilaginous matrix [75]. Short term (hours to days) studies have shown that the application of dynamic compression can enhance ECM biosynthesis in a variety of tissue engineering systems, including hydrogels and PLA/PGA scaffolds [75], [189], [194], [195]. Lee *et al.* (2000) [195] applied 15 % dynamic compressive strain, at 1 Hz to a chondrocyte-agarose hydrogel system and showed a 50 % increase in the GAG content for chondrocytes in the deep-zone. Buschmann *et al.* (1995) [189] found that dynamic compressive loading (3 % strain, 0.01-1 Hz over 10 hrs) increased proteoglycan levels by 6-25% and protein synthesis by 10-35 % in agarose systems, depending on the frequency of loading. In longer term studies, Mauck *et al.* (2003) [196] found a 2-fold and a 3-fold increase in the PG content and the collagen content in chondrocyte-agarose

hydrogels, respectively, with the application of intermittent compressive loading (10 % strain, 1 Hz, for 3 continuous cycles of 1 hr on/ 1 hr off, 5 days per week) over a two months period.

The complex mechanical loading applied to articular cartilage involves fluid-induced shear forces as well as compression under normal physiological conditions [191]. Waldman *et al.* (2003) [191] developed a custom bioreactor designed to apply dynamic shearing forces to cartilage constructs, in an attempt to exploit the use of tissue shear strain as the mechanical stimulation to modulate the constructs development *in vitro*. Cartilage constructs contained 40 % and 35 % more collagen and PGs, respectively, than those free-swelling controls after 4 weeks of intermittent shear stimulation. Most interestingly, these changes were obtained with a low shear strain amplitude with only a relative small amount of cycles applied per day (2 % cyclic shear strain, 1 Hz, 6 min per every second day) [191].

During mechanical loading, hydrostatic pressure is introduced within the cartilage by the initial resistance to fluid flow [75]. Bioreactors were developed to explore the potential of application of hydrostatic pressure on regulating the development of cartilage constructs. These were designed to apply hydrostatic pressure through pressurising fluid or gas in chambers [35], [190], [197]. Carver and Heath found that intermittent hydrostatic pressure (3.44 and 6.87 MPa of compression, 5 secs pressurised/15 secs depressurised, applied for 20 min intervals every 4 hrs for 5 weeks) applied to chondrocyte-PGA constructs enhanced the amount of GAGs content and that a higher level of applied pressure also increased the collagen production [190]. The results suggested there may be a minimum level of pressure required to stimulate ECM production. Mizuno *et al.* (2002) [197] also showed the PGs content in chondrocyte-collagen constructs increased after subjected them to cyclic hydrostatic pressure (2.8 MPa, 0.015 Hz for 15 days).

#### **1.9.4 Cartilage Tissue Engineering**

As stated in Section 1.8, the prevalence of OA is increasing due to the ageing population and an increase in related factors such as life expectancy and levels of obesity. The current dominant activity to tackle cartilage lesions is through the application of tissue engineering. There have been increasing efforts focused in the area of cartilage tissue engineering research over the past few decades. It offers a promising prospects for cartilage regeneration. It allows precise control in scaffold structures and mechanical properties, scaffold material selection, sources of cells and biological factors, all of which can be fine-tuned to achieve the biochemical and biomechanical properties specific to native cartilage [160].

There are many studies reporting attempts to engineer cartilage constructs. Most studies focused solely on investigating the biochemical properties of cartilage constructs developed using different combinations of the principles of tissue engineering [160], [166], [175], [176], [179], [198], [199]. Although data on the biosynthetic response of cells and the final histological

appearance of developed tissue are highly important evidences to demonstrate appropriate tissue production, it is also necessary to demonstrate the functionality of constructs. The functionality of cartilage constructs is largely influenced by its mechanical properties because the primary function of articular cartilage is to bear load. Thus, comprehensive mechanical testing is required to determine whether engineered cartilage constructs can behave similarly to native cartilage under mechanical loading. Often, studies claim the production of their tissue engineered constructs resemble hyaline-like cartilage [75], [166]. The constructs were shown to have upregulated ECM biosynthesis (notably GAGs and collagen content) and altered gene expression of the cells, leading to new ECM deposition and neo-tissue production. However, compared to native cartilage, they lacked the appropriate mechanical properties or no mechanical data was presented to support the claim of hyaline-like cartilage production [75], [166].

One of the main techniques used to create tissue engineered cartilage constructs *in vitro* is to utilise a cell seeded-gel (hydrogel) culture system. In this method, chondrocytes or MSCs are encapsulate within a gel scaffold composed of biopolymers (e.g. agarose) which can be subjected to biochemical (e.g. TGF- $\beta$ 3, TGF- $\beta$ 1 and BMPs) and/or physical (e.g. cyclic compression) stimuli to promote cartilage-like matrix production and tissue formation [75]. Hydrogels have considerable benefits (e.g. manipulable mechanical properties and controllable degradation rates through variations in their fabrication) that can provide appropriate structural matrix support for the encapsulated cells to function [160]. Mauck *et al.* (2003) [196] utilised chondrocyte-seeded agarose hydrogels which were subjected to intermittent deformational loading (10 % strain at 1 Hz, 3 consecutive cycles of 1 hr on and 1 hr off per day, 5 days per week) for two months. This particular loading regime resulted in constructs with increased GAG and collagen contents and a more uniform distribution of collagen type II. In addition, constructs achieved a Young's modulus of approximately 185 kPa and a dynamic modulus of approximately 1.6 MPa [196]. Lima *et al.* (2009) [200] also used an agarose hydrogel system, entrapping bovine chondrocytes. The chondrocytes encapsulated in hydrogels were cultured in a chemically-defined medium supplemented with biochemical stimuli (TGF- $\beta$ 3) for the first two weeks and physical stimulation (10 % unconfined compression initially and tapered to 2 % peak-to-peak deformation by Day 42 at 1 Hz, 3 hrs per day) was then applied either parallel with or after the period of TGF- $\beta$ 3 supplementation for a further 42 days. The resulting constructs following the discontinuation of TGF- $\beta$ 3 showed abundant GAG deposition and a uniform distribution of collagen type II. Constructs also obtained a Young's modulus of 1.3 MPa and a dynamic modulus of 4.1 MPa [200].

More recently, Levato *et al.* (2017) [201] attempted to load bioprintable hydrogels with articular cartilage-derived progenitor cells (ACPCs). A progenitor cell has the ability to drive towards a specific type of cell lineage (but more specific than a stem cell). ACPCs are isolated from a

cartilage source and are suggested to have a high potential to chondrogenic differentiation [201]. Gelatin methacryloyl (gelMA) hydrogels were used to encapsulate and culture ACPCs, MSCs and chondrocytes and used as bioinks for printing. ACPCs and chondrocytes were harvested from equine metacarpophalangeal cartilage while equine bone marrow was used to source the MSCs. By combining bioinks of ACPCs and MSCs in gelMA to co-culture the two cell types, a superior amount and quality of new cartilage matrix was produced within the bioprinted 3D cartilage construct *in vitro*. Histological findings showed it contained zonal-like architecture with defined superficial and deep regions, each with a distinct distribution of cellular and ECM (collagens and GAGs) components. The results indicated the possibility of using ACPCs as a complementary cell source in cartilage constructs production. However, this study solely investigated cell sources for cartilage tissue engineering, in particular the biological performance of ACPCs, in relation to MSCs and chondrocytes and did not provide the mechanical properties of the developed constructs. Nevertheless, the results in the study demonstrated the potential of using ACPC-laden hydrogels for cartilage regeneration as well as opened new avenues for the biofabrication of 3D constructs for *in vitro* tissue models [201].

Another popular approach in tissue engineering of articular cartilage is to use synthetic polymeric scaffolds. A study by Waldman *et al.* (2004) used a combination of chondrocytes seeded in porous calcium phosphate scaffolds and the application of intermittent compression (5 % strain at 1 Hz, 400 cycles every second day) for 4 weeks to create tissue engineered cartilage constructs. These constructs contained approximately 40 % more collagen and 30 % more PGs than the unstimulated controls and achieved a Young's modulus of 80 kPa [202]. In another study combining PCL scaffolds with adult human MSCs (hMSCs) to produce engineered cartilage constructs. A Young's modulus range from 100-400 kPa was obtained depending on the applied loading method (static or cyclic) [203].

The cartilage constructs produced by these methods achieved compressive moduli at the lower end of the values range for human articular cartilage [204], with the highest dynamic modulus reported being 4.1 MPa [200]. These constructs may therefore not be able to resist rigorous compressive and shear forces within the joint. Under physiological loading conditions, the magnitude of mechanical stresses applied to articular cartilage during light to moderate activities ranges between 1 and 6 MPa; therefore these constructs would appear to be insufficiently robust to restore cartilage areas that are subjected to higher levels of stress [204], [205]. However, post-implantation rehabilitation also needs to be considered and failure due to low modulus might only occur if the recipient's usual activities were resumed immediately after implantation of such a construct. Usually, controlled loading such as continuous passive motion (i.e. application of slow and low load) is gradually reintroduced to the joint after the surgical operation [206]. This gradual rehabilitation regime might promote further tissue formation *in situ* and increase the stiffness of implanted tissue over time. It allows time for integration of the

repair tissue to the surrounding native tissue. Thus, with the application of controlled gradual loading to the joint, the repair tissue could reach the appropriate moduli values required to withstand the high stresses imposed on cartilage at the repair site during normal physiological loading. However, engineered cartilage constructs with higher moduli could reduce this rehabilitation time and be advantageous in long-term repair but lateral integration of the construct with the surrounding native cartilage still needs to be achieved [207]. To date, there has been little success in creating functional constructs that have similar biochemical and mechanical properties to those of the surrounding native cartilage for implantation.

A recent method developed by Finlay *et al.* (2016) [1] used mechanical loading to engineer functional constructs *in vitro* for long term cartilage repair. Bovine synoviocytes were seeded onto non-woven polyethylene terephthalate (PET) scaffolds followed by chondrogenic culture for 4 weeks, after which cyclic compressive loading was applied for an hour at 1 Hz, 5 days per week for a further 84 days as shown in Figure 7. The engineered constructs achieved a cartilage-like histological appearance comparable to native cartilage. High dynamic compressive modulus values, with a mean of 15.2 MPa, were obtained from the constructs after 84 days of mechanical stimulation, comparable to the high end values for native cartilage. The high-modulus values obtained from the constructs was attributed to the bioreactor set up used in the experiments and the nature of the mechanical loading regime applied as the constructs matured. The application of compressive loading was achieved by using a force controlled bioreactor and silicone rings. The compressive strain applied to the constructs ranged between 13 % and 23 % depending on the mechanical properties of the immature constructs after 4 weeks in chondrogenic culture. This range of strains appeared to produce suitable stress within the deposited matrix of each construct, presumably via mechanotransductive effects on the residing cells, causing an anabolic response.

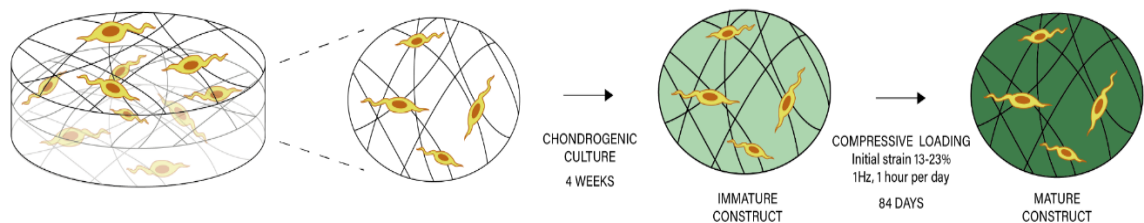


**Figure 7: Schematic of the mechanical loading regime used to create mechanically competent tissue engineered constructs. Figure adapted from [1].**

Under the conditions determined by the bioreactor set up and the confinement of the constructs within silicone rings, construct maturation was believed to cause the applied tissue strain values to change during different stages in construct development as shown in Figure 8. In the early stage of construct development (Day 0 and Day 28), the vast majority of the applied load would be taken up by the silicone ring surrounding each construct but some load would be applied to the cells within the construct causing them to experience a physiologically relevant level of stress that induces an anabolic response. Cells would react to this by upregulating the production and secretion of cartilage-like ECM in an attempt to “resist” the applied load. As the construct continued to mature with increased elaboration of cartilage-like ECM, this would cause an increase in both thickness and compressive stiffness (between Day 28 and Day 56). The accumulation of new ECM would distribute the load away from the cells, thereby reducing cellular stress. However, when the construct matures in this way, under the conditions of the bioreactor set up, a greater proportion of the 5 N load applied by the bioreactor plunger would be taken by the construct as well as increasing the strain applied. Thus, as the stiffness and thickness of the construct increase, the stress (and strain) applied would also increase and remain at a level that promotes further load-distributing- matrix deposition (Day 56). This would continue until the majority of the load is taken by the construct and not the silicone ring (at Day 84). At this point, the effect of mechanical loading on the construct would have reached a plateau and would mainly serve to maintain tissue composition, akin to the homeostasis of native articular cartilage. Finlay hypothesised this to be a “self-adapting” mechanism which causes the external stimulation (the applied stress and strain) to increase as the engineered cartilage become more robust, thereby subjecting the residing cells with consistent stimulation throughout culture to further deposit matrix in maturing the constructs [1]. However, the time period taken to produce such constructs was approximately three to four months which limits its suitability for translation to the clinic. In order to bring this method one step closer to clinical translation, reducing the culture period will increase the feasibility that it will be economically viable (as well as reducing the risk that something might go wrong during culture).

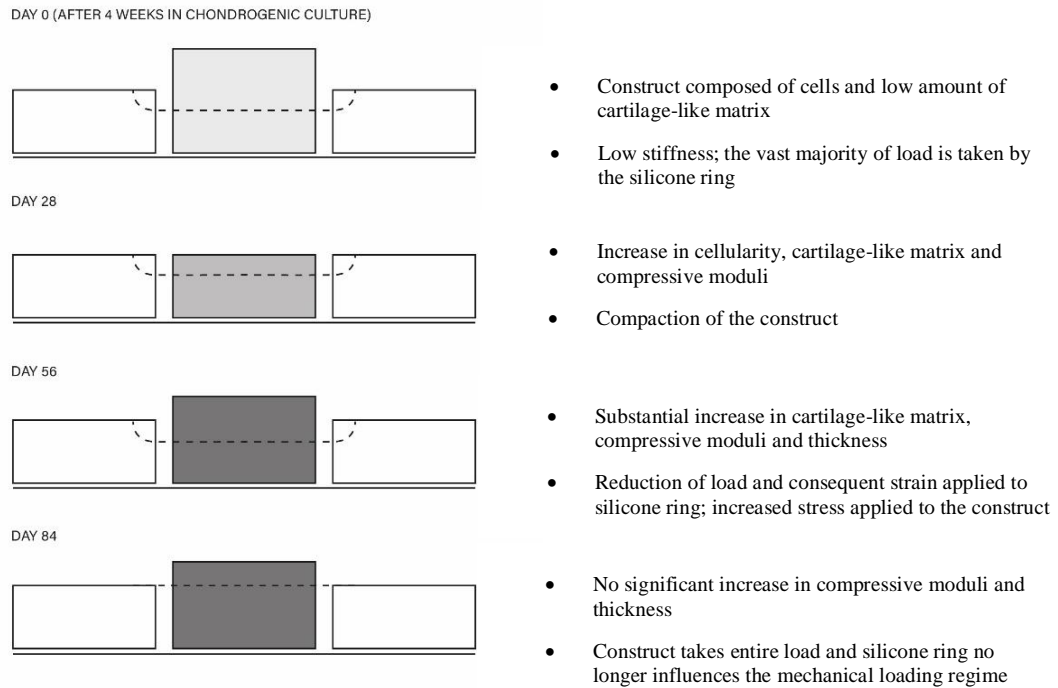


**Figure 8: Finlay's hypothesised mechanism explaining the stages in the development of cartilage-like constructs with the application of compressive loading. Adapted from [1].**

The black dotted line represents the estimated level of strain applied to the construct and silicone ring at each development stage.

## 1.10 Thesis Aims and Objectives

The ultimate goal of the work in this thesis was to bring the method developed by Finlay *et al.* (2016) [1] to engineer functional cartilage constructs one step closer to clinical translation, by accelerating construct development. Reducing the culture period would increase the feasibility of the method to become economically viable. By attempting to provide new insight into the mechanism(s) underpinning the construct's development, new, essential information for promoting matrix synthesis and deposition in future constructs might be derived. Such information could improve efficiency of construct growth with consequential benefits for increased potential for clinical translation and ultimately, patient benefit.

### 1.10.1 Overall Aim

The overall (long term) aim of this study was to improve the efficiency of construct maturation and accelerate the production of mechanically competent cartilage constructs by generating new insights in to the cellular response to applied load.

The effect of cellular deformation within constructs at different stages in their development, in particular the relationship between applied tissue strain and cellular strain, could provide insight on how best to modify the loading regime at different time points to accelerate tissue formation. In cartilage tissue engineering, it is important that an appropriate level of mechanical stress is

received by the cells to favour for the promotion of a chondrocyte-like phenotype and induction of deposition of an appropriate matrix for tissue maturation [208]. An appropriate cellular response to mechanical signals is also essential for the development of *in vitro* mechanically functional engineered cartilage tissue [209]. Thus, a sufficient amount of cell deformation is required to stimulate cells to produce ECM for tissue maturation. It is hypothesised that different magnitudes of applied compression are required for immature and mature constructs to maintain sufficient amount of cell deformation to induce ECM production (Figure 9). For a more mature construct, a greater load might be required to sustain the level of cell stimulation to promote further ECM production and deposition compared to an immature construct with reduced amount and quality of ECM.

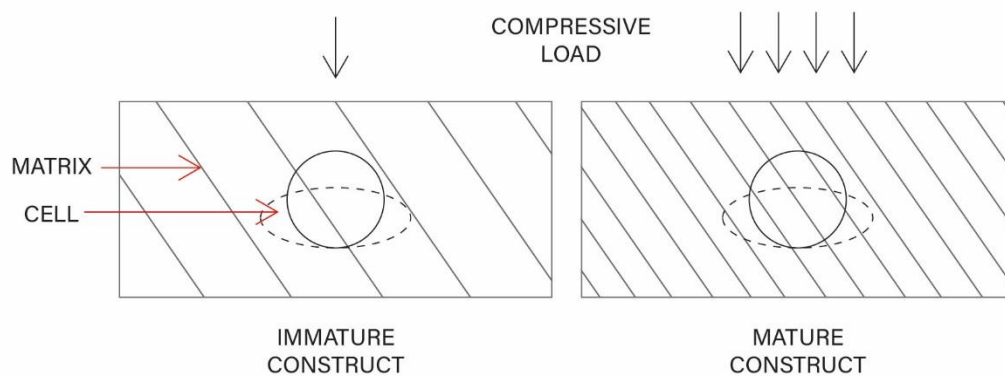


**Figure 9: Schematic of immature and mature constructs after application of different magnitudes of compressive load in order to maintain sufficient amount of cell deformation to stimulate ECM production. A greater applied load would be required for a more mature construct (with different matrix composition compared to immature construct) in order to sustain cell stimulation for further ECM deposition.**

Finlay *et al.* (2016) [1] proposed a underlying mechanism operating by which the immature constructs are transformed into cartilage-like constructs as a ‘self-adapting’ mechanism (see Section 1.9.4). However, the precise mechanism(s) behind the construct’s development, in particular at a cellular level has not been investigated. It is of interest to determine the mechanical stress experienced by the cells within constructs developed at different time points.

The specific aim of this thesis was therefore to study cell deformation behaviour in native cartilage and tissue engineered constructs developed at different time points under incremental compression in an attempt to explore Finlay’s hypothesised mechanism in developing cartilage-like constructs [1] and to address the relationship between applied tissue strain and cellular strain. To achieve this, a methodology for visualising, tracking, imaging and quantifying cell morphological changes within native and tissue engineered cartilage constructs whilst applying tissue compression needed to be developed.

### 1.10.2 Objectives

To determine the effects of compressive strains on cell deformation behaviour in native cartilage and tissue engineered constructs and to address the relationship between the applied tissue strain and cellular strain, the following objectives needed to be achieved:

- Development of a novel device for the application of accurately measured compressive load to native and tissue engineered cartilage constructs with simultaneous live cell imaging (Chapter 2).
- Development of a live cell staining and imaging method for visualisation of cell morphology and morphometric quantification in native and tissue engineered cartilage constructs (Chapter 3).
- Use of the novel compression device and staining and imaging methodologies (Chapter 2 and Chapter 3) to study cell deformation in native cartilage disks under application of incremental compressive strains in real time (Chapter 4).
- Development of cartilage constructs using the method developed by Finlay *et al.* (2016) [1] and use of the novel compression device and staining and imaging methodology (Chapter 2 and Chapter 3) to study cell deformation in constructs developed at different time points under application of incremental compressive strains in real time (Chapter 5).

## **Chapter 2 - Development of A Compression Device for the Application of Tissue Strain**

*This chapter describes the development of a novel compression device capable of applying tissue strains to native and tissue engineered cartilage and simultaneously allow real time visualisation of the changes in cell morphology. To determine the effects of incremental compressive strains on cell deformation behaviour in native cartilage disks (Chapter 4) and tissue engineered cartilage constructs (Chapter 5), the device was capable of delivering compressive strains in accordance with the range of strains that were hypothesised in Finlay *et al.* (2016) [1] used to engineer cartilage constructs and the physiological levels of applied native cartilage strain *in situ* (0 % - 30 % strain) to permit direct measurement of cell dimension *in situ* via confocal microscopy. The device was successfully optimised and used in further investigations as described in Chapter 4 and Chapter 5.*

### **2.1 Introduction**

To study cell deformation behaviour and its relationship to applied compressive strain in native cartilage disks (Chapter 4) and tissue engineered cartilage constructs (Chapter 5), a compression device was required for tissue strain application. In this chapter, the main aim was to develop a device capable of applying a range of precise tissue strain magnitudes and allow visualisation of cell deformation in real time.

Many types of compression devices had been developed and used in previous studies to assess the mechanical behaviour of chondrocytes under static tissue compression in cartilage explants [21], [51], [87], [133]–[138], [210], intact cartilage [85], [145] and isolated chondrocytes cultured in agarose gel [88], [142]–[144]. These compression devices were custom-designed and built specifically for each study to answer their research questions. In fixed cartilage explants studies, Clark *et al.* (2003) [138] and Choi *et al.* (2007) [137] compressed cartilage explants at a range of static load of physiological magnitudes using a cylindrical, flat ended indenter and polysulfone platens, respectively. Compressed cartilage were then fixed prior to the examination of cell deformation via confocal microscopy and histological observation, respectively. Thus, the compression devices used in these studies were only designed for tissue compression load application. In contrast, studies investigated the deformation behaviour of chondrocytes in non-fixed native articular cartilage and isolated chondrocytes seeded in agarose gel required an apparatus that was able to simultaneously apply tissue compression and allow real time visualisation of the changes in chondrocyte morphology [51], [87], [88], [110], [133]–[135], [137], [142]–[144]. These compression apparatuses only accommodated samples that were prepared to semi-cylindrical/strip shapes. However, tissue preparation by

cutting/sectioning the cartilage tissue after harvesting would compromise the tissue integrity and alter the material properties of the cartilage which consequently would affect the mechanical environment around the chondrocytes. In addition, fixed tissue may not reflect on the instantaneous properties of chondrocytes within the cartilage tissue. Thus, fixed and cut tissue approaches were avoided in this thesis. Due to the specificity in the designs of compression device used in previous studies, a novel device was therefore required to be developed specifically for non-fixed and non-cut samples (i.e. native cartilage disks and tissue engineered cartilage constructs) in this thesis, to allow compressive tissue strain application and simultaneous live cell imaging, in order to examine cell deformation behaviour under different magnitudes of compressive tissue strains. The different apparatuses used in the previous studies illustrated a variety of design characteristics that needed to be carefully considered for the development of the compression device in this study.

Application of dynamic compression would be the ideal for use in a device to be developed in this thesis for studying cell deformation behaviour in tissue engineered cartilage constructs (Chapter 5), in an attempt to better understand Finlay's hypothesised mechanism in developing cartilage-like constructs and to address the relationship between the applied tissue strain and cellular strain. As mentioned in Section 1.9.4, Finlay *et al.* (2016) [1] used a force controlled bioreactor for cyclic compressive loading application to engineer cartilage constructs. The bioreactor was developed to simulate, as closely as possible, the physiological demands upon cartilage. Compressive loading was applied to the constructs continually by the bioreactor for an hour at 1 Hz, 5 days per week during construct development which in itself mimics the physiological situation ( see Section 5.2.2 for full methodology). However, experimentally, it is difficult to record and quantify the three-dimensional (3D) changes to cell morphology in cyclic loading conditions due to the practical difficulties of loading in a controlled, physiological, dynamic manner and simultaneously capturing 3D morphological changes. To date, not many studies have investigated cell deformation behaviour in native or tissue engineered cartilage under dynamic loading. In addition, to the author's best knowledge, no study has managed to determine 3D measurements of cells within native and tissue engineered cartilage under cyclic loading. There have only been *in silico* studies that simulate the mechanical response of chondrocytes to cyclic compression loading using finite element modelling [211] and a study that measured the 2D deformation of isolated chondrocytes in agarose gel during both static and cyclic compressive loading [141].

In the previous studies of assessing cell deformation behaviour under static uniaxial compression in native cartilage explants or when seeded in agarose gel, chondrocytes were subjected to either confined [133], [134], [136] or unconfined [51], [87], [135], [143], [210] but unconfined loading has typically been used [87], [128]. In a device that utilised confined compression, a cartilage sample was often placed in a rigid chamber so that radial confinement was achieved [133], [134], [136]. Ideally, the dimension of the cartilage should be equal to the

internal dimension of the chamber to avoid any friction occurring at the interface. A porous platen would then be used to compress the cartilage so that exudation of interstitial fluid could occur in one direction [133], [134], [136]. Measurements under such loading can be difficult to achieve for native cartilage and especially for tissue engineered constructs due to their unpredictable growth (in all dimensions). This can be overcome by cutting both native and tissue engineered cartilage to size but this would affect the tissue mechanical integrity as previously mentioned in this section which would consequently change the local mechanical environment around the cells. In unconfined compression devices, two impermeable platens would often be used to compress the cartilage [51], [87], [135], [143], [210]. Cartilage samples would be allowed to deform radially in its cross-section, leading to fluid exudation from the circumference. Unconfined measurements would not be affected by cross-section irregularity, as it does with confined measurements and therefore it could be argued that this loading configuration is better suited to variable tissue engineered constructs. In addition, unconfined compression configuration would better replicate the loading scenario in the bioreactor used in Finlay *et al.* (2016) [1] for compressive loading application to engineer cartilage constructs ( see Section 5.2.2 for full methodology). During compressive loading, each construct was confined within a silicone ring that would be significantly stiffer than the constructs themselves. The compressive force generated in the bioreactor was applied to the constructs via impermeable loading platens and fluid flow would occur radially inside the constructs during compressive loading, similar to that observed in unconfined compression configuration. Thus, in this thesis, unconfined uniaxial static compression was selected as the loading method for the device.

The aim of the work in this chapter was to design and build a novel device for compressive tissue strain application and allow simultaneous live cell imaging in order to examine cell deformation behaviour within native and tissue engineered cartilage. The ability to apply accurate strain values to cartilage tissue/construct disks was a vitally important design aspect of the device. In order to have good control on the applied strain, a micrometer head (Mitutoyo, Japan, 148-201), with a low graduation of 10  $\mu\text{m}$  step and an accuracy of  $\pm 5 \mu\text{m}$  was used for compressive tissue strain application. It was also essential to consider the loading configuration with respect to the axis of the optical path microscope.

The aim of this study was approached via the following objectives:

- To outline the design specification for the compression device.
- To compare two compression device designs based on loading configuration perpendicular and parallel to the axis of the light path, respectively, to determine which best suited to the design specification (both designs used a micrometer for compressive tissue strain application).
- To manufacture the final version of compression device

- To validate the chosen compression device design; to determine the ability of coverslip to withstand a 5 N load, the extent of coverslip flexion under applied load and the micrometer accuracy for compressive tissue strains application.

## 2.2 Device design specification

Confocal microscopy was the imaging mode of choice in this thesis for visualisation of cellular deformation in native and tissue engineered cartilage constructs under compressive loading because of its ability to produce a 3D view of living cells within a given tissue/construct sample with minimal destruction (more detail in Section 3.1.1). Quantitative cell morphology measurements could be recorded using an image analysis software based on the 3D reconstruction of cells captured from the confocal image. The methodology used to visualise and quantify the cell deformation behaviour in native cartilage disks and tissue engineered cartilage constructs under compressive loading will be described in Chapter 3.

The aim of this chapter was to develop and build a compression device for the application of compressive tissue strain to assess the effects of incremental compressive strains on cell deformation in native cartilage disks (Chapter 4) and tissue engineered cartilage constructs developed at different time points (with and without loading in the bioreactor) (Chapter 5). Thus, the device was designed to allow confocal visualisation of the morphology of the respective embedded cells within native and tissue engineered cartilage whilst applying selected compressive strain accurately to the tissue or construct. To determine the effects of incremental compressive tissue strains on chondrocyte deformation behaviour in native cartilage disks, incremental static compressive tissue strain values of 10 % and 15 % were used in Chapter 4 to correspond to physiological range of native cartilage strains *in vivo* of between 0 % and 30 % [20], [35], [36]. In Finlay *et al.* (2016) [1], it was hypothesised that the loading regime was continually self-adjusting as the constructs developed i.e. the applied stress and strain increased with changes in constructs' stiffness and thickness (Section 1.9.4). The device being developed here therefore needed to be able to apply a range of compressive strains in accordance with the range of strains that were hypothesised in Finlay *et al.* (2016) [1] and the physiological levels of applied native cartilage strain *in situ* in order to study the cell deformation behaviour in native cartilage disks as well as in constructs developed at different time points.

For the device to achieve its purpose, a number of design requirements needed to be met. The device was required:

- To apply a range of compressive strain magnitudes in accordance with the range of strains that were hypothesised in Finlay *et al.* (2016) [1] and applied to native cartilage *in situ*.
- To keep cells and tissue viable for the duration of experiments.
- To mount onto the stage of a confocal microscope system.

- To accommodate native and tissue engineered cartilage disks with dimensions of approximately 5 mm in diameter and 1-2 mm in thickness.
- To allow confocal visualisation of the respective embedded cells at different regions of native and tissue engineered cartilage with good optical resolution.
- To be easily cleaned and maintained.
- To have sound optical qualities and material properties (e.g. biocompatibility and stiffness).
- To tolerate applied compression.

## **2.3 Compression Device Designs**

### **2.3.1 Loading configurations**

In previous confocal microscopy studies in determining chondrocyte deformation in non-fixed native cartilage explants [21], [51], [87], [133]–[136], [210], intact cartilage [85], [145] or in isolated chondrocytes in agarose gel [88], [142]–[144] under static compression, the compression devices followed either loading configurations perpendicular or parallel to the axis of the light path depending on the experimental set-up (e.g. different confocal microscope systems, sample shapes and region of interest used).

In this thesis, fixed and cut tissue approaches were avoided and therefore non-fixed disk shaped samples (i.e. native cartilage disks and tissue engineered cartilage constructs) were used. The two loading configurations considered for the device to accommodate disk shaped samples in this thesis are shown in Figure 10. The first loading configuration applied compression perpendicular to the axis of the microscope's objective (Figure 10A). By observing fluorescently labelled cells in this test configuration, this would enable visualisation of cells throughout the full depth of the sample. For example, in a native cartilage explant, this would theoretically enable visualisation of chondrocytes in different zones within the tissue. However, the downside of this set-up would be that only cells located at the circumferential edge could be observed as the imaging depth is limited by the laser penetration of the confocal microscope. In order to capture cell deformation changes under compression, high resolution images of cells are required and therefore a high magnification objective lens must be used. High magnification lenses usually have short working distances. This is not a problem if an inverted confocal microscope was to be used with this set-up. However, if an upright confocal microscope was used, the short working distance and the small gap between the sample and the lens could potentially cause difficulty when manoeuvring the microscope stage to locate cells for imaging.

The alternative loading configuration applied loading parallel to the optical path of the microscope (Figure 10B). By adopting this test configuration, visualisation of cell deformation on both sample surfaces would be facilitated. In a cartilage explant, it would be possible to visualise chondrocytes in the superficial and deep zones but visualisation of the middle zone

would be limited by the laser penetration of the confocal microscope. In this set-up, there is scope for greater manoeuvrability of the microscope stage, allowing observation of cell deformation at the outer edge and central regions of the sample surfaces. Based on these loading configurations, a design was initially proposed for each configuration.

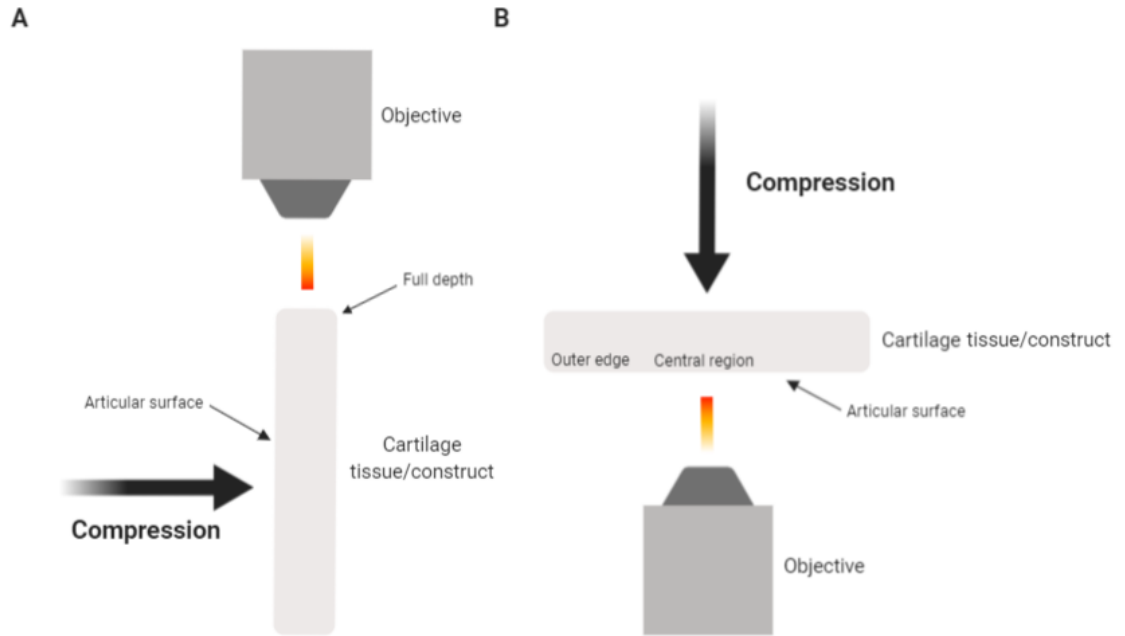


**Figure 10: Diagram showing the two potential loading configurations for the compression device; application of compression on a cartilage tissue/construct disk (A) perpendicular and (B) parallel to the axis of the light path of the confocal microscope.**

### 2.3.2 Compression Device Design Based on Loading Configuration

#### Perpendicular to the Axis of the Light Path

The design of a device incorporating the loading configuration perpendicular to the axis of the optical path is shown in Figure 11. It was important to be able to assemble/disassemble the individual components to make it easier to clean and maintain the device (Section 2.2). This device was created for use with an upright confocal microscope (Leica TCS-SP2, Leica Microsystems, Milton Keynes, UK). The overall device dimensions were 29.7 x 29 x 16 mm, allowing for fit onto the confocal stage. In addition, this device can accommodate native and tissue engineered cartilage disks with dimensions of approximately 5 mm in diameter and 1-2 mm in thickness.

The device comprises of a chamber in which three additional walls are placed inside; the front and back wall are fixed in place and the middle wall is able to slide along inset rods. The sample holder is positioned into a slot located in the front wall where a cartilage tissue/construct disk is oriented with the sample surface parallel to the face of the sample holder, while the compression platen slots into the middle wall. The compression platen aligns with the sample holder and the uniaxial compression would be applied parallel to the sample surface using a micrometer. The

micrometer asserts load directly onto the middle wall, which in turn moves the compression platen towards the sample to apply the desired strain. All of the components described above are assembled and placed inside a fluid chamber which can be filled with Live Cell Imaging Solution (described in Chapter 3) to maintain cell viability during imaging. For visualisation of cellular deformation in cartilage tissue/construct samples, the chamber height would be sufficient for a water immersion objective to descend into the culture medium close to the circumferential edge of the sample.

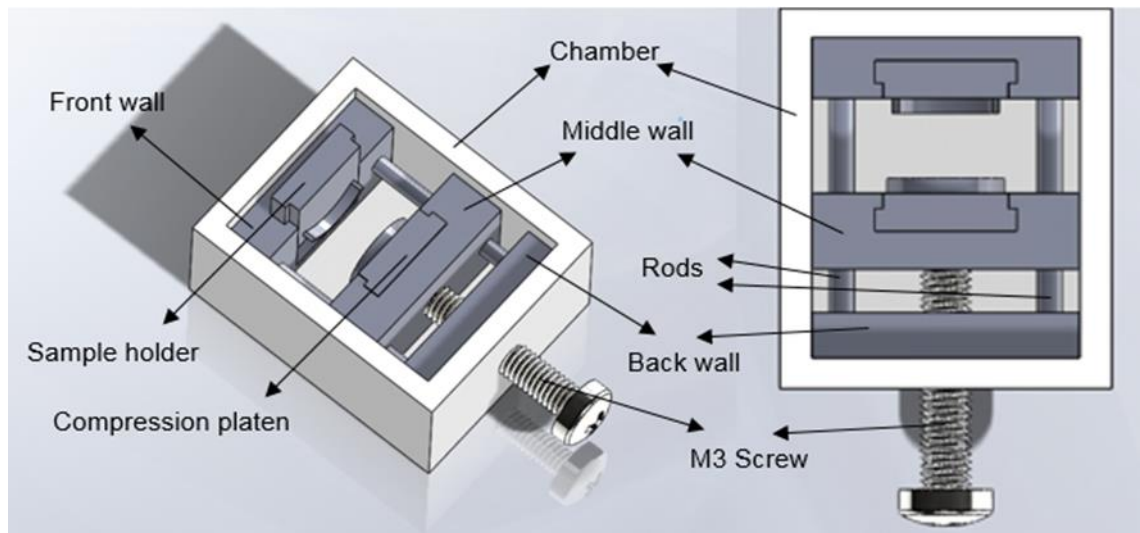


**Figure 11: Schematic of compression device design based on perpendicular loading configurations to the axis of the light path for use in an upright confocal microscope. The design features include a chamber, front, middle and back walls, a sample holder, a compression platen, rods and a M3 screw/micrometer. The compression device is presented in 3D and top views.**

### **2.3.3 Compression Device Design Based on Loading Configuration Parallel to the Axis of the Light Path**

The design of a device that accommodates the application of strain parallel to the plane of the microscope light path is shown in Figure 12. This device can accommodate native and tissue engineered cartilage disks with dimensions of approximately 5 mm in diameter and 1-2 mm in thickness. This device was created for use with an inverted confocal microscope system (Nikon A1R, Nikon Instruments Inc, Surrey, UK). The dimensions of the device allows it to mount upon the stage of the confocal microscope system, enabling visualisation of respective fluorescently labelled cells within native and tissue engineered cartilage subjected to static compression. The requirement of assembling individual components (for ease of cleaning) to form the device was also incorporated in this design.

The device consists of a well with an opening at the bottom, a coverslip, a platen, a magnetic disk, a brace, metal screws and a micrometer (Figure 12B). To set up the device, a coverslip is sealed to the open bottom of the well using silicone grease to provide fluid confinement within the well. A sample (i.e. native cartilage disks/tissue engineered cartilage constructs) would then be placed on top of the coverslip, inside the well (with the imaging surface faces down towards

the coverslip). The coverslip allows penetration of the laser from the confocal microscope through to the sample and reflect back to build up an image of the cells. The well would be filled with Live Cell Imaging Solution (described in Chapter 3) to maintain cell viability. A platen with an magnetic disk attached on top of it, that fitted and slid freely in the channels at either side of the well is positioned on top of the sample. The brace is then secured to the well by two metal screws with the micrometer fixed onto the brace by a small screw. A compressive displacement is achieved using a micrometer, which is applied in a direction parallel to the axis of the microscope light path. The micrometer connects with the platen via the magnetic disk in which load is asserted onto the platen, which in turn applied the desired strain onto the tissue.

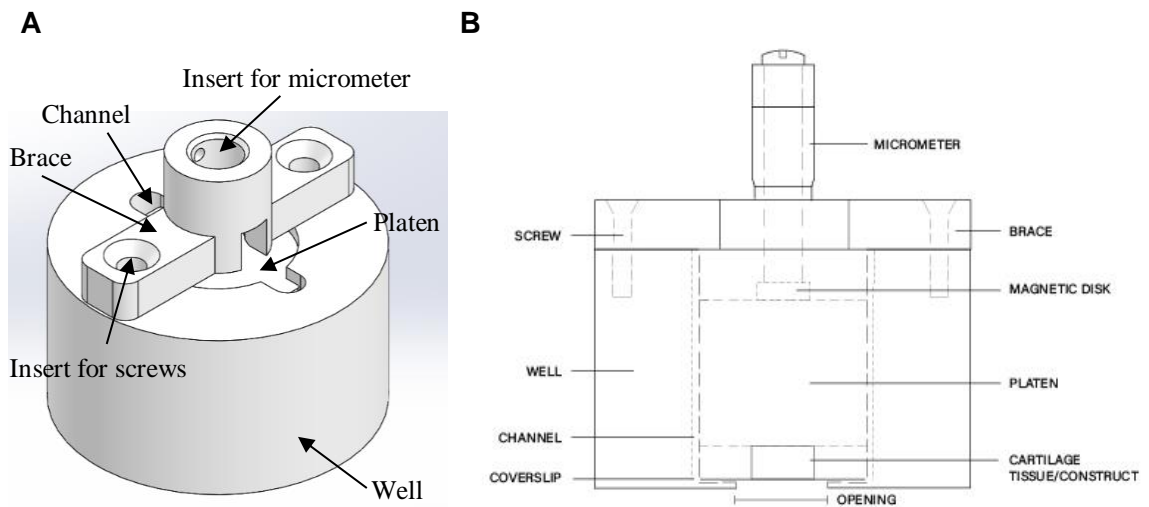


**Figure 12: (A) Schematic of the compression device design based on perpendicular loading configurations to the axis of the light path without the micrometer in a 3D view and (B) a sketch of the components (a well with an opening at the bottom, a coverslip, a platen, a magnetic disk, a brace, metal screws and a micrometer) which assemble to form the device in a side view. The compression device can be used to apply compressive tissue strains on native cartilage and tissue engineered cartilage construct disks.**

### **2.3.4 Final Design of Compression Device Based on Loading Configuration Parallel to the Axis of the Light Path**

Both proposed designs described based on different loading set-ups (described in Section 2.3.2 and Section 2.3.3) have their advantages and disadvantages. Ultimately, the configuration of parallel loading to the confocal optical path (Figure 10B) was selected as being more suitable for applying compressive load whilst visualising cells under confocal microscopy in this thesis than the perpendicular loading configuration (Figure 10A).

Loading perpendicularly to the light path enables visualisation of cells through the full depth of both cartilage tissue/construct disks as illustrated in Figure 10A. However, the biggest downside of this set-up is that confocal imaging is restricted to the circumferential edge only, due to the limited penetration depth of the laser. In unconfined compression, inhomogeneous strain fields occur near the edges of the tissues and thus it is better to avoid such regions [137]. In addition, the need to harvest the cartilage samples in the first place by drilling would have compromised

the cutting edge (i.e. the circumferential edge) (see Section 3.3.3). Dead chondrocytes are likely to be present at the cut periphery due to the increased temperature created from the drilling and the mechanical integrity would have been affected which consequently affect the mechanical environment around the cells in that region. It would be less than ideal to image a potentially damaged region. Another shortcoming of this set-up is the difficulty in locating cells from a small region (basically the thickness of the sample) for cell imaging. As well as the small gap, the short working distance on high magnification lenses contributes to this problem if an upright confocal system is used because it would be challenging to manoeuvre the microscope stage above such a small region.

One big advantage of using the proposed set-up of parallel loading to the optical path for strain application is that it can visualise living cells from the central region or outer edges on both cartilage tissue/construct disk surfaces (Figure 1B). However, the strain field along the central axis of the sample would be more homogenous than at the edges and therefore it is better to avoid the edges [137]. For native cartilage disks, the articulating surface/superficial zone is the sample area that is the least likely to be damaged following the harvesting process compared to the opposite surface where the deep zone is located. Living cells would therefore be expected to be found on the articulating surface. In addition, the cartilage tissue/construct disk surface provides a larger area so that there is a greater potential regions to image and easier for the microscope stage to manoeuvre during imaging. The only downside of this set-up is the limited visualisation of cells within the core of a disk due to lack of penetration of the laser.

After consideration of the advantages and disadvantages of both designs, application of compressive loading parallel to the optical path was selected to be used in the device (described in Section 2.3.3).

### **2.3.5 Compression Device Fabrication**

Manufacturing and assembling individual components to form the device was utilised to facilitate maintenance and to be able to comprehensively clean the device. Additive and traditional manufacturing methods were originally investigated as fabrication methods for the device. 3D printing was an attractive choice because it is a relatively inexpensive process with costs significantly lower than other manufacturing methods for the production of prototypes or one-off functional parts. Another attractive feature of 3D printing is the speed at which objects can be produced compared to traditional manufacturing methods. Designs can be uploaded from a CAD model and printed in a few hours. This allows rapid development, testing and verification of different design ideas with prototypes. In addition, the design can be easily altered by adjusting the digital print and therefore changes can be made easily and quickly before the design is finalised. This technology has good utility for the production of custom, one-off parts that would normally need more than one manufacturing processes to make. The

ability to build a part (with complex geometries) in one step makes this method more cost-effective and efficient.

Although additive manufacturing is an attractive method to use for manufacturing the device, the degree of precision required for the device components was not achieved from the 3D printers used in attempt to manufacture the device, therefore additive manufacturing was used only for the purpose of prototypes and assessing the design. Prototypes were produced to verify the design, form and fit of the device. Ultimaker 2, the 3D printer, and acrylonitrile butadiene styrene (ABS), the material, were used in the manufacture of the prototype at Xiros Ltd (Leeds, UK) prior to the fabrication of the compressive device.

Once the design was finalised, the device was manufactured by Kirkstall Precision (Leeds, UK) using traditional machining. Delrin<sup>®</sup> acetal homopolymer (Polyoxymethylene) (DuPont, USA) was selected as the material of choice to fabricate the device because it offers high compressive strength and stiffness so it can withstand the compressive forces imposed by the micrometer and will not deform [212]. It is also easily machineable so complex components could be manufactured. Choosing a medical grade Delrin<sup>®</sup> avoids any issues regarding biocompatibility. Due to all component parts of the device being in close proximity to the microscope optical path where the laser scans the tissue, matt black Delrin<sup>®</sup> was chosen as it could minimise back-scattered light and background fluorescence and therefore improve the quality of confocal images acquired.

## **2.4 Validation of Compression Device Final design**

### **2.4.1 Introduction**

Compression device design based on loading configuration parallel to the axis of the light path, as described in Section 2.3.3, was selected as the final version of the device. This then needed to be validated prior to use in later experiments. This device was created for use on the Nikon A1R inverted confocal microscope. Within the device, a 12 mm opening situated at the bottom of the well (Figure 13) was designed to accommodate different objective lenses for microscopic visualisation (see Section 3.4.5) and allow enough space to avoid high magnification lenses (i.e. 40x and 100x oil immersion objectives described in Section 3.4.5) hitting the opening edges of the well when manoeuvring the microscope stage. As compressive load is applied parallel to the optical path, the coverslip that is sealed to the bottom of the well where the opening is located could be potentially subjected to a high amount of force (Figure 13). For this set-up to work, the coverslip would be required to sustain the applied load and not shatter.

Commercially available coverslips come in a variety of thicknesses, typically range between 0.9 and 0.25 mm (e.g., Scientific Laboratory Supplies, Fisher Scientific and Boli Optics) and to accommodate their use with different objective lenses. Using an inappropriate coverslip

thickness can cause image degradation due to optical aberrations [213]. In order to achieve the best image quality (brightest, crispest, high resolution), a coverslip of the correct thickness is required, especially with higher magnification lenses. Most modern objectives are designed to be used with a 0.17 mm-thick coverslip [213]. With that in mind, the coverslip used in the device was also required to be strong enough to withstand the applied load as previously stated.

In addition to the coverslip itself, there needed to be sufficient support for the coverslip on top of the opening. Due to the exact measurement required to mount the device securely onto the microscope stage, any changes to the external diameter of the device (Figure 13) were restricted. With a 12 mm opening situated at the bottom of the device, the internal diameter of the device was required to be larger than the opening itself in order to provide an inner ledge within the well to provide support for the coverslip as shown in Figure 13. Thus, the proposed inner diameter of the device was 18 mm. Experimentation was therefore undertaken to validate whether an 18 mm internal diameter of the device provided sufficient support for the coverslip that is sealed on top of a 12 mm opening. The experimental set-up mimicked the load application that was planned to be delivered in the device during later investigations. The amount of load applied to the tissue/construct disks would be dependent on the strains to be identified in this thesis but a maximum load of 5 N, the same load applied in the bioreactor during the development of constructs, would be expected to be endured by the coverslip. Static load would be expected to be applied for a maximum duration of approximately 3-4 hrs during confocal imaging. Prior to the fabrication of the device, coverslips with different thicknesses ( $0.14 \pm 0.01$  mm and  $0.17 \pm 0.01$  mm) were therefore tested under 5 N of load for a duration of comparable length to determine the ability of coverslips to withstand applied load and if an 18 mm internal diameter of the device provided sufficient support. The coverslip capable of

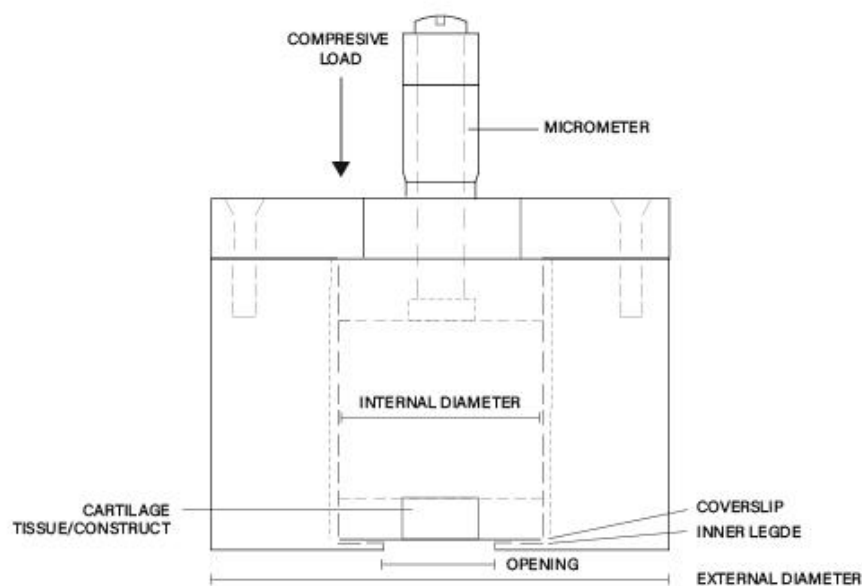


**Figure 13: A sketch of the compression device which shows the inner ledge required to provide support for the coverslip that is sealed on top of an opening at the bottom of the device to withstand the load applied parallel to the coverslip surface.**

consistently withstanding the maximum applied load of 5 N for over 4 hrs would then be suitable to use in the chosen device design.

Direct application of compressive load onto the coverslip would cause it to bend as shown in Figure 14. This flexion would need to be taken into consideration when applying accurate tissue strain values in later experimentations. The amount of coverslip flexion caused by applied load was therefore investigated once the device was manufactured. To accomplish this, coverslips of different thicknesses ( $0.14 \pm 0.01$  mm and  $0.17 \pm 0.01$  mm) were loaded in the device up to 700 g (~7 N) and the displacement values were recorded. A higher load than 5 N was chosen because it shows the glass flexion behaviour beyond the maximum applied load of 5 N that will be used in later experimentations.

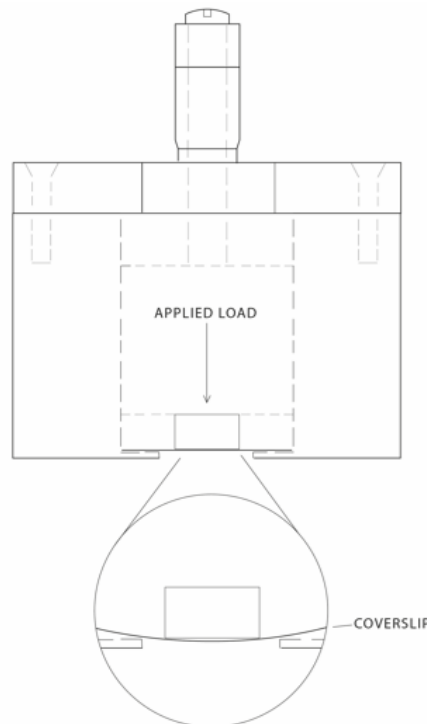


**Figure 14: A sketch of the compression device showing that when load is directly applied onto the coverslip, it would cause bending to the coverslip.**

Accurate application of compressive tissue strain was vital to the success of the planned investigations and a micrometer was selected for this purpose as part of the device design. Before the device was used for experimentations, the accuracy of the micrometer was validated against a Bose ElectroForce 3200 mechanical testing machine (TA Instruments Inc, New Castle, USA) because this machine is well suited for low force/displacement testing. Once the compression device was manufactured, the thickness of an acrylic disk (with similar dimensions to the cartilage tissue/construct disks to be used in the investigations) was recorded using the compression device and a Bose ElectroForce 3200 mechanical testing machine and compared to determine the accuracy and precision of the micrometer. Acrylic was chosen because of its high compressive modulus relative to the load being applied [214] and therefore it was assumed that the acrylic disk would not deform in the experimental set-ups. Native cartilage disks were also

tested to investigate the accuracy of the device because they are representative of future samples (Chapter 4) and cartilage disks are more likely to deform under small loads compared to the more resistant acrylic disk.

Thus, for the device to succeed, several investigations were carried out to characterise its performance. These included:

- Application of 5 N static load to coverslips of different thicknesses
- Coverslip flexion under applied load
- Validation of micrometer accuracy

## **2.4.2 Experimental Methodologies**

### **2.4.2.1 Application of 5 N Static Load to Coverslips of Different Thicknesses**

Prior to the manufacture of the device, coverslips with different thicknesses were tested with support around them (described previously, see Section 2.4.1) to determine their ability to withstand 5 N of load over periods of time commensurate with the expected experimental duration. Eighteen mm-diameter coverslips with thicknesses of  $0.14 \pm 0.01$  mm and  $0.17 \pm 0.01$  mm were used in this investigation and three coverslips from each thickness group were tested. The experimental set-up to study the ability of coverslips to withstand a 5 N applied load is shown in Figure 15. Two acrylic plastic blocks were set apart to a distance of 12 mm with a coverslip placed on top to replicate the opening at the bottom of the device. An acrylic disk, approximately 5 mm in diameter and 1.8 mm in height (similar dimensions to the tissue/constructs samples to be investigated later), was placed on top. A prototype of the device was manufactured as described previously (Section 2.3.5) in which the platen was used in this investigation. This was placed on top of the acrylic disk along with a weight of 510 g (5 N), overnight. The coverslips were then checked for any signs of damage, cracks and permanent deformation.

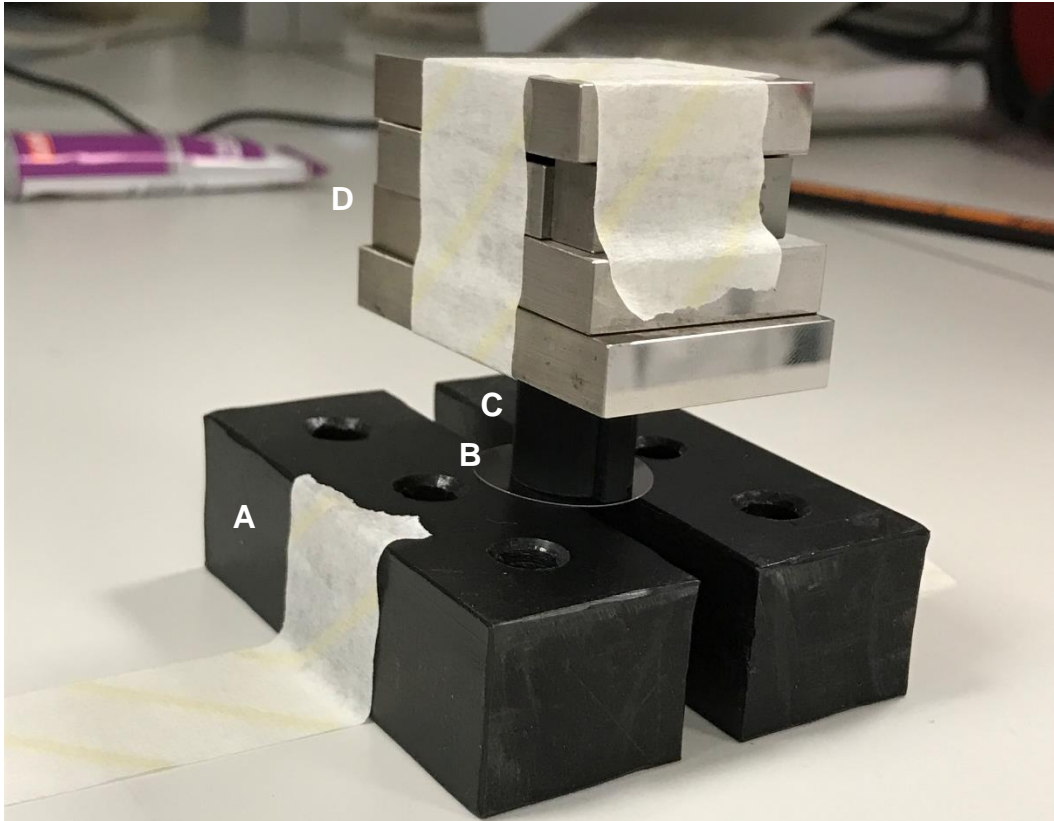


**Figure 15: Experimental set up for investigating coverslip ability to withstand 5 N applied load for protracted periods of time: (A) support plastic blocks, (B) coverslip, (C) the platen of the prototype device, (D), 5 N of applied load.**

#### **2.4.2.2 Coverslip Flexion under Applied Load**

The amount of coverslip flexion caused by applied load was determined on 18 mm-diameter coverslips with thicknesses of  $0.14 \pm 0.01$  mm and  $0.17 \pm 0.01$  mm ( $n=3$  per thickness group) once the device was manufactured. Coverslips were randomly selected and tested as described in the below protocol in order to compare the flexion behaviour between the two thickness groups. The compression device was fabricated as described previously (Section 2.3.5) in which the well and the platen were used in this investigation. First, a coverslip was sealed to the opening located at the bottom of the device using silicone grease. An acrylic disk (described Section in 2.4.2.1) was placed in the centre of the well to use as a sample to test the glass flexion under load. The acrylic disk was used because it would not deform under the selected load (700 g,  $\sim 7$  N) due to its high compressive strength [214]. The platen was then placed directly on top of the acrylic disk. Compressive load was applied using a Bose ElectroForce 3200 mechanical testing machine and the testing rig was set up as shown in Figure 16. A 10 N load transducer was fixed on the base of the rig frame to which a wide platen was attached. A smaller cylinder shaped platen was attached to the test rig actuator with two screws. The prepared compression device was placed at the centre in between the two platens. Under the control of the Bose Wintest software, the top platen was lowered to the compression device at a rate of 0.2 mm/s until a tare load of 0.02 N was reached to establish a ‘zero displacement’

position. At the 'zero displacement' position, the load was ramped up to 700 g ( $\sim 7$  N) in intervals of 50 g (10 secs hold at each interval) and the displacement values were recorded at each 50 g interval.

After identifying which coverslip thickness is suitable for use in the device, coverslips from the selected thickness group were tested in the same set-up but they were subjected to loads between 0.02 g and 700 g at a rate of 50 g/s, whilst recording displacement (at a rate of 200 Hz). Displacement/load profiles were obtained for six coverslips and a standard curve was created (Figure 18).



**Figure 16: Bose mechanical testing machine set up for coverlip deflection testing under compression: (A) connection to the actuator, (B, C) platens, (D) compression device and (E) connection to 10 N load transducer.**

#### **2.4.2.3 Validation of Micrometer Accuracy**

To validate the micrometer accuracy in the compression device against a Bose ElectroForce 3200 mechanical testing machine, an acrylic disk and bovine cartilage disks were used as samples. The full methodology for harvesting bovine cartilage disks is described in Section 3.3.3. Thickness measurements were obtained using both the compression device and a Bose ElectroForce 3200 mechanical testing machine.

To measure thickness utilising the compression device, the 'zero' position was first established by assembling the device together in the absence of any sample. First, a coverslip was sealed to the opening located at the bottom of the device using silicone grease prior to placing the platen on top. The micrometer was then secured to the device by the brace and lowered until it connected with the platen via the magnetic disk and the distance value displayed on the micrometer at this position was recorded as the zero position. The device was then set up again with the sample placed in the centre of the well filled with phosphate buffered saline (PBS) (Sigma-Aldrich, Irvine, UK, D8537). Prior to lowering the platen to the sample, the micrometer fixed to the brace was connected to the platen via the magnetic disk and secured to the device. The platen was then lowered towards the sample by the micrometer until the platen made contact with the sample. The distance value displayed on the micrometer was recorded at this position. Sample thickness was determined by the difference between the distances displayed on the micrometer with and without the sample. A Bose ElectroForce 3200 mechanical testing machine used to obtain thickness measurements was set up as described previously in Section 2.4.2.2 but without the device. The platens were brought together with a load of 200 g to establish a 'zero displacement' position, before being set apart by 3 mm. Within this space, a column of PBS was formed in which a sample was held. Under the control of the Bose Wintest software, the top platen was lowered at a rate of 0.2 mm/s until a tare load of 0.02 N was reached to determine the thickness.

Six repeats of an acrylic disk's thickness were recorded using both measurement methods. For native cartilage, six disks were measured.

### **2.4.3 Results**

#### **2.4.3.1 Ability of Coverslip to Withstand 5 N Static Load**

Prior to the fabrication of the device, coverslips with different thicknesses ( $0.14 \pm 0.01$  mm and  $0.17 \pm 0.01$  mm) were tested under 5 N of static load overnight with 3 mm of plastic blocks on each side of the coverslip to determine their ability to withstand applied load and to validate if an 18 mm internal diameter of the device provided sufficient support for the coverslips. No signs of damage or cracks and no permanent deformation were observed on the tested coverslips (n=3 per thickness group) with the application of load after 12 hrs.

#### **2.4.3.2 Coverslip Flexion under Applied Load**

The amount of coverslip flexion caused by applied load was determined on coverslips with thicknesses ( $0.14 \pm 0.01$  mm and  $0.17 \pm 0.01$  mm, n=3 per thickness group) once the device was fabricated. The displacement of  $0.17 \pm 0.01$  mm-thick coverslips appeared greater than that seen for coverslips with  $0.14 \pm 0.01$  mm thickness when the load was ramped up, suggesting that more flexion occurred in  $0.17 \pm 0.01$  mm-thick coverslips (Figure 17). However, there was no

statistical difference between the two coverslip thickness groups when compared using a repeated ANOVA test.

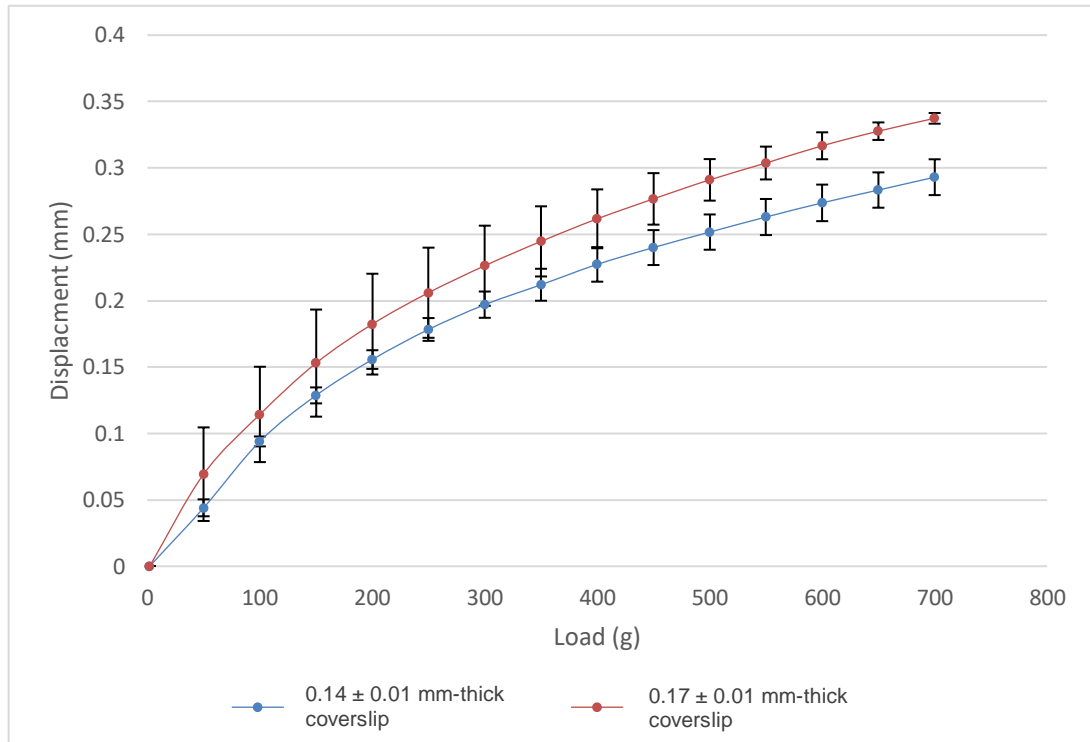


**Figure 17: Glass flexion profile of 0.14 ± 0.01 mm and 0.17 ± 0.01 mm-thick coverslips under load of 700 g.**

Displacements obtained by 0.17 ± 0.01 mm-thick coverslips were greater than 0.14 ± 0.01 mm-thick coverslips but no significant difference. Data represented as mean ± SD at each 50 g interval (n=3, per thickness group). Statistical analysis was determined by repeated ANOVA.

### 2.4.3.3 Validation of Micrometer Accuracy

The accuracy of the micrometer in the compression device was validated against a Bose ElectroForce 3200 mechanical testing machine with regards to thickness measurements. The thicknesses of an acrylic disk and bovine cartilage disks were recorded using both measurement methods. The thickness values for an acrylic disk measured by the device and a Bose ElectroForce 3200 mechanical testing machine were markedly similar. There was an absolute difference of 1.1 % between the values but no significant difference when tested statistically using a t-test (Table 1). Cartilage thickness measurements obtained by the same measurement methods were again similar. There was no statistically significant difference between measurements recorded using either methods when tested statistically using a paired sample t-test (Table 1).

**Table 1: Thickness measurements of an acrylic disk and bovine cartilage disks obtained using the compression device and a Bose Electroforce 3200 mechanical testing machine. There were no statistical significances found in thickness measurements of an acrylic disk (6 repeats) and bovine cartilage disks (n=6) between the two measurement methods. Data represented as mean  $\pm$  SD (n=6). Statistical analysis was determined by t-test for the acrylic disk and paired t-test for bovine cartilage disks.**

	Thickness obtained from compression device (mm)	Thickness obtained from Bose ElectroForce 3200 mechanical testing machine (mm)	Difference (%)
An acrylic disk	1.70 ( $\pm$ 0.020)	1.682 ( $\pm$ 0.012)	1.1 %
Bovine cartilage disks	1.52 ( $\pm$ 0.165)	1.473 ( $\pm$ 0.170)	3.1 %

## 2.4.4 Discussion

### 2.4.4.1 Ability of Coverslip to Withstand 5 N Static Load

Coverslips with different thicknesses ( $0.14 \pm 0.01$  mm and  $0.17 \pm 0.01$  mm) were examined under 5 N of static load for 12 hrs to determine their ability to withstand applied load and to validate if an 18 mm internal diameter of the device provided sufficient support. There was no visible signs of damage or cracks apparent on any coverslips and all of them returned to their original shape after a maximum load of 5 N was applied for 12 hrs which is a much longer duration than the load that would be applied in planned experimentations. Although the experimental set-up did not perfectly mimic the set up in the device (with only support provided on either side of, instead of completely around, the coverslip), sufficient support was provided from 3 mm of plastic blocks on each side of the coverslip because the coverslips withstood 5 N static load without any signs of damage, cracks and permanent deformation for an extensively longer duration than that in later experimentations. This would suggest that an 18 mm internal diameter of the device (with 3 mm of inner ledge around the coverslip) would provide enough support to withstand an applied load of 5 N with a 12 mm opening at the bottom of the device. In addition, the result does not provide information with regards to continued use of the same coverslip for different tissue samples. In later experimentations, a new coverslip would be used for different tissue samples to avoid cracking due to fatigue.

### 2.4.4.2 Coverslip Flexion under Applied Load

Due to load being directly applied onto the coverslip in the device, it was important to determine the amount of flexion the coverslip undergoes as the results of load application.

Different thicknesses of coverslips ( $0.14 \pm 0.01$  mm and  $0.17 \pm 0.01$  mm) were subjected to loads up to 700 g ( $\sim 7$  N) to determine if/how the coverslips flex under high load. Acrylic plastic has considerably high stiffness [214] and it was assumed that the acrylic disk would have negligible deformation in the experimental set-up, thereby the displacement observed would be the true flexion of the coverslip under load. There were no significant differences between the two coverslips with regards to displacement under load. This experiment was primarily conducted to give an indication as to how coverslips with different thicknesses would flex under load and the data was sufficient to meet that requirement, suggesting that both batches of coverslips were suitable to use in the device. Selecting the correct thickness of coverslip is important for optimal image quality. Most objective lenses are designed to be used with an 0.17 mm coverslip and therefore coverslips with  $0.17 \pm 0.01$  mm thickness were chosen to be used in the device for later experimentations.

To represent the trend that the coverslip flexes under load,  $0.17 \text{ mm} \pm 0.01$  mm coverslips were selected for displacement testing under load in order to create a standard curve (Figure 18). When calculating the applied tissue strain in later cell deformation experimentations, this standard curve was used to calculate the amount required to add on top of the selected tissue strain in order to compensate for the glass flexion caused by the particular load used to apply the selected tissue strain.

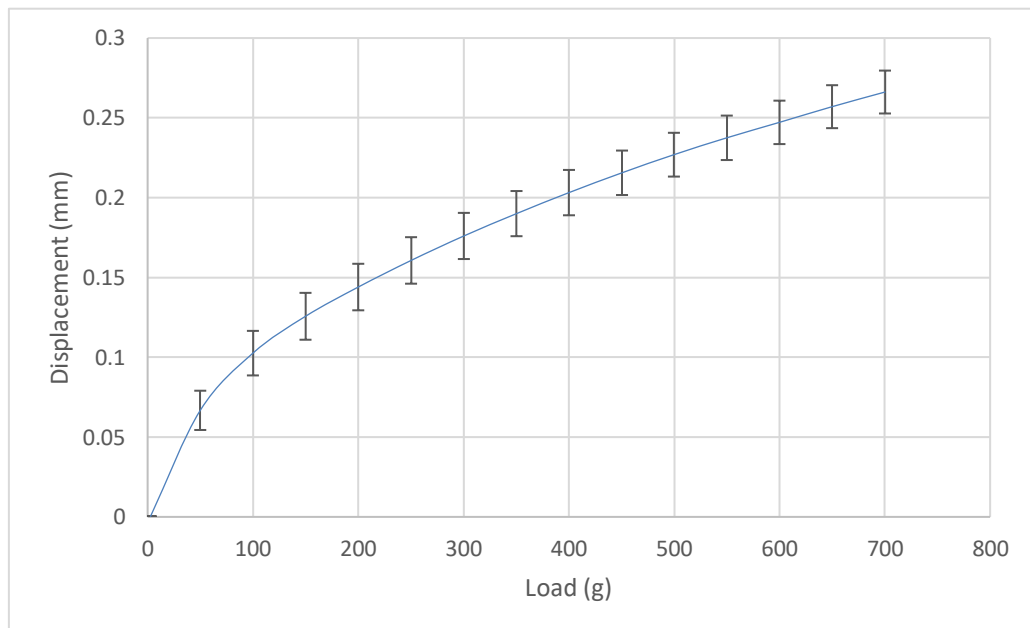


**Figure 18: Standard curve of displacement vs load for  $0.17 \text{ mm} \pm 0.01$  mm-thick coverslip. Data represented as mean  $\pm$  SD at each 50 g interval ( $n=6$ ).**

#### **2.4.4.3 Validation of Micrometer Accuracy**

The accuracy of the micrometer in the compression device was validated against a Bose ElectroForce 3200 mechanical testing machine. The thickness of an acrylic disk and bovine cartilage disks were measured using both measurement methods. An acrylic disk was used because it was assumed that it would not deform under the applied load (700 g,  $\sim 7$  N) due to its

high compressive stiffness [214]. In addition, native cartilage disks were measured because they are representative of future samples (Chapter 4) and they are more likely to deform under small loads compared to the more resistant acrylic disk. The thickness measurements obtained for an acrylic disk and bovine cartilage disks using the compression device and a Bose ElectroForce 3200 mechanical testing machine were significantly similar. The results suggest the micrometer and mechanical testing machine were sufficiently similar in their ability to measure displacement. It therefore determined that the micrometer was suitable to apply strain within the compression device.

### **2.4.5 Conclusion**

A 18 mm internal diameter of the device was proven to provide sufficient support (of 3 mm) around the coverslip to withstand 5 N of static load with a 12 mm opening window in the device for over 12 hrs. A coverslip thickness of  $0.17 \text{ mm} \pm 0.01 \text{ mm}$  was selected for use in the device because this particular thickness can accommodate most of the objective lenses. A standard curve was created to represent the trend of coverslip flexion under load. This information will be used in later experimentations when calculating the amount of displacement required to compensate for coverslip flexion in order to accurately apply tissue strain.

The accuracy of the micrometer was validated against a Bose ElectroForce 3200 mechanical testing machine with regards to thickness measurements. The measurements obtained by both methods were statistically similar, thereby it determined that the micrometer was suitable to apply strain within the compression device.

## **2.5 Discussion**

The aim of this chapter was to develop and build a compression device for compressive tissue strain application and to allow simultaneous confocal visualisation of cell deformation in real time to study cell deformation behaviour and its relationship to applied compressive strain in native cartilage disks (Chapter 4) and tissue engineered cartilage constructs (Chapter 5). Because an aim of this thesis was to determine cellular deformation within native and tissue engineered cartilage under different magnitudes of compressive strain, the device needed to be able to deliver compressive strains in accordance with the range of strains that were hypothesised in Finlay *et al.* (2016) [1] used to engineer cartilage constructs and the physiological levels of applied native cartilage strain *in situ* (0 % - 30 % strain). In addition, the ability to apply accurate strain values to cartilage tissue/construct disks was a vitally important design aspect of the device, thereby a micrometer head was selected for compressive strain application in the device. In this thesis, fixed and cut tissue were avoided and therefore the device was also required to accommodate non-fixed disk shaped samples (i.e. native cartilage disks and tissue engineered cartilage constructs).

This chapter investigated two potential compressive device designs based on loading configuration perpendicular and parallel to the axis of the optical path (described in Section 2.3.2 and Section 2.3.3, respectively). After consideration of the advantages and disadvantages of both designs, the compression device design based on loading configuration parallel to the axis of the light path was selected as the final version of the device. Several validation investigations on the compressive device were conducted to determine the dimensions of the device, the ability of the coverslip to withstand applied load and the micrometer accuracy. The findings suggested that a coverslip with a thickness of  $0.17 \text{ mm} \pm 0.01 \text{ mm}$  was capable to withstand the applied load within the compressive device and that the micrometer was suitable to apply strain within the compression device. Thus, a compressive device that is capable applying a range of compressive strains accurately to non-fixed disk shaped samples (i.e. native cartilage disks and tissue engineered cartilage constructs) and allow simultaneous confocal live cell imaging was successfully developed, ready for use to study the effects of incremental compressive strains on cell deformation behaviour in native cartilage disks (Chapter 4) and tissue engineered cartilage constructs (Chapter 5).

Many types of compression devices had been used in previous studies to examine the mechanical behaviour of chondrocytes under static tissue compression in cartilage explants [21], [51], [87], [133]–[138], [210], intact cartilage [85], [145] and isolated chondrocytes cultured in agarose gel [88], [142]–[144]. These devices followed either loading configurations perpendicular or parallel to the axis of the light path depending on the experimental set-up (e.g. confocal microscope systems used, specimen shapes used and the specimen region of interest). However, the majority of the devices were not suited for use in this thesis.

In fixed cartilage explants studies, these studies only required a loading device to apply tissue compression load to the cartilage during chemically fixation. Thus, fixed, compressed cartilage were examined for chondrocyte deformation after the fixation process. Clark *et al.* (2003) [138] compressed cat patella and femoral groove cartilage explants under static load of physiological magnitude using a cylindrical, flat ended indenter. The compressed cartilage were then chemically fixed prior to examination of cell deformation via histological observation. In a study by Choi *et al.* (2007) [137], porcine femoral condyle cartilage disks were compressed to 0%, 10%, 30%, and 50% strain using polysulfone platens and then chemically fixed.

Compressed cartilage were fluorescently immunelabelled for type-VI collagen to outline the PCM in order to examine the deformation behaviour of the chondrons from superficial, middle, and deep zone of the cartilage under different magnitudes of compressive tissue strains via confocal microscopy. The device being developed for this thesis was required to simultaneously apply compressive tissue strain to the sample and allow confocal visualisation of cell deformation in real time, thereby these devices described here were not suitable.

In the studies investigating chondrocyte deformation in non-fixed native articular cartilage and isolated chondrocytes seeded in agarose gel, a loading device was required to be able to simultaneously apply tissue compression and allow real time visualisation of chondrocyte deformation [51], [87], [88], [110], [133]–[135], [137], [142]–[144]. In a study by Guilak *et al.* (1995) [87], in which changes in chondrocyte morphology and local matrix deformation in the surface, middle and deep zones of canine articular cartilage explants subjected to physiological levels of tissue compression was investigated. A compressive device was designed to simultaneously apply unconfined static compression and accommodate imaging of chondrocytes within the full cartilage depth using an inverted confocal microscopy. To achieve this, Guilak *et al.* (1995) [87] adopted the approach of loading perpendicular to the optical axis. The compression device was placed within a Petri dish with a small hole drilled in the middle of the dish and a coverslip attached to the bottom of the hole to allow confocal visualisation. Compressive tissue strain was applied perpendicular to the tissue surface using a digital micrometer with two stainless steel platens. Semi-cylindrical test specimens were used by cutting the harvested cartilage cylindrical explants in half perpendicular to the articular surface and labelling with fluorescein dextran. Each cartilage specimen was placed in the compression device between two platens with the flat, exposed cross section faced down on the coverslip. This compression device allowed for the same group of chondrocytes from different zones within the cartilage to be imaged during a compressive strain of 0 % and 15 % and following removal of compression for quantification of changes in chondrocyte morphology and local matrix deformation [87]. However, the specimens used in this device required to be cut into a semi-cylindrical shape and this would affect the tissue mechanical integrity and consequently change the local mechanical environment around the cells. Thus, this was one of the reasons why a new device was needed to be developed in this thesis; to accommodate non-fixed and non-cut samples (i.e. native cartilage disks and tissue engineered cartilage constructs).

The compression device developed for this thesis was therefore capable of applying a range of compressive strains accurately to non-fixed disk shaped samples (i.e. native cartilage disks and tissue engineered cartilage constructs) and simultaneous allow examination of cell deformation via confocal imaging.

## **2.6 Conclusion**

The aim of this chapter was to the develop a novel compression device capable of delivering compressive strains to native and tissue engineered cartilage in accordance with the range of strains that were hypothesised in Finlay *et al.* (2016) [1] used to engineer cartilage constructs and the physiological levels of applied native cartilage strain in situ (0 % - 30 % strain) and simultaneously allow real time visualisation of the changes in cell morphology. Two potential compressive device designs based on loading configuration perpendicular and parallel to the axis of the optical path (described in Section 2.3.2 and Section 2.3.3, respectively) were

investigated and compared. After consideration of the advantages and disadvantages of both designs, the device design based on loading configuration parallel to the axis of the light path was chosen as the final version of the device. The compression device was successfully optimised and used in further investigations as described in Chapter 4 and Chapter 5.

## **Chapter 3 - Development of Methodology to Visualise Live Cells within Native and Tissue Engineered Cartilage**

*This chapter describes the development of a methodology for live cells visualisation within native and tissue engineered cartilage in order to study cell deformation behaviour and its relationship to applied compressive strain. Two staining methods (method using Acridine Orange and SiR-actin Probe and method using Hoechst 33342 and CellMask Green Plasma Membrane Staining) were developed and compared for their suitability for the required application in live cell sequential imaging within native and tissue engineered cartilage under non-loaded conditions as a prelude to subsequently determining cell deformation behaviour under compressive loads. It was determined that both staining methods were able to penetrate native and tissue engineered cartilage revealing morphology of the respective embedded cells. However, with the addition of ProLong® Live Antifade Reagent to aid the reduction in photobleaching, the dual staining method of Hoechst 33342 and CellMask Green plasma membrane stains showed superior fluorescence signal retention than the staining method of Acridine orange and SiR-actin after tracking selected cells on multiple confocal scans. Galvo scanning proved to be superior than resonant scanning when comparing the two microscope scanning modalities at retaining fluorescence signal after live cell sequential imaging. In summary, Hoechst 33342 and Cell Mask Green plasma membrane stains, together with ProLong® Live Antifade Reagent and galvo scanning were selected for use in all further experimentation for live cell visualisation in native and tissue engineered cartilage.*

### **3.1 Introduction**

To study cell deformation behaviour and its relationship to applied compressive strain in native cartilage disks (Chapter 4) and tissue engineered cartilage constructs (Chapter 5), a live cell staining method first needed to be established for cell morphology visualisation. In this chapter, the main aim was to establish and develop a method that was capable of visualising, tracking, imaging and quantifying 3D changes in cell morphology (shape and size) of living chondrocytes within native cartilage and bovine synoviocytes within tissue engineered cartilage during different magnitudes of static compressions. To visualise sub-cellular level within living tissue, there are many challenges to overcome and technical details to be tested, especially for live cells that needed to be imaged a multiple times. These included cell viability, stain(s) penetration, fluorescence crosstalk, imaging depth (which is affected by laser light depth penetration and the working distance (WD) of the objectives), microscope scanning modalities and photobleaching which would all be addressed in this chapter (discussed in Section 3.1.2).

For the purposes of this thesis, to visualise cell shape, a number of options were possible, either with actin or plasma membrane fluorescence staining. In addition, It is well established that the cellular response to mechanical stimulation is largely influenced by cell deformation (changes in shape) associated with the actin cytoskeleton. It would therefore be interesting to observe whether re-organisation of the actin filament network would occur, as well as determining the cell deformation behaviour in native and tissue engineered cartilage under different magnitudes of compressive strains.

### **3.1.1 Confocal Microscopy**

The 3D deformation behaviour of chondrocytes under static compression has been widely studied in cartilage explants and within other scaffold materials (e.g. agarose gel) using either confocal microscopy or histological evaluation [21], [51], [87], [88], [133]–[144]. The concept of confocal imaging was first introduced by Minsky (1957) [215] and the confocal principle has become the basic configuration of all modern confocal microscopes. Confocal laser scanning microscopy (CLSM) uses the principle of fluorescence excitation and emission to image biological samples (i.e. fixed or living cells and tissues) that have been labelled with one or more fluorescence stains [216]. Fluorescent molecule exhibits fluorescence which is a property of absorbing light of short wavelength and re-emitting light of long wavelength after a short period of time [217]. For any given fluorescent molecule, it has its own distinct excitation and emission energy levels meaning that light excitation and emission can occur only at specific wavelengths. Figure 19 shows the main components and the light paths in a basic CLSM configuration. The key to the confocal approach is the use of pinhole apertures to eliminate fluorescent signal from outside the plane of interest [213], [216], [218]. When a fluorescently labelled sample is imaged using a CLSM, a laser light beam (i.e. excitation light) (Figure 19, blue lines) is reflected towards an objective lens by the dichroic mirror (also known as the beamsplitter) in which the light focuses to a spot at a desired focal plane (i.e. focal point) in the sample [213], [218], [219]. The fluorescent molecules within the cone of illumination are excited by absorbing the light and results in light emission (i.e. fluorescence). The fluorescent light emitted by excited fluorescent molecules from within the focal plane (Figure 19, green lines) is then collected by the objective lens, passed back through the dichroic mirror and focused by a second lens through a pinhole onto a detector. A pinhole positioned in the light path between the objective lens and the detector ensures that only in focus fluorescence signal from the focal point passes through to the detector and any out of focus emission generated along the light path that is outside the objective focal point (i.e. above and below the focal plane) (Figure 19, grey dashed lines) is blocked [213], [218], [219]. This results in acquisition of the fluorescent signal from only the illuminated point. The confocal approach only collects the emission light from a single point at a time and therefore creates an image one pixel at a time [218], [219]. A two-dimensional image is created by scanning the sample in a raster pattern

using one or more scanning mirrors ‘galvanometer mirror’ [218], [219]. A raster scan pattern is when an area is scanned side to side in lines from top to bottom [218]. Typically, one mirror is responsible to direct the laser light beam in the x direction and the other in the y direction. Both mirrors work together to direct the excitation light to scan the sample in a raster fashion to create pixel by pixel in the x-y axis. The detector (e.g. photomultiplier tube (PMT)) collects the emission signal that passes through the pinhole and consequently convert them to an image [219]. This image represents a single ‘optical plane’ of the sample. A 3D volume image of the sample can be produced by scanning numbers of optical planes (sections/slices) and computationally stacking them using a microscopy software (Z stack) [213], [218].

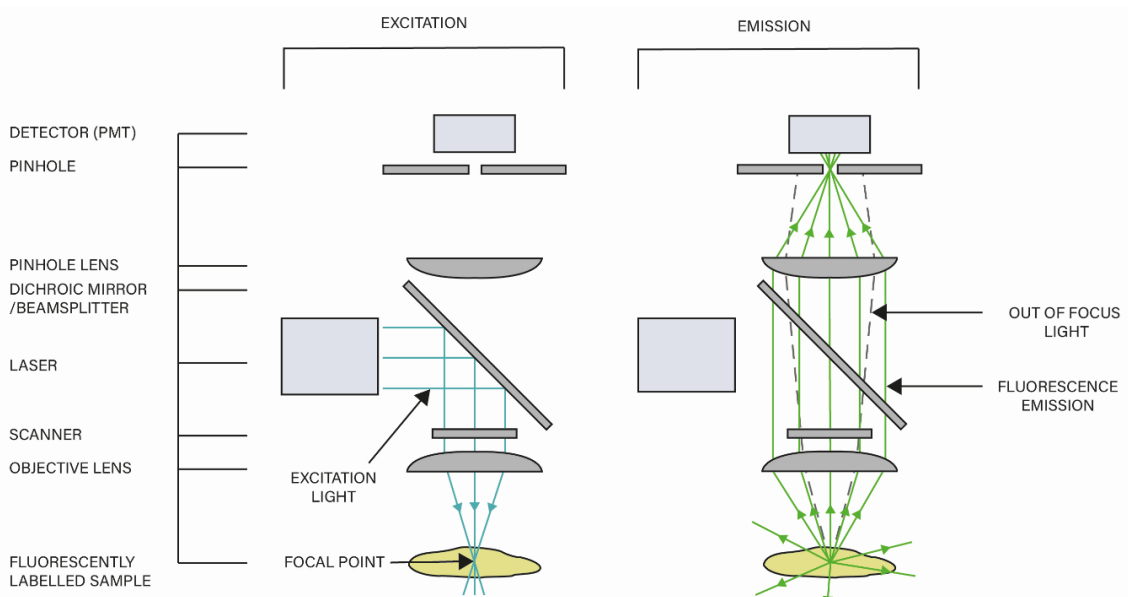


**Figure 19: Schematic of the confocal laser scanning microscopy (CLSM) principle, showing the main components and the excitation and emission light paths. Excitation light (blue lines) is focused to a spot at a desired focal plane (i.e. focal point) in the fluorescently labelled sample. Fluorescent light (green lines) is collected by the objective lens and focused by a second lens through a pinhole onto a detector. Any out of focus emission generated along the light path that is outside the objective focal point (e.g. above and below the focal plane - grey dashed lines) is blocked. Figure adapted from [213].**

The confocal imaging approach offers many advantages over conventional fluorescence imaging [213], [218], [220]. In a conventional fluorescence microscope, the excitation light illuminates the entire field of view of the sample and thereby fluorescence emits throughout the entire depth of the sample (or as deep as the excitation light is able to penetrate), including the regions that are not of interest (i.e. planes above and below the focal plane) and the focal plane. Much of the emitted light, collected from regions outside the focal plane would contribute to an out of focus blur to the image and a consequent reduction in image resolution [213]. In confocal microscopy, imaging occurs through a pinhole that restricts fluorescence emission of the sample to a focal point, with most of the illumination from regions above and below the focal plane being blocked and thus prevented from contributing to the image [213], [218], [220], [221]. In addition, the pinhole also eliminates points of light in the focal plane (except the focal point).

As a result of removal of out of focus light, a sharp image of the sample can be produced with significant enhancement in both axial and lateral optical resolution and in signal to noise ratio. Thus, confocal microscopy can produce high resolution and high signal to noise images [213], [216], [218], [220], [221]. Another major advantage of the confocal microscope is the ability to create a confocal image (i.e. optical section) from a single plane through optical sectioning which allows visualisation of thick samples ( $> 20\mu\text{m}$ ) (i.e. tissues) internally without having to physically section the sample [213], [220], [221]. In addition, it can acquire a series of confocal images (i.e. optical sections from different focal planes) to produce a 3D image dataset (z stack) from a thick sample, enabling the visualisation, reconstruction and quantitation of 3D structures/features from the sample volume [213], [220], [221]. Due to its ability to remove out of focus light and its optical sectioning property to permit the acquisition of high resolution and high signal to noise 3D images, confocal microscopy was selected as the visualisation system used for this thesis.

### **3.1.2 Challenges in Live Cell Imaging in Tissue**

Imaging live cells within tissue introduces many challenges that need to be overcome. Fluorescent labelling of cells within living tissue can be problematic [222]–[224]. The stains are required to penetrate the tissue to specifically label the cells. If multiple fluorophores are used, fluorescence crosstalk, a common problem, is possible and must be avoided [213]. Crosstalk is when the emission spectra of a fluorophore overlaps and extends into the spectra area of other fluorophores, resulting in bleed-through artefacts that might complicate the interpretation of the resulting image [213]. In other words, emission of a fluorophore is collected by more than one detector. The simplest solution to crosstalk is to select fluorophores that do not overlap in the emission spectra. In addition, sequential excitation scanning (i.e. channel series described in Section 3.4.5) should be used so that only one laser is scanning at any particular time to minimise the occurrence of crosstalk. If crosstalk is unavoidable, spectral unmixing is a technique that could be used after acquisition to allow separation of fluorophores with overlapping spectra [225]. Thus, selecting the appropriate fluorescent stains to label the cells within native and tissue engineered cartilage is vital when providing an accurate representation of cell morphology in this thesis.

Live cell imaging is further complicated by the need to keep the live cells/tissues viable prior to and during imaging because any stress experienced by the cells would affect cell behaviour [213], [222], [223]. For example, cells transportation (e.g. across campus or between buildings) could potentially induce significant stress to the cells because of the motion and the changes in temperature associated with the transportation [213]. Thus, it is vitally important to provide suitable environmental conditions (i.e. temperature, pH, CO<sub>2</sub> and humidity) for cells/tissues to replicate *in vivo* cell dynamics as accurate of a representation as possible [213], [222], [223]. An environmental chamber could be used to control the environmental conditions during imaging

as well as the use of physiological medium that keeps cells healthy at ambient atmosphere and temperature [213], [222], [223], [226].

Imaging depth has always been a challenge in biological tissue imaging. The penetration depth is typically limited to 50-100  $\mu\text{m}$  for confocal microscopy depending on the sample transparency and the wavelength of the excitation light [213], [227]–[229]. This is due to light absorption and scattering by the tissue specimens. When imaging deep into a tissue, image quality could worsen as a result of fluorescent light being scattered, absorbed and defocused as it passes back through the tissue and consequently very little emitted fluorescence reaches the detectors [228], [230]. For every specimen, there is a depth, dependent on the tissue density, at which light scattering occurs and where traditional fluorescence techniques are no longer effective. Generally, longer wavelength light has a deeper penetration depth than shorter wavelength light due to less light absorption and scattering [213], [228]. The working distance (WD) (vertical distances between the front of the objective and the closest sample surface when the sample is focused) of the objective could also affect the imaging depth [213]. Typically, the imaging depth reduces as the WD decreases along with increased magnification and the objective's numerical aperture (NA). Imaging thick tissue sample with a lower NA, longer WD objective would improve the imaging depth, but with lower resolution and sensitivity. Thus, when selecting the objective used for live cell imaging in this thesis, a balance between image resolution and imaging depth must be considered.

Another challenge in live cell imaging is to minimise photobleaching effect whilst maintaining high signal to noise ratio required for the image resolution [213], [222], [223]. Thus, in this thesis, it was important that the microscope, detector (i.e. comparison of microscope scanning modalities) and image acquisition settings (i.e. laser light exposure time, excitation light intensity, optical section thickness and number of optical sections) were optimised to maximise image resolution while minimising photobleaching effect in live cell imaging (discussed in Section 3.6). Photobleaching is the irreversible destruction of the fluorophore that can occur due to photochemical modification which leads to fluorescence fading during observation and consequently loss its ability to fluoresce permanently [222], [224], [231]–[233]. When fluorescent molecules are excited by light, it leads to photons to be absorbed and causes a shift from the ground energy state (S) to the singlet-energy level (S\*) [233]. Energy can be dissipated by emission of fluorescence, or in radiation less processes such as internal conversion (a transition from a higher to a lower electronic state) and intersystem crossing to the excited triplet state (T\*) [233]. However, excited fluorophores, either in a singlet (S\*) or triplet (T\*) state, can undergo permanent structural change that causes a loss in its ability to fluoresce and thereby become a photobleached molecule [233]. In the triplet state, it permits the excited dye molecules to interact with their environment (oxygen molecules dissolved in sample media) for a much longer time (milliseconds instead of nanoseconds) [233]. Interactions between oxygen (O<sub>2</sub>) and excited triplet state dye molecules may create singlet oxygen (<sup>1</sup>O<sub>2</sub>) which has a longer

lifetime than the triplet excited fluorophores, allowing more time for further interactions with other excited dye molecules and causing further degradation [233]. All these chemical reactions depend on both the singlet oxygen concentration and the distance between the fluorophore and intracellular components such as proteins and lipids [233]. Thus, the amount of photons emitted (fluorescence) before a fluorophore is permanently destroyed depends both on the nature of the fluorophore and on its environment [233]. In this thesis, fluorescence signal loss due to photobleaching would result in lack of detail for cell morphology and therefore could potentially affect the accuracy of quantitative data on cell deformation obtained from the images. The proposed imaging approach in this thesis would require the stains to be capable for sequential imaging of cells multiple times without signal loss therefore it was especially important that this was addressed. Thus, long illumination time and high laser intensity must be avoided to reduce photobleaching. Another way to aid the reduction in photobleaching is to deplete oxygen from the imaging media as oxygen is one of the main actors in photobleaching [222], [233].

### **3.1.3 Actin Staining**

Staining actin filaments can show the overall shape and structure of the cell. There are many commercially available stains and probes for labelling actin cytoskeleton in living and fixed cells in order to determine and track the structure and function of the filaments.

The gold standard for labelling actin is to use F-actin marker phalloidin [234]–[236]. Phalloidin, a bicyclic peptide from a family of toxins in the death cap mushroom (*Amanita phalloides*), only binds specifically to F-actin at the junction between the actin subunits and does not bind to other forms of actin [235], [237]. Fluorescent phalloidin conjugates utilise phalloidin to selectively bind to small and large F-actin with a 1:1 stoichiometric ratio between phalloidin and actin subunits whilst the fluorescent dye provides fluorescence visualisation; this therefore reduces non-specific background staining [237]. Fluorophores such as Alexa Fluor<sup>®</sup> dyes (e.g. Invitrogen Alexa Fluor<sup>®</sup> 488) coupled with phalloidin are commonly used fluorescent probes for labelling F-actin and claimed to be superior in brightness and photostability across the full spectral range. However, due to phalloidin being not cell-permeable, fixation and permeabilisation steps are required for its use or it must be microinjected into live cells prior to imaging [236], [238]. Furthermore, phalloidin binding stabilises F-actin which subsequently perturbs its normal assembly and dynamics and therefore limits its applicability for live imaging of actin filaments [236], [239].

In living cells, actin structures can be visualised either by incorporating fluorescently labelled actin through microinjection (technically demanding) or by overexpression [237], [239]. The technique of overexpressing a fusion protein composed of actin monomers and a fluorescent protein, such as green fluorescent protein (GFP) has been widely used [239], [240]. It requires manipulation of the cellular genetics by transfecting the target cells with expression vectors that

carry the actin-GFP fusion proteins [240]. GFP-actin DNA vectors are readily transfected into human cell lines [237]. However, primary cells, tissues and many non-mammalian cells are often difficult, impractical or unreliable to transfect [237]. In addition, GFP-labelled actin is known to interfere with cytoskeletal dynamics during cell cytokinesis and migration [241], cell deformation [242], [243] and cell-matrix adhesion [237], [240], [244]. Alternatively, fluorescent actin-binding proteins or domains have been used as a less disruptive method for visualising actin structures in live cells [236], [237], [239], [240]. Such commonly used live-probes include fusions of LifeAct [240], [245], F-tractin and Utrophin [239] to a fluorescent protein (e.g. green fluorescent protein (GFP)) [236], [240]. Compared to Actin-GFP, studies have reported that LifeAct-GFP displays better definition of the actin organisation and dynamics without affecting the biomechanical properties of either the entire cells or the actin cortex [240], [245]. Moreover, fluorescent probes based on the actin binding domain of Utrophin have shown to obtain clear visualisation of F-actin distribution in living and fixed cells and distinguish between stable and dynamic F-actin [239]. Although these probes have been successful in labelling F-actin, they still need to be introduced into cells either via protein transfection reagents (plasmid or viral vectors) or microinjection [239], [245].

In recent years, a probe conjugating silicon-rhodamine (SiR) to a ligand desbromo-desmethyl-jasplakinolide which binds to filamentous actin (F-actin), SiR-actin, was developed for labelling actin filaments in living cells [238], [240], [246]. The membrane permeable characteristic of SiR-actin allows for labelling of actin inside live cells without the need to transfect and overexpress fluorescently labelled proteins such as actin monomers or actin binding proteins which makes it easy to use [238], [247], [248]. Other advantages of SiR-actin over the other methods include its use in living cells without fixation and its far-red absorption and emission wavelengths which doesn't overlap with other commonly used fluorophores to avoid crosstalk. Other key properties of SiR-actin such as its fluorogenicity and high specificity to F-actin provide clear visualisation of actin filaments with a high signal to noise ratio [238], [247], [248]. Due to these beneficial features, SiR-actin was selected as a potential candidate stain for determining cell morphology and the actin structures and dynamics in living native and tissue engineered cartilage during tissue deformation in this thesis.

By coupling a nuclear stain with the actin probe, it would help to identify the actin filaments associated with each cell as well as cell morphology and, therefore Acridine orange was chosen to visualise cell nuclei. Acridine orange is a cell permeant nucleic acid dye, and was thus suitable for live cell imaging applications. In addition, there was minimal crosstalk between the two stains as the overlap in the emission spectra is insignificant. Acridine orange emits between 490 and 645 nm ( $\lambda_{Em\ max}$  526 nm) and SiR-actin displays a far-red emission between 600nm and 850nm ( $\lambda_{Em\ max}$  674nm).

### **3.1.4 Plasma Membrane Staining**

Apart from actin filament staining to visualise cell shape, plasma membrane staining is also a convenient marker for highlighting cell boundaries. There are many probes that are available for staining the plasma membrane. One method used for labelling cell membranes is the CellMask (Green, Orange and Red) plasma membrane stains. According to the manufacturer's descriptions, CellMask stains are amphipathic molecules which provide a lipophilic moiety for membrane loading and consist of a negatively charged hydrophilic dye that is able to anchor the probe in the plasma membrane. CellMask stains are able to provide bright, robust and uniform staining of plasma membrane across various mammalian cell types and are slow to internalise. They also rapidly stain plasma membrane in live cells. Thus, CellMask Green plasma membrane stain was chosen to determine its potential application in staining plasma membrane as a means of highlighting cell morphology. In addition, Hoechst 33342 dye was selected to couple with CellMask Green plasma membrane to label cell nuclei and identify cells because there is minimal overlap between the two stains on the emission spectra.

## **3.2 Objectives**

In this chapter, the main aim was to establish and develop a method that was capable of visualising, tracking, imaging and quantifying 3D changes in cell morphology (shape and size) of living chondrocytes within native cartilage disks and bovine synoviocytes within tissue engineered cartilage constructs during different magnitudes of static compressions. The method developed needed to allow stains to penetrate the matrix and provide specific and highly resolved visualisation of cell morphology for 3D quantification measurements. In addition, because an aim of this thesis was to determine the cellular deformation behaviour within native and tissue engineered cartilage under different magnitudes of compressive strain, the stains needed to label the cells and allow the operation of the confocal microscope to track and image selected cells multiple times without significant signal loss. Fluorescence signal loss needed to be avoided as this would result in lack of detail for cell morphology and therefore could potentially affect the accuracy of quantitative data on cell deformation obtained from the images.

The aim of this study was approached via the following objectives:

- To characterise and optimise SiR-actin stain on bovine synoviocyte monolayers.
- To characterise a dual staining method of Acridine orange and SiR-actin stains on bovine synoviocyte monolayers, native cartilage and synoviocyte-polyethylene terephthalate (PET) immature constructs to determine the ability to penetrate tissue samples, label cell nuclei and the F-actin structures and image selected cells multiple times without significant signal loss.

- To characterise an alternative dual staining method of Hoechst 33342 and CellMask Green plasma membrane stains on bovine synoviocyte monolayers, native cartilage and synoviocyte/PET immature constructs to determine the ability to penetrate tissue samples, label cell nuclei and the plasma membrane and image selected cells multiple times without significant signal loss.
- To examine the effects of photobleaching with the use of ProLong<sup>®</sup> Live Antifade Reagent in both staining methods.
- To compare image acquisition in the confocal microscope using a traditional galvo scanner and a high speed resonant scanner to potentially retain fluorescence signal.

Evaluation of the two staining methods (described in Section 3.4.1 and Section 3.4.3) and determination of which one was best suited for live cell imaging within native and tissue engineered cartilage was conducted under non-loaded conditions as a prelude to subsequently determining cell deformation behaviour under different compressive loads (described in Chapter 4 and Chapter 5). Once a staining method was established, an appropriate confocal imaging setting for tracking changes in cell morphology within native and tissue engineered cartilage subjected to different amounts of tissue deformation was determined. An overview of the experimental plan with variations of staining is depicted in Figure 21-24.

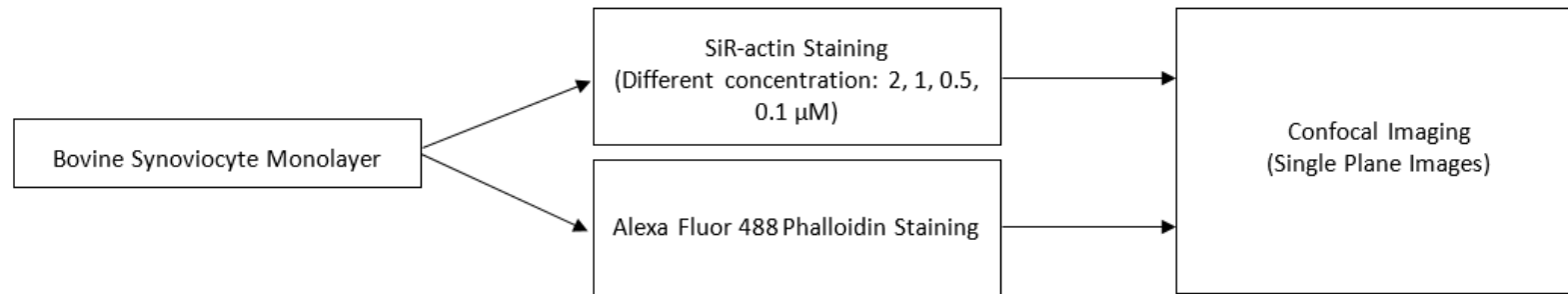


**Figure 20: Overview of experimental plan for optimising SiR-actin stain and comparing with Alexa Fluor® Phalloidin stain on bovine synoviocyte monolayers.**

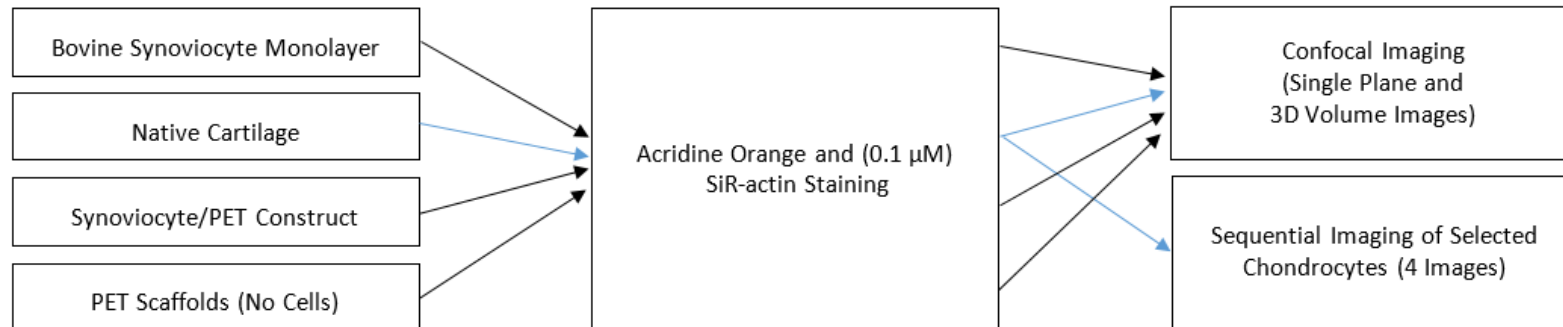


**Figure 21: Overview of experimental plan for characterising a dual staining method of Acridine orange and SiR-actin stains on bovine synoviocyte monolayers, native cartilage and synoviocyte-polyethylene terephthalate (PET) immature constructs to determine the ability to penetrate tissue samples, label cell nuclei and the F-actin structures and image selected cells multiple times without significant signal loss.**

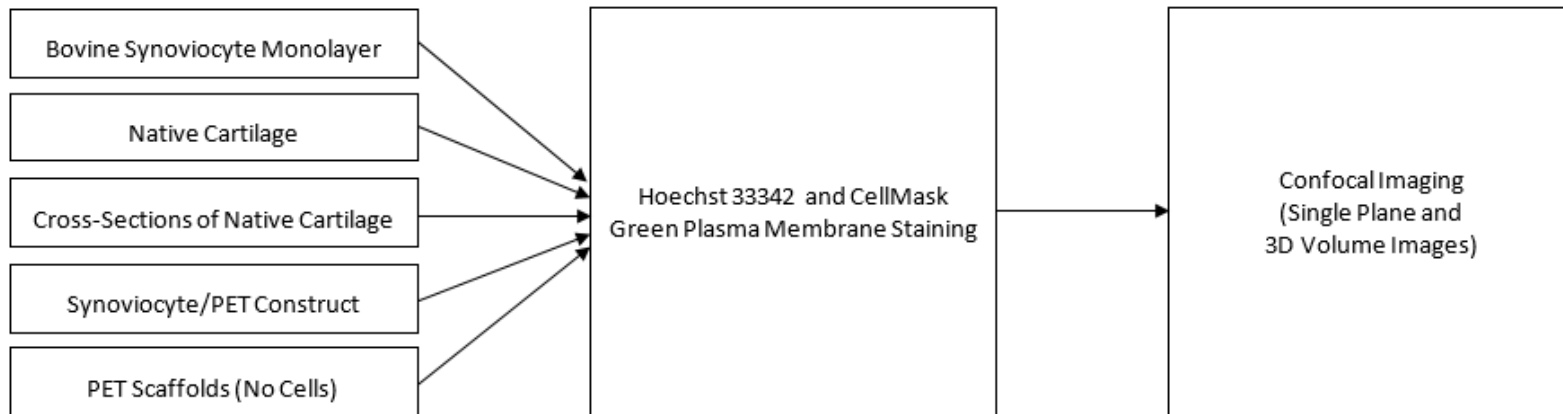


**Figure 22: Overview of experimental plan for characterising a dual staining method of Hoechst 33342 and CellMask Green plasma membrane stains on bovine synoviocyte monolayers, native cartilage and synoviocyte-polyethylene terephthalate (PET) immature constructs to determine the ability to penetrate tissue samples, label cell nuclei and the F-actin structures.**

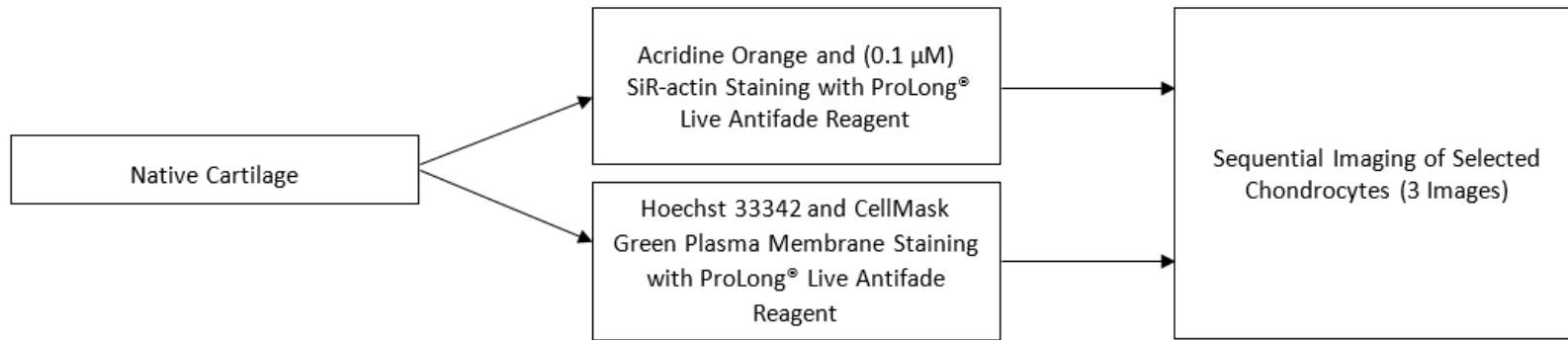


**Figure 23: Overview of experimental plan for examining the effects of photobleaching with the use of ProLong® Live Antifade Reagent in both staining methods.**

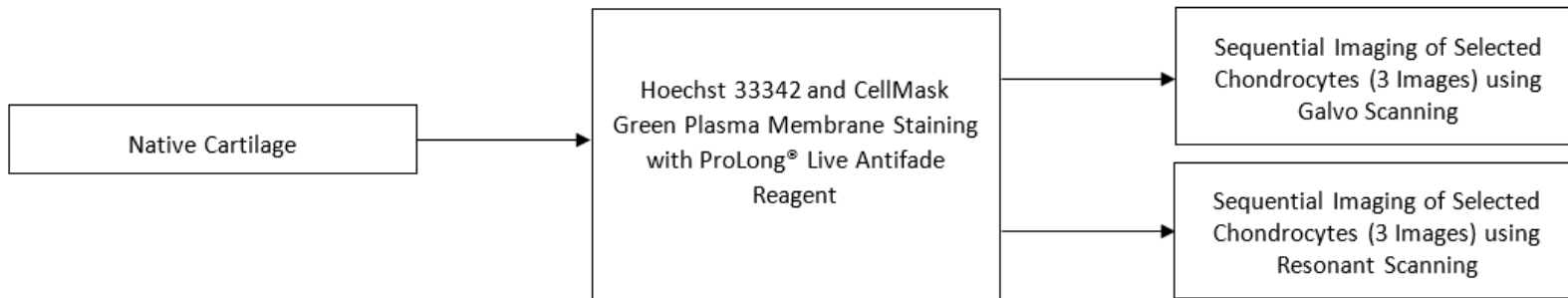


**Figure 24: Overview of experimental plan for comparing image acquisition in the confocal microscope using a traditional galvo scanner and a high speed resonant scanner to potentially retain fluorescence signal.**

### 3.3 Experimental Methodologies

#### 3.3.1 Cell Isolation and Monolayer Expansion

Cell isolation and monolayers expansion followed the method described in Finlay *et al.* (2016) [1]. Bovine synoviocytes were obtained from the synovia of approximately 6 month old bovine metatarsophalangeal joints. The legs were first cleaned with warm soapy water, followed by removal of skin without compromising the joint capsule. The joint was dissected aseptically using sterile surgical tools to open up the joint in order to expose the synovium. The synovium was removed before placing it in Dulbecco's PBS (written in full in Section 2.4.2.3) with 1 % 100x antibiotic (AB) (Sigma-Aldrich, Irvine, UK, P4333) (final concentration of AB in solution was 100 units/mL penicillin and 0.1 mg/mL streptomycin). The synovium was then cut into small pieces and placed in 0.25 % (w/v) collagenase 1A (Sigma-Aldrich, Irvine, UK, C9891) within Dulbecco's Modified Eagles Medium/Ham's F12 medium (DMEM/F12) (Gibco by ThermoFisher Scientific, Northumberland, UK, 21041025) at 37°C for 3 hrs. Once digested, the solution was filtered through a 70 µm nylon meshed cell strainer (Corning Life Sciences B.V., Amsterdam, Netherlands, 352350) before it was centrifuged at 100 g for 6 mins. The supernatant was then removed and the pellet was resuspended before seeding into 175 cm<sup>2</sup> tissue culture flasks (Corning Life Sciences B.V., Amsterdam, Netherlands, 431080), containing growth medium (which consisted of DMEM/F12 medium supplemented with 10 % foetal bovine serum (FBS) (Sigma-Aldrich, Irvine, UK, F7524), 1x AB and 2 mM L-glutamine (Sigma-Aldrich, Irvine, UK, G7513). Bovine synoviocytes were incubated at 37°C, 5 % CO<sub>2</sub> and above 90 % humidity. When confluence reached approximately 90 %, cells were passaged by trypsinisation. Growth medium was removed and the cells washed with PBS. Trypsin-EDTA (0.25 % w/v) (Sigma-Aldrich, Irvine, UK, T4049) was added to the cells for approximately 5 mins to induce cell detachment. The resulting cell suspension was then centrifuged at 100 g for 5 mins before the supernatant was removed and the pellet was resuspended in growth medium and re-seeded into 175 cm<sup>2</sup> tissue culture flasks at 5,000 cells/cm<sup>2</sup>. Medium change occurred every 3-4 days. Cells between passage 1 and 3 were used for all of the experiments described in this thesis.

To determine cell number for seeding, an aliquot of cell suspension combined with Trypan blue (Sigma-Aldrich, Irvine, UK, T8154) was added to a haemocytometer. Cells (located in three random squares in the haemocytometer) were counted manually under a light microscope. The cell concentration can be calculated using the following formula:

$$\text{Total cells/mL} = \frac{\text{Total cells counted} \times 10^4 \times \text{dilution factor (2)}}{\text{number of counted squares}}$$

### **3.3.2 Synoviocyte Monolayer Culture for Staining with SiR-actin**

To prepare synoviocyte monolayer for confocal imaging, synoviocytes were trypsinised and re-seeded at 7000 cells/cm<sup>2</sup> on 6-well cell culture plates (Corning Life Sciences B.V., Amsterdam, Netherlands) with each well containing 5 mL of growth medium. The cell monolayers were cultured in the incubator at 37°C and 5 % CO<sub>2</sub>. Medium change occurred every 3-4 days. When cells reach approximately 80 % confluency (cultured up to 7 days), both staining methods; Acridine orange coupled with SiR-actin stains and Hoechst 33342 combined with CellMask Green plasma membrane stains (described in Section 3.4.1 and Section 3.4.3) were applied prior to confocal imaging.

### **3.3.3 Harvesting of Osteochondral Plugs for Cartilage Disks**

Osteochondral plugs (5 mm in diameter were used as a source for cartilage disks as native cartilage samples) were obtained from the (relatively flat) medial and lateral regions of the patellofemoral groove of bovine knee joints. The joint was opened by removing remnant joint capsule tissue and other connective tissue using a scalpel, leaving the patellofemoral groove exposed. Only joints showing no visible defects were used. The articular surface was kept hydrated by dripping PBS on to the surface throughout the procedure. The initial outlines circumscribing the desired plug were marked on the cartilage surface using a plain ended corer. A drill mounted with a customised drill-aided corer was then used to drill down into the subchondral bone at the marked locations. Upon completion, the resulting osteochondral plug was snapped in-situ and removed from the joint surface with the aid of a plain ended corer. The extracted plugs were washed and placed in PBS before transferring them to PBS containing 10x AB for 20 mins. Once the plugs were sterilised, the subchondral bone ends were removed from the osteochondral plugs by a scalpel to leave as close to full depth cartilage as possible. The cartilage disks were then placed into culture conditions within a 24-well cell culture plate (Corning Life Sciences B.V., Amsterdam, Netherlands), with growth medium (DMEM/F12 medium supplemented with 10 % FBS, 1x AB and 2 mM L-glutamine) for a maximum three days prior to confocal imaging.

### **3.3.4 Production of Synoviocyte/PET Immature Constructs**

To fabricate synoviocyte/PET immature cartilage constructs, bovine synoviocytes, non-woven PET scaffolds (Xiros Ltd., Leeds, UK) and biochemical stimuli were used. For the purposes of stain testing, mechanical loading was not applied to the constructs during their development.

#### **3.3.4.1 Preparation of Non-Woven PET Fibre Scaffolds**

Non-woven PET fibre scaffolds provided by Xiros Ltd. for this project were plasma treated to improve cell attachment. Woven PET scaffold is clinically used in ligament repair and has been FDA approved. Non-woven PET fibre scaffolds were provided as sheets with dimensions of 20

x 60 mm and a porosity of 90.2 % by volume that resulted in 0.9 mm thickness. This was produced with the 97 % porosity scaffold by plastic compression, with heating, which causes a reduced in scaffold thickness and porosity. The PET sheets were cut into 5 mm disks using a custom-made cutter under aseptic conditions. Prior to the fabrication of constructs, the scaffolds were subjected to ultra violet (UV) radiation for a total of 30 mins (with 15 mins of exposure on each side of the scaffold) to ensure sterility before being used.

#### **3.3.4.2 Cell Isolation, Monolayer Expansion and Dynamic Cell Seeding**

Synoviocytes were isolated and expanded as described in Section 3.3.1. In brief, synoviocytes were isolated from bovine synovium via collagenase digest for 3 hrs at 37°C. The digest was filtered and centrifuged before the pellet was resuspended and seeded into tissue culture flasks. Synoviocytes were cultured in DMEM/F12 medium supplemented with 10 % FBS, 1x AB and 2 mM L-glutamine at 37°C, 5 % CO<sub>2</sub> and above 90 % humidity. When approximately 90 % confluency was reached, cells were passaged by trypsinisation and re-seeded at 5000 cells/cm<sup>2</sup>. Medium change occurred every 3-4 days. Cells between passages 1 and 3 were used for experimentation.

Once sufficient cell numbers had been reached, a 250,000 cells/mL suspension was prepared prior to the dynamic cell seeding procedure. A 1 mL aliquot of cell suspension along with a PET disk were inserted in a 2 mL capacity polypropylene tube (Sarstedt, Leicester, UK, 72.695). Each tube was then inserted into an in-house built, dynamic seeding apparatus, as shown in Figure 25. The dynamic seeding device consisted of a pair of rollers (one of which is connected to a DC electrical motor), two cylindrical steel disks connected by four shafts with twelve 10 mm holes where tubes were inserted and two cylindrical steel plates (attachable to the steel disks with screws for fixing the tubes in place). These components were assembled together to allow the inserted tubes filled with cells suspension and the PET scaffold to rotate at a rate of approximately 0.25 Hz. The dynamic cell seeding device was placed in the incubator at 37°C for 24 hrs to allow the cells to attach to the PET scaffold.

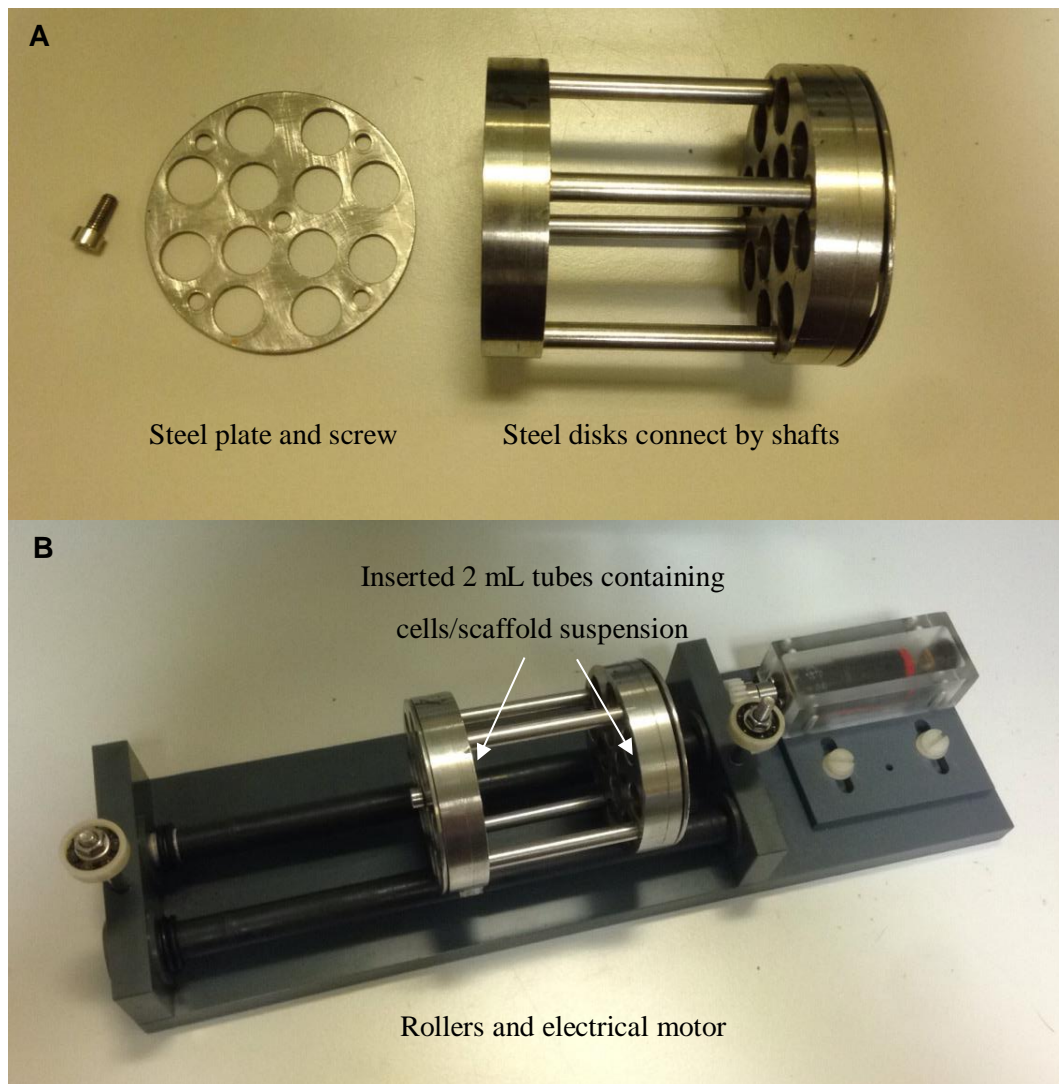


**Figure 25:** (A) Components of two steel disks with twelve 10 mm holes (connected by four shafts) and two steel plates (attachable with screws to the steel disks) combine together and (B) place on a pair of rollers (one of which is connected to a DC electrical motor) to form the assembled dynamic cell seeding device to allow the inserted tubes filled with cells/PET scaffold suspension to rotate at a rate of approximately 0.25 Hz.

### 3.3.4.3 Chondrogenic Culture of Synoviocytes on PET Scaffolds

Each cell-PET construct was transferred into a single well of a 24-well cell culture plate after the seeding was completed. Each construct was submerged in 1 mL of chondrogenic medium, which consisted of DMEM/F12 medium supplemented with, 10 ng/mL transforming growth factor  $\beta$ 3 (TGF- $\beta$ 3) (PeproTech, London, UK, 100-36E), 50  $\mu$ g/mL L-ascorbic acid-2-phosphate sesquimagnesium salt hydrate (Sigma-Aldrich, Irvine, UK, A8960),  $10^{-7}$  M dexamethasone (Sigma-Aldrich, Irvine, UK, D4902), 1x Insulin-Transferrin-Selenium (ITS) (ThermoFisher Scientific, Northumberland, UK, 51300-044), 1x AB and 2 mM L-glutamine. Chondrogenic medium was freshly made prior to application due to the instability of TGF- $\beta$ 3 and ascorbic acid-2-phosphate in solution. The plates were placed in the incubator at 37°C and 5 % CO<sub>2</sub>. Cultures were kept under these conditions for 12 weeks. Medium was changed every 3-4 days.

### **3.4 Analytical Methods**

#### **3.4.1 Live Cell Staining for Cell Nuclei and Actin Filaments with Acridine Orange and SiR-actin Stains**

For visualisation of F-actin structure and cell morphology in live bovine synoviocyte monolayers, native cartilage and synoviocyte/PET immature constructs, Acridine orange (Invitrogen, Paisley, UK, A1301) and SiR-actin (TeBu-bio, Peterborough, UK, 251SC001) were used to stain cell nuclei and F-actin, respectively.

A 1 mM stock solution of SiR-actin live probe was prepared by dissolving the content of the vial of SiR-actin in 50  $\mu$ L of anhydrous dimethyl sulfoxide (DMSO) (Sigma-Aldrich, Irvine, UK 276855). The stock solution was diluted with DMEM/F12 medium to make up staining solutions with different concentrations of the probe (2, 1, 0.5 and 0.1  $\mu$ M) and applied to synoviocyte monolayers in order to determine the desired staining concentration of SiR-actin required to visualise F-actin. Verapamil (10  $\mu$ M) (TeBu-bio, Peterborough, UK, 21910-1111), a broad spectrum efflux pump inhibitor, was added to each staining solution to improve on staining efficiency [238]. Growth medium in each well was replaced by different staining solutions, ensuring that cells were submerged in the solutions. The plates were placed in the incubator at 37°C and 5 % CO<sub>2</sub> overnight (approximately 12 hrs of labelling time). Once labelling was completed, cell monolayers were washed once with Live Cell Imaging Solution (Molecular probes by ThermoFisher Scientific, Northumberland, UK, A14291DJ) before imaging. Live Cell Imaging Solution is a physiological medium developed specifically for live cell imaging applications (live cell imaging, dye loading and wash steps). According to the manufacturer's instructions, it is an optically clear, physiological solution buffered with HEPES at pH 7.4 which can keep cell healthy for up to 4 hrs at ambient atmosphere and temperature. In addition, it provides better optical clarity and signal to noise ratio than standard media.

Once optimal staining of F-actin was achieved, the combination of Acridine orange and SiR-actin was applied to four different samples; i) bovine synoviocyte monolayers cultured in growth medium, ii) cartilage disks obtained from the patellofemoral groove of bovine knee joints and cultured in growth medium, iii) immature cartilage constructs generated by dynamically seeding bovine synoviocytes on PET scaffolds and cultured in chondrogenic medium for 12 weeks and iv) PET scaffolds (no cells) cultured in growth medium. Medium in each well was replaced by a staining solution of 0.1  $\mu$ M SiR-actin and 10  $\mu$ M Verapamil in DMEM/F12 medium for F-actin labelling. The samples were then placed in the incubator at 37°C and 5 % CO<sub>2</sub> overnight (approximately 12 hrs of labelling time). The samples were washed once with Live Cell Imaging Solution before labelling nuclei with Acridine orange (1  $\mu$ g/mL) in DMEM/F12 medium for 30 mins at 37°C. Three wash steps with Live Cell Imaging Solution were applied to the samples to

remove any residual staining. All samples were placed in Live Cell Imaging Solution prior to imaging. Staining solutions were freshly prepared for each experimental set up.

### **3.4.2 Alexa Fluor<sup>®</sup> 488 Phalloidin Staining for F-actin Visualisation**

To compare staining of SiR-actin with the more commonly used F-actin marker, phalloidin (e.g. Alexa Fluor<sup>®</sup> 488 phalloidin) [234], [249] for labelling of F-actin, synoviocyte monolayers cultured in a 6-well cell culture plate were used. The monolayers were washed with PBS three times before and after being submerged in 10 % neutral buffered formalin (NBF) (Sigma-Aldrich, Irvine, UK, HT501128) for 15 mins to fix the cells. Cell membranes were then permeabilised with 0.1 % Triton-X (Sigma-Aldrich, Irvine, UK, T8787) in PBS for 20 mins followed by three PBS washes. The monolayers were then incubated with Alexa Fluor<sup>®</sup> 488 phalloidin stain (Molecular probes by ThermoFisher Scientific, Northumberland, UK, A12379), at a 1 in 10 dilution for 2 hrs at room temperature, protected from light. Three PBS washes on monolayers were completed after which they were submerged and stored in fresh PBS prior to confocal imaging.

### **3.4.3 Live Cell Staining for Cell Nuclei and Plasma Membrane using Hoechst 33342 and CellMask Green Plasma Membrane Stains**

Bovine synoviocyte monolayers, chondrocytes within native cartilage and synoviocytes within synoviocyte/PET immature constructs were stained with Hoechst 33342 (ThermoFisher Scientific, Northumberland, UK, 62249) and CellMask Green plasma membrane (Molecular probes by Thermo Scientific, Northumberland, UK, C37608). A combined staining working solution of 1 µg/mL Hoechst 33342 and 1x CellMask Green plasma membrane (prepared from 1000x concentrated stain solution) were freshly prepared with DMEM/F12 medium prior to application to samples. A sufficient volume of the stain working solution was applied to completely cover the synoviocyte monolayers in a 6-well cell culture plate, the native cartilage and the immature constructs in a 24-well cell culture plate. The plates were covered with aluminium foil to protect from the light and incubated at 37°C and 5 % CO<sub>2</sub> for 40 mins. The monolayers and tissue samples were then washed three times in Live Cell Imaging Solution before visualisation using an Nikon A1R inverted confocal microscope (Nikon Instruments Inc, Surrey, UK). Staining solutions were freshly prepared for each experimental set up.

### **3.4.4 Live Cell Staining with the Addition of ProLong<sup>®</sup> Live Antifade Reagent**

The effect of addition of ProLong<sup>®</sup> Live Antifade Reagent to potentially reduce photobleaching was investigated on native cartilage specimens. Following dual staining of Acridine orange and SiR-actin stains, and Hoechst 33342 and CellMask Green plasma membrane on native cartilage disks as described in Section 3.4.1 and Section 3.4.3, respectively, ProLong<sup>®</sup> Live Antifade

Reagent (Invitrogen by Thermo Fisher Scientific, Northumberland, UK, P36975) was diluted in 1:100 with Live Cell Imaging Solution and applied to the samples in the dark at 37°C for 2 hrs before sequential imaging using a Nikon A1R inverted confocal microscope. Sequential imaging allows selected cells to be tracked and imaged through a series of 3D volume images. Given that both SiR-actin and CellMask Green plasma membrane stains were used to define cell boundaries, the ability of both stains to retain fluorescence signal after tracking identified cells three times via sequential imaging, with the addition of ProLong<sup>®</sup> Live Antifade Reagent, were determined and compared. The full method of sequential imaging is described in Section 3.4.5.6.

### **3.4.5 Confocal Microscopy Imaging**

#### **3.4.5.1 Confocal Imaging of Synoviocyte Monolayers Following Staining with SiR-actin, Alexa Fluor<sup>®</sup> 488 Phalloidin or Combined Acridine Orange and SiR-actin Stains**

All confocal images of synoviocyte monolayers stained with either different concentrations of SiR-actin, Alexa Fluor<sup>®</sup> 488 phalloidin or a staining combination of Acridine orange and SiR-actin were acquired using a Leica TCS-SP2 upright confocal laser scanning microscope (Leica Microsystems, Milton Keynes, UK). The 6-well cell culture plates containing the stained synoviocyte monolayers were placed on the stage of the confocal microscope and cells were randomly selected for imaging. Using a 20x water-immersion objective lens (HCX APO 0.5 numerical aperture (NA), Leica Microsystems, Milton Keynes, UK) and the 633 nm Helium-neon laser selected to excite SiR-actin, 1024 x 1024 pixel images of synoviocyte stained with different concentrations of SiR-actin were captured with four-times line averaging. Averaging is usually used in image acquisition to improve image quality by adding the sum of pixel values from the specified number of scan and using the average as the final value in the image. Line averaging is a form of averaging which scans each line for a specified number of times prior to moving to the next line. This is repeated for all lines in the frame and the pixel data collected is averaged to produce an image with reduced noise and improved signal to noise ratio.

For the comparison of synoviocytes stained with either Alexa Fluor<sup>®</sup> 488 phalloidin or SiR-actin, confocal images (1024 x 1024 pixels) were recorded using a 63x water-immersion objective (HCX APO 0.9 NA, Leica Microsystems, Milton Keynes, UK) with four-times line averaging and lasers at excitation/emission wavelengths of 488/520 nm and 652/674 nm, respectively. Images of SiR-actin stained synoviocytes (use for comparison with Alexa Fluor<sup>®</sup> 488 phalloidin labelled synoviocytes) were compiled and pseudo coloured to green using Leica Confocal Software (Leica Microsystems, Milton Keynes, UK).

To acquire images (512 x 512 pixels) of synoviocytes stained with Acridine orange and SiR-actin, objective lenses with various magnifications (20x and 63x) and digital zooms were used with four-times line averaging. The 543 nm Argon laser and the 633 nm Helium-neon laser were used to excite Acridine orange and SiR-actin, respectively. Unidirectional scanning and channel series were selected to capture all images. Channel series enables sequential scanning mode which means only one laser is scanning at any particular time, this therefore reduces fluorescence crosstalk where emission from one fluorophore is detected by more than one detector. Images were compiled using Leica Confocal Software and Acridine orange and SiR-actin were pseudo coloured to blue and green, respectively.

#### **3.4.5.2 Confocal Imaging of Native Cartilage and Synoviocyte/PET Immature Constructs Following Staining with Combined Acridine Orange and SiR-actin Stains**

All 3D volume images (Z stack) of cells within native cartilage and immature cartilage constructs were acquired using an Nikon A1R inverted confocal microscope. The 488 nm Argon laser and 641 nm solid state laser were selected to excite Acridine orange and SiR-actin stains, respectively. Unidirectional galvo scanning and channel series were used to capture all images. Individual tissue samples were placed inside the compression device without load application and with the imaging surface (i.e. the deep zone) faced down onto the coverslip, as described in Section 2.3.3. The tissue was submerged in Live Cell Imaging Solution to maintain hydration and cell viability during imaging. The device (with no load applied to the tissue) was mounted onto the stage of the microscope. Chondrocytes and synoviocytes were randomly selected from the central region (radially) of the native cartilage and Synoviocyte/PETimmature construct, respectively. To determine the ability of both stains to penetrate through both tissue samples, serial optical sections of 512 x 512 pixels were recorded at an interval of 1.25  $\mu\text{m}$ /section with no line averaging using a 20x air objective (PL APO 0.75 NA, Nikon Instruments Inc, Surrey, UK). Three dimensional volume and maximum projection images were reconstructed from the series of optical sections using Nikon NIS-Elements software (Nikon Instruments Inc, Surrey, UK) and Acridine orange and SiR-actin were pseudo coloured to blue and green, respectively. Maximum projection is a method that projects 3D data (the voxel with the highest intensity values from the sections throughout the volume) onto a single plane image.

#### **3.4.5.3 Confocal Imaging of Synoviocyte Monolayers, Native Cartilage and Synoviocyte/PET Immature Constructs Following Staining with Combined Hoechst 33342 and CellMask Green Plasma Membrane Stains**

All 3D volume images (Z stack) were acquired using an Nikon A1R inverted confocal microscope. The 405 nm solid state and 488 nm Argon laser were selected to excite the Hoechst 33342 and CellMask Green plasma membrane stains, respectively. Unidirectional galvo

scanning and channel series were used to capture all images. For visualising synoviocytes in monolayers, the 6-well cell culture plate was mounted directly onto the stage of the confocal microscope and serial optical sections of 512 x 512 pixels at an interval of 0.2  $\mu\text{m}$ /section with no line averaging were recorded using a 20x air and 40x oil immersion objective lens (20x PL APO 0.75 NA and 40x S Fluor 1.30 NA, Nikon Instruments Inc, Surrey, UK). For all experimentations that involved tissue samples, they were placed in the non-loaded compression device filled with Live Cell Imaging Solution (with the imaging surface either the superficial surface or the deep zone faces down onto the coverslip, as described in Section 2.3.3) and mounted on the stage of confocal microscope. To determine the ability of both stains for cell visualisation via penetrating through native cartilage and immature cartilage constructs, a series of optical sections of 512 x 512 pixels at 1.25  $\mu\text{m}$  intervals with no line averaging were captured using a 20x air objective (PL APO 0.75 NA). Three dimensional volume images were compiled using Nikon NIS-Elements software.

#### **3.4.5.4 Determination of Staining Penetration using Cross-Sections of Native Cartilage**

In preparation for determining the extent of penetration of Hoechst 33342 and CellMask Green plasma membrane stains in to native cartilage, cross-sectional slices (approximately 1 mm thick) were prepared from the stained cartilage disks from the central axis of the articular surface down to the deep zone using a scalpel. The cross sectional slices were then imaged by acquiring a series of optical sections of 512 x 512 pixels at 6.22  $\mu\text{m}$  intervals using a 10x air objective (PL Fluor 0.30 NA, Nikon Instruments Inc, Surrey, UK) to produce an overall view of the cross-section. Unidirectional galvo scanning and channel series were used to capture all images. Maximum projection images were reconstructed from the series of optical sections using Nikon NIS-Elements software.

#### **3.4.5.5 Sequential Imaging of Selected Chondrocytes in Native Cartilage Following Staining of Acridine orange and SiR-actin**

In order to study the effect(s) of incremental compressive loading on cell deformation in living native cartilage and immature cartilage constructs, selected cells must be visualised multiple times without significant signal loss. An imaging acquisition protocol of a sequential series of four 3D volume images (as shown in Figure 26) was used to determine the ability of SiR-actin to retain fluorescence signal during tracking and imaging selected cells multiple times. A set of four sequential volume (Z stack) images was chosen because this would allow examination of changes in cell morphology (shape and size) from the uncompressed state to the deformed state following application of various magnitudes of compressive tissue strain in later cellular deformation experiments. Following application of Acridine orange and SiR-actin (described in Section 3.4.1), the stained native cartilage sample was placed in the compression device

(without load application) filled with Live Cell Imaging Solution and with the imaging surface either superficial surface or the deep zone faced down onto the coverslip, as described in Section 2.3.3 prior to mounting on the stage of the microscope. Chondrocytes located in the superficial surface and the deep zone of native cartilage were examined under non-loaded conditions as a prelude to subsequently determining cell deformation behaviour in native and tissue engineered cartilage under different compressive loads (described in Chapter 4 and Chapter 5). Chondrocytes from the central region (radially) of the tissue were randomly selected from a depth of 20-30  $\mu\text{m}$  inside the tissue and tracked by capturing a sequential series of four volumes images. To capture a volume image of selected chondrocytes in both the superficial surface and the deep zone, a series of optical sections of 512 x 512 pixels at 0.2  $\mu\text{m}$  intervals were taken using a 100x oil immersion objective (Plan APO 1.40 NA, Nikon Instruments Inc, Surrey, UK) with unidirectional galvo scanning and no line averaging. Thin optical section thickness (0.2  $\mu\text{m}$ ) was selected to achieve high z-resolution that could provide sufficient pixel details to resolve 3D cell morphology. No line averaging was applied in order to reduce scanning time on tissue samples and consequently minimise the risk of photobleaching. After 30 mins of equilibrium time, a further another volume image was recorded of the same selected cells in the same area. The procedure was repeated for two additional volume images of the same selected cells in the same area to complete the sequential series of four volume images. Images were compiled using Nikon NIS-Elements software.

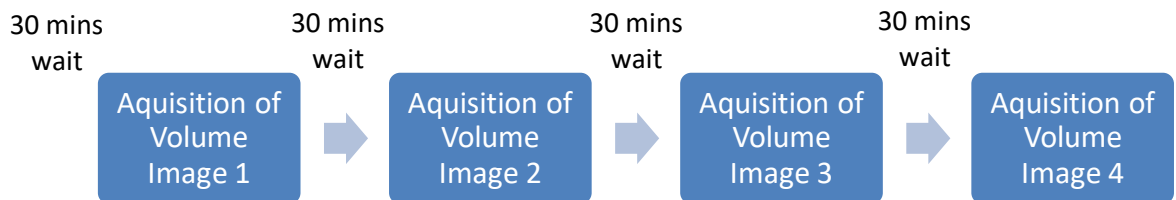


**Figure 26: A confocal imaging protocol consisting of a sequential series of four 3D volume images was used to determine the ability of SiR-actin to retain fluorescence signal after tracking and imaging selected cells multiple times. This protocol was applied to chondrocytes located in the superficial surface and the deep zone of native cartilage.**

#### **3.4.5.6 Comparison in Sequential Imaging of Selected Chondrocytes in Native Cartilage Between Staining of SiR-actin and CellMask Green Plasma Membrane with the addition of ProLong<sup>®</sup> Live Antifade Reagent**

Given that SiR-actin and CellMask Green plasma membrane stains were used to define cell boundaries, the ability to retain fluorescence signal after tracking identified cells multiple times were compared between the two stains, with the addition of ProLong<sup>®</sup> Live Antifade Reagent to potentially reduce photobleaching. An imaging acquisition protocol of sequential 3D volume images as described in Section 3.4.5.5 was used, except a sequential series of three images

instead of four. Following application of either dual staining of Acridine orange and SiR-actin stains, and Hoechst 33342 and CellMask Green plasma membrane with the addition of ProLong<sup>®</sup> Live Antifade Reagent on native cartilage (described in Section 3.4.4), experimentation was conducted under non-loaded conditions as a prelude to subsequently determining cell deformation behaviour in native and tissue engineered cartilage under different compressive loads (described in Chapter 4 and Chapter 5). In brief, a stained native cartilage sample was placed in the compression device (without load application) filled with ProLong<sup>®</sup> Live Antifade Reagent and with the imaging surface either superficial surface or the deep zone faced down onto the coverslip, as described in Section 2.3.3. The device was then mounted on the stage of the microscope. Chondrocytes from the central region (radially) of a sample of native cartilage were randomly selected from a depth of 20-30  $\mu\text{m}$  inside the tissue and tracked by capturing a sequential series of three volumes (Z stack) images. Three volume images (512 x 512 pixels and 0.2  $\mu\text{m}$  optical section thickness per a volume image) of the same identified cells in the same area were conducted sequentially with 30 mins of waiting time apart. Unidirectional galvo scanning, channel series and no line averaging were used to capture all images. Lasers were set at 5 % of full power to minimise stain bleaching. In addition, the pinhole was set at the theoretical optimum of 1 Airy units (Au) to provide a diameter that gives the best compromise between light throughput, noise and resolution. Images were compiled using Nikon NIS-Elements software.

#### **3.4.5.7 Sequential Imaging of Selected Chondrocytes in Native Cartilage using Galvo and Resonant Scanning Systems Following Staining of Hoechst 33342 and CellMask Green Plasma Membrane with the Addition of ProLong<sup>®</sup> Live Antifade Reagent**

To examine which scanning system was best in order to retain fluorescence signal of stain, a series of three volume images of chondrocytes in the same sample of native cartilage was captured using the galvo and resonant scanner systems on an Nikon A1R inverted confocal system. Experimentation was conducted on native cartilage under non-loaded conditions as a prelude to subsequently determining cell deformation behaviour in native and tissue engineered cartilage under different compressive loads (described in Chapter 4 and Chapter 5). Following application of Hoechst 33342 and CellMask Green plasma membrane (described in Section 3.4.4), the stained cartilage sample was placed in the non-loaded compression device filled with ProLong<sup>®</sup> Live Antifade Reagent (with the imaging surface faces down onto the coverslip, as described in Section 2.3.3) and the device was mounted on the stage of the microscope. Chondrocytes from the central region (radially) of a sample of native cartilage were randomly selected at a depth of 20-30  $\mu\text{m}$  within the tissue. The 405 nm solid state and 488 nm Argon laser were used to excite Hoechst 33342 and CellMask Green plasma membrane stains respectively. For the galvo scanner, lasers were set at 5 % of full power with no line averaging

and the pinhole was set at the theoretical optimum of 1 Au to provide a diameter that gives the best compromise between light throughput, noise and resolution. To set up the resonant scanning, 30 % of full laser power was used with sixteen-times line averaging and the pinhole was set at 1 Au. When a higher speed scanner is used, increase in laser power and line averaging are required to compensate on the shorter pixel dwell time which means less photon influx per pixel and consequently lower signal to noise ratio. A volume image (22.25  $\mu\text{m}$  in depth) was recorded by taking serial optical sections of 512 x 512 pixels at 0.2  $\mu\text{m}$  intervals with a 40x oil immersion objective (S Fluor 1.30 NA). Three volume images of cells in the same area were collected every 30 min as described in Section 3.4.5.6. Six cartilage samples were imaged using either the galvo and resonant scanning system in total. Images were compiled and change in fluorescence intensity (%) was recorded following three sequential images using Nikon NIS-Elements software.

## **3.5 Results**

### **3.5.1 Characterisation and Optimisation of SiR-actin Stain on Synoviocyte Monolayers**

#### **3.5.1.1 Confocal Microscopy of Synoviocyte Monolayers Stained with Different Concentrations of SiR-actin**

The different concentrations of SiR-actin applied to bovine synoviocytes appeared to have little effect on the resulting fluorescence intensity (Figure 27). This suggests the lowest concentration (0.1  $\mu\text{M}$ ) of SiR-actin provided adequate signal and was suitable to label actin filaments in live bovine synoviocytes.

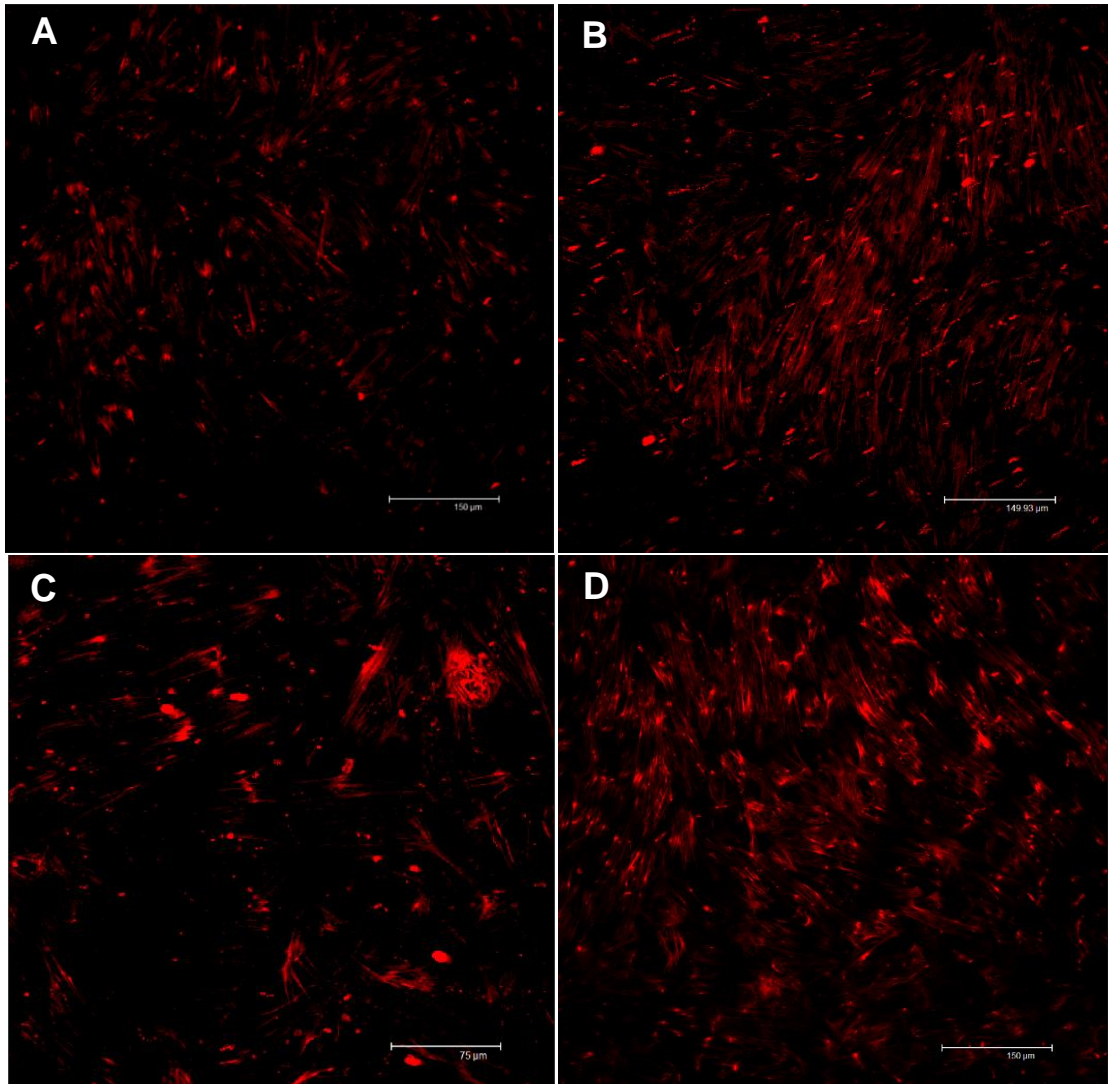


**Figure 27: Confocal images of bovine synoviocytes stained with different concentrations of SiR-actin (red) for F-actin; (A) 2  $\mu$ M, (B) 1  $\mu$ M, (C) 0.5  $\mu$ M and (D) 0.1  $\mu$ M SiR-actin.**

Fluorescence intensity was similar in synoviocyte monolayers applied with different concentrations of SiR-actin.

### **3.5.1.2 Comparison of SiR-actin and Alexa Fluor<sup>®</sup> 488 Phalloidin Stains for F-actin visualisation**

Confocal images of live bovine synoviocytes stained with SiR-actin and Alexa Fluor<sup>®</sup> 488 phalloidin revealed similar actin filament organisations and structures (Figure 28), respectively, confirming that SiR-actin is highly specific to labelling F-actin. Spherical stained structures were visible in the image of synoviocytes stained with SiR-actin (Figure 28B) which could potentially be stain debris.

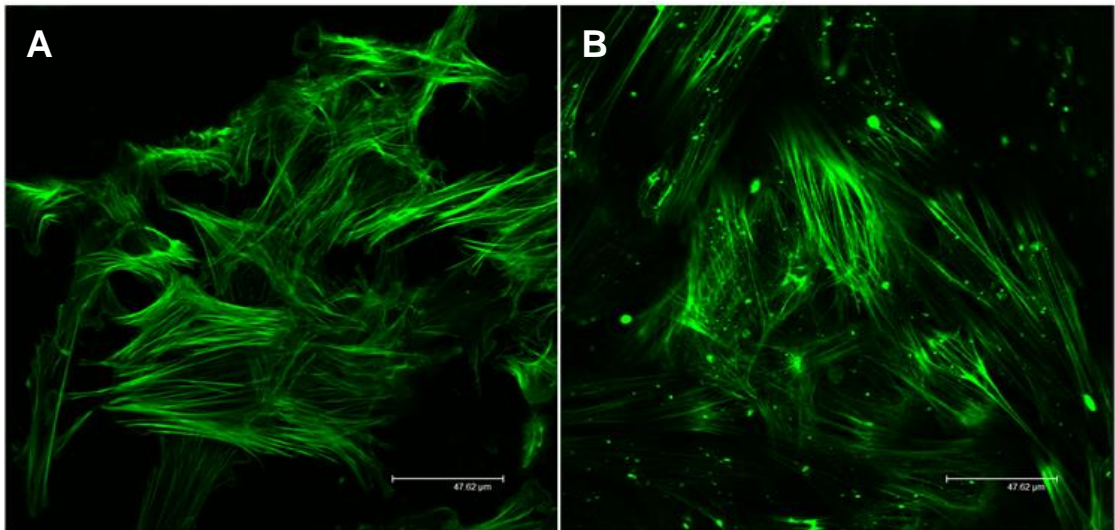


**Figure 28: Parallel staining of bovine synoviocyte monolayers using (A) Alexa Fluor® 488 phalloidin and (B) SiR-actin (pseudo coloured to green).**

Staining of both Alexa Fluor® 488 phalloidin and SiR-actin revealed similar actin filament organisations and structures. Spherical stained structures also appeared in the image of synoviocytes stained SiR-actin.

### **3.5.2 Characterisation of the Dual Staining Method of Acridine Orange and SiR-actin Stains on Synoviocyte Monolayers, Native Cartilage and Synoviocyte/PET Immature Constructs**

#### **3.5.2.1 Confocal Microscopy of Synoviocyte Monolayers Stained with Acridine Orange and SiR-actin**

Following staining of Acridine orange (1 µg/mL) and SiR-actin (0.1 µM), living synoviocyte monolayers were imaged via confocal microscopy. The staining combination of Acridine orange and SiR-actin to label the nuclei (blue) and actin filaments (green), respectively, revealed cell morphology (overall shape) in the live bovine synoviocytes (Figure 29). Images in Figure 29 revealed F-actin in live bovine synoviocytes to be highly organised, forming bundles and 3D networks (Label 1, Figure 29E) along with different lengths of filaments (Label 2, Figure 29A). Staining also appeared to reveal globular actin (Label 3, Figure 29E). Acridine orange revealed cell nuclei (Label 4, Figure 29F) and denser staining within some regions of nuclei was observed, potentially indicating the presence of nucleoli (Label 5, Figure 29D and Figure 29F). Acridine orange was also faintly visible in the cytoplasm (Label 6, Figure 29F). Cell-cell interactions and adhesion plaques were also observed (Label 7, Figure 29D).

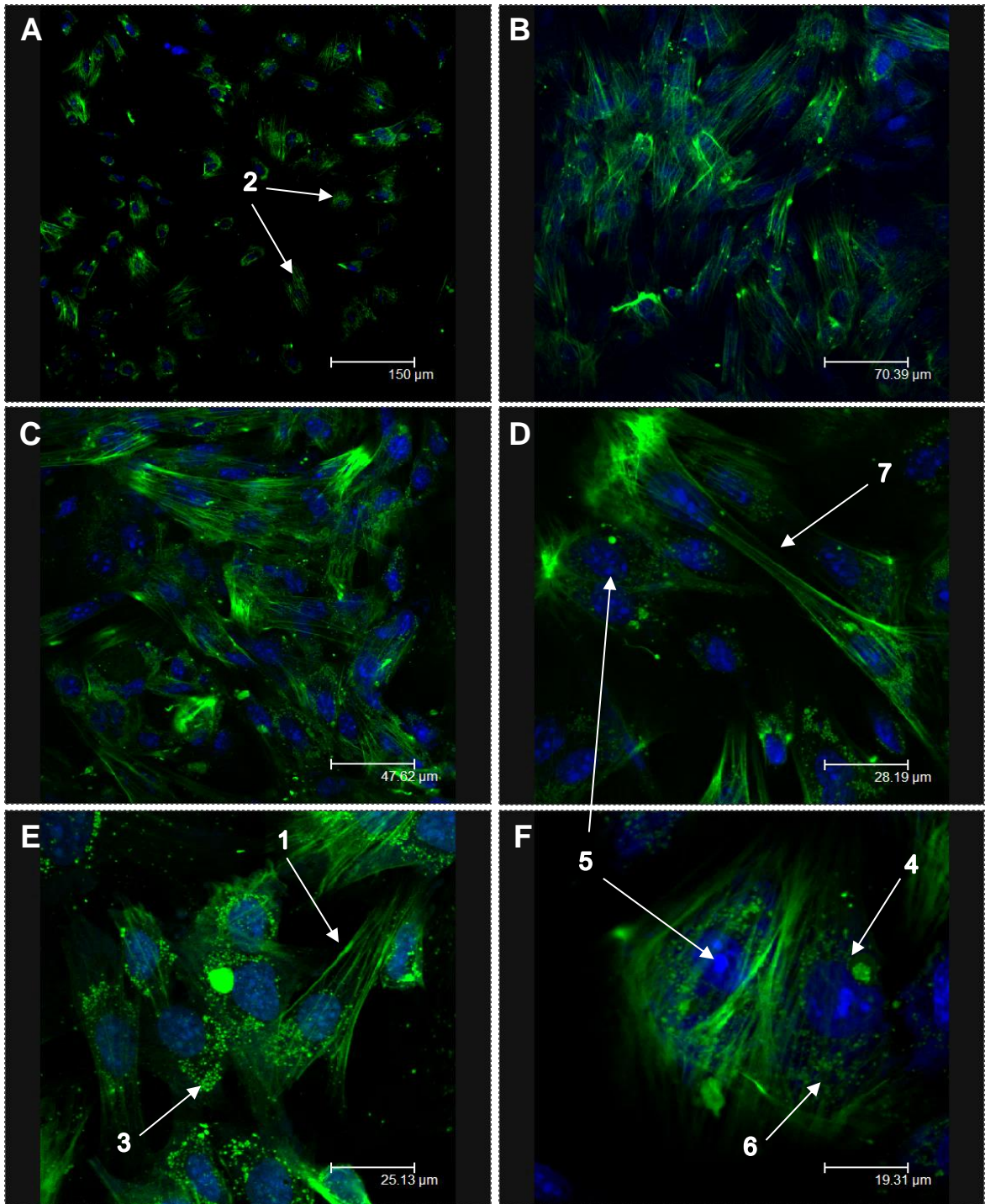


**Figure 29: Confocal images of live bovine synoviocyte monolayers labelled with Acridine orange (pseudo coloured to blue) and SiR-actin stains (pseudo coloured to green) for staining of nuclei and actin filaments, respectively, were visualised using (A-F) various magnifications and digital zooms.**

Bundles and 3D networks of actin filaments (Label 1) were observed along with different lengths of filaments (Label 2). Staining also revealed the assembly and disassembly of actin filaments with globular-actin (Label 3) appeared to be visible along with actin filaments. Nuclei (Label 4) were labelled with Acridine orange and denser staining was observed in some regions of the nuclei compared with others, potentially indicating the presence of nucleoli (Label 5). Acridine orange was faintly visible in the cytoplasm (Label 6). Cell-cell interactions and adhesion was also observed (Label 7).

### **3.5.2.2 Confocal Microscopy of Cells Stained with Acridine Orange and SiR-actin within Native Cartilage and Synoviocyte/PET Immature Constructs**

The 3D volume images showed both Acridine orange and SiR-actin stains had penetrated through native cartilage and synoviocyte/PET immature constructs and labelled cell nuclei and actin filaments, respectively (Figure 31). Both 3D volume and maximum projection images of the deep zone of native cartilage revealed chondrocytes with a rounded morphology which were arranged in columns (Figure 30A and Figure 31A), as would be expected. From the 3D volume and maximum projection images of the synoviocyte/PET immature construct, synoviocytes appeared to have a spindle-like morphology and were distributed relatively evenly throughout the construct (Figure 30C and Figure 31B). They were more densely packed than the chondrocytes in native cartilage and difficult to distinguish one cell from another. Low level staining was observed with the PET scaffold control (no cells) in Figure 30E and Figure 31C, indicating a low level of non-specific stain was present at the selected wavelengths. However, the staining intensity was insignificant compared to the fluorescently labelled nuclei and actin filaments associated with the cells in native cartilage and synoviocyte/PET immature constructs. For the negative, non-stained controls shown in Figure 30B, Figure 30D and Figure 30F, there was no visible staining present, inferring that the staining methodology developed to stain nuclei and F-actin does not exhibit false positive staining.

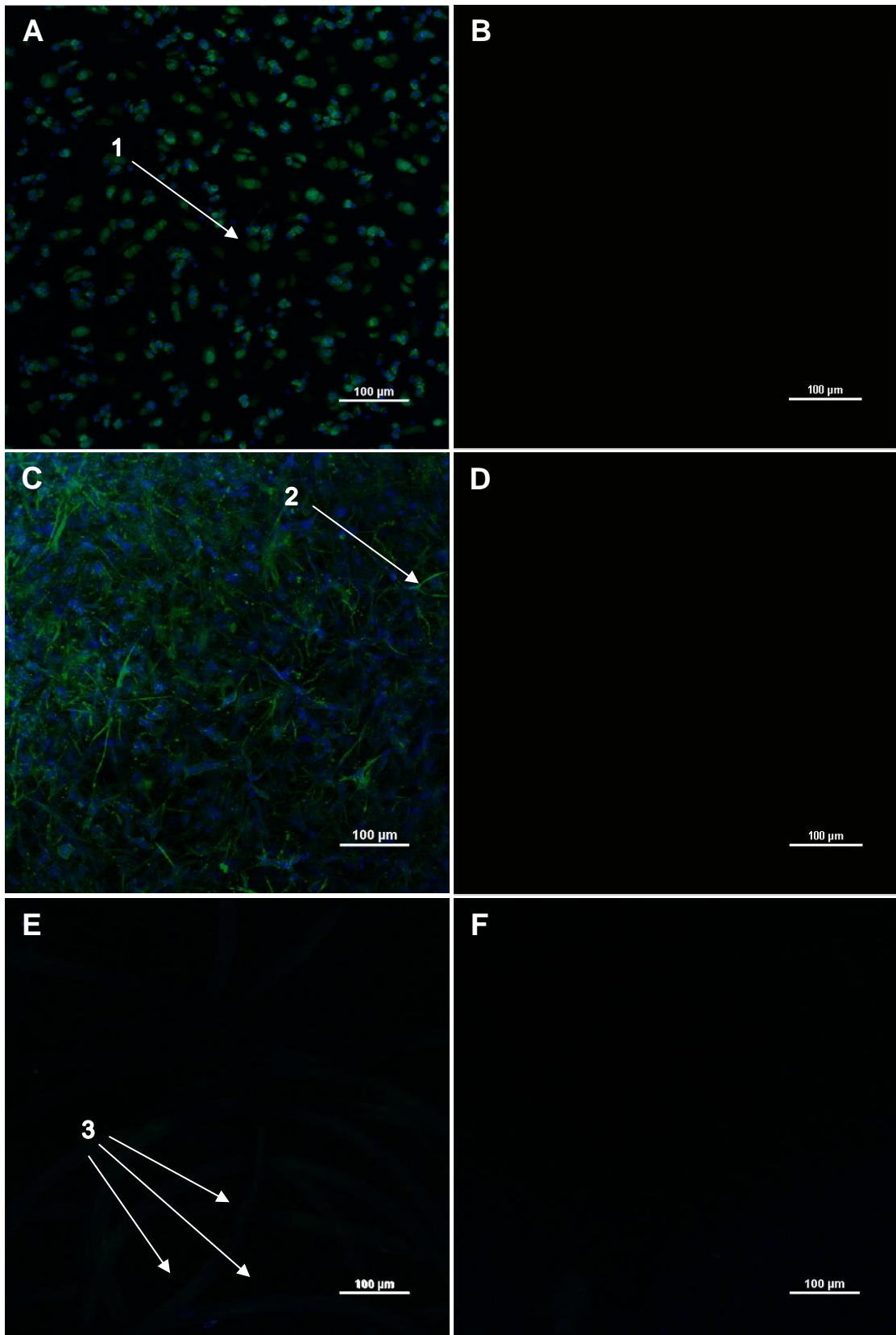


**Figure 30: Maximum projected confocal images of (A) native articular cartilage, (C) synoviocyte/PET immature cartilage construct and (E) a PET scaffold stained with Acridine orange (pseudo coloured to blue) and SiR actin (pseudo coloured to green) for nuclei and actin filaments, respectively; and non-stained samples, (B) native articular cartilage, (D) synoviocyte/PET immature cartilage construct and (F) a PET scaffold.**

Individual chondrocytes located in the deep zone of cartilage appeared rounded in shape (Label 1) and synoviocytes in the synoviocyte/PET immature construct revealed a spindle-like morphology (Label 2). Low level staining of Acridine orange was observed with the PET scaffold control (Label 3). There was no visible staining present in non-stained controls.

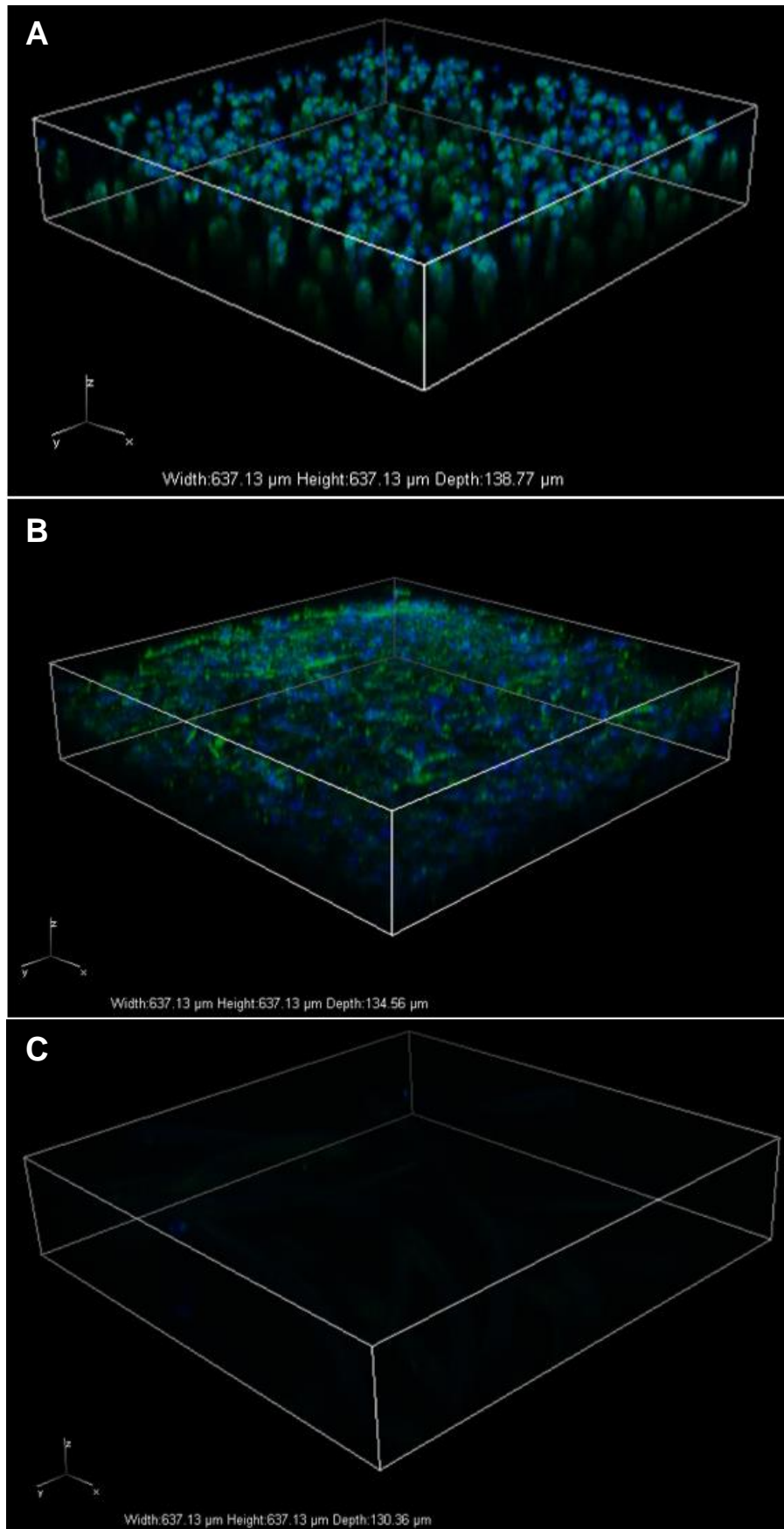


**Figure 31: 3D volume images of (A) native articular cartilage, (B) synoviocyte/PET immature cartilage construct and (C) a PET scaffold stained with Acridine orange (pseudo coloured to blue) and SiR-actin (pseudo coloured to green) for nuclei and actin filaments, respectively. Images are presented in the XYZ-plane.**

Images revealed the stains had penetrated through native cartilage and synoviocyte/PET immature construct and labelled A) chondrocytes and B) synoviocytes, respectively. Low level staining of Acridine orange was observed with C) the PET scaffold control.

### **3.5.2.3 Retention of Fluorescence Signal after Sequential Imaging of Selected Chondrocytes in Native Cartilage**

After application of a staining combination of Acridine orange and SiR-actin (as described in Section 3.4.1), confocal microscopy was used to sequentially image selected chondrocytes in the superficial surface and the deep zone of native cartilage. A series of four 3D volume images was used to record specific chondrocytes in the superficial and deep zone of native cartilage, as shown in Figure 32 and Figure 33, respectively. The fluorescence signal of SiR-actin was seen to decrease in the sequential series of images of chondrocytes in the superficial surface of native cartilage, with the loss of signal more visible images 1 and 2 (Figure 32). In addition, there was a considerable loss in fluorescence signal between the images captured in the deep zone, in particular fading was more pronounced towards the end of the series (between images 3 and 4) (Figure 33). Due to a significant loss in fluorescence signal, details on cell morphology were lost.

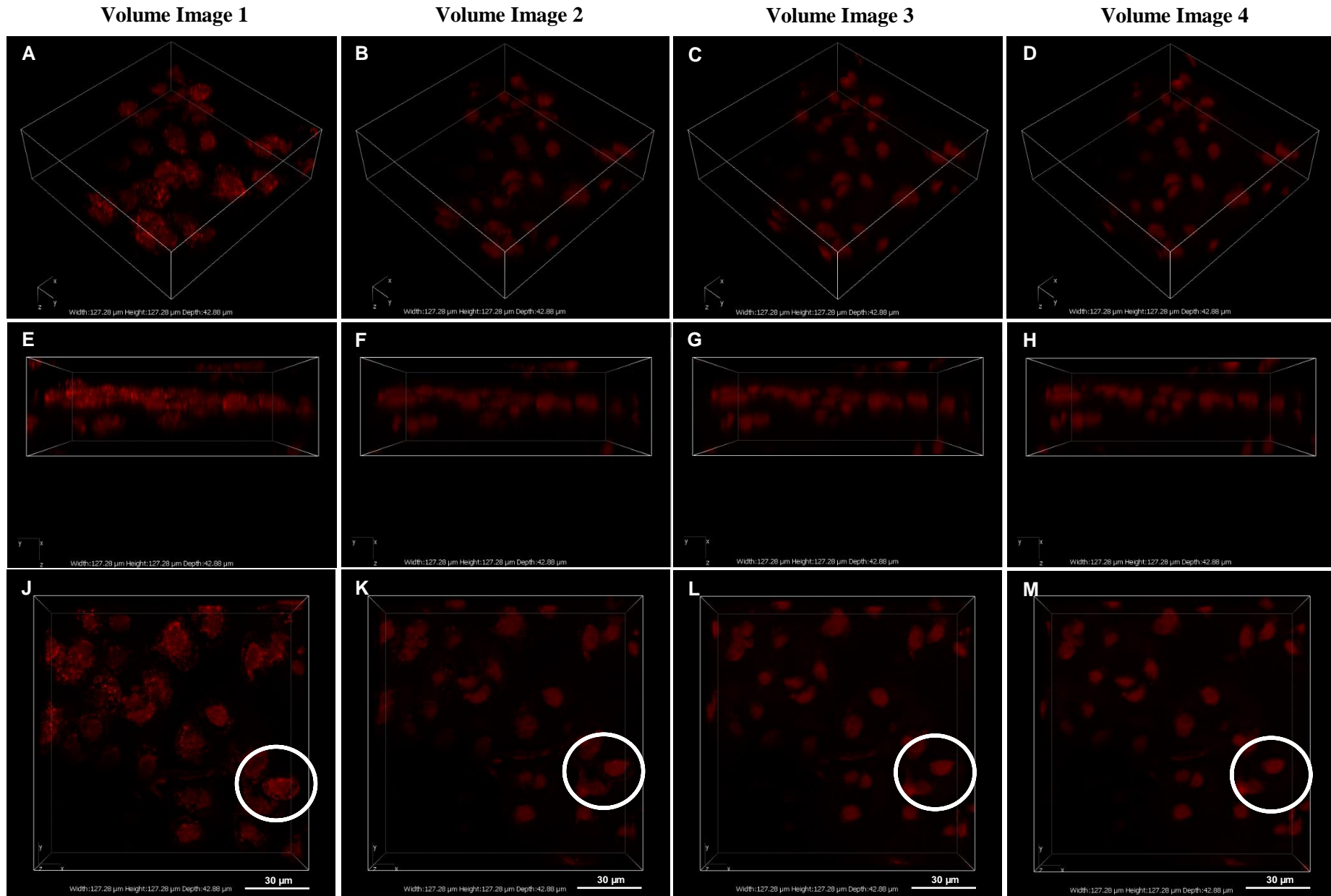


**Figure 32: A sequential series of four 3D volume images of selected chondrocytes on the superficial surface of bovine cartilage, images 1-4 (left to right) displayed in the SiR-actin (Red) channel in various planes: (A-D) XZY-plane, (E-H) XZ-plane and (J-M) Z-plane.**

There was a considerable loss in fluorescence signal between the images. Example of loss of fluorescence signal highlighted with circle.

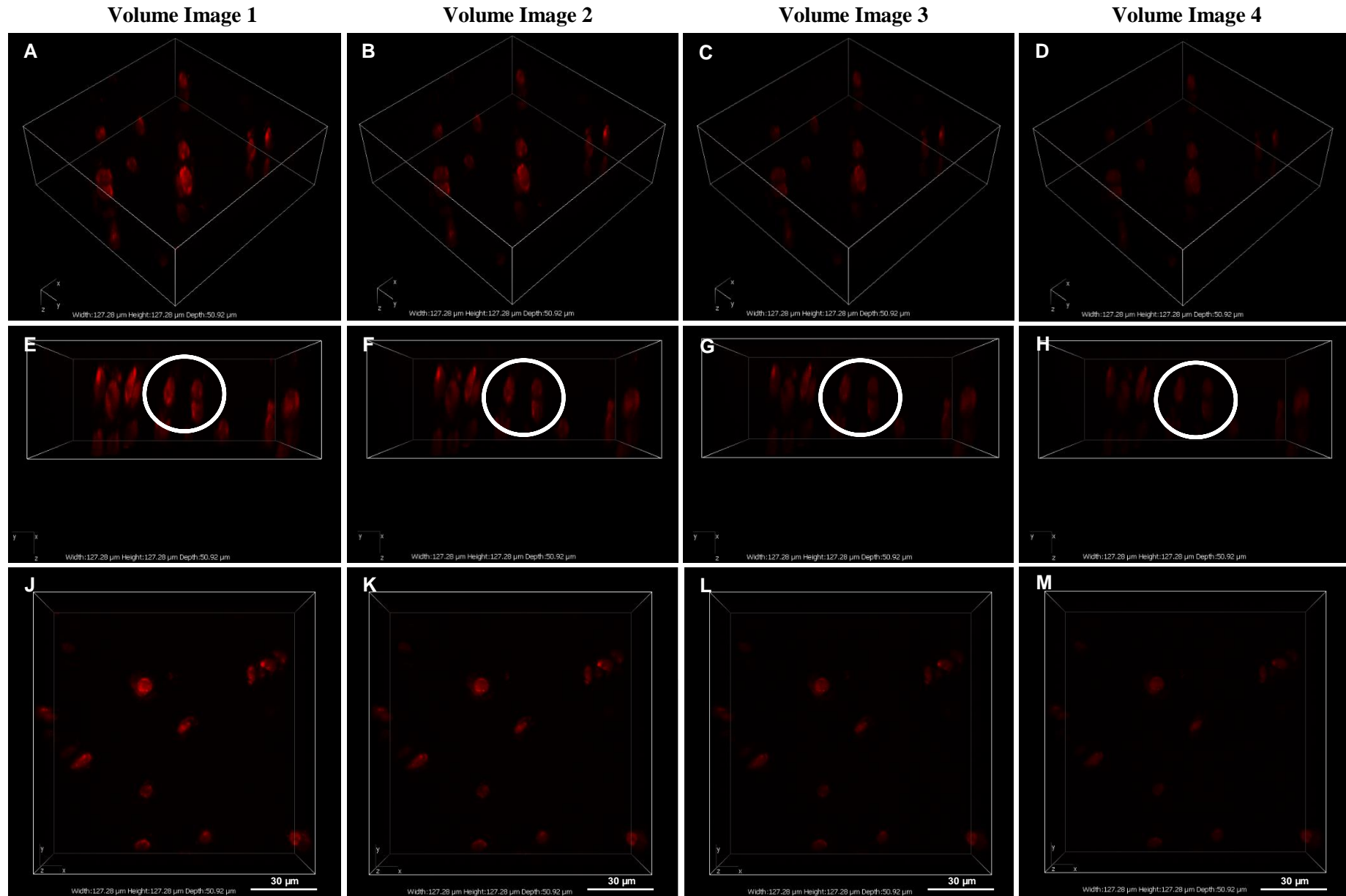


**Figure 33: A sequential series of four 3D volume images of selected chondrocytes at the deep zone of bovine cartilage, images 1-4 (left to right) displayed in the SiR-actin (Red) channel in various planes: (A-D) XYZ-plane, (E-H) XZ-plane and (J-M) Z-plane.**

There was a considerable loss in fluorescence signal between the images. Example of loss of fluorescence signal highlighted with circle.

### 3.5.3 Characterisation of the Dual Staining Method of Hoechst 33342 and CellMask Green Plasma Membrane Stains on Synoviocyte Monolayers, Native Cartilage and Synoviocyte/PET Immature Constructs

#### 3.5.3.1 Confocal Microscopy of Synoviocyte Monolayers Stained with Hoechst 33342 and CellMask Green Plasma Membrane Stains

The 3D volume images of live bovine synoviocytes, cultured in monolayer and stained with Hoechst 33342 and CellMask Green plasma membrane stains revealed high contrast labelling of cell nuclei and plasma membrane. The staining combination of Hoechst 33342 and CellMask Green plasma membrane stains provided an excellent fluorescence signal with minimal background noise, enabling clear visualisation of synoviocyte morphology including overall shape (Figure 34).

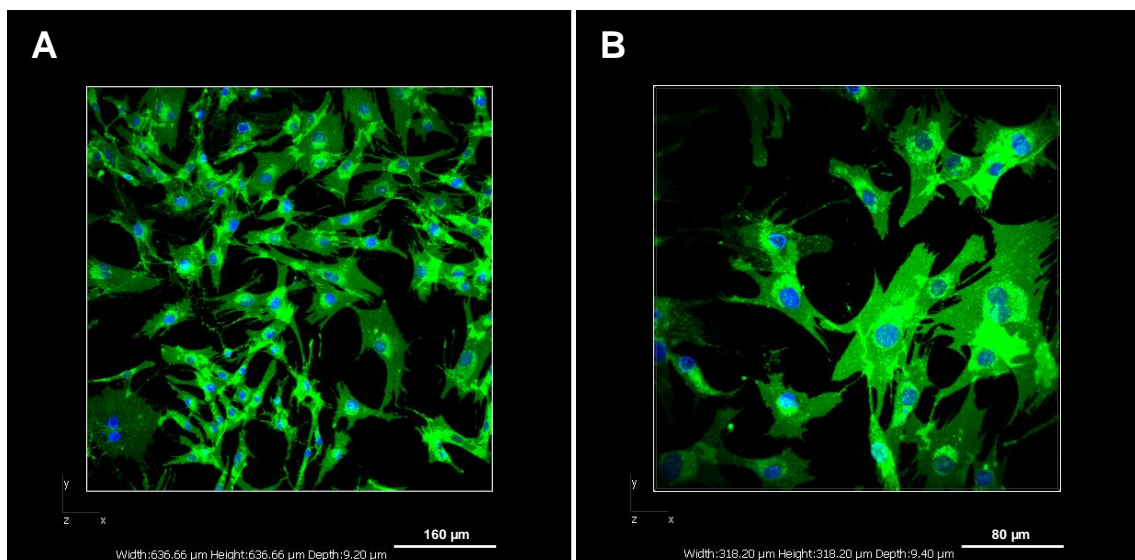


**Figure 34: 3D volume images of live bovine synoviocyte in monolayer cultures stained with Hoechst 33342 (blue) and CellMask green plasma membrane stains (green) for nuclei and plasma membrane, respectively. Cells were visualised by (A) a 20x air and (B) a 40x oil-immersion objectives. Images are presented in the Z-plane.**

Staining revealed synoviocyte morphology and shape with excellent fluorescence signal and minimal background noise.

#### 3.5.3.2 Confocal Microscopy of Cells within Native Cartilage and Synoviocyte/PET Immature Constructs Stained with Hoechst 33342 and CellMask Green Plasma Membrane Stains

Following staining of Hoechst 33342 and CellMask Green plasma membrane, native cartilage and synoviocyte/PET immature constructs were imaged via confocal microscopy. The 3D volume images showed both stains had penetrated through the tissue samples and successfully labelled cell nuclei and plasma membrane (Figure 35 and Figure 36). The images of native

cartilage revealed chondrocytes with flattened morphology within the superficial area of the tissue (Label 1, Figure 35A and Figure 36A). The CellMask Green plasma membrane staining appeared to have also labelled the pericellular matrix that surrounds chondrocytes, providing visualisation of chondrons in the superficial area (Label 3, Figure 35A and Figure 36A). In the deep zone of native cartilage, the images showed a rounded appearance for chondrocytes which were uniformly distributed throughout the tissue (Label 2, Figure 35B and Figure 36B), as would be expected.

The 3D volume images of synoviocyte/PET immature constructs showed densely packed synoviocytes to have a spindle-like morphology and an even distribution throughout the construct constructs (Label 4, Figure 35C and Figure 36C), with an appearance similar to that of synoviocytes SiR-actin stained (Section 3.5.2.2). The staining provided highly resolved visualisation of cell shape within the construct. Blue fluorescence signal was observed with the PET scaffold control (no cells), indicating that the Hoechst 33342 stain had been bound to the scaffold fibres (Label 5, Figure 35D and Figure 36D). The scaffold fibres appeared to have a high affinity to Hoechst 33342 and consequently fluoresce at the same wavelength as cell nuclei. Negative, non-stained controls showed no visible staining present, suggesting no autofluorescence.

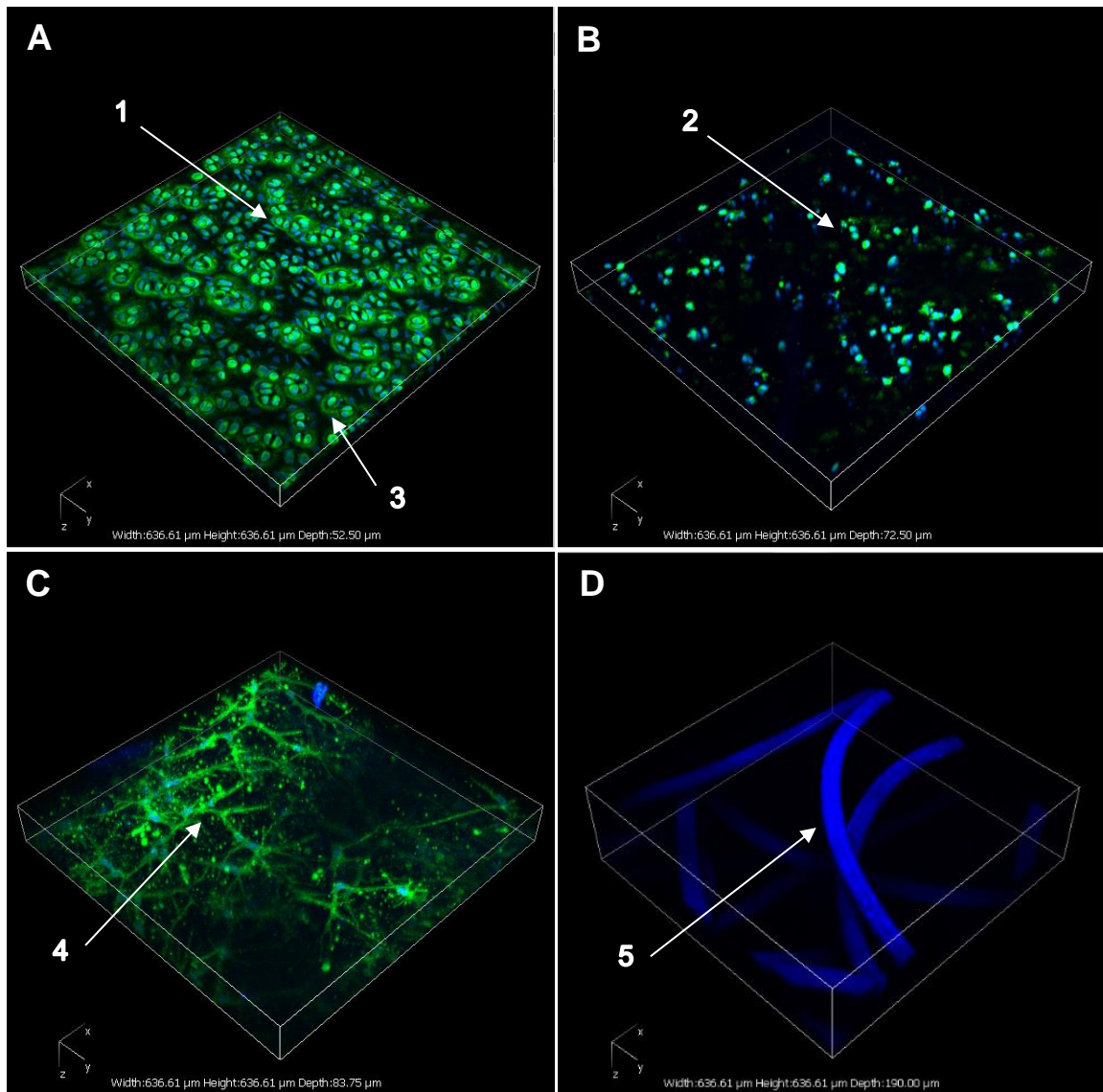


**Figure 35: 3D volume images of (A) superficial surface, (B) the deep zone of native articular cartilage, (C) synoviocyte/PET immature cartilage construct and (D) a PET scaffold stained with Hoechst 33342 (blue) and CellMask green plasma membrane stains (green) for nuclei and plasma membrane, respectively. Images are presented in the XYZ-plane.**

Individual chondrocytes located in the superficial and the deep zone of cartilage appeared flattened (Label 1) and rounded (Label 2) in shape, respectively. Staining appeared to have also labelled the pericellular matrix that surrounds chondrocytes (Label 3). Synoviocytes within the synoviocyte/PET immature construct appeared to have a spindle-like morphology and a random distribution throughout the construct (Label 4). Blue fluorescence signal was picked up by the scaffold fibres in the PET scaffold control (no cells) (Label 5).

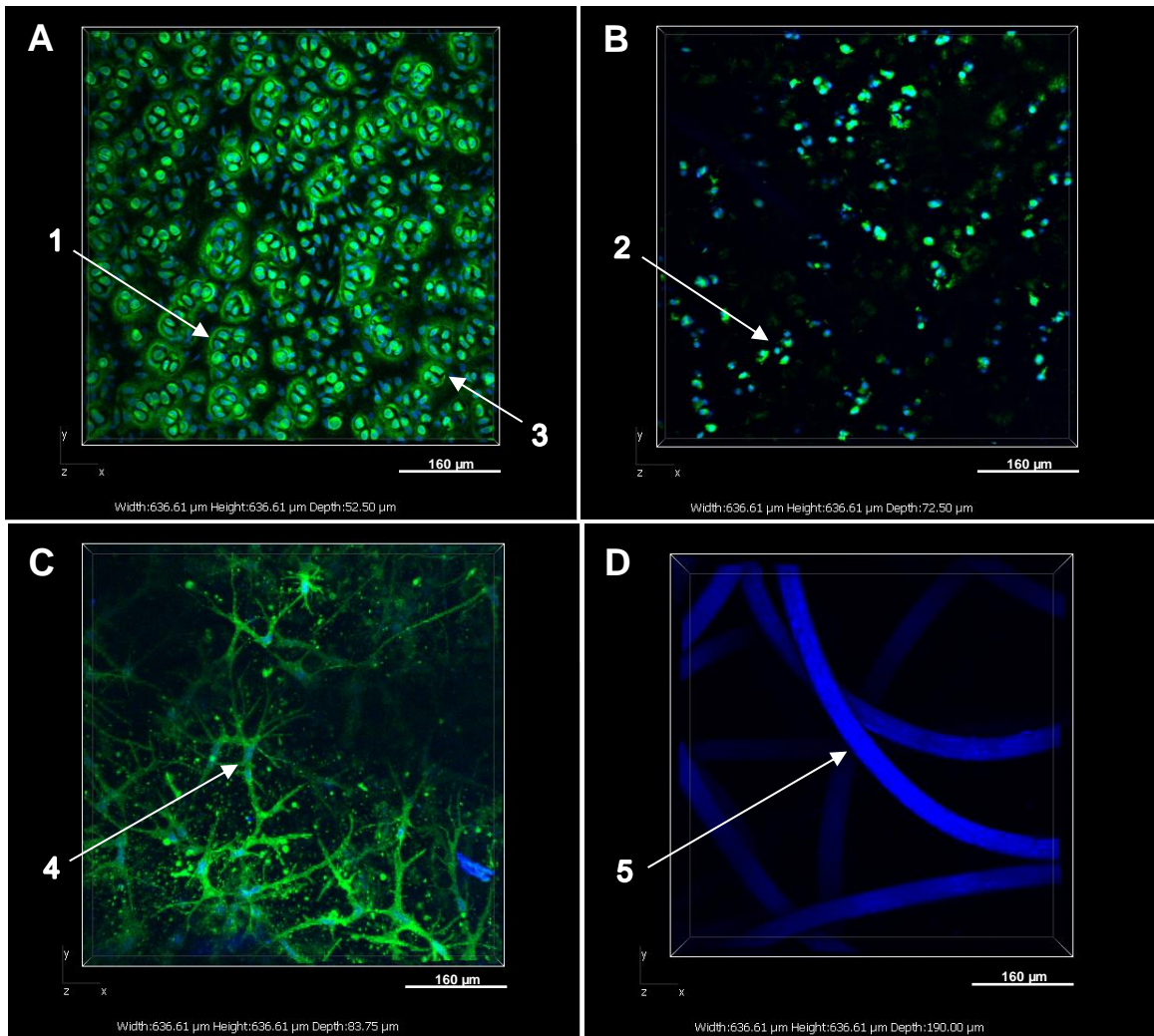


**Figure 36: 3D volume images of (A) superficial surface, (B) the deep zone of native articular cartilage, (C) synoviocyte/PET immature cartilage construct and (D) a PET scaffold stained with Hoechst 33342 (blue) and CellMask green plasma membrane stains (green) for nuclei and plasma membrane, respectively. Images are presented in the Z-plane.**

Individual chondrocytes located in the superficial and the deep zone of cartilage appeared flattened (Label 1) and rounded (Label 2) in shape, respectively. Staining appeared to have also labelled the pericellular matrix that surrounds chondrocytes (Label 3). Synoviocytes within the synoviocyte/PET immature construct appeared to have a spindle-like morphology and a random distribution throughout the construct (Label 4). Blue fluorescence signal was picked up by the scaffold fibres in the PET scaffold control (no cells) (Label 5).

### 3.5.3.3 Tissue Penetration of Hoechst 33342 and CellMask Green Plasma Membrane in Native Cartilage

Confocal image of cross-sectional slices of stained native cartilage revealed that both Hoechst 33342 and CellMask Green plasma membrane stains had penetrated through the full thickness of the tissue and were able to provide cell visualisation by labelling nuclei and plasma membranes, respectively (Figure 37).

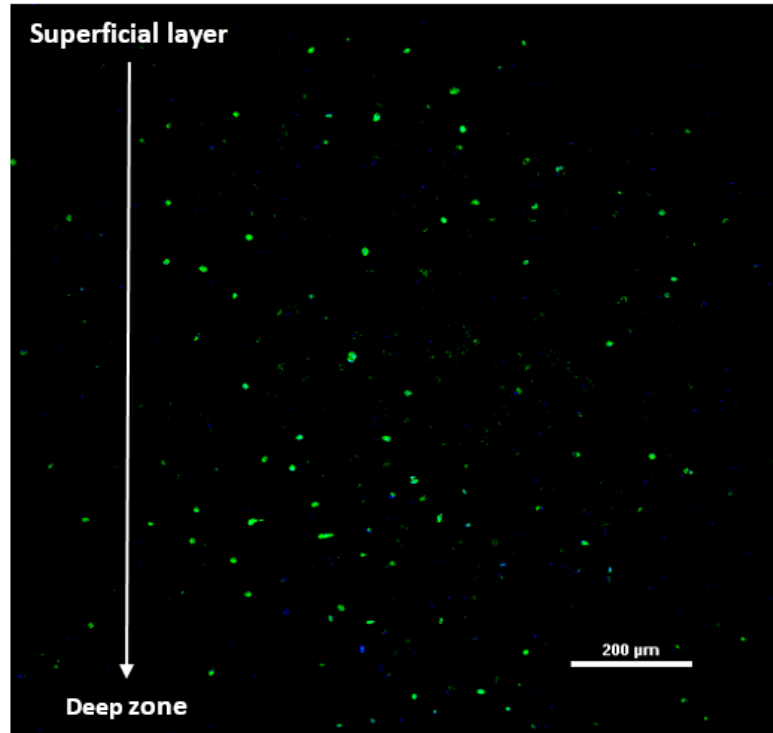
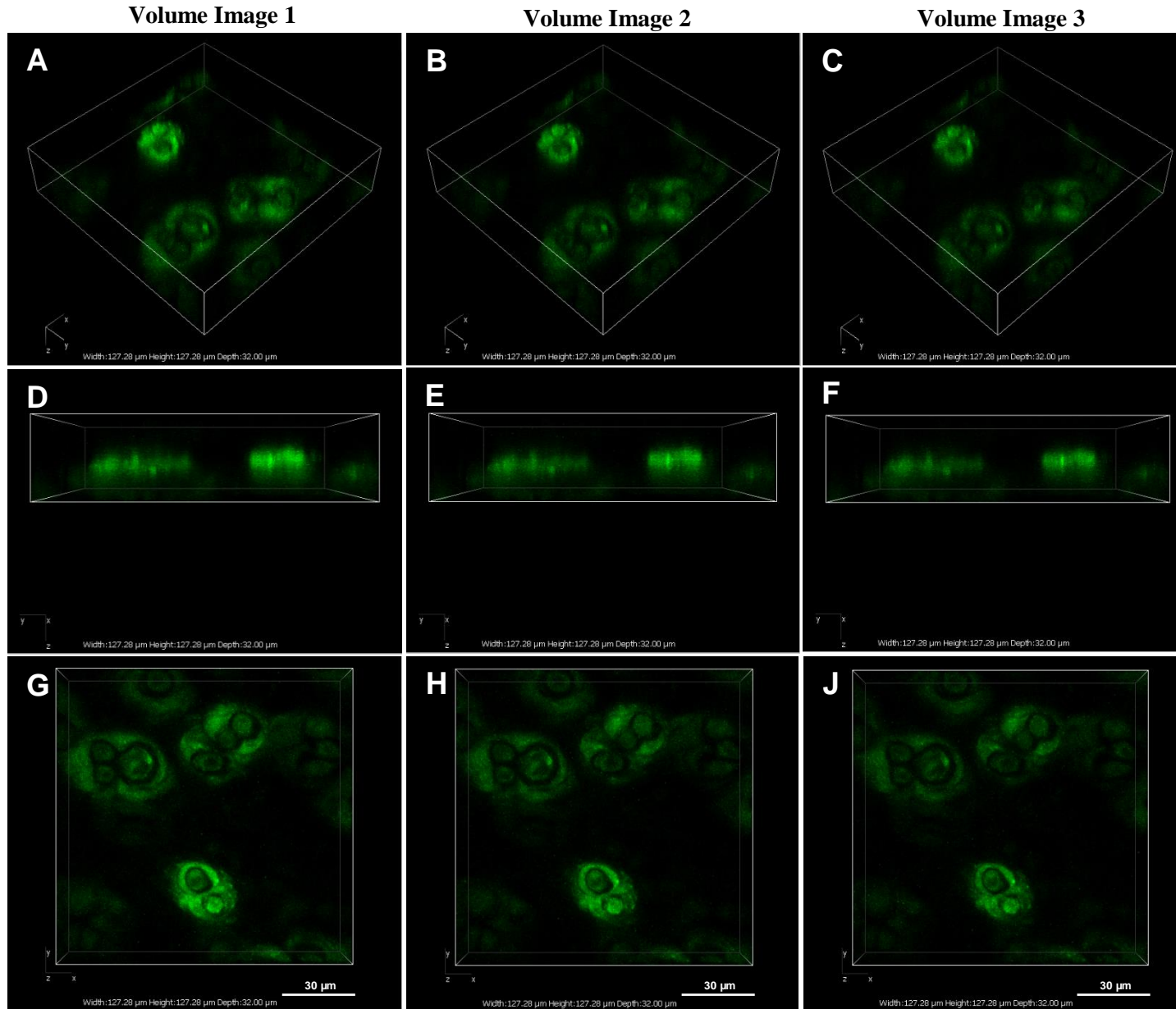


Figure 37: Confocal image of cross section of native articular cartilage stained with Hoechst 33342 and CellMask green plasma membrane revealed both stains penetrated through the full thickness of the tissue from the superficial layer down to the deep zone.

### 3.5.4 Effect of Addition of ProLong<sup>®</sup> Live Antifade Reagent on Retention of Fluorescence Signal after Sequential Imaging of Selected Chondrocytes in Native Cartilage

With the addition of ProLong<sup>®</sup> Live Antifade Reagent, the ability to retain fluorescence signal in native cartilage after tracking selected cells through multiple times were compared between the staining methods of Hoechst 33342 coupled with CellMask Green plasma membrane and Acridine orange combined with SiR-actin. After application of stains, confocal microscopy was used to sequentially image selected cells in the samples. The intensity of the fluorescence signal of CellMask Green plasma membrane stain in native cartilage was seen to be similar between the three sequential images and was much superior to that seen for SiR-actin stained cartilage (Figure 38 and Figure 39), indicating that the CellMask Green plasma membrane stain may be better at retaining its signal. With the addition of ProLong<sup>®</sup> Live Antifade Reagent in the staining method, SiR-actin appeared to retain its signal better than previous experimentation but fading still occurred (Figure 39).



**Figure 38: A sequential series of three 3D volume images of selected chondrocytes on the superficial surface of bovine cartilage, images 1-3 (left to right) displayed in the CellMask green plasma membrane (Green) channel in various planes: (A-C) XYZ-plane, (D-F) XZ-plane and (G-J) Z-plane.**

Similar fluorescence signal intensity was observed between three sequential volume images following staining of CellMask green plasma membrane coupled with ProLong® Live Antifade Reagent.

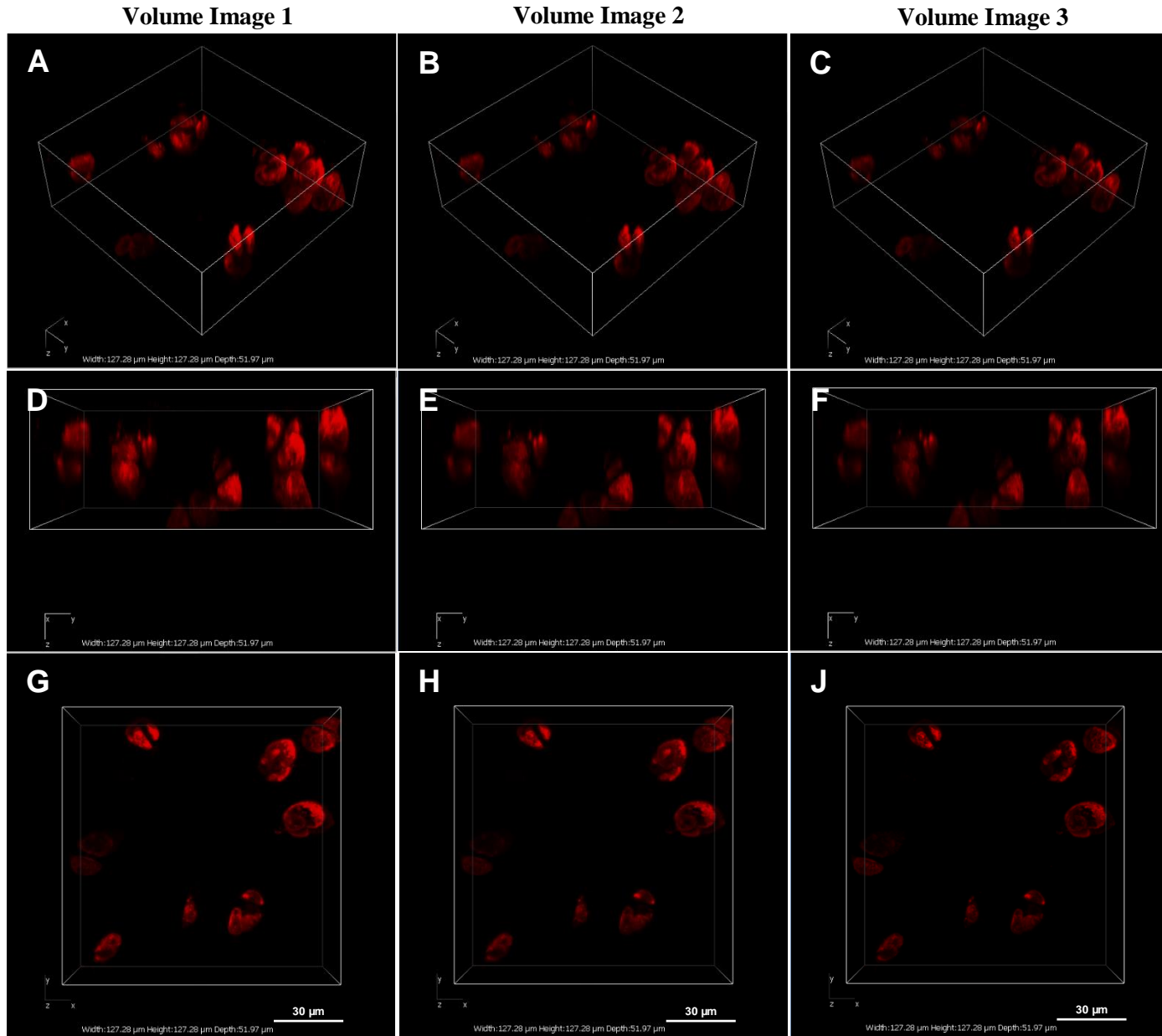


**Figure 39: A sequential series of three 3D volume images of selected chondrocytes in the deep zone of bovine cartilage, images 1-3 (left to right) displayed in the SiR-actin (Red) channel in various planes: (A-C) XYZ-plane, (D-F) XZ-plane and (G-J) Z-plane.**

With the addition of ProLong<sup>®</sup> Live Antifade Reagent in the staining method, SiR-actin improved on retaining fluorescence signal following the capture of three sequential images compared to previous experimentation but fading still occurred.

### 3.5.5 Retention of Fluorescence Signal after Sequential Imaging of Selected Chondrocytes in Native cartilage using Galvo and Resonant Scanning with the Addition of ProLong<sup>®</sup> Live Antifade Reagent

Following application of Hoechst 33342 and CellMask Green plasma membrane stains with the addition of ProLong<sup>®</sup> Live Antifade Reagent, the change in fluorescence signal following the capture of a series of three volume images was measured and compared between image acquisition methods using either galvo or resonant scanning. Approximately 90 % of the fluorescence signal was retained when galvo scanning was used compared to 83% for resonant scanning after the images were recorded (Figure 40).

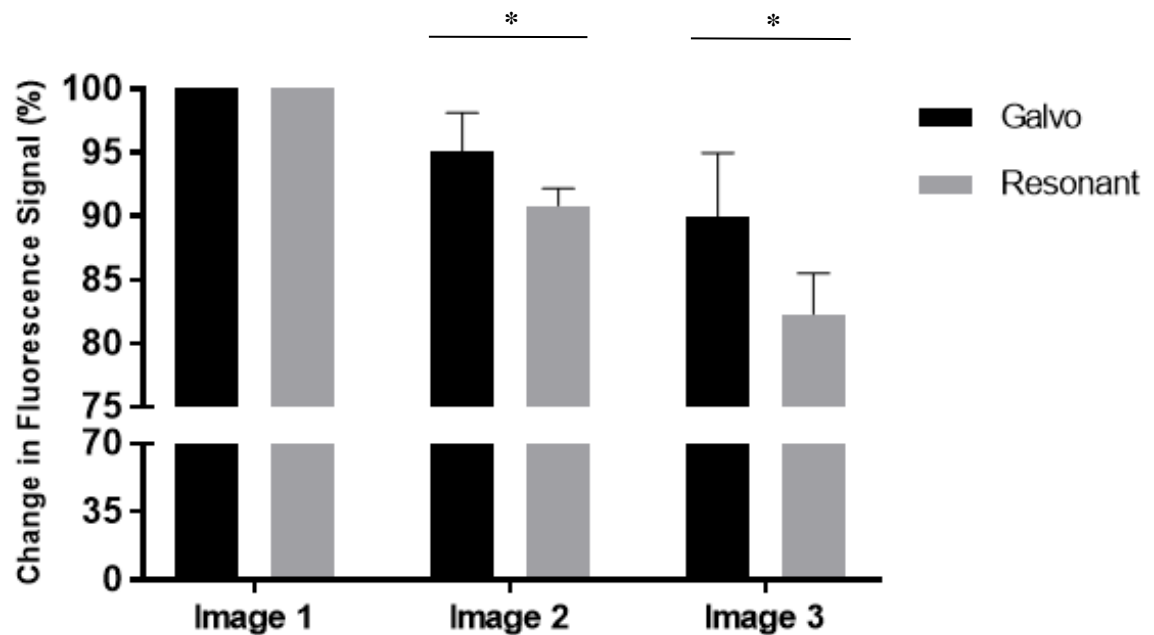


**Figure 40: Change in mean fluorescence intensity after selected chondrocytes were sequentially imaged three times under non-loaded conditions using traditional galvo and high speed resonant scanning in the confocal microscope.**

Significantly greater loss of fluorescence signal was observed with the use of resonant scanner. Data represented as means  $\pm$  SD (n=6). Statistical difference determined by paired t-test (\*  $\equiv$  p < 0.05).

## 3.6 Discussion

The aim of this chapter was to develop a live cell staining method that was able to fluorescently-label cells and allow the operation of the confocal microscope to track and image 3D changes in cell morphology (shape and size) of living chondrocytes within native cartilage and bovine synoviocytes within tissue engineered cartilage during different magnitudes of static compressions via sequential imaging. Thus, the method developed needed to allow stains to penetrate the dense matrix and provide specific and highly resolved visualisation of cell morphology for 3D quantification measurements. In addition, because an aim of this thesis was to determine the cellular deformation behaviour within native and tissue engineered cartilage

under different magnitudes of compressive strain, the stains needed to label the cells inside both tissue samples and be capable of imaging selected cells multiple times without significant signal loss. Fluorescence signal loss would result in lack of detail for cell morphology and therefore could potentially affect the accuracy of quantitative data on cell deformation obtained from the images.

This chapter investigated two potential staining methods; i) a dual staining method of Acridine orange and SiR-actin stains and ii) a dual staining method of Hoechst 33342 and CellMask Green plasma membrane stains for application in live cell imaging in native and tissue engineered cartilage. To determine which staining method was best suited, both staining methods were evaluated on synoviocyte monolayers, bovine cartilage disks and synoviocyte/PET immature constructs under non-loaded conditions as a prelude to subsequently determining cell deformation behaviour in native and tissue engineered cartilage under different compressive loads (described in Chapter 4 and Chapter 5). The effects of photobleaching with the use of ProLong<sup>®</sup> Live Antifade Reagent in both staining methods were evaluated. In addition, an appropriate confocal imaging setting for tracking changes in cell morphology within native and tissue engineered cartilage subjected to different amounts of tissue deformation was determined.

### **3.6.1 Characterisation and Optimisation of SiR-actin Stain on Synoviocyte Monolayers**

Staining actin filaments allows visualisation of the overall cell shape. A number of various methods and probes are currently available for labelling actin in living cells which apply the principle of fusing fluorescent protein to different actin-binding proteins or domains, such as LifeAct [240], [245], utrophin and F-tractin [239], as well as the technique of expression of GFP-actin (as described in Section 3.1.3) [234], [236], [240]. Although these techniques have been successful in visualisation of F-actin in living cells, there is still a need to introduce them into cells either via protein transfection reagents (plasmid or viral vectors) or microinjection which could be time-consuming and problematic [239], [245].

A novel membrane permeable fluorescent probe called SiR-actin was recently developed to bind to F-actin in living cells without the need to overexpress fluorescently labelled proteins [238], [246]. It was chosen as a potential marker in this study to label F-actin and provide visualisation of the overall cell shape in living native cartilage and synoviocyte/PET immature constructs because of its membrane permeable characteristic, fluorogenity properties as well as high specificity to F-actin [238]. To the best of the author's knowledge, SiR-actin has never been applied to native cartilage and cartilage constructs before, therefore, in this thesis, its use was first optimised on cell monolayers. Bovine synoviocyte were selected for this as this is the cell type used to produce the tissue engineered cartilage in Finlay *et al.* (2016) [1] and in this thesis.

To evaluate SiR-actin as a potential marker for labelling F-actin, the desired concentration to obtain strong staining in synoviocyte was first determined, following by a comparison of SiR-actin staining with the more widely used F-actin marker, phalloidin (e.g. Alexa Fluor<sup>®</sup> 488 phalloidin) [234], [249].

There is little literature available that provides a recommended SiR-actin concentration to use for labelling F-actin in live cell imaging of cartilage specimens. However, a range of concentration between 0.1 to 2  $\mu\text{M}$  have been used in previous studies to label actin in various types of cells and tissues [238], [246], [249]–[251]. Este *et al.* (2016) [246] revealed that the periodic organisation (ring-shaped pattern) of actin and spectrin subcortical cytoskeleton is not just a distinctive feature of hippocampal neurons but rather a fundamental characteristic of cells in the nervous system with stimulated emission depletion (STED) super resolution microscopy. SiR-actin probe (0.1  $\mu\text{M}$ ) was used by Este *et al.* to discover the formation of a subcortical periodic actin structure in the axons of live rat dorsal root ganglion neurons, cortical neurons, striatal neurons and granule cells from the cerebellum [246]. In another study by Romarowski *et al.* (2018) [249], 0.1  $\mu\text{M}$  SiR-actin was also used, in combination with super-resolution microscopy, to effectively reveal the regions that contain F-actin within the head of live mouse sperm cells and observe the dynamic changes of F-actin prior to and during acrosomal exocytosis. In a study by Magliocca *et al.* (2017) [250], in which 1  $\mu\text{M}$  of SiR-actin and SiR-tubulin probe were used, actin and tubulin cytoskeletal dynamics were analysed in proliferating induced pluripotent stem cells (iPSCs) and iPSC-derived neurons following treatments with de-polymerisation. The use of both SiR probes with live cell time-lapse imaging allowed Magliocca *et al.* (2017) to monitor the rapid re-organisation of the cytoskeleton in both iPSC and iPSC-derived neurons after induced de-polymerisation [250]. Furthermore, a SiR-actin concentration of 2  $\mu\text{M}$  was used by Klementieva *et al.* (2016) [251] to study the fine structure and remodelling of actin filaments within tumour tissue. The SiR-actin probe combined with live cell imaging provided an efficient way to visualise the fine details of actin cytoskeleton in tumour tissues of two mouse models at high resolution and allowed Klementieva *et al.* (2016) to demonstrate for the first time that the actin structure of cancer cells in tumour *in vivo* differs from that in cancer cells *in vitro* and in normal tissues [251].

Since SiR-actin is developed from a derivative of Jasplakinolide, a drug that is known to stabilises actin and has shown to be cytotoxic, the only potential disadvantages are the possible alternation of actin dynamics and induced phototoxicity effects in living cells [238]. However, it has been reported that at concentrations up to 3  $\mu\text{M}$  SiR-actin did not alter the mitotic spindle morphology and the duration of mitotic formation [238]. In addition, SiR-actin did not have cytotoxicity effects toward primary human fibroblasts over a period of 24 hrs of time-lapse imaging as well as showed no detectable effect on proliferation in cultured HeLa cells when a concentration up to 0.1  $\mu\text{M}$  was used [238]. Since higher concentrations could impair actin

dynamics and have cytotoxicity effects, it is recommended to minimise the concentration of SiR-actin up to or equal to 0.1  $\mu\text{M}$  for long term live cell imaging [238].

In this study, a concentration of SiR-actin that provides good staining intensity with minimal undesirable effects on cell viability was desired. For this reason, different concentrations of SiR-actin (0.1 to 2  $\mu\text{M}$ ) were investigated on synoviocyte monolayers to identify a suitable concentration for visualising the structure and dynamics of F-actin without interference. There seemed to be no discernible difference in staining intensity when synoviocytes in monolayer culture were stained with different concentrations of SiR-actin. A concentration of 0.1  $\mu\text{M}$  SiR-actin (in accordance to the manufacturer recommendations to avoid undesirable effects) resulted in bright fluorescent signal in the synoviocytes in comparison to those other concentrations used, suggesting that this concentration could provide a sufficient amount of SiR-actin molecules for labelling F-actin. Elevated concentration of SiR-actin is suggested to have undesirable effects on actin filaments, as described previously in this section. Lukinavicius *et al.* (2014) [238] suggested that there is a concentration window where these undesirable effects are minimal and showed that low imaging concentrations (equal or below 0.1  $\mu\text{M}$ ) had little phototoxicity, did not affect actin dynamics and provided a high signal to noise ratio. It is evident that by keeping the concentration of the stain as low as possible would avoid or minimise the undesirable effects. In this study, SiR-actin at 0.1  $\mu\text{M}$  provided a bright fluorescent signal that is adequate to identify cell shape and, therefore 0.1  $\mu\text{M}$  was chosen as the concentration of SiR-actin used following the preliminary experiment described in this thesis.

Since phalloidin, a fluorescent derivative of phallotoxins, is traditionally used as the gold standard marker for labelling actin filaments [234], [249] and according to the manufacturer, Alexa Fluor<sup>®</sup> 488 phalloidin is a F-actin specific probe often used by researcher, it was used to benchmark against SiR-actin in terms of morphological comparison of labelled cell features [252]. Confocal images of synoviocytes labelled with SiR-actin and Alexa Fluor<sup>®</sup> 488 phalloidin revealed similar labelled filamentous structures, indicating that actin filaments were being stained by the SiR-actin to a similar extent to those stained using the more widely used Alexa Fluor<sup>®</sup> phalloidin. Spherical stained structures was also visible in the image of synoviocytes stained with SiR-actin (Figure 28B). This might potentially be stain debris, however this is unknown.

### **3.6.2 Characterisation of the Dual Staining Method of Acridine Orange and SiR-actin Stains on Synoviocyte Monolayers, Native Cartilage and Synoviocyte/PET Immature Constructs**

The strategy of these experiments was to evaluate SiR-actin as a potential marker to determine cell morphology and actin filament structures in living native cartilage and tissue engineered constructs which would ultimately be subjected to different incremental compressive strains in

later experimentations. In order to achieve this, the stain was required to penetrate in to tissue samples and provide specific and highly resolvable labelling of cell morphology. Most importantly, the stain must be able to retain its fluorescence signal after tracking and imaging of selected cells multiple times in order to study the effect(s) of incremental loading on cell deformation behaviour in native and tissue engineered cartilage.

By using a staining combination of Acridine orange and SiR-actin, confocal images of synoviocyte monolayers, native cartilage and synoviocyte/PET immature constructs showed highly resolved cell morphology, supporting the use of Acridine orange and SiR-actin for the required live cell imaging applications. By coupling a nuclear stain with the actin probe, it helped to identify the actin filaments associated with each cell as well as cell morphology. However, it was more difficult to distinguish cell boundaries in synoviocyte/PET immature constructs due to the synoviocytes being so densely packed. The actin cytoskeleton is well-known in forming a 3D dynamic network that is able to assemble and disassemble to provide mechanical support for the cell in response to mechanical stimulation [104]. In addition, it is physically associated with cell adhesions which link to cells to their ECM and to neighbouring cells [253]. These details were observed in confocal images of monolayers of live synoviocyte, revealing in particular highly organised bundles and networks of actin filaments (Label 1, Figure 29E) and cell-cell adhesions (Label 7, Figure 29D). In addition, staining also revealed the assembled and disassembled actin filaments in bovine synoviocytes; globular-actin was visible along with actin filaments (Label 3, Figure 29E). Although actin filaments are able to assemble/disassemble, they do not simply switch between the polymerised and depolymerised state [105]. Instead, F-actin elongates steadily in the presence of actin monomers [105]. This explains why actin filaments with different lengths were observed in the confocal images shown here (Label 2, Figure 29A).

Within the fluorescently labelled nuclei (Label 4, Figure 29F), denser staining of Acridine orange was observed in some regions of the nuclei compared with others, potentially indicating the presence of nucleoli (Label 5, Figure 29D and Figure 29F). Nucleoli are responsible for the transcription of ribosomal RNA and the synthesis of ribosomes and therefore a high concentration of RNA and DNA is present in these sub-organelles [254]. Since Acridine orange is a cell permeable nucleic acid stain that binds to single/double stranded DNA and RNA, nucleoli were identified with dense staining within the nuclei. In addition, Acridine orange was faintly visible in the cytoplasm (Label 6, Figure 29F). Likewise, this may be due to ribosomes, (composed of RNA molecules for the translation process into proteins) which are found in the cytoplasm.

Both Acridine orange and SiR-actin stains appeared to have penetrated through the native cartilage and synoviocyte/PET immature constructs and were able to reveal the morphology of chondrocytes and synoviocytes, respectively (Figure 31). As expected, chondrocytes had a

round morphology and were arranged in columns in the deep zone of native cartilage (Figure 30A and Figure 31A). In synoviocyte/PET immature constructs, synoviocytes were seen as spindle-like structures with actin filaments branching out to other actin filaments in surrounding synoviocytes and were scattered relatively evenly throughout the construct (Figure 30C and Figure 31B). In addition, the synoviocytes were more densely packed than the chondrocytes in native cartilage and difficult to distinguish one cell from another. This observation revealed that cell-cell interactions might be occurring within the construct. Cell-cell interaction plays a role in the mechanotransduction process as actin filaments are able to transmit intercellular forces arising from cell-cell adhesion and respond by triggering mechanotransduction signalling pathways to increase matrix synthesis and deposition in maturing the construct [101]. These observations were therefore encouraging data which supported the use of Acridine orange and SiR-actin for determining cell morphology in native cartilage and tissue engineered constructs for later cell deformation studies.

Due to light absorption and scattering by tissue specimens, laser light penetration depth has always been a challenge in biological tissue imaging which plays a role in the achieved imaging depth [213]. It was noted that confocal microscopy was unable to visualise cells throughout the full thickness of native cartilage and synoviocyte/PET immature constructs. This was most likely due to the density of both tissues being too great (even in constructs at the early stage of development) causing absorption and scattering which consequently prevented light penetration. The maximum penetration depth was therefore limited to between 100-140  $\mu\text{m}$  (with a 20x air objective) and consequently restricted visualisation to the sample surfaces. This meant that only the articular surface and the deep zone of native cartilage could be observed (i.e. by inverting the sample). However, the depth of penetration is generally limited to 50-100  $\mu\text{m}$  for confocal microscopy [213]. Previous studies that have examined 3D deformation behaviour of chondrocytes in native cartilage achieved the maximum imaging depth of around 40-50  $\mu\text{m}$  without cutting the tissue to expose the cross-sectional area [85], [145]. Han *et al.* (2010) [145] took Z stack images of chondrocytes from the superficial surface to a depth of 40  $\mu\text{m}$  inside the cartilage, whilst Madden *et al.* (2013) [85] managed to image chondrocytes between the superficial surface and 50  $\mu\text{m}$  depth (both studies used a 40x water immersion objective). However, another contributing factor in determining the imaging depth is the working distance (WD) (vertical distances between the front of the objective and the closest sample surface when the sample is focused) of the objective [213]. Typically, the depth of imaging decreases as the WD decreases along with increased magnification and the objective's numerical aperture (NA). Imaging thick tissue sample with a lower NA, longer WD objective would improve the imaging depth, but with lower resolution and sensitivity. However, the use of a higher magnification objective (with a higher NA) would limit the imaging depth into the sample due to a trade-off of a shorter WD. The 40x water immersion objective used by Han *et al.* (2010) [145] and Madden *et al.* (2013) [85] which had an NA of 0.8 would have partly contributed to the limited depth

achieved compared to that achieved with a 20x air objective (0.75 NA) in this study. Nevertheless, a significant improvement on penetration depth was achieved with the dual staining method of Acridine orange and SiR-actin stains in this study in comparison to those previously achieved in the field. Penetration depth could be further improved by increasing excitation light intensity but this would then increase the likelihood of photobleaching, causing the fluorescent marker to lose the ability to fluoresce throughout the required time period. As penetration depth is a limitation of using confocal microscopy to image tissue samples in this thesis, the regions of interest was restricted to the regions in which the confocal microscope was capable of imaging.

Significant loss of fluorescence signal was observed and consequently loss of details of cell morphology when selected chondrocytes in the superficial surface and the deep zone were sequentially imaged four times (Figure 32 and Figure 33). There are at least two potential factors that could explain the reduced fluorescence intensity seen after sequentially imaging:

- a) SiR-actin effluxes from the cells over the duration of experimentation; unbound or non-specific binding of SiR-actin doesn't fluoresce.
- b) Long exposure to light causes photobleaching to occur and consequently fluorophores lose their fluorescence permanently.

The labelling efficiency of SiR-actin was reported to vary with cell types, depending in particular on the expression level of efflux pumps [238]. SiR-actin molecules can be removed from the cells via efflux pumps, consequently resulting in low staining efficiency [238]. Verapamil is a known broad-spectrum efflux-pump inhibitor [255] which could block efflux of fluorophores and it was recommended by the manufacturer to add it to the SiR-actin staining solution to reduce such effect [238]. It was reported that the addition of Verapamil improved staining substantially in cell lines that showed low labelling efficiency [238]. It is possible that Verapamil unbind from the efflux pumps during the duration of experimentation and results in low signal intensity. However, Mishra et al. (2019) [256] showed that the supplementation of 100 nM of Verapamil with SiR-actin staining prolonged retention of the probe in the study to determine the turnover dynamics of actin cytoskeleton in human bone-marrow derived MSCs following lineage diverging culture. In addition, SiR-actin signal started to fade at different time between the sequential images of chondrocytes captured in two native cartilage disks (Figure 32 and Figure 33). As both cartilage disks were harvested from the same bovine knee joint and cultured and imaged in the same conditions (except the use of different laser power for imaging), this perhaps suggests the signal loss might be related to the image acquisition settings. This therefore tends to reduce the potential of (a) as the primary driver explaining the significant loss of fluorescence.

In the deep zone, the loss of SiR-actin signal was substantially more noticeable in later images of the sequential series, between images 3 and 4 (Figure 33). This provides evidence to suggest

(b) is likely to be the predominant driving factor to explain the results. As described in Section 3.1.2, photobleaching occurs when a fluorophore is permanently damaged and unable to fluoresce due to photo-induced chemical alteration and covalent modification [222], [224], [231]–[233]. Photobleaching can happen from long exposure to the excitation light. To reduce the occurrence of this, the intensity level of the excitation light should be kept as low as possible but it still needs to be sufficient to excite the fluorophores to fluoresce. In the case of the work described here, the laser power was set at 5 % to sequentially image chondrocytes in the deep zone (Figure 33). However, around 25 % of laser power was used to capture chondrocytes in the superficial surface and loss of signal was more significant from image 1 and 2 (of Figure 32), indicating that the intensity level of excitation light might be too high and potentially caused rapid photobleaching. This illustrated the excitation light intensity is required to be low in order to minimise photobleaching.

Even if the level of excitation light was kept to a minimum, it is not uncommon to detect fluorescence fading after sequentially imaging a region of interest (ROI) repeatedly. This is because a long exposure time partly contributes to photobleaching as well as high light intensity [223]. The duration required for acquisition of repeated images of a ROI still exposes sample to a low intensity of light for a long period and photobleaching would inevitably occur. It could be argued that acquiring four repeated images in the same region of native cartilage, as carried out here, was pushing beyond the capability of the SiR-actin stain. Some fluorescent molecules have a very short useful lifetime, after which fading occurs and they only emit a few hundred photons while some can emit a large number of photons (tens of millions) before becoming permanently bleached [233]. The number of photons emitted before photobleaching occurs depends on both on the nature of the fluorescence molecule and on its environment [233]. In this study, 5 % of laser power was used to image chondrocytes in the deep zone of native cartilage and yet loss of fluorescence intensity was observed, with fading being more pronounced in the later images (Figure 33), suggesting that the acquisition time (exposure time to light) required to record four sequential volume images was too long, causing photobleaching and so beyond the useful lifetime of SiR-actin. It was therefore decided that a maximum of three sequential images would be used to track cells within the native cartilage and tissue engineered constructs.

Overall the staining method using Acridine orange and SiR-actin proved to provide specific and highly resolved visualisation of cell morphology for cells in monolayers, native cartilage and immature cartilage constructs. However, significant fluorescence signal loss was observed when four sequential images were recorded for selected chondrocytes in native cartilage. The loss of cell morphology details due to the faded fluorescence signal would affect the measurements during any quantification from the images. This compromised the prospect of utilising the staining method of Acridine orange and SiR-actin in native cartilage and tissue engineered constructs. The confocal images using Verapamil point towards photobleaching as being the

predominant driver that caused the reduced signal. Effects could be made to reduce photobleaching by minimising exposure to excitation light, such as limiting light intensity and exposure time [223]. Light intensity could be reduced by lowering laser power or decreasing pinhole size. Exposure time depends on the number of repeated images, the number of optical sections per image and the size of an optical section. It was proposed to reduce the number of sequential images from four to three in order to reduce exposure time to the sample. In addition, the use of antifade protection in mounting medium such as ProLong<sup>®</sup> Live Antifade Reagent could help reduce photobleaching [222]. This works by reducing the oxygen available for photo-oxidation reactions that promote photobleaching. Thus far, the photobleaching prevented SiR-actin from being a promising marker for cell morphology labelling the samples used in this thesis and a means to reduce photobleaching would therefore need to be devised. Alternatively, a switch to a more photo-stable fluorochrome would be required.

### **3.6.3 Characterisation of the Dual Staining Method of Hoechst 33342 and CellMask Green Plasma Membrane Stains on Synoviocyte Monolayers, Native Cartilage and Synoviocyte/PET Immature Constructs**

Apart from the use of actin filaments staining to identify cell shape, plasma membrane staining can be a convenient marker for highlighting cell boundaries. A traditional approach for membrane labelling is the use of lipophilic dyes such as Dil and DiO [257]. However, they internalise rapidly in live cells which offers a very small window for imaging. Fluorescent wheat germ agglutinin (a plant lectin), has also been typically used as a membrane stain [258]. Staining using lectins depends upon the binding of lectin-conjugates to certain cell surface sugars (e.g. glycoproteins or glycolipids) and as a result, inconsistent staining can occur with different cell types. Another way to label cell membranes is the use of CellMask plasma membrane stain, a commercially available stain. According to descriptions provided by the manufacturer, it is an amphipathic molecule which provides a lipophilic moiety for membrane loading and consists of a negatively charged hydrophilic dye that is able to anchor the probe in the plasma membrane therefore it can rapidly stain plasma membranes across various mammalian cell types as well as providing robust and uniform staining. In addition, the manufacturer claims it internalises slower compared to the traditional approaches that were described above. Thus, CellMask Green plasma membrane stain was chosen to determine its potential application in staining plasma membrane as a means of highlighting cell morphology. In addition, Hoechst 33342 dye was selected to couple with CellMask Green plasma membrane to label cell nuclei and identify cells.

Hoechst 33342 and CellMask Green plasma membrane staining was apparent throughout the depth of a cross-sectional native cartilage sample (Figure 37), suggesting both stains were able

to penetrate the full thickness of tissue and permit visualisation of the chondrocytes. Confocal images of stained synoviocyte monolayers, native cartilage and synoviocyte/PET immature constructs revealed bright staining of cell nuclei and membranes and consequently provided highly resolved cell morphology (Figure 34-36). Chondrocytes located in different regions of native cartilage clearly showed different morphologies. Flattened and rounded chondrocytes were revealed in the superficial surface and the deep zone, respectively, as would be expected (Figure 35A-B and Figure 36A-B) [8]. Staining appeared to have also labelled the pericellular matrix surrounding the chondrocytes in the superficial zone (Figure 35A and Figure 36A). However, clear cell boundaries could still be visualised from the images, therefore permitting future analysis of cell deformation in later studies. The spindle-like morphology of synoviocytes in the synoviocyte/PET immature constructs was clearly labelled but it was difficult to distinguish the cell boundaries due to the synoviocytes being so densely packed (Figure 35C and Figure 36C). Lower penetration depth (around 50-80  $\mu\text{m}$ ) was achieved for native cartilage and synoviocyte/PET immature constructs stained with Hoechst 33342 and CellMask Green plasma membrane stains, in comparison to that achieved with the dual staining of Acridine orange and SiR-actin stains. This is most likely because shorter wavelength light (blue/green) which is used to excite the CellMask Green plasma membrane stain, experiences greater absorption and scattering than longer wavelength light (far red) (used to excite the SiR-actin stain) and therefore results in shallower penetration depth [213], [228]. However, the penetration depth achieved by using Hoechst 33342 and CellMask Green plasma membrane stains was similar to the range achieved by previous studies in the field (as described in Section 3.6.2) [85], [145]. Thus, the preliminary results suggested that the Hoechst 33342 and CellMask Green plasma membrane stains were promising for use in revealing cell morphology in these tissue samples.

#### **3.6.4 Effect of Addition of ProLong<sup>®</sup> Live Antifade Reagent on Retention of Fluorescence Signal after Sequential Imaging of Selected Chondrocytes in Native Cartilage**

As mentioned before in Section 3.1.2, the staining method must be able to track and image selected cells in tissue samples repeatedly without significant loss of fluorescence signal. The fluorescence fading that occurs following the capture of a series of images would directly affect the accuracy of the quantitative data on cell deformation because cell measurements are recorded from the images. Previous results in this chapter showed that SiR-actin stain significantly lost fluorescence intensity during the time period required to capture sequential confocal volume images, possibly due to photobleaching.

ProLong<sup>®</sup> Live Antifade Reagent is a commercially available product which the manufacturer claims it metabolises these singlet oxygen molecules, resulting in increased signal intensity and duration whilst keeping the background signal low. Thus, the effect of the addition of ProLong<sup>®</sup>

Live Antifade Reagent on the retention of fluorescence signal after sequential imaging of selected chondrocytes in native cartilage were compared between the staining methods of Acridine orange combined with SiR-actin and Hoechst 33342 coupled with CellMask Green plasma membrane.

SiR-actin was better at retaining its signal with the addition of ProLong<sup>®</sup> Live Antifade Reagent (Figure 39), compared to without the use of ProLong<sup>®</sup> Live Antifade Reagent as seen previously (Figure 32 and Figure 33), though some signal loss was still observed. This suggested that ProLong<sup>®</sup> Live Antifade Reagent provided protection against the effects of photobleaching of the stain. Given that molecular oxygen is one of main actors in the photobleaching process, it is possible that ProLong<sup>®</sup> Live Antifade Reagent protected SiR-actin molecules from environmental molecular oxygen by metabolising singlet oxygen molecules which consequently resulted in lowering the rate of photobleaching and improving the survival period of SiR-actin.

Following three sequential volume images of chondrocytes in native cartilage, the CellMask Green plasma membrane stain (Figure 32) retained almost all of the fluorescence signal unlike the SiR-actin staining to which it was compared (Figure 33). This indicated that these stains exhibit different photostability under the same illumination conditions (same dose of light and imaging acquisition settings), with CellMask being more photo-stable. With the presence of ProLong<sup>®</sup> Live Antifade Reagent in the imaging solution to potentially provide environmental protection to fluorophores, it is likely that CellMask Green plasma membrane would have a greater total number of photons available for emission before bleaching compared to SiR-actin resulting in reasonable images, where photobleaching was negligible. According to the manufacturer, there is a possibility that CellMask Green plasma membrane stain could internalise 90 mins after the removal of the staining solution. The data here showed distinct staining for the entire duration of image acquisition (approximately 120 mins), suggesting minimal internalisation.

Overall, the Hoechst 33342 and CellMask Green plasma membrane stains with the addition of ProLong<sup>®</sup> Live Antifade Reagent have the ability to provide specific and highly resolved visualisation of cell morphology in native cartilage and immature constructs. Following the capture of three sequential volume images, it would appear that CellMask Green plasma membrane stain is a high photostability stain with negligible photobleaching effects. SiR-actin was not able to retain its fluorescence signal, even with the addition of ProLong<sup>®</sup> Live Antifade Reagent. These data suggest that CellMask Green plasma membrane stain was more superior to SiR-actin at retaining fluorescence signal after repeatedly imaging selected cells within a dense tissue.

### **3.6.5 Retention of Fluorescence Signal after Sequential Imaging of Selected Chondrocytes in Native cartilage using Galvo and Resonant Scanning**

The previous preliminary data had shown that the staining method of Hoechst 33342 and CellMask Green plasma membrane was able to follow selected chondrocytes in native cartilage by capturing three sequential 3D volume images without significant fluorescence loss. The next stage was to investigate the appropriate confocal microscope settings for image acquisition.

To be able to quantify cell morphology changes in native and tissue engineered cartilage samples under incremental compression in later experimentations, it was important to obtain high resolution images that could observe the fine detail of cell morphology with visible contrast between the features of interest (cell morphology) and the background. Resolution is dependent on the wavelength of light used to excite fluorophore ( $\lambda$ ) and the numerical aperture (NA) of the objective lens [259]. Rayleigh's criterion is a rule of thumb used to estimate the achievable maximum lateral resolution:

$$R_{xy} = \frac{1.22\lambda}{2NA}$$

For example, cell features could be resolved at ~200 nm lateral resolution if labelled with a green fluorophore, such as CellMask Green plasma membrane stain ( $\lambda = \sim 500$  nm) and imaged with a high-NA oil immersion objective (NA = 1.3). Axial resolution is generally about two or three times worse than lateral resolution (~400-600 nm in this example). Fluorophores excite by shorter wavelength light (blue/green) generally achieve higher resolution than those illuminate by longer wavelength light (red) [213]. In this study, by using shorter wavelength fluorophore (i.e. CellMask Green plasma membrane stain) to label native cartilage and immature constructs, it appeared to achieve better resolution for imaging cell morphology compare to SiR-actin (long wavelength fluorophore) (Figure 30 and Figure 36). However, this came with the trade-off of a shallower penetration depth (as described in Section 3.6.2 and Section 3.6.3).

Objective is perhaps considered as the most important component in an optical microscope because it is primarily responsible for the quality of images that could be produced by the microscope [213], [260], therefore choosing the appropriate objective for the experiments is critically important. The NA of the objective is generally considered as the most important design feature when selecting an objective lens and not the magnification because it is an indicator of the resolution that could be achieved for a given objective lens [260]. It also affects the depth of imaging into the sample (as described in Section 3.6.2). An objective lens with a high NA is capable to achieve higher resolution (i.e. smaller features can be resolved) and has a greater light-collecting ability (i.e. more efficient at capturing fluorescence) but with reduce depth of imaging [213]. When selecting the objective for the imaging method here, a balanced between image resolution and imaging depth must be considered. The NA between 40x, 60x and 100x oil lenses were similar (NA = 1.3, 1.4 and 1.4, respectively). However, the 40x lens

had a longer WD than the other objectives, which would allow more space to manoeuvre the lens during focusing on the sample and improve the imaging depth into the sample without compromising too much on the resolution. Typically as the magnification increases, the objective would have to be closer to the sample in order to focus which results in shorter WD and consequently reduces the imaging depth into the sample [213].

In addition, image brightness is influenced by the objective magnification which is inversely proportional to the magnification squared [260]. In other words, image intensity decreases drastically with increased magnification. This is because there is a fixed amount of light per area and when an area is magnified (increase in magnification), a smaller area is being observed and therefore the light level is decreased which consequently results in dimmer image. Elevation of laser power could improve image brightness but this would also increase the risk of photobleaching [213]. Thus, an objective with the highest NA but having the lowest possible magnification still capable of providing adequate resolution and imaging depth is recommended for fluorescence live cell imaging in low light level settings [260].

For these reasons, a 40x oil-immersion lens was selected for use in these studies instead of a 100x oil-immersion lens (used in previous sequential imaging experiments as described in Section 3.4.5.5 and Section 3.4.5.6) because it maintains reasonably high NA compared to the 100x lens so the magnification of 40x would still produce good enough resolution for cell morphology visualisation and measurements but with higher image signal intensity and an increase in imaging depth.

In addition to obtaining high resolution images, it was also important to minimise the photobleaching effect. Photobleaching can be addressed/decreased by reducing excitation light exposure by limiting exposure time and light intensity to a minimum while retaining a high signal to noise ratio required for the image resolution [223]. Thus, it was proposed that the laser power was kept at the lowest possible level of illumination and 5% was selected because it was proved to provide good staining signal intensity in previous experiments with minimal loss of fluorescence signal. The exposure time to illuminate a tissue sample was also kept at a minimum. Photobleaching can occur when scanning too long on the ROI therefore sample focus and imaging acquisition settings were established on a neighbouring region to reduce the time spent illuminating the ROI when not capturing images before returning to the ROI for image acquisition. For the volume image acquisition settings, it was proposed to use a smaller image depth (approximately 20  $\mu\text{m}$ ) that is still capable to track a population of cells and keep the same optical section thickness (0.2  $\mu\text{m}$ ) as previously in the preliminary experiments (Section 3.4.5.5 and Section 3.4.5.6) to reduce illumination time in ROI but still provide the z-resolution required for sufficient pixel details to resolve 3D cell morphology. In addition, line averaging (described in Section 3.4.5.1) was not applied to reduce the laser exposure time on a tissue sample and consequently decrease the risk of photobleaching.

A Nikon A1R inverted confocal microscopy was equipped with two scanning systems: a traditional galvo (non-resonant) and a high speed resonant scanners. Thus, image acquisition in the confocal microscope using a traditional galvo scanner and a high speed resonant scanner to potentially retain fluorescence signal were compared. It has previously been demonstrated that resonant scanning with a faster scan speed was able to suppressed photobleaching better compared to galvo scanning [261], however, this was not found to be the case in this study. Galvo scanning appeared to be superior at retaining the fluorescence signal compared to resonant scanning (Figure 40). There was a significant difference in fluorescence intensity loss following each sequential image captured between the two scanning systems ( $p < 0.05$ , Figure 40).

One possible explanation for this is that the current version of the resonant scanner might not be compatible for this particular imaging application. The image quality was poor with high noise background when resonant scanning was used for image acquisition, suggesting that the capacity of the scan head was pushed beyond optimal. Part of what defines the image resolution captured from a resonant scanner is the ability of the electronics to sample the image and create pixels quickly [261]. Higher sample scanning rates means more pixels can be created in the same amount of time, and therefore the electronics can generate a more highly resolved image. Image quality is also defined by the ability of the resonant scanner to reduce the noise contribution to the final image [261]. Reduced noise not only aids improvement of the overall quality of the image but, with shorter pixel dwell time and potentially less signal, is also effective in maximising signal to noise ratio. In the case of the current version of the resonant scan head used here, it is possible that it was not able to create the pixels needed fast enough to produce the image resolution required to define cell morphology and the quality of the electronics was not good enough to reduce the noise level of the final images. In order to compensate for the poor image resolution, laser power and line averaging needed to be set higher which increased excitation light intensity and illumination time on the sample, which potentially leads to photobleaching. With continual enhancements of the quality of the electronics in resonant scan heads, there are now commercially available resonant scanners such as a Nikon HD high-speed resonant scanner (Nikon A1R HD25) reported to be efficient in producing sharp sequential images with good resolution [261]. Thus, the possibilities of examining the capability of a Nikon HD resonant scanner for live cell imaging in cartilage tissue could be explored in future work.

A possible explanation for the low signal to noise ratio observed when using the resonant scanner here is that the conventional photomultiplier tubes (PMTs) installed in the current A1R confocal system might not have the efficiency to detect the low signal potentially caused by a shorter pixel dwell time (resulted from faster sample scanning rate). With a higher sensitivity detector, such as a Nikon GaAsP detector (Nikon C2-DUVB), that has a high signal to noise ratio and more than double the efficiency of conventional PMTs, the acquisition of fluorescent signals with less laser power applied to the sample is possible, which results in less photobleaching [213], [262]. The confocal images of chondrocytes in articular cartilage captured using a Nikon C2-DUVB GaAsP detector on a C2 confocal microscope in a demonstration showed no discernible difference of fluorescence signal loss (Figure 41). However, the Nikon HD resonant scanner and the GaAsP PMT were not available to use in this thesis. The galvo scanning showed to be superior at retaining fluorescence signal than the resonant scanning with the current A1R confocal microscope, therefore galvo scanning was selected as the sequential image acquisition method for further cell deformation experiments.

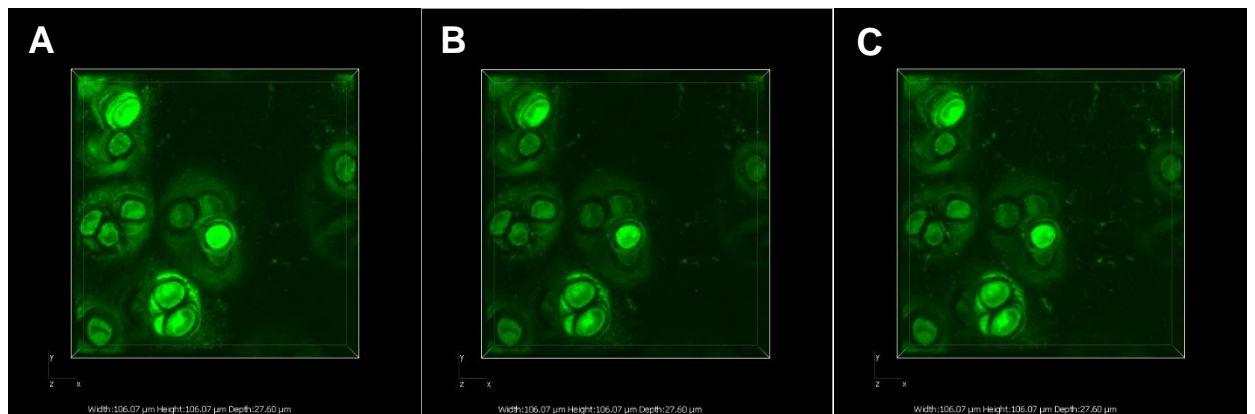


**Figure 41: A sequential series of three 3D volume images of selected chondrocytes on the articular surface of bovine cartilage captured using the C2-DUVB GaAsP detector on a Nikon C2 confocal microscope, displayed in the CellMask Green plasma membrane (Green) channel in Z-plane: (A-C) image 1 to 3.**

### 3.6.6 Conclusion

The staining method of Acridine orange and SiR-actin provided for visualisation of specific and highly resolved cell morphology in bovine synoviocyte monolayers, native cartilage and synoviocyte/PET immature constructs. However, significant fluorescence signal loss was observed and consequently loss of details on cell morphology when selected chondrocytes in the superficial surface and the deep zone were sequentially imaged. A means to reduce photobleaching therefore needed to be devised. With the addition of anti-photobleaching, ProLong<sup>®</sup> Live Antifade Reagent to aid the reduction in photobleaching, SiR-actin still showed some signal loss.

The dual staining method of Hoechst 33342 and CellMask Green plasma membrane stains was selected as an alternative method to visualise, track and image cell morphology in native cartilage and tissue engineered constructs in this thesis due to its ability to provide highly

resolved visualisation of cell morphology in monolayers, native cartilage and synoviocyte/PET immature constructs. In addition, it was because with the addition of ProLong<sup>®</sup> Live Antifade Reagent, the CellMask Green plasma membrane stain was more superior to the SiR-actin stain at retaining fluorescence signal following the capture of three sequential images.

Following application of Hoechst 33342 and CellMask Green plasma membrane stains with the addition of ProLong<sup>®</sup> Live Antifade Reagent on native cartilage, galvo scanning proved to be superior than resonant scanning at retaining the fluorescence signal after the capture of three sequential volume images of chondrocytes in native cartilage in the current Nikon A1R confocal microscope used in this thesis, therefore it was selected as the image acquisition method used in further cell deformation studies in native and tissue engineered cartilage.

In summary, Hoechst 33342 and Cell Mask Green plasma membrane stains, together with ProLong<sup>®</sup> Live Antifade Reagent and galvo scanning will be used for all further experimentation.

## **Chapter 4 - Effect of Compressive Strains on Cell Deformation in Native Cartilage**

*This chapter investigates the effects of incremental compressive strains on the deformation behaviour of live bovine chondrocytes within cartilage disks subjected to different magnitudes of compressive tissue strains, in an attempt to verify a novel cell deformation measurement method (i.e. a live cell staining technique for live cell confocal imaging to label and visualise chondrocytes within cartilage disks, a custom designed compression device for tissue strain application and a custom workflow on Amira software for cell deformation quantification analysis) developed in this thesis prior to cell deformation experiments in tissue engineered constructs and compare the observed findings to previous studies in the literature. It is the first time that the same population of live superficial zone chondrocytes was tracked to determine the 3D deformation behaviour under incremental tissue strains (10 % and 15 %) in non-fixed bovine cartilage disks. Confocal images of the same chondrocytes were captured (i) at zero strain, (ii) 10 % and (iii) 15 % applied tissue strains and Amira software used to quantitate chondrocyte morphometric parameters including: cell length, width, height, volume and sphericity. A significant change in chondrocyte shape, size and volume in response to incremental cartilage compressive strains was observed. These deformational changes were substantially greater than the applied tissue strains, suggesting that large changes in chondrocyte morphology might occur in the superficial zone under compressive tissue strains. It is possible that chondrocyte deformation was largely influenced by the local ECM structure and composition as well as partly modulated by the physical properties of PCM and the chondrocyte itself. Cell deformation may therefore be considered to be a function of applied tissue load and local cartilage matrix structure. The findings observed in the present study were consistent with previous deformation measurements of superficial zone chondrocytes in cartilage explants. This suggests that a novel methodology to visualise, image and quantify live cell morphology developed in this thesis was capable to determine changes in chondrocyte 3D morphology within native cartilage disks under incremental static compressive tissue strains.*

### **4.1 Introduction**

Articular cartilage, a highly hydrated connective tissue, facilitates load transmission and provides a low-friction surface for articulation of diarthrodial joints to protect underlying bone and joint functions [22], [144]. The health and function of the diarthrodial joint is largely influenced by the local mechanical environment of specialised cartilage cells (chondrocytes) which are responsible for synthesis and degradation of the unique extracellular matrix that gives cartilage its strength and load-bearing function [21], [22], [84], [139], [144]. Chondrocytes in articular

cartilage detect and respond to mechanical signals through mechanotransduction mechanisms in conjunction with other environmental and genetic factors to regulate their metabolism [12], [21], [22], [66], [82], [83], [86]. This capability provides a means by which articular cartilage can alter its structure and composition in response to changes in *in vivo* loading in the diarthrodial joint in order to meet the physical demands placed upon the body [21], [87].

One mechanism by which chondrocytes may detect alterations in their mechanical environment during cartilage deformation is through direct stress transmission from the ECM causing deformation (changes in shape and volume) of the chondrocytes themselves which in turn generate signals that regulate metabolic and biosynthetic activities [59], [65], [87], [94], [95]. Chondrocytes may be exposed to complex mechanical and osmotic environments during articulation of joints, including compressive and tensile stresses and strain, fluid flow as well as changes in hydrostatic pressure, osmotic pressure and ionic gradients, which in turn may influence the biosynthetic response of chondrocytes *in situ* [139]. In attempts to understand the complex environment around the chondrocyte within the tissue resulting from applied load, several studies have investigated the deformation behaviour of chondrocytes using theoretical and numerical analyses [95], [146]–[148]. The results indicated that the tissue's ultrastructural anisotropy and its depth-dependent inhomogeneous mechanical properties significantly influence the local mechanical environment of the chondrocyte [95], [146]–[148]. Furthermore, the mechanical properties of the chondrocyte itself and the pericellular matrix (PCM), a narrow tissue region which completely surrounds the chondrocytes and together with enclosed cell (s) has been termed the "chondron" [263], were also found to influence the deformational response of chondrocytes to compressive loading [95], [146]–[148].

Chondrocyte deformation has been widely investigated in previous studies under static compression, generally with the use of confocal microscopy or histological observation in native cartilage explants [21], [51], [87], [133]–[138], [210], intact cartilage [85], [145] and isolated chondrocytes seeded in agarose [88], [140]–[144]. These studies measured aspects of cell morphology (lateral and axial diameter), deformation index (aspect ratio of cell), cross-sectional area and cell volume to assess the effect of static compression on chondrocytes. In native cartilage, it was observed that static loading had major impact on the shape and volume of chondrocytes and that the resulting significant changes were greatly influenced by their local ECM deformation [21], [85], [87], [137], [145]. It was also found that chondrocytes responded differently to loading according to their location throughout the depth of the tissue [87], [137]. Moreover, the findings suggested that PCM plays a biomechanical role in the cartilage by regulating the local mechanical and osmotic environments of the chondrocyte in a depth dependent manner [85], [87], [137], [145]. For isolated chondrocytes seeded in agarose gels, it has been shown that the matrix developed by chondrocytes was largely influenced by the extent of cell deformation [142]. The results indicated an increase in matrix elaboration which led to a decrease in cell deformation under static loading [142]. These studies have greatly improved our

understanding of cartilage and chondrocyte mechanics and provide an important foundation for the present study.

Many approaches have been used in earlier studies to determine the deformation behaviour of chondrocytes under static compression in cartilage explants. Fixed tissue approaches were used by Clark *et al.* (2003) [138] and Choi *et al.* (2007) [137] but these study may not reflect on the instantaneous properties of chondrocytes within the cartilage tissue. Some studies investigated chondrocyte deformation in non-fixed articular cartilage with semi-cylindrical/strip samples under either one compressive strain level [87], [134], [210] or a range of compressive strain levels [133], [135]. However, sample preparation by cutting the cartilage tissue would compromise the tissue integrity and alter the material properties of the cartilage which consequently would affect the mechanical environment around the chondrocytes. Thus, fixed and cut tissue approaches should be avoided. Wu *et al.* (2001) [136] managed to examine sheep chondrocyte deformation within cylindrical cartilage specimens at two compression levels under live cell conditions. The same chondrocytes were followed but only changes in chondrocyte 2D morphology were measured. Thus, to the author's best knowledge, no study has managed to track the same chondrocytes and examine the changes in 3D morphology in cartilage disks subjected to different compressive strain levels, without cutting and fixing the tissue.

The aim of the work described in this chapter was to investigate the deformation response of a given population of chondrocytes in the articular zone of bovine cartilage disks subjected to different magnitudes of static compressive strains under live cells imaging condition and compare this to previous measurements in the literature prior to moving on to determining the effect(s) of incremental loading on cell deformation behaviour in tissue engineered constructs (Chapter 5). In Chapter 2, a compression device that adapts a parallel loading configuration to the confocal light path was developed for compressive tissue strain application whilst allowing microscopic visualisation of cell morphology in native and tissue engineered cartilage. In Chapter 3, two staining methods were examined for live cell visualisation and imaging in native cartilage and tissue engineered constructs. The confocal images showed that Hoechst 33342 and CellMask Green plasma membrane stains penetrated both native cartilage and tissue engineered constructs and provided specific and highly resolved visualisation of cell morphology. In addition, retention of fluorescent signal was shown to be superior to the alternative staining method using Acridine orange and SiR-actin after sequential imaging of selected chondrocytes in native cartilage. This led to the conclusion that use of Hoechst 33342 and CellMask Green plasma membrane staining was for the method of choice for visualising, tracking, imaging and quantifying changes in chondrocyte morphology (shape and size) within cartilage explants subjected to incremental magnitudes of compressive strains.

To observe the effects of incremental compressive tissue strains on chondrocyte deformation behaviour in bovine cartilage disks, both the compression device and the staining method of

Hoechst 33342 and CellMask Green plasma membrane developed previously in this thesis were used. Static compressive strains of 10 and 15 % were selected to correspond to physiological levels of cartilage strain range between 0 % and 30 % [130], [210], [264]. In addition, these strain levels were used in previous studies, therefore it would be easier to compare the results to the literature. Due to the limited penetration depth with the confocal system, deep tissue visualisation (i.e. chondrocytes in the middle zone of native cartilage) was not possible (as discussed in Section 3.6.2). Chondrocytes in the articular surface were selected for the investigation because dead cells may potentially be present in the vicinity of the cut surface required to acquire the cartilage disk which is located in the deep zone. In addition, the cutting of cartilage would have mechanically damage and disrupt the matrix which affects the local mechanical environment around the chondrocytes and consequently could alter the cell deformation behaviour [265]. Previous studies found that cutting of cartilage induced tissue and cell swelling near the cut surface which were likely caused by loosening of collagen fibril tension [265], [266].

Prior to the cell deformation experiment in native cartilage, the viability of chondrocytes within cartilage disks needed to be tested. In this study, the cartilage disks were cultured for up to 3 days after harvesting from the bovine osteochondral plugs because of the practicality of harvesting tissue (i.e. harvesting take most of the day in another laboratory) and the logistic of a weekly tissue delivery from the abattoir. It was important to ensure that the chondrocytes are healthy before live cell imaging. In addition, following this, potential errors in the morphometric measurements introduced by photobleaching of the stains were assessed.

The aim of this study was approached via the following objectives:

- To examine the viability of chondrocytes within bovine cartilage disks cultured for up to 3 days after harvesting by Live/Dead<sup>®</sup> staining and XTT reduction assay.
- To assess the potential errors in the morphometric measurements introduced by photobleaching of the stains.
- To determine the effects of incremental compressive strains on chondrocyte deformation behaviour within the superficial zone of native cartilage in the uncompressed state and during applied compressive tissue strains of 10 % and 15 %.

An overview of the experimental plain is depicted in Figure 42.

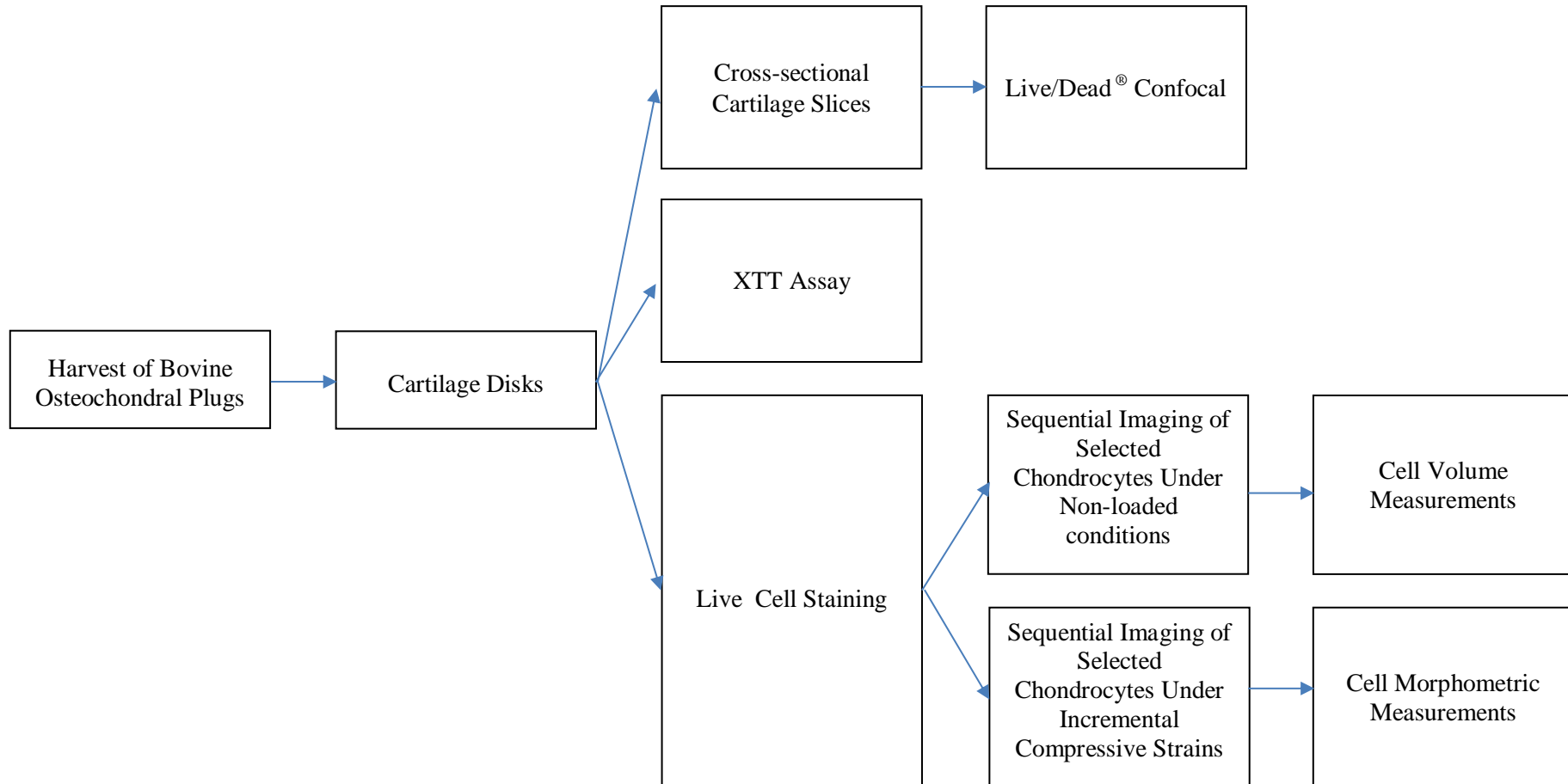


**Figure 42: Overview of experimental plan for determining the effects of incremental compressive strains on chondrocyte deformation behaviour within the superficial zone of native cartilage.**

## **4.2 Experimental Methodologies**

### **4.2.1 Harvest of Osteochondral Plugs for Cartilage Disks**

Osteochondral plugs, used as a source for native cartilage disks (5 mm in diameter), were harvested from the (relatively flat) medial and lateral regions of the patellofemoral groove of bovine knee joints as stated in Section 3.3.3. In brief, the articular surface of the patellofemoral groove was kept hydrated by PBS. A drill equipped with an in-house customised drill-aided corer was used to drill down from the cartilage surface into the subchondral bone. The osteochondral plug was then snapped *in situ* and removed from the joint surface with the aid of a plain ended corer. The extracted plugs were washed in PBS before transferring them in to PBS containing 10x AB (written in full in Section 3.3.1) for 20 mins. The subchondral bone ends were removed from the osteochondral plugs using a scalpel to leave as close to full depth cartilage as possible. The cartilage disks not tested immediately were cultured in DMEM/F12 medium supplemented with 10 % FBS, 1x AB and 2 mM L-glutamine at 37°C, 5 % CO<sub>2</sub> and above 90 % humidity for up to 3 days prior to cell viability determination, metabolic activity quantification and confocal imaging.

## **4.3 Analytical methods**

### **4.3.1 Metabolic Activity Quantification on Native Cartilage Disks After Harvest of Osteochondral Plugs Using XTT Assay**

Chondrocyte metabolic activity within the cartilage disks obtained from osteochondral plugs was quantified using the XTT assay which measures cellular metabolism of a tetrazolium salt, 2,3-bis-[2-methoxy-4-nitro-5-sulfophenyl]-2H-tetrazolium-5-carboxanilide (XTT) [267]–[269]. XTT is cleaved by dehydrogenase enzymes in the mitochondria of metabolically active cells and reduced to an orange coloured formazan salt [270]. Given that reduction of XTT can only occur in metabolically active cells, the measured absorbance at 450 nm directly correlates to the number and metabolic activity of viable cells [271]. The XTT assay is a more convenient method than previously used MTT assays because it forms a soluble formazan product which can be measured directly from culture [267], [270]. It has been reported that the sensitivity of XTT assay is similar to or better than that of the MTT assay [271]. In addition, it is a safer method than past assays that use radiolabelled thymidine.

Cell viability in native cartilage was analysed using an XTT based *in vitro* toxicology assay kit (Sigma-Aldrich, Irvine, UK, TOX-2). Pre-weighted cartilage tissue harvested from the osteochondral plugs was chopped into small pieces using a scalpel and placed into a well of a 12-well cell culture plate filled with 0.5 mL of growth medium (DMEM/F12 medium supplemented with 10 % FBS, AB and 2 mM L-glutamine). XTT working solution was made

up of 0.8 mL of 1 mg/mL XTT and 1.2 mL of growth medium and 0.5 mL of this XTT working solution was added to the well. A blank well with just the XTT solution (0.5 mL of growth medium and 0.5 mL XTT working solution) and no tissue was included. The plate was incubated for 4 hrs at 37°C in 5 % CO<sub>2</sub> with gentle agitation. Following this, the XTT solution was removed from each well, including the blank well and retained into 2 mL tubes.

Tetrazolium product was then extracted from the tissues using 0.5 mL of DMSO added to each well for an hour at room temperature, in the dark, by gentle shaking. The 1 mL XTT solutions and the corresponding DMSO/tissue suspensions were then pooled before transferring three aliquots of 100 µL of each sample into a 96-well microplate (Corning Life Sciences B.V., Amsterdam, Netherlands). Absorbances were measured at 450 nm and 690 nm using a microplate spectrophotometer (ThermoFisher Scientific, Northumberland, UK). The absorbances at 690 nm were subtracted from those at 450 nm followed by subtraction of the average blank reading (no tissue sample) to remove background measurements and XTT content calculated *per* gram of tissue. Three cartilage disks per culture duration of day 0 (immediately after harvest), 1, 2 and 3 (a total of 12 cartilage disks harvested from the patellofemoral groove of two bovine knee joints) were used for XTT assay.

#### **4.3.2 Cell Viability Determination on Cross-Sections of Native Cartilage Disks After Harvest of Osteochondral Plugs: Confocal Microscopy and Live/Dead<sup>®</sup> Staining**

A Live/Dead<sup>®</sup> Viability/Cytotoxicity Kit (Molecular probes by ThermoFisher Scientific, Northumberland, UK, L3224) was used to determine the cell viability within the cartilage tissue. Discrimination of live from dead cells was achieved by simultaneously staining with green-fluorescent calcein-acetoxymethyl ester (calcein AM) ( $\lambda_{\text{Ex/Em}}$  494/517 nm) and red-fluorescent ethidium homodimer-1 (EH) ( $\lambda_{\text{Ex/Em}}$  528/617 nm) which both fluoresce at different wavelengths. Calcein AM readily passes through intact cell membranes and converts to calcein when it is in contact with intracellular esterases and consequently fluoresces. Ethidium homodimer-1 can only pass through damaged cell membranes to enter cells and upon binding with exposed DNA increases its fluorescence 40-fold. Thus, live cells would show green fluorescence whilst dead cells would show red fluorescence upon fluorophore excitation. This provided a visualisation of cell viability within native cartilage cultured with different durations.

A Live/Dead<sup>®</sup> working solution was made up of 2.5 µL of 4mM calcein AM, 5 µL 2 mM EH and 10 mL of PBS. Prior to stain application, cartilage disks were washed with PBS three times before two cross-sectional slices (approximately 1 mm thick) per cartilage disk were prepared by cutting perpendicular to tissue surfaces from the central axis of the disks with a scalpel.

Cartilage slices were placed in wells of a 24-well cell culture plate and 1 mL of the Live/Dead<sup>®</sup> working solution was added to each cartilage slice. The plate was then incubated for an hour in

the dark at 37°C. The cartilage slices were washed three times in PBS before visualisation via an Nikon A1R inverted confocal microscope and images compiled using Nikon NIS-Elements software. Two cartilage disks per culture duration of day 0 (immediately after harvest), 1, 2 and 3 (a total of 8 cartilage disks harvested from the patellofemoral groove of two bovine knee joints) were used to prepare two cartilage slices from each cartilage disk for Live/Dead<sup>®</sup> staining.

### **4.3.3 Live Cell Staining of Native Cartilage Disks for Cell Nuclei and Plasma Membrane using Hoechst 33342 and CellMask Green Plasma Membrane Stains**

Chondrocytes within the cartilage disks harvested from the osteochondral plugs were stained with Hoechst 33342 and CellMask Green plasma membrane as described previously (Section 3.4.4). Only flat cartilage disks were used in the experiment. In brief, a combined staining working solution of 1 µg/mL Hoechst 33342 and 1x CellMask Green plasma membrane were freshly prepared in DMEM/F12 medium and applied to the cartilage disks placed in a 24-well cell culture plate. The plate was covered with aluminium foil to protect it from the light and incubated at 37°C and 5 % CO<sub>2</sub> for 40 mins. Cartilage disks were then washed three times in Live Cell Imaging Solution. Following on from the wash step, ProLong<sup>®</sup> Live Antifade Reagent was applied to cartilage disks in dark at 37°C for 2 hrs before visualisation using a Nikon A1R inverted confocal microscope.

### **4.3.4 Confocal Image acquisition**

#### **4.3.4.1 Live/Dead<sup>®</sup> imaging of Cross-Sections of Native Cartilage Disks**

Volume images of the Live/Dead<sup>®</sup> stained cross sectional slices obtained from the cartilage disks cultured for up to 3 days (as described in Section 4.3.2) were acquired using an Nikon A1R inverted confocal microscope, recorded by taking serial optical sections of 512 x 512 pixels at 3 µm intervals perpendicular to the articular surface with a 10x air objective (PL Fluor 0.30 NA) to produce an overall view of the cross-section. The 488 nm Argon laser and the 561 nm solid state laser were used to excite calcein and ethidium homodimer-1 respectively. Lasers were set at 10 % of full power. The pinhole was set at 1 Au. Unidirectional galvo scanning and channel series were used to capture two volume images per cartilage slice. Two cartilage slices obtained from each cartilage disk (n=2 per culture duration of day 0 (immediately after harvest), 1, 2 and 3) were labelled with Live/Dead<sup>®</sup> staining and imaged.

#### **4.3.4.2 Sequential Imaging of Selected Chondrocytes in Native Cartilage Disks under Non-loaded Conditions Following Staining with Hoechst 33342 and CellMask Green Plasma Membrane after the Addition of ProLong<sup>®</sup> Live Antifade Reagent**

Sequential imaging of selected chondrocytes within the superficial zone of native cartilage disks (stained with Hoechst 33342 and CellMask Green plasma membrane for cell nuclei and plasma membrane, respectively, as previously described in Section 4.3.3) was performed under non-loaded conditions to assess whether photobleaching of CellMask Green plasma membrane stain may introduce errors into the morphometric measurements. Stained native cartilage disk was placed in the compression device (without load application) filled with Live Cell Imaging Solution and with the imaging surface faced down onto the coverslip, as described in Section 2.3.3, prior to mounting on the stage of a Nikon A1R inverted confocal microscope. The same group of chondrocytes selected in each cartilage disk was observed throughout the experiment. Three sequential volume images of selected chondrocytes were acquired in each non-compressed cartilage disk at a 30 min interval. A total of five cartilage disks harvested from the patellofemoral groove of two bovine knee joints were imaged.

To determine the effects of incremental compressive strains on chondrocyte deformation behaviour, sequential imaging of selected chondrocytes within the superficial zone of stained native cartilage disks was performed under incremental compressive strains. Three sequential volume images of selected chondrocytes were acquired in the uncompressed state and during applied compressive strains of 10 % and 15 % using a Nikon A1R inverted confocal microscope. The same group of chondrocytes from each cartilage disk was imaged under the selected strain levels throughout the experiment. A total of four cartilage disks harvested from the patellofemoral groove of two bovine knee joints were compressed and imaged using the experimental procedure described in Section 4.3.5.3. Volume image acquisition is described in this section.

The 405 nm Solid state and 488 nm Argon lasers were used to excite Hoechst 33342 and CellMask Green plasma membrane stains, respectively. Lasers were set at 5 % of full power to minimise photobleaching. In addition, the pinhole was set at 1 Au to provide a diameter that gave the best compromise between light throughput, noise and resolution. Unidirectional galvo scanning and channel series were used to capture all images. Chondrocytes from the central region (radially) of the articular surface of native cartilage were randomly selected at a depth of 20-30  $\mu\text{m}$  inside the tissue. Volume images (approximately 20  $\mu\text{m}$  in depth) were recorded by taking serial optical sections of 512 x 512 pixels at 0.2  $\mu\text{m}$  intervals with a 40x oil immersion objective (S Fluor 1.30 NA). Typically, around 20-30 chondrocytes were captured within the imaging depth of field.

### **4.3.5 Cartilage Compressive Strain Application**

To determine the change in morphology of chondrocytes in the articular zone of native cartilage under different magnitudes (10 % and 15 %) of uniaxial unconfined compressive tissue strains, the compression device described in Chapter 2 was used for overall tissue strain application.

The thickness of the cartilage disks used here was first measured using the Bose ElectroForce 3200 mechanical testing machine. The mechanical testing rig was set up to determine the zero displacement point (as described in Section 2.4.2.3). In brief, the top platen of the testing rig was lowered at a rate of 0.2 mm/s towards the bottom platen until the two platens were brought together with a force of 100 N to establish a 'zero displacement' position, before being set 2 mm apart. The cartilage disk was then placed in between the two platens and the top platen was lowered at a rate of 0.2 mm/s until the load signal read a tare load of 0.02 N. The distance between the two platens at this tare load was defined as the cartilage thickness.

To determine the final compressed thickness that corresponded to the selected compressive tissue strains (10 % and 15 %), the amount of compressive displacement required to be applied to the tissue surface by the micrometer of the compression device was calculated knowing the cartilage thickness. For example, 10 % strain of a cartilage disk with thickness of 1 mm would correspond to a deformation of 100  $\mu\text{m}$ , which corresponds to a compressed thickness of 900  $\mu\text{m}$ . Thus, 100  $\mu\text{m}$  of displacement would be applied to the tissue using the micrometer.

In Chapter 2, it was determined that the coverslip used in the compression device would undergo flexion during load application and it was important to take this into account when calculating the load required to compress the cartilage. To achieve this, each cartilage disk was placed in between the two platens of the Bose ElectroForce 3200 mechanical testing machine and the top platen was lowered at a rate of 0.2 mm/s until the load signal read a tare load of 0.02 N. The cartilage disk was then subjected to loads up to 700 g at a rate of 50 g/s, whilst recording the displacement (at a rate of 200 Hz). The amount of load required to apply selected compressive tissue strains (10 % or 15 %) to the cartilage was then determined from the cartilage displacement and load data. To determine the amount of displacement attributable to the coverslip flexes, the displacement that corresponded to the load required to apply the selected compressive strain to the cartilage was read from the standard curve of displacement/load for the coverslip (Section 2.4.4.2). The amount of displacement caused by coverslip flexion was added on top of the compressive displacement that corresponds to selected tissue strain in order to compensate for the glass flexion effect.

The compression device was set up as described previously (Section 2.3.3) for strain application to the cartilage. Figure 43A shows all the components of the device (i.e. a well with an opening at the bottom, a coverslip, a platen, a magnetic disk, a brace, metal screws and a micrometer) assembled to form the compression device. In brief, the coverslip was sealed to the bottom of the device well using silicone grease. The individual cartilage disk (stained with Hoechst 33342

and CellMask Green plasma membrane for cell nuclei and plasma membrane, respectively, as previously described in Section 4.3.3) was placed articular surface down on the coverslip before filling the well with ProLong<sup>®</sup> Live Antifade Reagent in Live Cell Imaging Solution to maintain hydration and cell viability during imaging. To assemble the top half of the device, the micrometer was fixed onto the brace by a small screw along with the platen that was connected to the micrometer by a magnetic disk. The top half of the device was secured to the well via the brace by two metal screws. The compression device was then attached to the stage of an Nikon A1R inverted confocal microscope (Figure 43B). The experimental procedure used to compress the cartilage disk and sequentially image selected chondrocytes in the articular zone in the uncompressed state and during incremental compressive tissue strains of 10 % and 15 % is shown in Figure 44. To define the '0 % strain' position (the uncompressed state), the platen was lowered by the micrometer to the distance equal to the cartilage thickness. The '0 % strain' position was held for 30 mins before compressive strains were applied. A volume image of the selected chondrocytes in the uncompressed state was captured (as previously described in Section 4.3.4.2) prior to application of compression. A compressive tissue strain of 10 % (the compressive displacement that corresponded to this selected strain combined with the additional coverslip flexion displacement) was then applied in a direction parallel to the tissue surface, using the micrometer. The cartilage disk was allowed to equilibrate for 30 mins and another volume image was recorded of the deformed state of selected chondrocytes in the same region. The cartilage disk was then further compressed by manual turning of the micrometer to yield compressive strain of 15 % (the compressive displacement that corresponded to this selected strain combined with the additional coverslip flexion displacement) and allowed to reach equilibrium for 30 mins before a final volume image of the same chondrocytes was recorded.

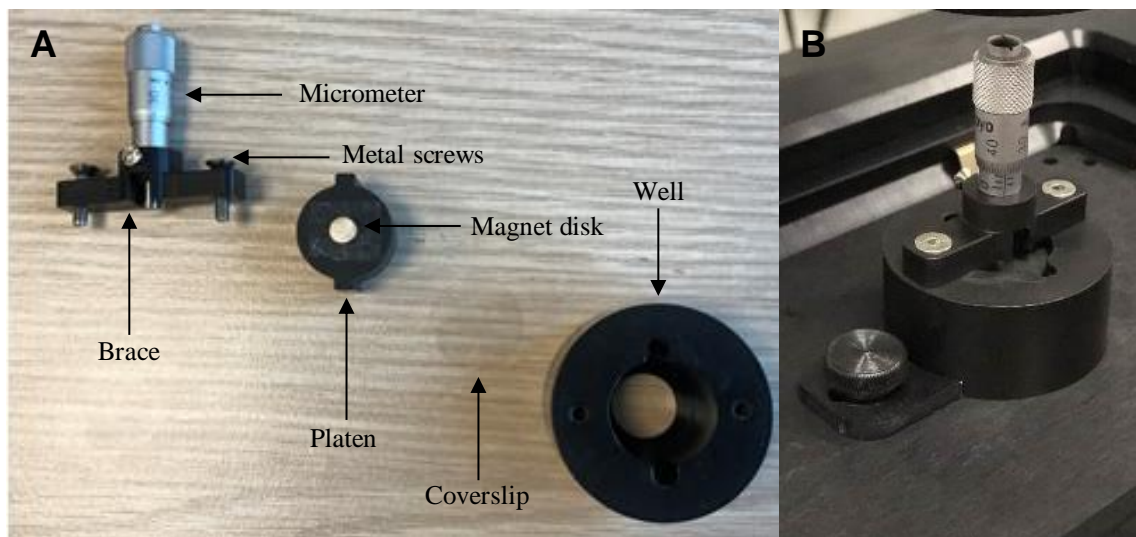


**Figure 43: (A) All the components of the device (a well with an opening at the bottom, a coverslip, a platen, a magnetic disk, a brace, metal screws and a micrometer) assembled to form the compression device. (B) The compression device mounted on the stage of an Nikon A1R invert confocal microscope system enabling precise compressive tissue strain application while visualising cell deformation behaviour under confocal microscopy.**

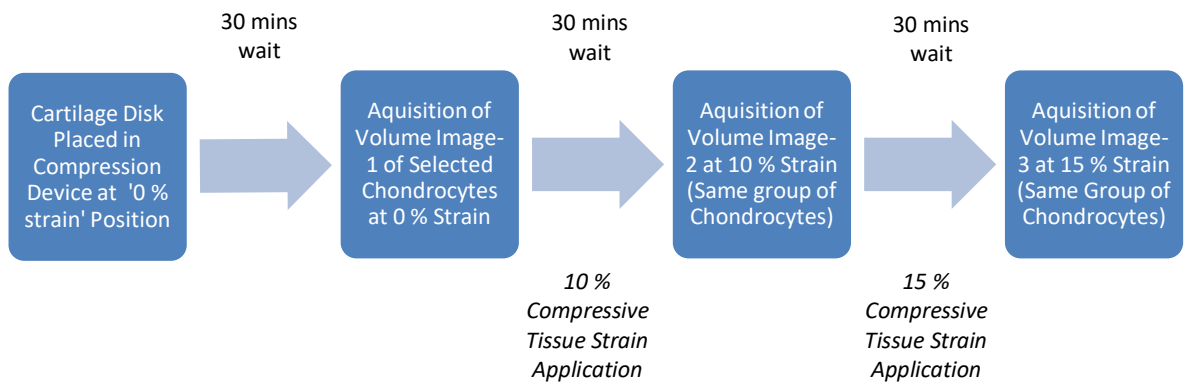


**Figure 44: Flow diagram of the experimental procedure used to sequentially image selected chondrocytes in the articular zone of native cartilage disk in the uncompressed state and during applied static compressive strains of 10 % and 15 %.**

### 4.3.6 Confocal Image Analysis

#### 4.3.6.1 Volume Measurements of Chondrocytes in Uncompressed Cartilage using Repeated Confocal Scans

Chondrocyte volume measurements were recorded on the sequential volume images acquired in non-compressed cartilage disks (as described in Section 4.3.4.2) using Nikon NIS-Elements software. The (3D) confocal volume images were loaded onto the software and processed for cell volume measurements. Images were subjected to intensity thresholding which results in binary images for cell volume measurements. Intensity thresholding is a process that determines the pixels to be included in the binary image by defining threshold limits based on intensity pixel values and thus distinguishes regions of interest (i.e. the cells in this thesis) for analysis. In other words, this process masks regions of interest in an image to be included in the binary image and segment them from unwanted regions. Once threshold limits were defined, the same threshold was then applied for all the images. Volume measurements were calculated from the resulting thresholded binary images. The measurements were performed on the same chondrocytes (n=3 cells per cartilage disk) in all repeated images captured in each cartilage disk (for a total of 5 cartilage disks harvested from the patellofemoral groove of two bovine knee joints). A total of 15 cells (from five cartilage disks) were measured.

#### 4.3.6.2 Quantification of Chondrocyte Deformation

For the purposes of image processing, 3D rendering and cell morphometric quantification, Amira software (ThermoFisher Scientific, Northumberland, UK) was used. A custom workflow was specifically developed by the author to analyse (raw) 3D confocal volume images of cells and perform cell morphometric measurements within native and tissue engineered cartilage (chondrocytes within native cartilage disks in this chapter and synoviocytes within tissue

engineered cartilage in Chapter 5) in order to quantify cell deformation behaviour under incremental compressive strains. The custom workflow, as shown in Figure 45, was created by selecting and combining several modules used for image processing, cells identification and data analysis (i.e. 3D rendering and cell morphology measurements on the identified cells). Modules including ‘Gaussian Filter’, ‘Interactive Thresholding’, ‘Fill Holes’, ‘Remove Small Spots’, ‘Border Kill’ (only applied to chondrocytes in the chapter), ‘Arithmetic’ used for image processing and modules such as ‘Volume rendering’ and ‘Label Analysis’ were used for image analysis (i.e. 3D rendering and cell morphometric measurements). Once the workflow was satisfactory (i.e. the order of modules and their settings), the workflow was applied on every image set to perform the same analysis. It was important to be consistent across comparison so that a fair analysis was conducted. The 3D images were analysed by travelling through the custom workflow in Amira and processed by each module in order.

Upon starting the chondrocyte deformation quantification analysis on the sequential images of chondrocytes acquired under incremental compressive strains (as described in Section 4.3.5), the confocal volume images were first converted to 16 Bit greyscale TIFF images and separated into two image stacks of the nuclei and plasma membrane using Fiji (National Institutes of Health, Maryland, USA) before being imported to Amira software for image processing and analysis. Image voxel (i.e. 3D equivalent of a pixel) size was set to define the spatial dimensions of the image stack. The custom workflow was then applied to the image stacks in which the image stack of the plasma membrane travelled through the workflow and were processed by each module in order followed by the image stack of the nuclei (Figure 45).

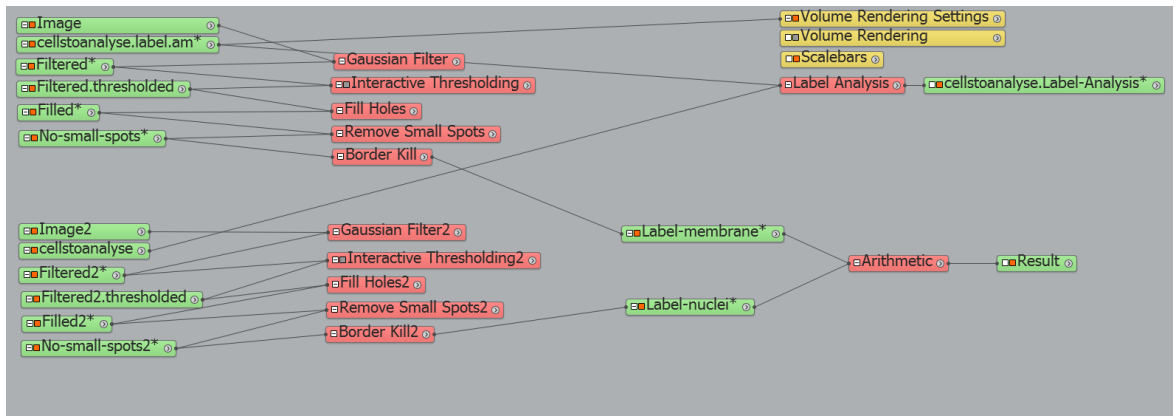


**Figure 45: The control panel of Amira software displaying the custom workflow used to process the confocal volume images of cells and perform 3D rendering and cell morphometric measurements.**

Firstly, a Gaussian filter was used to smoothen the raw image stacks in order to reduce noise and preserve cell edges. Filtering is typically applied to raw data as a pre-processing denoising technique to enhance (cell) edge detection for the image segmentation stage so that it can later be analysed effectively. The identifying pixels in an image at which the image brightness/signal intensity changes dramatically are typically defined as edges and this is known as edge detection. Example XY-orthoslices from the raw image stacks of the nuclei and plasma

membrane of chondrocytes, along with the filtered slices after the application of '*Gaussian filter*' module are shown in Figure 46. Orthoslice is a 2D orthogonal slice from a particular plane.

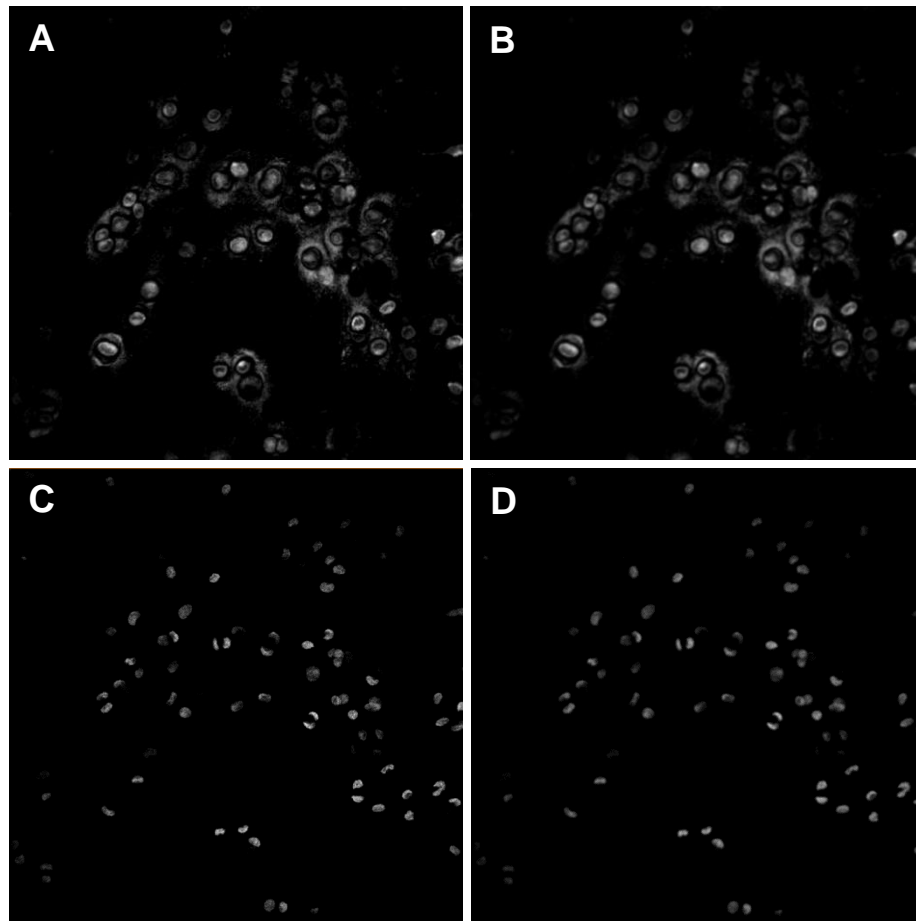


**Figure 46:** *XY*-orthoslices of the plasma membrane of chondrocytes from (A) 'raw' and (B) 'filtered' image data and the cell nuclei from (C) 'raw' and (D) 'filtered' image data, showing before and after the application of '*Gaussian filter*' module used to smooth the raw data in order to reduce noise and preserve cell edges.

The 'filtered' data were then segmented to determine the location and geometry of the nuclei and plasma membrane of chondrocytes (in their respective image stacks). Image segmentation is a process used to separate a digital image into a number of regions/phases (also known as image objects), where each region has a set of pixels with certain visual characteristics (e.g. colour, intensity and texture). In other words, it is a process that allocates a label to every pixel in an image and pixels that share similar characteristics would be assigned with the same label which identify the region associated with those pixels. This process is typically conducted to locate objects and boundaries (e.g. contour lines or curves that outline the shape of the objects) in a digital image. The main goal of segmentation is to simplify the representation of an image and present it in a more meaningful way (i.e. divide it into a number of distinct regions/phases), allowing further analysis to be readily performed on each region. The resulting segmented image could be made up of a set of regions/objects (i.e. different labels) that collectively cover

the entire image or a set of contours (the outline of the shape of objects) extracted from the image.

In this thesis, interactive thresholding was used for image segmentation to locate and label the nuclei and plasma membrane from the image stacks for further quantitative analysis. The concept behind the approach of interactive thresholding is to mask and label the region of interest by setting threshold levels with a visual feedback. In this study, the threshold intensity range to separate the nuclei and plasma membrane of chondrocytes from the background (in each of their respective image stacks) were selected through interactive, visual pixel evaluation. By overlapping greyscale (i.e. filtered image) and segmented images, threshold intensity values were assigned to the pixels representing the nuclei or plasma membrane in their respective image stacks. An immediate 2D visual feedback (preview) was used to modify and evaluated the threshold values in multiple 2D optical slices to ensure the labelling matches the nuclei and plasma membrane in their respective 3D image stacks. The chosen threshold values were then applied to the filtered data using the '*Interactive Thresholding*' module. As a result, an output binary image stack of the labelled pixels (i.e. 'segmented' image data) was generated. Example XY-orthoslices of the nuclei and plasma membrane of chondrocytes before and after interactive thresholding are shown in Figure 47. The labelled pixels that are identified as the nuclei and plasma membrane of chondrocytes are displayed in blue in the 'segmented' image data (Figure 47).

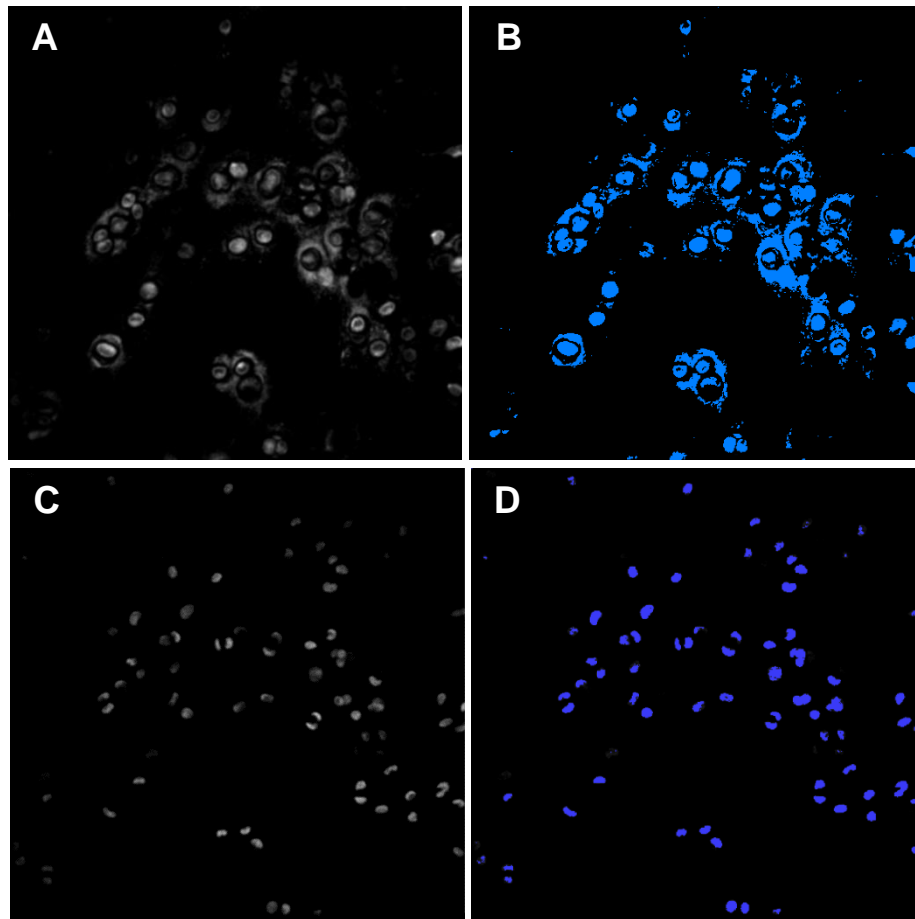


**Figure 47: XY-orthoslices of the plasma membrane of chondrocytes from (A) ‘filtered’ and (B) ‘segmented’ image data and the cell nuclei from (C) ‘filtered’ and (D) ‘segmented’ image data, showing before and after the application of ‘Interactive Thresholding’ module used to determine the location and geometry of the plasma membrane and nuclei of chondrocytes.**

Following interactive thresholding, the labelled pixels that represent the nuclei and plasma membrane are displayed in dark blue and light blue, respectively, in their respective ‘segmented’ image data.

Due to high contrast between phases of nuclei/background and plasma membrane/background, segmentation was reasonably straightforward using interactive thresholding. However, there is a minor complication introduced by the nature of fluorescence staining and image acquisition (uneven staining intensity in cells). The staining intensity of the nuclei and plasma membrane were slightly irregular across the chondrocytes. The majority of pixels that represent the nuclei and plasma membrane were selected by the threshold levels in interactive thresholding. However, some pixels, that were supposed to be assigned to either the nuclei or plasma membrane (in their respective image stacks) but were not within the threshold levels, were excluded. To overcome this issue, the ‘Fill Holes’ module was used to fill incompletely labelled objects (i.e. the nuclei or plasma membrane in their respective image sets). Example XY-orthoslices of the nuclei and plasma membrane of chondrocytes before and after the *Fill Holes*’ module are presented in Figure 48. The red arrows in Figure 48 indicate where the pixels were

excluded because they lied outside the threshold level range but were supposed to be assigned to either the nuclei or plasma membrane (in their respective image stacks).

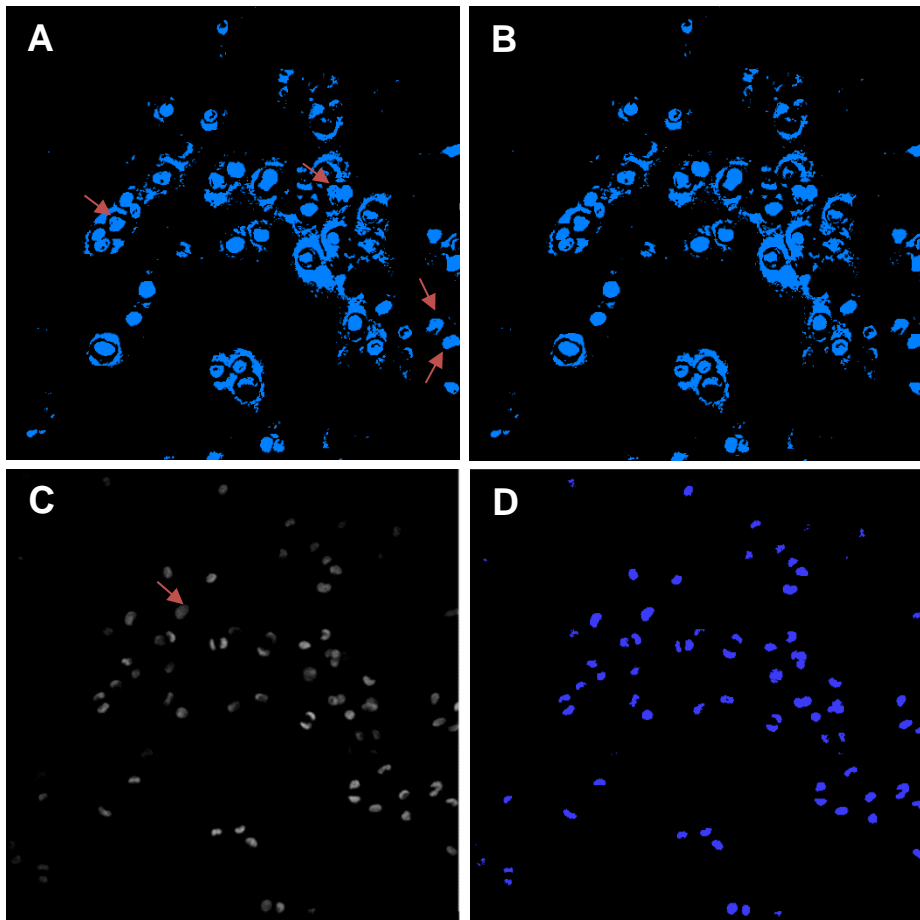


**Figure 48:** XY-orthoslices of the plasma membrane of chondrocytes from (A) 'segmented' and (B) 'filled holes' image data and the cell nuclei from (C) 'segmented' and (D) 'filled holes' image data, showing before and after the application of 'Fill Holes' module used to fill incompletely labelled objects.

Incompletely labelled nuclei and plasma membrane of chondrocytes highlighted with red arrows which were filled using the 'Fill Holes' module.

The 'filled holes' image sets were further processed by applying the 'Remove Small Spots' module. This was to clean up the image stacks and provide a more accurate visualisation of the cells. A volume size threshold was defined for each image stack to preserve the nuclei and the cell bodies while eliminate extraneous objects too small to be the nuclei and cells. Example 2D orthoslices of the 'filled holes' image sets of the nuclei and plasma membrane from pre and post 'Remove Small Spots' module application are shown in Figure 49 (red arrows). The last image processing step was to remove incomplete objects near the border through the application of the 'Border Kill' module. This means incomplete cells that were located at the border would not be included for further analysis. Example 2D orthoslices of the 'removed small spots' image sets of the nuclei and plasma membrane from pre and post 'Border Kill' module application are shown in Figure 49 (orange arrows).

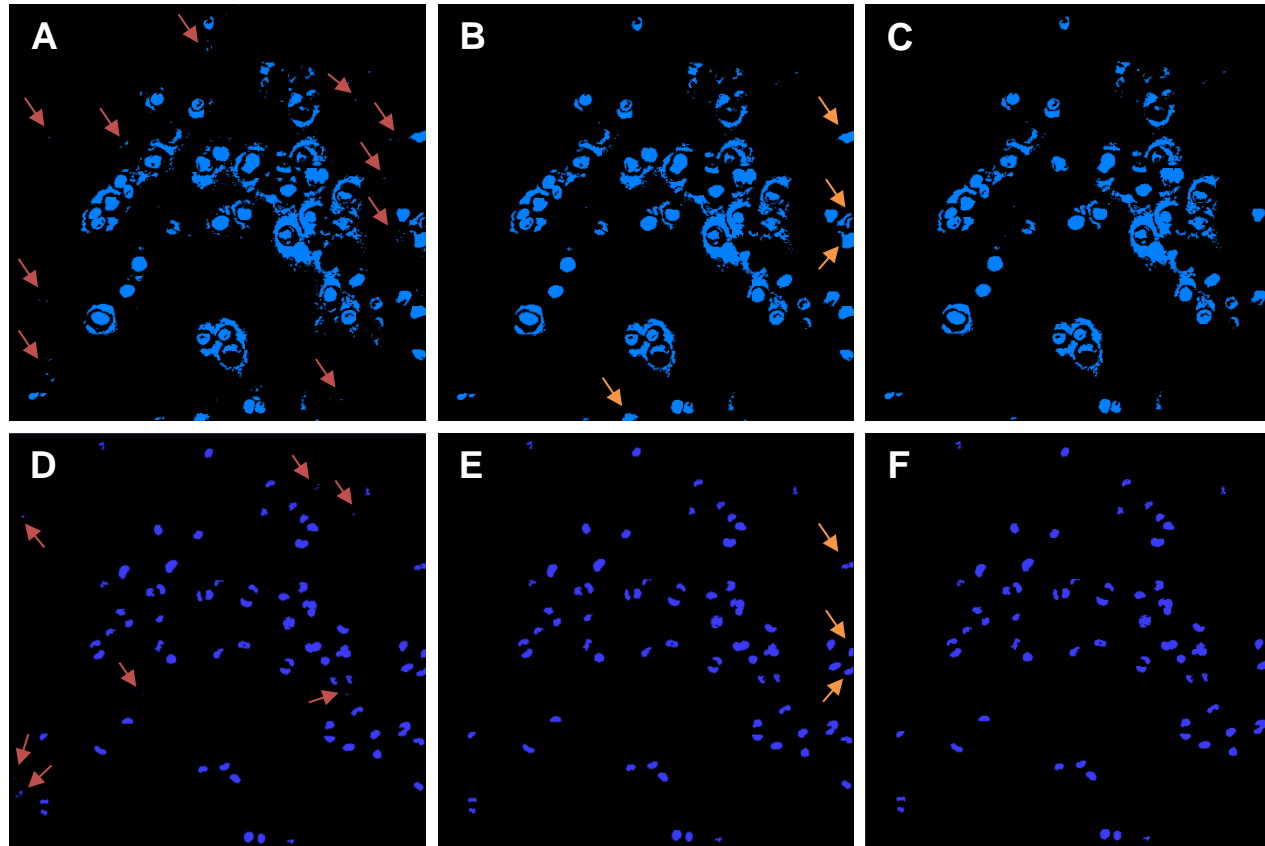


**Figure 49:** *XY-orthoslices of the plasma membrane of chondrocytes from (A) ‘filled holes’, (B) ‘removed small spots’ and (C) ‘border killed’ image data and the cell nuclei from (D) ‘filled holes’, (E) ‘removed small spots’ and (F) ‘border killed’ image data, showing before and after the application of the ‘Remove Small Spots’ module and the ‘Border Kill’ module.*

Removal of extraneous objects too small to be the nuclei and chondrocytes highlighted with red arrows. Removal of incomplete objects (i.e. the nuclei and plasma membrane of chondrocytes) near the border highlighted with orange arrows.

Once both image stacks were processed through the workflow by each module in order, they were then merged together by using the '*Arithmetic*' module to create an binary image that highlights the nuclei and plasma membrane of chondrocytes (Figure 50).

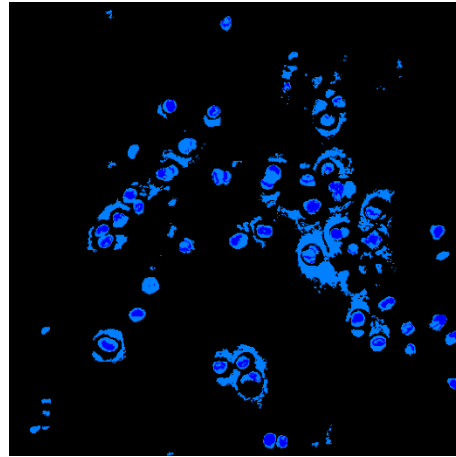


**Figure 50: XY-orthoslice of the image data after merging together both the processed image stacks of the nuclei and plasma membrane of chondrocytes using the '*Arithmetic*' module prior to the cells identification step.**

The nuclei and plasma membrane of chondrocytes are displayed in dark blue and light blue, respectively, in the processed, merged image stack.

The next stage of the image analysis process was to identify and select chondrocytes from the processed, merged image stack of the nuclei and plasma membrane of chondrocytes for 3D rendering and morphometric quantification analysis. The cells identification stage was conducted using the Image Segmentation Editor of Amira. The Image Segmentation Editor is a workroom that provides a variety of tools and functions for semi-automated and manual segmentation. It is typically used for interactive segmentation tasks. It can be used to correct or refine previously labelled regions/objects by automated segmentation module (i.e. interactive thresholding used for nuclei and plasma membrane segmentation in this thesis). It also allows the user to identify and extract a particular region/regions from the 3D data for further analysis. In this study, the '*Interactive Thresholding*' module was used previously to segment the potential nuclei and plasma membrane of chondrocytes from their respective image stacks. Further editing was conducted using the Image Segmentation Editor to identify and extract chondrocytes from the 3D processed data for 3D rendering and morphometric quantification analysis. By default, the Image Segmentation Editor operates in a 2D-view mode which normally displays one XY-orthoslice of a 3D image. Figure 51 is a screenshot of the Image Segmentation Editor's interface which shows an XY-orthoslice from the processed, merged image stack; highlighting the boundaries of the potential nuclei and plasma membrane in blue and green, respectively.

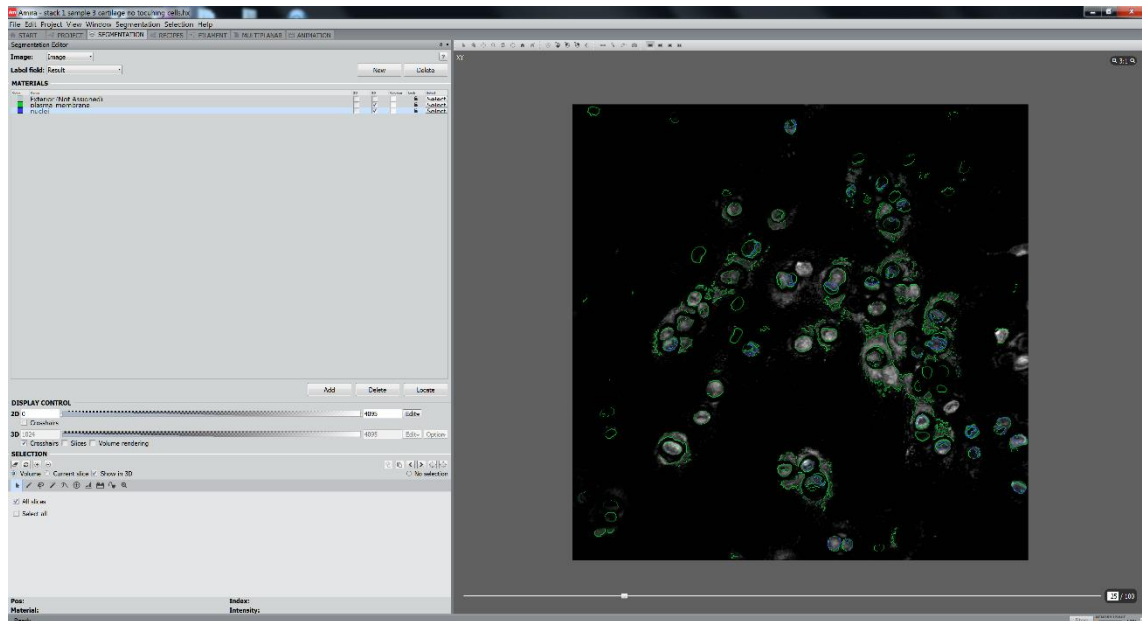


**Figure 51:** The interface of Amira's Image Segmentation Editor displaying an XY-orthoslice from the processed, merged image stack which highlights the boundaries of the potential nuclei (blue) and plasma membrane (green).

By using the Image Segmentation Editor, it was capable of easily picking out chondrocytes that had clear cell boundaries from the 3D processed image stack. In this case of clear cell boundaries, the nuclei and plasma membrane of chondrocytes were merged together and identified as individual chondrocytes. An example of this is demonstrated in Figure 52; a chondrocyte was identified by selecting the nuclei (Blue boundary selected in red, Figure 52A) and its corresponding plasma membrane (Green boundary selected in red, Figure 52A) and registering the two parts as a chondrocyte (Red boundary, Figure 52B,).

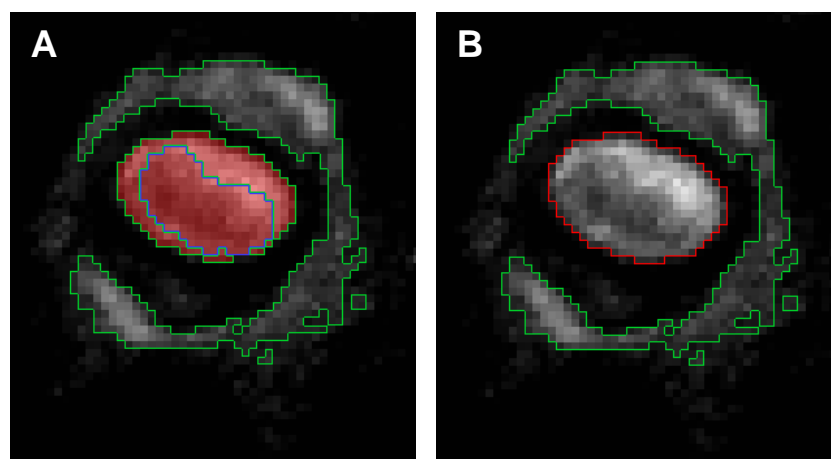


**Figure 52:** An example of cells identification using the Image Segmentation Editor in the case of clear cell boundaries; (A) a nucleus (blue boundary selected in red) and its corresponding plasma membrane (green boundary selected in red) were selected and register the two parts as (B) an individual chondrocyte (red boundary).

However, in some cases, the cell boundaries were ill-defined (as demonstrated in Figure 53) where the cells were touching unwanted surroundings (i.e. pericellular matrix) and each other. This made the cells identification step more challenging and an extra step was required to separate touching chondrocytes or remove pericellular matrix from the chondrocytes. The lasso tool from the Image Segmentation Editor was used to manually define dividing lines in 2D to separate different objects (i.e. separation of touching chondrocytes and removal of pericellular matrix) so chondrocytes identification were made possible. This extra step was required to be completed each cell on every 2D image that made up the 3D data. Once this was completed, cell boundaries could be defined more easily. The plasma membrane and the corresponding nuclei were then merged together to be identified as individual chondrocytes for morphometric measurements. An example of this is demonstrated in Figure 53; two chondrocytes were in close contact which made it hard to distinguish cell boundaries (Figure 53A). To overcome this, the lasso tool was used to manually define a dividing line in 2D to separate the two chondrocytes (White arrow, Figure 53B). This was completed on every 2D image that made up the 3D data, resulting in two separated chondrocytes (Figure 53C). Once clear cell boundaries were refined, the plasma membrane and the corresponding nuclei were selected and registered as chondrocytes.

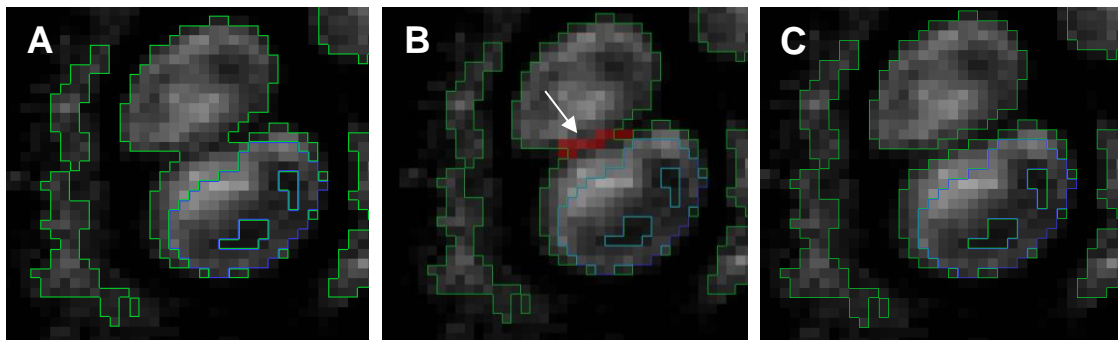


**Figure 53: An example of cells identification using the lasso tool from the Image Segmentation Editor in the case of ill-defined cell boundaries; (A) two chondrocytes were in close contact which made it hard to distinguish cell boundaries, (B) a diving line (white arrow) was manually defined by the lasso tool in every 2D image that made up the 3D data, (C) two separated chondrocytes as a result of the extra step taken with the lasso tool to refine cell boundaries, allowing the two chondrocytes to be identified for 3D rendering and cell morphometric measurements.**

The identified chondrocytes were then extracted to create a label image stack named ‘cellstoanalyse’ for 3D rendering and cell morphometric measurements. Figure 54A shows an 2D orthoslice from the resulting ‘cellstoanalyse’ image stack following the cell identification step, highlighting the chondrocytes (labelled with yellow boundaries) selected for further analysis. Figure 54B shows an 2D orthoslice of the corresponding selected chondrocytes (labelled in red) from the processed, merged image stack of the nuclei and plasma membrane.

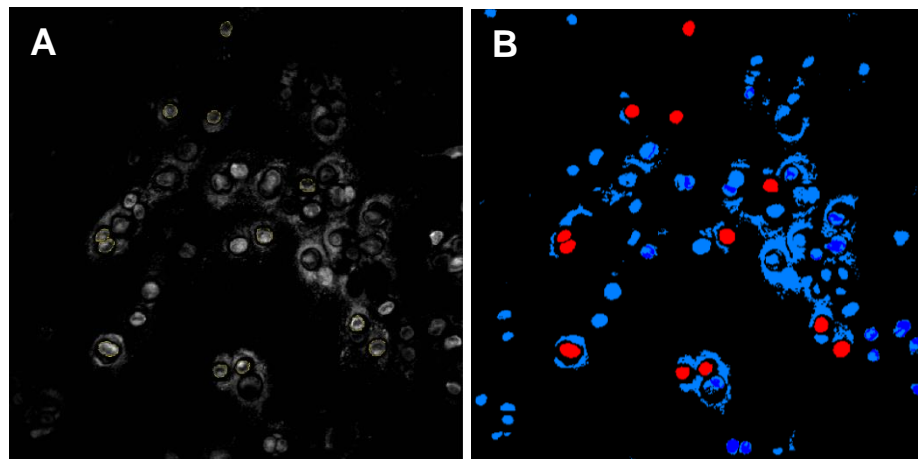


**Figure 54: XY-orthoslices of (A) the ‘cellstoanalyse’ image stack following the cell identification step which highlights the chondrocytes (yellow boundaries) selected for 3D rendering and cell morphometric measurements and (B) the processed, merged image stack of the nuclei and plasma membrane showing the corresponding selected chondrocytes (red).**

The ‘*Label Analysis*’ module was used to carry out cell morphometric measurements on the identified chondrocytes from the label image stack. Cell morphometric parameters including cell length, width, height and volume were selected from the measure port along with sphericity (which was manually inserted specific equation) and saved as a new measure group for cell morphometric quantification (Figure 55). Cell length and width were defined along the major and minor axes of the cell cross-section perpendicular to cell height (Figure 56). Height was defined as the maximum distance between the vertical coordinates of all the vertices (perpendicular to cartilage surface) on the Z-axis (Figure 56). Sphericity is the measures of how closely the shape of an object approaches that of a mathematically perfect sphere and this was defined as the ratio of the surface area of a sphere (with the same volume as the given cell) to the surface area of the cell. A sphericity value of 1 corresponds to a perfect a sphere, any value less than 1 indicates departure from the sphere, with lower values signifying least spherical structures. Once measurements were saved and selected from the measure port in Amira, the ‘*Label Analysis*’ module was applied to the ‘cellstoanalyse’ image stack to perform the morphometric measurements. An example analysis spreadsheet of the morphometric measurements conducted on selected chondrocytes is shown in Figure 57.

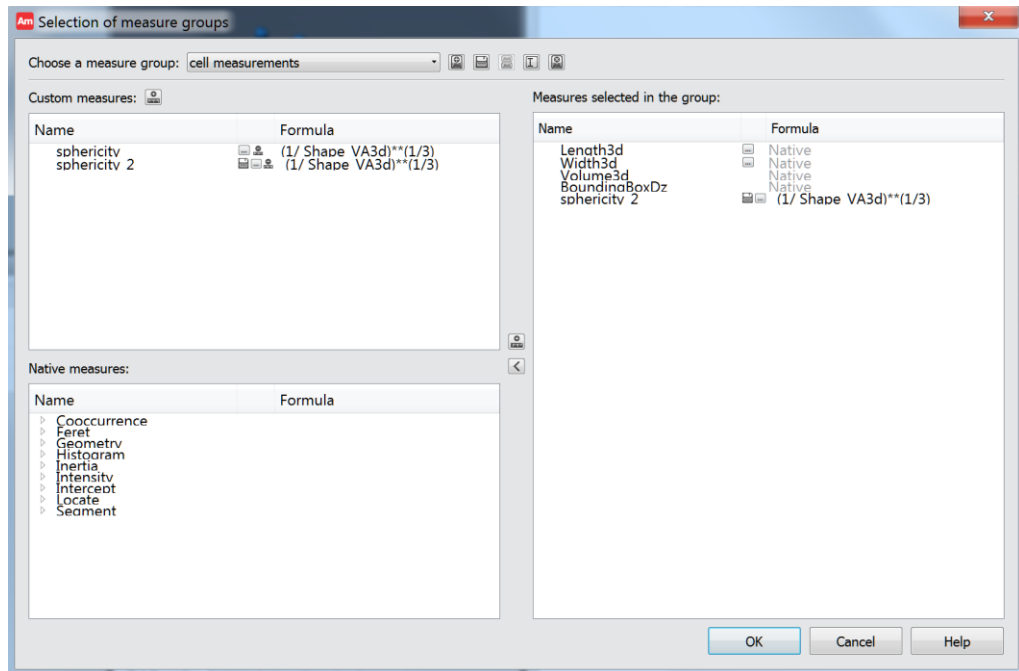


**Figure 55:** The measure port was used to select cell morphometric parameters including cell length, width, height, volume and sphericity (which was manually inserted specific equation) and create a new measure group for cell morphometric quantification.

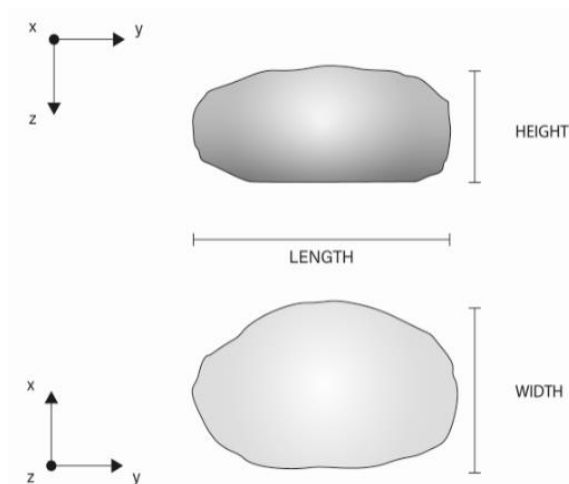


**Figure 56:** Definition of cell morphology parameters. Cell length and width were defined along the major and minor axes of the cell cross-section perpendicular to its height. Height was defined as the maximum distance between the vertical coordinates of all the vertices on the Z-axis.

	Length3d	Width3d	FeretShape3d	Volume3d	BoundingBoxDz	EqDiameter	sphericity_2	index	Materials
1	12.3247	9.81861	1.28441	559.84	12.2	10.2256	0.857113	1	cells
2	17.3374	10.2462	1.66428	931.786	9.8	12.1182	0.634033	2	
3	13.6651	10.3307	1.27088	617.808	10.6	10.567	0.885985	3	
4	12.3423	9.55671	1.26272	518.632	10.6	9.96828	0.859928	4	
5	11.5632	7.4602	1.52452	381.017	7	8.9946	0.860411	5	
6	12.962	9.91011	1.26247	591.745	9.4	10.4163	0.824049	6	
7	12.8235	9.51211	1.21537	512.943	9	9.9317	0.781123	7	
8	15.4717	9.21128	1.6342	733.973	8.6	11.1916	0.834862	8	
9	13.9408	10.8355	1.27153	741.892	10.6	11.2317	0.885104	9	
10	12.2544	9.62682	1.22615	428.145	9.4	9.35113	0.846739	10	
11	13.0282	8.86652	1.447	546.232	8.6	10.1421	0.785129	11	
12	0.260898	0.260898	3.37022	0.07688	0.2	0.52756	1.34159	12	

**Figure 57: An example analysis spreadsheet displaying the cell morphometric measurements performed on selected chondrocytes.**

Three dimensional reconstruction of the selected chondrocytes from the ‘cellstoanalyse’ image was then performed following the cell morphometric measurements using the ‘Volume Rendering’ module. The 3D rendering of chondrocytes was used for 3D visualisation purpose. Figure 58 shows an example of 3D rendering of selected chondrocytes.

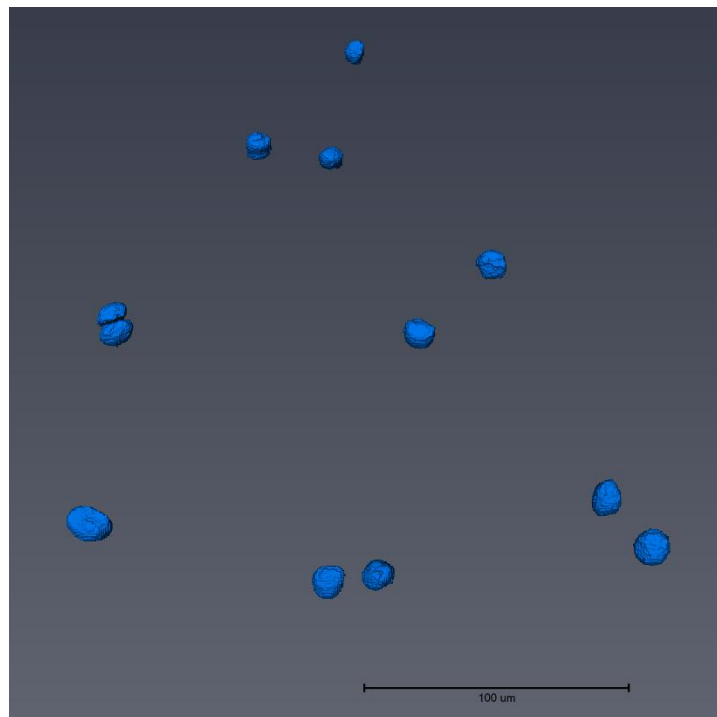


**Figure 58: 3D rendering of selected chondrocytes from the label ('cellstoanalyse') image for 3D shape visualisation purpose.**

As described in Section 4.3.4.2, three sequential volume images of selected chondrocytes from the superficial zone of cartilage disks (n=4, obtained from the medial and lateral regions of the patellofemoral groove of two bovine knee joints) were acquired under zero, 10 % and 15 % applied tissue compressive strains using confocal microscopy in order to determine the effects of incremental compressive strains on chondrocyte deformation behaviour in native cartilage. In other words, the same group of chondrocytes from each cartilage disk was imaged under the selected strain levels throughout the experiment. All confocal volumes images of chondrocytes were analysed using the custom workflow described in this section to quantify cell deformation behaviour under incremental compressive tissue strains. It was important to reduce bias associated with manual measurements so that a fair analysis was conducted, therefore the

custom workflow was applied on every image set with the same modules, module order and settings. Due to the extra step required to identify chondrocytes in the cases of ill-defined cell boundaries (i.e. chondrocytes touching pericellular matrix and each other) which was extremely time-consuming and required considerable effort and concentration, this led to low chondrocyte numbers for analysis in this study. Consequently, 3D rendering and cell morphometric measurements were performed on a total of the same 37 chondrocytes from four cartilage disks under the selected strain levels, with data collected for 6-11 chondrocytes per cartilage disk.

## **4.4 Results**

### **4.4.1 The Effect of Culture Duration on Chondrocyte Metabolism and Viability within Native Cartilage**

In this study, cartilage disks culture was required because it was not possible to regularly harvest fresh osteochondral plugs (i.e. the source for cartilage disks) from bovine knee joints due to the logistic of a weekly tissue delivery from the abattoir. Thus, a culture period of up to 3 days was used to investigate the effect of culture duration on chondrocyte metabolism and viability within cartilage disks as it was important to ensure that the chondrocytes were healthy before live cell imaging. XTT assay and Live/Dead<sup>®</sup> imaging were used to determine the effect of length of time in culture on chondrocyte metabolism and viability within native cartilage disks harvested from bovine osteochondral plugs.

XTT assays of cartilage disks cultured for different durations from day 0 to 3 indicated similar metabolic activity, suggesting that the culture times used here had no measurable effects on chondrocyte viability in native cartilage up to Day 3 (Figure 59). Live/Dead<sup>®</sup> images of cross-sectional slices obtained from cartilage disks cultured up to Day 3 showed densely distributed live chondrocytes through the depth of the tissue and some dead chondrocytes were visualised (Figure 60 and Figure 61). Live/Dead<sup>®</sup> images in the XZ-plane revealed chondrocytes in the depth of about 200  $\mu\text{m}$  below the cut surface showed that the majority of the dead chondrocyte were located at the cut surface (Figure 61).

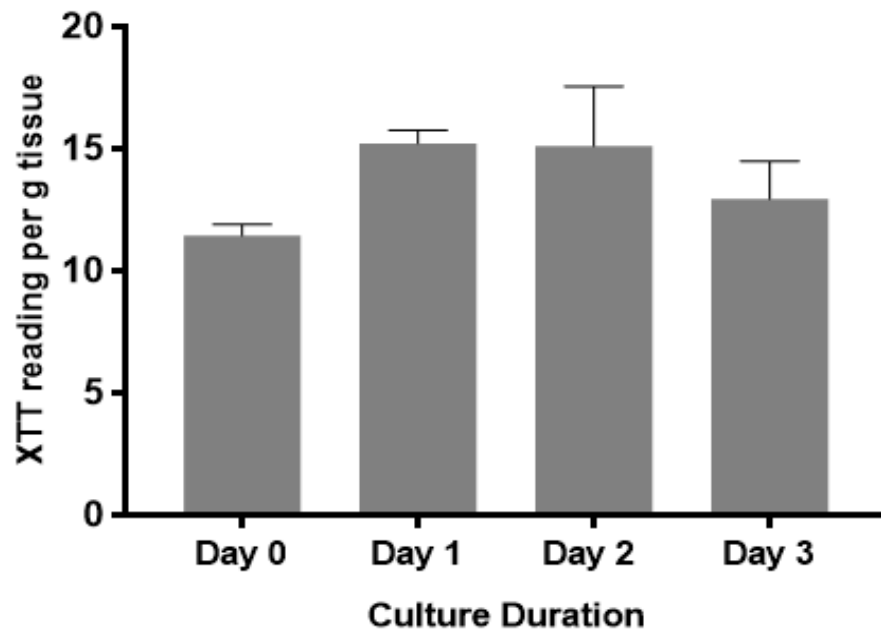


**Figure 59: Viability assessment of cartilage disks harvested from osteochondral plugs after up to 3 days in culture. Chondrocyte metabolic activity was assessed by XTT assay.**

There were no statistical significances found between cartilage samples in culture for different time durations (up to Day 3). Data represented as means  $\pm$  SD (n=3). Statistical analysis was determined by the Kruskal–Wallis test.

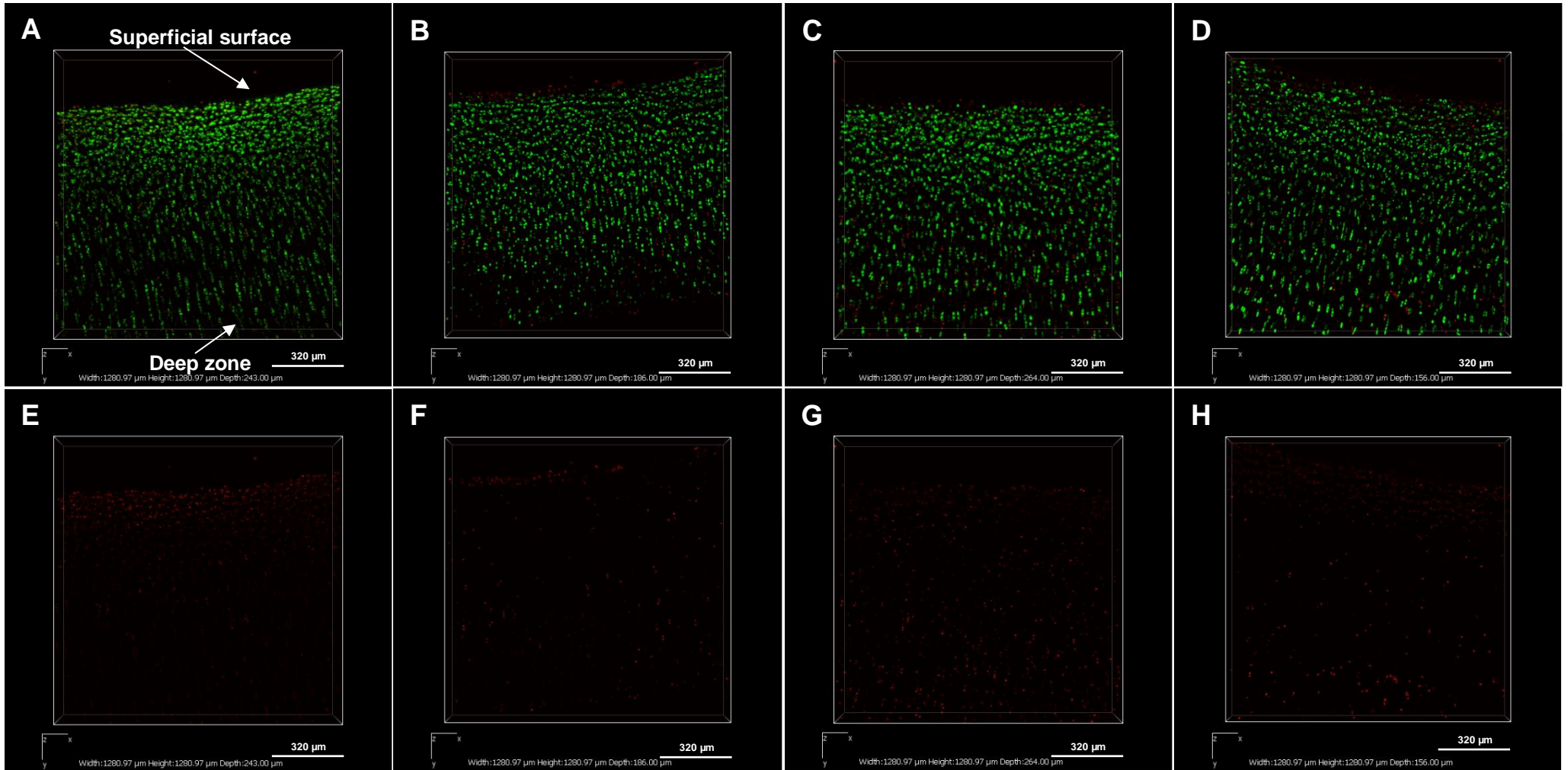


**Figure 60: Live/Dead<sup>®</sup> confocal volume images of chondrocytes in cartilage slices obtained from bovine cartilage disks cultured in different periods of time from Day 0 to 3; (A, E) Day 0, (B, F) Day 1, (C, G) Day 2 and (D, H) Day 3. Images revealed chondrocytes through the depth of the cartilage slices from the superficial zone down to the deep zone labelled with (A-D) both live and dead staining and (E-H) dead staining only. Images are presented in the Z-plane.**

Green  $\equiv$  live cells. Red  $\equiv$  dead cells. Live cells appeared throughout the depth of tissue cultured under different culture durations and some dead cells were visualised. Scale bar 320  $\mu$ m.

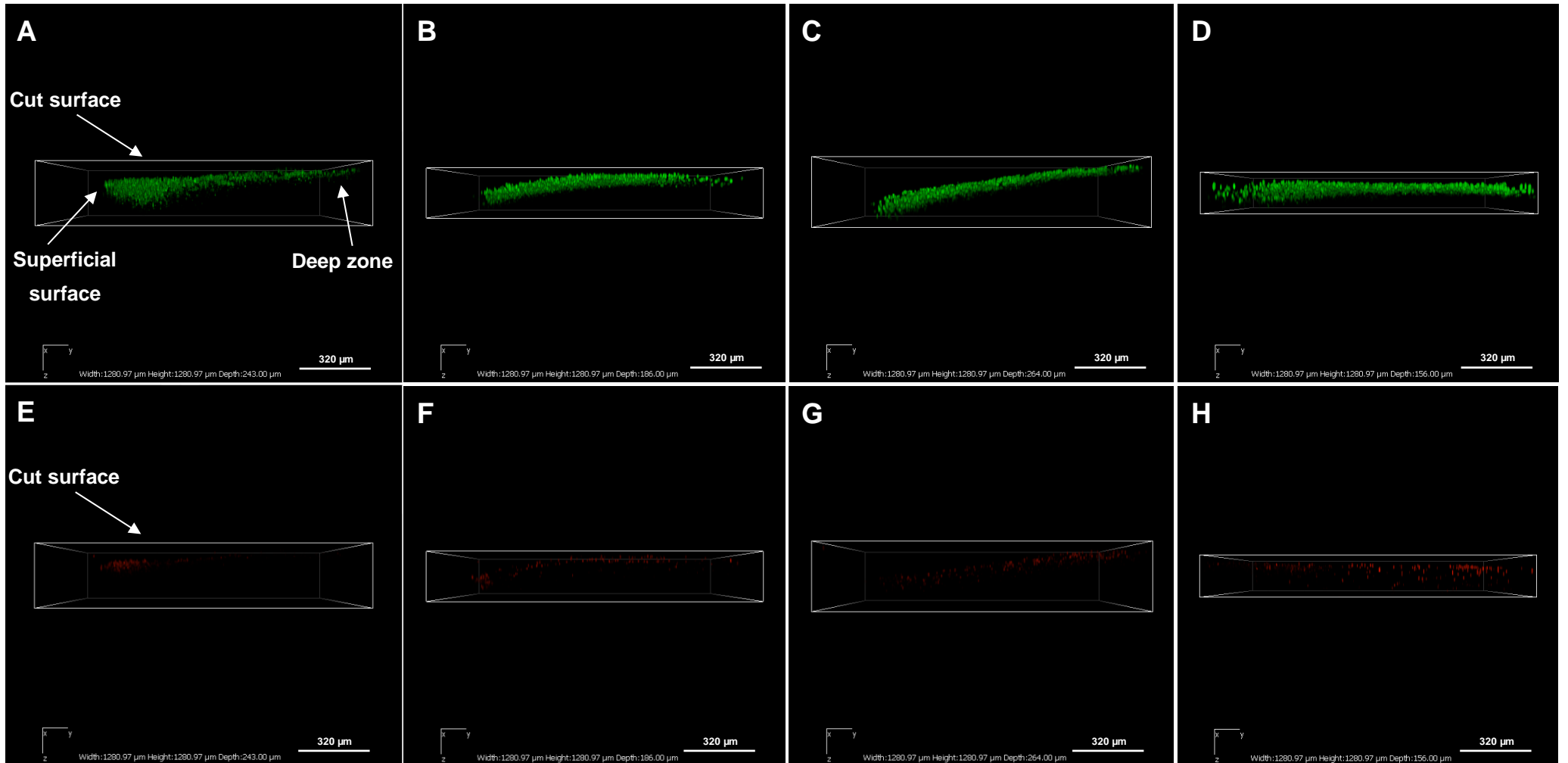


**Figure 61: Live/Dead<sup>®</sup> confocal volume images of chondrocytes in cartilage slices obtained from bovine cartilage disks cultured in different periods of time from Day 0 to 3; (A, E) Day 0, (B, F) Day 1, (C, G) Day 2 and (D, H) Day 3. Images show (A-D) live and (E-H) dead. Images are presented in the XZ-plane.**

Green  $\equiv$  live cells. Red  $\equiv$  dead cells. Live cells appeared throughout tissue depth while the majority of dead cells were visualised near the cut surface of the cross-sectional tissue slices. Arrows highlighting the cut surface in the XZ-plane. Scale bar 320  $\mu$ m.

#### **4.4.2 Chondrocyte Volume Changes in Uncompressed Native Cartilage with Repeated Confocal Scans**

In order to assess whether photobleaching of CellMask Green plasma membrane stain may introduce errors into the morphometric measurements, three sequential images of selected chondrocytes within the superficial zone of cartilage disks were acquired under non-loaded conditions. Cell volume measurements were performed on the same chondrocytes (n=3 cells per cartilage disk) in all repeated images captured in each cartilage disk (for a total of 5 cartilage disks harvested from the patellofemoral groove of two bovine knee joints).

Changes in chondrocyte volume were determined after the capture of three repeated confocal images in uncompressed cartilage disks. Chondrocyte volume normalised to the original volume (Image 1) after the repeated confocal images is shown in Figure 62. There was a significant decrease in normalised chondrocyte volume after each capture, of 2.1 % between Image 1 and Image 2 and 4.5 % between Image 1 and Image 3 ( $p < 0.0001$  and  $p < 0.001$ , Figure 62). This most likely indicates the errors (%) in the morphometric measurements were introduced by photodestruction of the CellMask Green plasma membrane stain. It was important to examine the measurement errors associated with the staining method because photobleaching of CellMask Green plasma membrane stain would result in loss of detail for cell morphology and consequently affect the accuracy of morphometric measurements. Thus, the measurement errors introduced by the staining method needed to be taken into account for the morphometric quantitative data as a limitation of the staining method.

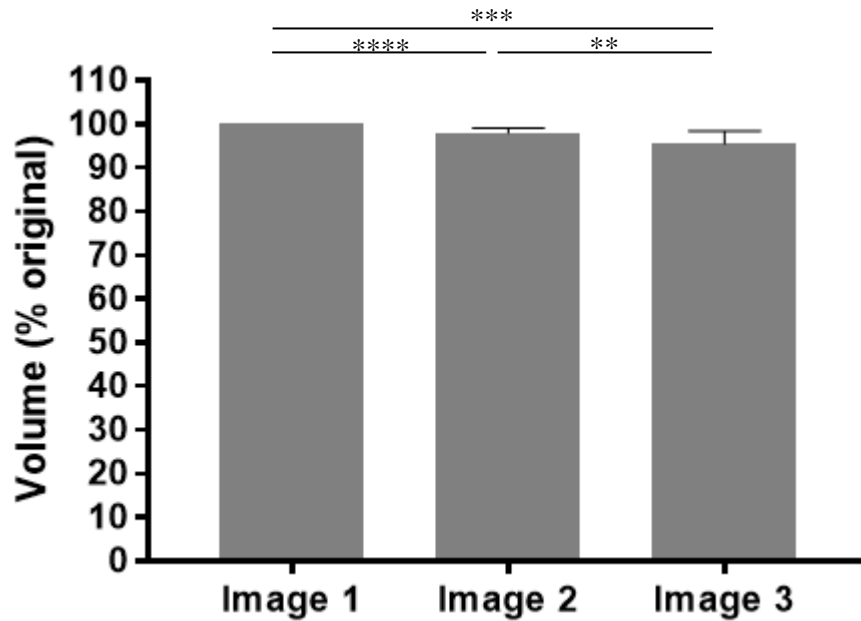


**Figure 62: Changes in the volume of chondrocytes in uncompressed cartilage disks with three repeated confocal scans. There was a slight decrease in normalised chondrocyte volume following capture of repeated confocal images and the changes were significant.**

Data represented as means  $\pm$  SD (n=15 from 5 cartilage disks). Statistical analysis was determined by one way repeated ANOVA after data normality was determined. Turkey's post hoc test was used for comparison between uncompressed chondrocytes captured with repeated confocal images. \*\*  $\equiv$   $p < 0.01$ , \*\*\*  $\equiv$   $p < 0.001$ , \*\*\*\*  $\equiv$   $p < 0.0001$ .

#### **4.4.3 Quantification of Chondrocyte Deformation under Incremental Compressive Tissue Strains In Native Cartilage Disks via Amira: Morphometric Measurements**

In order to determine the effects of incremental compressive strains on chondrocyte deformation behaviour in native cartilage, cell morphometric data was collected from volume images of selected chondrocytes in the superficial zone of cartilage disks acquired sequentially at zero, 10 % and 15% applied compressive tissue strains. A dual staining method of Hoechst 33342 and CellMask Green plasma membrane stains was used to label chondrocytes within cartilage disks. Each cartilage disk was placed in to the newly develop device (see Chapter 2) and viewed under confocal microscopy at the selected strain levels. After an equilibration period of 30 mins in each case, images of the same chondrocytes were acquired and Amira software used to quantitate chondrocyte morphometric parameters including: cell length, width, height, volume and sphericity (see Section 4.3.6.2 for full methodology). Cell morphometric data was collected for 6-11 chondrocytes per cartilage disk and from four cartilage disks obtained from the (relatively flat) medial and lateral regions of the patellofemoral groove of two bovine knee joints. A total of the same 37 chondrocytes from four cartilage disks under the selected strain levels were analysed for cell deformation quantification.

The resulting data is presented in three different ways to fully demonstrate the trends and changes in each parameter and to facilitate comparisons: (1) absolute measurements for each chondrocyte at each strain level; (2) mean values  $\pm$  SD and percentage (%) change in dimension compared to baseline (zero strain) for all chondrocytes in each of the four cartilage disks compare statistically at each strain level and (3) mean values  $\pm$  SD and % change in dimension compared to baseline (zero strain) for all chondrocytes combined in each cartilage disk following application of compressive strains.

#### **4.4.3.1 Absolute Morphometric Measurements for Each Chondrocyte at Each Strain Level in Each of the Four Cartilage Disks**

Absolute measurements of cell length, width, height, volume and sphericity for a total of the same 37 chondrocytes in the superficial zone of four bovine cartilage disks following application of compressive tissue strains (0 %, 10 % and 15 %) are presented in Figure 63 and Figure 64. Figure 63 and Figure 64 illustrates all of the raw data for each chondrocyte in each cartilage disk at each strain level.

Following application of compressive tissue strain, there was no clear trend for changes in chondrocyte length and width (Figure 63A-H). Chondrocyte height and volume appeared to decrease in all cartilage disks at each strain level (10 % and 15 %) (Figure 63J-M and Figure 64A-D). Sphericity appeared to be consistent, except in Cartilage Disk 2 which appeared to increase (Figure 64E-H). These trends were tested statistically for whole populations of chondrocytes in each of the four cartilage disks at each strain level (see Section 4.4.3.2).

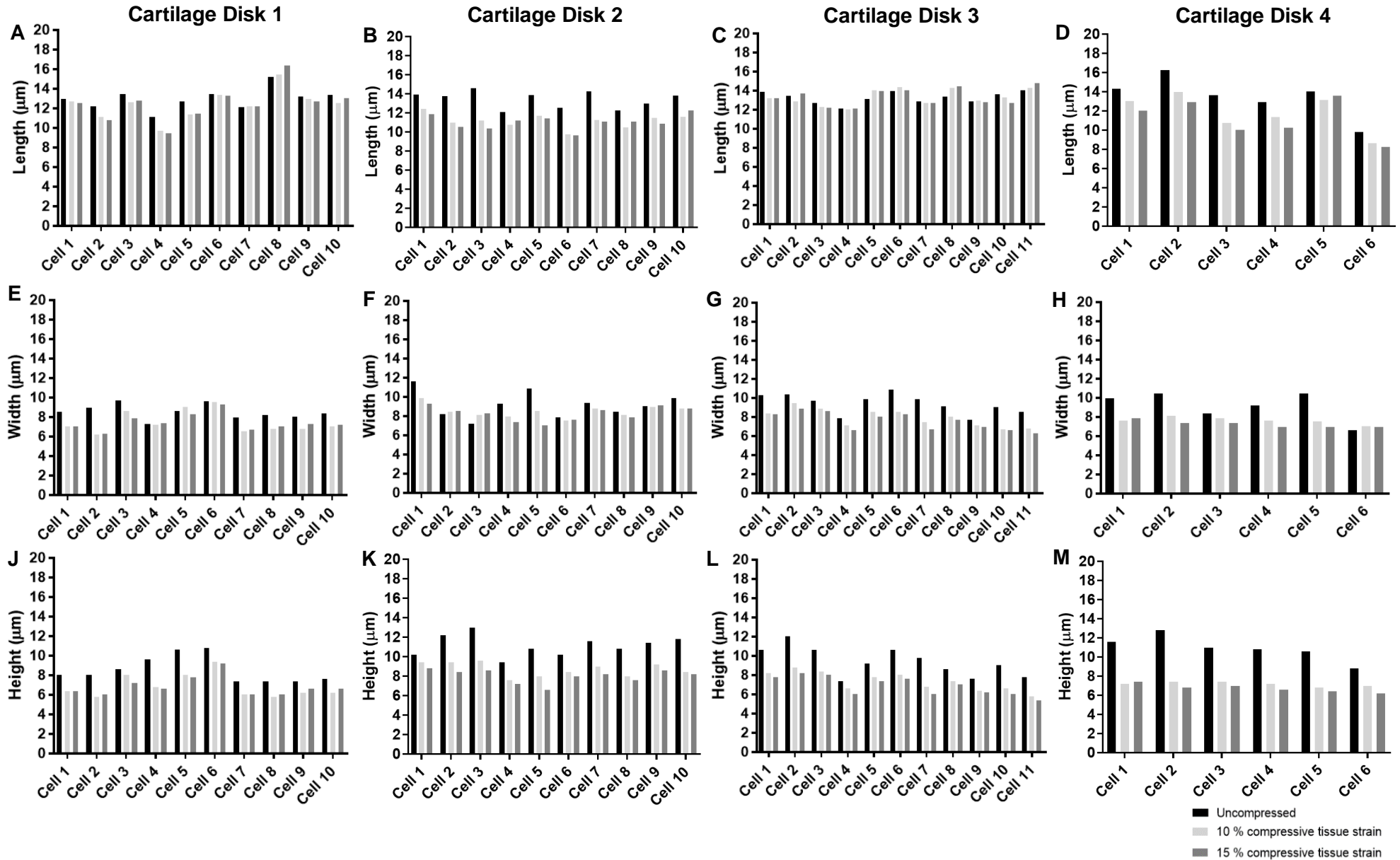


**Figure 63: Absolute morphometric measurements for each individual chondrocyte (n=37) in the superficial zone of each of the four bovine cartilage disks (1-4 = left to right columns) at the selected compressive strain levels of 0 %, 10 % and 15 %; (A, B, C, D) Chondrocyte length, (E, F, G, H) width and (J, K, L, M) height. There was no clear trend for changes in individual chondrocyte width and length with the application of compressive tissue strain. Chondrocyte height appeared to decrease with application of compressive tissue strain.**

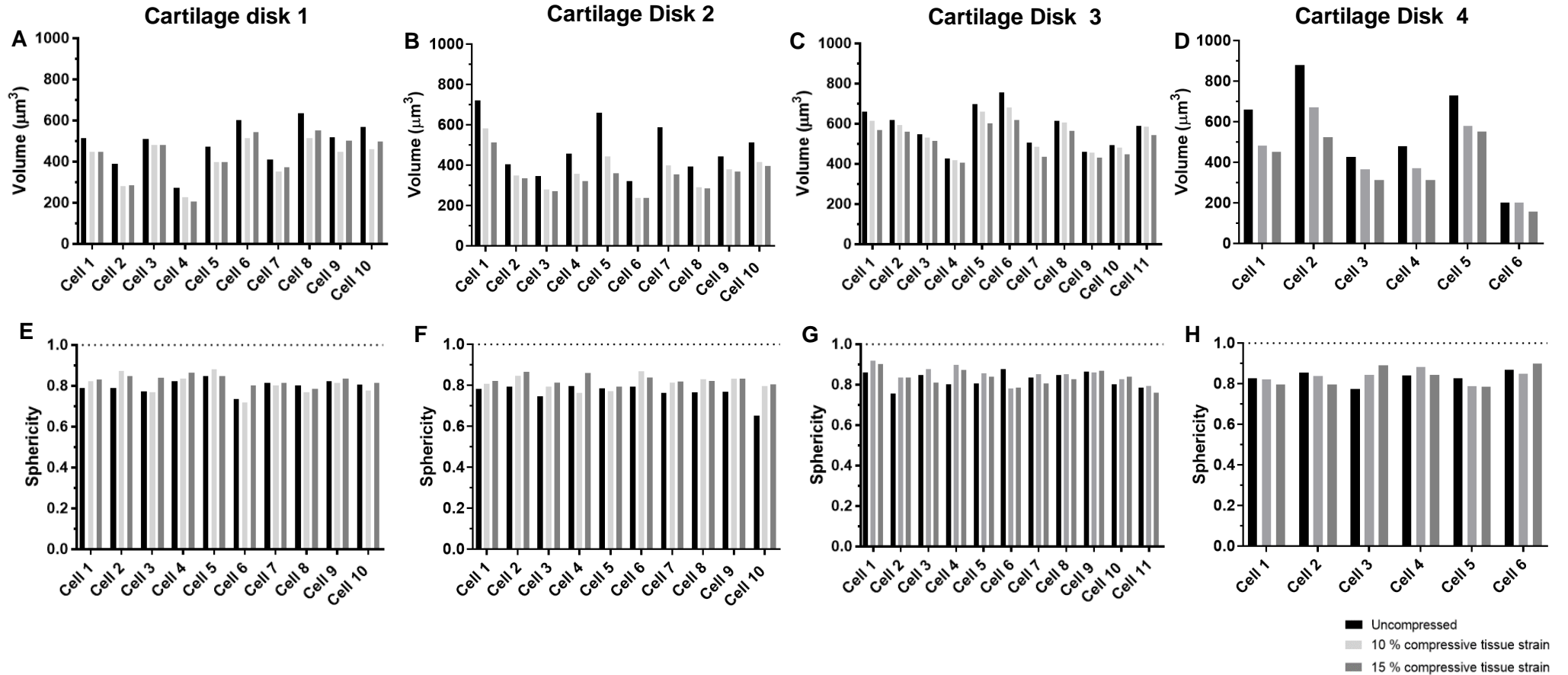


**Figure 64:** Absolute morphometric measurements for each individual chondrocyte ( $n=37$ ) in the superficial zone of each of the four bovine cartilage disks (1-4 = left to right columns) at the selected compressive strain levels of 0 %, 10 % and 15 %; (A, B, C, D) chondrocyte volume and (E, F, G, H) sphericity. *Dotted line* in (E, F, G, H) indicates the value of a perfect sphere. Chondrocyte volume appeared to decrease with application of compressive tissue strain. Sphericity remained consistent in all cartilage disks, apart from chondrocytes in Cartilage Disk 2 where sphericity appeared to increase with application of compressive tissue strain.

#### **4.4.3.2 Mean values $\pm$ SD of and Percentage (%) Change in Morphometric Measurements Compared to Baseline (Zero Strain) for All Chondrocytes in Each of the Four Cartilage Disks Following Application of Compressive Strains**

Changes in chondrocyte length, width, height, volume and sphericity for all chondrocytes (n=37) in the superficial zone of each of the four bovine cartilage disks following application of 10 % and 15 % compressive tissue strains are shown as mean values  $\pm$  SD in Figure 65 and Figure 66 and percentage (%) compared to baseline (zero strain) in Figure 67 and Figure 68. The population means and % change (from zero strain) of each morphometric parameter for all chondrocytes in each of the four cartilage disks at each strain level were statistically tested to determine any significant differences in the dimensions.

The application of compressive tissue strains of 10 % and 15 % had significant observable effects on the morphology of chondrocytes. Mean values of length and width for chondrocytes in each of the four cartilage disks decreased with applied compressive tissue strain, with the decrease being statistically significant in Cartilage Disk 1, 2 and 4, and Cartilage Disk 1,3 and 4, respectively (Figure 65A-D). Chondrocytes in Cartilage Disk 1 obtained a significant decrease in length, from an average of  $13 \pm 1.1 \mu\text{m}$  at 0 % strain to  $12.4 \pm 1.5 \mu\text{m}$  at 10 % applied tissue strain ( $p < 0.05$ , Figure 65A) which corresponds to a percentage change of -4.7 % ( $p < 0.05$ , Figure 67A). The width significantly reduced, from a mean value of  $8.5 \pm 0.7 \mu\text{m}$  at the uncompressed tissue state to  $7.5 \pm 1.1 \mu\text{m}$  and  $7.4 \pm 0.9 \mu\text{m}$  at 10 % and 15 % applied strains, respectively ( $p < 0.05$  and  $p < 0.01$ , Figure 65A). The corresponding percentage change in width compared to baseline (zero strain) were -12.3 % and -12.4 % at 10 and 15 % tissue strains, respectively ( $p < 0.05$  and  $p < 0.01$ , Figure 67A). In Cartilage Disk 2, a significant decrease in mean length value was observed, reducing from  $13.4 \pm 0.9 \mu\text{m}$  at 0 % applied strain to  $11.2 \pm 0.7 \mu\text{m}$  and  $11 \pm 0.7 \mu\text{m}$  at 10 % and 15 % applied strains, respectively but with no significant change in mean width with applied compressive tissue strain ( $p < 0.0001$  and  $p < 0.001$ , Figure 65B). The corresponding percentage change in mean length compared to baseline (zero strain) were -16.6 % and -17.4 % at 10 and 15 % tissue strains, respectively ( $p < 0.0001$  and  $p < 0.001$ , Figure 67B). In contrast, chondrocytes in Cartilage Disk 3 showed a significant decrease in mean width at each strain level (10 % and 15 %), from a mean value of  $9.4 \pm 1 \mu\text{m}$  at the uncompressed tissue state to an average of  $7.9 \pm 0.9 \mu\text{m}$  and  $7.6 \pm 0.9 \mu\text{m}$  at 10 % and 15 % applied tissue strains, respectively, but no significant changes were observed in mean length with applied compressive tissue strain ( $p < 0.0001$ , Figure 65C). The corresponding percentage decrease in mean width compared to baseline (zero strain) were -15.6 % and -19.4 % at 10 and 15 % tissue strains, respectively ( $p < 0.0001$ , Figure 67C). In Cartilage Disk 4, length significantly decreased from a mean of  $13.5 \pm 2.1 \mu\text{m}$  at the uncompressed tissue state to  $11.8 \pm 1.9 \mu\text{m}$  and  $11.2 \pm 2 \mu\text{m}$  at 10 % and 15 % applied tissue strains ( $p < 0.01$ , Figure 65D), along

with a significant reduction in width between 0 % and 15 % applied tissue strains, from a mean of  $9.2 \pm 1.5 \mu\text{m}$  to  $7.2 \pm 0.4 \mu\text{m}$  ( $p < 0.05$ ). The corresponding percentage change in mean length compared to baseline (zero strain) were -12.5 % and -17.2 % at 10 and 15 % tissue strains, respectively, ( $p < 0.01$ , Figure 67D) and the percentage change in mean width compared to baseline (zero strain) was -19.4 % at 15 % tissue strain ( $p < 0.05$ ).

Reduction in mean values of height for chondrocytes in each of the four cartilage disks were observed following application of compressive tissue strain (Figure 65E-H). This decrease was statistically significant in all cartilage disks and at all applied strain levels, except between 10 % and 15 % tissue strains in Cartilage Disk 1 and 4 ( $p < 0.01$ , Figure 67E-H). Mean values of chondrocyte height in Cartilage Disk 1-4 significantly decreased from  $8.5 \pm 1.3 \mu\text{m}$ ,  $11.1 \pm 1.1 \mu\text{m}$ ,  $9.4 \pm 1.5 \mu\text{m}$ ,  $10.9 \pm 1.3 \mu\text{m}$  at the uncompressed tissue state to  $6.9 \pm 1.2 \mu\text{m}$ ,  $8.7 \pm 0.7 \mu\text{m}$ ,  $7.3 \pm 1 \mu\text{m}$ ,  $7.2 \pm 0.2 \mu\text{m}$  at 10 % applied tissue strain ( $p < 0.01$ ) and  $6.8 \pm 1 \mu\text{m}$ ,  $8 \pm 0.7 \mu\text{m}$ ,  $6.9 \pm 1 \mu\text{m}$ ,  $6.7 \pm 0.4 \mu\text{m}$  at 15 % applied tissue strain, respectively ( $p < 0.001$ ).

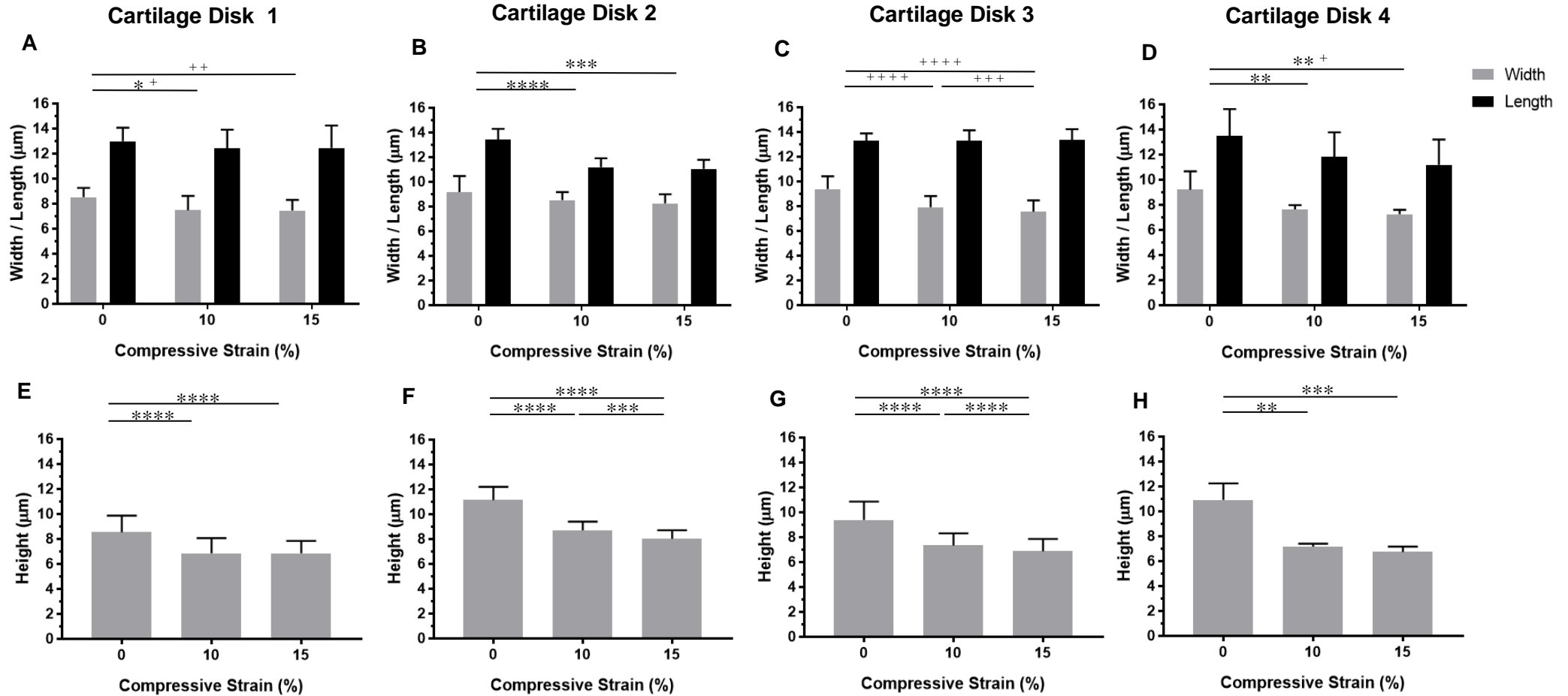
The corresponding percentage change in mean height for chondrocytes in each of the four cartilage disks are shown in Figure 67E-H. In Cartilage Disk 1, the height of chondrocytes significantly decreased from baseline (zero strain) by 19.6 % and 19.5 % at 10 % and 15 % tissue strains, respectively ( $p < 0.0001$ , Figure 67E). The significant percentage drop in chondrocyte height compared to baseline (zero strain) in Cartilage Disk 2 was by 21.6 % at 10 applied tissue strain and 27.6 % at 15 % applied tissue strain ( $p < 0.0001$ , Figure 67F). The percentage change in chondrocyte height from baseline (zero strain) in Cartilage Disk 3 was decreased by 22.3 % and 26.3 % at 10 % and 15 % tissue strains, respectively ( $p < 0.0001$ , Figure 68G). In Cartilage Disk 4, the height of chondrocytes significantly decreased from baseline (zero strain) by 33.6 % and 37.9 % at 10 % and 15 % tissue strains, respectively ( $p < 0.001$  and  $p < 0.0001$ , Figure 68H). The magnitude of percentage change in chondrocyte height compared to baseline (zero strain) appeared to vary across the cartilage disks, with chondrocytes in Cartilage Disk 1, 2, 3 and 4 significantly dropped by an average of 19.5 %, 27.6 % and 26.3 % and 37.9 %, respectively, following application of 15 % compressive tissue strain ( $p < 0.0001$ , Figure 67E-H). A greater change in chondrocyte height was observed from the uncompressed state to 10 % applied strain compared to between 10 % and 15 % strain in all cartilage Disks (Figure 67E-H).

Figure 66A-D shows the mean volume values for chondrocytes in each of the four cartilage disks decreased with applied compressive tissue strain. Volume reduction was statistically significant in all cartilage disks and at all applied strain levels, except between 10 % and 15 % applied tissue strains in Cartilage Disk 1 ( $p < 0.05$ , Figure 66A-D). Mean values of chondrocyte volume in Cartilage Disk 1-4 significantly decreased from  $490 \pm 108 \mu\text{m}^3$ ,  $486 \pm 134 \mu\text{m}^3$ ,  $579 \pm 102 \mu\text{m}^3$ ,  $599 \pm 256 \mu\text{m}^3$  at the uncompressed tissue state to  $413 \pm 98 \mu\text{m}^3$ ,  $374 \pm 98 \mu\text{m}^3$ ,  $556$

$\pm 86 \mu\text{m}^3$ ,  $446 \pm 168 \mu\text{m}^3$  at 10 % applied tissue strain and  $429 \pm 114 \mu\text{m}^3$ ,  $345 \pm 77 \mu\text{m}^3$ ,  $517 \pm 75 \mu\text{m}^3$ ,  $386 \pm 150 \mu\text{m}^3$  at 15 % applied tissue strain, respectively ( $p < 0.05$ ).

The corresponding percentage change in mean volume for chondrocytes in each of the four cartilage disks are shown in Figure 68A-D. In Cartilage Disk 1, the volume of chondrocytes significantly decreased from baseline (zero strain) by 15.8 % and 13.4 % at 10 % and 15 % tissue strains, respectively ( $p < 0.0001$  and  $p < 0.01$ , Figure 68A). The significant percentage drop in chondrocyte volume compared to baseline (zero strain) in Cartilage Disk 2 was by 22.5 % at 10 applied tissue strain and 27.6 % at 15 % applied tissue strain ( $p < 0.0001$ , Figure 68B). The percentage change in chondrocyte volume from baseline (zero strain) in Cartilage Disk 3 was decreased by 3.6 % and 10.2 % at 10 % and 15 % tissue strains, respectively ( $p < 0.01$  and  $p < 0.0001$ , Figure 68C). In Cartilage Disk 4, the volume of chondrocytes significantly decreased from baseline (zero strain) by 17.9 % and 29.9 % at 10 % and 15 % tissue strains, respectively ( $p < 0.05$  and  $p < 0.001$ , Figure 68D). Changes in chondrocyte volume appeared to vary across four cartilage disks (Figure 68A-D). At 15 % applied tissue strain, percentage change in chondrocyte volume compared to baseline (zero strain) was dropped by an average of 13.4 %, 27.6 %, 10.2 % and 29.9 % in Cartilage Disk 1, 2, 3 and 4, respectively ( $p < 0.01$ , Figure 68A-D).

Mean values of sphericity remained consistent with no significant different following the application of 10 % and 15 % tissue strains, except in Cartilage disk 1 and 2 ( $p < 0.05$ , Figure 66E-H). In Cartilage disk 1, there was a significant increase in chondrocyte sphericity, from a mean value of  $0.80 \pm 0.03$  at the uncompressed tissue state to  $0.83 \pm 0.02$  ( $p < 0.05$ ) at 15 % applied tissue strain ( $p < 0.05$ , Figure 66E) which corresponds to a percentage increase of 3.6 % ( $p < 0.05$ , Figure 68E). A significant increase in sphericity was observed in Cartilage Disk 2, increasing from an average of  $0.77 \pm 0.04$  at the uncompressed tissue state to  $0.81 \pm 0.03$  and  $0.83 \pm 0.02$  at 10 % and 15 % applied tissue strains ( $p < 0.05$  and  $p < 0.01$ , Figure 66F) which correspond to a percentage increase of 6.5 % and 8.5 %, respectively ( $p < 0.05$  and  $p < 0.01$ , Figure 68F).



**Figure 65:** Mean values  $\pm$  SD of morphometric measurements for all chondrocytes (n=37) in the superficial zone of each of the four bovine cartilage disks (1-4 = left to right columns) at the selected compressive tissue strain levels of 0 %, 10 % and 15 %; (A, B, C, D) chondrocyte width and length and (E, F, G, H) height. Mean values of chondrocyte width decreased with applied tissue strain, with the decrease being statistically significant in Cartilage Disk 1, 3 and 4. Mean values of chondrocyte length decreased with applied tissue strain and a significant difference was seen in Cartilage Disk 1, 2 and 4. Significant decrease in mean values of chondrocyte height was observed in all cartilage disks at each tissue strain level.

Statistical differences were performed using one way repeated ANOVA with compressive strain as the between subject factor after data normality was determined. Turkey's post doc test was used for comparison between chondrocytes in the uncompressed state and during 10 and 15 % compression. The \* marking indicates significant differences in length and height measurements and the + marking determines statistically significant in width measurements. \* and +  $\equiv$  p < 0.05, \*\* and ++  $\equiv$  p < 0.01, \*\*\* and +++  $\equiv$  p < 0.001, \*\*\*\* and ++++  $\equiv$  p < 0.0001.

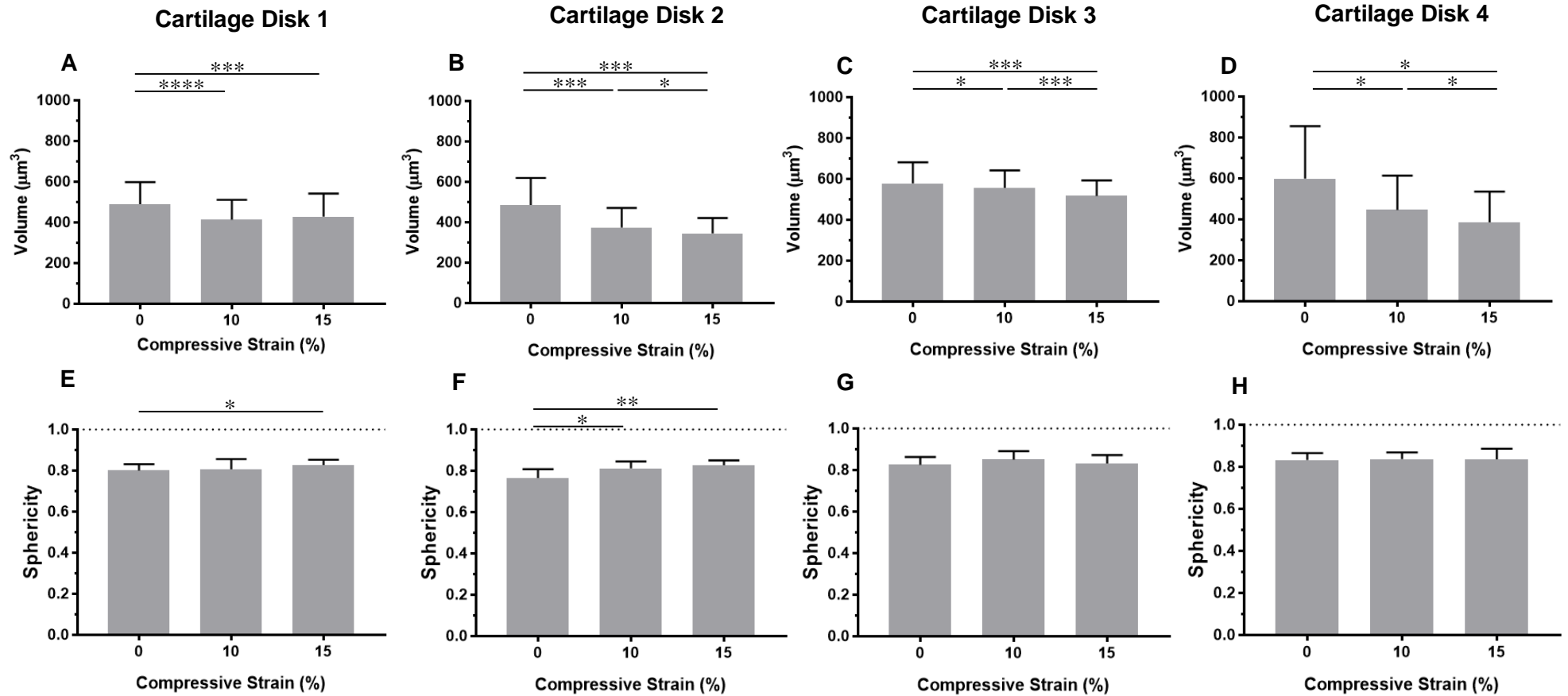


**Figure 66:** Mean values  $\pm$  SD of morphometric measurements for all chondrocytes ( $n=37$ ) in the superficial zone of each of the four bovine cartilage disks (1-4 = left to right columns) at the selected compressive tissue strain levels of 0 %, 10 % and 15 %; (A, B, C, D) chondrocyte volume and (E, F, G, H) sphericity. Dotted line in (E, F, G, H) indicates the cell shape for a perfect sphere. Significant decrease in mean values of chondrocyte volume was observed with application of 10 % and 15 % compressive tissue strains except between 10 % and 15 % strains in Cartilage Disk 1. Mean values of chondrocyte sphericity remained largely consistent irrespective of applied tissue strain, apart from a significant increase in Cartilage Disk 1 at 15 % applied tissue strain and in Cartilage Disk 2 at each tissue strain level.

Statistical analysis was performed using one way repeated ANOVA with compressive strain as the between subject factor after data normality was determined. Turkey's post doc test was used for comparison between chondrocytes in the uncompressed state and during 10 and 15 % compression. \*  $\equiv$   $p < 0.05$ , \*\*  $\equiv$   $p < 0.01$ , \*\*\*  $\equiv$   $p < 0.001$ , \*\*\*\*  $\equiv$   $p < 0.0001$ .

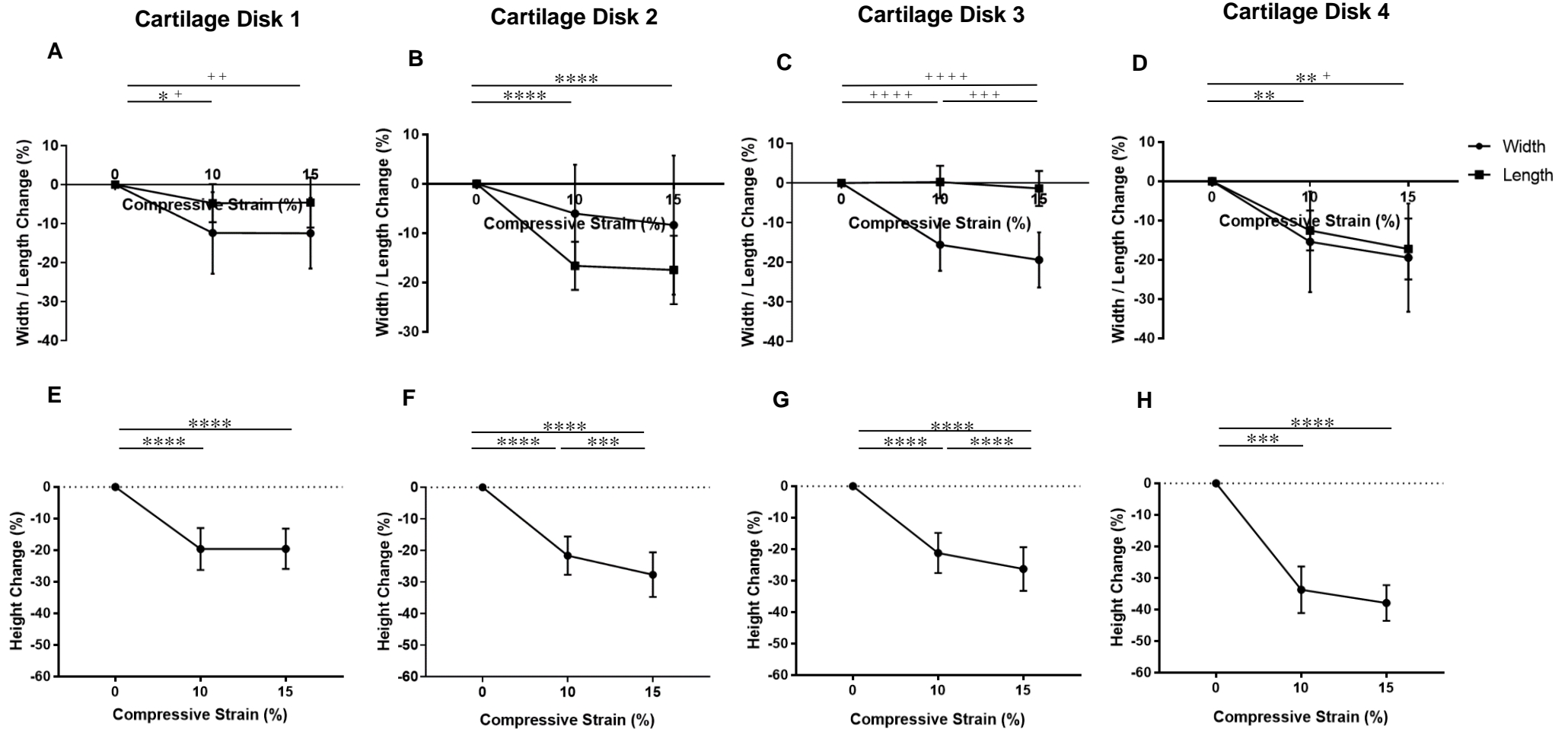


**Figure 67: Percentage (%) change in morphometric measurements from baseline (zero strain) for all chondrocytes (n=37) in the superficial zone of each of the four bovine cartilage disks (1-4 = left to right columns) following application of 10 % and 15 % compressive tissue strains; (A, B, C, D) chondrocyte width and length and (E, F, G, H) height. Percentage change in chondrocyte width decreased with applied tissue strain, with the decrease being statistically significant in Cartilage Disk 1, 3 and 4. Percentage change in chondrocyte length decreased with applied tissue strain and this was significant in Cartilage Disk 1, 2 and 4. Percentage change in chondrocyte height also significantly decreased at each tissue strain level.**

Statistical analysis was performed using one way repeated ANOVA with compressive strain as the between subject factor after data normality was determined. Turkey's post doc test was used for comparison between chondrocytes at the uncompressed state, during 10 and 15 % compression. The \* marking indicates significant difference in length and height measurements and the + marking determines statistically significant in width measurements. \* and +  $\equiv$   $p < 0.05$ , \*\* and ++  $\equiv$   $p < 0.01$ , \*\*\* and +++  $\equiv$   $p < 0.001$ , \*\*\*\* and ++++  $\equiv$   $p < 0.0001$ .

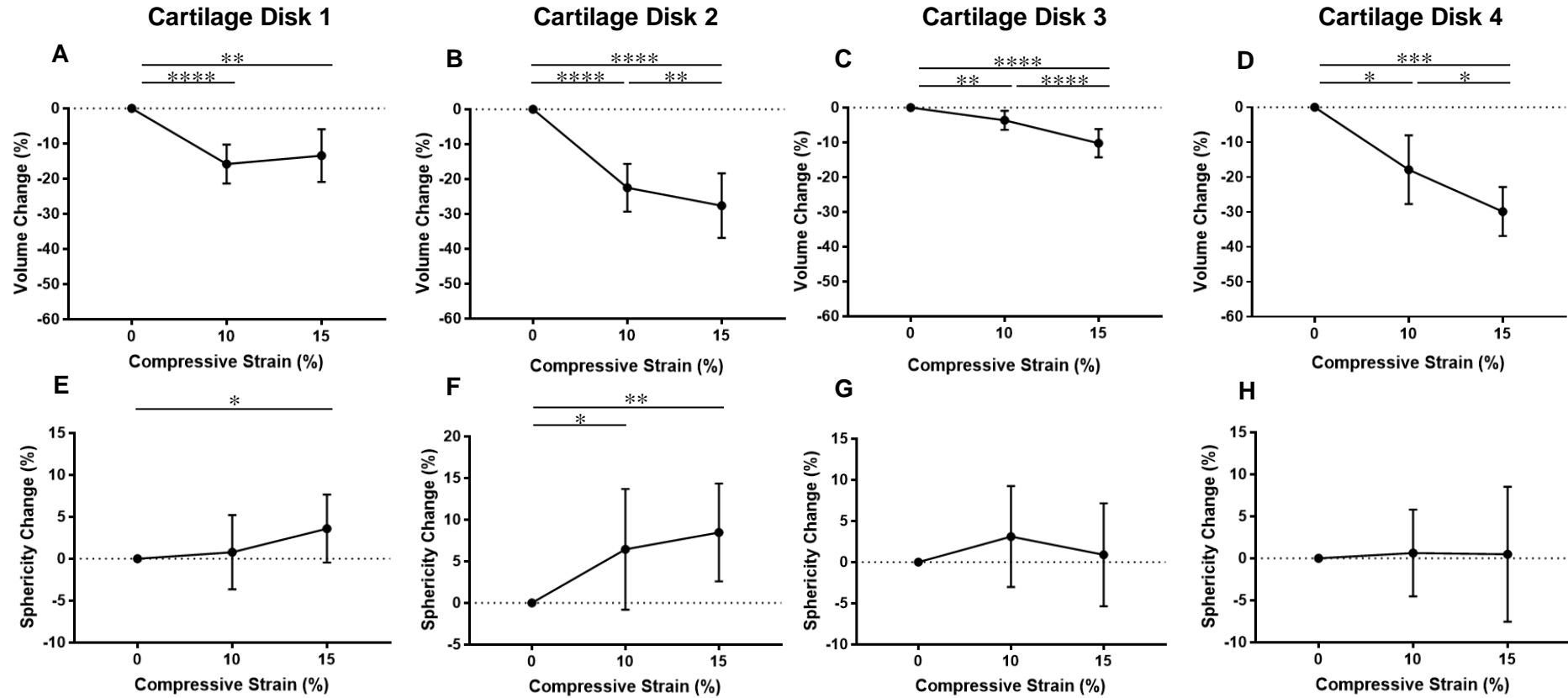


**Figure 68: Percentage (%) change in morphometric measurements from baseline (zero strain) for all chondrocytes (n=37) in the superficial zone of each of the four bovine cartilage disks (1-4 = left to right columns) following application of 10 % and 15 % compressive tissue strains; (A, B, C, D) chondrocyte volume and (E, F, G, H) sphericity. Percentage change in chondrocyte volume significantly decreased with applied tissue strain. Significant increase in percentage change in chondrocyte sphericity was only observed in Cartilage Disk 1 at 15 % applied tissue strain and in Cartilage Disk 2 at each tissue strain level.**

Statistical differences were performed using one way repeated ANOVA with compressive strain as the between subject factor after data normality was determined. Turkey's post doc test was used for comparison between chondrocytes at the uncompressed state, during 10 and 15 % compression. \*  $\equiv p < 0.05$ , \*\*  $\equiv p < 0.01$ , \*\*\*  $\equiv p < 0.001$ , \*\*\*\*  $\equiv p < 0.0001$ .

#### **4.4.3.3 Morphometric Measurements Presented as Mean values $\pm$ SD and Percentage (%) Change Compared to Baseline (Zero Strain) for All Chondrocytes Combined in Each Cartilage Disk Following Application of Compressive Strains**

Changes in chondrocyte length, width, height, volume and sphericity for all chondrocytes (n=37) in the superficial zone combined from all bovine cartilage disks (n=4) following application of 10 % and 15 % compressive tissue strains are shown as mean values  $\pm$  SD and % change compared to baseline (zero strain) in Figure 69 and Figure 70.

The mean value of length for all chondrocytes (n=37) combined in each cartilage disk significantly reduced at each strain level (10 % and 15 %), from an average of  $13.3 \pm 1.1 \mu\text{m}$  at the uncompressed tissue state to a mean of  $12.3 \pm 1.5 \mu\text{m}$  and  $12.1 \pm 1.6 \mu\text{m}$  at 10 % and 15 % applied tissue strains, respectively ( $p < 0.0001$ , Figure 69A). The corresponding significant percentage drop in length compared to baseline (the uncompressed tissue state) were 7.7 % and 9.1 % at 10 and 15 % tissue strains, respectively ( $p < 0.001$  and  $p < 0.0001$ , Figure 69D). The mean width value for all chondrocytes combined from all cartilage disks significantly decreased from a mean of  $9.1 \pm 1.1 \mu\text{m}$  at the uncompressed state to an average of  $7.9 \pm 0.9 \mu\text{m}$  and  $7.7 \pm 0.8 \mu\text{m}$  at 10 % and 15 % applied tissue strains, respectively ( $p < 0.0001$ , Figure 69B). The width of chondrocytes significantly decreased compared to baseline (zero strain) by 12.1 % and 14.6 % at 10 % and 15 % applied tissue strains, respectively ( $p < 0.0001$ , Figure 69E).

The overall mean value of height for 37 chondrocytes from all cartilage disks significantly reduced at each strain level (10 % and 15 %), from an average of  $9.9 \pm 1.7 \mu\text{m}$  at the uncompressed tissue state to a mean of  $7.6 \pm 1.1 \mu\text{m}$  and  $7.2 \pm 1 \mu\text{m}$  at 10 % and 15 % applied tissue strains, respectively ( $p < 0.0001$ , Figure 69C). The corresponding percentage decrease in height compared to baseline (zero strain) was 23 % and 26.7 % at 10 and 15 % tissue strains, respectively ( $p < 0.0001$ , Figure 69F) which were greater than the applied tissue strains.

Figure 70A and Figure 70C shows the mean volume value and percentage change in volume compared to baseline (zero strain) for 37 chondrocytes combined from four cartilage disks decreased with applied compressive tissue strain. The overall mean value of volume significantly reduced from a mean of  $533 \pm 148 \mu\text{m}^3$  at the uncompressed tissue state to an average of  $450 \pm 127 \mu\text{m}^3$  and  $425 \pm 119 \mu\text{m}^3$  at 10 % and 15 % applied tissue strains, respectively ( $p < 0.0001$ , Figure 70A). The mean volume of chondrocytes was decreased by 14.3 % at 10 % applied tissue strain and 19 % at 15 % applied tissue strain which were greater than the applied tissue strains and the reduction was statistically significant at both applied cartilage strains ( $p < 0.0001$ , Figure 70C).

The overall mean value of sphericity for all chondrocytes combined in each cartilage disk significantly increased from an average of  $0.80 \pm 0.04$  at the uncompressed state to a mean of

$0.82 \pm 0.04$  and  $0.83 \pm 0.03$  at 10 % and 15 % applied strain ( $p < 0.05$  and  $p < 0.01$ , Figure 70B) which correspond to a percentage increase of 3 % and 3.6 %, respectively ( $p < 0.05$  and  $p < 0.01$ , Figure 70D).

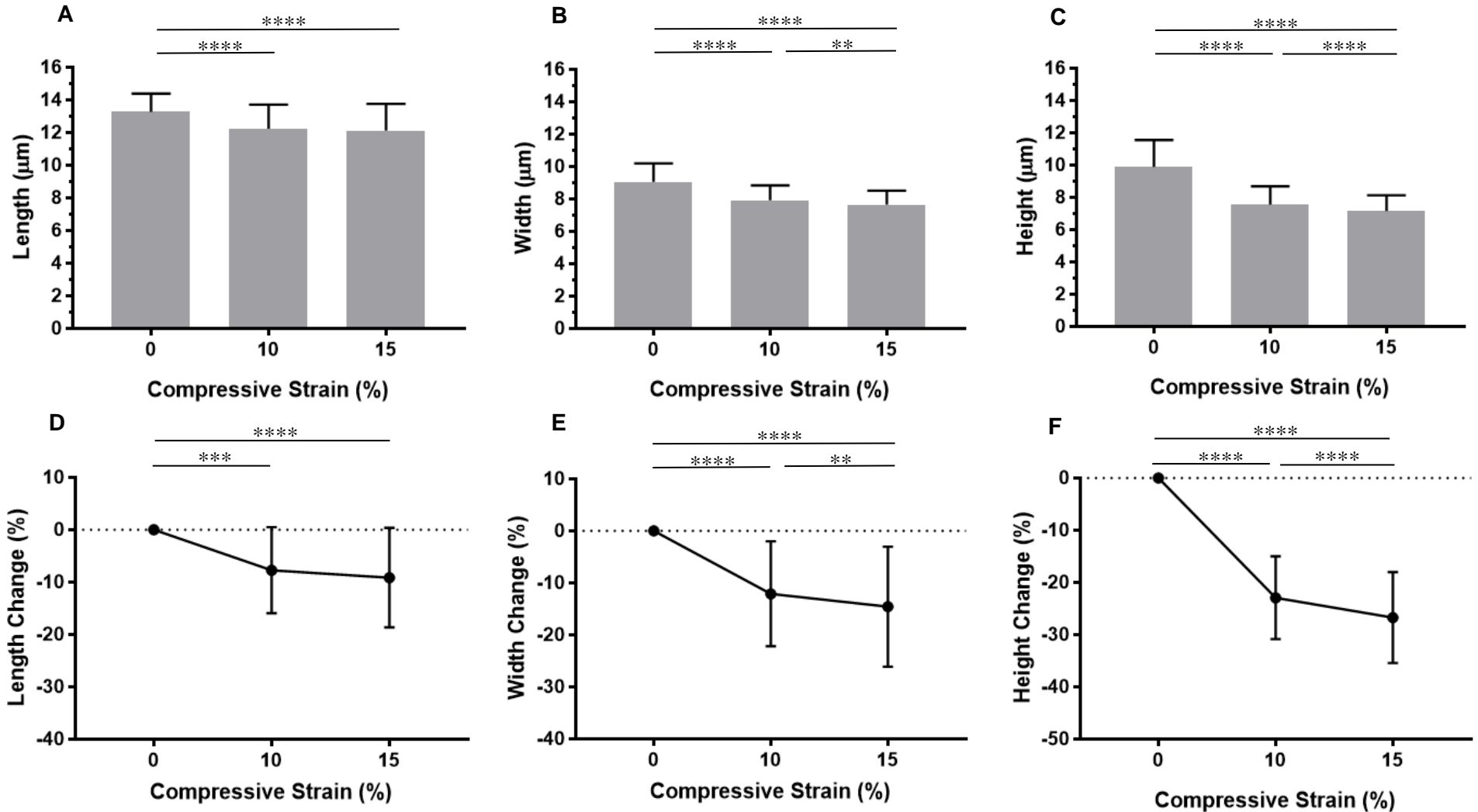


**Figure 69: Morphometric measurements for all chondrocytes (n=37) in the superficial zone combined from all bovine cartilage disks (n=4) following application of 10 % and 15 % compressive tissue strains; (A, D) chondrocyte length, (B, E) width and (C, F) height. The data is presented in (A, B, C) mean values and (D, E, F) percentage change from baseline (zero strain). The chondrocytes combined in each cartilage disk showed chondrocyte length, width and height significantly decreased at each tissue strain level.**

Statistical differences were performed using one way repeated ANOVA with compressive strain as the between subject factor after data normality was determined. Turkey's post doc test was used for comparison between chondrocytes at the uncompressed state, during 10 and 15 % compression. \* ≡ p < 0.05, \*\* ≡ p < 0.01, \*\*\* ≡ p < 0.001, \*\*\*\* ≡ p < 0.0001.

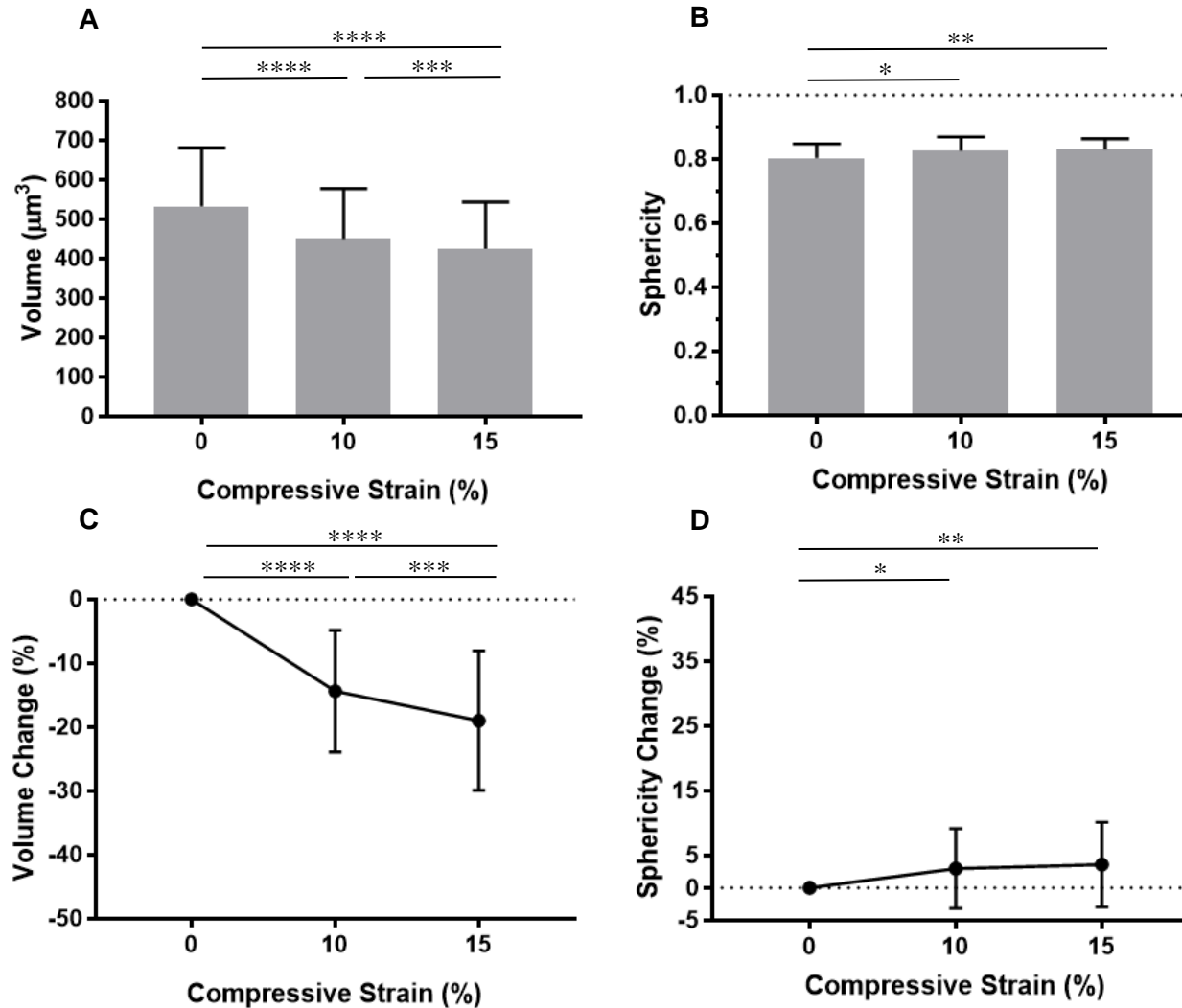


**Figure 70: Morphometric measurements for all chondrocytes (n=37) in the superficial zone combined from all bovine cartilage disks (n=4) following application of 10 % and 15 % compressive tissue strains; (A, C) chondrocyte volume and (B, D) sphericity. The data is presented in (A, B) mean values and (C, D) percentage change from baseline (zero strain). Dotted line in (B) indicates the cell shape as a perfect sphere. The chondrocytes combined in each cartilage disk showed chondrocyte volume significantly decreased and sphericity significantly increased at each tissue strain level.**

Statistical differences were performed using one way repeated ANOVA with compressive strain as the between subject factor after data normality was determined. Turkey's post doc test was used for comparison between chondrocytes at the uncompressed state, during 10 and 15 % compression. \*  $\equiv p < 0.05$ , \*\*  $\equiv p < 0.01$ , \*\*\*  $\equiv p < 0.001$ , \*\*\*\*  $\equiv p < 0.0001$ .

## **4.5 Discussion**

The aim of this study was to use a novel compression device and a dual live cell staining method of Hoechst 33342 and CellMask Green plasma membrane stains (as described in Chapter 2 and Chapter 3, respectively) specifically developed to allow observation of chondrocytes in real time under confocal microscopy to determine the chondrocyte deformation behaviour in the superficial zone of bovine cartilage disks under zero, 10 % and 15 % applied tissue compressive strains in order to address the relationship between applied tissue deformation and cellular strain. Native bovine cartilage disks were used in this study as a readily available cartilage source prior to moving on to determining the effect(s) of incremental applied compressive tissue strain on cell deformation behaviour in engineered constructs (Chapter 5). Prior to the experiment, the effect of culture duration on chondrocyte metabolism and viability were accessed by XTT reduction assay and Live/Dead<sup>®</sup> staining. Due to cartilage disks not being imaged immediately after harvest and being cultured for up to 3 days, it was necessary to assess whether the chondrocytes were viable before live cell imaging and if the length of culture duration would affect chondrocyte metabolism and viability within cartilage disks. In addition, it was also necessary to determine the potential errors introduced in the morphometric measurements by photobleaching of the CellMask Green plasma membrane stain prior to the experiment because photobleaching effects could affect the accuracy of acquired quantitative data from images. Thus, due to requiring to image the a sample three times at the strains stated above, three sequential images of selected chondrocytes from the superficial zone of cartilage disks were acquired under non-loaded condition and cell volume measurements were performed on the selected chondrocytes in all repeated images captured in each cartilage disk to determine any dimensional changes in the morphometric measurements introduced by photobleaching.

### **4.5.1 The Effect of Culture Duration on Chondrocyte Metabolism and Viability within Native Cartilage**

For practical reasons, all native bovine cartilage disks not tested immediately after harvest were cultured in DMEM/F12 medium at 37°C for up to 3 days until the time of live cell imaging. Prior to experimentation, it was necessary to check cell viability within the cartilage disks in culture under growth medium following harvest and monitor whether culture duration would affect cell metabolism and viability, because this could have a direct influence on cell behaviour and consequent cell measurements in both loaded and non-loaded conditions.

Cell viability is normally defined by the integrity of cell membrane and/or the cell's metabolic activity [269]. In the current study, the effects of culture duration on cell viability within native cartilage was analysed by XTT reduction assay and Live/Dead<sup>®</sup> staining [267], [268]. It was found that consistent values for XTT conversion were recorded and no significant differences

were detected between cartilage disks cultured for different time durations, from day 0 to day 3 (Figure 59). This would indicate that similar levels of cell metabolic activity were detected in all cartilage disks, suggesting tissues could be maintained in culture for (at least) up to 3 days without a significant effect on cell viability. XTT conversion is dependent on the number of viable cells and the reading is based on an average conversation or output from the entire cell population. The metabolic activity observed here might be similar after three days but variations in cell metabolic rate and cell number in cartilage disks could affect results for this study. There could be instances where higher number of chondrocytes metabolising slowly in some cartilage disks and lower number of chondrocytes metabolising quickly in other cartilage disks which potentially results in similar XTT values. Due to natural variations in the rate of cellular metabolism and cell number within cartilage disks, it was necessary to perform XTT assay along with Live/Dead<sup>®</sup> imaging to complement the observations and help support the XTT data. Thus, cell viability of cultured bovine cartilage disks was also evaluated using Live/Dead<sup>®</sup> staining on cartilage slices obtained from the disks. This revealed that at day 0 (freshly harvested cartilage), the majority of chondrocytes were alive throughout the depth of the cartilage tissue (Figure 60 and Figure 61) and there was a layer of dead or dying chondrocytes present on the cut surface (Figure 61). After 1, 2 and 3 days in culture, there were no noticeable changes in the Live/Dead<sup>®</sup> staining pattern of the cartilage, suggesting the chondrocytes within the cartilage were still viable in culture for up to 3 days. This was in agreement with the XTT data and consequently supports the idea that chondrocyte viability could be maintained in cartilage for up to 3 days. The dead chondrocyte layer located at the cut surface could be the result of the cutting process in preparing the tissue slices, which would have led to some peripheral cell death. It is known that mechanical damage to cartilage can cause cell death [269], [272]. Procedures such as harvesting osteochondral plugs by coring, cutting the bone ends to harvest cartilage disks (described in Section 4.2.1) and cutting cartilage disks to produce cartilage slices (described in Section 4.3.2) would have resulted to inevitable damage to the cells and the ECM at the cut periphery. In addition, there was a suggestion that there were relatively greater numbers of red stained (dead) chondrocytes in the 3 day cultured cartilage (Figure 61H), perhaps cell viability started to decrease but this was a qualitative observation only and was not supported by the quantitative data.

The results here suggest that incubation of bovine cartilage disks in DMEM medium maintains chondrocyte viability and metabolism for up to 3 days after harvesting. In earlier studies, tissue and cell viability have been investigated in cartilage explants for long-term culture [269], [273]–[275]. However, it is difficult to compare the observation in the present study with previous studies because of the differences between source of cartilage, methods of harvesting, size of explants, medium and culture times used. In an attempt to evaluate the approach of non-invasive monitoring of tissue viability in long-term *ex vivo* organ culture model of osteochondral tissue, healthy, induced cell apoptosis and induced cell necrosis porcine femoral osteochondral plugs

were cultured in DMEM medium for 20 days and molecular markers, such as glucose, lactate dehydrogenase (LDH), alkaline phosphatase (AP), glycosaminoglycans (GAGs), and matrix metalloproteinase (MMP-2 and MMP-9), in the organ culture conditioned medium were used to indicate changes in tissue viability along with the commonly used methods (XTT assay and Live/Dead imaging) [269]. It was found that chondrocytes within healthy osteochondral tissue did not lose membrane integrity and tissue viability was sustained in culture for up to 20 days. In a study by Bain *et al.* (2008) [273], the use of serum-free chondrogenic medium to preserve allografts of articular cartilage and maintain the native mechanical and biochemical properties in long-term culture was investigated. Juvenile bovine cartilage explants (both chondral and osteochondral) extracted from the femoral condyles remained stable following culture in serum-free chondrogenic medium for up to 6 weeks, with no changes in the mechanical properties, biochemical content and cell viability. In another study, osteochondral plugs extracted from the bovine metacarpalphalangeal joints was used to investigate the metabolic dynamics of cartilage explants following harvest and culture *in vitro* over a long-term period [275]. Biochemical properties (i.e. cell viability, cell number, proteoglycan (PG) content and collagen content) of the harvested osteochondral plugs were maintained over a cultured period of up to 17 days, with the biochemical changes remained the most stable between Day 2 and Day 10 of the culture period. Although it is difficult in comparing and contrasting data obtained using different experimental parameters, the results in the present study and earlier findings suggest cell viability in harvested cartilage disks could be sustained *in vitro* for a period of 3 days under culture and therefore cartilage disks cultured up to a maximum 3 days were used in this study.

#### **4.5.2 Volume Changes of Chondrocytes in Uncompressed Native Cartilage Following Repeated Confocal Scans**

Having established that harvested cartilage disks remained viable *in vitro* for up to 3 days, it was then necessary to determine any dimensional changes in the morphometric measurements introduced by photobleaching of the stains prior to the cell deformation experiment in cartilage disks.

In Chapter 3, the ability of Hoechst 33342 and CellMask Green plasma membrane stains to retain fluorescent signals in native cartilage disks during and after tracking selected chondrocytes on multiple confocal scans was investigated. Few photobleaching effects were detected following the capture of three sequential volume images of chondrocytes in uncompressed native cartilage. Photobleaching would result in loss of fluorescent signal and consequent detail for cell morphology, and therefore could potentially affect the accuracy in obtaining quantitative data on cell deformation from collected images. In this chapter, quantitative analysis (i.e. chondrocyte volume measurement) was conducted on repeated confocal volume images of chondrocytes in uncompressed bovine cartilage disks.

Changes in chondrocyte volume in uncompressed bovine cartilage disks were noted after the capture of three repeated confocal images (Figure 62). There was a significant decrease in normalised chondrocyte volume for the same chondrocytes between the images, reducing by 2.1 % and 4.5 % between Image 1 and Image 2, and Image 1 and Image 3, respectively ( $p < 0.0001$  and  $p < 0.001$ , Figure 62). This indicated that photobleaching had potentially affected the morphometric measurements as hypothesised. Although the drop in measured chondrocyte volume was statistically significant, the overall morphology of the chondrocyte was relatively stable over the capture of three repeated images with only minor errors introduced by the staining method.

Photobleaching of fluorescent stains is a commonly known problem when conducting morphometric measurements over repeated scans. Several previous studies investigated the effect of compressive strain on chondrocyte deformation in native cartilage have taken into account of the potential error that photobleaching might introduce to morphometric measurements over repeated scans. Prior to a study that quantified the 3D changes in chondrocyte morphology in cartilage explants by Guilak *et al.* (1995) [87], changes in chondrocyte volume with repeated confocal scans were determined in uncompressed cartilage in order to assess whether photobleaching of the fluorescent stain introduced error into the morphometric measurements. No significant changes in volume were observed over five repeated scans during an hour period, which indicated that the morphology of chondrocytes was relatively stable over the duration of the experiment and that photobleaching had minimal effect on the morphometric measurements. An *in situ* intact rabbit cartilage study on superficial zone chondrocyte deformation under compressive tissue strains (0-80 %) by Madden *et al.* (2013) [85] carried out a separate experiment similar to that conducted by Guilak to examine the photobleaching effects on morphometric measurements. It was found that a small amount of chondrocyte volume was lost that might be attributed to photobleaching even though this effect was not statistically significant. However, Madden believed that it may have contributed to the final quantitative measurements. Nevertheless, it is important to take into account of the potential error that photobleaching might introduce to measurements. Thus, the measurement errors associated with the staining method in this thesis was taken into account for morphometric measurements as a limitation of the staining method.

#### **4.5.3 The Effect of Incremental Compressive Tissue Strains on Chondrocyte Deformation in Native Cartilage**

The deformation behaviour of chondrocytes has been investigated extensively in cartilage explants under static compression [21], [51], [87], [133]–[138], [210]. However, to the author's best knowledge, no study has managed to track the same population of live chondrocytes and determine the 3D morphological changes in non-fixed and non-cut cartilage disks during different compressive strain levels. Thus, the aim of this study was to determine the

chondrocyte deformation behaviour within the superficial zone of non-fixed bovine cartilage disks during different compressive tissue strain levels in equilibrium conditions and compare this to previous studies in the literature in order to verify the method prior to cell deformation experiments in tissue engineered constructs. Changes in chondrocyte 3D morphology were examined in response to incremental compression of bovine cartilage disks by tracking and making morphometric measurements of the same population of chondrocytes at 0 %, 10 % and 15% applied compressive tissue strains. Incremental static compressive tissue strain values of 10 % and 15 % were used in this study to conform within the physiological range of native cartilage strains *in vivo* of between 0 % and 30 % [130], [210], [264]. In addition, these strain levels have been used in other studies in the literature and this would allow for more meaningful comparison of results [85], [87], [137], [144]. Only cells that had clear cell boundaries were analysed for cell deformation quantification.

Cartilage disks stained Hoechst 33342 and CellMask Green plasma membrane stains (described in Section 4.3.3) were placed in to the newly developed device (see Chapter 3) and viewed under confocal microscopy at the selected levels. After an equilibration period of 30 mins in each case, confocal volume images of the same chondrocytes in the superficial zone of cartilage disks was acquired sequentially and Amira software used to quantitate chondrocyte morphometric parameters including: cell length, width, height, volume and sphericity (see Section 4.3.6.2 for full methodology). Cell morphometric data was collected for 6 to 11 chondrocytes per cartilage disk and from four cartilage disks from the patellofemoral groove of two bovine knee joints. A total of the same 37 cells from four cartilage disks under the selected strain levels were analysed for chondrocyte deformation quantification. These measurements will serve as a baseline for more physiologically-relevant dynamic studies in the future beyond this thesis.

In the present study, the morphology of the superficial zone chondrocytes in the uncompressed state within bovine cartilage disks were similar with the findings in previously reported studies on different articular cartilage sources (discussed later within this section). The major finding of this study showed that chondrocytes underwent significant changes in morphology, size and volume following application of compressive tissue strains. The most prominent effects on morphology were changes in cell height and volume while changes in lateral dimensions (cell length and width) and sphericity were much smaller. The chondrocyte deformation response observed in this study is likely influenced significantly by the structure and composition of the ECM and pericellular matrix (PCM) surrounding the chondrocyte and the chondrocyte itself. Under compressive loading, chondrocytes perceive alterations in their local mechanical environment through direct stress transmission from the ECM to the chondrocytes causing them to restructure their cytoskeleton and deform accordingly [87], [95].

Application of compressive tissue strains resulted in changes in chondrocyte height and volume. A significant decrease in cell height was observed in chondrocytes in all cartilage disks ( $p < 0.01$ , Figure 65E-H). The overall chondrocyte height reduced from an average of  $9.9 \pm 1.7 \mu\text{m}$  in the uncompressed tissue state to a mean of  $7.2 \pm 1 \mu\text{m}$  at 15 % applied tissue strain (Figure 69C). The magnitude of overall reduction in chondrocyte height were 23 % and 26.7 % under 10 % and 15 % compressive tissue strains (Figure 69F). Reduction in chondrocyte height was perhaps to be expected as the measurements were recorded in the same (z axis) direction as the applied compressive strain. The chondrocyte height change under compression of cartilage can be used as an indication of axial cellular compressive strain. Compression of native cartilage also resulted in a significant reduction in chondrocyte volume ( $p < 0.0001$ , Figure 70A and Figure 70C). The overall volume of chondrocytes was decreased from an average of  $533 \pm 148 \mu\text{m}^3$  in the non-loaded tissue state to a mean of  $425 \pm 119 \mu\text{m}^3$  at 15 % strain (Figure 70A). Volume was reduced by 14.3 % and 19 % at 10 % and 15 % applied tissue strains, respectively (Figure 69C) and were statistically significant at both applied strains.

A greater change in height was observed from the uncompressed state when 10 % compressive strain was applied compared to the difference in height associated with an increase from 10 % and 15 % strain in all cartilage disks (Figure 69C and Figure 69F). This suggests greater cell deformation occurs when greater tissue strain is applied. Compression of cartilage would be expected to generate internal stresses that are withstood by the ECM, resulting in deformation and a substantial amount of mechanical stress would be presumably transmitted to the PCM and chondrocytes [276]. It therefore seems reasonable to hypothesise that a greater degree of applied tissue strain would result in larger cellular strain.

The changes in chondrocyte height and volume were greater than the applied tissue strains, indicating a significant change in chondrocyte morphology in the superficial layer of compressed native cartilage. This illustrates the low compressive modulus of superficial layer relative to the other zones, resulting in greater matrix deformation and consequently larger changes in height and volume under compressive tissue strains; i.e. overall cartilage deformation is not uniform throughout its cross-section with the superficial zone deforming more than the average overall deformation. The significant reduction in chondrocyte volume also demonstrated chondrocyte has the ability to regulate their cytoplasmic volume in response to changes in osmotic and mechanical environment surrounding it. Differences in ECM biochemical composition and ultrastructure between the zones directly influences the mechanical properties throughout the tissue depth (as described in Section 1.4) [146], [148] and therefore explains why the superficial zone would deform more and consequently backing up the significant reduction in chondrocyte height and volume observed in this study.

The superficial zone of articular cartilage has several unique structural features which contribute to its low compressive modulus relative to the middle and deep zone (as described in Section

1.2) [51]. The collagen fibres are oriented parallel to the articular surface compared to a perpendicular orientation in the deep zone [51]. The proteoglycan concentration is lower in the superficial zone than the deep zone [51]. In addition, the superficial ECM is characterised by higher permeability than the other zones [51]. Due to the unique superficial structural features, lateral fluid exudation would occur more easily under cartilage compression in the surface compared with the other zones [51]. Thus, the ECM in the superficial layer is typically the most compliant and bears a large proportion of the deformation for physiologically relevant tissue strains (10 % - 30 % strain), resulting in greater matrix deformation (higher local ECM strain causes greater cell fluid exudation) and consequently a larger reduction in chondrocyte height and volume as observed in this study [51], [85].

The findings in this study correspond with the previous measurements of the zonal variation in chondrocyte shape recorded in cartilage explants [87], [137] under unconfined static compressions which showed reduction in chondrocyte height and volume with increasing compressive tissue strains. The findings in a study by Choi *et al.* (2007) [137] demonstrated that cell compressive strains were 27 %, 21 % and 2.2 % in the superficial, middle and deep zones, respectively, when a porcine cartilage explant was subjected to 10 % applied strain. In Guilak's study, chondrocyte height was shown to reduce by 25.6 %, 18.8 % and 20.7 % and volume were dropped by 21.8 %, 15.5 % and 17.5 % in the superficial, middle and deep zones of canine cartilage explants, respectively, under 15 % tissue strain [87]. These studies have provided evidence of the complex and inhomogeneous mechanical environment surrounding chondrocytes within native adult articular cartilage [87], [137]. The magnitude of the morphological changes in chondrocytes under compressive loading was reported to be highly dependent on the depth of the tissue, with highest deformation in the superficial zone and lowest in the deep zone. This was consistent with the significantly greater local ECM strain recorded in the superficial layer compared to the middle and the deep zones [87], [137]. Although cell morphology measurements were not recorded in the middle and deep zone in this current study, the large reduction in chondrocyte height and volume observed in this study is consistent with previous measurements under static compression in the superficial layer of cartilage explants, therefore it is in general agreement that greatest cell deformation occur in the superficial zone [87], [137].

The effects of compressive tissue strain on the lateral measurements (i.e. length and width) and sphericity were less prominent compared to the findings in height and volume of the chondrocytes. The changes in chondrocyte lateral dimensions within the cartilage disks are shown in Figure 65A-D and Figure 67A-D. The overall trend of the lateral changes of chondrocytes showed chondrocyte length and width to decrease (Figure 69). The absolute magnitude of change in sphericity was very small, with sphericity increasing from  $0.8 \pm 0.04$  at 0 % strain to  $0.82 \pm 0.04$  and  $0.83 \pm 0.03$  at 10 % and 15% applied tissue strain, respectively, and this does not reflect a drastic change in cell shape (Figure 70B). Taken together the

sphericity data for cell shape was relatively consistent between the uncompressed and compressed states. There was a significant increase in sphericity between 0 % and 10 % applied strains and between 0 % and 15 % applied strains which were 3 % and 3.6 %, respectively (Figure 70D). Given the photobleaching effect introduced measurement errors (2.1 % and 4.5 %) to the deformation data measured between confocal images captured at 0 %, 10 % and 15 % applied strain (discussed in Section 4.5.2), it may have contributed to the variance observed in sphericity. Taken together all the deformation metrics, it appeared that chondrocytes maintained a similar shape but only partially maintained their size (decrease in length, width, height and volume but maintain sphericity) in response to unconfined compressive static strains.

The observed overall changes in the morphology of superficial zone chondrocyte (decrease in length, width, height and volume but maintain sphericity) within bovine cartilage disks subjected to compressive tissue strains are believed to be attributed to the local matrix environment around the chondrocytes. The local matrix composition and structure play an important role in influencing the mechanical properties of the superficial zone of cartilage and consequently affects the micromechanical environment surrounding the chondrocytes. In particular, the interaction between the collagen network and the swelling (fluid) pressure (generated by negative charges from the PGs and the ionic constituents of the synovial fluid) within the ECM directly influence the stresses, strains and fluid flow in and around the chondrocytes and, therefore, would play a significant role in the mechanical response of chondrocytes under compressive loading [95], [148]. However, the deformation response of chondrocytes observed in this study cannot be solely explained by the ECM ultrastructure, composition and the mechanical properties of the superficial zone. Earlier studies showed that PCM modulates cell deformation and volume changes during cartilage compression [85], [95], [137], [146], [148]. The PCM is believed to play an important role in controlling the biomechanical environment in and around chondrocytes under mechanical and osmotic loading conditions by transmitting and transforming mechanical signals from the ECM to the chondrocytes [147], [148]. PCM is a narrow region rich in negatively charged PGs (including aggrecan, hyaluronan and decorin) and collagen fibres (mainly type IV collagen as well as types II and IX collagen) that completely surrounds the chondrocyte [87], [137], [143], [146].

Previous studies have demonstrated that the ECM and PCM surrounding chondrocytes affect the chondrocytes' ability to regulate their deformation response under mechanical and osmotic loading conditions [137], [146], [147]. With the collagen fibres oriented parallel to the articular surface and in combination with the swelling (fluid) pressure induced by interplay of mobile ions in the physiological interstitial fluid and the negatively fixed charge in the PGs inside the ECM and PCM in the superficial zone, internal stresses can exist in the uncompressed tissue and induce lateral strain to the chondrocytes [95], [147]. Under static compression of cartilage, the tension acting on the collagen fibrils in the ECM would increase [147]. As a consequence, this would generate a higher stress environment within the chondrocyte vicinity and, therefore,

apply higher lateral strains for the chondrocytes [147]. These conditions would transmit to the PCM and produce high tension for the pericellular fibrils, resulting in increased stiffness and consequently limit chondrocyte radial expansion [147]. Fluid pressure would also build up within the ECM, inside the chondrocytes as well as the PCM surrounding the chondrocytes during static compressive loading of cartilage [95], [147]. As a result of cartilage compression and as a consequence of an increase in radial strains on the chondrocytes and fluid pressure generated within the ECM, PCM and inside the chondrocytes, lateral fluid exudation of the tissue would occur in order to reduce the fluid pressure in the local ECM [95]. This would lead to the fluid inside the chondrocyte to escape, resulting in a decrease in chondrocyte axial diameter (height) and volume which highly likely complement with the observed findings in this study [95].

During the stress relaxation period (where tissue is kept under a constant strain condition for some finite interval of time), the ECM has been reported to recoil to almost its original dimensions and induced chondrocytes to recoil laterally in a similar manner under an equilibrium compressive state [95]. Likhitpanichkul *et al.* (2005) [95] found that the ECM expanded laterally as a result of tissue lateral fluid exudation during the application of unconfined compression and caused the chondrocyte to expand laterally while being axially compressed [95]. This resulted in a slight increase in ECM volume since the lateral expansion dominated the axial compression [95]. The ECM then recoiled to almost its original dimension gradually until it reached an equilibrium state, inducing the chondrocytes to recoil laterally in a similar manner [95]. As a result of the recoiling process of the tissue under static compression, chondrocytes would be exposed to high tension due to the radial diameter being compressed by the stiff collagen fibrils, in combination with the stiff ECM due to high fluid pressure and, thus, increased high lateral strain [95]. The chondrocyte lateral deformation was therefore speculated to be highly influenced by the magnitude of fluid pressure within the ECM (which is relative to the permeability of ECM) that acts on the chondrocytes [95]. In addition to the recoiling of chondrocytes, this would force more fluid inside the chondrocytes to exudate, resulting in further reduction in volume [95]. The amount of recoiling chondrocyte radial diameter would partly influence the magnitude in chondrocyte volume changes.

Theoretical models found that the chondrocyte deformational response was also further dictated by the mechanical properties of PCM and the chondrocyte itself [95], [147]. The models demonstrated that 'Stiff' PCM (with high fixed charge density induced by the PGs and stiffer pericellular fibrils) further decreased chondrocyte height and exerted greater lateral compression to the chondrocytes due to high swelling pressure which caused chondrocyte lateral strain to increase and recoiled the radial diameter beyond its original dimensions compared to 'less stiff' PCM with lower fixed charge density (lower swelling pressure) and collagen fibril stiffness [95], [147]. The stiffness of the chondrocyte itself also had an effect on the deformation behaviour [95]. Chondrocytes with lower Donnan osmotic pressure was found to modulate to

behave like a softer material and, therefore, the (lateral and axial) deformation was larger compared to those with higher Donnan osmotic pressure [95]. Thus, the effect on cell deformation of PCM and the mechanical properties of chondrocytes themselves should not be neglected and we can assume these effects might have partly contributed to the measurements of chondrocyte height, length and width in this study despite the unknown values of the local ECM and PCM strains.

The observed reduction in chondrocyte length and width in this study could therefore be attributed to the combination of the characteristic of tissue radial deformation and the mechanical properties of PCM and the chondrocyte itself. In addition, the reduction in axial diameter caused by the applied compressive strain combined with the recoiling of chondrocyte radial diameter (dictated by the permeability of the ECM, the stiffness of PCM and chondrocyte itself) may therefore help explain the significant reduction in chondrocyte volume observed in this study. The mechanical properties of ECM and PCM should be investigated along with the chondrocyte deformation response under compression in future studies.

There was slight variation in the deformation response of individual chondrocytes within each cartilage disk (Figure 63 and Figure 64), suggesting the mechanical environment around the chondrocytes differed slightly. The measurements of the cell deformation response were recorded on chondrocytes located within a volume of approximately  $2.023 \text{ cm}^3$  (3D confocal image size:  $318 \times 318 \times 20 \text{ }\mu\text{m}$ ) in each cartilage disk, it can therefore be assumed that there was no drastic variation in ECM composition and its mechanical properties within the sample area. The observed differences in chondrocyte deformation response could be related to the physical properties of PCM and the chondrocyte itself as discussed previously in this section. The stiffness of the pericellular matrix and the chondrocyte itself contributes to its ability to regulate shape and volume under mechanical and osmotic loading conditions [95], [147]. Therefore, slight differences in the PCM structure and composition and the stiffness of the chondrocyte may contribute to the differences in chondrocyte deformation observed within each cartilage disk in this study.

There was considerable variation in the deformation response of individual chondrocytes between cartilage disks that were harvested from areas within the same joint region (medial and lateral patellofemoral groove) (Figure 65-68), suggesting the mechanical environment of ECM differed even where cartilage disks were harvested from the same joint region and raising questions about the validity of assuming that chondrocytes within a given zone of articular cartilage experience the same mechanical loading. One possible reason for the observed differences in cell deformation behaviour between cartilage disks harvested from the patellofemoral groove could be attributed to the variation in the load, contact area and stresses acting on the patellofemoral groove during normal activities [277], [278] giving rise to site-specific variations in ECM properties and chemistry. The amount of applied joint stresses are

variable and depend on the degree of flexion and the amount of weight is put on the ground [277]. During articulation between the patellofemoral groove cartilage and the opposing patellar cartilage, the patella has movement in multiple planes with contact point (area) changes between the two joint surfaces throughout the range of motion and the loads transmitted change too, and hence to the different level of applied stresses arising as a result [277]. The stress placed on the joint surface is defined as the resultant compression force acting on the joint (which is dependent on the joint angle and muscle tension) divided by the patellofemoral joint contact area [277]. A high compression force combined with a small contact area would result in high joint stress acting on the cartilage surface [277]. In addition, the amount of joint stress acting on the cartilage surface depends on the type of activities [277], [278]. Studies have demonstrated human applied forces of 1.3 times body weight (BW) during level walking and 5.6 times BW during running [279]. Cartilage disks used in this study were harvested from (two) knees of two different cattle. The amount/type of activities would vary between the cattle and therefore would reflect the difference in the amount in which the patellofemoral joints were stressed. As a consequence of variable stress level acting on the patellofemoral groove cartilage throughout the range of motion and during different activities, matrix structural differences might have evolved and influence the mechanical properties of the local cartilage that consequently affect the mechanical environment surrounding the chondrocytes. The observed differences in cell deformation behaviour between cartilage disks might also arise from biological variabilities among cattle from different ages, cattle breeds and genders. Therefore it seems reasonable that the slight different deformation behaviour between cartilage disks harvested from the knees of two different cattle could be attributed to biological variation and variation in applied loads and stresses in different areas of the patellofemoral grooves.

#### **4.5.3.1 Morphometric Measurements Comparisons with Previous Chondrocyte Deformation Studies**

In the present study, the mean ( $\pm$  SD) length, width, height, volume and sphericity of the chondrocytes in the uncompressed state were  $13.3 \pm 1.1 \mu\text{m}$ ,  $9.1 \pm 1.1 \mu\text{m}$ ,  $9.9 \pm 1.7 \mu\text{m}$ ,  $533 \pm 148 \mu\text{m}^3$  and  $0.80 \pm 0.04$ , respectively. The uncompressed chondrocyte morphology recorded in this study was similar to the findings in previously reported studies on articular cartilage in the literature. In a study by Guilak *et al.* (1995) [87], the length, width, height and volume measurements conducted in the superficial area of articular cartilage explants were  $15 \pm 1.6 \mu\text{m}$ ,  $15 \pm 1.9 \mu\text{m}$ ,  $4.8 \pm 1.8 \mu\text{m}$  and  $876 \pm 422 \mu\text{m}^3$ , respectively. Another study conducted by Han *et al.* (2010) [145] determined length, width, height and volume to be  $11.3 \pm 0.3 \mu\text{m}$ ,  $8.6 \pm 0.2 \mu\text{m}$ ,  $5.1 \pm 0.1 \mu\text{m}$  and  $250 \pm 9 \mu\text{m}^3$  in intact native cartilage attached to its native bone respectively. A mean volume of approximately  $500 \mu\text{m}^3$  was recorded in a study conducted by Choi *et al.* (2007) [137]. The measurements obtained in the current study were the same in magnitude

compared to the studies reported in the literature but the absolute values different to other studies which were also differed from one another.

The deformation of chondrocytes observed in this study was compared to those previously reported in cartilage explant and intact cartilage under static unconfined 15 % compressive strain (Figure 71). Superficial zone chondrocyte deformation from a cartilage explant study by Guilak *et al.* (1995) [87] and an intact cartilage study by Madden *et al.* (2013) [85] were used for comparison with the present study and only the available data (cellular compressive strain and volume measurements) are presented. The compressive cell strain and volume were similar in the current study compared to that found in the cartilage explant study by Guilak *et al.* (1995) [87] but much greater than that of the intact cartilage study by Madden *et al.* (2013) [85].

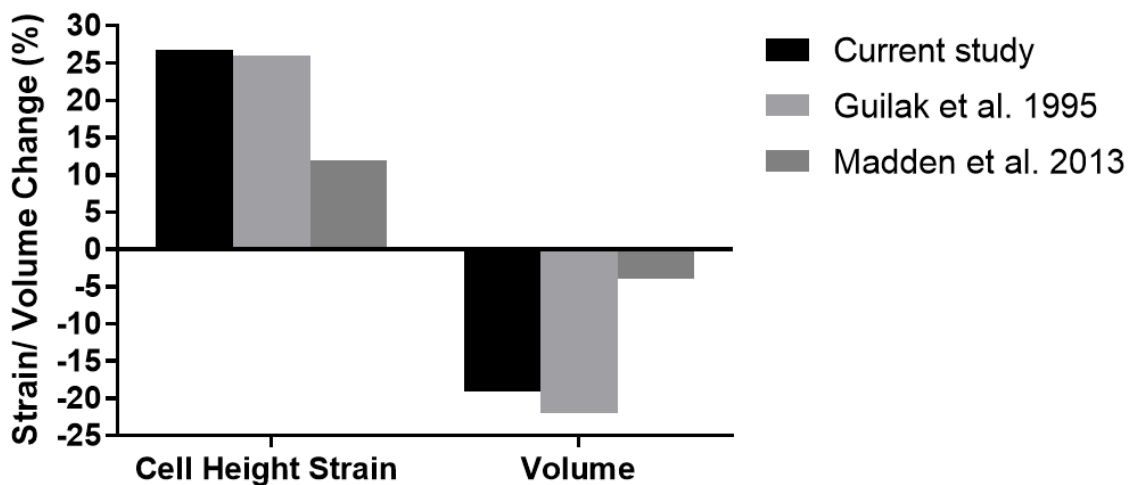


**Figure 71: Comparison of data (% strain/volume change) obtained in the current study for chondrocyte height strain and volume (black bars) and previous studies using cartilage explants(light grey bars) and intact cartilage (dark grey bars). In all cases, results are presented for an applied tissue compressive strain of 15 %.**

The observed differences in the morphometric measurements (at the uncompressed state and under 15 % applied tissue strain) may be associated with the use of different species and different measurement joint sites [85], [265], [280], [281]. Porcine femoral condyle and canine patellofemoral groove cartilage were used in studies of Choi *et al.* (2007) [137] and Guilak *et al.* (1995) [87], respectively, while (New Zealand White) rabbit retropatellar and femoral condyle cartilage were used in studies carried out by Han *et al.* (2010) [145] and Madden *et al.* (2013) [85], respectively, compared to the bovine patellofemoral groove cartilage used in the present study. It has been previously demonstrated that significant differences exist in the biochemical composition and the biomechanical properties of ECM among species despite their anatomic similarity [280]. Furthermore, the matrix composition and the biomechanical properties have been reported to significantly vary in different sites (patella groove and femoral condyles) within a patellofemoral joint, possibly due to differing in functional requirements, loading patterns and topography of the different sites [280], [282]. Athanasiou *et al.* (1991) [280] tested five species (bovine, canine, human, monkey and rabbit) of knee joint cartilage harvested from “high” (lateral and medial femoral condyles) and “low” (patellar groove) load

bearing areas of the distal femur for their biomechanical properties (aggregate modulus, Poisson's ratio and permeability). The results indicated significant differences in material properties between species and sites [280]. The material properties of the patellar groove (high permeability, low aggregate modulus and Poisson's ratio) suggested that it can be compressed greater and faster compared to the other tested sites, allowing rapid fluid transport to achieve a fast stress distribution under high applied load in order to create a congruent patellofemoral articulation [280]. The differences in material properties of articular cartilage among species and in different sites of the patellofemoral joint reflect on the differences in matrix biochemical composition which consequently affect the local mechanical environment around the chondrocytes. Madden *et al.* (2013) [85] also found that cell deformation was dependent on joint site in which chondrocytes from the rabbit femoral condyle and patellar cartilage showed different deformation behaviour under tissue compression. Structural differences may have likely evolved to adapt mechanically and consequently influence the local cartilage mechanical properties [85].

Another factor that may partly contribute to the observed difference is age. Structural changes associated with age include softening of articular surface, a reduction in the amount of proteoglycan, and alteration in fibrous structure (fibrillation), leading to a compromised ECM with loss of matrix integrity, tensile strength and stiffness [283]. These changes subsequently alter the mechanical environment of chondrocytes [145], [147]. The use of different measurement methods, such as staining techniques, imaging methods and tissue compression methods used (discussed in Section 2.5), could also attribute to the differences in the morphometric measurements (at the uncompressed state and under 15 % applied tissue strain).

The sample preparation (cartilage explants versus intact cartilage attached to its bone) was thought to be attributed to the observed differences in cell deformation between the current study and the study by Madden *et al.* (2013) [85] (Figure 71). Intact cartilage attached to its bone was used in Madden *et al.* (2013) [85] compared to cartilage explants used in Guilak *et al.* (1995) [87] and in the current study. It is possible that the tissue integrity in the explant was compromised by removing the underlying bone in sample preparation, causing disruption to the cartilage matrix and possible loosening to the collagen fibril tension [265]. Consequently, this may cause lateral fluid exudation of tissue to occur more easily and allow more fluid inside the chondrocyte to escape, resulting in larger cellular compressive stain (greater reduction in cell height) and volume changes in cartilage explant observed by Guilak *et al.* (1995) [87] and the current study.

The observed differences in uncompressed chondrocyte morphometric measurements and the magnitude of the differences in chondrocyte compressive strains and volume changes illustrates the difficulty in comparing observations in the current study to previous studies due to the use of different measurement methods, sample preparation and cartilage harvested from different

animals, different joint sites and age of the experimental animals. Nevertheless, the chondrocyte deformation data observed in this study was in general agreement with those reported in the previous cartilage explant studies [87], [137]. This infers that despite all the variations, such as species, activity levels, age and different measurement methods, that there appears to be a range of cell deformations within healthy cartilage across all species studied. In addition, this suggests that a novel methodology to visualise, image and quantify live cell morphology developed in this thesis was capable of determining chondrocyte deformation in compressed native cartilage disks. The imaging method lent itself to image analysis to provide quantitative data on cell deformation. Thus, the methods used in this study to determine changes in cell morphology will be utilised to examine the cell deformation behaviour in tissue engineered constructs under compression in order to understand the mechanism behind construct development and to optimise construct maturation in the longer term.

## **4.6 Conclusion**

To the author's best knowledge, no study has managed to track the same population of live chondrocytes and determine the 3D morphological changes in cartilage disks under different compressive strain levels. It is the first time that the superficial zone chondrocyte 3D deformation behaviour was determined under incremental compressive tissue strains (10 % and 15 %) in non-fixed bovine cartilage disks using live cell imaging and a custom designed compression device. Chondrocytes underwent significant changes in shape, size and volume in response to cartilage compression. These deformational changes were substantially greater than the overall applied tissue strains, indicating that large changes in chondrocyte morphology might occur in the superficial zone during periods of physiological compressive loading. Cartilage in this zone is known to have a lower compressive modulus than other zones in the articular cartilage resulting in a consequently greater matrix deformation and larger changes in chondrocyte morphology. Chondrocyte deformation was presumed to be largely influenced by the local ECM environment as well as partly modulated by the mechanical properties of PCM and the chondrocyte itself. Chondrocyte deformation may therefore be considered to be a function of applied tissue load and local cartilage matrix structure.

The findings in the current study were consistent with previous deformation measurements of superficial zone chondrocytes in cartilage explants in another specie [87]. The very similar deformation measurements across species where the explant method was used lends weight to the argument that chondrocyte behaviour perhaps is similar across species. The findings in the present study also suggests that a novel methodology to visualise, image and quantify live cell morphology developed in this thesis was capable of determining changes in chondrocyte 3D morphology in compressed native cartilage disks. The experimental strategy was therefore used to examine the cell deformation response in tissue engineered constructs in the later study (Chapter 5).

## **Chapter 5 - Effect of Compressive Strains on Cell Deformation in Cartilage Constructs**

*Having developed a staining method used for live cell confocal imaging to label and visualise cells within 3D native and tissue engineered cartilage, a novel compression device for tissue strain application and a custom workflow on Amira software capable for cell deformation quantification analysis, this chapter investigates the effects of incremental compressive strains on the deformation behaviour of live synoviocytes within cartilage constructs developed at different time points, in an attempt to better understand the mechanism behind the construct's development and to address the relationship between the applied tissue strain and cellular strain. Constructs were created using the mechanical loading method developed by Finlay et al. (2016) [1]; bovine synoviocytes were dynamically seeded on PET scaffolds followed by incubation in chondrogenic culture for 4 weeks before being subjected to cyclic compressive loading for an hour at 1 Hz, 5 days per week for 28 or 56 days. The maturation of constructs were analysed by collagen, sulphated glycosaminoglycan (sGAG) and DNA content, dynamic compressive modulus, histological staining characteristics (Alcian blue / Sirius red) and immunohistochemical staining characteristics (collagen type I and collagen type II). Confocal images of randomly selected synoviocytes were captured (i) at zero strain, (ii) an estimated percentage in applied compressive strain during mechanical loading in the bioreactor and (iii) 28 % applied compressive strain for both loaded and non-loaded constructs developed at different time points (Day 0, 28 and 56). Synoviocyte deformation quantification was conducted on the randomly selected synoviocytes in loaded and non-loaded constructs after 56 days of culture using Amira software. Synoviocyte morphometric parameters included cell length, width, height, volume and sphericity. The constructs developed in this study revealed only a small amount of cartilage-like matrix (according to collagen content, sGAG content, histological and immunohistochemical staining) in comparison to those in Finlay et al. (2016) study which resulted in correspondingly low compressive modulus. The primary reason for the differences could be related to the starting thickness (porosity) of the scaffolds used in the constructs, emphasising the importance of scaffold material's dimension, pre-culture period and mechanical loading in promoting a chondrocyte-like phenotype, leading to cartilage-matrix and mechanical properties within the constructs. No significant change was observed in synoviocyte morphology within Day 56 loaded constructs under the estimated strain applied to the construct during mechanical loading and 28 % compressive tissue strain. It is possible that the microenvironment around the measured synoviocytes may contribute to the observed effects, in particular the stiffness of the constructs and the site-specific ECM quality that would have led to variable quantities of collagen type II and GAG within the constructs. A further study with*

*larger sample size and lower scaffold porosity as originally intended is required to give a better insight into the mechanism behind the construct's development and the relationship between applied tissue strain and the cellular strain within the constructs. Nevertheless, a novel methodology to visualise, image and quantify live cell morphology within cartilage constructs under incremental static compressive tissue strains was achieved.*

## **5.1 Introduction**

Finlay *et al.* (2016) [1] attempted to engineer functional cartilage constructs for long term cartilage repair *in vitro* using mechanical stimulation. Constructs were created through the combining of PET scaffolds and bovine synoviocytes followed by incubation in chondrogenic culture for 4 weeks before being subjected to cyclic compressive loading for an hour at 1 Hz, 5 days per week for 28, 56 or 84 days. The resulting constructs achieved high compressive modulus and cartilage-like histological appearance comparable to that of native cartilage. The high-modulus values obtained from the constructs was hypothesised to be related to the nature of the mechanical loading regime applied as the constructs matured. The application of compressive mechanical loading was designed to apply appropriate stress and strain to the pre-cultured synoviocyte/PET constructs through the use of a force controlled bioreactor and silicone rings. Under the conditions determined by the bioreactor set up and the confinement of the constructs within silicone rings, applied strain to the constructs was regulated to between 13 % and 23 %. This strain value appeared to produce suitable stress within the deposited matrix of each construct, presumably via mechanotransductive effects on the residing cells, causing an anabolic response. The application of mechanical loading to the constructs initially triggered a surge of cell proliferation, followed by continued deposition of cartilage-like matrix. As the cells continued to respond and adapt to the challenge of mechanical loading, this apparently increased the construct thickness together with increased compressive stiffness of the construct. As this effect continued, a greater proportion of the load applied by the bioreactor was taken by the construct as well as increasing the strain applied (because of an increase in construct thickness). The stress (and strain) experienced by the cells remained at a level that promoted further matrix deposition. This effectively created a self-regulating mechanical regime where consistently increasing the thickness and the compressive stiffness of the construct occurred in conjunction with increased applied stress and strain [1]. This would presumably continue until the stress and strain levels reached a homeostatic level, i.e. when the majority of the applied load from the bioreactor is taken by the construct [1]. However, the time period taken to produce such constructs (approximately three to four months) limits its suitability for translation to the clinic. If a long culture period remains then the manufacturing costs will be high. This will not be an issue if the manufacturing costs can be offset by selling at a high price for the end product. However, if the end product cannot be sold at a price that offsets the production costs, then it will not be economically viable and the efficiency of construct development needs be

accelerated. Thus, in order to bring this method one step closer to clinical translation, reducing the culture period will increase the feasibility that it will be economically viable (as well as reducing the risk that something might go wrong during culture).

In native cartilage, chondrocytes are responsible for the elaboration and maintenance of extracellular matrix (ECM) that gives cartilage its strength and load-bearing function [21], [22], [139]. Previous studies have shown that mechanical loading modulates the biosynthetic response of chondrocytes *in vivo* [121], [122] and *in vitro* [123]–[128], demonstrating the importance of mechanical loading on cartilage homeostasis [93], [278], [284]. Chondrocytes are sensitive to changes in their environment and the level of their metabolic response is dependent on the type, magnitude and frequency of the applied mechanical loading [142], [285]. Chondrocytes in articular cartilage detect and respond to mechanical signals through mechanotransduction in conjunction with other environmental and genetic factors to regulate their metabolism [21], [22]. The mechanical signals are transferred to the chondrocytes through force transmission from the ECM resulting in cellular deformation (changes in shape and volume) [59], [65], [87], [94], [95]. Many studies have investigated the deformation behaviour of chondrocytes in cartilage explants [21], [87], [139] and for chondrocytes within other scaffold materials (e.g. isolated chondrocytes seeded in agarose) [88], [140]–[143] under static compression. In Chapter 4, the deformation response of a given population of chondrocytes from the superficial zone of bovine articular cartilage disks was examined. The findings showed that changes in chondrocyte shape and volume in native cartilage under unconfined static compression were consistent with previously published measurements. It is believed that chondrocyte deformation is closely associated with deformation of ECM as well as modulation by the mechanical properties of the pericellular matrix (PCM) and the chondrocyte itself. However, under tissue deformation, the local mechanical environment (i.e. matrix content and composition) around chondrocytes in native cartilage will not be comparable to those in cartilage constructs because native cartilage has distinct structural heterogeneities; matrix heterogeneity and depth-dependent heterogeneity [286]. Matrix heterogeneity refers to the different matrices that surround a chondrocyte in native cartilage; a PCM (the immediate layer of matrix outside a chondrocyte), a territorial matrix (TM), and an interterritorial matrix (IM), also known as ECM (the bulk of the matrix in cartilage) [286]. In contrast, the matrix of engineered constructs was found to be relatively homogeneous based on histology [1]. From histology, it was observed that there was an increase in Alcian blue staining (which corresponds to sGAG content), from very little at the beginning of culture to dense at the end of culture, comparable to native cartilage [1]. However, a hierarchical native cartilage structure was not observed.

In order to promote or maintain differentiation of synoviocytes to a chondrocyte-like phenotype in the constructs and consequently the production of the desired cartilaginous matrix, a sufficient amount of compressive load is required to stimulate the cells to respond in the

required manner. The role of synoviocytes in producing and maintaining ECM is crucial to the maturation of the tissue. However, the magnitude of strain transmitted through the ECM and directly acting on the cells that corresponds to the applied external load during the different stages in construct development is unknown and is yet to be determined. To date, such constructs have been examined from a tissue level with histological and immunochemical visualisation of cell and matrix distribution but no attempt has been made to visualise the constructs at the level of a single cell. Therefore, the aim of the work described in this chapter was to examine the deformation behaviour of living synoviocytes within cartilage constructs under incremental compressive tissue strains in order to address the relationship between applied tissue strain and cellular strain. This involved identification of the actual mechanical regime experienced by the synoviocytes in the constructs at different time points of their development during mechanical loading. To fulfil the aim, it was proposed that cellular deformation would be examined under the estimated tissue strain experienced by the constructs in the bioreactor during construct development (as described in Section 5.3.7). A compressive strain of 28 % was also used in the experiments in an attempt to determine how synoviocytes would respond under conditions approaching maximum physiological loading (physiological range lies between 0 % and 30 % [130], [210], [264]), in terms of any changes in cell morphology (shape and size).

The work would also hopefully provide new insight into the mechanism(s) underpinning the construct's development and provide essential information for promoting matrix synthesis and deposition in future constructs. In addition, a better understanding of the effect of cellular deformation within constructs developed at different stages could improve efficiency of construct growth with consequential benefits for increased potential for clinical translation.

The aim of this study was approached via the following objectives:

- To fabricate cartilage constructs using synoviocyte/PET scaffold constructs using the mechanical loading method developed by Finlay *et al.* (2016) [1].
- To assess the effects of mechanical loading on the maturation of constructs at different time points (Days 0, 28 and 56) of development by determination of compressive dynamic moduli, collagen, sulphated glycosaminoglycan (sGAG) and DNA content, histological staining with Alcian blue/Sirius red and immunohistochemical staining for collagens type I and type II.
- To determine the effects of incremental compressive strains on cell deformation behaviour in constructs developed at different time points in the uncompressed state, during estimated strain subjected by the bioreactor and at 28 % tissue strain. This was achieved by live cell imaging, utilising the live cell staining method of Hoechst 33342 and CellMask green plasma membrane stains (described in Chapter 2) and confocal microscopy to fluorescently label and visualise synoviocytes in the constructs whilst

using the novel compression device developed specifically for tissue strain application (described in Chapter 3) and Amira software for cell deformation quantification analysis.

An overview of the experimental plain is depicted in Figure 72.

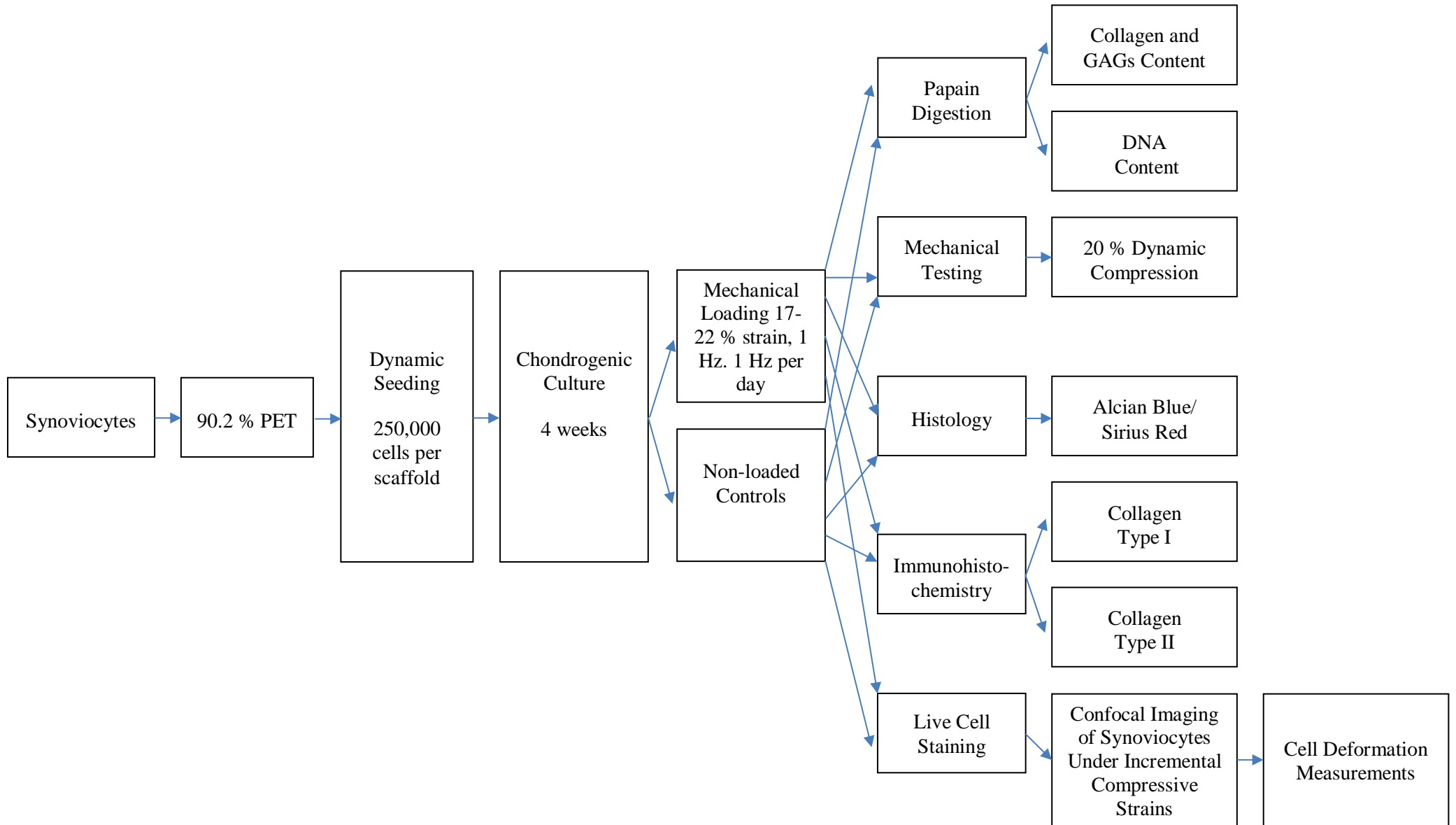


Figure 72: Overview of experimental plan for determining the effect of incremental compressive strains on cell deformation behaviour in cartilage constructs.

## **5.2 Experimental Methodologies**

### **5.2.1 Cell isolation, Monolayer Culture, Dynamic Seeding and Chondrogenic Culture of Synoviocytes on PET Scaffolds**

Synoviocytes were isolated, expanded *in vitro*, dynamically seeded on to PET scaffolds and cultured under static chondrogenic conditions as stated in Section 3.3.3. In brief, synoviocytes were isolated from bovine synovium via collagenase digest for 3 hrs at 37°C. The digest was filtered and centrifuged before the pellet was resuspended and seeded into tissue culture flasks. Synoviocytes were cultured in DMEM/F12 medium supplemented with 10 % FBS, 1x AB and 2 mM L-glutamine at 37°C, 5 % CO<sub>2</sub> and above 90 % humidity. When approximately 90 % confluency was reached, cells were passaged by trypsinisation and re-seeded at 5000 cells/cm<sup>2</sup>. Medium change occurred every 3-4 days. Cells between passages 1 and 3 were used for experimentation.

Once sufficient amount of cell numbers had been achieved, a 250,000 cells/mL suspension was prepared. An aliquot of 1 mL cell suspension coupled with a PET scaffold disk were inserted in a 2 mL capacity polypropylene tube. Each tube was then inserted into a dynamic seeding apparatus built in-house and rotated at a rate of approximately 0.25 Hz. The dynamic cell seeding device was placed in the incubator at 37°C for 24 hrs to allow the cells to attach to the PET scaffold.

Once seeding was completed, each cell-PET construct was transferred into a single well of a 24 well cell culture plate. Each construct was submerged in 1 mL of chondrogenic medium, which consisted of DMEM/F12 medium supplemented with, 10 ng/mL TGF-β<sub>3</sub>, 50 µg/mL L-ascorbic acid-2-phosphate sesquimagnesium salt hydrate, 10<sup>-7</sup> M dexamethasone, 1x ITS, 1x AB and 2 mM L-glutamine. Chondrogenic medium was freshly made prior to application due to the instability of TGF-β<sub>3</sub> and ascorbic acid-2-phosphate in solution. The plates were placed in the incubator at 37°C. Cultures were kept under these conditions for 4 weeks. Medium change occurred every 3-4 days.

### **5.2.2 Mechanical Loading of Synoviocyte/PET Constructs**

Following 4 weeks in chondrogenic culture, application of mechanical loading to constructs was achieved using an in-house built compressive bioreactor that was used previously in Finlay *et al.* (2016) [1]. The aim of applying mechanical stimulation to the pre-cultured constructs was to further develop the immature constructs towards a mechanically functional cartilage-like tissue. The mechanical stimulus required to potentially induce mechanotransduction and anabolic matrix synthesis was defined as one that generates stress and strain to the neo-tissue elaborated within the constructs within physiological ranges comparable to those experienced within native cartilage.

The response of immature constructs (after 4 weeks of chondrogenic culture but before the mechanical loading commenced i.e. Day 0) to compressive load was examined previously by Finlay *et al.* (2016) [1]. This identified that the appropriate loading regime for application onto immature constructs was between 13 % and 30 %. These values are specific to constructs upon commencement of the mechanical loading. The authors showed that the loads measured at strains below 10 % were almost negligible, indicating little stress was being transmitted to the matrix and residing cells, whereas at strains greater than approximately 13 %, the recorded load increased exponentially, demonstrating the potential for stress to be transmitted to the matrix and the resident cells. An upper limit of 30 % strain was chosen (approaching the maximum values of strain observed in native cartilage) because it was believed that the “loose” matrix developed within the construct in the early stages was unlikely to transmit damaging forces to the cells.

The compressive bioreactor (Figure 73) was built to apply cyclic compressive loading to constructs within a custom culture apparatus (Figure 74). Its external dimensions of 250 x 235 x 100 mm<sup>3</sup> allowed it to be placed within an incubator. This maintained standard culture conditions (i.e 37°C, 5 % CO<sub>2</sub> and greater than 90 % humidity) whilst allowing application of mechanical loading. The bioreactor consisted of 12 loading channels which could be set individually to apply a uni-axial force of between 0.5 and 10 N.

The loading mechanism of the bioreactor is briefly described as follows (see Figure 73). The bioreactor is driven by a 12 volt DC motor (A) connected to an assembly of a gear box (B), timing belt and pulley system (C) which causes two cam shafts (D) (only one cam shaft is visible in Figure 73) to rotate at a frequency of 1 Hz. As the cam shaft rotates, it causes twelve connected transmission shafts (F) to reciprocate vertically at the same frequency, therefore loading samples contained within the culture chambers beneath. The ends of the transmission shafts are where the plungers and culture apparatus are linked to the bioreactor by connectors (H). A C-shaped follower (with roller) (E) was used to ensure the transmission shaft moved with the rotating cam shaft. The waveform of the transmission shaft and the plunger is governed by the cam's geometry. The bioreactor was force controlled and the force delivered by each plunger comprised the weight of the plunger assembly (which includes the C-shaped follower (with roller), transmission shaft, plunger and the associated connectors) and load exerted from a pre-compressed spring (G). For the application of the minimum force (0.5 N), the spring is removed. In contrast, for the application of maximum force (10 N), a spring is installed and highly compressed to produce the required force.

The bioreactor compresses up to twelve samples that are placed within two custom culture chambers, with each construct cultured in a separate well of a chamber that is located beneath six bioreactor loading channels. Referring to Figure 74, each chamber consists of six separate wells (L), a lid (K), six plungers each with a diameter of 8 mm (J) and six connectors that link

the plungers and the transmission shafts (I). The well is 14 mm in depth and 14 mm in diameter and can accommodate up to 900  $\mu\text{L}$  of culture medium. When these components are assembled, the plungers were aligned with the centres of the wells within the culture chamber by the small holes in the lid (the large holes permit gaseous exchange). Moreover, during assembly, a flexible polyurethane film (Smith & Nephew, Watford, UK, Opsite Flexigrid, 4631) was affixed on the underside of the culture lid in order to seal the rim of each chamber and the exits of the plungers so the culture chamber contents are protected from contamination whilst allowing gas exchange and movement of the plungers. All culture components were made out of stainless steel 316 because of its good biocompatibility under *in-vitro* conditions. During the non-loading periods, the assembled culture apparatus could be disconnected from the bioreactor as a standalone piece of equipment, therefore allowing simultaneous culture of many constructs within multiple culture chambers.

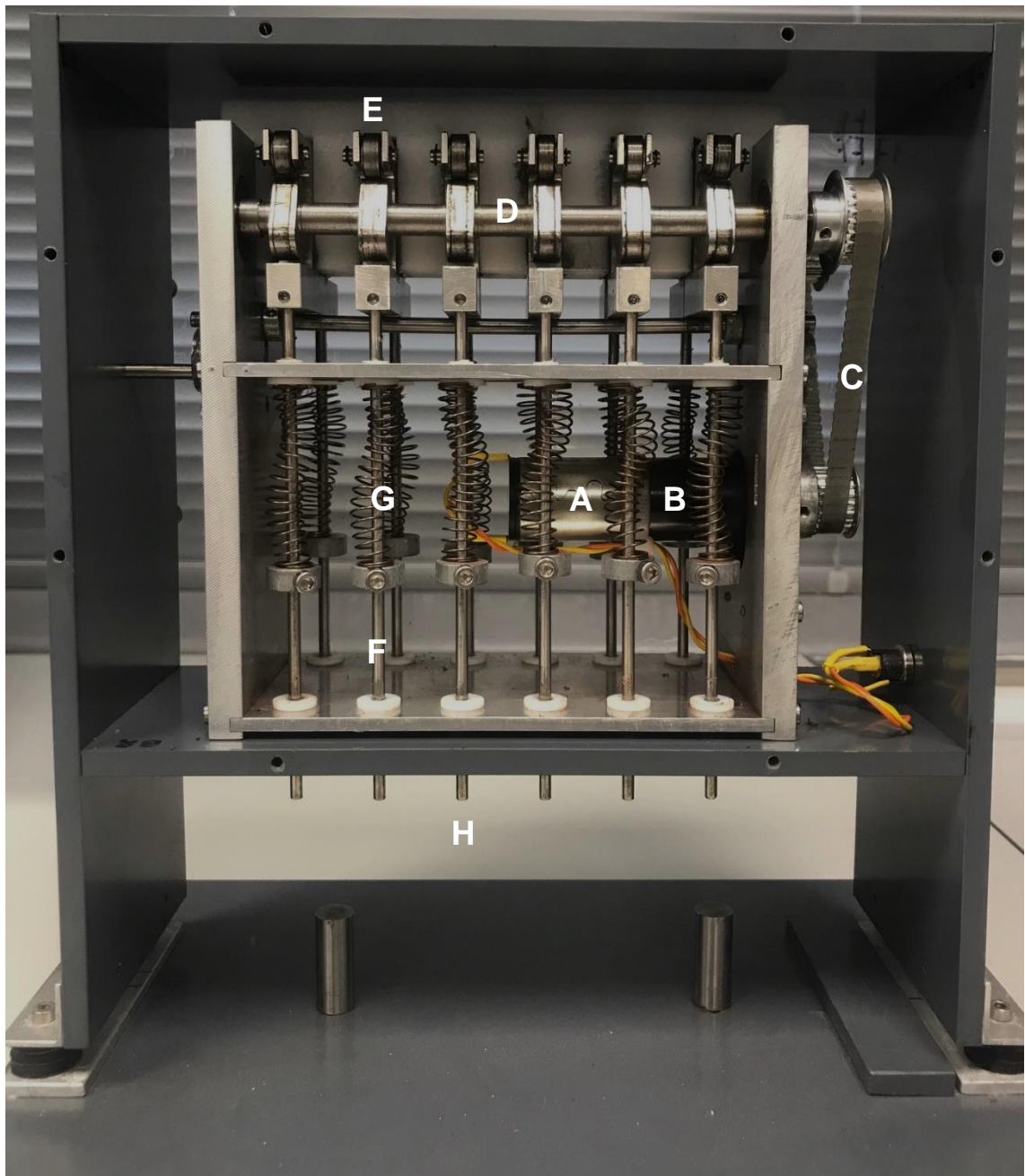


**Figure 73:** Internal assembly of the in-house built cyclic compressive bioreactor; (A) 12 volt DC motor, (B) gear box, (C) timing belt and pulley system, (D) cam shaft, (E) C-shaped follower with roller in contact with cam and connected to (F) transmission shaft and (G) pre-compressed spring and (H) the end of transmission shaft where the plunger and culture apparatus joined by connector (illustrated in Figure 74I).



**Figure 74: Components of culture apparatus for in-house built cyclic compressive bioreactor; (I) connector to the bioreactor (illustrated in Figure 73H) and (J) plungers, (K) culture lid, (L) culture chamber and (M) assembly of these components.**

The following setup was adapted to apply compressive loading in a quasi-displacement controlled modality, by the introduction of a silicone ring within each well of the culture chambers that would be significantly stiffer than the constructs. It was proposed to modify the loading mechanism of the bioreactor from a force controlled setup to a custom-construct displacement control setup because the previous study [287] demonstrated that the average force required to compress constructs by 20 % was 0.16 N, which was below the minimum force the bioreactor can apply (0.5 N). It was deemed to be unwise to tamper with the original load controlled mechanism used in the bioreactor in order to apply the desired compression (0.16 N) because the bioreactor was effective at applying consistent load over a great amount of cycles.

In addition, whilst it was technically simple to reduce the minimum force applied by the bioreactor, there was a significant negative consequence in applying such low load. The flexible and breathable membrane that covers the lid of the culture apparatus to ensure sterility of the constructs and the surrounding medium imparts resistance to the movement of the plungers during the motion of the transmission shafts. The effect of this resistance to such a low load would likely be considerable, variable and difficult to determine, thus a displacement controlled mechanism was adapted. A relatively high force of 5 N applied by the bioreactor was therefore selected to avoid any potential consequences with regards to the effects of the resistance from the polyurethane membrane. Another advantage of confining the constructs within silicone rings was that this could reduce potential lateral construct displacement within the culture wells during mechanical loading and consequently ensure the constructs were loaded centrally during each loading cycle, reducing the incidence of construct displacement. As the constructs were loaded within the confines of a silicone ring that would be significantly stiffer than the constructs themselves, it was assumed that the constructs would have negligible stiffness with regards to the surrounding silicone rings and, thereby, the plunger displacement would only be influenced by the silicone ring when the bioreactor applied a force of 5 N. By knowing the compressive modulus of the silicone material as well as the dimensions of the silicone ring and the force applied by the bioreactor, the distance which the plunger travels could be determined. Construct strain applied by the bioreactor was, therefore dependent on the plunger displacement and construct thickness.

A silicone elastomer (Sylard<sup>®</sup> 184, VWR International; Lutterworth, UK, 634165S) was chosen for silicone ring fabrication because of its known biocompatibility and its predictable behaviour under compressive loading. Finlay *et al.* (2016) [1] tested the mechanical behaviour of the silicone material and found that cured silicone had a stiffness value of 2.64 MPa which is substantially stiffer than the constructs that had been cultured for 4 weeks under chondrogenic conditions (0.2 MPa at 20 % compressive strain). Finlay [1] also found out that the silicone elastomer rings strained on average by 3.3 % when subjected to a cyclic load of 5 N by a bioreactor plunger within a culture chamber. By knowing the amount the silicone rings strained on average under cyclic loading of 5 N, compressed thickness of silicone rings can be calculated which was used to calculate the applied tissue strain.

Following 4 weeks of chondrogenic culture, the synoviocyte/PET scaffold constructs were removed from their wells and their thickness measured using sterile Vernier callipers (accuracy of  $\pm 10 \mu\text{m}$ ). Silicone rings with various thicknesses (between 1650  $\mu\text{m}$  and 1750  $\mu\text{m}$ ) were fabricated (described in Section 5.2.3) in order to accommodate the application of the selected strain range by selecting rings of appropriate thickness from a range of rings of different thicknesses. To achieve a desired strain in the range between 13 % and 30 %, a silicone ring of specific thickness was matched with each construct. Those constructs with a measured thickness of between 1970  $\mu\text{m}$  and 2210  $\mu\text{m}$  were selected. This corresponded to a strain between 17 %

and 22 %. For example, when a silicone ring with a thickness of 1650  $\mu\text{m}$  was compressed in the bioreactor by a plunger with 5 N force, the resulting 3.3 % strain would correspond to a deformation of 55  $\mu\text{m}$ , which corresponds to a compressed height of 1595  $\mu\text{m}$ . If a construct with a measured thickness of 1970  $\mu\text{m}$  was compressed within this silicone ring under the assumption the construct has negligible stiffness in comparison to the silicone ring, we can assume it would be deformed to a final height of 1595  $\mu\text{m}$  (by implementation of the silicone ring that limited the travel of the plunger) which corresponds to an applied strain of 19 %.

Constructs that met the thickness criteria were placed into a bioreactor culture well. Any that were not within the construct thickness range between 1970  $\mu\text{m}$  and 2210  $\mu\text{m}$  were returned to culture within the confinement of silicone rings and used as experimental controls (i.e. non-loaded constructs) for the remainder of the culture period. The silicone rings matched with the non-loaded constructs therefore theoretically yielded the desired strain range between 13 % and 30 % if they were placed under in the bioreactor during mechanical loading. The corresponding silicone ring to each non-loaded construct was later used to determine the amount of applied construct strain for cell deformation examination (see Section 5.3.8).

The spring was pre-compressed to apply 5 N of force in the bioreactor. This was validated by placing a transducer from the Bose ElectroForce 3200 mechanical testing machine beneath the connector to the plunger of the bioreactor and ensuring the transmission shaft was at its lowest position. Constructs within each culture chamber well were loaded into the bioreactor each day for an hour (5 day per week) and subjected to 5 N of force at a frequency at 1 Hz. After each loading period, the constructs were checked to ensure they had not been displaced from the confinement of the silicone ring during loading. All constructs continued to receive chondrogenic medium throughout the remainder of the culture periods, with medium change every 3-4 days.

Constructs were removed from culture at Days 0 (i.e., at the end of the 4-week static culture period), 28 and 56 to be processed for analysis.

### **5.2.3 Silicone Ring Fabrication**

In order to apply physiologically relevant mechanical loading to the pre-cultured (immature) constructs using a displacement controlled mechanism in the bioreactor, they were confined within silicone rings during mechanical loading (as described in Section 5.2.2). A silicone elastomer (Sylgard<sup>®</sup> 184, VWR International; Lutterworth, UK, 634165S) was used to fabricate the silicone rings.

The procedure for silicone rings fabrication is described as follows. Following the manufacturers' instructions, Sylgard<sup>®</sup> 184 silicone elastomer base was combined with Sylgard 184 curing agent in a 10:1 ratio, mixed vigorously and degassed under vacuum. Referring to Figure 75, whilst still in the liquid phase, a syringe was used to draw up the silicone and slowly

injected it in between (A) two glass plates. The space between the two glass plates is governed by (B) a U-shape spacer which determines the resulting polymerised silicone thickness. The glass plates were held in place by (C) clamps to ensure correct spacing. During this process, any visible bubbles in the silicone migrated to the surface where they dissipated. The entire apparatus (Figure 75) was moved to a drying cabinet at 40°C to accelerate curing overnight.

Once cured, the clamps were removed and the plates were submerged under water. The plates were then slowly prised apart, leaving a silicone sheet on one of the plates which was carefully peeled away. Silicone rings were then produced using a custom made circular cutter, of internal diameter 6 mm and external diameter 14 mm. The rings were further modified by removing 1 mm of the external diameter from four sides with a scalpel to create four edges perpendicular to each other (Figure 76). This ensured the rings fitted in to the wells of the bioreactor, allowing fluid movement but avoiding displacement of constructs occurring during loading. Silicone rings with thicknesses ranging between 1.65 mm and 1.75 mm were fabricated by using spacers of different thicknesses to accommodate constructs with various thicknesses in order to apply the selected strain range. Silicone ring thickness was confirmed with Vernier calipers. Silicone rings were rinsed in PBS prior to a wash in 70 % ethanol and then autoclaved to ensure sterility before introduction to culture conditions.

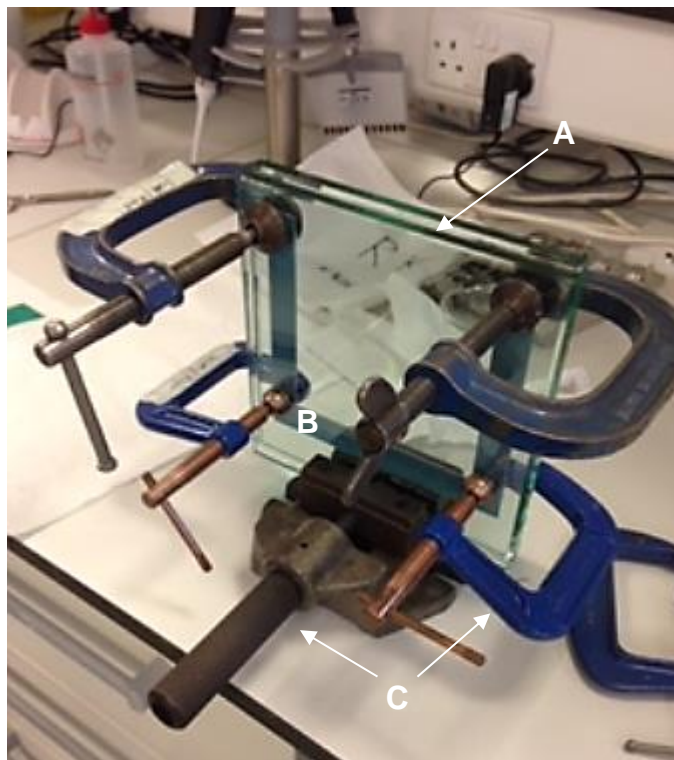


**Figure 75: Assembly of the apparatus used to fabricate cured silicone sheets for silicone rings; (A) liquid silicone injected in between two glass plates where (B) a U-shaped spacer is held by (C) clamps to ensure correct spacing.**

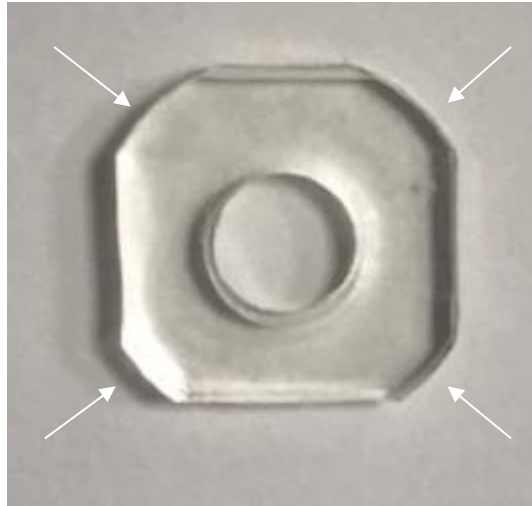


**Figure 76: Example of a modified silicone ring. Silicone rings (internal diameter 6 mm and external diameter 14 mm) were further modified by removing 1 mm of the external diameter from four sides (white arrows) to create four edges perpendicular to each other to ensure the rings fitted in to the wells within the culture chambers of the bioreactor, allowing fluid movement but avoiding displacement of constructs occurring during loading.**

## **5.3 Analytical Methods**

### **5.3.1 Papain Digestion and Collagen, Sulphated Glycosaminoglycan and DNA Quantification**

#### **5.3.1.1 Papain Digestion**

Before collagen, sGAG and DNA quantification could be carried out, the contents of the constructs needed to be solubilised. Papain was previously used by Hoemann *et al.* (2002) [288] on milligram quantities of cartilage and was shown to consistently solubilise tissue and cells, whilst retaining the collagen, sGAG and DNA content from degradation.

Following culture of constructs at each experimental time point (days 0, 28 and 56), they were washed in PBS and cut into smaller pieces before placing at 60°C for 24 hrs in sterile 1.5 mL screw cap microtubes (Elkay Laboratory Products, Basingstoke, UK, 021-4153) with 0.5 mL of 0.2 µm filter-sterilised papain digestion buffer [5 mM L-cysteine (Sigma-Aldrich, Irvine, UK, 168149), 100 mM Na<sub>2</sub>HPO<sub>4</sub> (Fisher Scientific UK, Leicestershire, UK, S9763), 5 mM EDTA (Sigma-Aldrich, Irvine, UK), pH 7.5] containing 125 mg/mL papain type III (Sigma-Aldrich, Irvine, UK, P4762). The resulting solution was stored frozen at -80°C until analysed (n = 6 for each time point). Bovine articular cartilage specimens were digested in the same manner as the constructs for collagen, sGAG and DNA quantification in native bovine cartilage as a form of positive control.

### 5.3.1.2 Collagen Quantification

The amount of collagen in the constructs was determined using the hydroxproline (HYP) assay. This imino acid is a major component in collagen and can be used for its indirect quantification since it comprises approximately 13.5 % of the total collagen content [289]. The HYP assay is a colorimetric assay in which a chromophore is formed from HYP via reaction with p-dimethylaminobenzaldehyde [290], [291].

A 30  $\mu$ L aliquot of papain digested construct was placed in a sterile 1.5 mL screw cap microtube which was placed in a hot plate for evaporation. Following this, 50  $\mu$ L of 2M NaOH (Sigma-Aldrich, Irvine, UK) was added to the microtube before placing in the autoclave at 121°C. Ten microlitres of this were added to a well in a 96-well microplate along with 90  $\mu$ L of Chloramine-T solution [1.27 g chloramine-T (Sigma-Aldrich, Irvine, UK, 402869) in 20 mL n-propanol in 100 mL acetate citrate buffer (50 g citric acid monohydrate, 12 mL glacial acetic acid, 120 g sodium acetate trihydrate, 34 g NaOH to pH 6.5 in 1 L). The plate was placed in a sealed bag in a water bath for 25 mins at 65°C. Samples were then mixed with 100  $\mu$ L of freshly prepared Ehrlich's reagent (3.8 mL of 60 % perchloric acid (VWR Chemicals, Lutterworth, UK) slowly added to 1.5 g p-dimethylaminobenzaldehyde (Sigma-Aldrich, Irvine, UK, D2004) in 6.2 mL n-propanol (Sigma-Aldrich, Irvine, UK, 34871) and incubated at 60°C for 20 mins. Absorbance at 550 nm (excited at 480 nm) was read using a microplate spectrophotometer. Bovine articular cartilage specimens were tested as per the experimental constructs in order to determine the typical amount of collagen in native tissue and use as a reference for construct comparison.

Hydroxproline standards were prepared using 1 mg/mL L-hydroxproline (Sigma-Aldrich, Irvine, UK, 41875). A range HYP standards of 4  $\mu$ g/ $\mu$ L to 20  $\mu$ g/ $\mu$ L was produced. Each standard then followed the same process to that of experimental samples; evaporation, combination with NaOH, autoclaving, combination with Chloramine-T solution and Ehrlich's reagent before fluorescence being read. Triplicates were carried out for all experimental samples and HYP standards.

### 5.3.1.3 Sulphated Glycosaminoglycan Quantification

sGAG content of constructs was determined using a Dimethylmethylene Blue (DMMB) assay. sGAG is an important component of cartilage and DMMB, a cationic dye, can be used to detect GAGs in solution [292]. Upon binding to sGAG, DMMB undergoes a change in colour in the absorption spectrum [293], [294].

A 1  $\mu$ L aliquot of papain digested construct was added to a well of a 96-well microplate before combining with 99  $\mu$ L of PBE buffer. Two hundred microlitres of DMMB solution (40 mM NaCl, 40 mM glycine, 46  $\mu$ M DMMB, to pH 3) was added to each well, pipette mixed and incubated for 5 mins at room temperature before absorbance was read at 525 nm using a microplate

spectrophotometer. Bovine articular cartilage specimens were tested as per the experimental constructs in order to determine the typical amount of sGAG in native tissue and use as a reference for construct comparison.

sGAG standards were prepared from 2.5 mg/mL chondroitin sulphate (Sigma-Aldrich, Irvine, UK, C4384). A 10  $\mu$ L aliquot of the chondroitin sulphate solution was added to 990  $\mu$ L PBE buffer. This was then serially diluted with PBE buffer to produce a range of 0.25 and 2  $\mu$ g of standards. One microlitre aliquots of each standard solution were added to 99  $\mu$ L of PBE buffer before combining with 200  $\mu$ L of DMMB solution within a 96-well microplate, pipette mixed, incubated for 5 mins at room temperature and absorbance read at 525 nm. Triplicates were carried out for all experimental samples and sGAG standards.

#### **5.3.1.4 DNA Quantification**

DNA content was determined in the constructs as a surrogate measure for cell numbers and was performed using the Quant-iT<sup>™</sup> PicoGreen<sup>®</sup> assay (Invitrogen, Paisley, UK, P7589). The PicoGreen assay kit contained Quant-iT<sup>™</sup> PicoGreen<sup>®</sup> dsDNA reagent, 20x TE buffer and Lambda DNA standard. Picogreen is a fluorescent probe that binds double stranded DNA (dsDNA) and upon binding to dsDNA, fluorescence enhances 1000 fold [295]. Picogreen also binds to single stranded DNA and RNA but fluorescence enhancement is dramatically lower compared to dsDNA binding [295]. According to the manufacturer, the sensitivity of Picogreen is 400 fold greater compared to Hoechst 33258 (another commonly used DNA quantification molecule; a fluorochrome called bisbenzimidazole).

A 10  $\mu$ L aliquot of the papain digested construct was added to 290  $\mu$ L of 1x TE buffer (10 mM Tris-HCL and 1 mM EDTA, at pH 7.5). Fifty microlitres of this was combined with 50  $\mu$ L PicoGreen working solution (35  $\mu$ L PicoGreen concentrate, 6965  $\mu$ L TE buffer) and added to a well of a 96-well microplate. Fluorescence was read at 520 nm (excited at 480 nm) using a microplate spectrophotometer after the plate was incubated at room temperature for at least 5 mins. Bovine articular cartilage specimens were tested as per the experimental constructs in order to determine the typical amount of DNA in native tissue and use as a reference for construct comparison.

DNA standards were prepared from 100  $\mu$ g/mL bacteriophage lambda DNA which was provided with the PicoGreen reagent (Invitrogen, Paisley, UK, P7581-Ccomponent C). Twenty microlitres of 100  $\mu$ g/mL bacteriophage lambda DNA were added to 980  $\mu$ L TE buffer. This was then serially diluted with TE buffer, to create a range of concentrations between 1  $\mu$ g/mL and 1 ng/mL. Fifty microlitres of each standard was combined with 50  $\mu$ L PicoGreen working solution before fluorescence being read. Triplicates were carried out for all experimental samples and DNA standards.

### 5.3.2 Dynamic Mechanical Testing

A dynamic mechanical testing method was used because it simulates functional physiological loading and an appropriate response of the constructs [296]. The (compressive) modulus of loaded and non-loaded constructs was measured at each time point (Days 0, 28 and 56) when subjected to dynamic unconfined compression. The Young's modulus ( $E$ ) (under tension or compression) is defined as stress ( $\sigma$ ) divided by strain ( $\varepsilon$ ) (Equation 1) and used to describe the stiffness of a material.

$$E = \frac{\sigma}{\varepsilon} \quad (\text{Eq. 1})$$

Engineering stress ( $\sigma$ ) is defined as Force ( $F$ ) acting on the cross sectional area ( $A_o$ ) of the sample (Equation 2).

$$\sigma = \frac{F}{A_o} \quad (\text{Eq. 2})$$

Strain ( $\varepsilon$ ) is defined as the ratio of deformation ( $\Delta L$ ) of the sample compared to its original length ( $L_o$ ) (Equation 3).

$$\varepsilon = \frac{\Delta L}{L_o} \quad (\text{Eq. 3})$$

In order to calculate stiffness of the constructs, measurements of cross-sectional area, thickness and force in combination with deformation were required. The Instron ElectroPuls<sup>TM</sup> E3000 (Instron, High Wycombe, UK) was used to dynamically test the constructs, as shown in Figure 77. Referring to Figure 77, a 250 N transducer (G) was secured to the base of the rig frame, to which a mechanical action wedge grip (F) was attached. A second mechanical grip (B) was connected to the test rig actuator (A). Two metallic platens (with diameters greater than the test samples) were placed and secured in the two grips ((C) and (E)). The top platen (C) was lowered with a force of 100 N to bring the two platens together before establishing a 'zero' displacement position'. A distance of 2.5 mm was then set apart between them. A column of PBS was formed between the platens in which a construct was suspended (D).



**Figure 77: Dynamic mechanical testing rig set up; (A) actuator, (B, F) mechanical actin wedge grips, (C,E) platens, (D) space where top platen lowered to form PBS column with suspended construct and (G) 250 N load transducer.**

The thickness of each construct was first measured. Under the control of the Instron WaveMartix software (Instron, High Wycombe, UK), the top platen was lowered at a rate of 50  $\mu\text{m/s}$  and stopped until a tare load of  $-0.02\text{ N}$  was reached. The load data obtained were then filtered through a rolling average of 20 data points to reduce noise. Construct thickness was read as the distance between the two facing surfaces of the platens at this tare load. The top platen was then positioned at this distance and subjected the construct to 10 cycles of 20 % cyclic strain of a triangular waveform at 1 Hz as shown in Figure 78. Both force and resulting compressive deformation of the construct were simultaneously recorded.

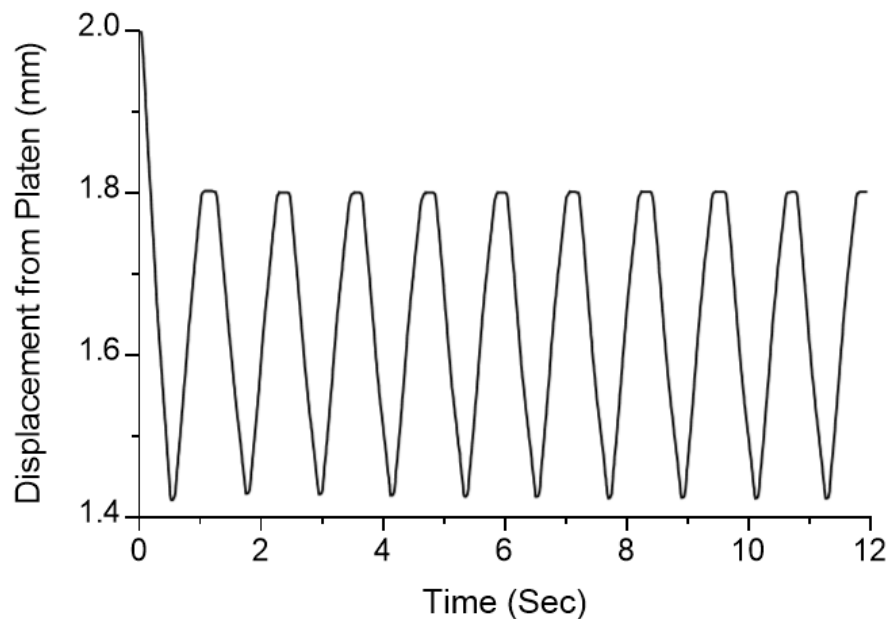


**Figure 78: Example of 10 cycles of 20 % strain triangular waveform at 1Hz applied to constructs for the means of dynamic mechanical testing.**

The 4 last loading cycles (out of 10) were selected for measuring the compressive moduli of the constructs as it was previously shown by Finlay *et al.* (2016) [1] that a number of cycles were required in order to reach a steady state in the loading behaviour of the constructs. This steady state was achieved by the time of the first 6 cycles. Hence, the final 4 cycles were used for mechanical testing. Stress-strain curves were plotted from the displacement/force data obtained from these 4 later cycles, to which a best-fit exponential curve was fitted. Curves obtained illustrated a non-linear stress/strain relationship (Figure 79). A tangent modulus of the construct was calculated by differentiating the exponential best-fitted curve and obtaining the gradient at strain value of 18 %. All data handling was carried in OriginPro 8.1.

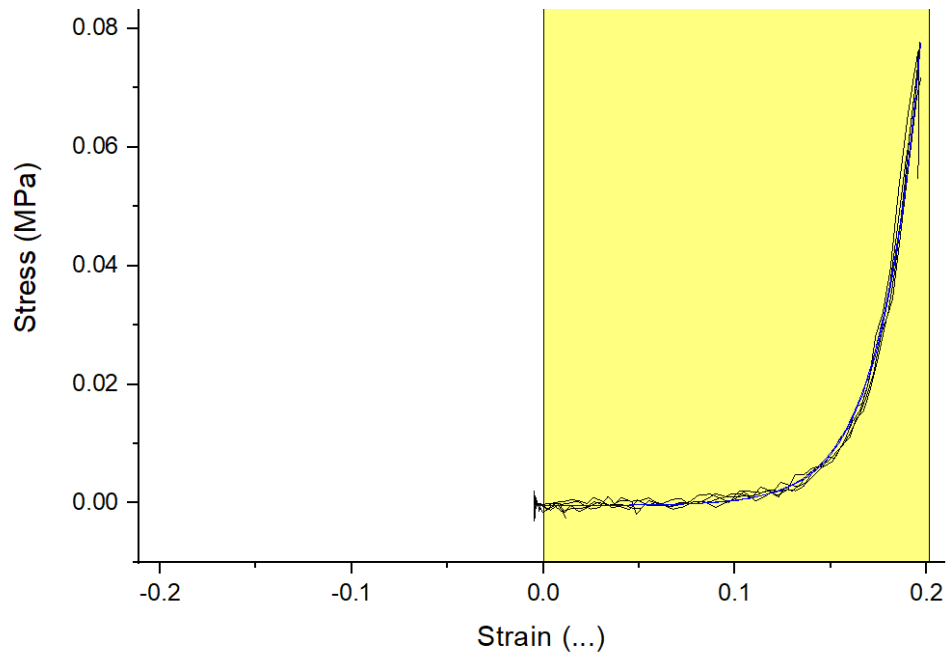


**Figure 79: Example of typical engineering stress vs strain curve acquired from dynamic mechanical testing. Exponential fit (blue line) made between 0.0 and 0.2 strain.**

### **5.3.3 Fixation, Embedding and Sectioning of Constructs**

In order to evaluate construct histology, loaded and non-loaded constructs (n = 3 for each time point) were removed from culture and washed in PBS to remove excess medium before submerging in 10 % NBF (CellPath, Newtown, UK, BAF-6000-08A) for at least 30 mins to fix the tissue. Fixed constructs were then stored in PBS ready for embedding and sectioning.

Embedding and sectioning of the fixed constructs were performed by Covance Laboratories Ltd (Harrogate, UK). A 3 mm wide central region was cut from the 5 mm diameter construct discs using a scalpel prior to embedding. The cut strip was then embedded in paraffin wax within an enclosed tissue processor, with the cut face positioned parallel to the resulting block to create longitudinal sections with regards to the disc face. In brief, samples were dehydrated through increasing concentrations of ethanol followed by multiple xylene treatments to remove the ethanol. The final step of embedding was to infiltrate the melted paraffin wax into the sample by the aid of vacuum. Once the wax had cooled and solidified, the samples were sectioned to a thickness of 5  $\mu\text{m}$  using a rotary microtome. Sections were floated on water at 45°C to remove any wrinkles formed during sectioning and mounted onto Superfrost Plus slides (VWR, Lutterworth, Leicestershire, UK, 631-0446) and left to dry. The resulting sections were transported back (apart from a Day 56 non-loaded construct lost during transportation) and stored at room temperature until analysed by histological and immunohistochemical staining.

Bovine osteochondral plugs (n=3) were used as positive and negative controls for Alcian blue/Sirius red staining and immunohistochemical staining (i.e. collagen type II and collagen type I). The tissue plugs were processed as per the experimental constructs (i.e. fixed,

embedded and sectioned) with the exception of being decalcified prior to being embedded. Decalcification was achieved by placing the tissue plugs in 14 % EDTA at room temperature with agitation for 3 weeks. Decalcification was validated by X-ray.

### **5.3.4 Histological Staining and Light Microscopy of Sectioned Constructs**

Histological staining was used to provide a visual impression on the gross distribution of different components present in each section and to some limited extent, an indication of the amount of such material within the section based on the staining density [297].

A staining combination of Alcian blue/Sirius red stains were used to highlight GAGs and collagen fibre distribution, respectively. The deeper the staining of Alcian blue and Sirius red, the greater the concentration of GAGs and collagen.

#### **5.3.4.1 Alcian Blue/Sirius Red Staining Methodology**

Sections were taken to water; firstly by clearing the paraffin wax with xylene for at least 5 mins before washing in absolute ethanol twice (5 mins each) and a final wash in water (1 min).

Sections were stained with Weigert's haematoxylin (Atom Scientific, Hyde, UK) for 10 mins to visualise cell nuclei, followed by a water step to remove excess stain. Sections were stained with Alcian blue (Merck Chemicals Ltd, Gillingham, UK, 1.01647.0500) for 10 mins. Excess stain was removed by a water wash (1 min). Sections were then stained with the Picosirius red kit (Polysciences Inc, Eppelhem, Germany), by placing in phosphomolybdic acid for 2 mins. Picosirius red stain was applied for 45 mins and followed by application 1N hydrochloride acid (HCl) for 2 mins and 70 % ethanol for 45 secs.

Sections were then dehydrated in two washes in absolute ethanol (5 mins each) and cleared in xylene for 5 mins. Finally, the sections were mounted in p-xylene bis-pyridinium bromide (DPX) (Sigma-Aldrich, Irvine, UK, 317616) before visualisation by the Olympus BX50 light microscope. Images were compiled using Nikon NIS-Elements software. Positive controls were produced using decalcified osteochondral plugs and proceeded as described in the above protocol.

#### **5.3.4.2 Immunohistochemistry and Light Microscopy of Sectioned Constructs**

Immunohistochemistry uses the principle of antibodies binding to a specific antigen to detect and localise target proteins within a histological sample [298]. When antibodies have been raised against a particular antigen, they will bind to that antigen. An antibody that is conjugated with a detectable molecule e.g. the fluorophore fluorescein, can localise the antigen.

Immunohistochemistry methodology used in this study adapted these basic principles in which primary and secondary antibodies were used. Primary antibodies specific to collagen type I and collagen type II were raised commercially in an animal host (e.g. mouse) and were provided

purified. The primary antibodies were applied to sections of the experimental tissue and allowed to bind to their target antigen. A secondary antibody, raised against the immunoglobulins of the specific animal host of the primary antibody was then applied to the sections in order to identify the first antibody in the sample. The secondary antibody was conjugated to horse radish peroxidase (HRP) permitting localisation of target proteins via light microscopy. Upon the completion of primary and secondary antibodies binding and incubation with a chromogenic substrate, a brown precipitate is formed at the site of bound antibodies which consequently localise the antigens under investigation.

Sections were taken to water; firstly by clearing the paraffin wax with xylene for at least 5 mins before washing in absolute ethanol twice (5 mins each) and a final wash in water (1 min).

Endogenous tissue peroxidase was blocked by immersion of sections in 2 % H<sub>2</sub>O<sub>2</sub> for 20 mins followed by a PBS wash. An antigen retrieval step took place by submerging the sections in boiled antigen unmasking solution for 5 mins (Vector Laboratories, Peterborough, UK, H-3301) for immunohistochemical staining of collagen type I and 0.1 % chymotrypsin at 37°C for 30 mins (within 0.1 % CaCl<sub>2</sub>, at pH 7.8) (Sigma-Aldrich, Irvine, UK, C4129) for immunohistochemical staining of collagen type II, followed by a PBS wash. Sections were then blocked with normal goat serum (Dako, Ely, UK, X0907) for 20 mins to reduce non-specific binding and washed with PBS. Following this, sections were incubated with a primary antibody overnight at 4°C. Primary antibodies used were raised against collagen type I (Abcam, Cambridge, UK, monoclonal ab6308) and collagen type II (Calbiochem, Nottingham, UK, monoclonal II-4C11) and were diluted at 1 in 50 and 1 in 600 respectively. Sections were then washed with PBS before incubation with secondary antibodies for 30 mins as per the EnVision™ kit's instructions ((Dako, Ely, UK, K5007). Once incubation was completed, sections were further washed with PBS and chromogenic substrate applied for 10 mins. Developed sections were washed with water, counterstained within Harris's Haematoxylin (ThermoScientific, Northumberland, UK, 6765002) for 3 mins, water washed and submerged in Scott's tap water for 2 mins before a final water wash.

Sections were then dehydrated in two washes in absolute ethanol (5 mins each) and cleared in xylene for 5 mins. Finally, the sections were mounted in DPX before visualisation by the Olympus BX50 light microscope. Images were compiled using Nikon NIS-Elements software.

Negative controls were generated using Day 56 construct and decalcified osteochondral plug sections by omitting the primary antibody step from the above protocol and then proceeding as described. Positive controls were produced using decalcified osteochondral plugs and proceeded as per the experimental constructs. For osteochondral plugs, articular cartilage was used as a collagen type II positive tissue; subchondral bone was used as a collagen type I positive tissue.

### **5.3.5 Live Cell Staining of Cell Nuclei and Plasma Membrane for Synoviocytes within Constructs using Hoechst 33342 and CellMask Green Plasma Membrane**

Synoviocytes within loaded and non-loaded constructs were stained with Hoechst 33342 and CellMask green plasma membrane in order to visualise cell nuclei and plasma membrane as described in Section 3.3.2.3. In brief, a combined staining working solution of 1 µg/mL Hoechst 33342 and 1x CellMask green plasma membrane was freshly prepared with DMEM/F12 medium and applied to samples placed in a 24-well cell culture plate. The plate was covered with aluminium foil to protect it from the light and incubated at 37°C and 5 % CO<sub>2</sub> for 40 mins. Constructs were then washed three times in Live Cell Imaging Solution. Following on from the wash step, diluted ProLong Live Antifade Reagent was applied to samples which were then incubated in the dark at 37°C for 2 hrs before visualisation via the Nikon A1R confocal microscope.

### **5.3.6 Confocal Imaging Acquisition of Selected Synoviocytes in Constructs Following Staining after the Addition of ProLong™ Live Antifade Reagent**

Volume images of synoviocytes within the constructs were acquired using the Nikon A1R inverted confocal microscope. The 405-nm Solid state and 488-nm Argon lasers were used to excite Hoechst 33342 and CellMask green plasma membrane stains, respectively. Lasers were set at 5 % of full power and the pinhole at 1 Au. Unidirectional galvo scanning and channel series were used to capture all images. Synoviocytes from the central region of the tissue surface were randomly selected at a depth of 20-30 µm inside the tissue. Volume images were recorded by taking serial optical sections of 512 x 512 pixels at 0.2 µm intervals with a 40x oil immersion objective (S Fluor 1.30 NA). A total of five constructs from each loaded and non-loaded groups were imaged.

### **5.3.7 Application of Compressive Strain to Synoviocyte/PET Scaffold Constructs**

The mechanical loading regime developed by Finlay *et al.* (2016) [1] that was used to create high modulus cartilage-like constructs was hypothesised to be a self-regulating system driven by the maturation of the developing constructs themselves. In the early stage of construct development, the vast majority of the applied load would be taken by the silicone ring surrounding each construct but some load would be applied to the cells within the construct causing them to experience a physiologically relevant level of stress that induces an anabolic response [1]. Cells would react to this by upregulating the production and secretion of cartilage-like ECM in an attempt to “resist” the applied load [1]. As the construct continued to mature

with increased elaboration of cartilage-like ECM, this would cause an increase in both thickness and compressive stiffness [1]. The accumulation of new ECM would distribute the load away from the cells, thereby reducing cellular stress [1]. However, when the construct matures in this way, under the conditions of the bioreactor set up, a greater proportion of the 5 N load applied by the bioreactor plunger would be taken by the construct as well as increasing the strain applied [1]. Thus, as the stiffness and thickness of the construct increase, the stress and strain applied would also increase and remain at a level that promotes further load-distributing- matrix deposition [1]. This would continue until the majority of the load is taken by the construct and not the silicone ring [1]. At this point, the effect of mechanical loading on the construct would have reached a plateau and would mainly serve to maintain tissue composition, akin to the homeostasis of native articular cartilage [1]. Thus, Finlay *et al.* (2016) [1] proposed this to be a “self-adapting” mechanism.

In order to provide a better understanding of Finlay’s hypothesised mechanism in developing cartilage-like constructs and to address the relationship between applied tissue strain and cellular strain in constructs developed at different time points, it was proposed to examine cell deformation under the estimated strain applied by the bioreactor during mechanical loading (customised to each construct) and with a compressive strain of 28 % in loaded constructs. Non-loaded controls were also examined under the two strain levels at each time point (the estimated strain if it was placed under 5 N of load in the bioreactor and compressive strain of 28 %).

To determine the morphometric changes in synoviocytes within loaded and non-loaded constructs developed at different time points (Days 0, 28 and 56) under different magnitudes of uniaxial unconfined compressive tissue strain (the estimated amount of strain subjected to the constructs within the bioreactor during mechanical loading and 28 %), the compression device described in Chapter 2 was used. The thickness of the construct was first measured using the Bose ElectroForce 3200 mechanical testing machine. The mechanical testing rig was set up to determine the zero displacement point as described in Section 2.4.2.3. In brief, the top platen of the testing rig was lowered at a rate of 0.2 mm/s towards the bottom platen until the two platens were brought together with a force of 100 N to establish a ‘zero displacement’ position, before being set 2.5 mm apart. The construct was then placed in a horizontal position between the two platens and the top platen was lowered at a rate of 0.2 mm/s until the load signal read a tare load of 0.02N. The distance between the two platens at this tare load was defined as the construct thickness.

To determine the estimated strain applied to the construct when placed under 5 N of load in the bioreactor, each construct was mechanically tested under a load of 5 N within the confines of the corresponding silicone ring that was used during mechanical loading in the case of the loaded constructs and during static chondrogenic culture for non-loaded constructs (as described in Section 5.2.2). The construct, along with the silicone ring, were placed within the Instron

ElectroPuls™ E3000 mechanical testing rig which was set up as described in Section 5.3.2. However, the top platen in the set up was replaced by a bioreactor plunger. Between the space of the plunger and the bottom platen, a column of PBS was formed in which the construct-silicone ring was held in a horizontal position centrally to the space. The combined construct-silicone ring was then subjected to a static compressive load of 5 N, therefore mimicking the loading inside the bioreactor. The resulting displacement was recorded and the deformed thickness was obtained. The estimated strain percentage subjected to the construct under 5 N load within the bioreactor during mechanical loading was calculated by the deformation (the original construct thickness minus the resulting deformed thickness under 5 N load) divided by the original construct thickness times a hundred. The amount of compressive displacement required to be applied to the construct surface by the micrometer in the compression device to yield the estimated strain subjected to the constructs during mechanical loading was determined as the amount of deformation under 5 N load.

To determine the final compressed thickness that corresponded to tissue strain of 28 %, the amount of compressive displacement required to be applied by the micrometer to the tissue surface was calculated knowing the construct thickness. For example, 28 % strain of a construct with thickness of 2 mm would correspond to a deformation of 560 µm, which would correspond to a compressed height of 1440 µm. Thus, 560 µm of displacement would be applied to the construct using the micrometer.

In chapter 2, it was determined that the coverslip used in the compression device would undergo flexion during load application and it was important to take this into account when calculating the load required to compress the construct. To achieve this, each construct was placed in between the two platens of the Bose ElectroForce 3200 mechanical testing machine and the top platen was lowered at a rate of 0.2 mm/s until the load signal read a tare load of 0.02 N. The construct was then subjected to loads up to 700 g at a rate of 50 g/s, whilst recording the displacement at 200 Hz. The amount of load required to apply selected compressive tissue strains (the estimated strain applied by the bioreactor during mechanical loading or 28 %) specifically to each construct was then determined from the construct displacement/ load data. To determine the amount of displacement attributable to the coverslip flexes, the displacement that corresponded to the load required to apply the selected compressive strain to the construct was read from the standard curve of displacement/load for the coverslip (see chapter 2). The amount of displacement caused by coverslip flexion was added on top of the compressive displacement that corresponds to selected tissue strain in order to compensate for the glass flexion effect.

The compression device was set up as described in Section 2.3.3 for tissue strain application. As demonstrated in Figure 43 in Section 4.3.5, all the components, such as a well with an opening at the bottom, a coverslip, a platen, a magnetic disk, a brace, metal screws and a micrometer,

assembled to form the compression device in which attached to the Nikon AIR confocal microscope stage. In brief, the coverslip was attached to the bottom of the device well using silicone grease. The individual stained construct was placed on the coverslip before filling the well with diluted ProLong live antifade reagent in Live Cell Imaging Solution to maintain hydration and cell viability during imaging. To assemble the top half of the device, the micrometer was fixed onto the brace by a small screw along with the platen that was connected to the micrometer by a magnetic disk. The top half of the device was secured to the well via the brace by two metal screws. The experimental procedure used to compress the tissue engineered construct and image selected synoviocytes in the uncompressed state and during selected compressive tissue strains (the estimated strain applied by the bioreactor during mechanical loading or 28 %) is shown in Figure 80. To define the '0 % strain' position (the uncompressed state), the platen was lowered by the micrometer to the distance equal to the construct thickness. This position was held for 30 mins before compressive strains were applied. Synoviocytes from the central region of the construct were randomly selected at a depth of 20-30  $\mu\text{m}$  inside the tissue. Volume images of the selected synoviocytes in the non-loaded state were captured prior to application of compression. Approximately 40 to 50 synoviocytes were typically captured in the field of a volume image. A compressive tissue strain equal to the estimated strain applied to each construct by the bioreactor during mechanical loading (including compensation for additional coverslip flexion displacement) was then applied in a direction parallel to the tissue surface, using the micrometer. The construct was allowed to equilibrate for 30 mins and volume images were recorded of the synoviocytes which were randomly selected from the central region of the tissue. The construct was then further compressed by manual turning of the micrometer to yield a compressive strain of 28 % and allowed to reach equilibrium for 30 mins before synoviocytes were again randomly selected from the central region of the construct for the final capture of volume images. Different populations of synoviocytes were selected and imaged in the uncompressed state and during the two levels of applied strain because it was not possible to track the same synoviocytes throughout each procedure as the constructs were highly cellular and the cells were densely packed within the constructs developed at the early time points (Days 0 and 28). A total of five constructs from each loaded and non-loaded group at each time point (Days 0, 28 and 56) were compressed and imaged using this experimental procedure.

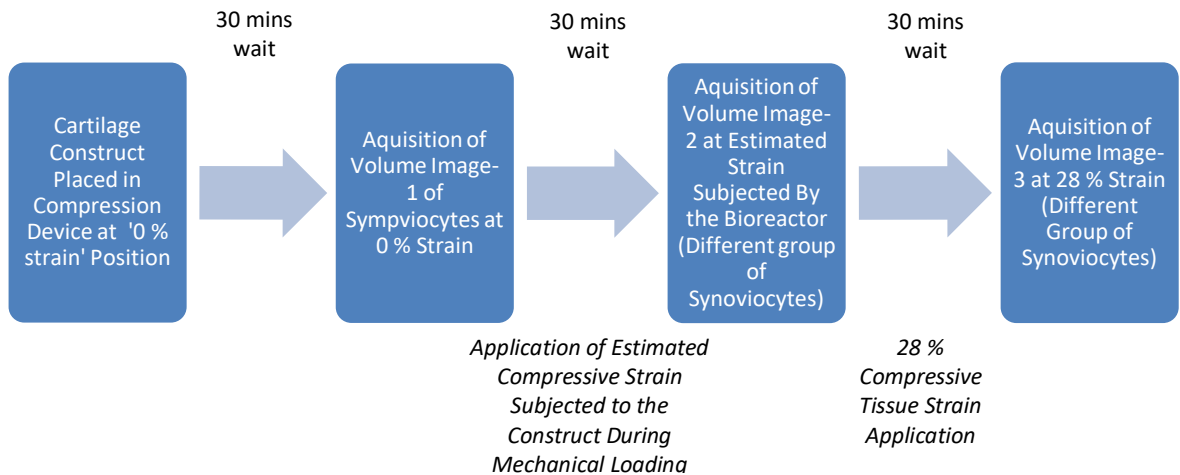


**Figure 80: Flow diagram of the experimental procedure used to sequentially image synoviocytes in the tissue engineered constructs in the uncompressed state and during estimated compressive strain subjected to the construct during mechanical loading and 28 % compressive tissue strain.**

### 5.3.8 Confocal Image Analysis

#### 5.3.8.1 Quantification of Synoviocyte Deformation

Amira software was used for quantification of any morphometric changes of synoviocytes in constructs under different conditions of loading. A custom workflow, specifically developed by the author, was used to analysis 3D confocal volume images of cells and perform cell morphometric measurements in order to quantify cell deformation behaviour under incremental compressive strains (see Section 4.3.6.2 for full methodology). The custom workflow was created by selecting and combining several modules used for image processing, cells identification and data analysis (i.e. 3D rendering and cell morphology measurements on the identified cells). For cell deformation quantification on volume images of synoviocytes acquired under different magnitudes of compressive strains in this Chapter, the *'Border Kill'* module in the workflow (as described in Section 4.3.6.2) was excluded. In brief, volume images of synoviocytes were converted to 16 Bit greyscale TIFF images and separated into two image stacks of the nuclei and plasma membrane prior to importing them to Amira software. Image voxel size was set and the custom workflow was then applied on the image stacks to perform 3D reconstruction and morphometric measurements of synoviocytes.

First, images were smoothed using a Gaussian filter to reduce noise and preserve cell edges, followed by interactive thresholding for image segmentation in order to identify and label the nuclei and the plasma membrane (cell boundaries), respectively. Image sets were further processed by applying modules such as the *'Fill Holes'* and *'Remove Small Spots'* modules to fill incompletely labelled objects i.e. the nuclei or plasma membrane in their respective image sets and eliminate extraneous objects too small to be the nuclei and cells, respectively. Once

both image stacks were processed through the workflow by each module in order, they were then merged together by using the 'Arithmetic' module to create a binary image that highlights the nuclei and plasma membrane of synoviocytes. The next stage was to identify and select synoviocytes from the process, merged image stack for 3D rendering and morphometric quantification analysis. However, this was not a straight forward task; synoviocytes within the constructs were highly confluent and present in tight, dense collections of cells and consequently many of them touched and overlapped each other which made it difficult to recognise and separate them as individual synoviocytes. An extra step was conducted to segment synoviocytes from other touching synoviocytes by manually defining dividing lines with the use of the 'lasso tool' from the Image Segmentation Editor of Amira on each synoviocyte on every 2D image that made up the 3D data. Once clear cell boundaries were refined, the plasma membrane and the corresponding nuclei were selected and registered as synoviocytes (Yellow boundaries, Figure 81). The identified synoviocytes were then extracted to create a label image stack for 3D rendering and cell morphometric measurements.



**Figure 81: XY-orthoslices of the processed, merged image stack which highlights the boundaries of the potential nuclei (blue) and plasma membrane (green). Synoviocytes segmented from other touching synoviocytes with the use of the lasso tool and registered as synoviocytes (yellow boundaries) for 3D rendering and cell morphometric measurements.**

A 'Volume Rendering' module was used for 3D reconstruction of selected synoviocytes for 3D visualisation purpose (Figure 82). The 'Label Analysis' module was used to carry out cell morphometric measurements on the identified synoviocytes. Morphometric parameters, including cell length, width, height, volume and sphericity were selected to determine cell deformation behaviour in loaded and non-loaded constructs under incremental compressive strains.

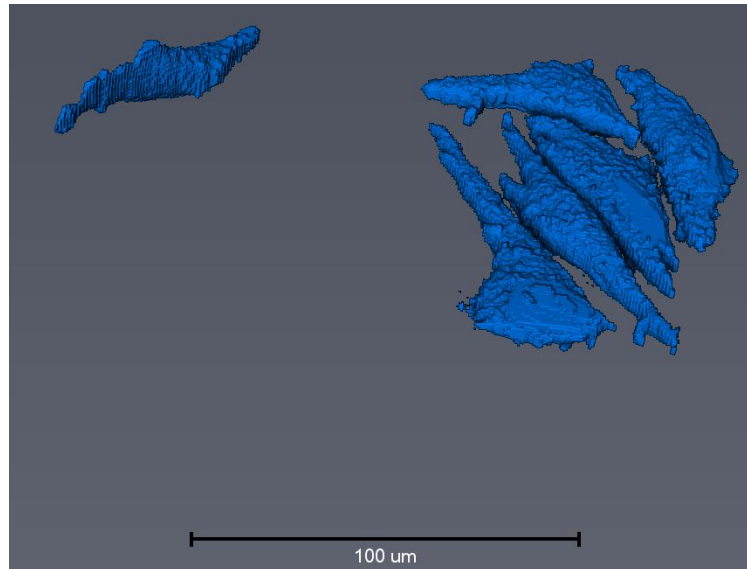


**Figure 82: 3D rendering of selected synoviocytes from the label image for 3D shape visualisation purpose.**

However, morphometric measurements were performed only on loaded and non-loaded constructs at time point Day 56 because it was not possible to identify cell edges in constructs at early time points (Day 0 and 28) due to the high density of cells within those constructs as is evident in the confocal images (Figure 103-105). Where measurements were possible, 10 synoviocytes were selected from confocal images of each construct (two constructs from each loaded and non-loaded groups) in the uncompressed state, during estimated strain experienced by the constructs during mechanical loading and applied strain of 28 % for morphometric measurements.

## **5.4 Results**

### **5.4.1 Collagen, Sulphated Glycosaminoglycan and DNA Content of Synoviocyte/PET Constructs Subjected to Compressive Mechanical Loading**

The effect of mechanical loading on the biochemical composition and cellularity of maturing constructs was determined by measuring their collagen, sGAG and DNA content measured using HYP, DMMB and PicoGreen assays respectively.

From Day 0 to Day 56, there was a significant increase in the collagen content for both loaded and non-loaded constructs with no apparent differences between the two groups at each time point throughout the entire culture period ( $p < 0.05$ , Figure 83). Compared with native cartilage, the constructs had less collagen content (Figure 83).

The sGAG content of both loaded and non-loaded constructs significantly increased between Day 0 and Day 28 ( $p < 0.001$  and  $p < 0.05$ , Figure 84). No statistical differences in sGAG content were seen between loaded and non-loaded constructs at any of the time points. Native cartilage had a significantly greater amount of sGAG compared to the constructs at any time point (Figure 84).

The cellular (DNA) content of non-loaded constructs significantly increased within the first 28 days of culture and continued at an elevated level for the remaining culture period (to 56 days) but was not statistically different to that at Day 28 ( $p < 0.05$ , Figure 85). For loaded constructs, there was also significant increase in DNA content throughout the entire 56 days of culture ( $p < 0.01$ , Figure 85). Loaded constructs had significant greater amount of DNA than non-loaded constructs at Day 28 and Day 56 ( $p < 0.001$  and  $p < 0.01$ , Figure 85). Native cartilage had significantly less DNA content than both loaded and non-loaded constructs, apart from at Day 0 (Figure 85).

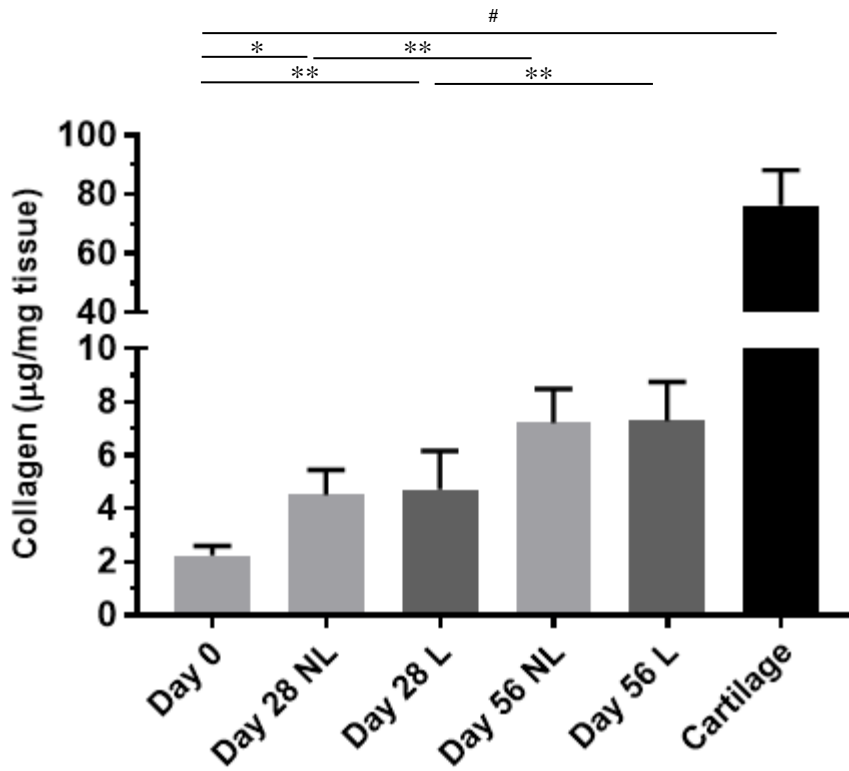


**Figure 83: Collagen content of synoviocyte/PET constructs following pre-culture in chondrogenic medium for 4 weeks and then subjected to a mechanical loading regime for either 28 or 56 days. L ≡ Loaded (dark grey), NL ≡ Non-loaded constructs (light grey) and Cartilage ≡ Native cartilage (black).**

No significant differences were seen between loaded and non-loaded constructs at each individual time point. Significant increase in collagen content was observed from Day 0 to Day 56 in both loaded and non-loaded constructs. The collagen content in native cartilage was significant greater than the loaded and non-loaded constructs. Data represented as means ± SD (n=6). Data was analysed by one way ANOVA. \* indicates significant difference in non-loaded and loaded constructs and # indicates significant difference in comparison with the native cartilage. \* ≡ p < 0.05, \*\* ≡ p < 0.01.

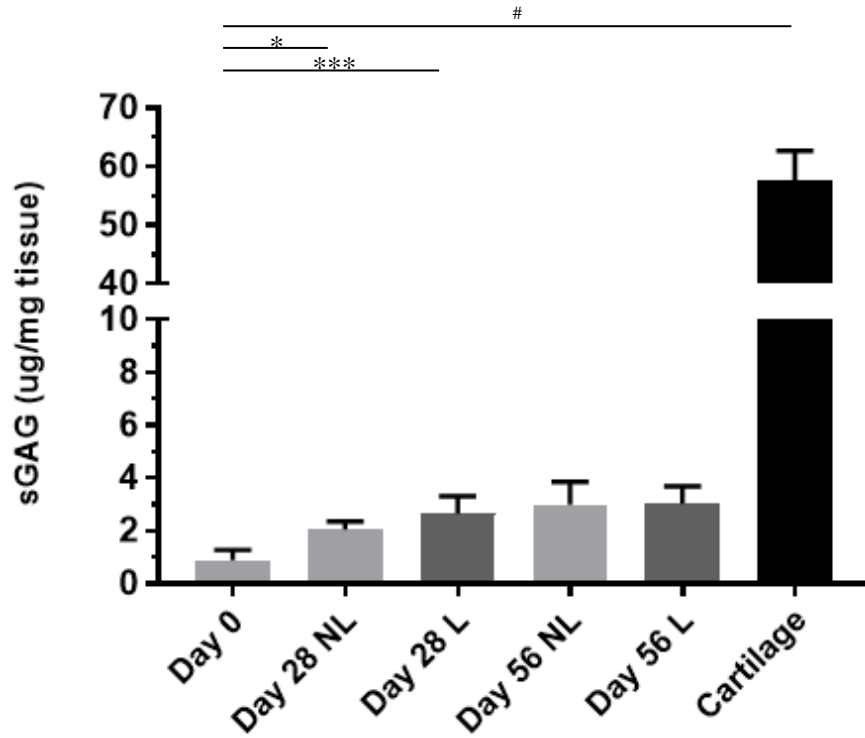


**Figure 84: sGAG content of synoviocyte/PET constructs following pre-culture in chondrogenic medium for 4 weeks and then subjected to a mechanical loading regime for either 28 and 56 days. L ≡ Loaded (dark grey), NL ≡ Non-loaded constructs (light grey) and Cartilage ≡ Native cartilage (black).**

No significant differences were seen between loaded and non-loaded constructs at each individual time point. Significant increase in sGAG content was observed from Day 0 to Day 28 in both loaded and non-loaded constructs. Native cartilage was associated with significantly greater sGAG content compared to both loaded and non-loaded constructs at each individual time point. Data represented as means  $\pm$  SD (n=6). Data was analysed by one way ANOVA. \* indicates significant difference in non-loaded and loaded constructs and # indicates significant difference in comparison with the native cartilage. \*  $\equiv$   $p < 0.05$ , \*\*\*  $\equiv$   $p < 0.001$ .

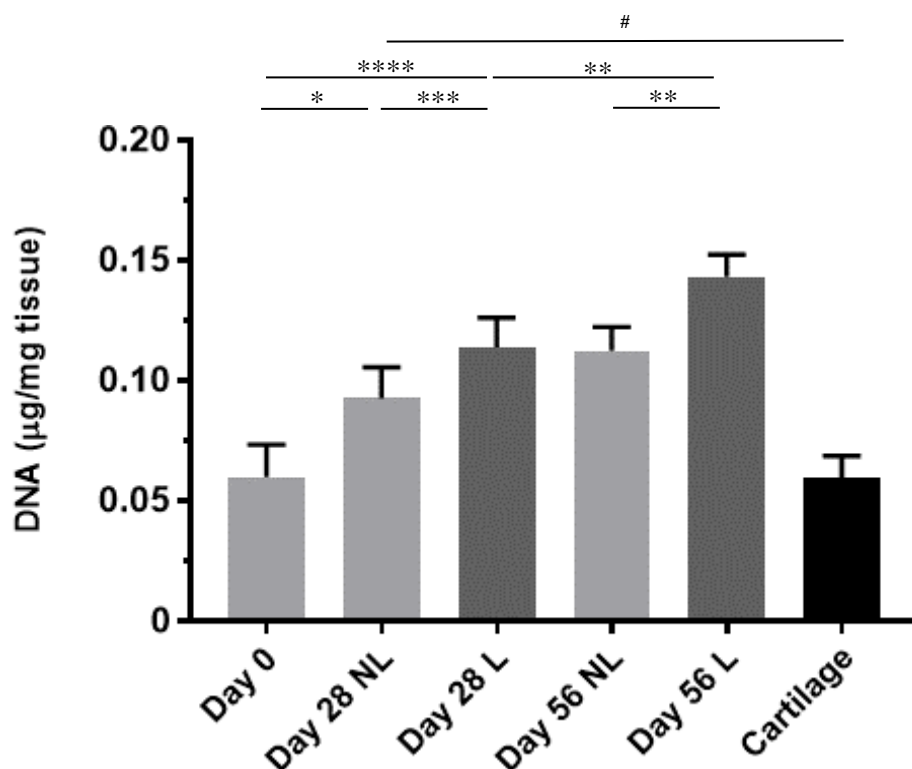


**Figure 85: DNA content of synoviocyte/PET constructs following pre-culture in chondrogenic medium for 4 weeks and then subjected to a mechanical loading regime for either 28 and 56 days. L ≡ Loaded (dark grey), NL ≡ Non-loaded constructs (light grey) and Cartilage ≡ Native cartilage (black).**

Significantly greater DNA content was seen in loaded constructs compared to non-loaded constructs at each individual time point. Significant increase in DNA content was observed from Day 0 to Day 28 in both loaded and non-loaded constructs and this continued to be statistically significant from Day 28 to Day 56 in loaded constructs. No significant differences were seen between native cartilage and constructs at Day 0 but DNA content in native cartilage was significant lower than in both loaded and non-loaded constructs at Day 28 and Day 56. Data represented as means ± SD (n=6). Data was analysed by one way ANOVA. \* indicates significant difference in non-loaded and loaded constructs and # indicates significant difference in comparison with the native cartilage. \* ≡ p < 0.05, \*\* ≡ p < 0.01, \*\*\* ≡ p < 0.001, \*\*\*\* ≡ p < 0.0001.

#### **5.4.2 Compressive Moduli of Pre-Cultured Synoviocyte/PET Constructs Subjected to Compressive Mechanical Loading**

In order to determine and compare the mechanical properties of the constructs that were subjected to compressive loading with those of non-loaded controls, the dynamic compressive moduli of the constructs were measured as previously described in Section 5.3.2. Stress-strain curves were then plotted from the displacement/force data, followed by best-fit exponential curves fitted to the plotted data and tangent moduli calculated at a strain value of 18 %.

Compressive modulus measured at 18 % strain of non-loaded and loaded synoviocyte/PET constructs following pre-culture in chondrogenic medium for 4 weeks and then subjected to a mechanical loading regime for either 28 and 56 days are shown in Figure 86 and summarised Table 2. At 18 % strain, the moduli of non-loaded constructs increased gradually at each time

point, from an average of  $0.07 \pm 0.01$  MPa at Day 0 to a mean of  $0.39 \pm 0.16$  MPa at Day 56 (Table 2). Loaded constructs had a significant increase in moduli at Day 28 (average of  $0.58 \pm 0.29$  MPa) ( $p < 0.01$ , Figure 86); these loaded constructs had a higher mean value at Day 56 ( $0.88 \pm 0.45$  MPa) but this was not significantly different to Day 28 (Table 2). Loaded constructs had greater moduli values than non-loaded constructs at each time point, with a significant difference observed at Day 56 ( $p < 0.01$ , Figure 86). At Day 28, loaded constructs had 2x greater moduli values than the non-loaded constructs and 2.3x at Day 56 (Figure 86). Thus, the greatest effect of mechanical loading on constructs compressive moduli occurred between Day 28 and Day 56.

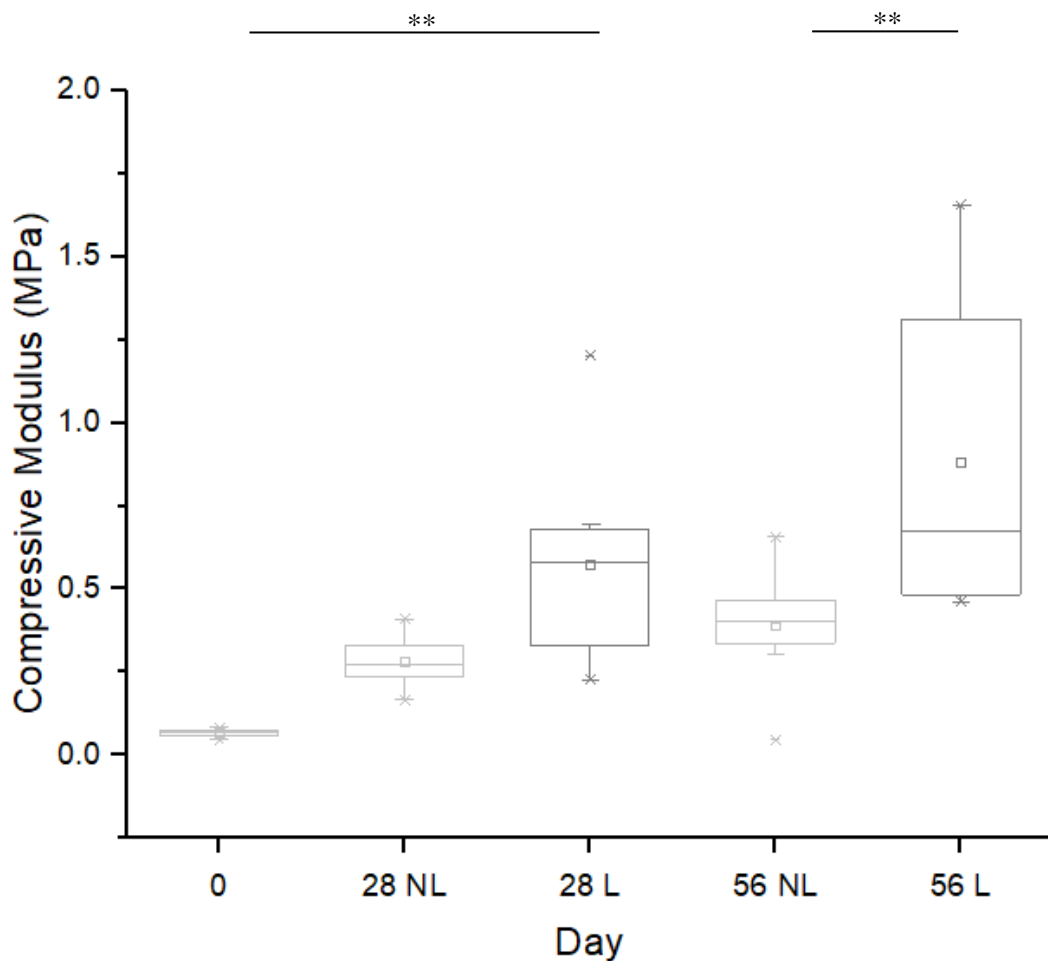


**Figure 86: Compressive moduli measured at 18 % strain for synovioocyte/PET constructs under 1 Hz 20 % cyclic strain following pre-culture in chondrogenic medium for 4 weeks and then subjected to a mechanical loading regime for either 28 and 56 days. L  $\equiv$  Loaded (dark grey) , NL  $\equiv$  Non-loaded constructs (light grey).**

No significant differences were observed between loaded and non-loaded constructs except for moduli of loaded constructs which was significantly greater at Day 56 compared with non-loaded constructs. Significant increase in moduli was observed from Day 0 to Day 28 in loaded constructs. Data was analysed by one way ANOVA. \*\*  $\equiv$   $p < 0.01$  ( $n=8$ ).

**Table 2: Tangential compressive modulus measured at 18 % strain of non-loaded and loaded synoviocyte/PET constructs following pre-culture in chondrogenic medium for 4 weeks and then subjected to a mechanical loading regime for either 28 and 56 days.**

	Non-loaded construct modulus at 18 % Strain ( $\pm$ SD) (MPa)	Loaded construct modulus at 18 % Strain ( $\pm$ SD) (MPa)
Day 0	0.067 ( $\pm$ 0.011)	0.067 ( $\pm$ 0.011)
Day 28	0.282 ( $\pm$ 0.07)	0.575 ( $\pm$ 0.288)
Day 56	0.389 ( $\pm$ 0.163)	0.882 ( $\pm$ 0.448)

### **5.4.3 Histology of Pre-Cultured Synoviocyte/PET Constructs Subjected to Compressive Mechanical Loading**

In order to identify matrix components and provide a visual impression of cellular and matrix distribution within the constructs, histological and immunohistochemical staining were used. A histological staining combination of Alcian blue/Sirius red was used to visualise sGAG and collagen, respectively, and immunohistochemistry was used to identify collagen Type I and collagen Type II. Collagen Type II and high levels of sGAG are classical markers for cartilage, detection of their presence would support the deposition of cartilage-like matrix [25], [299]. Collagen Type I is not found in cartilage (with the exception of small quantities at the superficial layer) [300] and was therefore used as a negative maker.

As a control, the histological appearance of a decalcified bovine osteochondral plug, probed with antibodies for collagen type I or collagen type II is shown in Figure 87. Collagen type II staining was observed in the articular cartilage (Figure 87A), as would be expected. Staining for collagen type II was not seen in the bone (Figure 87A), again, as would be expected. Collagen type I staining was observed in the bone and not seen on the articular cartilage layer (Figure 87C), also as would be expected. There was no evidence of co-localisation of the two antibodies. The results showed that the antibodies were reacting in a specific manner and were therefore, suitable to use on experimental constructs.

Negative immunohistochemical control sections (where incubation of the primary antibody had been omitted) are shown in Figure 87B, Figure 87D and Figure 88. There was no visible staining present, indicating the wash steps and the secondary antibody procedure did not cause false positive staining.

The histological appearance of the loaded and non-loaded constructs at different time points (Day 0, 28 and 56) of the culture period are shown in Figure 89 to 102. The data are summarised below.

At Day 0 (i.e. after 4 weeks pre-culture in chondrogenic medium but before application of mechanical loading), a low level of staining was seen for collagen type I, collagen type II and with Alcian blue (Figure 89 to 91).

By Day 28, there was a noticeable increase in immunostaining for Collagen type II and in staining with Alcian blue in both loaded and non-loaded constructs, suggesting the deposition of cartilage-like matrix (Figure 92 to 98). However, the staining intensity for both Collagen type II and Alcian blue were still low in comparison to that seen in the native cartilage (Figure 87A and 87C). Staining for Collagen type II and Alcian blue was primarily found at the edges of the construct and either the top or bottom face of the construct (it was not possible to determine which way up the constructs had been position after processing), suggesting the laying down of cartilage-like matrix appeared to first occur at these regions of the construct. This was particularly apparent in one of the non-loaded constructs (Figure 93) and two of the loaded constructs (Figure 95 and Figure 97). Collagen type I immunostaining slightly increased throughout all constructs compared to those at Day 0. There were no discernible differences in staining between loaded and non-loaded construct by Day 28, apart from one of the non-loaded constructs having a considerably stronger staining intensity for collagen type II and Alcian blue than other constructs (Figure 93). In addition, with regards to construct shape, loaded constructs had a uniform shape (Figure 93 to 97) whilst non-loaded constructs were non-uniform (this is particularly evident in Figure 92 and Figure 94).

By Day 56, there was no discernible differences in any of the staining in non-loaded constructs compared with those at Day 28, with the exception that one of the non-loaded constructs displayed further increase in staining for Alcian blue at the periphery of the construct, as shown in Figure 98. There was slight increase in Alcian blue staining at Day 56 for loaded constructs compared to those at Day 28. Strong Alcian blue staining appeared around the circumferential edge of the loaded constructs (this is particularly evident in Figure 100 and Figure 102) and low level staining occurred in areas toward the cores of two of the constructs (Figure 100 and Figure 102). In addition, at Day 56 there were visible differences in histological appearance between loaded and non-loaded constructs. Loaded constructs had greater staining intensity than the non-loaded constructs at Day 56, apart from one non-loaded construct with strong Alcian blue staining at the surface, as seen in Figure 98. Both loaded and non-loaded constructs had a uniform shape but non-loaded construct thickness was considerably thicker than the loaded construct ones.

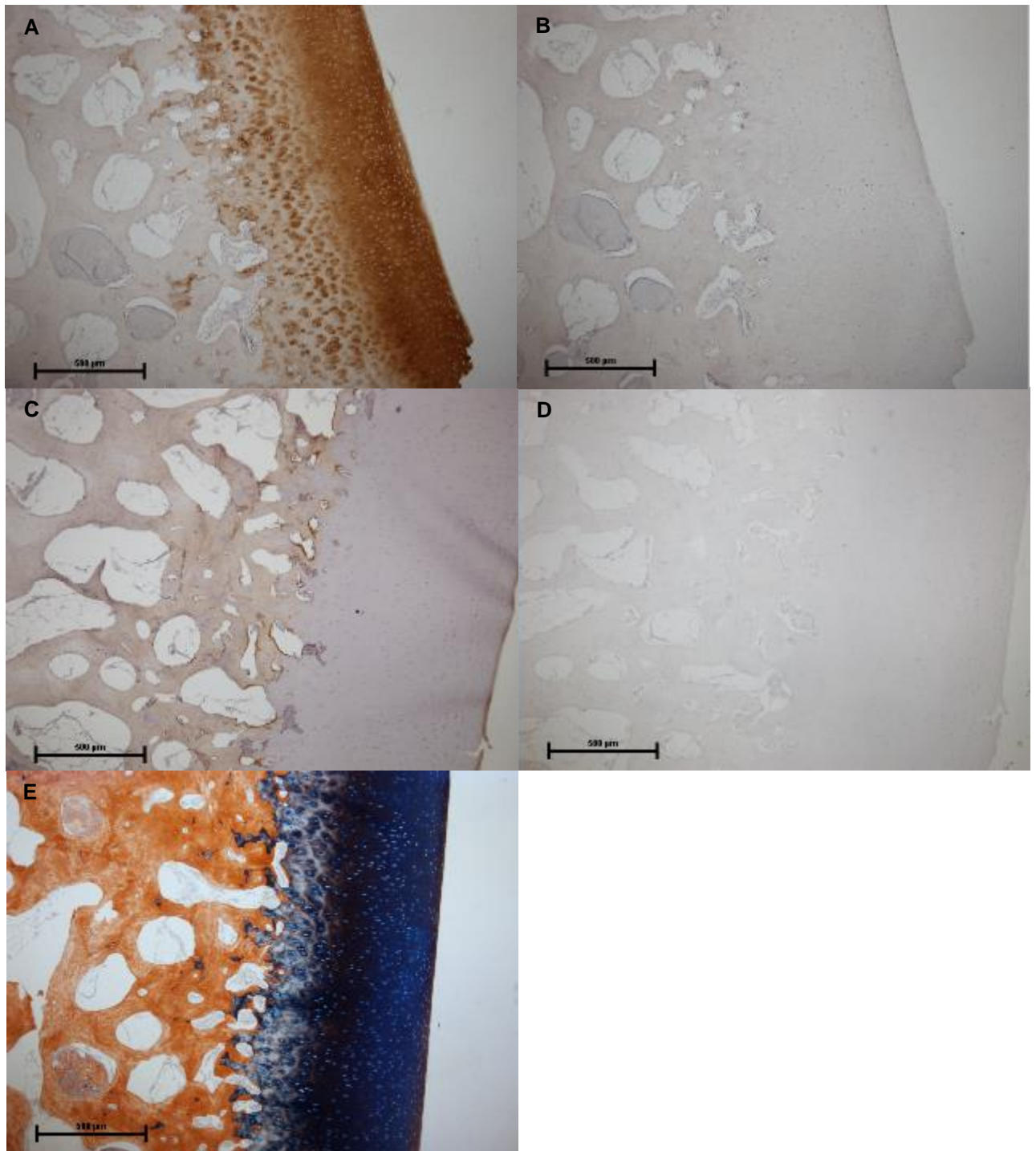


**Figure 87: Histological appearance of sections of decalcified bovine osteochondral plugs. Sections stained with (A) antibodies to Collagen type II, (C) antibodies to Collagen type I, (E) Alcian blue/Sirius red and without the inclusion of either (B) Collagen type II or (D) Collagen type I primary antibody.**

(A) Strong positive Collagen type II staining was seen for the articular cartilage and no staining in the subchondral bone, (B) no collagen type II staining was seen in either articular cartilage and subchondral bone for controls, (C) no Collagen type I staining was seen in articular cartilage but positive type I staining was evident in subchondral bone, (D) no Collagen type I staining was seen in either articular cartilage and subchondral bone in controls. Scale bar 500 µm, (E) strong Alcian blue staining of articular cartilage and strong Sirius red staining of subchondral bone were seen.

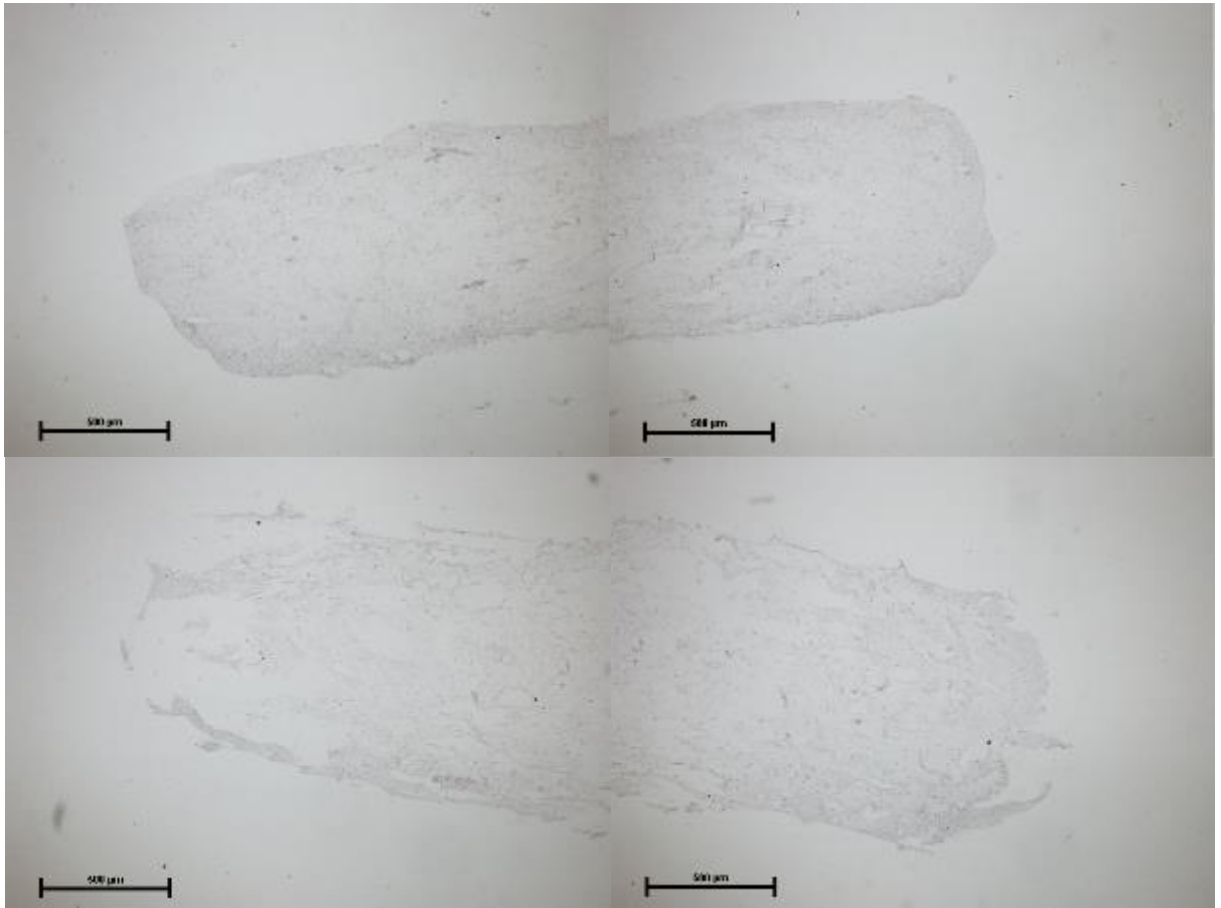


**Figure 88: Negative controls for immunochemistry. Histological appearance of sections from two constructs at Day 56 of mechanical loading stained without the inclusion of either Collagen type I or Collagen type II primary antibodies. Two images captured from each end of the constructs are collaged and shown in each case, representing the entire construct.**

There was a lack of staining throughout the sections, suggesting an absence of non-specific staining. Scale bar 500  $\mu\text{m}$ .

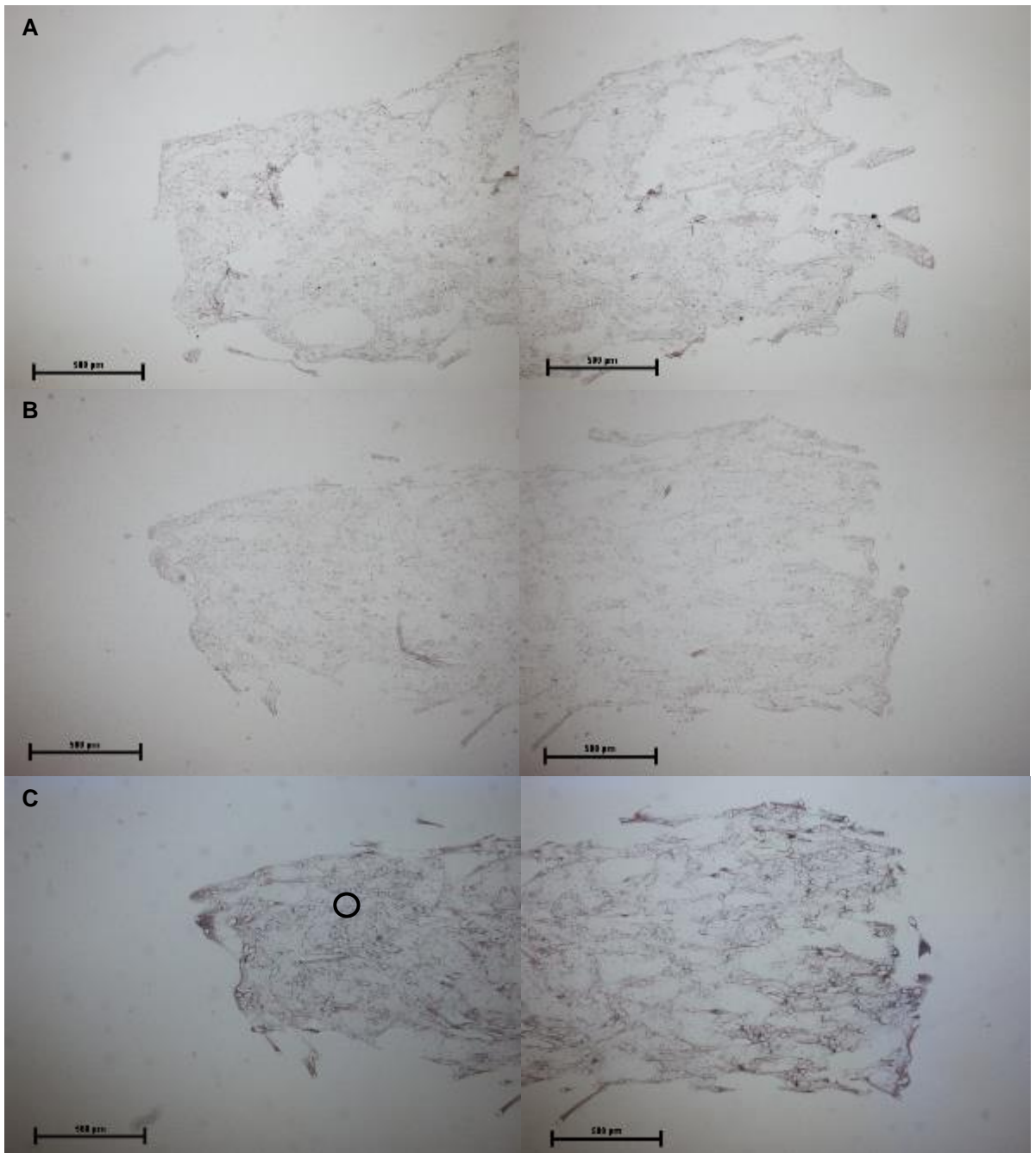


**Figure 89: Histological appearance of sections from a construct at Day 0 (Sample 1) after 4 weeks of pre-culture in chondrogenic medium (prior to application of mechanical loading). Sections stained with (A) antibodies to Collagen type I, (B) antibodies to Collagen type II and (C) Alcian blue/Sirius red. Two images captured from each end of the constructs are shown collaged in each case, representing the entire construct.**

There was no obvious immunostaining for both collagen types and a lack of blue or red staining in the Alcian blue/Sirius red stained sections. Circle highlighting PET scaffold fibre. Scale bar 500 µm.

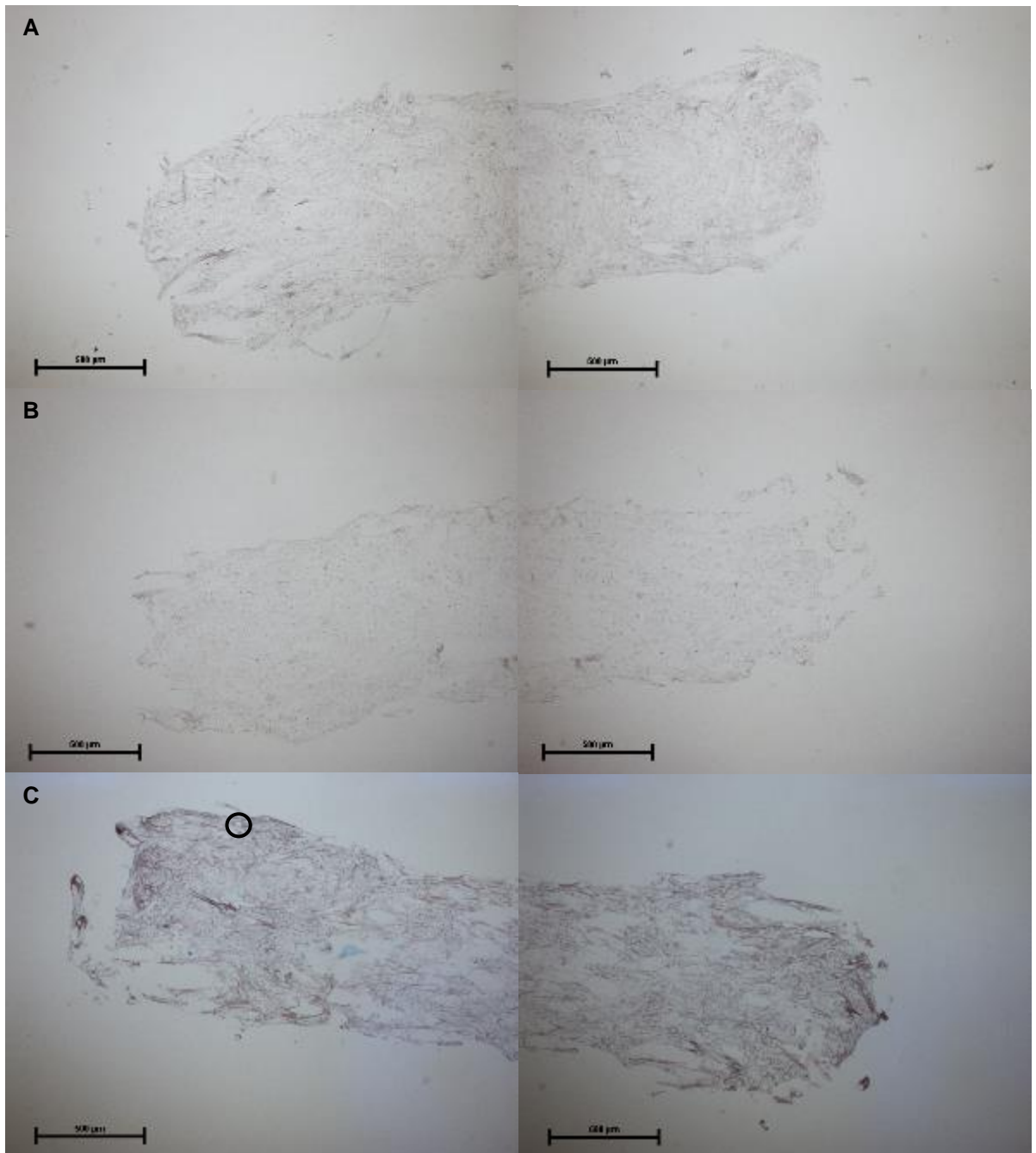


**Figure 90: Histological appearance of sections from a construct at Day 0 (Sample 2) after 4 weeks of pre-culture in chondrogenic medium (prior to application of mechanical loading). Sections stained with (A) antibodies to Collagen type I, (B) antibodies to Collagen type II and (C) Alcian blue/Sirius red. Two images captured from each end of the constructs are shown in each case, representing the entire construct.**

There was no obvious immunostaining for both collagen types and a lack of blue or red staining in the Alcian blue / Sirius red stained sections. Circle highlighting PET scaffold fibre. Scale bar 500 µm.

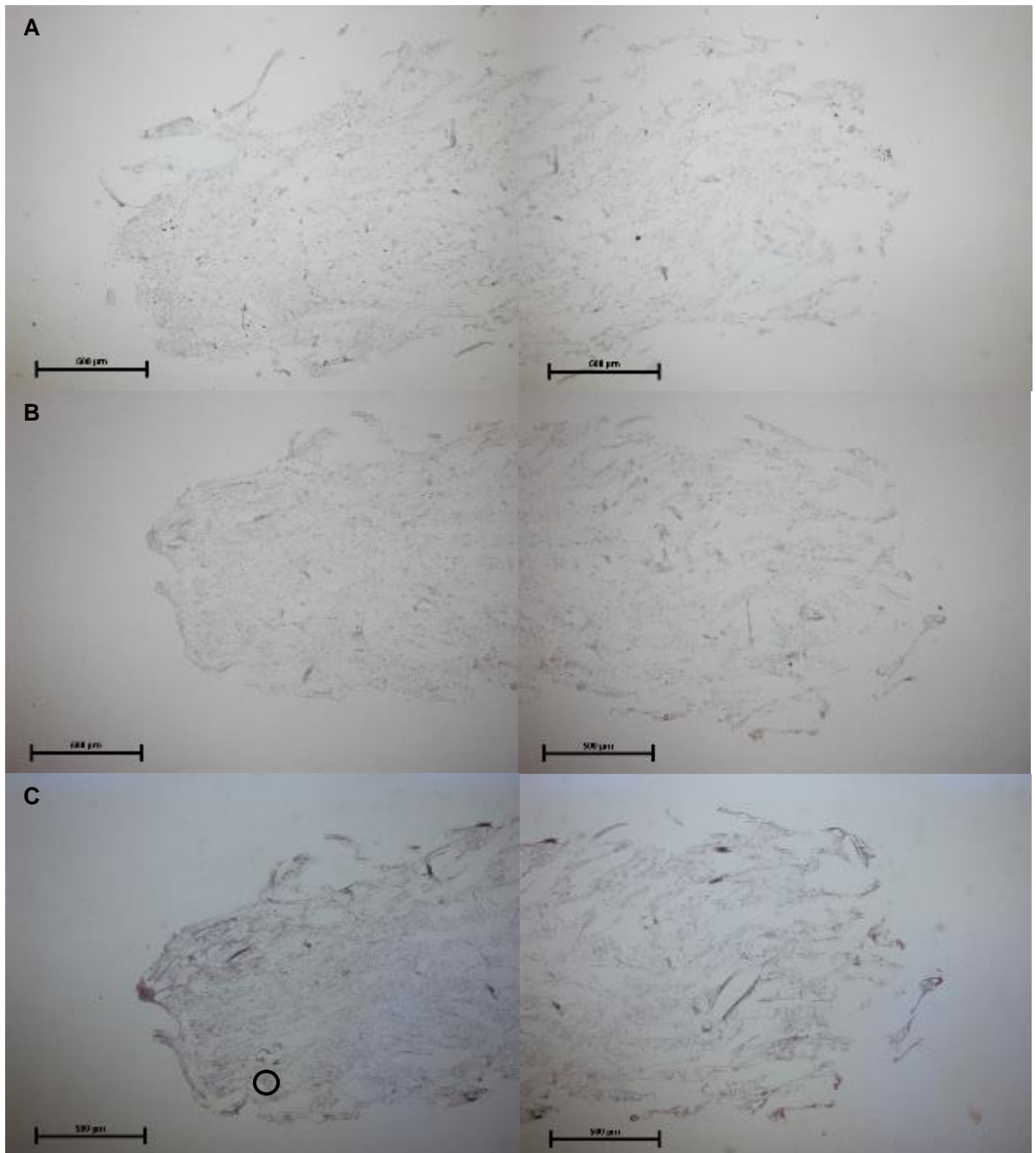


**Figure 91: Histological appearance of sections from a construct at Day 0 (Sample 3) after 4 weeks of pre-culture in chondrogenic medium (prior to application of mechanical loading). Sections stained with (A) antibodies to Collagen type I, (B) antibodies to Collagen type II and (C) Alcian blue / Sirius red. Two images captured from each end of the constructs are shown collaged in each case, representing the entire construct.**

There was no obvious immunostaining for both collagen types and a lack of blue or red staining in the Alcian blue / Sirius red stained sections. Circle highlighting PET scaffold fibre. Scale bar 500 µm.

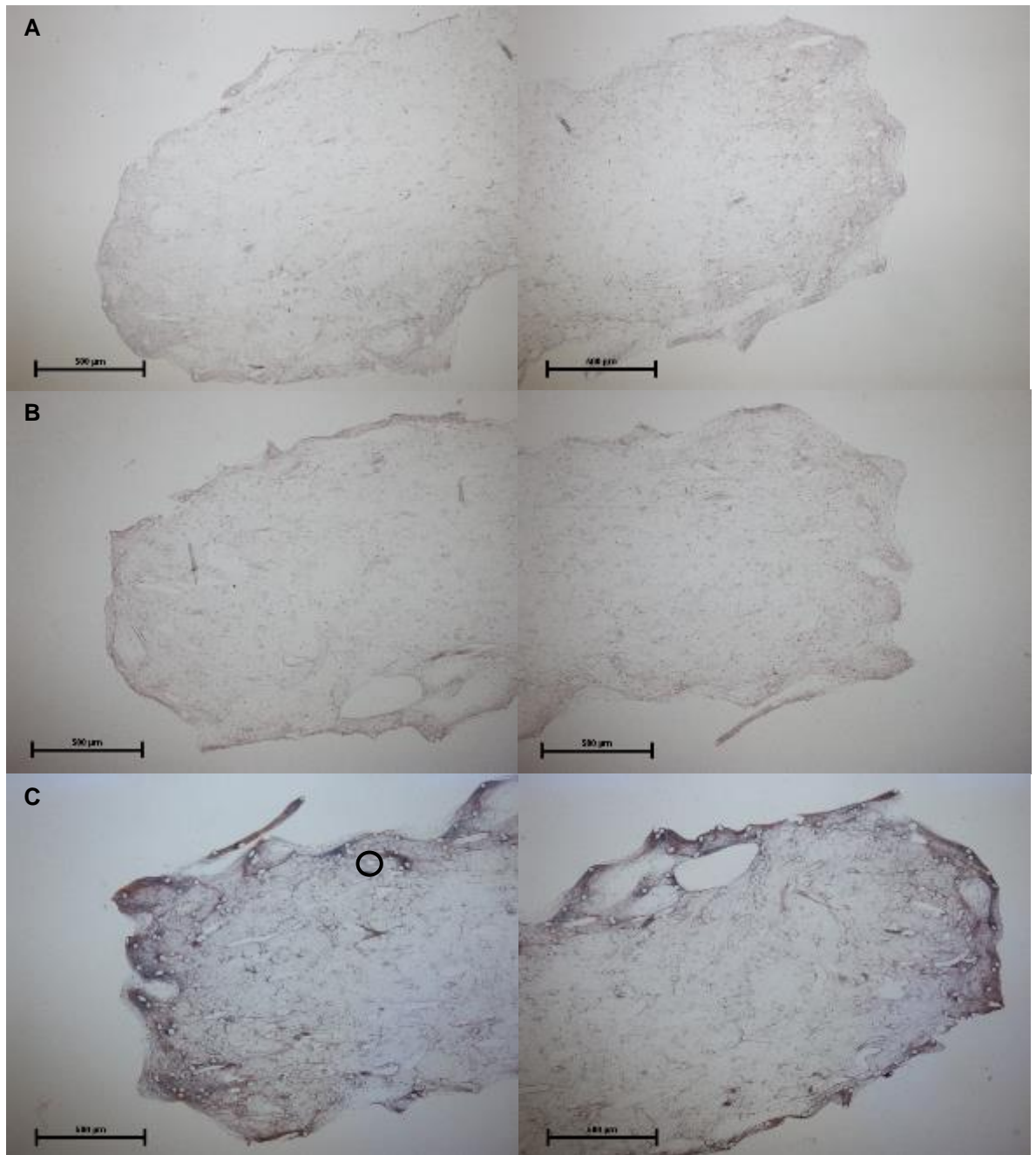


**Figure 92: Histological appearance of sections from a non-loaded construct at Day 28 (Sample 1) of culture without the presence of mechanical loading. Sections stained with (A) antibodies to Collagen type I, (B) antibodies to Collagen type II and (C) Alcian blue / Sirius red. Two images captured from each end of the constructs are shown collaged in each case, representing the entire construct.**

There was a slight increase in staining for collagen type II and Alcian blue, compared to constructs at Day 0. Also note the non-uniform cross-sectioned shape. Circle highlighting PET scaffold fibre. Scale bar 500 µm.

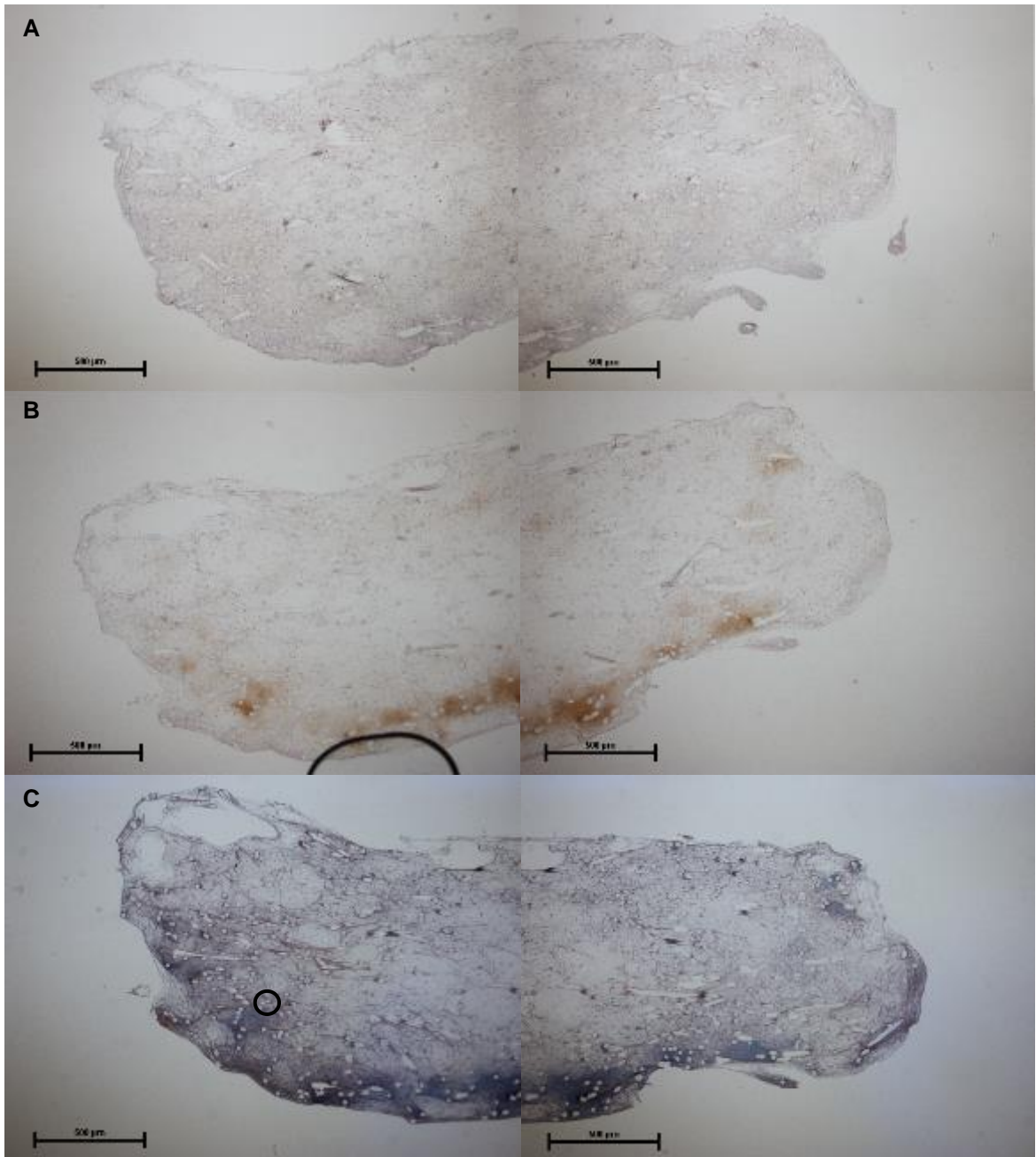


**Figure 93: Histological appearance of sections from a non-loaded construct at Day 28 (Sample 2) of culture without the presence of mechanical loading. Sections stained with (A) antibodies to Collagen type I, (B) antibodies to Collagen type II and (C) Alcian blue / Sirius red. Two images captured from each end of the constructs are shown collaged in each case, representing the entire construct.**

There was an increase in staining for collagen type II and Alcian blue, compared to constructs at Day 0. Also note the non-uniform cross-sectioned shape. Circle highlighting PET scaffold fibre. Scale bar 500 µm.

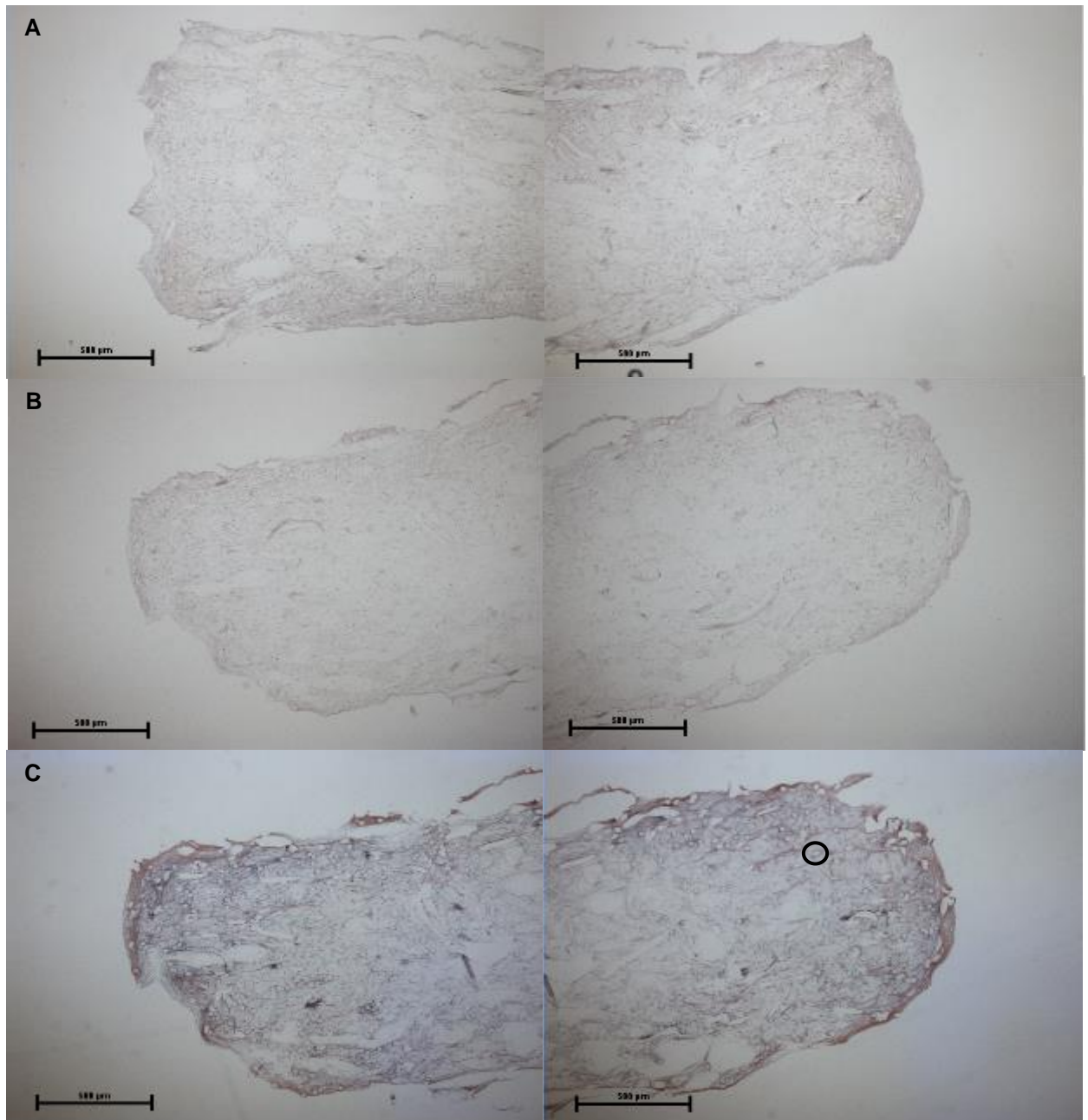


**Figure 94: Histological appearance of sections from a non-loaded construct at Day 28 (Sample 3) of culture without the presence of mechanical loading. Sections stained with (A) antibodies to Collagen type I, (B) antibodies to Collagen type II and (C) Alcian blue / Sirius red. Two images captured from each end of the constructs are shown collaged in each case, representing the entire construct.**

There was a slight increase in staining for collagen type II and Alcian blue, compared to constructs at Day 0. Also note the non-uniform cross-sectioned shape. Circle highlighting PET scaffold fibre. Scale bar 500 µm.

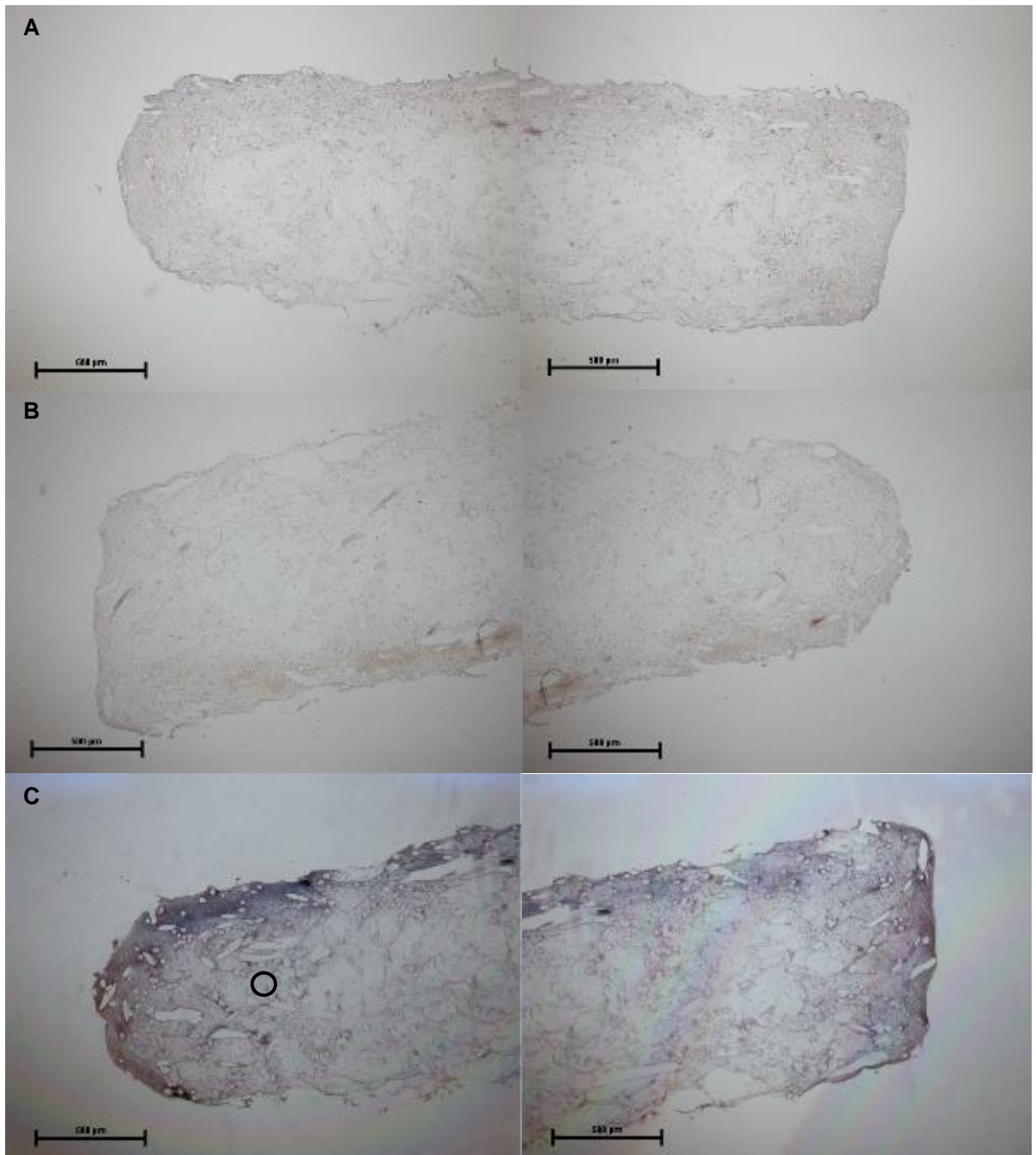


**Figure 95: Histological appearance of sections from a loaded construct at Day 28 (Sample 1) of culture with the presence of mechanical loading. Sections stained with (A) antibodies to Collagen type I, (B) antibodies to Collagen type II and (C) Alcian blue / Sirius red. Two images captured from each end of the constructs are shown collaged in each case, representing the entire construct.**

There was a slight increase in staining for collagen type II and Alcian blue, compared to constructs at Day 0. Circle highlighting PET scaffold fibre. Scale bar 500  $\mu\text{m}$ .

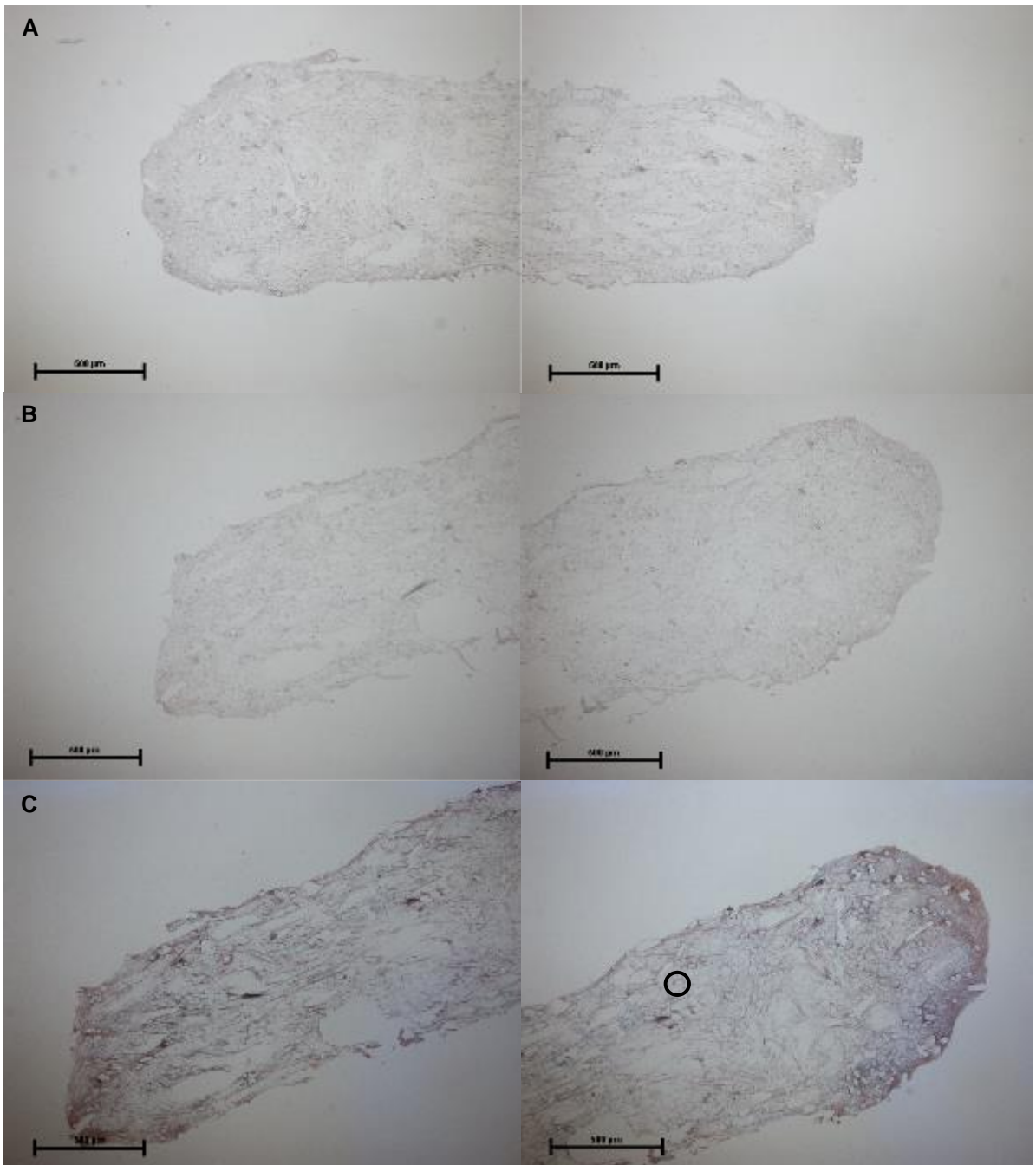


**Figure 96: Histological appearance of sections from a loaded construct at Day 28 (Sample 2) of culture with the presence of mechanical loading. Sections stained with (A) antibodies to Collagen type I, (B) antibodies to Collagen type II and (C) Alcian blue / Sirius red. Two images captured from each end of the constructs are shown in each case, representing the entire construct.**

There was a slight increase in staining for collagen type II and Alcian blue, compared to constructs at Day 0. Circle highlighting PET scaffold fibre. Scale bar 500 µm.

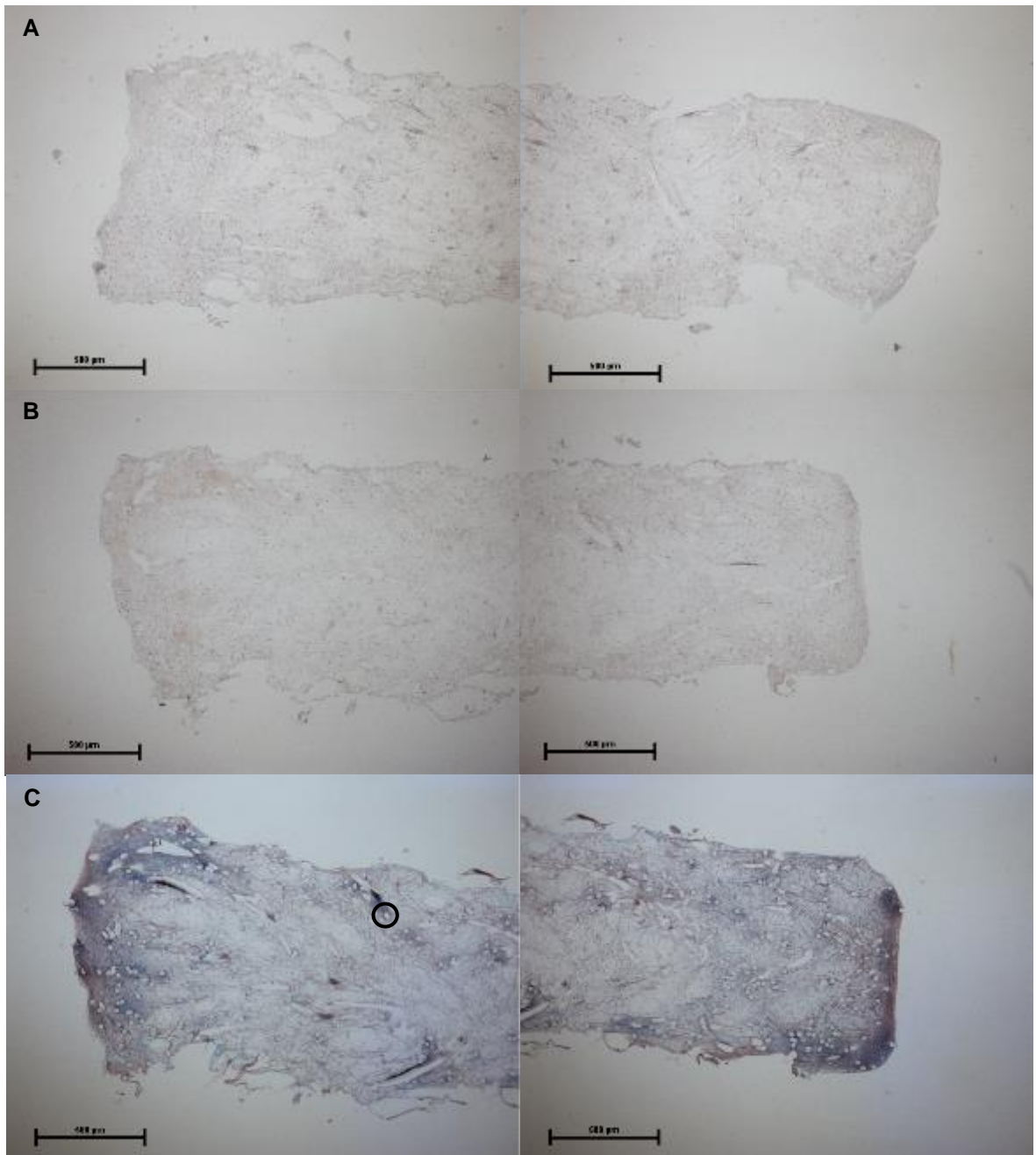


**Figure 97: Histological appearance of sections from a loaded construct at Day 28 (Sample 3) of culture with the presence of mechanical loading. Sections stained with (A) antibodies to Collagen type I, (B) antibodies to Collagen type II and (C) Alcian blue / Sirius red. Two images captured from each end of the constructs are shown collaged in each case, representing the entire construct.**

There was a slight increase in staining for collagen type II and Alcian blue, compared to constructs at Day 0. Circle highlighting PET scaffold fibre. Scale bar 500  $\mu\text{m}$ .

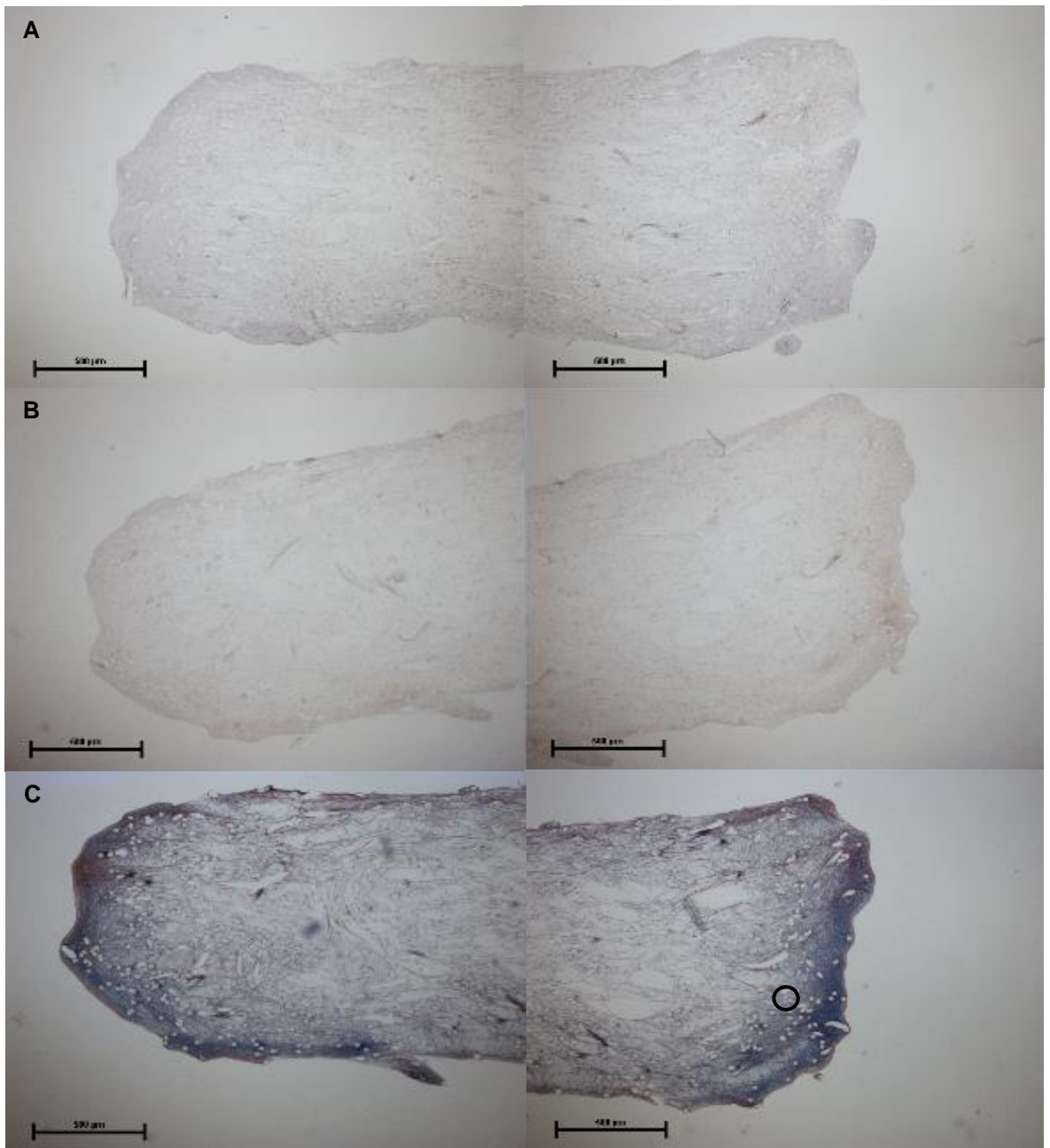


**Figure 98: Histological appearance of sections from a non-loaded construct at Day 56 (Sample 1) of culture without the presence of mechanical loading. Sections stained with (A) antibodies to Collagen type I, (B) antibodies to Collagen type II and (C) Alcian blue / Sirius red. Two images captured from each end of the constructs are shown collaged in each case, representing the entire construct.**

Further increased staining for Alcian blue and similar staining intensity for collagen type II, together with increased construct thickness, in comparison to Day 28 can be seen. Circle highlighting PET scaffold fibre. Scale bar 500 µm.

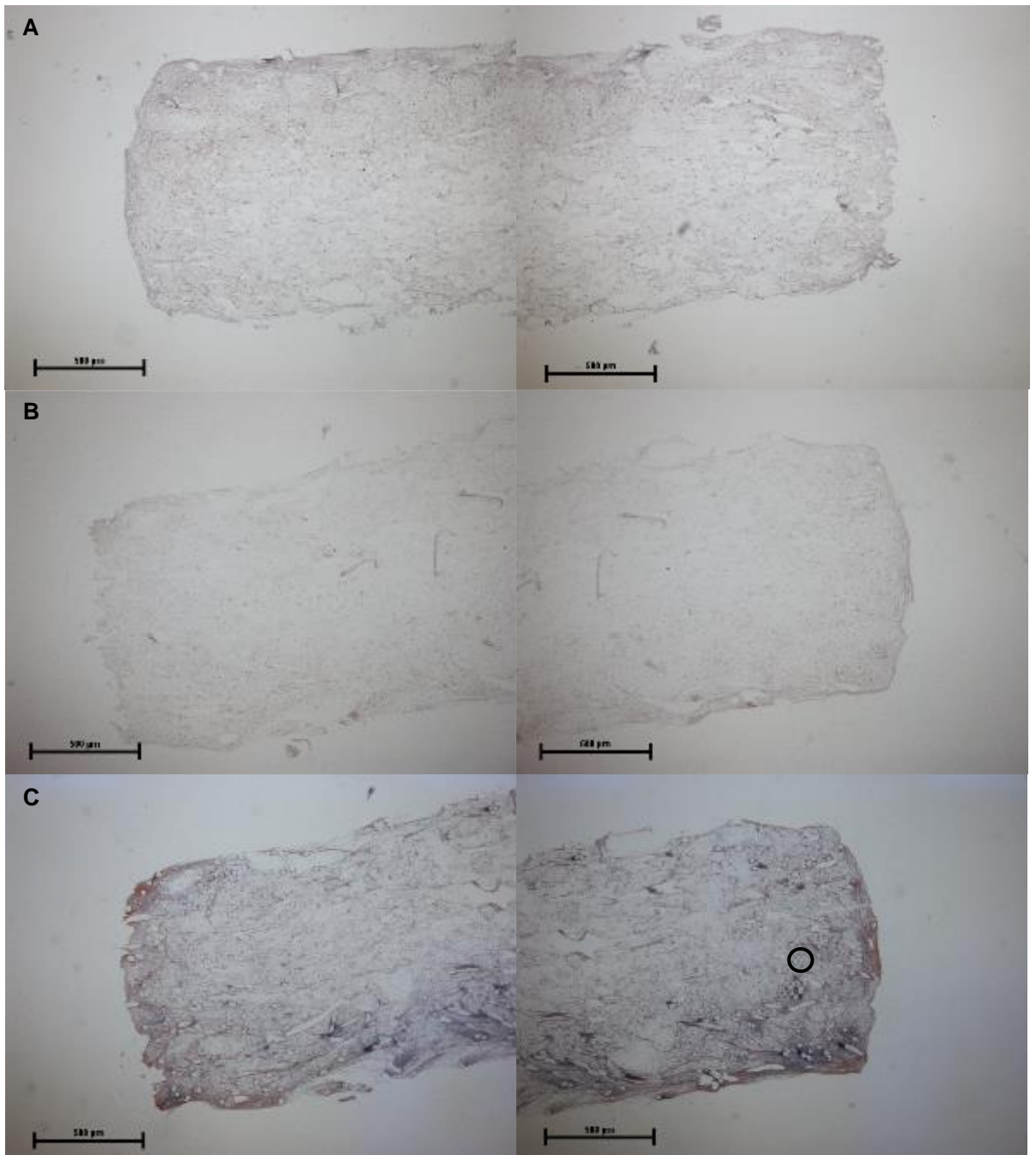


**Figure 99: Histological appearance of sections from a non-loaded construct at Day 56 (Sample 2) of culture without the presence of mechanical loading. Sections stained with (A) antibodies to Collagen type I, (B) antibodies to Collagen type II and (C) Alcian blue / Sirius red. Two images captured from each end of the constructs are shown in each case, representing the entire construct.**

Similar staining intensity for collagen type II and Alcian blue, together with an increased uniform construct cross-sectional thickness can be seen when compared to Day 28. Circle highlighting PET scaffold fibre. Scale bar 500  $\mu\text{m}$ .

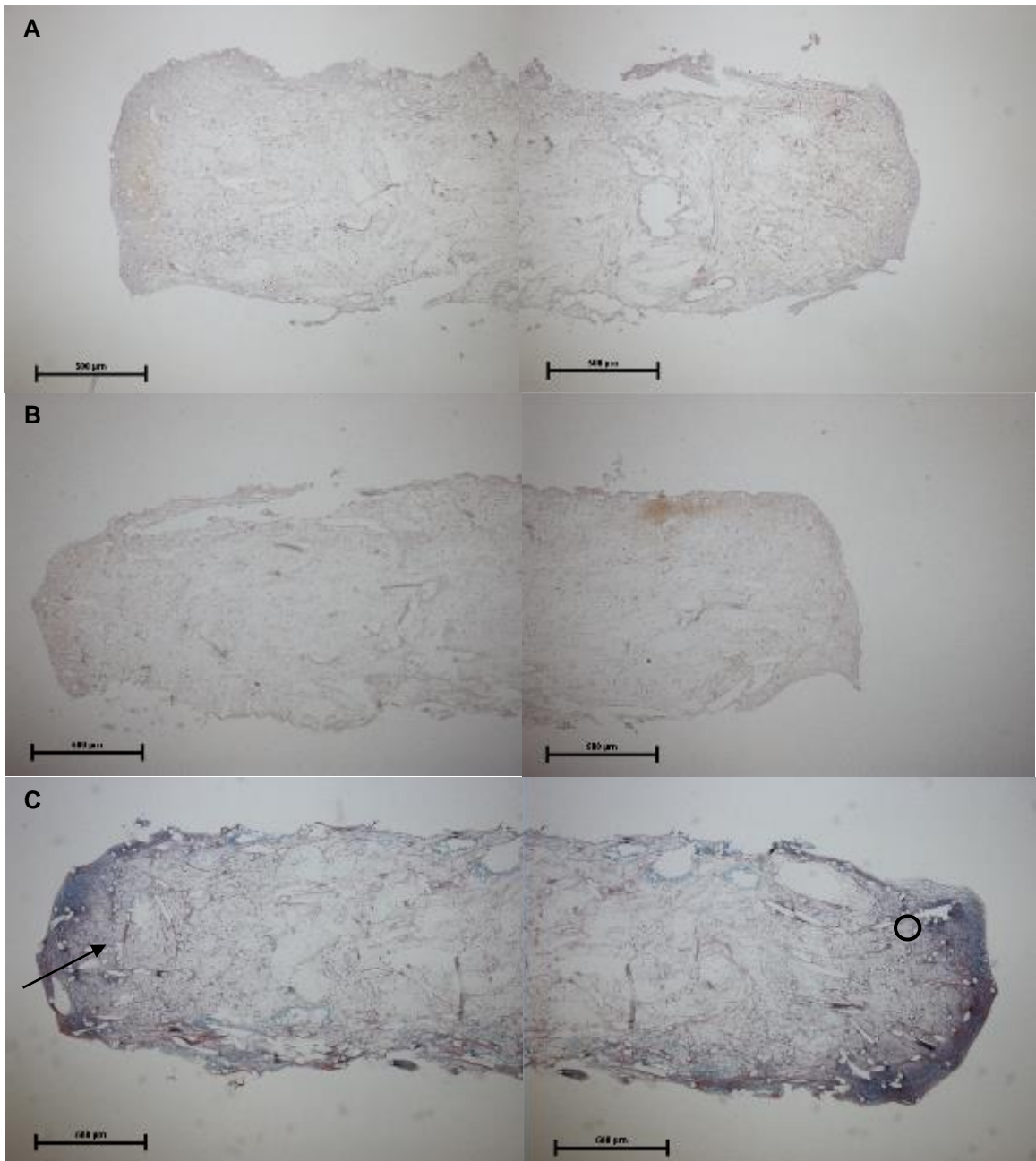


**Figure 100: Histological appearance of sections from a loaded construct at Day 56 (Sample 1) of culture with the presence of mechanical loading. Sections stained with (A) antibodies to Collagen type I, (B) antibodies to Collagen type II and (C) Alcian blue / Sirius red. Two images captured from each end of the constructs are shown collaged in each case, representing the entire construct.**

A similar staining intensity for collagen type II and Alcian blue, can be seen compared to Day 28. There was also a decreased construct thickness, compared with non-loaded constructs. Arrow indicating cartilage-matrix deposited in locations toward the core of the construct. Circle highlighting PET scaffold fibre. Scale bar 500 µm.



**Figure 101: Histological appearance of sections from a loaded construct at Day 56 (Sample 2) of culture with the presence of mechanical loading. Sections stained with (A) antibodies to Collagen type I, (B) antibodies to Collagen type II and (C) Alcian blue / Sirius red. Two images captured from each end of the constructs are shown collaged in each case, representing the entire construct.**

A similar staining intensity for collagen type II and Alcian blue, can be seen compared to Day 28. There was also a decreased construct thickness, compared with non-loaded constructs. Circle highlighting PET scaffold fibre. Scale bar 500  $\mu\text{m}$ .

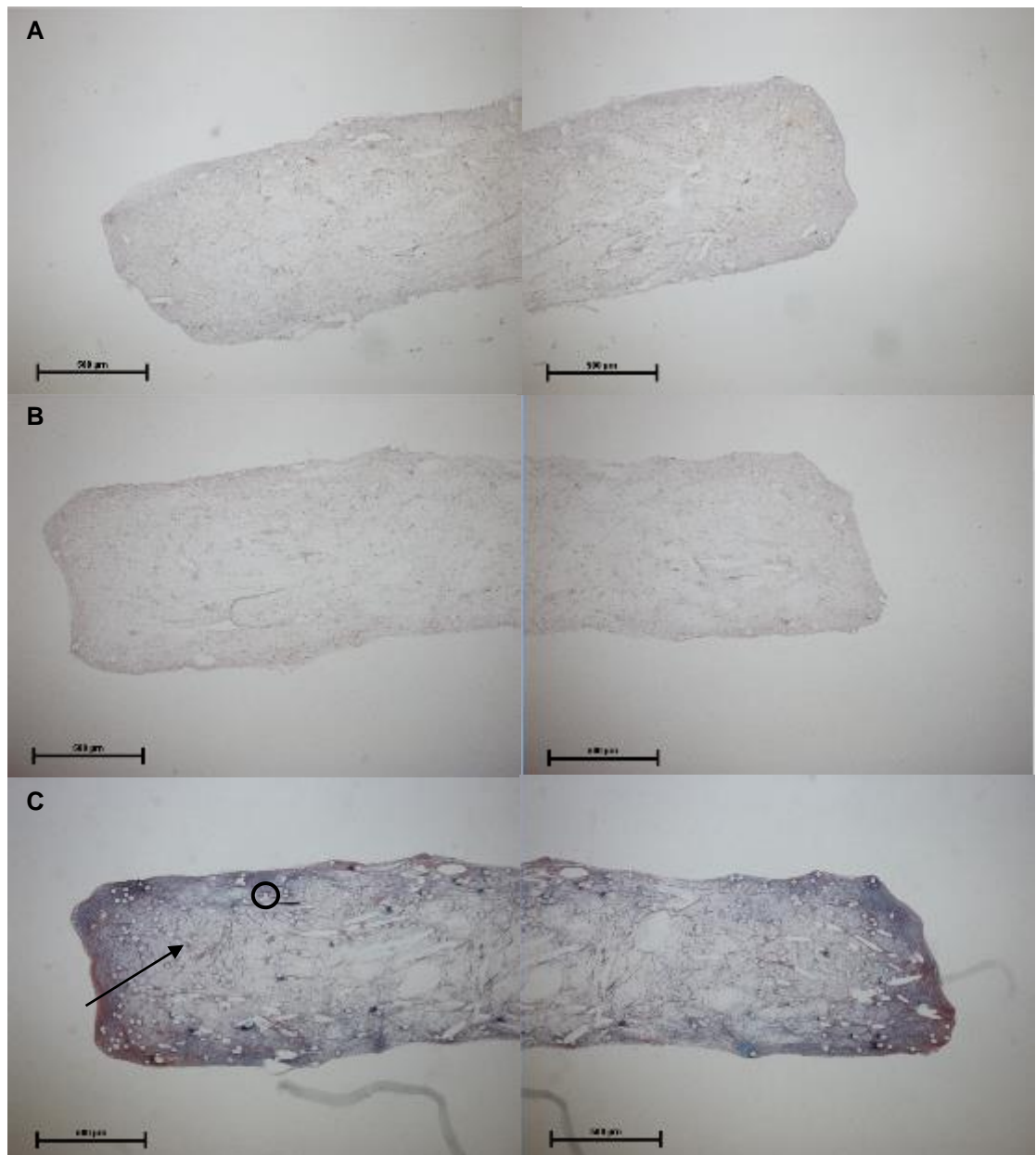


**Figure 102: Histological appearance of sections from a loaded construct at Day 56 (Sample 3) of culture with the presence of mechanical loading. Sections stained with (A) antibodies to Collagen type I, (B) antibodies to Collagen type II and (C) Alcian blue / Sirius red. Two images captured from each end of the constructs are shown collaged in each case, representing the entire construct.**

A similar staining intensity for collagen type II and Alcian blue, can be seen compared to Day 28. There was also a decreased construct thickness, compared with non-loaded constructs. Arrow indicating cartilage-matrix deposited in locations toward the core of the construct. Circle highlighting PET scaffold fibre. Scale bar 500  $\mu\text{m}$ .

#### **5.4.4 Confocal Microscopy of Synoviocytes within Compressed and Uncompressed Constructs under Incremental Compressive Strains**

In order to determine the cellular deformation behaviour in constructs subjected to incremental compressive strains, staining using Hoechst 33342 and CellMask green plasma membrane stains (described in Chapter 3) was used to fluorescently label and visualise the synoviocytes within the constructs, coupled with confocal microscopy. A novel compression device (described in Chapter 2) was then used for tissue strain application. Confocal images of randomly selected synoviocytes were captured (i) in the uncompressed state, (ii) during an estimated strain applied by the bioreactor during mechanical loading and (iii) during 28 % compressive strain for both loaded and non-loaded constructs developed at different time points (Day 0, 28 and 56) (Figure 103 to 107). Five constructs from each loaded and non-loaded group were imaged. Two constructs in each group are displayed in this section. There was a considerable change in synoviocyte morphology between loaded and non-loaded constructs developed at different time points (Day 0, 28 and 56) (Figure 103 to 107).

At Day 0 of the mechanical loading experiment (i.e. after 4 weeks of pre-culture in chondrogenic medium but before the mechanical loading commenced), large numbers of synoviocytes were observed within the uncompressed, immature constructs (Figure 103A and Figure 103D). Cells within the dense population of synoviocytes appeared to be thin and elongated in shape and were found to congregate in clusters near the PET scaffold fibres within the constructs (Label 1, Figure 103). Due to the synoviocytes being so densely packed, it was not possible to determine the individual cell boundaries that is a necessary requirement for morphometric measurements, presenting an extremely difficult challenge for cell deformation quantification analysis later in this study. During the application of compressive strains (estimated strain subjected during mechanical loading and the maximum 28 % strain applied), synoviocyte boundaries remained difficult to identify due their close proximity to one another (Figure 103B, Figure 103C, Figure 103E and Figure 103D).

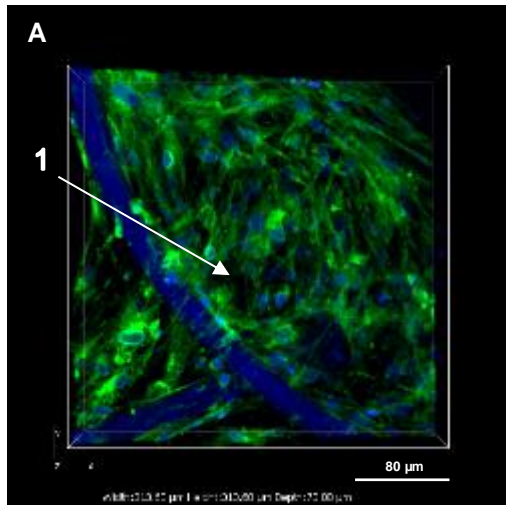
The morphology and distribution of synoviocytes within non-loaded constructs are shown in Figure 104 and Figure 106. At Day 28, synoviocytes remained spindle-like in morphology (Label 1, Figure 104). There was no discernible difference in morphology between synoviocytes in non-loaded constructs at Day 28 (Figure 104) and those in Day 0 (Figure 103). Large numbers of synoviocytes continued to congregate closely together (Figure 104) similar to the observation seen in Day 0 constructs (Figure 103). By Day 56, some synoviocytes became more spread in morphology with larger projected areas but the majority remained elongated in shape (Label 2 and Label 3, Figure 106). Synoviocytes with a spread morphology perhaps suggested that they may be undergoing differentiation. Thin protrusions in spreading synoviocytes were observed in non-loaded constructs at Day 56 (Figure 106), indicating that cell-cell and cell-matrix interactions and adhesions may be taking place. These thin projected areas would

comprise of the cell's internal cytoskeleton (actin filaments, microtubules and intermediate filaments) which allows the synoviocyte to move and connect to other synoviocytes or the ECM, via their respective cadherins and integrins. The synoviocytes at Day 56 (Label 1, Figure 106) were more sparsely distributed compared to earlier time points (Day 0 and 28), allowing the clear identification of cell boundaries and consequently making it possible for cell deformation quantification analysis later in this study.

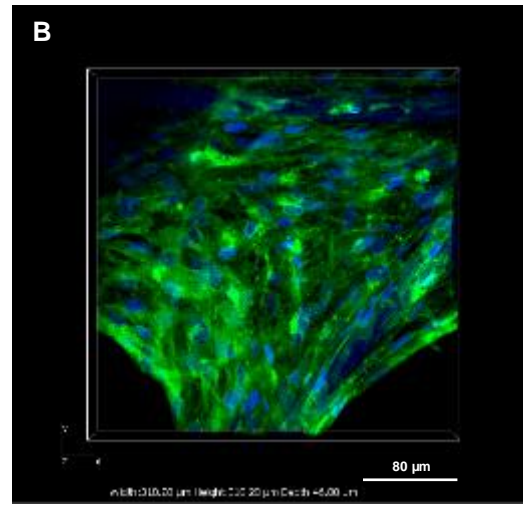
The morphology and distribution of synoviocytes within loaded constructs changed significantly throughout the entire 56 days of culture (Figure 105 and Figure 107). At Day 28, synoviocytes were more spread in morphology (Label 1, Figure 105) compared to those at Day 0 and those seen in the non-loaded constructs at Day 28 (Figure 103 and Figure 104), perhaps indicating that synoviocytes were stimulated towards differentiation by the mechanical loading. Synoviocytes were sparsely distributed within the loaded constructs at Day 28 (Label 3, Figure 105) compared to those in Day 0 and those in non-loaded constructs at Day 28 (Figure 103 and Figure 104). Some synoviocytes were seemingly in close proximity with each other and thin cellular protrusions were observed, suggesting that cell-cell and cell-matrix interactions might be taking place (Label 1, Figure 105). By Day 56, synoviocytes continued to be spread in morphology and were sparsely distributed (Label 1 and Label 2, Figure 107). Thin cellular protrusions were still seen in these spreading synoviocytes, suggesting continual cell-cell and cell-matrix interactions and adhesions within the constructs. Due to the sparse distribution of synoviocytes in loaded constructs, synoviocytes with clear cell boundaries could be identified and so analysed for cell deformation later in this study.

Sample 1 – Day 0

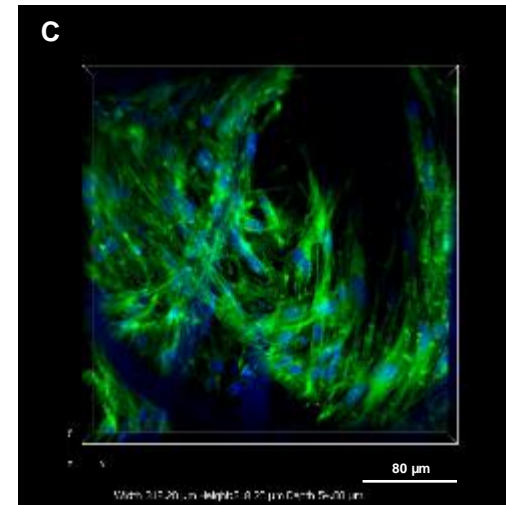
0 % strain



23 % strain

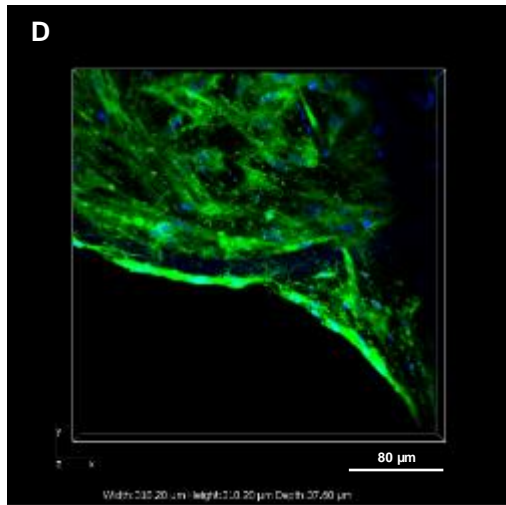


28 % strain

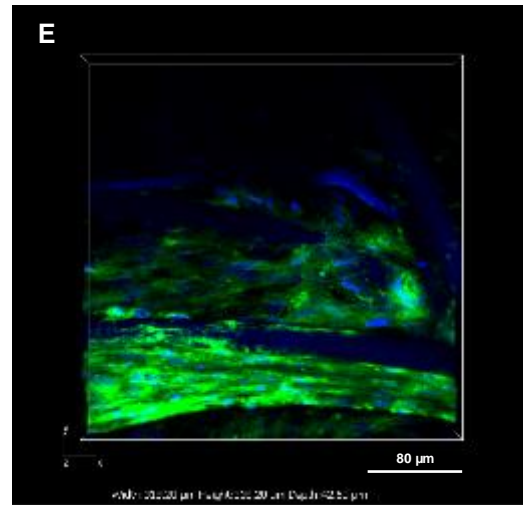


Sample 2 – Day 0

0 % strain



23% strain



28 % strain

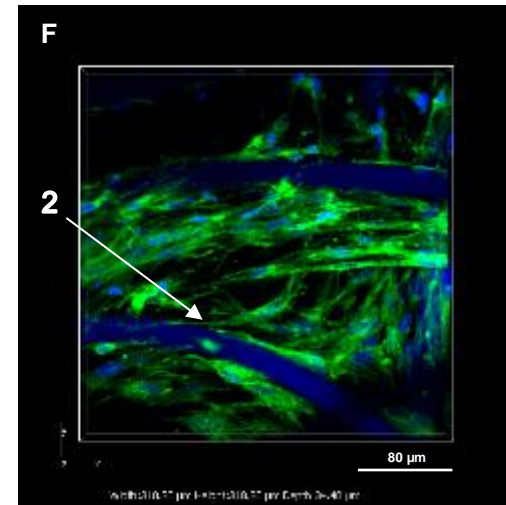
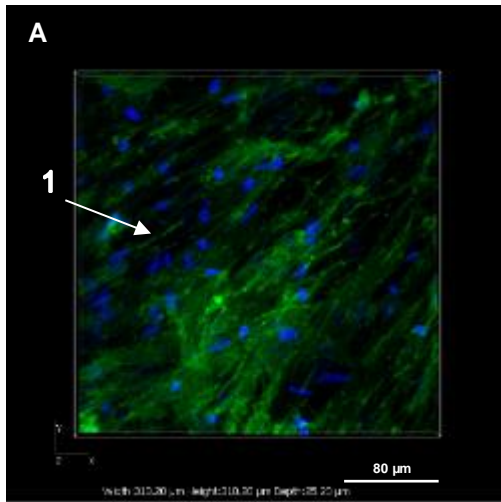


Figure 103: 3D volume images of synoviocytes in both uncompressed and compressed state within two construct samples (1,2) at Day 0 stained with Hoechst 33342 (blue) and CellMask green plasma membrane stains (green) for nuclei and plasma membrane respectively; images of synoviocytes captured during 0 %, estimated strain applied during mechanical loading (23 % for both samples) and 28 % compressive tissue strain in Sample 1 (A, B, C) and Sample 2 (D, E, F). Images are presented in the Z-plane.

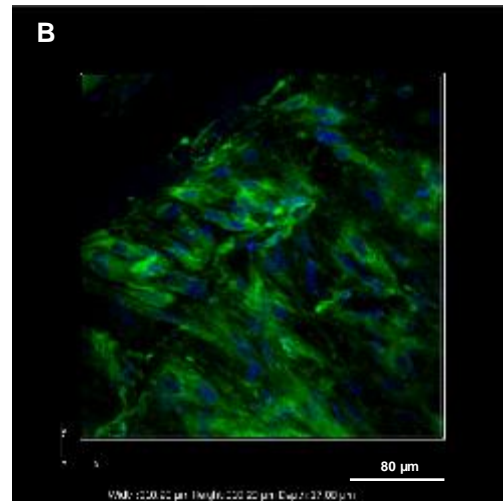
Dense populations of synoviocytes with spindle-like morphologies could be seen around the scaffold fibres in both uncompressed and compressed states within constructs at Day 0 (Label 1). Blue fluorescence signal was picked up by the scaffold fibres in the PET scaffold (Label 2). Scale bar 80 μm.

Sample 1 – Non-loaded – Day 28

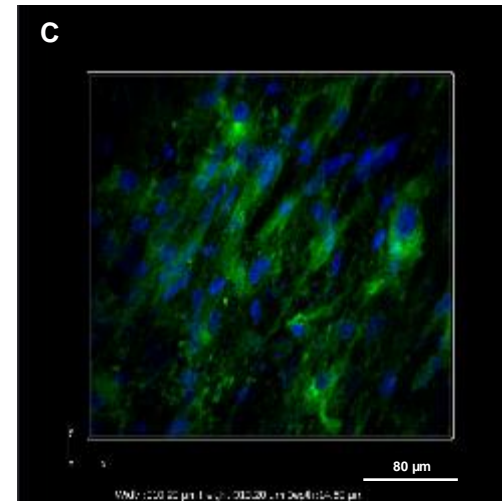
0 % strain



23 % strain

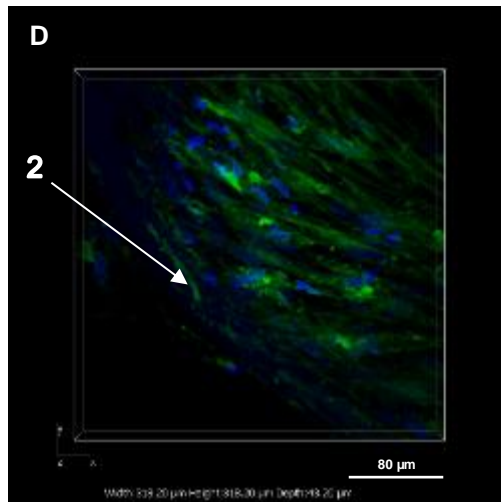


28 % strain

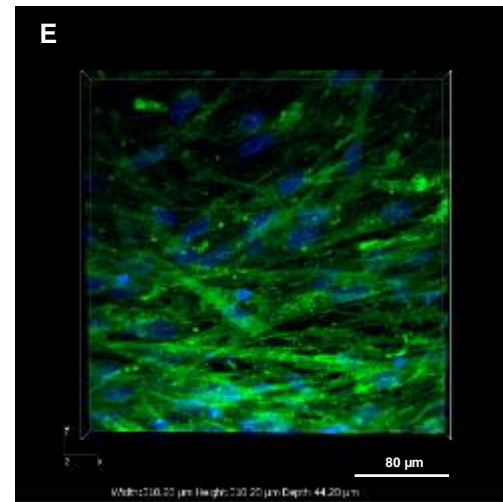


Sample 2 – Non-loaded – Day 28

0 % strain



22.4 % strain



28 % strain

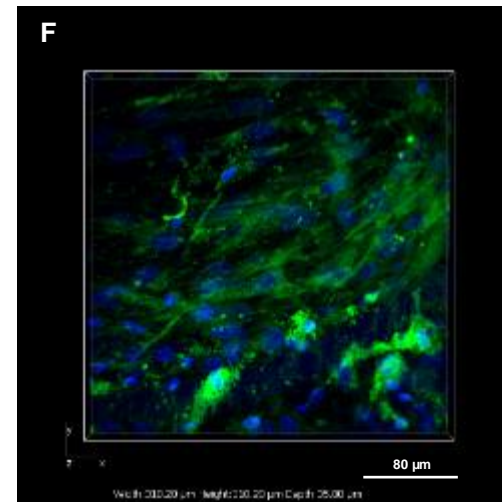
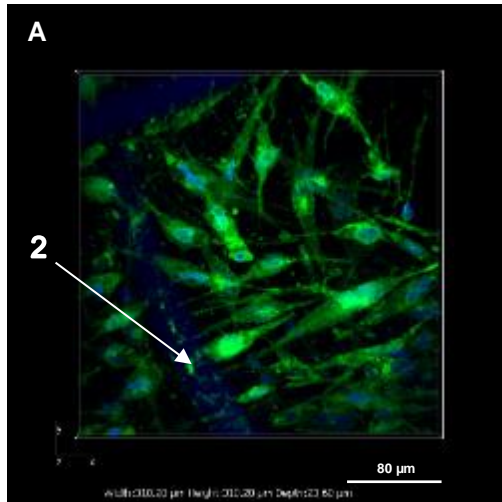


Figure 104: 3D volume images of synoviocytes in both uncompressed and compressed state within two non-loaded construct samples (1,2) at Day 28 stained with Hoechst 33342 (blue) and CellMask green plasma membrane stains (green) for nuclei and plasma membrane respectively; images of synoviocytes captured during 0 %, estimated strain applied during mechanical loading (23 % for Sample 1 and 22.4 % for Sample 2) and 28 % compressive tissue strain in Sample 1 (A, B, C) and Sample 2 (D, E, F). Images are presented in the Z-plane.

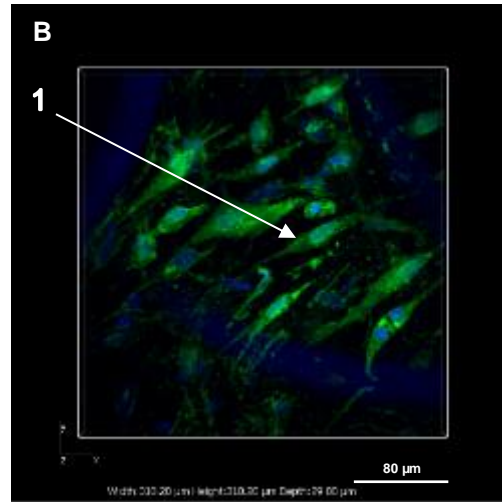
Dense populations of synoviocytes with spindle-like morphologies could be seen in both uncompressed and compressed states within the non-loaded constructs at Day 28 similar to those seen at Day 0 (Label 1). Blue fluorescence signal was picked up by the scaffold fibres in the PET scaffold (Label 2). Scale bar 80 μm.

**Sample 1 – Loaded – Day 28**

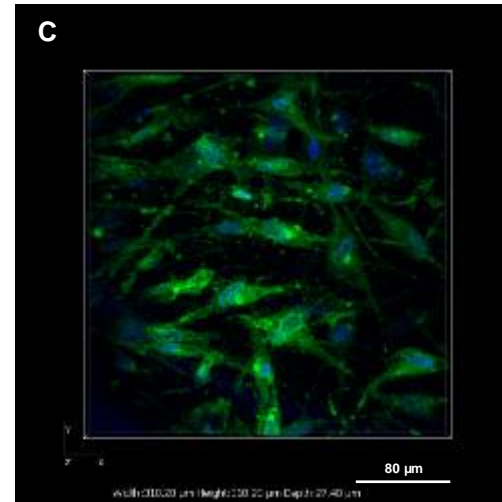
**0 % strain**



**13.2 % strain**

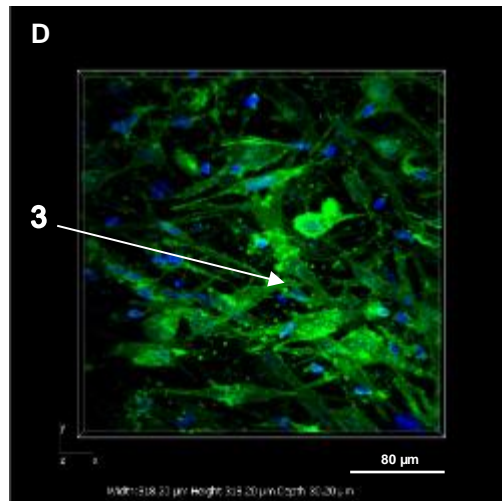


**28 % strain**

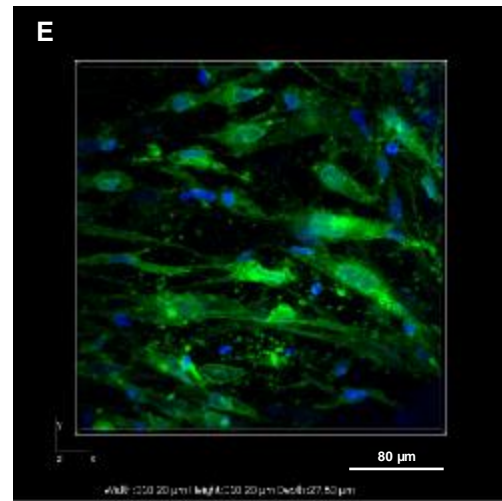


**Sample 2 – Loaded – Day 28**

**0 % strain**



**13.5 % strain**



**28 % strain**

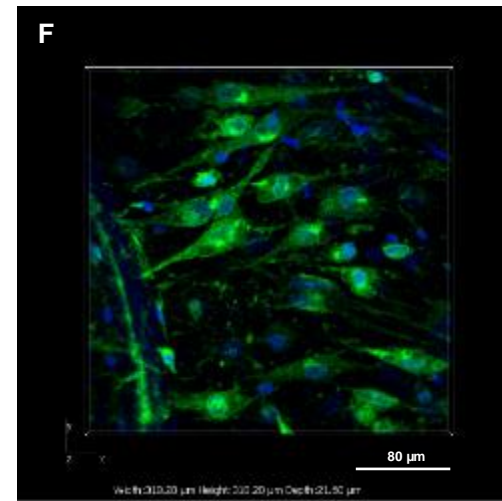


**Figure 105: 3D volume images of synoviocytes in both uncompressed and compressed state within two loaded construct samples (1,2) at Day 28 stained with Hoechst 33342 (blue) and CellMask green plasma membrane stains (green) for nuclei and plasma membrane respectively; images of synoviocytes captured during 0 %, estimated strain applied during mechanical loading (13.2 % for Sample 1 and 13.5 % for Sample 2) and 28 % compressive tissue strain in Sample 1 (A, B, C) and Sample 2 (D, E, F). Images are presented in the Z-plane.**

A more spread synoviocyte morphology with thin cellular protrusions can be seen in both the uncompressed and compressed state within the loaded constructs at Day 28 compared to those at Day 0 and those in non-loaded constructs at Day 28 (Label 1). Synoviocytes were also more sparsely distributed though still in close proximity with each other, suggesting of cell-cell interactions (Label 3). Blue fluorescence signal was picked up by the scaffold fibres in the PET scaffold (Label 2). Scale bar 80 μm.

**Sample 1 – Non-loaded – Day 56**

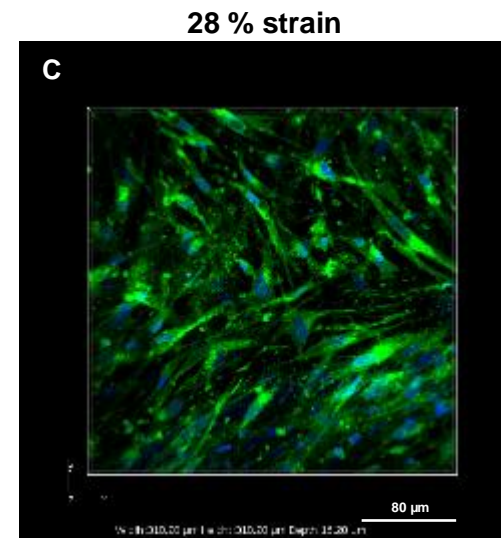
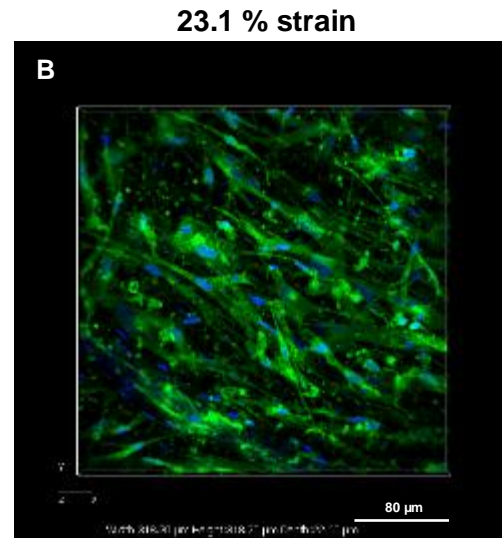
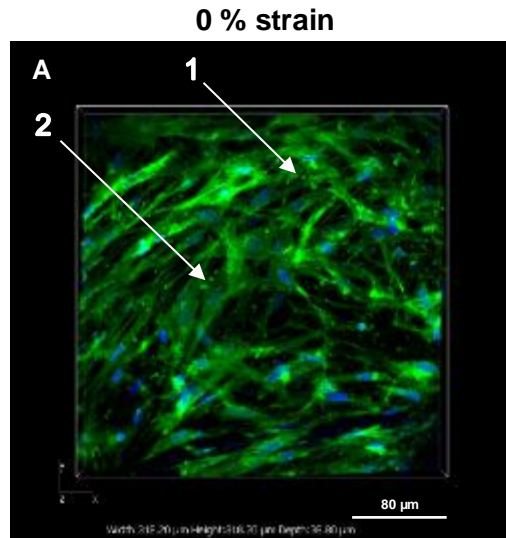
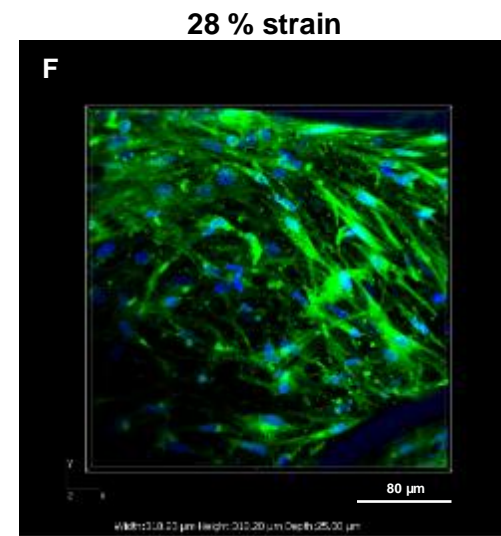
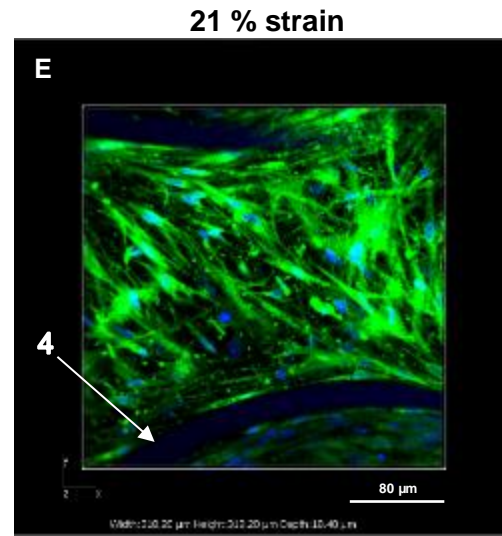
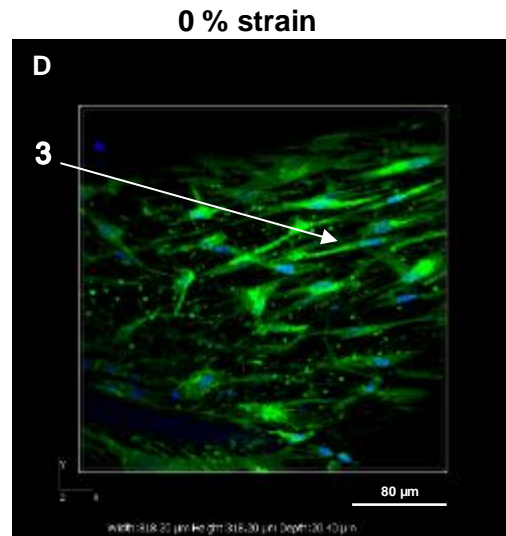


**Figure 106: 3D volume images of synoviocytes in both uncompressed and compressed state within two non-loaded construct samples (1,2) at Day 56 stained with Hoechst 33342 (blue) and CellMask green plasma membrane stains (green) for nuclei and plasma membrane respectively; images of synoviocytes captured during 0 %, estimated strain applied during mechanical loading (23.1 % for Sample 1 and 21 % for Sample 2) and 28 % compressive tissue strain in Sample 1 (A, B, C) and Sample 2 (D, E, F). Images are presented in the Z-plane.**

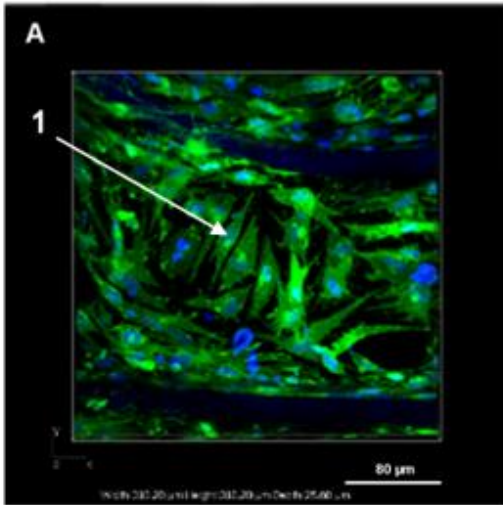
**Sample 2 – Non-loaded – Day 56**



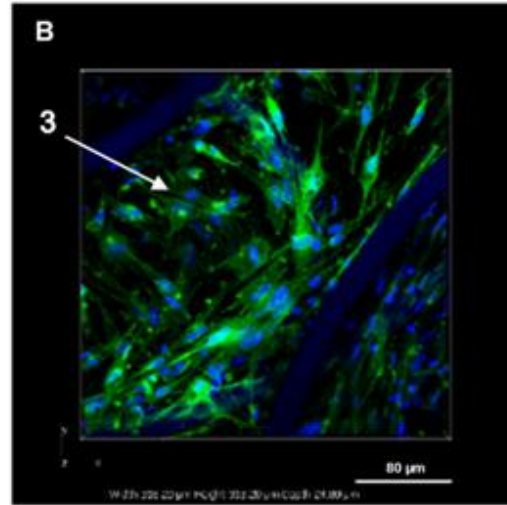
The majority of synoviocytes appeared to be spindle-like in shape (Label 3) but some could be seen with a more spread morphology (Label 2) in both uncompressed and compressed states within the non-loaded constructs at Day 56, in comparison to those in non-loaded constructs at Day 28. Synoviocytes distributed more sparsely within the construct compared to earlier time points (Day 0 and non-loaded constructs at Day 28) (Label 1). Blue fluorescence signal was picked up by the scaffold fibres in the PET scaffold (Label 4). Scale bar 80 μm.

Sample 1 – Loaded – Day 56

0 % strain



14.7 % strain



28 % strain

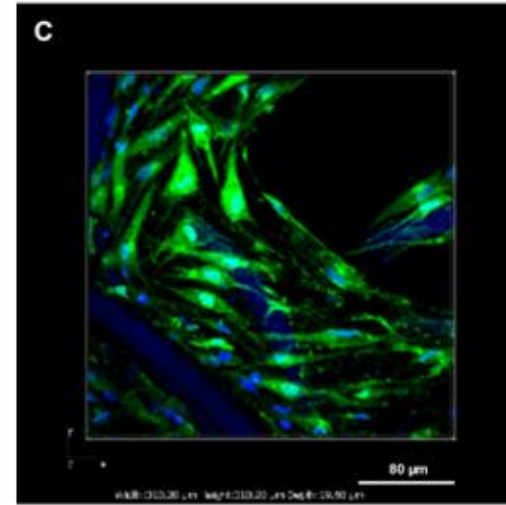
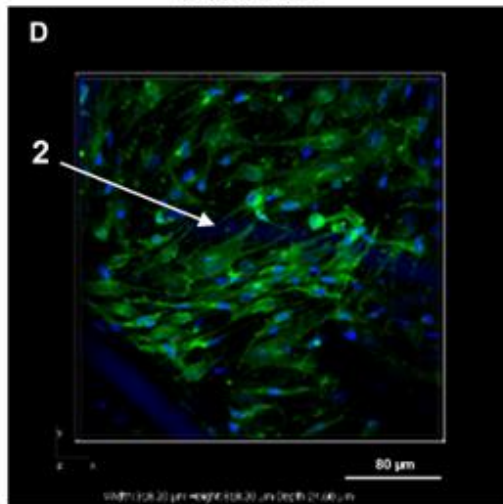


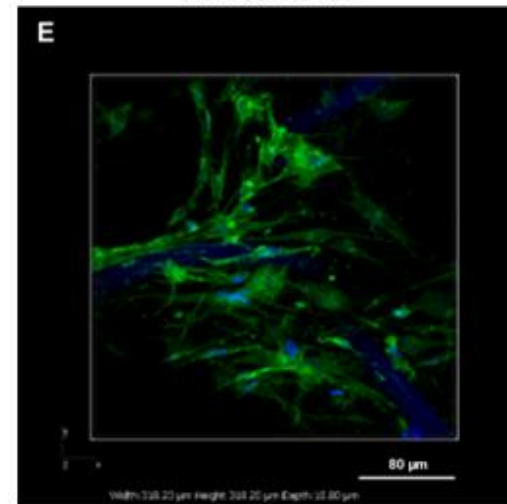
Figure 107: 3D volume images of synoviocytes in both uncompressed and compressed state within two loaded construct samples (1,2) at Day 56 stained with Hoechst 33342 (blue) and CellMask green plasma membrane stains (green) for nuclei and plasma membrane respectively; images of synoviocytes captured during 0 %, estimated strain applied during mechanical loading (14.7 % for Sample 1 and 12.4 % for Sample 2) and 28 % compressive tissue strain in Sample 1 (A, B, C) and Sample 2 (D, E, F). Images are presented in the Z-plane.

Sample 2 – Loaded – Day 56

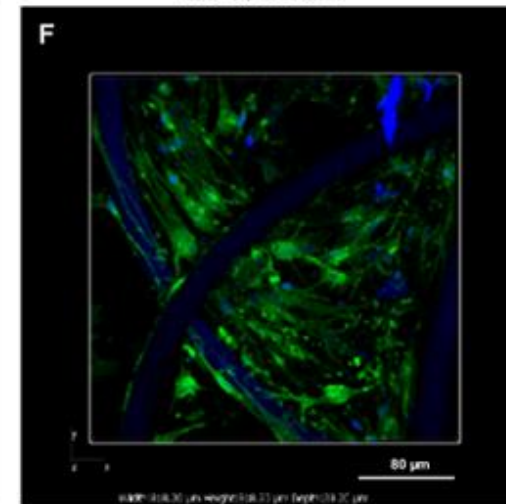
0 % strain



12.4 % strain



28 % strain



A spread morphology for the synoviocytes, together with multiple thin cell processes were seen in both uncompressed and compressed states within the loaded constructs at Day 56, similar to those in loaded constructs at Day 28 (Label 1). The cell density was also more sparse compared with Day 0 and with unloaded constructs though cells were still in close proximity with one another, suggesting the possibility of cell-cell interactions (Label 3). Blue fluorescence signal was picked up by the scaffold fibres in the PET scaffold (Label 2). Scale bar 80 μm.

#### **5.4.5 Quantification of Synoviocyte Deformation under Incremental Compressive Tissue Strains In Constructs via Amira: Morphometric Measurements**

In order to determine the deformation behaviour of synoviocytes in constructs under compressive tissue strains, confocal images of synoviocytes were captured as previously described in Section 5.3.7 in an uncompressed state and during applied compressive strains for both loaded and non-loaded constructs developed at different time points. Constructs stained with Hoechst 33342 and CellMask Green plasma membrane stains were placed in to the newly developed device (see Chapter 3) and viewed under confocal microscopy at (i) zero strain, (ii) an estimated percentage in applied compressive strain during mechanical loading in the bioreactor and (iii) 28 % applied compressive strain. After an equilibration period of 30 mins in each case, images of different populations of synoviocytes were acquired. However, constructs developed at Day 0 and Day 28 were excluded for synoviocyte deformation quantification analysis due to the extremely high cell densities within these constructs which consequently made identification of the outline of the synoviocytes (necessary for morphometric measurements) impossible. Morphometric changes were therefore only recorded and compared between loaded and non-loaded constructs after 56 days of culture as synoviocytes showed defined boundaries at this time point (as shown in Figure 106 and Figure 107). Data was collected for 10 different synoviocytes in each case per construct and from two different constructs in each loaded and non-loaded group. Amira software was used to quantify synoviocyte morphometric parameters including: cell length, width, height, volume and sphericity (see Section 4.3.6.2 for full methodology). The resulting data is presented as mean values  $\pm$  SD for all synoviocytes in each of the two constructs per loaded and non-loaded groups and compared statistically at each strain value.

In loaded constructs in the uncompressed state, the mean ( $\pm$  SD) volume, sphericity, height, length and width of the synoviocytes were  $6203 \pm 1348 \mu\text{m}^3$  and  $4341 \pm 1409 \mu\text{m}^3$ ,  $0.42 \pm 0.05$  and  $0.41 \pm 0.08$ ,  $14.2 \pm 2.3 \mu\text{m}$  and  $9.8 \pm 1.4 \mu\text{m}$ ,  $85.2 \pm 16.2 \mu\text{m}$  and  $90.1 \pm 23 \mu\text{m}$  and  $15.9 \pm 1.2 \mu\text{m}$  and  $12 \pm 1.4 \mu\text{m}$  in Sample 1 and Sample 2, respectively (Table 3). In uncompressed non-loaded constructs, the mean ( $\pm$  SD) volume, sphericity, height, length and width of the synoviocytes were  $6804 \pm 2904 \mu\text{m}^3$  and  $6179 \pm 2320 \mu\text{m}^3$ ,  $0.30 \pm 0.07$  and  $0.32 \pm 0.03$ ,  $11.6 \pm 2.1 \mu\text{m}$  and  $9.4 \pm 2.9 \mu\text{m}$ ,  $138.1 \pm 43.6 \mu\text{m}$  and  $122.4 \pm 27.3 \mu\text{m}$  and  $18.3 \pm 3.4 \mu\text{m}$  and  $15.4 \pm 4.3 \mu\text{m}$  in Sample 1 and Sample 2, respectively (Table 3). There were no discernible differences in morphometric measurements between uncompressed synoviocytes within loaded and non-loaded constructs at Day 56.

Application of incremental compressive tissue strains on non-loaded constructs resulted in significant observable effects on synoviocyte morphology. Morphometric changes for synoviocytes in each non-loaded construct sample ( $n = 2$ ) following application of compressive

tissue strains are presented as mean values  $\pm$  SD in Figure 108A-H. Synoviocyte volume tended to decrease in non-loaded constructs with applied tissue strain (Figure 108C and Figure 37E), with the decrease being statistically significant only in Sample 2 when comparing synoviocytes in the uncompressed state and those at 28 % strain ( $p < 0.05$ , Figure 108E) and synoviocytes under an estimated strain applied to the constructs during mechanical loading in the bioreactor (21 %) compared to those at 28 % compressive tissue strain ( $p < 0.05$ , Figure 108E). Under the application of estimated strain applied during mechanical loading in the bioreactor (23.1 % strain for Sample 1 and 21 % for Sample 2, respectively) and 28 % compressive cartilage strain, sphericity appeared to be consistent with no significant differences (Figure 108B and Figure 108F). Cell height in Sample 2 tended to decrease with applied tissue strain but it was not statistically significant (Figure 108G). However, a significant decrease in cell height was observed for Sample 1 at 23.1 % and 28 % applied tissue strain ( $p < 0.01$  and  $p < 0.0001$ , Figure 108C). Following application of incremental compressive tissue strain, there was no significant effects on the length and width of the synoviocytes in non-loaded construct samples (Figure 108D and Figure 108H), apart from a significant reduction in cell width in Sample 1 between cells in the uncompressed state to compared to those at the estimated strain applied during mechanical loading in the bioreactor (23.1 %) and 28 % strain ( $p < 0.01$ , Figure 108D).

The morphometric measurements of synoviocytes within loaded constructs following application of compressive tissue strains are presented in Figure 109A-H. Following applied tissue strains to loaded constructs (estimated applied strain during mechanical loading in the bioreactor of 14.7 % for Sample 1 and 12.4 % for Sample 2, respectively, and 28 % compressive strain), no significant difference was observed in cell volume, height, width and length of synoviocytes (Sample 1 and Sample 2) (Figure 109). There was also no significant change in sphericity in both loaded constructs (Sample 1 and Sample 2), with the exception that a significant decrease in sphericity was observed in Sample 1 between synoviocytes at 0 % and those at 28 % applied strain ( $p < 0.05$ , Figure 109).

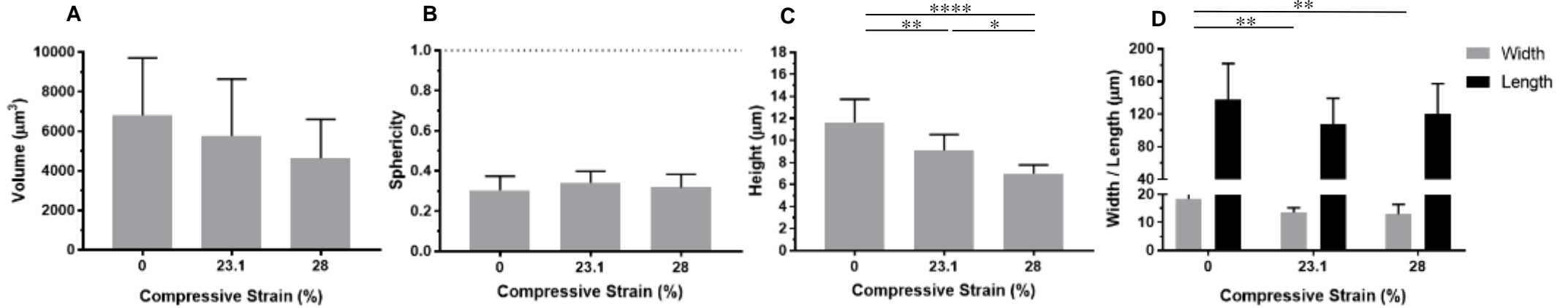
**Table 3: Mean values  $\pm$  SD of morphometric measurements for 10 different synoviocytes in the uncompressed state from two constructs in each of the loaded and non-loaded group at Day 56; cell volume, sphericity, height, length and width.**

Day 56	Volume	Sphericity	Height	Length	Width

	( $\pm$ SD) ( $\mu\text{m}^3$ )	( $\pm$ SD)	( $\pm$ SD) ( $\mu\text{m}$ )	( $\pm$ SD) ( $\mu\text{m}$ )	( $\pm$ SD) ( $\mu\text{m}$ )
Non-loaded Sample 1	6804 $\pm$ 2904	0.30 $\pm$ 0.07	11.6 $\pm$ 2.1	138.1 $\pm$ 43.6	18.3 $\pm$ 3.4
Non-loaded Sample 2	6179 $\pm$ 2320	0.32 $\pm$ 0.03	9.4 $\pm$ 2.9	122.4 $\pm$ 27.3	15.4 $\pm$ 4.3
Loaded Sample 1	6203 $\pm$ 1348	0.42 $\pm$ 0.05	14.2 $\pm$ 2.3	85.2 $\pm$ 16.2	15.9 $\pm$ 1.2
Loaded Sample 2	4341 $\pm$ 1409	0.41 $\pm$ 0.08	9.8 $\pm$ 1.4	90.1 $\pm$ 23	12 $\pm$ 1.4

Sample 1 – Non-loaded – Day 56

- 236 -



Sample 2 – Non-loaded – Day 56

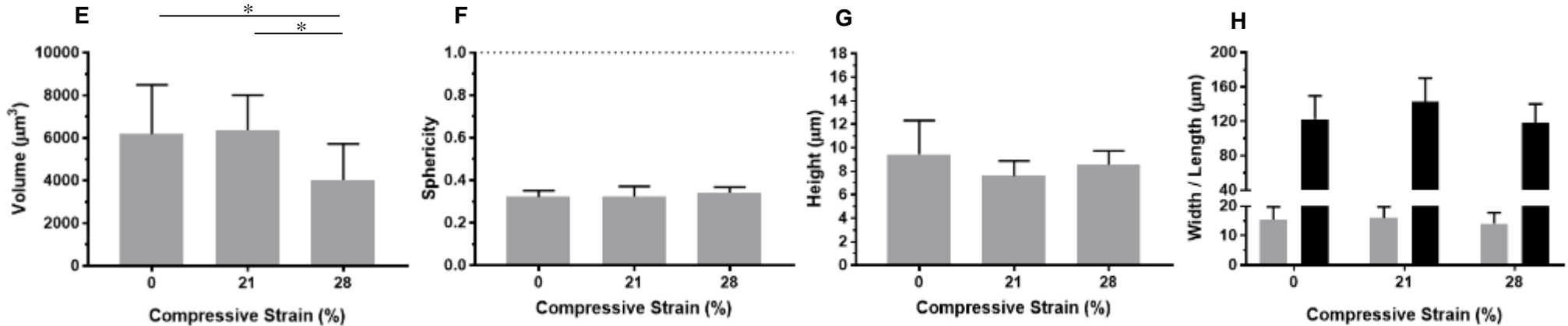
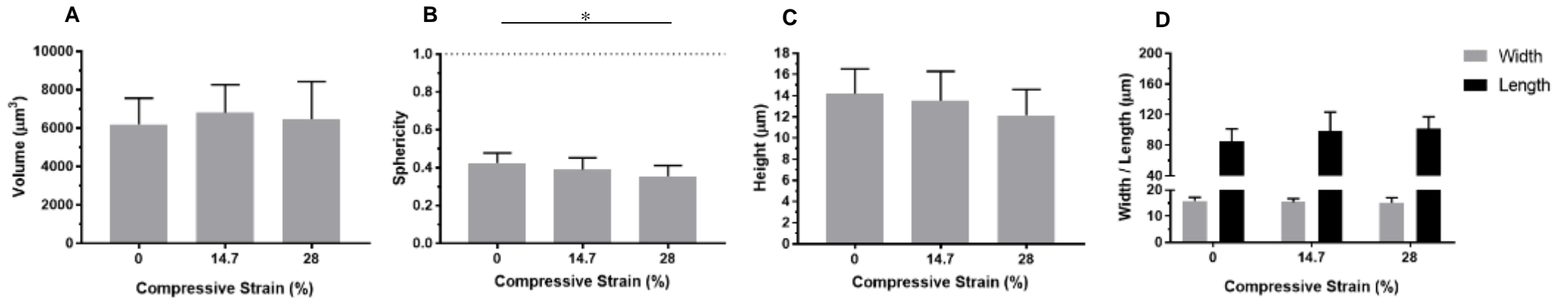


**Figure 108: Mean values  $\pm$  SD of morphometric measurements for 10 different synoviocytes from two non-loaded construct samples at Day 56 (Sample 1 and Sample 2 = top and bottom rows) under different experimental conditions (uncompressed state, estimated strain experienced by the constructs during mechanical loading in the bioreactor (23.1 % for Sample 1 and 21 % for Sample 2, respectively) and 28 % compressive tissue strain); cell volume, sphericity, height, width and length for sample 1 (A, B, C, D) and sample 2 (E, F, G, H). Dotted line in (B, F) indicates the value for a perfect sphere. A significant decrease in cell volume was only observed in Sample 2 between synoviocytes in the uncompressed state and those at 28 % strain. Sphericity remained largely consistent irrespective of applied tissue strain in both samples. Significant decrease in cell height was only observed for synoviocytes in Sample 1 with application of 23.1 % and 28 % compressive tissue strains. No significant differences in cell length and width with applied tissue strain were observed in both samples, apart from significant decreases in cell width in Sample 1 at 23.1 % and 28 % strain.**

Statistical analysis was performed using one way ANOVA with compressive strain as the between subject factor after data normality was determined. Turkey's post doc test was used for comparison between synoviocytes within non-loaded constructs in the uncompressed state and during estimated compressive strain applied during mechanical loading (23.1 % for Sample 1 and 21 % for Sample 2, respectively) and 28 % compression. \*  $\equiv$   $p < 0.05$ , \*\*  $\equiv$   $p < 0.01$ , \*\*\*\*  $\equiv$   $p < 0.0001$ .

**Sample 1 – Loaded – Day 56**



**Sample 2 – Loaded – Day 56**

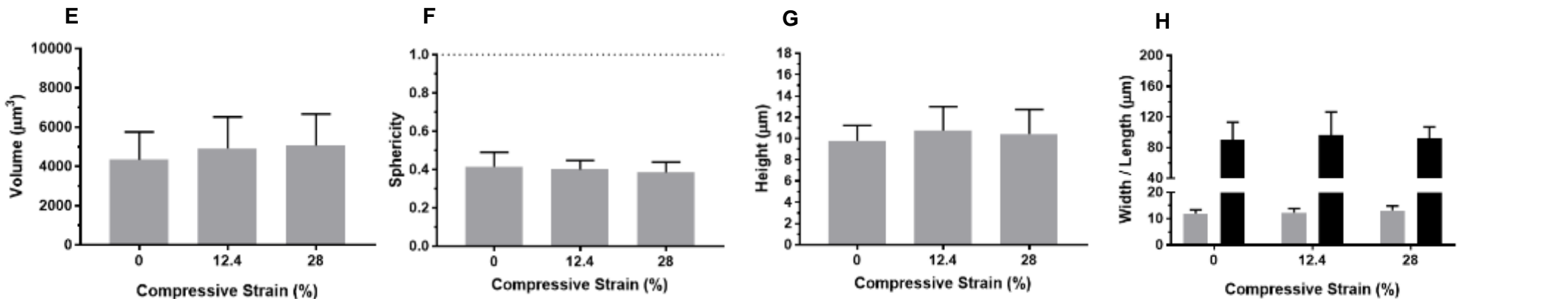


**Figure 109: Mean values ± SD of morphometric measurements for 10 different synoviocytes from two loaded construct samples at Day 56 (Sample 1 and Sample 2 = top and bottom rows) under different experimental conditions (uncompressed state, estimated strain experienced by the constructs during mechanical loading in the bioreactor (14.7 % for Sample 1 and 12.4 % for Sample 2, respectively) and 28 % compressive tissue strain); cell volume, sphericity, height, width and length for Sample 1 (A, B, C, D) and Sample 2 (E, F, G, H). Dotted line in (B, F) indicates the value for a perfect sphere. No significant change in cell volume, height, length and width were observed for all samples with applications of estimated strain applied during mechanical loading in the bioreactor and 28 % compressive tissue strain. Sphericity also remained largely consistent irrespective of applied tissue strain in both samples, apart from a significant decrease in sphericity in Sample 1 between synoviocytes in the uncompressed state and those at 28 % strain.**

Statistical analysis was performed using one way ANOVA with compressive strain as the between subject factor after data normality was determined. Turkey’s post hoc test was used for comparison between synoviocytes within loaded constructs in the uncompressed state and during estimated compressive strain applied during mechanical loading (14.7 % for Sample 1 and 12.4 % for Sample 2, respectively) and 28 % compression. \* ≡ p < 0.05.

## 5.5 Discussion

The aim of this study was to determine cell deformation behaviour under compression in cartilage constructs developed at different time points in order to gain a better understanding on the loading mechanism that was previously used by Finlay *et al.* (2016) [1] for the creation of mechanically functional constructs for long term cartilage repair. The relationship between applied tissue strain and resulting cellular strain was of particular interest. By understanding the effect of the mechanical loading to which the residing cells are subjected within constructs developed at different stages, information for improving the rate of quality matrix deposition would be provided which in turn would provide consequential benefits for accelerated clinical translation.

In Finlay *et al.* (2016) study [1], there was no significant difference in compressive modulus values and histological appearance for constructs after 56 and 84 days of mechanical loading. This suggested that the constructs had reached a plateau in mechanical stiffness. For this reason, constructs that had been cultured  $\pm$  loading for up to 56 days were used in this study.

The progress of construct maturation was assessed by analysing the collagen, sGAG and DNA content, compressive moduli and histological appearance of loaded and non-loaded constructs at each time point (Day 0, Day 28 and Day 56). Synoviocyte morphology within the constructs at the different time points was viewed by the use of confocal microscopy under incremental compressive strains (estimated strain experienced by each construct during mechanical loading within the bioreactor and 28 % compressive tissue strain). Due to the high cell density of the synoviocytes within the constructs at earlier time points, the morphometric changes were measured and quantified only in loaded and non-loaded constructs at Day 56. From these results, the protein (sGAG and collagen) and DNA content along with the histological findings and compressive properties of the constructs might be associated with the cell deformation characteristics observed within both loaded and non-loaded constructs.

### 5.5.1 The Effect of Compressive Mechanical Loading on the Collagen and Sulphated Glycosaminoglycan Content of Pre-Cultured Synoviocyte/PET Constructs

The collagen content of all constructs was found to significantly increase between Day 0 and Day 28 and also between Day 28 and Day 56 for those constructs subjected to mechanical loading ( $p < 0.05$ , Figure 83). The sGAG content also increased significantly in both loaded and non-loaded constructs between Day 0 and Day 28 but remained at a similar level at Day 56 ( $p < 0.05$ , Figure 83). There were no significant differences in both collagen and sGAG content between loaded and non-loaded constructs at each time point (Figure 82 and Figure 83).

Collagen (primarily type II collagen) and glycosaminoglycans are typically found as major ECM components within native articular cartilage. The significant increase in collagen and sGAG content seen in the constructs after 28 days suggests an ECM that has characteristics similar to native cartilage was initially deposited during synoviocyte differentiation under chondrogenic medium conditions during this time period. At Day 56, the observed sustained higher levels of collagen and sGAG indicate further elaboration of cartilage-like matrix within the constructs. The deposition of a cartilage-like matrix in the constructs was further supported by the increased intensity of Alcian blue staining and type II collagen immune-positive staining, with low immune-positive staining for type I collagen in constructs at Day 28 and Day 56 (Figure 92 to Figure 102). The increased collagen and sGAG content observed in the constructs during the entire culture period was also commensurate with an observed increase in compressive moduli (Figure 86).

There were no statistically significant differences in both increased collagen and sGAG content between loaded and non-loaded constructs at each time point (Figure 83 and Figure 84). This suggests that both phenomena are caused by a shared circumstance, such as the factors (dexamethasone and TGF- $\beta$ 3) contained in the chondrogenic medium, which both were cultured in. The synoviocytes were initially seeded onto PET fibre scaffolds and placed in chondrogenic medium for 4 weeks, in order to initiate the differentiation of synoviocytes and begin the lay down of cartilage-like matrix. However, the lack of histological staining with Alcian blue and collagen type II seen in Day 0 constructs in this study (Figure 89 to Figure 91) suggested that only a very small amount of matrix that is similar to that of native cartilage had been produced and this is in line with Finlay *et al.* (2016) results. As the synoviocytes continued to differentiate in chondrogenic medium for the next 28 days, an increased but still small amount of the desired cartilage-like matrix was laid down, as indicated by the increase in collagen and sGAG content (Figure 83 and Figure 84) and in histological staining (Figure 92 to Figure 97) for cartilage matrix. A steady elaboration of cartilage-like matrix by the synoviocytes as a function of their increasing exposure to chondrogenic medium continued in all constructs up to Day 56. The findings of collagen and sGAG analysis in conjunction with the low intensity of histological staining for cartilage-like matrix (despite staining by Alcian blue and collagen type II antibodies increasing at Day 28 and remaining at a consistent intensity at Day 56) observed in both loaded and non-loaded constructs at Day 28 and Day 56 suggests it took longer than 4 weeks to initiate the formation of the desired matrix and cellular phenotype that is receptive to mechanical loading. This is further supported by the morphological changes in synoviocytes observed at Day 28 in loaded constructs and at Day 56 in non-loaded constructs (Figure 105 and Figure 106), where there were only limited shifts in cell morphology from the original spindle shaped, to a more spread morphology (i.e. large projected areas).

Both the collagen and sGAG content of loaded and non-loaded constructs were significantly lower than that of native cartilage (Figure 83 and Figure 84). This observation corresponds with

the histological findings of low Alcian blue staining and type II collagen immune-positive staining throughout the loaded and non-loaded constructs at Day 56 (Figure 98 to Figure 102) in comparison to the high intensity of staining observed in the native cartilage (Figure 87A and Figure 87E). Although cartilage-like matrix deposition in constructs was indicated by the increased collagen and sGAG content and histological staining from Day 0, the amount of matrix produced by the synoviocytes after 56 days of culture was still very low compared with native cartilage which is reflected by the low compressive modulus values (Table 2).

### **5.5.2 The Effect of Compressive Mechanical Loading on the DNA Content of Pre-Cultured Synoviocyte/PET Constructs**

After the first 28 days of application of mechanical loading to the constructs, the DNA content (used as a measure of cellularity within the constructs) significantly increased within both loaded and non-loaded constructs, in comparison to those at Day 0 ( $p < 0.0001$  and  $p < 0.05$ , Figure 85). Continual increase in DNA content was observed within both loaded and non-loaded constructs throughout the remaining culture period at Day 56 but it was only statistically significant in loaded constructs ( $p < 0.01$ , Figure 85). The significant increase in cellular content in loaded and non-loaded constructs at Day 28 indicated an increase in cell proliferation and this presumably continued for loaded constructs up to Day 56. This significant increase in DNA content (and therefore cell numbers) throughout the entire culture period observed only in loaded constructs suggests that the mechanical loading was stimulating cell proliferation rather than differentiation in to a mature chondrocyte phenotype at this later time period. These data also imply that the magnitude of the loading sensed by the cells was not harmful, leading to cell apoptosis or necrosis and net cell loss. The effect of mechanical stimulation on cell proliferation has previously been investigated on chondrocytes in 3D culture [90], [301]–[304]. Studies have demonstrated a modulation in the proliferative response to mechanical loading by chondrocytes in 3D culture and this is believed to be regulated by the mechanotransduction processes through different pathways such as stretch-activated ion channels [301] and integrins (specifically  $\alpha_5\beta_1$ ) [90]. Significant observations from these studies were that enhanced proliferation caused by mechanical loading occurs primarily where immature chondrocytes were involved and secondly for cells that have adopted a chondrogenic phenotype (e.g. after treatment with TGF- $\beta_3$ ) [90]. The process of cartilage growth in a joint is a complex one and consists of multiple stages, with immature chondrocytes initially proliferating in response to mechanical loading followed by the maturation stage i.e. differentiation in to mature chondrocytes [305]–[307]. In the current work, after 4 weeks of pre-culture in chondrogenic medium, the DNA data suggests the synoviocytes are behaving in a similar manner to immature chondrocytes which started to proliferate in response to mechanical loading throughout the culture period to Day 56. The observation that cell proliferation occurs with cells that are in a “receptive” phenotype also implicate the importance of pre-culture in chondrogenic medium (that contains TGF- $\beta_3$ ) in this study in order

to ensure that the synoviocytes are expressing the relevant integrins and becoming more chondrocyte-like. TGF- $\beta$  is known to regulate metabolic processes in articular cartilage and numerous studies have demonstrated that the provision of TGF- $\beta$  can influence the phenotypic status of the cells in order to re-express a chondrogenic phenotype [308]–[311]. However, the effect of mechanical loading had not stimulated observable cell differentiation.

The DNA content of non-loaded constructs initially increased significantly at Day 28 and did not change significantly between Day 28 and Day 56. In addition, significantly greater DNA content was observed in loaded constructs compared to those in non-loaded constructs at each time point. This implies that mechanical loading might be the cause for the significant increase in cell proliferation at the later time point of Day 56. As expected, native cartilage had significantly less DNA content than both loaded and non-loaded constructs (apart from at Day 0) due to a sparse population of chondrocytes in articular cartilage (Figure 85).

### **5.5.3 Histological Appearance of Pre-Cultured Synoviocyte/PET Constructs Subjected to Compressive Mechanical Loading**

Histological analysis (of collagen types I and II, and Alcian blue/Sirius red) supported the protein (collagen and sGAG) content of the developing constructs, as stated in previous sections.

At Day 28, histological images revealed that the cellular and matrix distribution was similar in loaded and non-loaded constructs (Figure 92 to Figure 97). The majority of the cells were located at the edges and either the top or bottom face of the constructs which appeared to have a flatter morphology and this is where the first evidence of a cartilage-like matrix (staining positive for collagen type II and sGAG) had been synthesised and deposited. This could be due to nutrient availability, where the surface of the construct would have the greatest amount of nutrient available, potentially facilitating more cells to proliferate and differentiate into a chondrocyte-like phenotype [312], [313].

Histological differences observed at Day 56 were apparent between loaded and non-loaded constructs (Figure 98 to Figure 102). By Day 56, there was evidence of a slight increase in staining intensity of cartilage-like matrix revealed around the periphery of the loaded constructs (in comparison to Day 28 constructs) (Figure 98 to Figure 102), indicating more cartilage-like matrix was laid down. In addition, although it's not apparent throughout their cross-section, it was evident that the histological staining of cartilage-like matrix was found in regions near the cores of the loaded constructs following an initial non-homogenous matrix deposition on the periphery of the constructs (indicated by arrow in Figure 100 and Figure 102). It could be suggested that the majority of cells are yet to further differentiate into chondrocyte-like cells, consequently affecting the deposition of cartilage-like ECM. Cells were seemingly differentiating to more classic chondrocyte-like cells in some locations within the loaded

constructs, such as the surfaces and regions toward the cores of the constructs, based on the presence of their associated cartilage-like matrix. This is further supported by the confocal findings of significant morphological changes in synoviocytes at the periphery of the loaded constructs at Day 56 (Figure 107). It was assumed that when the mechanical loading was applied during the culture period, it would trigger the cells to favour matrix synthesis and deposition. However, the lack of abundant histological staining of cartilaginous matrix observed in loaded constructs at Day 56 in this study suggests that very little cartilage-like matrix was laid down by the cells in response to the mechanical stimulation (Figure 100 to Figure 102).

In non-loaded constructs it was evident that histological staining only occurred at the periphery throughout the culture period. Under free swelling conditions, the cells within the constructs are seemingly differentiating based on their local environmental conditions and variations (e.g. nutrient availability and cell density), leading to some regions (e.g. the edges of the constructs) assuming a more classic chondrocyte-like phenotype with associated matrix and other regions (e.g. the core of the construct) not so.

Another visual difference between loaded and non-loaded constructs after Day 56 was the overall shape of the constructs themselves. Loaded constructs had a more consistent thickness and disc-like cross-sectional shape through the culture period, whilst the non-loaded constructs appeared non-uniform with marked variation and were thicker. The application of mechanical loading along with the confinement of the silicone ring appeared to compact the constructs and inhibit extraneous growth in all aspects that did not follow the overall margins of the construct. The lateral displacement was limited when the edges of the construct came into contact with the silicone ring under mechanical loading. This would have resulted in unintended circumferential loading, limiting extraneous growth in that plane. In non-loaded constructs, the growth was not physically limited in any aspects except in the lateral plane by the confinement of the silicone ring, thereby leading to constructs with non-uniform cross-sectional shape and non-consistent thickness. These constructs would not be appropriate for use in the clinical setting because a cartilage replacement should be smooth and level, allowing it to follow the curvature of the neighbouring native cartilage surface to avoid abnormally high stress generation and support smooth articulation.

#### **5.5.4 The Effect of Compressive Mechanical Loading on the Compressive Moduli of Pre-Cultured Synoviocyte/PET Constructs**

The compressive moduli of non-loaded constructs (measured at 18 % strain), on average, increased gradually throughout the culture period but there was no significant difference at each time point (Figure 86 and Table 2). This slight increase is likely due to the continual culture of constructs in chondrogenic medium, resulting in the cells steadily laying down cartilage-like matrix [186]. This is supported by the observed increase in collagen content (Figure 83), initial

increase in sGAG content followed by consistent sGAG level (Figure 84) and consistent level of DNA content (Figure 85) throughout the entire culture period. The suggestion of matrix deposition is further supported by the increase in histological staining for cartilage matrix between Day 0 and Day 28 which remained consistent by Day 56 (Figure 92 to Figure 94). Nevertheless, the amount of detectable cartilage-like matrix remained low in non-loaded constructs.

The compressive moduli for loaded constructs increased significantly between Day 0 and Day 28 and but there was no statistical difference in compressive modulus values between Day 28 and Day 56 (Figure 86 and Table 2).

The cause of the increase in compressive moduli in loaded constructs from Day 0 to Day 28 could be similarly attributed to that suggested for the non-loaded constructs, i.e. due to an increase in cartilage-like matrix being deposited as is evident by comparable histological findings (noticeable increase in Alcian blue and collagen type II staining in both loaded and non-loaded constructs) (Figure 92 to Figure 97). As suggested previously, during this period the increased collagen and sGAG content in both loaded and non-loaded constructs is caused by a shared circumstance such as the chondrogenic medium. Given the similarity of the protein content (collagen and sGAG) and the histological staining of cartilage matrix in loaded and non-loaded constructs at Day 28, it is likely that the chemical cues in the chondrogenic medium and the biological conditions (i.e. nutrient availability and cellular density) during this period remain highly influential in determining the matrix production and resulting construct stiffness. It is presumed that mechanical loading will only have a predominating effect on cellular phenotype with the formation of a (stiffer) construct in the presence of accumulated cartilage-like matrix. In this case, as there were no significant differences in modulus values between the two experimental groups, mechanical loading has not had an obvious effect on cartilage-matrix formation at this early stage but has had an effect on cellular behaviour, as supported by the significant differences observed in the increase in cellularity between loaded and non-loaded constructs (Figure 85). There is, however, another contributor (apart from increased deposition of cartilage-like matrix) that could enhance the stiffness of the loaded constructs. At Day 28, the histological images showed that the thickness of loaded constructs appeared to have decreased with the application of compression, compared to a thickening observed in the non-loaded constructs (Figure 92 to Figure 97) (discussed in Section 5.5.3), potentially indicating compaction/consolidation of the laid down matrix. As the loaded and non-loaded constructs have statistically similar collagen and sGAG content and histological staining, the differences between compressive moduli could be partly attributed to matrix compaction/consolidation.

At Day 56, after the surge in proliferation that was evident between Day 0 and Day 28 and the suggestion of cartilage-like matrix production during the first 28 days of mechanical loading, it was presumed that plenty of cells are present and potentially receptive to mechanical loading via

the relevant integrins and in association with relevant cartilaginous matrix molecules. Therefore, it might be expected that the cells would be in an ideal position to react to the mechanical challenge by depositing more cartilage-like matrix to resist the compression, thereby substantially increasing the compressive moduli of the constructs. The compressive moduli of the loaded constructs, on average, increased from Day 28 to Day 56, but this was not statistically significant (Figure 86 and Table 2). This unexpected phenomenon might suggest that not much new cartilage-like matrix was produced in response to mechanical stimulation between 28 and 56 days of loading. This is further indicated by the similar (low) histological staining for cartilage-like matrix observed in loaded constructs at Day 28 and Day 56 (Figure 100 to Figure 102), in contrast to the histologically mature and high stiffness constructs developed in Finlay *et al.* (2016) [1]. One possible reason for the observed lack of cartilage-like matrix deposition and the low compressive moduli obtained for constructs after 56 of mechanical loading in this study might be the starting thickness/porosity of the PET scaffold used in the present study. The scaffold material (with 97.0 % porosity) was initially heat compressed in order to yield scaffolds with an overall porosity of 90.2 % by volume and 0.9 mm thickness. However, after the heat compression process in this study, the resulting scaffold thickness was on average  $1.85 \pm 0.24$  mm which was twice the thickness than expected (those used in Finlay *et al.* (2016) [1]). There are a couple of factors that may help explain the observed differences in scaffold thickness, such as quality control of the PET material (i.e. were new measurements of porosity made after each batch, to ensure that any variability in the source material and the heat pressing process were taken into account?), differences in thickness measurement techniques and the preservation of scaffold properties. It is likely that the scaffold properties was not retained due to the scaffold material used in this study was over 10 years old and therefore possibly displayed a recovery of its thickness. As a result of increased scaffold thickness but still with the same amount of fibres, an increase in porosity would be expected and this could potentially affect the rate of matrix production and deposition. These data suggest that the scaffold used in the present study had a greater porosity than that (90.2 % porosity) used by Finlay *et al.* (2016) [1]. Prior to the 2016 study, Finlay investigated the effect of scaffold porosity variation on matrix production and deposition with different cell types [287]. Combinations of scaffolds of differing porosities (90.2 % - 97 %) and cell types such as human foetal osteoblastic cells (hFOB), bovine synoviocytes and human bone marrow mesenchymal stem cells (BM-MSC) were used to determine the best combination to produce the greatest quantity of matrix [287]. The protein content in conjunction with the SEM images of the cell-scaffold constructs after 4 weeks in chondrogenic culture illustrated that scaffold with the lowest porosity 90.2 % (from 97 %) was the most advantageous in promoting matrix production and filling of the scaffold with all three cell types [287]. Cell-scaffold constructs produced with a scaffold of 90.2 % porosity were completely filled with cells and matrix compared to those

constructs used scaffolds with the highest porosity of 97 % which only partial filling up to 50 %.

There are a number of potential factors that could influence matrix deposition that are associated with an increased in scaffold porosity. One possible factor could be a reduction of the potential surface area for cellular attachment leading to a lower number of cells being present in the constructs after seeding and hence an overall reduction matrix production. However, there was an equal weight of fibres present in the scaffolds used in both studies and the consequent total surface area available for cellular attachment would be the same irrespective of changes in porosity. In addition, the cellular (DNA) content obtained in this study for both loaded and non-loaded constructs at each time point was comparable to those in the 2016 study [1]. This was therefore unlikely to be the causative factor to explain the observed low cartilage-like matrix deposition and low compressive moduli obtained in constructs in this study. A more significant factor associated with increased porosity is the resulting increase in void volume between fibres in the scaffolds used in the present study compared with the 2016 study, therefore requiring more matrix to fill the scaffold. The resulting increase in void space with respect to increased thickness is thus likely to have contributed to the observed lack of cartilage-like matrix deposition and the low compressive moduli obtained in constructs in this study. Increasing scaffold porosity would also yield increased distance between scaffold fibres that could potentially prevent cells from bridging between scaffold fibres, leading to reduced cell-cell interactions and causing a delay in promoting a cell phenotype with increased matrix synthesis and deposition. Cell-cell interactions play a crucial role in tissue formation through cell signalling, allowing cells to communicate with each other in response to alterations in their microenvironment. It has been implicated in the literature that cell-cell interaction is an important factor during the differentiation of mesenchymal cells towards osteoblastic and chondrogenic phenotypes (in addition to cell-matrix interactions) [314], [315]. Direct mechanical signals originated from the mechanical loading of constructs or signals from another synoviocyte can be sensed by a synoviocyte and are likely to be transferred to their neighbouring synoviocytes through cell-cell contacts [316]. Transmission of mechanical forces can occur via cadherins which are cell-cell adhesion transmembrane molecules [317]. They are able to bridge plasma membrane and link other synoviocytes to allow cells to communicate with each other in response to changes in their microenvironment [317]. Confocal images of synoviocytes within constructs at Day 0 in his study (Figure 103) provided evidence to suggest that increased distance between scaffold fibres as a result of increased porosity is likely to be the primary driver for reduced matrix production and consequent low compressive moduli obtained in constructs in this study (Figure 86). Confocal images revealed synoviocytes were located on scaffold fibres and where fibres are in close proximity to one another (as shown in Figure 103) whilst a sparse number of synoviocytes were observed in areas with larger inter-fibrillar gaps. This suggests that cell-cell interactions primarily occurred in areas with small inter-fibrillar

gaps, allowing the cells to bridge the gaps to promote a chondrocyte-like phenotype with increased matrix synthesis and deposition in order to fill the pores of the scaffold. A scaffold with a higher porosity would have a greater proportion of large inter-fibrillar gaps than scaffolds with lower porosity, such as those used in the 2016 study. As a consequence, the occurrence of cell-cell interactions would be limited which could hinder the development of a desired phenotype and subsequent cartilaginous matrix deposition and, therefore less matrix filled pores within the scaffolds is likely. This is supported by the lack of Alcian blue and collagen type II staining for the constructs in this study.

During the same stage of construct development (between Day 28 and Day 56) in Finlay's 2016 study, a substantial increase in compressive moduli was observed for the loaded constructs and the histological findings revealed clear differences between loaded and non-loaded constructs [1]. The compressive modulus occurred in conjunction with intense, homogenous histological staining for Alcian blue and collagen type II throughout the loaded constructs. Finlay provided evidence to show that suitably applied mechanical stimulation is a predominating factor in developing and maintaining chondrocyte-like phenotype and consequent cartilaginous matrix deposition [1]. The low compressive moduli obtained in this study suggests using a scaffold with suitable porosity is essential in promoting cartilaginous matrix synthesis and deposition which is believed to be time dependent. More porous scaffolds might take longer for cell-cell interactions to occur and if the porosity is greater than a threshold value, these interactions might not happen at all. Thus, in this study, use of a scaffold with higher porosity has potentially hindered the rate of cell differentiation and matrix deposition within the constructs which in turn resulted in lower matrix synthesis and deposition after the pre-culture period. It was originally assumed that when mechanical loading was initially applied during experimental culture, this stimulation to the cells would favour matrix synthesis and deposition. However, this was not observed in this study, presumably due to the issues described above in respect of scaffold porosity. The data in this study suggests that the cells hadn't differentiated to the same extent as in previous studies and therefore the effect of loading had been only to promote cell proliferation rather than enhance matrix secretion.

The bioreactor was set up in such a way that at Day 0 (following the 4 weeks in chondrogenic culture) it applied strain to constructs at magnitudes between 17 % to 22 %, as determined by the stiffness of the silicone rings and the applied load of 5 N by the pre-compressed springs within the bioreactor. It is possible that insufficient amounts of initial cartilage-like matrix had been laid down within the constructs during the 4 week pre-culture period, potentially due to using a scaffold with higher porosity. This would then result in the matrix might being insufficiently stiff – or insufficiently cartilage-like - to be able to transmit the mechanical signals to the cells, further hindering the rate of cell differentiation and matrix deposition. The histological images of constructs at Day 0 revealed the lack of cartilage-like matrix present within the constructs (Figure 89 to Figure 91). Matrix stiffness has been implicated in regulating

gene expression and cell fate, such as in directing the differentiation of mesenchymal stem cells [84]. Interestingly, ECM stiffness can also influence cell phenotype [84]. Articular chondrocytes can respond to the mechanical loads imposed on their matrix through mechanotransduction. This is a process in which cells can sense and respond to the biophysical properties of the extracellular environment through integrin-mediated adhesion, converting them to biochemical signals that modulate the metabolic activity of the cells [89], [90]. The external mechanical forces induce matrix strains and associated stresses, which promote assembly of the cytoskeleton into actin stress fibres and focal adhesions and drive a variety of signalling cascades, inducing the desired mechanotransductional effects [84]. In order to transmit the applied external mechanical forces from the matrix to the cells and consequently influence cell differentiation and matrix production, the matrix is required to have a sufficient stiffness [84]. In the case of the constructs used in this study, the lack of a competent matrix at the outset of the introduction of mechanical loading would preclude these mechanotransduction events from taking place, or at least mean that they would be much less common.

The idea of confining the constructs within silicone rings was that the rings would initially take the majority of the load applied from the bioreactor and apply strains between 17% and 22 % on the constructs to produce suitable stress within the deposited matrix and residing cells, triggering anabolic effects. Cells would react to the compressive loading by upregulating the production of cartilage-like matrix that can distribute the load away from the cells, reducing cellular stress in an attempt to “resist” the applied load. This accumulation of new matrix would then cause the constructs to marginally increase its thickness (by matrix deposition causing an increased amount of sGAG and consequently bound water) and its compressive stiffness. As the cells continued to lay down cartilage-matrix in response to the mechanical stimulation, the stiffness and thickness of the constructs would eventually become comparable to that of the silicone rings, thereby the constructs would effectively take a greater proportion of the applied load as well as increasing the strain applied. This consequently would maintain cellular mechanical stimulation and induce continued anabolic effects, effectively creating a positive feedback loop, steadily increasing the thickness and the compressive stiffness of the constructs. This loop would continue until the majority of the load applied from the bioreactor would be taken by the constructs and not by the surrounding silicone ring.

However, by Day 56 in the current study, the stiffness of all of the constructs had not developed beyond the stiffness of the silicone rings (compressive modulus of 0.88 MPa (Day 56 loaded-constructs) vs 2.64 MPa (cured silicone) respectively at 18 % strain), indicating that the silicone ring was still taking up the majority of the load. In addition, the thickness of the loaded constructs at Day 56 (Figure 100 to Figure 102) remained the same as that at Day 28 (Figure 95 to Figure 97). This again suggests that the mechanical loading might not have been effective in inducing the anabolic effects observed in Finlay’s 2016 study. The DNA content of constructs in the current study showed that cell proliferation remained high during the 56 days, suggesting

that the cells were behaving as immature chondrocytes rather than fully differentiated cells (see above), further supporting the contention that the constructs in this study were “immature” during the loading period and therefore unable to elaborate a competent matrix as described previously.

It seems likely therefore, that for scaffolds of higher porosity, such as those used here, a longer pre-cultured period may be required to ensure sufficient ECM is laid down and that the quality of the ECM is cartilage-like, with a higher starting compressive stiffness, plus the cells themselves would then be sufficiently mature to be able to respond to mechanotransductive signals. The data in this study suggests scaffold porosity is clearly an important factor to take in to account when considering scaffold (and therefore construct) design. It is possible that above a certain porosity (as yet unknown), the approach used here might not be feasible.

Loaded constructs on average had higher compressive modulus values than non-loaded but the difference only reached statistical significance at Day 56. This may be that by Day 56, the cells within the constructs were beginning to produce a more cartilage-like ECM. In Finlay’s 2016 study, a significant difference in compressive modulus values between loaded and non-loaded constructs was observed at each time point of the loading period and the rate of increase in compressive moduli for the loaded constructs accelerated dramatically between Day 28 and Day 56. The compressive moduli of loaded constructs developed at Day 56 (mean of 12.1 MPa) were 12- x higher than those developed in this study (mean of 0.88 MPa). This further emphasises that there was a delay in matrix deposition in this study, potentially caused by the use of thicker scaffold pads with increased porosity and consequent reduction in cell-cell interactions, as suggested previously in this section. This also further emphasises the importance of an optimal dimension for the scaffold material, pre-culture period and mechanical loading in promoting a chondrocyte-like phenotype, leading to superior cartilage-like matrix and consequent mechanical properties within the constructs.

Given the similarity in collagen and sGAG content obtained in loaded and non-loaded constructs through the experimental period, the relative increase in compressive moduli in loaded constructs at Day 56 can not be solely explained by the accumulation of matrix but rather by the quality of matrix (both composition and density). The histological images obtained from constructs at Day 56 revealed differences between loaded and non-loaded constructs (Figure 98 to Figure 102). Loaded constructs had apparently slightly greater deposited matrix (as judged by staining with antibodies to collagen type II and Alcian blue staining) in comparison to the non-loaded constructs (Figure 100 and Figure 102). In addition, low staining of cartilage-like matrix appeared in areas towards the cores of the loaded constructs. This perhaps suggests it is moving towards filling the pores at the cores of the constructs with cartilaginous matrix but the rate of matrix deposition is slower than expected. Following the initial non-homogenous deposition of matrix after Day 28, an imbalance of intra-construct regions would occur as more matrix was

deposited. It is possible that those regions with more cartilage-like matrix (i.e. in the circumferential edge of the construct) will be stiffer and possibly swell more, therefore these regions would be able to take a greater proportion of the applied mechanical load. As this process continues it could reach a tipping point where the mechanical stimulation in the stiffer areas would become not favourable to matrix deposition, leading it to slow down. This would continue until other regions have 'caught up' and resulted in a similar matrix composition. Histological staining found in areas towards the cores of the constructs at Day 56 is evident that these regions had deposited cartilage-like matrix in order to catch up to the other stiffer regions with similar matrix composition. The mechanical stimulation to the temporarily-suspended regions would then tip back to one that favoured matrix synthesis. This proposed process would eventually result in uniform cross-section and homogenous matrix distribution as seen in Finlay's study. Based on the experimental data in this study, it is possible that the accumulation of cartilage-like matrix might have continued if the constructs had been cultured with applied mechanical loading to a later time point and subsequently produce constructs with relatively homogenous cartilage-like matrix and higher moduli values. This proposed process is highly theoretical and would require further experimentations with a prolong culture duration (up to Day 84) to determine the cause of the slower rate of matrix deposition with the use of thicker scaffold pads.

Overall, moduli of both loaded and non-loaded constructs in this study followed the same trend as that reported in Finlay's study [1] in that values increased with in time and loaded constructs had significantly higher moduli at each time point than the non-loaded constructs. However, the values obtained from the Finlay's study were substantially higher than those observed in this study. This is strongly correlated with the intensity of histological staining of cartilaginous matrix in each of the study which revealed homogenous and regional matrix deposition in Finlay's and the current study, respectively. This further emphasises the lack of cartilaginous matrix deposited in constructs in this study and thereby resulted in constructs with substantially low compressive moduli.

### **5.5.5 Morphometric Appearance and Distribution of Synoviocytes in Constructs under Incremental Compressive Tissue Strains**

Synoviocytes within both loaded and non-loaded constructs were visualised by confocal imaging in their uncompressed state and during static incremental compressive tissue strains; an estimated strain experienced by the constructs within the bioreactor during mechanical loading (this was construct-specific, see Section 5.3.7) and 28 % compressive tissue strain (corresponding to near maximum physiological loading which lies in the physiological range of 0 % to 30 % [130], [210], [264]) in order to determine cellular deformation behaviour.

Due to the limited capability of the confocal microscopy, such as the restricted laser penetration into the cartilage constructs, it was not possible to visualise synoviocytes in regions near the cores of the constructs. Thus, this study was limited to the morphometric appearance and distribution of synoviocytes at the periphery of the constructs, with images captured from the surface to a depth of approximately 40/50  $\mu\text{m}$ . It would also have been ideal if repeat measurements had been made on the same cell, or at least in the same population of several cells but this was not possible. Different populations of synoviocytes were imaged because the cells were densely populated within those constructs developed at the early time points (Day 0 and 28) which made it impossible to track a single cell population. In addition, the Z-range (the total depth) of each image was varied to accommodate visualisation of different populations of synoviocytes.

A clear difference in morphometric appearance and distribution of synoviocytes was observed between loaded and non-loaded constructs (Figure 103 to Figure 107). Synoviocytes appeared thin and elongated in shape in constructs at Day 0 (Figure 103) and their morphometric appearance remained similar in non-loaded constructs at Day 28 (Figure 104), suggesting that the majority of synoviocytes had not undergone differentiation with no sign of morphological change, which consequently leads to the low cartilage-matrix deposition as shown in the histological images (Figure 92 to Figure 94). By Day 56, the majority of synoviocytes still remained in an elongated shape but some had started to spread with larger projected areas (Figure 106). This perhaps indicates that the synoviocytes were starting to differentiate towards a more chondrocyte-like phenotype and increasing the production and deposition of cartilage-like matrix.

In contrast, by Day 28, there was evidence of cell morphological changes in loaded constructs (Figure 105). Synoviocytes were found to be more spread in appearance and had become more sparsely distributed compared to the fibroblast-like morphology observed at Day 0 (Figure 105). In response to biochemical and biomechanical signals, morphological change, such as cell shape and size, can be an indication of phenotype differentiation/de-differentiation [318]. Alterations in chondrocyte morphology have been strongly suggested to relate to changes in chondrocytic phenotype [208], [209]. It has been well documented that the *in vitro* 2D culture of chondrocytes induces a switch in phenotype from chondrocytic (differentiated) to fibroblast-like (de-differentiated) [209]. These changes are evidenced by the loss of a spherical/ellipsoid morphology and a decline in the expression of chondrocyte-specific type II to type I collagen ratio [319], [320]. The morphological changes of synoviocytes observed in the loaded constructs at Day 28 in the present study suggested the promotion towards a chondrocyte-like phenotype, resulting in secretion of cartilage-like ECM. This is further supported by the histological staining of cartilage-like matrix including collagen type II and sGAG found around the periphery of the loaded constructs.

Chondrogenesis is the process by which cartilage is formed, involving stem-cell differentiation to mature chondrocytes and the secretion of molecules that form the ECM through the coordinated effects of growth/differentiation factors and ECM components [97], [315]. Chondrocyte differentiation is a multistep process characterised by successive changes in cell morphological features and gene expression [97]. For cartilage tissue engineering, the maintenance of a chondrocytic phenotype is crucial to produce cartilage-like matrix [208]. Research efforts have been made to develop *in vitro* culture methods and medium supplementation to improve on matrix metabolism to favour a hyaline-like matrix [208], [321]. It has been implicated in the literature that cell-cell interaction is an essential event for chondrocytic differentiation and the initial formation of cartilage-like matrix [314]. It is evident that cell-cell interactions occurred within the loaded constructs at Day 28 as some synoviocytes appeared in close proximity with each other (Figure 104). In this study, seeded synoviocytes within the constructs were cultured in chondrogenic medium to stimulate cell proliferation and initial chondrogenic-like differentiation for synthesis and deposition of a foundation of matrix. By Day 28, the effect of mechanical loading coupled with the chondrogenic conditions was likely to have promoted further chondrocyte-like differentiation and cartilaginous matrix production as supported by the evidence seen in the current study.

Cell-matrix interactions are also implicated to be significant for the regulation of many biological processes important to homeostasis and repair of articular cartilage [97]. ECM is vital to the form and function of soft connective tissues and cells are responsible for building and maintaining the ECM [84]. Chondrocytes within cartilage establish the ECM during development, maintain it in health, remodel it during environmental adaptations and repair it in response to diseases and injury [84]. Conversely, as well as providing structural support to the chondrocytes and maintaining tissue under mechanical loads, ECM influences many chondrocyte functions including migration, adhesion, differentiation and survival. It also plays an important instructional role in cell signalling, providing biochemical and biomechanical cues that influence the above range of chondrocyte activities. These cues are passed on from the ECM to the cell via recognition of ECM proteins by the transmembrane receptors called integrins [89], [91]. They have two main functions: 1) attachment between the ECM and the cell and 2) signal transduction from the ECM to the cell [97]. In addition to the biochemical cues that regulate cellular functions, ECM is able to store a range of cellular growth factors, acting as a depot for them [97]. Changes to the physiological conditions can trigger protease activities that cause release of growth factors locally, leading to rapid and local growth-factor-mediated activation of cellular functions [97]. In particular, proteoglycans (PGs) help trap and store growth factors within the ECM [97]. Once secreted, the molecules aggregate with the matrix [97]. As a result, resident cells produce the components that make up the ECM via exocytosis [322].

Chondrocytes can detect and respond to the mechanical load acting on the articular cartilage that are perceived by resident chondrocytes as stimuli through integrin-mediated mechanotransduction [89], [90]. External mechanical forces (such as applied tissue compression) are known to modulate the metabolic activity of articular chondrocytes and are transmitted through, or exerted on, constituents of the ECM, matrix receptors and intracellular structures via cell-matrix interaction [84], [90]. To increase differentiation towards a chondrocyte-like phenotype in tissue engineered cartilage, appropriate mechanical stress is crucial in order for the cells to receive the suitable signals for the production of a resilient, load-bearing cartilaginous ECM [208]. Thus, the expression of cartilaginous matrix proteins is essential for the development of suitable *in vitro* engineered cartilage tissue [209]. In this study, in order to maximise the effects of mechanical loading to promote further differentiation and deposition of cartilage-like matrix, the ECM needs to contain cartilaginous components that the cells can adhere to, so mechanical signals can be transmitted from ECM to the cells. During the mechanical loading of constructs, the external applied tissue strain would induce matrix strains and associated stresses, which potentially promote assembly of the cytoskeleton into actin fibres and focal adhesions [84]. Cell-matrix adhesion involves both binding to ECM proteins and to the actin cytoskeleton [91]. Spreading of synoviocytes with large projected area and development of thin protrusions observed in loaded constructs at Day 28 and Day 56 (Figure 105 and Figure 107) might suggest the occurrence of interactions between synoviocytes and the ECM as cell spreading and development of large focal adhesion and actin stress fibres are morphological features which characterise cell-matrix adhesion [84], [91]. Cells are able to detect the ECM rigidity and adjust the applied tension accordingly [91]. Cells experience high traction forces when bound to stiff matrix through the formation of robust actin stress fibres and focal adhesions and the consequent of larger spread areas [91]. On softer matrices with less force applied, this leads to less well developed actin fibres and focal adhesion [91]. The presence of defined thin protrusions of synoviocytes observed in the loaded constructs perhaps indicate that mechanical loading is having a predominating effect on cellular phenotype via cell-matrix interactions and synoviocytes are reacting to the mechanical stimuli with the subsequent formation of a relatively stiff matrix in order to increase the stiffness of the constructs to resist compression. With the slight increase in histological cartilage-like ECM staining and significant increase in compressive modulus values observed in loaded constructs compared to the non-loaded constructs at Day 56, this further emphasises that synoviocytes are responding to the compression applied on the constructs that are transmitted through from the ECM as mechanical signals by modulating towards a chondrocyte-like phenotype and increasing deposition of cartilaginous ECM. This further emphasises the importance of mechanical loading in producing 'phenotypically correct' chondrocyte-like cells, leading to cartilage-like matrix and consequent mechanical properties within the constructs.

### **5.5.6 The Effect of Incremental Compressive Tissue Strains on Synoviocyte Deformation in Constructs: Morphometric Measurements**

In order to provide a better understanding of Finlay's hypothesised mechanical mechanism in developing cartilage-like constructs [1] and to address the relationship between applied tissue strain and resulting cellular strain in constructs developed at different time points, cell deformation was examined and quantified under incremental static compressive tissue strain values that corresponded to the estimated amount of strain applied to the constructs by the bioreactor during mechanical loading (customised to each construct as described in Section 5.3.7) and at 28 % strain (corresponding to conditions approaching maximum physiological loading which lies in the physiological range of 0 % to 30 % [130], [210], [264]).

Confocal images of synoviocytes within loaded and non-loaded constructs developed at different time points revealed that the cells were densely populated, in particular during the earlier culture period (Day 0 and Day 28) (Figure 103 to Figure 105). This made it extremely difficult to identify the cell boundaries, which is an essential feature required for 3D quantification analysis of synoviocyte morphology, therefore only morphological changes of cells within constructs at Day 56 were able to be measured. Tracking the same population of cells from the uncompressed state to being under different magnitudes of compressive tissue strain was also incredibly difficult because the field of view on the confocal microscope changes with the application of compressive tissue strain. This, in addition to the high density of cells within the constructs made cell identification very challenging. Analysis was therefore conducted on different populations of synoviocytes during their uncompressed state and under incremental compressive tissue strains within constructs at Day 56.

In this study, changes in synoviocyte 3D morphology in response to incremental static compressive tissue strains were examined and measured using Amira software from the confocal volume images of synoviocytes within loaded and non-loaded constructs captured at Day 56. Cell morphology was measured 30 mins after the application of compressive loading, assumed to represent the equilibrium response. These measurements serve as a baseline for more physiologically-relevant dynamic studies in the future. Only synoviocytes that had clear cell boundaries were analysed for cell deformation quantification. Due to the difficulty of cell boundary identification and extremely time consuming quantification analysis process, ten different synoviocytes were measured under different experimental conditions (uncompressed state, estimated compressive strain experienced by the constructs under 5 N load applied by the bioreactor and 28 % compressive tissue strain) from two constructs in both experimental groups (loaded and non-loaded constructs). In addition, morphometric parameters, such as cell width, length, height, volume and sphericity, were measured on synoviocytes located at the periphery of the constructs due to the limitation with laser penetration on the confocal system.

The morphometric measurements of uncompressed synoviocytes corresponded with the cell appearance observed in the confocal images of non-loaded and loaded constructs at Day 56. When considering cell sphericity measurement, a value of 1 corresponds to a perfect a sphere, any value less than 1 indicates departure from the sphere, with lower values signifying least spherical structures. Lower values of sphericity ( $0.30 \pm 0.07$  and  $0.32 \pm 0.03$  for non-loaded Sample 1 and Sample 2, respectively) were obtained for synoviocytes in non-loaded constructs, indicating that they were more elongated in shape in comparison to those in loaded constructs which had higher sphericity values ( $0.42 \pm 0.05$  and  $0.41 \pm 0.08$  for loaded Sample 1 and Sample 2, respectively) (Table 3).

There were no detectable differences in cell volume and height between uncompressed synoviocytes in loaded and non-loaded constructs (Table 3).

When measured under the estimated strain experienced by the construct during mechanical loading (14.7 % and 12.4 % strain for Sample 1 and Sample 2 respectively) and 28 % compressive strain, there were no significant changes in synoviocyte morphology within loaded constructs other than a significant decrease in sphericity observed in Sample 1 between synoviocytes at 0 % and compared to those at 28 % applied strain ( $p < 0.05$ , Figure 109B).

In contrast, application of compressive tissue strain had variable but significant effects on synoviocyte morphology in non-loaded constructs (Figure 108). Synoviocyte volume significantly decreased in Sample 2 between synoviocytes at 0 % and those at 28 % strain ( $p < 0.05$ , Figure 108E) and synoviocytes under an estimated strain applied to the constructs during mechanical loading in the bioreactor (21 %) compared to those at 28 % applied strain ( $p < 0.05$ , Figure 108E). A significant decrease in synoviocyte height was observed in Sample 1 between synoviocytes at 0 % and those under an estimated strain applied to the constructs during mechanical loading in the bioreactor (23.1 %) and at 28 % applied strain ( $p < 0.01$  and  $p < 0.0001$ , Figure 108C). In addition, a significant reduction in cell width was observed in Sample 1 between synoviocytes at 0 % to compared to those at the estimated strain applied during mechanical loading in the bioreactor (23.1 %) and 28 % strain ( $p < 0.01$ , Figure 108D).

The lack of changes in cell morphology under application of compressive tissue strains in the Day 56 loaded constructs were surprising as previous analysis had indicated that these constructs were beginning to show some early signs of differentiation to a more chondrocyte-like phenotype and had a higher modulus value than the non-loaded constructs. Based on the experimental data in this study, it seems likely that the lack of a homogeneous cartilaginous matrix observed in the loaded constructs at Day 56 in comparison to those in Finlay's 2016 study could influence the deformation behaviour of synoviocytes in a similar site-specific way.

It is presumed that internal mechanical stress generated during compression of the construct is primarily borne by the matrix and transmitted to the cells [84], [90]. This would be detected by

the cells causing them to experience a level of stress which induces cell morphology changes. However, matrix stiffness around the cells plays a critical role in transmitting the mechanical stress and so influencing cell phenotype [84]. Constructs with low amount of cartilage-like matrix (ones developed in this study) will deform more readily as the matrix will not be able to bear the load which reduces the transmission of mechanical stress and strain to the cells. In contrast, constructs with homogeneity of stiff matrix (such as those produced in Finlay's study) will bear and transmit more of the load to the cells. The construct will only be able to bear load and transfer force/deformation to the residing cells if there is a stiff enough foundation of matrix otherwise the foundation will deform instead. Histological images (Figure 100 to Figure 102) revealed that the amount of cartilage-like matrix produced after Day 56 of mechanical loading still remained low in these constructs compared to the homogeneity of matrix deposited in the constructs developed in Finlay's study, suggesting the constructs might not have had a sufficient amount of foundations of matrix (and consequently not stiff enough) to bear and distribute the load across the constructs and therefore possibly an insufficient level of stress was sensed by the cells and consequent no significant change in cell morphology occurred. Indeed, the stiffness of all of the constructs at Day 56 had not developed beyond the stiffness of the silicone ring (compressive modulus of 0.88 MPa (Day 56 loaded-constructs) vs 2.64 MPa (cured silicone) respectively at 18 % strain) which means the silicone ring was still taking the vast majority of the load.

Inspecting the histological images of both loaded and non-loaded constructs taken from Day 56 revealed inhomogenous staining, suggesting that there were distinct regions with variable quantities of collagen type II and sGAG within the constructs that could also influence the deformation behaviour of synoviocytes (Figure 98 to Figure 102). This will, in turn, give rise to different regions within these constructs with variable compressive stiffnesses. Under tissue compression, a stiffer region will be able to bear and transmit more the internal stress generated from the load than a less stiff region. The histological images of loaded constructs at Day 56 revealed strong Alcian blue staining (which corresponds to sGAG content) around the circumferential edge, the region where confocal images of synoviocytes were taken (Figure 100 to Figure 102). However, it is not possible to identify the exact locations which the confocal images of synoviocytes were captured in order to map these to the histological findings. Given that strong Alcian blue staining appeared but limited change in synoviocyte morphology was detected at the superficial of the Day 56 loaded constructs under compressive tissue strains, this perhaps suggests that the regions where the synoviocytes were visualised had denser matrix but the synoviocytes did not experience much deformation because regions with less stiff matrix would deform much more readily. In addition, the proposed assumption of stiffness differences in regions with variable amount of matrix may explain the different deformation behaviour of synoviocytes observed in the two non-loaded constructs, giving rise to the variable changes in morphology that were seen under compressive tissue strains. Consequently, it could be assumed

that the microenvironment around the measured synoviocytes may contribute to the differences in synoviocyte deformation observed within the two non-loaded constructs. However, based on all the experimental results in this study, there is an insufficient amount of data to support the proposed assumptions for explaining the effects of deformation behaviour of synoviocytes within the loaded and non-loaded cartilage constructs. Site-specific differences in ECM quality, including stiffness, might explain the variability of response of the cells under compressive loading. For both loaded and non-loaded constructs, the lack of a homogenous matrix renders the data collection problematic. In addition, there will be differences in the cell deformation behaviour between static and dynamic loading. Even if there are no/little observable changes in cell morphology after 30 mins of static compression, this does not mean that the cells don't experience force/deformation whilst in the bioreactor i.e. dynamic conditions.

It is not possible to provide a huge amount of information regarding the effects of mechanical loading on cellular deformation within constructs created at different stages of development. There are limitations presented in this study. By not tracking the same population of cells, greater variability was added to the data. In addition, it was extremely difficult to identify cells with clear boundaries for morphometric measurements due to how densely populated they were within the constructs. Hence, only 10 cells were measured per experimental parameters (i.e. different strain levels) and groups (loaded and non-loaded constructs at Day 56). The small sample size could potentially increase the margin of error which can affect the confidence level of the study, especially given the heterogenous nature of the matrix as revealed in the histological findings. In addition, only cells that had clear boundaries were measured in this study and by selecting a sub population of cells this could potentially skew the data. In order to determine the predominant factor that caused the observed effects on synoviocyte morphology in this study and to address the relationship between applied tissue strain and the cellular strain, constructs with higher compressive modulus and more matrix deposition with greater homogeneity need to be developed. In addition, more cells need to be measured to increase the sample size, and if possible, track the same population of cells to improve the accuracy of the mean value of the measurements. For future experimental studies, by tracking the changes in cell morphology, the cell locations within the construct (i.e. top or bottom surface of the construct) and the matrix distribution around the cells with confocal and histological imaging for each experimental parameter (strain levels) and groups (loaded and non-loaded constructs developed at different time points), it will provide a better insight into the mechanism behind the construct's development and the relationship between applied tissue strain and the cellular strain within the constructs. Nevertheless, a methodology to visualise, image and quantify live cell morphology within cartilage constructs under incremental static compressive tissue strains was successfully developed, paving the way for more future cell deformation experiments to occur.

## **5.6 Conclusion**

The deformation behaviour of live synoviocytes within cartilage constructs under incremental compressive tissue strains was examined in order to better understand the mechanism behind the construct's development and to address the relationship between the applied tissue strain and cellular strain. The constructs developed in this study revealed only a small amount of cartilage-like matrix in comparison to those in a previous 2016 study which resulted in correspondingly low compressive modulus values. The main reason for the differences may be related to the starting porosity of the scaffolds used in the constructs, emphasising the need to understand the relationship between PET scaffold porosity, cell seeding density and time to differentiation. There was no significant change in synoviocyte morphology within loaded constructs under the estimated strain experienced by the construct during mechanical loading and 28 % compressive strain. It was likely that the microenvironment around the measured synoviocytes may contribute to the observed effects, in particular the stiffness of the constructs and the matrix heterogeneity that would have led to variable quantities of collagen type II and GAG within the constructs. However, a further study with larger sample size is required to give a better insight into the mechanism behind the construct's development and the relationship between applied tissue strain and the cellular strain within the constructs. Nevertheless, a novel methodology to visualise, image and quantify live cell morphology within cartilage constructs under incremental static compressive tissue strains was accomplished.

## Chapter 6 - General Discussion

*This chapter discusses the challenges faced during the investigations of cell deformation behaviour in native and tissue engineered cartilage explants by drawing together the issues raised in discussions within previous chapters and offers potential strategies for future work to address these challenges. The development of live cell staining and imaging methodologies and the design and production of a novel compression device used for static tissue compressive strain application are points of particular note.*

### 6.1 Introduction

Chondrocytes are responsible for the development, maintenance, remodelling and repair of the extracellular matrix (ECM) in articular cartilage [53]. The ECM is very versatile and influences many tissue functions in addition to its structural role including cell proliferation, adhesion, migration, differentiation and cell death [53], [84], [97]. Mechanical compression is known to modulate the metabolic and biosynthetic activities of chondrocytes [87], [90], [95].

Chondrocytes are able to sense and respond to the mechanical signals imposed by the ECM and convert them into biochemical signals through the mechanotransduction process, which is believed to be mediated by the transmembrane receptor, integrin [89]–[91]. In cartilage tissue engineering, it is important that an appropriate level of stress is received by the cells to favour for the promotion of a chondrocyte-like phenotype and induction of deposition of an appropriate matrix for tissue maturation [208]. An appropriate cellular response to mechanical signals is also essential for the development of *in vitro* engineered cartilage tissue [209].

Finlay *et al.* (2016) [1] attempted to engineer *in vitro* functional cartilage constructs for long term cartilage repair using mechanical stimulation. The resulting constructs achieved high compressive modulus and cartilage-like histological appearance comparable to that of native cartilage. It was hypothesised that a self-regulating mechanical regime had developed that increased the applied stress and strain in conjunction with the maturing constructs' stiffness and thickness. These two processes were believed to be generated as a consequence of the bioreactor set-up, in particular construct confinement within a silicone ring, and consequently initiated and maintained significant cellular mechanical stimulation to induce continued matrix production for formation of cartilage-like constructs. As stated previously in this section, an appropriate amount of stress is required to be transmitted from the ECM to the cells in order to promote an increased biosynthetic response (i.e. matrix production and deposition). However, the precise mechanism(s) behind the construct's development, in particular at a cellular level had not been

investigated. For future translation of the constructs, it would be of interest to identify the mechanical stress experienced by the cells within constructs developed at different time points. The aim of this thesis was therefore to study cell deformation behaviour in live native cartilage and tissue engineered constructs developed at different time points under incremental compression in an attempt to understand Finlay's hypothesised mechanism in developing cartilage-like constructs and to address the relationship between applied tissue strain and cellular strain. To achieve this, a methodology for visualising, tracking, imaging and quantifying cell morphological changes within native and tissue engineered cartilage under incremental compressive strains needed to be developed. A novel compression device capable of applying tissue strains to native and tissue engineered cartilage and simultaneously allow real time visualisation of the changes in cell morphology was developed (Chapter 2). A live cell staining using Hoechst 33342 and CellMask Green plasma membrane stains in conjunction with confocal microscopy was also developed to visualise, track, image cell morphological changes under applied tissue strains (Chapter 3). In addition, a custom workflow was developed on Amira visualisation and analysis software for cell deformation quantification analysis via morphometric measurements. All the research tools mentioned above were then used to determine the cellular deformation behaviour within native cartilage disks (Chapter 4) and cartilage constructs (Chapter 5) subjected to incremental compressive strains.

In this chapter, challenges raised during the development of the required research tools and the difficulties, both technical and biological, inherent in the studies of cellular deformation in both native and tissue engineered cartilage under incremental compression will be discussed.

## **6.2 Development of a Novel Device for Application of Compressive Loads with Simultaneous Live Cell Imaging**

Numerous previous studies have investigated the effect of compressive strain on chondrocyte metabolism and deformation, mechanotransduction signalling pathways and cartilage biomechanical behaviour *in vitro* using many different approaches including: isolated chondrocytes in agarose gel [88], [140]–[144], chondrocytes in native cartilage explants [51], [87], [133]–[136], fixed cartilage tissue [137], [138] and intact cartilage fully attached to its native bone [85], [145]. Many compression devices with different designs have been specifically developed in order to aid these studies and their research questions. However, none of the devices used in previously published studies were suitable for the experimental approach required for this thesis because fixed and cut tissue approaches were avoided (described in Section 2.1). Thus, a novel device was required to be developed to accommodate non-fixed and non-cut native cartilage disks and tissue engineered cartilage constructs and allow simultaneous application of compressive tissue strain and live cell imaging, in order to address the aim of the

work in this thesis; to examine cell deformation behaviour in live native cartilage disks and tissue engineered constructs developed at different time points under different magnitudes of compressive tissue strains.

A loading apparatus which adopted a loading configuration of perpendicular loading to the confocal laser path was developed to investigate the depth-varying compressive properties of human femoral head articular cartilage [135]. The device was specifically modified from a similar approach previously used by the same group to determine the variation of the equilibrium confined compression modulus of bovine articular cartilage with depth [133], [134]. The design of the apparatus allowed observation of chondrocytes in the full depth of a cartilage explant subjected to graded levels of equilibrium confined compression. Semi-cylindrical cartilage samples were used by cutting the harvested cartilage disk in half perpendicular to the articular surface and fluorescently stained the chondrocytes nuclei with ethidium homodimer-1. Each cartilage sample was placed between two porous stainless steel platens inside the confining chamber of the custom designed testing apparatus and overall tissue compressive displacements of 0, 8, 16, 24 and 32 % were achieved by advancing one of the platens slowly. The cartilage sample was allowed to stress relax for 60 mins at each compression level, the equilibrium load was measured and the tissue surface (perpendicular to the articular surface) was imaged to obtain the position of the chondrocytes within the tissue depth using an inverted epi-fluorescence microscope. The intra-tissue strain in each zone (from the articular surface to the deep zone) within the tissue depth was calculated from the images that captured the position changes of the centroids of fluorescent chondrocyte nuclei for each compressed state relative to the uncompressed reference state. In a study by Guilak *et al.* (1995) [87], changes in chondrocyte morphology and local matrix deformation in the surface, middle and deep zones of canine articular cartilage explants under physiological levels of tissue compression were quantified. A similar compressive loading apparatus which adopted the approach of loading perpendicular to the optical axis of the microscope's objective was used in conjunction with inverted confocal microscopy to allow visualisation of chondrocyte morphology within the full tissue depth and application of unconfined static compression. Compressive tissue strain was applied perpendicular to the tissue surface using a digital micrometer with stainless steel platens. Semi-cylindrical cartilage samples were also used (similar to those in Chen *et al.* (2001) [135] and labelled with fluorescein dextran. This set-up, allowed for the same single chondrocyte or group of chondrocytes from different zones within the cartilage explant to be imaged in an uncompressed state, during a strain of 15 % and following removal of compression for quantification of changes in chondrocyte morphology and local matrix deformation. The devices used in both studies could only accommodate cartilage samples cut into a semi-cylindrical shape and this would affect the tissue mechanical integrity and

consequently change the local mechanical environment around the cells. In this thesis, the device was required to accommodate non-fixed, non-cut samples (i.e. native cartilage disks and tissue engineered cartilage constructs) and therefore these devices were not suitable for the experimental approach required for this thesis.

In another study, a novel loading (indentation) system was built to use on a upright confocal microscope permitting simultaneous loading and real-time observation of chondrocytes in an intact cartilage sample fully attached to its native bone and measuring cell deformation under controlled loading conditions [281]. The indentation system consisted of a light transmissible indenter (that was fixed on the microscope stage and with a glass tip), a sample holder, a piezo actuator, a load cell and a displacement transducer. The system was mounted on the stage of a confocal microscope and the light transmissible indenter placed directly in front of the objective (an approach of applying loading parallel to the optical axis of the microscope's objective). Compressive loading was applied by the actuator from beneath the sample holder, with the tissue sample kept in PBS and held in fixed dental cement, pushing the tissue towards the underside of the fixed glass indenter. With this set-up, cell deformation in response to given loads could be imaged and measured in real-time directly underneath the loaded articular surface. This custom designed indentation system was used in another two studies conducted by the same group in 2010 and 2013 [85], [145]. The study in 2010 utilised this loading system to compare chondrocyte deformation between healthy and early osteoarthritis fully intact lapine cartilage attached to its native bone under compressive loading [145], whilst the other study determined chondrocyte deformations *in situ* under compressive loads ranging from physiological to extreme (0 % to 80 % tissue strain) in two regions of rabbit knee joints (femoral condyles and patellae) [85]. These studies wanted to investigate the intrinsic behaviour of chondrocytes in their physiological environment therefore they were particularly interested in preserving the tissue integrity and maintaining the chondrocytes in its native environment (i.e. intact cartilage attached to its native bone). Due to the specificity to intact cartilage samples fully attached to its native bone and the complexity of the loading system used in these studies, it was decided that it was not suitable for the purposes of the work to be carried out in this thesis.

The different loading devices used in previously published studies were designed and built specifically for each study in order to achieve the measurements required to test their respective hypotheses in different imaging applications. Some of the studies required the loading device to simultaneously apply compression and accommodate imaging to full cartilage depth whilst other studies were interested in determining the chondrocyte behaviour in fully intact cartilage and were consequently restricted to one region of the cartilage, the articular surface. However, these devices were considered not suitable for experiments in this thesis because none of the

devices were able to accommodate non-fixed, non-cut cartilage disk and tissue engineered cartilage construct samples and allow simultaneous application of compressive tissue strain and live cell imaging. Thus, a novel device was required to be developed in order to address the aim of the work in this thesis.

The compression device developed for this thesis (see Section 2.3.3) was required to be capable of applying a range of precise compressive strain magnitudes and allow confocal imaging of cell deformation in real time in order to study the cell deformation behaviour in native and tissue engineered cartilage disks under incremental compression. It was important to minimise compromising tissue integrity through sample cutting as much as possible as alteration to the 3D structure of cartilage samples could affect the structural and mechanical environment around the cells, which in turn would potentially affect the cell mechanics. In addition, fixed tissue approaches such as that used by Clark *et al.* (2003) and Choi *et al.* (2007) [137] were avoided as the instantaneous properties of cells within the cartilage samples would be lost in fixed tissue. Thus, the device was required to accommodate native and tissue engineered cartilage disks with dimensions of approximately 5 mm in diameter and 1-2 mm in thickness. It also needed to keep cells within the cartilage tissue samples viable for the duration of experiments.

Based on these design requirements for studying cell deformation behaviour in compressed native and tissue engineered cartilage in this thesis, a new device for applying precise levels of static compressive strain to native and tissue engineered cartilage disks was developed (see Chapter 2). The compression device was specially designed to allow simultaneous visualisation of vital cells within native and tissue engineered cartilage disks by mounting it upon the stage of an (Nikon A1R) inverted confocal microscope and applying static compressive strain. As discussed in Section 2.3, two approaches of parallel and perpendicular loading to the focal plane of the microscope's objective were considered. However, the configuration of loading parallel to the confocal optical path was adopted because its advantages outweigh those of the perpendicular loading approach to the optical axis, in particular for practical reasons associated with the need to visualise live cells within the samples and the access to more regions (central region of both surfaces) of the samples. A simple and effective way to apply precise compressive strain was conducted through the use of a micrometer. The accuracy of strain application was validated against the Bose ElectroForce 3200 mechanical testing machine by measuring the thickness of cartilage tissue (which is more representative for future samples in the experimentations in this thesis) and a more resistant acrylic disk. The result suggested that the micrometer and mechanical testing machine were sufficiently similar in their ability to measure displacement. Therefore it was decided that the micrometer was suitable to apply strain within the compression device. In addition, the design of the developed compression device was validated and optimised in terms of the dimensions of the components that made up the device

(i.e. coverslip thickness, the internal diameter of the well and the opening window for cell visualisation) and the ability to withstand 5N of load (the same load applied in the bioreactor during the development of constructs).

Chondrocytes are responsible for the synthesis of ECM components of cartilage, including Type II collagen and proteoglycan (PG) [139]. From the literature, studies have illustrated that the biosynthetic responses of chondrocytes could be affected by applied mechanical load [121]–[128] *In vitro* studies of chondrocyte metabolism showed that static loading and loading below a frequency of 0.001 Hz resulted in biosynthetic inhibition, whereas dynamic loading enhanced stimulation to tissue synthesis [127], [128], [131], [188]. For example, static compression has been shown to reduce chondrocyte PG and protein synthesis [131], [323]. In contrast, dynamic compression has been demonstrated to stimulate the biosynthetic response of chondrocytes, though the level of these responses are largely dependent on the amplitude and frequency of the applied mechanical load [124], [127], [128], [131], [188], [211].

The experimental condition used in this study to study cell deformation was that of static loading. Although this is likely to reflect the native and tissue engineered cartilage response to loading at physiological compressive levels, they do not take into account of the time-dependent variation on the local mechanical environment in and around the cells. Articular cartilage of major load bearing joints is exposed to a complex dynamic loading environment during normal activity [130], [324]. Chondrocytes within cartilage under physiological conditions may be subjected to a variety of mechanical loading in their local environment, including compressive and tensile stresses and strain, fluid flow, hydrostatic pressure and osmotic pressure [139]. The local cellular environment, which largely influences cell deformation behaviour [95], [146]–[148], under cyclic tissue loading would not be comparable to that under static loading, therefore the cell deformation behaviour observed in native and tissue engineered cartilage disks in this thesis during steady-state conditions may be different to that seen in the same samples subjected to cyclic compression.

Chondrocytes deformation behaviour has been extensively investigated, generally under static compressive loading, in native cartilage [21], [87], [137] and in other scaffold materials, such as agarose [88], [142]–[144], [325]. Conversely, not many studies to date have investigated the deformation of chondrocyte under dynamic loading. In addition, to the author's best knowledge, no study has managed to determine 3D measurements of cells within native and tissue engineered cartilage under cyclic loading. This is due to the practical difficulties of loading in a controlled, physiological, dynamic manner and simultaneously capturing 3D morphological changes. A study by Knight *et al.* (1998) [141] investigated the deformation behaviour of isolated chondrocytes in agarose during cyclic loading. From their deformation index (X/Y) data, which represented the ratio of cell diameters measured parallel (X) and perpendicular (Y)

to the axis of compression, they found that the level of chondrocyte deformation during cyclic loading (between 0 % and 15 % compressive strain at a frequency of 0.3 Hz) was initially similar to that observed during static 15 % compressive strain but reduced over the 20 mins period of cyclic loading, attributable to the cyclic nature of loading. In contrast, the level of deformation stayed constant throughout the static loading duration [141]. Wu and his co-workers (2006) utilised a finite element model to determine the mechanical response of chondrocytes subjected to unconfined cyclic compressive loading [211]. The results showed that chondrocyte deformation was location-dependent within a homogenous cartilage matrix during cyclic loading and that deformation was further affected by load magnitude. However, the frequency of cyclic loading was found to have no significant effect on cell deformation. It was therefore speculated that biosynthetic responses of chondrocytes to cyclic loading depend upon cell location and load magnitude [211]. Another study conducted by Chanhine *et al.* (2007) [139] investigated the deformation behaviour of single chondrocytes and their local mechanical environment under transient loading. The experimental results showed that a significant increase in compressive strain occurred in the microenvironment of the chondrocyte under transient loading, with the compressive strain recorded to be approximately 7 x higher in the intracellular region and 5 x higher in the pericellular matrix (PCM) than the ECM at peak ramp. The experimental result was incorporated in to a finite element model of chondrocyte deformation which demonstrated a significant strain amplification mechanism in the intracellular region. The results suggested that the PCM acts as a mechanical transducer for the chondrocyte, by amplifying the ECM strains to within and around the cellular environment during transient loading and at equilibrium and this amplification mechanism could possibly regulate chondrocyte mechanotransduction [139].

The compression device developed in this thesis was used for application of static compressive strain. However, application of dynamic compression in the device would better replicate the loading experienced by the cells within the constructs. This is because cartilage tissue engineered constructs developed in this thesis and in the study conducted by Finlay *et al.* (2016) [1] were created by applying a dynamic mechanical loading regime using a force controlled bioreactor. However, experimentally, it is difficult to record and quantify the three-dimensional (3D) changes to cell morphology in cyclic loading conditions due to the practical difficulties of loading in a controlled, physiological, dynamic manner and simultaneously capturing 3D morphological changes (as indicated by the few previously published dynamic loading studies). Thus, unconfined uniaxial static compression was selected as the loading method for the device. Nevertheless, the morphometric measurements obtained under static compression in this thesis, both in the native and tissue engineered cartilage deformation experimentation, were still meaningful and will serve as a baseline for more physiologically-relevant dynamic studies in the

future beyond this thesis. In addition, the compression device may be used in studies to examine cell deformation in different cartilage preparations, including isolated cells in agarose gel, cartilage/bone explants and fixed cartilage tissue as well as different connective tissues (i.e. tendon and ligament) and investigations to determine the chondrocyte biosynthetic responses under static compression.

In order to more closely resemble the mechanical conditions experienced by the cells within the constructs during construct development, a more 'physiologically-relevant' study using dynamic loading should be conducted. Further experimental work to modify the existing compression device or develop a new loading apparatus to apply controlled, physiological, dynamic compression would be required. In addition, silicone rings (used during mechanical loading of the constructs in this thesis and in the study conducted by Finlay *et al.* (2016) [1]) could be incorporated to the dynamic loading set-up of the device to further replicate the mechanical conditions that the constructs were subjected to during the development process in order to address the relationship between the applied dynamic compressive strain and cellular strain. It is possible that video microscopy (high contrast video imaging) [139], [141] and potentially 3D time-lapse imaging could be used for capturing images of cells during the application of cyclic loading on the constructs. However, the speed of the image acquisition must be quick enough to capture cell deformation during the unstrained and strained phases.

### **6.3 Live Cell Staining and Imaging Methodology**

A live cell staining and imaging method that was capable of visualising, tracking and imaging changes in cell morphology within native and tissue engineered cartilage during different magnitudes of static compressions was successfully established and developed in this thesis. The essential requirements for the desired staining method (discussed in Chapter 3) included 1) allows stains to penetrate samples of both native cartilage and engineered cartilage constructs, 2) provides specific and highly resolved visualisation of cell morphology for 3D quantification and 3) tracks and images cells multiple times without significant signal loss. Fluorescent staining has been consistently used to label living cells. In Chapter 3, two staining methods used for cell visualisation (method using Acridine Orange and SiR-actin Probe and method using Hoechst 33342 and CellMask Green Plasma Membrane Staining) were developed and compared for their suitability for the required application in live cell sequential imaging within native and tissue engineered cartilage under non-loaded conditions as a prelude to subsequently determining cell deformation behaviour under compressive loads. It was found that both staining methods were able to penetrate native and tissue engineered cartilage revealing morphology of the respective embedded cells. However, the dual staining method of Hoechst 33342 and CellMask Green plasma membrane stains showed superior fluorescence signal

retention compared to the staining method of Acridine orange and SiR-actin during and after tracking selected cells on multiple confocal scans. Fluorescence signal loss would result in loss of cell morphology detail and therefore could potentially affect the accuracy of quantitative data obtained from the images. It appeared that CellMask Green plasma membrane stain was more photo-stable in comparison to the SiR-actin probe under the same illumination conditions (same dose of laser and imaging acquisition settings) which decreased the likelihood of photobleaching, an effect where a fluorophore degrades slowly following excitation leading to its permanent damage and consequent inability to fluoresce [230]. This would inevitably introduce potential errors in any morphometric measurements obtained from the subsequent images, therefore the staining method of Hoechst 33342 and CellMask Green plasma membrane was chosen as the staining method for this thesis.

It was originally proposed to track the same population of the respective cells in native and tissue engineered constructs under incremental compressive strains but it was not possible to do this for cartilage constructs as they were highly cellular and the cells were densely packed within the constructs developed at early time points (Day 0 and 28) (which will be discussed later in this chapter). Nevertheless, it was still important to minimise the occurrence of photobleaching.

In addition to the staining method itself, microscopy system selection, imaging conditions and image acquisition settings could also influence the retention of the fluorescence signal together with the photobleaching effect. Therefore these were carefully considered in this thesis.

Confocal laser scanning microscopy (CLSM) was used as the visualisation system used for this thesis. CLSM is a high resolution imaging technique that uses the principle of fluorescence excitation to enable optical sectioning of non-transparent samples (could be fixed or living cells and tissues) that have been labelled with one or more fluorescence stains [228].

Chondrocyte deformation has been investigated in previous studies under static compression, generally with the use of confocal microscopy in native cartilage explants [21], [51], [87], [133]–[138], [210], intact cartilage [85], [145] and isolated chondrocytes seeded in agarose [88], [140]–[144]. Confocal microscopy is based on point illumination of a sample with a laser, which the laser is scanned across the sample to construct optical section, and spatial filtering of the returning light emission with a pinhole to block out of focus light from outside the focal plane [228]. Confocal microscopy offers several advantages over conventional optical microscopy. The major advantages of the confocal microscopy include the removal of out of focus light to increase optical resolution, the ability to construct a non-invasive 3D view of the sample by collecting of serial optical sections (Z stack) and the ability to record real time changes occurring at the cellular level [326]. Due to the advantageous features and the best

available system at the time, an Nikon A1R inverted confocal microscope was used for the experimentations in this thesis.

In Chapter 3, attempts to minimise the occurrence of photobleaching with regards to imaging conditions and image acquisition settings were described. The use of ProLong® Live Antifade Reagent was investigated. This is a reagent which is able to metabolise the free radical singlet oxygen molecules generated during imaging that can degrade neighbouring dye (stain) molecules. As discussed in Section 3.3.5, experimental data suggested that the presence of ProLong antifade reagent in the imaging solution provided environmental protection to fluorophores which aided the retention and duration of the fluorescence signal [327]. No previous chondrocyte deformation studies have used any antifade reagents to aid with photobleaching effects. In a study by Madden *et al.* (2013) [85], in which superficial zone chondrocyte deformation in intact rabbit cartilage under compressive tissue strains (0-80 %) was investigated, photobleaching effects was believed to be contributed to the morphometric measurements in the final confocal scans which may have led to measurement errors and potentially constraint image acquisition over longer time duration. Guilak (1995) [210], examined changes in 3D morphology of the nuclei of chondrocytes during compression of canine patellofemoral groove cartilage explants using confocal microscopy, also found rapid photobleaching effects without the use of antifade reagents. In addition (as discussed in Chapter 3), image acquisition settings were optimised based on the photo-stability of the stains and the capability of the current Nikon A1R inverted confocal microscope used in this thesis with regards to minimise the chances of photobleaching. It is well known that there is risks of photobleaching to the sample (cells/tissues) associated with high intensity of excitation light and long repeated exposure time [223]. In addition, the breakdown products of the fluorophore can also be toxic to a cell so it is likely to suffer from phototoxicity effect if fluorophores are excited near the ultra-violet portion of the spectrum which can lead to direct cell damage from the light source [230]. As observed in Chapter 3, with the excitation light kept to a minimal, fluorescence fading of SiR-actin was detected after sequentially imaging a region of interest within native cartilage samples repeatedly four times, suggesting that acquiring four repeated images in the same region of native cartilage was beyond the capability of the stain and that the exposure time to excitation light was too long. It was therefore proposed that three sequential images would be used to track chondrocytes within the native cartilage. Some previous chondrocyte deformation studies, such as Schinagl *et al.* (1996) [134] and Turunen *et al.* (2013) [328], ensured photobleaching was kept to a minimal by using lower laser power and reduced excitation light exposure time.

In addition to minimisation of the photobleaching effect, it was also important to obtain high resolution images (with clear visible contrast between the features of interest and the

background) to capture the cell morphology changes in native and tissue engineered cartilage samples under incremental compression for quantification analysis. Resolution is defined as the minimum distance between two points on a sample that can be defined by a certain level of contrast between them [329]. In other words, resolution is the amount of details that an image holds. Higher resolution means more fine details and an ability to capture smaller structures [230]. A number of strategies can be employed to increase the resolution of an image. In theory, image resolution in confocal microscopy depends on the numerical aperture (NA) of the objective and the wavelength of the light [228], [259], [329], [330].

The NA determines the resolving power of an objective [260]. The higher the NA of an objective, the better the resolution. In addition, the total resolution of the entire microscope system is dependent on the NA of the microscope's condenser, therefore correct alignment of the microscope optical system is also essential to ensure maximum resolution [331]. When selecting the objective for the imaging method here, there was no difference in NA between 40x, 60x and 100x oil lenses. The 40X lens had a higher working distance (vertical distances between the front of the objective and the closest surface to the sample when the sample is focused) than the other objectives, which allowed for more space available to manoeuvre the lens during focusing on the sample. This magnification still provided a good enough resolution (having similar NA to the other two objectives) with better overall image brightness (image brightness decreases as magnification increases [260]). It was therefore chosen as the objective for all of the experimental studies in this thesis.

However, in practice, the theoretical maximum resolution of the confocal microscope is often not achieved [329]. In live cell imaging experiments, experimental limitations and the properties of the sample itself also dictate the realistic resolution possible for imaging [332]. In addition, the capability of a microscope to produce high resolution images would also be worthless if sufficient contrast was not achieved [332]. Image contrast is created by differences in signal intensity and/or colour which allow features or details in an image to become visible [332]. In other words, the ability of a feature to stand out with respect to background and other adjacent details is a measure of image contrast [332]. Hence, the influence of noise and the amount of signal intensity (noise to signal ratio) would affect the image contrast and consequently resolution and quality of the resulting images [329]. Since resolution requires a certain level of contrast and contrast is affected by the noise to signal ratio, the image contrast level attained in practice is ultimately determined by the interaction of the sample with light (the number of photons detected), the dynamic range of signal and the efficiency of the optical system in conjunction with the ability to reliably record the photons collected within the detector [332]. In the experiments in this thesis, experiential factors such as the type of sample (cartilage explants and constructs), the image acquisition protocol (tracking the same population of chondrocytes

within native cartilage with sequential imaging and tracking different populations of synoviocytes within tissue engineered constructs), cell viability and photobleaching dictated the amount of light intensity and duration of exposure placed on the sample, consequently determining the attainable resolution. For example, to reduce the photobleaching effect, the laser power level and the excitation light exposure time should be kept as low as possible. However, limitation to light intensity and exposure duration would result in a reduction in signal to noise ratio and low contrast level, consequently affecting the resolution of the image. In contrast, low amounts of signals from the fluorophores can be improved by increasing the light intensity to provide more energy to excite them but there is then a risks of photobleaching. In addition, low signals can be improved by opening the pinhole in front of the detector to allow more illumination to pass through to the sample [329], [333]. The overall intensity and signal to noise ratio will seem to improve but the detector will be picking up the unwanted extrafocal signal from planes outside the focal plane, and consequently the axial resolution deteriorates [333]. Thus, there is a trade-off between photobleaching and image quality. Given that image contrast may be dictated by these factors, the best resolution possible within the constraints imposed by the experiment was attempted.

In the development of the imaging method used in this thesis, the image acquisition setting was optimised with respect to minimisation of the photobleaching effect without sacrificing image quality too much. As discussed in Section 3.6.5, keeping these considerations in mind, it was proposed that the laser power was kept at 5 % so it was as low as possible to minimise any photobleaching effect but was still able to provide enough light to excite the fluorophores to yield the number of photons detected to provide the contrast required for high resolution images. The pinhole was set at the theoretical optimum of  $1 \text{ Au}$  to provide a diameter that gave the best compromise between light throughput, noise and resolution and no line averaging (normally used to reduce noise) was used to reduce illumination time in order to minimise the photobleaching effect. In addition, the 3D image depth was set at approximately  $20 \text{ }\mu\text{m}$  with  $0.2 \text{ }\mu\text{m}$  optical section intervals to reduce the exposure time in ROI (kept in mind that 3 sequential images are captured in each ROI) but still capable of tracking a population of cells.

Optimisation of image acquisition settings achieved the best output capability of the confocal system available at the time of this thesis. Confocal microscopy is one of the most widely used imaging technique in tissue engineering research [227], [228], [334], but there are many other commercial advanced imaging systems and optical instrumentations available that have the capability to improve image resolution without introducing photobleaching effect.

The use of a high-speed resonant scanner, such as the Nikon A1R HD25 or the Olympus FV3000RS hybrid scanner, coupled with a high sensitivity detector could potentially improve on image contrast and consequently on resolution and reduce photobleaching and phototoxicity

[262]. Resonant scanning was designed to improve scanning speed. It is driven by a different waveform than (traditional) galvo scanners, which adapts a linear sawtooth wave. It uses a high frequency sinusoidal wave which can translate into speeds up to 30 frames per second. With the improved scan speed, the resonant scanner is capable of scanning the sample and creating pixels required for the image much quicker compared with the galvo scanner. This means that a higher sampling rate could create more pixels in the same amount of time resulting in better resolution images. In addition to quicker scan speeds, shorter dwell time to capture an image would be of benefit in reducing the photobleaching and phototoxicity effects from laser irradiation. However, shorter pixel dwell times could also potentially result in less signal detected and a consequent reduction in image resolution. By incorporating a highly sensitive detector such as a Nikon A1-DUVB-2 GaAsP detector with resonant scanning, this would be able to collect weak fluorescence signals without increasing laser power or opening the pinhole of the detector to increase excitation light which compromises image quality [213]. However, the suggested scanners and detectors have not been used in previous studies to examine cell deformation in native and tissue engineered cartilage and therefore these could be explored in further experimental work.

A shortcoming that became apparent during the development of the live cell staining and imaging method used in this thesis was the restriction of the tissue regions in which cells could be imaged and examined. Although the image resolution is very high, confocal microscopy has a very limited penetration depth [228], [230], [335], [336]. Typically, the penetration depth is limited to roughly 50-100  $\mu\text{m}$  for confocal microscopy depending on the sample transparency and the wavelength of the excitation light [213], [227]–[229]. When focusing deep into a sample, image quality could deteriorate as a result of fluorescent light returned from the sample becoming scattered, absorbed and defocused as it passes back through the sample and consequently very little emitted fluorescence reaches the detectors [228], [230]. For every sample, there is a depth at which light scattering occurs and where traditional fluorescence techniques are no longer effective. Generally, longer wavelength light has a deeper penetration depth than shorter wavelength light due to less light absorption and scattering [213], [228]. For the experiments in this thesis, the penetration depth was limited to around 50-80  $\mu\text{m}$  beneath the sample surface, meaning only cells located at the periphery of the cartilage tissues were imaged. In comparison to the range previously achieved in the field, studies examining 3D deformation behaviour of chondrocytes in native cartilage achieved the maximum imaging depth of around 40-50  $\mu\text{m}$  without cutting the tissue to expose the cross-sectional area [85], [145]. Thus, the penetration depth achieved by using Hoechst 33342 and CellMask Green plasma membrane stains in this thesis was similar to the range previously achieved in the field.

It is possible that multiphoton microscopy could be used as an alternative approach to improve the penetration depth in to the samples as required by this study. The multiphoton system typically has at least a twofold improvement in the imaging penetration, allowing imaging at much deeper levels than the confocal microscope [213], [227], [228], [230]. The penetration depth of multiphoton microscopy is approximately 400  $\mu\text{m}$  but it can reach up to 1 mm or higher depending on the transparency of the sample [227]. It uses much longer wavelengths of light (near-infrared) to excite the fluorescent molecules which scatter less than the visible (short) wavelength that is normally used in the confocal microscopy as it scans through tissue, thus enabling deeper penetration [227], [228], [230]. In addition, infrared wavelengths have a much lower phototoxic effect to living cells and tissues than excitation light near the ultra-violet wavelengths [230]. In multiphoton imaging, two-photon fluorescence microscopy is the most commonly used form [227]. It relies on two low energy photons being absorbed simultaneously by a single fluorophore to excite and subsequently to generate fluorescence [227], [228]. This process requires a high intensity of photons and is typically achieved by using ultra-short pulsed laser illumination which provides sufficient photon density at the focal point [228]. Excitation achieved by two-photon collision is restricted to the focal plane where the high intensity laser light is most concentrated, thus producing a natural pinhole effect that filters the out-of-focus light [227], [228], [230]. As a result of no out-of-focus absorption (from regions above and below the focal plane), the multiphoton detector collects all the emission light from the excitation, minimising signal loss (compared to confocal microscopy which uses a pinhole to eliminate out-of-focus light from the focal region), therefore a greater proportion of the excitation light is used to penetrate the tissue, allowing deeper penetration [227], [228], [230]. In addition, there is no out-of-focus light that will contribute to the image which results in consequent excellent image contrast. In addition to the excitation being restricted to only the focal plane, there is significantly less photobleaching and phototoxicity (two major limitations of imaging living cells and tissues by fluorescence microscopy) and sample can be imaged for a much longer period compared to confocal microscopy, where fluorophores along the whole illumination path are excited [227], [228], [230]. For these reasons, multiphoton microscopy could be used to improve on imaging penetration and photobleaching for further experimental work. With the improved imaging penetration, it might be possible to assess the chondrocyte deformation within the middle zone of native cartilage without causing damage and disruption to the chondrocytes and the matrix by cutting the sample.

## **6.4 Quantification of Cell Deformation via Amira Software**

Examination of cells by microscopy has been the primary method for studying cellular dynamics and function in life science research for decades [228], [230], [337]. If the cells (either in two-dimensional (2D) or three-dimensional (3D) cultures) are stained appropriately,

visualisation can be captured through the acquisition of fluorescence images by advanced imaging systems, such as confocal microscopy and multiphoton microscopy [337], [338]. These imaging systems are capable of collecting large numbers of high resolution images of cells in a short space of time for time-lapse experiments and live cell imaging studies. However, a bottleneck exists at the image analysis stage with regards to the long analysis time required to extract cell measurements from the fluorescence images. There are many image analysis software tools available for extracting quantitative measurements of cell parameters, such as morphology, count, intensity and texture, from either 2D or 3D fluorescence image data [338]. Open access software tools, such as ImageJ and The Visualization Toolkit have been used in studies to quantify cell morphological changes within cartilage explants and isolated chondrocytes in agarose [51], [85], [145], [328]. However, software such as ImageJ is generally used more towards manual analysis of individual images [337], [338]. Macros can be written in ImageJ in order to adapt it to specific image analysis tasks but this would require the researchers to learn a programming language [337]. Some studies utilised custom programmes written in commercial software (i.e. ImagePro and Matlab) or Java to view, identify, measure and track cells within cartilage tissues in 2D and 3D images under unstrained and strained conditions [94], [137], [144], [337], [339]. By developing their own scripts or code in the software, this can accommodate image analysis tasks specific to their studies. Although specific for purpose, customised in house image analysis solutions are not available for all to use and therefore limit the ability to compare data from different groups.

Amira software, a 2D-5D visualisation and data analysis software [340], was used in the current study to measure cell parameters including: cell length, width, height, volume and sphericity in 3D fluorescence images in order to quantify cell morphological changes under incremental static tissue compression. This particular image analysis tool was chosen because the software interface is user-friendly and easy-to-use which allows researchers who might not have extended expertise in computer programming to easily perform cell dynamics quantification analysis. In addition, Amira is a highly interactive software in which the data set can be displayed as graphics throughout each stage of software operation to visually support users in data analysis. The software was designed to analyse data from various imaging systems (i.e. micro-CT, Ultrasound, MRI and confocal microscopy) and handle large data sets in different file format. The software also adopts a modular design that enables the creation of custom workflow of combined modules to provide flexibility and specificity to the study. Thus, it is not targeted to a particular imaging application but has the capability to accommodate many experimental set-ups (i.e. counting, tracking or measuring morphology of various sized objects, from particles to entire cells) that present unique challenges for processing and analysing the imaging data. Different modules can be mixed and matched in numerous ways, customised to a

particular imaging task or application. Another major advantage of Amira software is that the image processing step can be conducted in an automated fashion once the custom workflow has been set up and saved. Upon the completion of image processing and cells identification steps, the software is also able to simultaneously perform 3D volume rendering and various measurement of cell morphology parameters (as mentioned pervious in this section) in a high throughput manner. Although Amira is relatively new to the market, the software has been used in published work where similar image analysis demands to those required in the current work were needed to be met. Amira has been used to measure porosity, surface area and volume from images of the microstructure of various types of samples (i.e. bituminous coal [341], Arkose rock [342] and used molten carbonate fuel cell cathodes [343]) captured using various imaging systems (i.e. micro-CT and X-ray microtomography). To the author's best knowledge, it is the first time it has been used for quantitative image analysis of native and tissue engineered cartilage under static compressive strain.

A custom workflow was developed by the author on Amira software specifically to analyse the confocal images and perform cell morphometric measurements within native and tissue engineered cartilage (see Chapter 4 and Chapter 5, respectively) in order to quantify cell deformation behaviour under incremental compressive strains. The image analysis process, which consisted of three stages: image processing, cells identification (also called segmentation) and data analysis (measurements), was conducted in a semi-automated fashion. This would reduce bias due to subjective observation and the time required for cell morphology evaluation from the confocal images. Several modules were selected and combined to form the workflow used for the current image analysis application and each module setting was adjusted appropriately in order to address the three image analysis steps. Once the workflow was satisfactory, the order of modules and their settings were saved and the workflow was applied on every image set to perform the same analysis. Upon starting the analysis, the 3D data from the confocal images was separated into images of cell nuclei and plasma membrane and loaded into the software. Both set of images travelled through the workflow and were processed by each module in order. Modules including '*Gaussian Filter*', '*Interactive Thresholding*', '*Fill Holes*', '*Remove Small Spots*' and '*Border Kill*' (only applied to chondrocytes in the cartilage deformation experiment) were used to process the images. The processing stage was particularly important in the image analysis process as it cleans up the images, reducing noise levels, which helps to improve accuracy on the cells identification stage. It was performed automatically and only required a short analysis time per image. The resulting processed images highlighted objects that were potentially nuclei and plasma membrane based on fluorescence intensity and both images were then merged together prior to the cells identification step.

Next, the cells identification stage was conducted in which cells were recognised and selected from the processed images for morphometric measurements. However, this stage posed the most challenging problem for the image analysis process in the current study. The software allows the user to segment structures or regions of interest in 3D images using a variety of automatic, semi-automated and manual tools. In the current study, the software was capable of easily picking out cells that had clear cell boundaries from the 3D confocal image data sets (all the 2D slices). In this case of clear cell boundaries, the nuclei and plasma membrane of cells were merged together and identified as individual cells for morphometric measurements. However, it was not straight forward in some cases where cells were touching unwanted surroundings (i.e. pericellular matrix (PCM)) and each other. In work described in Chapter 4, the chondrocytes within the native cartilage were well-dispersed but chondrocytes were in close contact in some occasions and the green CellMask plasma membrane stain appeared to have stained the PCM around the chondrocytes as well as the plasma membrane. In the case of work described in Chapter 5, the synoviocytes within the cartilage constructs were confluent and present in tight, dense collections of cells, in particular in both loaded and non-loaded constructs at Day 0 and Day 28. Since synoviocytes were highly densely populated within the constructs, many of them touched and overlapped each other, which made it difficult to recognise and separate them as individual synoviocytes. For this reason, cell measurements were only performed on confocal images of synoviocytes within Day 56 constructs. In addition to the high density of synoviocytes within the constructs, analysis was conducted on different populations of synoviocytes during their uncompressed state and under incremental tissue compression because tracking the same population was incredibly difficult as the field of view changed with the application of tissue compression. These issues are highlighted in both Chapters 4 and Chapter 5 and made cells identification a lot more challenging and an extra step was needed to separate touching chondrocytes or remove PCM from the chondrocytes and separate touching synoviocytes within native and tissue engineered cartilage, respectively. Thus, morphometric measurements were made possible by manually defining dividing lines in 2D with the use of the lasso tool to separate different objects in order to achieve the removal of PCM and separation of touching cells.

Once this was completed, cell nuclei and plasma membrane could be found more easily and were merged together to be identified as individual cells for morphometric measurements. However, objects separation needed to be conducted manually on each cell on every 2D image that made up the 3D data, and therefore this extra step to identify cells for morphometric measurement was extremely time-consuming and required considerable effort and concentration. Consequently, this led to low sample numbers in both native and tissue engineered cartilage deformation experiments. Cell morphometric measurements were

performed on the same 37 cells from four cartilage samples under the selected strain levels in the native cartilage experiment, whilst data was collected on 10 different synoviocytes at each strain level per construct and from two different constructs in each loaded and non-loaded group in the cartilage construct experiment. Madden *et al.* (2013) [85] examined morphological changes of the same chondrocytes in cartilage samples from two regions of the rabbit knee joint (femoral condyles and patellae) and managed to measure 4-8 chondrocytes per sample from four cartilage samples per joint region. In another study, Han *et al.* (2010) [145] quantified chondrocyte deformation in healthy and early osteoarthritis (OA) intact articular cartilage under static compression and the same group of chondrocytes (a total of 48 chondrocytes per experimental group) were tracked for quantitative morphometric measurements. The number of cells measured in this thesis was therefore similar to those of previous studies achieved in the field. It is possible that these studies might also experience similar challenges imposed on the measurement method in this thesis.

In order to reduce the time required for the cells identification stage during image analysis and consequently increase sample numbers in the current study, the use of a more specific stain to define cell borders could avoid the time-consuming segmentation step used to exclude unwanted objects, such as the PCM, from the chondrocytes in the cell deformation study in compressed native cartilage (Chapter 4). Whilst the ability to specifically visualise defined cell borders is important for effective cells identification in the image analysis process, the stain is also required to retain the fluorescence signal after repeated imaging. In addition to the densely packed synoviocytes observed in the cell deformation study in cartilage constructs (Chapter 5), it was problematic to recognise and separate clumped synoviocytes for morphometric measurements. In some cases, it was not possible to identify individual synoviocytes due to undefined cell borders. In other cases, dividing lines between touching synoviocytes were easier to identify and these were segmented manually in every 2D image that formed the 3D data on the software but this imposed a significant constraint on the speed of the image analysis process. It is possible to decrease the number of synoviocytes being imaged by reducing the depth image to a monolayer of cells within the constructs. This could potentially avoid observing some touching synoviocytes in the vertical z-axis. In addition, tracking the same synoviocyte during its uncompressed state and under incremental tissue compression could be achieved by applying the strain more slowly to the selected value while following the synoviocyte live on the confocal microscope before acquiring the image. However, this approach is extremely time-consuming and could induce photobleaching effects. It would not be possible to speed up the image analysis process for densely distributed touching synoviocytes on the x-y axis unless the cell seeding concentration were to be lowered at the beginning of construct development.

Once the cells were segmented, the last stage was to perform morphometric measurements on identified cells. In the current study, measurements such as cell length, width, height and volume were selected as well as manually inserted specific equation (i.e. sphericity) on the software. When the measurements settings were saved, the software was able to perform this stage automatically and could be used to reproduce the analysis on all of the image data sets which consequently saved time and reduced subjective bias associated with manual measurements. In this work, Amira software demonstrated the capability to analysis 3D confocal image data and perform cell morphometric measurement in a semi-automated fashion and has the potential to progress to automation with improvement on sample staining technique and adjustment to the image acquisition method.

## **6.5 Chondrocyte Deformation within Native Cartilage**

Many studies have been conducted to investigate chondrocyte deformation in native cartilage explants [21], [51], [87], [133]–[139], intact cartilage [85], [145] and isolated chondrocytes in agarose gel [88], [140]–[144].

In the present study, the deformation response of chondrocytes within bovine cartilage disks subjected to incremental compression was investigated in order to address the relationship between applied tissue deformation and cellular strain. It's the first time, to date, that a given population of articular zone chondrocytes within bovine cartilage explants was compressed under 10 % and 15 % compressive tissue strain and repeated confocal images of the same chondrocytes captured and tracked under live cell conditions in the uncompressed state and during the two applied compressive strains (as described in Chapter 4). Cell morphometric measurements were recorded to determine changes in 3D chondrocyte morphology in response to incremental tissue compression. The major findings of Chapter 4 showed that articular zone chondrocytes underwent significant changes in morphology, size and volume with overall tissue compression and these deformational changes were substantially greater than the applied tissue strains. The chondrocyte deformation observed in this study together with data previously reported in the literature [85], [87], [133]–[137], [145] suggest that the deformation response is associated with the local microenvironment around the chondrocytes. In particular, the PCM is believed to play a critical role in controlling the mechanical environment in and around the chondrocytes. In addition, the significant deformation changes observed in the study were presumed to be due to the specific composition and structure of the superficial matrix and its mechanical properties [51]. This is because the large axial compressive cellular strain reported in this study is consistent with previous measurements of cell strain under compression in the superficial layer of cartilage explants [87], [137]. Thus, the mechanical properties of ECM and

PCM around the chondrocytes should be investigated along with the cell deformation response under compression in future studies.

It is possible to determine the local ECM strains by labelling cell nuclei to measure the change in vertical distance between given groups of cells at each applied compression level. Label-free techniques, such as second harmonic generation (SHG) imaging, could be used to reveal differences in the architecture and organisation of the collagen within ECM and enable observation of the microenvironment around chondrocytes between loaded and non-loaded states [300], [344]. SHG imaging, an extension to multiphoton microscopy, is a non-linear optical process that has the ability to generate second harmonic signals from non-centrosymmetric structures (i.e. collagen, myosin and microtubules) when excited by ultra-short laser light [344]–[347]. This complementary technique to multiphoton microscopy utilises the excitation of two photons (induced by the incident laser beam) which simultaneously interact with dense non-centrosymmetric structures (like collagen in cartilage ECM) and convert into a single photon of exactly the same total energy and twice the frequency, without absorption and re-emission of photons [347], [348]. It can provide 3D, submicron resolution images of collagen in cartilage and has the capability to penetrate in to tissue to a depth of up to a few hundreds of micrometres (which is one of the benefits in using infrared excitation in multiphoton microscopy) without any need for tissue sectioning and staining [345], [348]. Examination and characterisation of surface morphology of cartilage, structural, morphological and organisation alteration in collagen and the detection of different collagen types were achieved by using SHG imaging in healthy or osteoarthritic native articular cartilage and in cartilage under (tensile) strain conditions [345]–[349].

In addition to fluorescence staining for cell visualisation, immunostaining of type VI collagen (i.e. a primary anti-collagen type VI antibody, followed by a FITC conjugated fluorescent secondary antibody) [339] or keratan sulphate (i.e. a primary anti-keratan sulphate antibody used with rhodamine conjugated fluorescent secondary antibody) [143] could be used to delineate the PCM region under applied tissue compression as these matrix molecules are generally present in PCM. By using multiphoton fluorescence and SHG microscopy together, it is possible to define the deformation changes in chondrocytes, PCM and ECM in order to examine the relationship between cellular, PCM and ECM strains in different zones within the cartilage prior to and during incremental compression.

## **6.6 Synoviocyte Deformation within Cartilage Constructs**

Finlay *et al.* (2016) [1] attempted to engineer functional cartilage constructs *in vitro* for long term cartilage repair using mechanical stimulation. Constructs were created through the combining of PET scaffolds and bovine synoviocytes followed by incubation in chondrogenic

culture for 4 weeks before being subjected to cyclic compressive loading for 1 hr at 1 Hz, 5 days per week for 28, 56 or 84 days. To date, no attempt has been made to investigate the constructs at the level of the single cell. The aim of the study in this thesis was to better understand the mechanism(s) behind the construct's development and to address the relationship between applied compressive strains and cellular strain. In order to fulfil the aim, a novel compression device and a dual staining method using Hoechst 33342 and CellMask Green plasma membrane (as described in Chapter 2 and Chapter 3, respectively) were specifically developed and used in conjunction with confocal microscopy to determine the deformation response of living synoviocytes within cartilage constructs (at different time points of their development) subjected to incremental compression. Cellular deformation was examined under the estimated tissue strain applied to the constructs in the bioreactor during mechanical loading. A higher compressive strain of 28 % was also used in this study in an attempt to access how synoviocytes would react under conditions approaching maximum physiological loading which lies in the physiological range of 0 % to 30 % [130], [210], [264], in terms of any changes in cell morphology.

The histological and compressive moduli findings revealed that the constructs created in this study appeared to have a lack of cartilage-like matrix and low compressive moduli after 56 days of culture under loaded and non-loaded conditions in comparison to those in Finlay's study (as discussed in Section 5.5) [1]. It is believed that the use in this study of a scaffold with higher porosity potentially limited cell-cell interactions within the constructs which could have hindered the rate of cell differentiation and subsequent cartilaginous matrix deposition, and therefore resulted in less matrix filled pores within the scaffold. It is possible that more porous materials take longer for these kinds of interactions to occur and if the porosity is greater than a threshold value, it might not happen at all. The DNA data also suggested that the mechanical loading was stimulating cell proliferation rather than differentiation therefore the synoviocytes hadn't differentiated to the same extent as previously observed in Finlay's study [1]. In addition to the use of a scaffold with higher porosity, it is possible that insufficient initial cartilage-like matrix had been deposited, indicated by the histological images after the 4-week pre-culture period, as a result of the synoviocytes being early in their journey towards differentiation to a chondrocyte-like phenotype. This would mean that synoviocytes may be unable to elaborate the correct cartilage-like matrix and/or enough amount of matrix (and thus insufficiently stiff) to be able to transmit mechanical signals to the synoviocytes in mechnotransduction. Also, whilst the matrix deposited might not be competent for the transmission of mechanical signals to the synoviocytes, the cells themselves may not have had the correct phenotype to be able to respond in the way that was seen previously. Based on the histological findings, there was also a lack of homogenous cartilaginous matrix with variable quantities of collagen type II and sGAG in

distinct regions within both loaded and non-loaded constructs at Day 56. It is possible that this is also due to the use of a thicker scaffold material (with higher porosity) which could have hindered the rate of cell differentiation and consequently affected the deposition of cartilage-like matrix within the constructs.

As discussed in Section 5.5.6, there were no significant changes in cell morphology under incremental compression in the Day 56 loaded constructs. It seems likely that this was influenced by the lack of a homogenous cartilaginous matrix. Histological analysis showed that there were distinct regions with variable cartilage-like matrix present within the constructs and these could give rise to different regions with variable compressive stiffnesses. Given that more GAGs appeared but no significant synoviocyte deformation was detected at the superficial of the Day 56 loaded constructs under compressive tissue strains, this perhaps suggests that the regions where the synoviocytes were visualised had denser matrix but the synoviocytes did not experience much deformation because regions with less stiff matrix would deform much more readily. The different deformation behaviour of synoviocytes observed in the two non-loaded constructs may also be explained by the proposed assumption of stiffness differences in regions with variable amount of cartilage-like matrix. Based on all the experimental results in this study, there was an insufficient amount of data to support the proposed assumption of site-specific differences in ECM quality, including stiffness, for explaining the effects of deformation response of synoviocytes within the loaded and non-loaded constructs. It was not possible to identify the exact locations which the confocal images of synoviocytes were captured and map these to the histological findings. Thus, the lack of a homogenous matrix renders the data collection problematic.

The difficulties, both biological and technical, inherent in this study, were clearly the reasons why it was not possible to provide much information with regards to the effects of mechanical loading on cellular deformation within constructs created at different stages of development. Thus, in order to determine the predominant driving factor in explaining the observed effects on synoviocyte morphology and to address the relationship between applied tissue strain and cellular strain, constructs with higher compressive modulus and more matrix deposition with greater homogeneity needed to be developed. By using scaffolds with the same porosity as the previous study for future experimental studies, constructs with homogenous distribution of cartilaginous matrix and fully differentiated chondrocytes could potentially be created. Consequently with further differentiation cells would be distributed more sparsely within the constructs which would make cells identification easier and allow more cells to be measured to increase the sample size. This would also allow tracking changes in cell morphology from the same population of cells possible in order to improve the accuracy of the mean value of the measurements. In addition, tracking the cell location within the construct (i.e top or bottom

surface of the construct) and the matrix distribution around the measured cells with confocal and histological imaging could provide a better insight into the effects of compressive loading on cellular deformation for each experimental parameter (strain levels) and groups (loaded and non-loaded constructs created at different stages of development). It is possible that the proposed technique of utilising the multiphoton fluorescence and SHG imaging together (described in Section 6.5) could be used simultaneously to observe the changes in cell morphology and the local microenvironment around the measured synoviocytes. Multiphoton and SHG microscopy can be used to visualise fluorescently labelled synoviocytes, and the collagen structure around the synoviocytes within the ECM, respectively. Thus, this study has highlighted the importance of scaffold selection for engineering the constructs and the need for more information on, for example, initial cell seeding density for subsequent matrix development and cell differentiation. Despite the shortcomings, this study provides a platform upon which to build for future cell deformation experimental studies.

## Chapter 7 - Conclusion

This investigation sought to determine cell deformation in native and tissue engineered cartilage under incremental tissue compression and to address the relationship between applied tissue deformation and cellular strain.

To summarise the findings:

- A novel compression device which uses a configuration of loading along the focal axis of the (Nikon A1R) confocal microscope was successfully developed to allow visualisation of cells within native and tissue engineered cartilage in real time, under controlled static unconfined compressive loading conditions.
- A dual staining method of Hoechst 33342 and CellMask Green plasma membrane stains with superior retention of fluorescence signal following the repeat capture of three sequential volume images was developed and used to visualise, track and image cell morphology in native cartilage and tissue engineered constructs under controlled loading conditions..
- Image acquisition settings of the confocal microscope were optimised to achieve the best resolution possible within the constraints, both technical and biological, imposed within the experiments. Galvo scanning proved to be more superior at retaining the fluorescence signal compared to resonant scanning and was therefore selected as the image acquisition method used in the experiments.
- Significant changes in deformation of chondrocytes in the superficial zone of bovine cartilage explants were determined under 10 % and 15 % compressive tissue strains. This represented the first time that incremental strain levels were applied and the 3D deformation behaviour of the same chondrocytes tracked within the cartilage tissue. These deformation changes were substantially greater than the overall applied tissue strains suggesting that large morphological changes might occur in the superficial zone of cartilage during physiological compressive loading. It is likely that the local ECM environment as well as the PCM around the chondrocyte may contribute to the observed effects.
- For engineered constructs, only a small amount of cartilage-like matrix deposition was seen in contrast to the previous 2016 study, with correspondingly low compressive modulus values. The primary reason for the differences may be related to the starting porosity of the scaffolds used in the constructs, emphasising the need to understand the relationships between scaffold porosity, cell seeding density and time to cell differentiation. Synoviocyte morphology did not change significantly within loaded constructs under the estimated strain experienced by the construct during mechanical

loading and under 28 % compressive strain. The observed effects were likely be influenced by the microenvironment around the measured synoviocytes, in particular the stiffness of the constructs and the matrix heterogeneity that would have led to distinct regions with variable quantities of collagen type II and GAG.

It is concluded that a novel methodology to visualise, track, image and quantify cell morphology within native and tissue engineered cartilage under static tissue compression was accomplished. This provides a platform upon which to build for future cell deformation experimental studies.

## Chapter 8 - Future work

The achievements and the findings of this study present numerous possibilities for future work. The long term aim of this study was to provide a better understanding on the loading mechanism that was previously used by Finlay *et al.* (2016) [1], in particular the mechanism (s) underpinning the construct's development.

For the cartilage deformation experiment described in Chapter 4, it was highlighted that the mechanical properties of ECM and PCM around the chondrocytes need to be investigated along with the cell deformation response under incremental compression in a future study. It was believed that chondrocyte deformation was largely influenced by the local ECM as well as the PCM around the chondrocyte.

Following the cartilage construct deformation experiment described in Chapter 5, a future study would need to be carried out. In order to determine the effects of incremental compression on synoviocyte deformation within constructs created at different stages of development and to address the relationship between applied tissue strain and the cellular strain, constructs with higher compressive modulus and more matrix deposition with greater homogeneity would need to be created. In addition, more synoviocytes need to be measured to increase the sample size and if possible, track the same population of cells in order to improve the accuracy of the measurements. The proposed assumption of site-specific differences in ECM quality, including stiffness, explaining the observed effects on synoviocyte morphology in this study could also be tested. As discussed in Section 5.5, the aim would be to track the changes in synoviocyte morphology, the synoviocyte locations within the construct and the matrix distribution around the synoviocytes for each experimental parameter (strain levels) and groups (loaded and non-loaded constructs developed at different time points).

The success of the methodology developed here to visualise, track, image and quantify cell morphology within native and tissue engineered cartilage under static tissue compression presents an interesting platform for future study to investigate cell deformation under more 'physiologically-relevant' dynamic loading. Further work on modifying the existing compression device or developing a new loading apparatus to apply controlled, physiological, dynamic compression could be conducted to study the effects of dynamic compressive loading on the cell deformation behaviour within native and tissue engineered cartilage and to address the relationship between the applied dynamic compressive strain and cellular strain. As discussed in Section 6.2, the compression device could be used in studies to examine cell deformation in different cartilage preparations, including isolated cells in agarose gel, cartilage/bone explants and fixed cartilage tissue as well as different connective tissues (i.e.

tendon and ligament) and investigations to determine the chondrocyte biosynthetic responses under static compression.

## Chapter 9 - References

- [1] S. Finlay, B. B. Seedhom, D. O. Carey, A. J. Bulpitt, D. E. Treanor, and J. Kirkham, "In vitro engineering of high modulus cartilage-like constructs," *Tissue Eng. Part C Methods*, vol. 22, no. 4, pp. 382–397, 2016.
- [2] Y. Sasazaki, R. Shore, and B. B. Seedhom, "Deformation and failure of cartilage in the tensile mode," *J. Anat.*, vol. 208, pp. 681–694, 2006.
- [3] A. Swann and B. Seedhom, "Improved techniques for measuring the indentation and thickness of articular cartilage," *Proc. Inst. Mech. Eng.*, vol. 203, no. 3, pp. 143–150, 1989.
- [4] M. Nordin and V. H. Frankel, *Basic Biomechanics of the Musculoskeletal System*. 2001.
- [5] V. C. Mow and C. T. Hung, "Biomechanics of articular cartilage," in *Basic Biomechanics of the Musculoskeletal System*, 4th Editio., M. Nordin and V. H. Franklin, Eds. Baltimore: Lippincott Williams & Wilkins, 2001, pp. 60–101.
- [6] N. P. Cohen, R. J. Foster, and V. C. Mow, "Composition and dynamics of articular cartilage: Structure, function, and maintaining healthy state," *J. Orthop. Sports Phys. Ther.*, vol. 28, no. 4, pp. 203–215, 1998.
- [7] A. M. Bhosale and J. B. Richardson, "Articular cartilage: structure, injuries and review of management.," *Br. Med. Bull.*, vol. 87, pp. 77–95, 2008.
- [8] A. J. S. Fox, A. Bedi, and S. a Rodeo, "The basic science of articular cartilage: structure, composition, and function.," *Sports Health*, vol. 1, no. 6, pp. 461–8, Nov. 2009.
- [9] C. A. McDevitt and J. Marcelino, "Composition of Articular Cartilage.pdf," *Sports Med. Arthrosc.*, no. 2, pp. 1–12, 1994.
- [10] R. A. Stockwell, *Biology of Cartilage Cells*. Cambridge: Cambridge University Press, 1979.
- [11] M. F. Venn, "Variation of chemical composition with age in human femoral head cartilage," *Ann. Rheum. Dis.*, vol. 37, no. 2, pp. 168–174, 1978.
- [12] V. C. Mow and R. Huiskes, *Basic Orthopaedic Biomechanics and Mechano-Biology*, 3rd Editi. Lippincott Williams & Wikins, 2005.
- [13] U. P. Palukuru, C. M. McGoverin, and N. Pleshko, "Assessment of hyaline cartilage matrix composition using near infrared spectroscopy," *Matrix Biol.*, vol. 38, pp. 3–11, Sep. 2014.
- [14] C.-H. Chang, F.-H. Lin, T.-F. Kuo, and H.-C. Liu, "Cartilage tissue engineering,"

*Biomed. Eng. Appl. Basis Commun.*, vol. 17, pp. 61–71, 2005.

- [15] C. C. Wang, C. T. Hung, and V. C. Mow, “An analysis of the effects of depth-dependent aggregate modulus on articular cartilage stress-relaxation behavior in compression,” *J. Biomech.*, vol. 34, pp. 75–84, 2001.
- [16] S. Zhou, Z. Cui, and J. Urban, “Nutrient gradients in engineered cartilage: metabolic kinetics measurement and mass transfer modeling,” *Biotechnol. Bioeng.*, vol. 101, no. 2, pp. 408–421, 2008.
- [17] B. E. Ingelmark, “The nutritive supply and nutritional value of synovial fluid,” *Acta Orthop. Scand.*, vol. 20, no. 2, pp. 144–155, 1950.
- [18] A. Maroudas and P. Bullough, “Permeability of articular cartilage,” *Nature*, vol. 219, pp. 1260–1261, 1968.
- [19] C. A. Poole, “Articular cartilage chondrons: Form, function and failure,” *J. Anat.*, vol. 191, no. 1, pp. 1–13, 1997.
- [20] F. S. Chen, S. R. Frenkel, and P. E. Di Cesare, “Repair of articular cartilage defects: part I. basic science of cartilage healing,” *Am. J. Orthop.*, vol. 28, no. 1, pp. 31–33, 1999.
- [21] F. Guilak, W. R. Jones, and H. P. G. M. L. Ting-Beall, “The deformation behavior and viscoelastic properties of chondrocytes in articular cartilage,” *Biorheology-Oxford-*, vol. 37, pp. 27–44, 2000.
- [22] A. Mobasheri, S. D. Carter, P. Marti, and M. Shakibaei, “Integrins and stretch activated ion channels ; putative components of functional cell surface mechanoreceptors in articular chondrocytes,” *Cell Biol. Int.*, vol. 26, no. 1, pp. 1–18, 2002.
- [23] F. Berthiaume, T. J. Maguire, and M. L. Yarmush, “Tissue Engineering and Regenerative Medicine: History, Progress, and Challenges,” *Annu. Rev. Chem. Biomol. Eng.*, vol. 2, pp. 403–430, 2011.
- [24] H. S. Vasiliadis, J. Wasiak, and G. Salanti, “Autologous chondrocyte implantation for the treatment of cartilage lesions of the knee: a systematic review of randomized studies,” *Knee Surg. Sports Traumatol. Arthrosc.*, vol. 18, no. 12, pp. 1645–55, Dec. 2010.
- [25] D. Eyre, “Collagen of articular cartilage,” *Arthritis Res.*, vol. 4, no. 1, pp. 30–35, 2002.
- [26] N. D. Broom and H. Silyn-Roberts, “The three-dimensional ‘knit’ of collagen fibrils in articular cartilage,” *Connect. Tissue Res.*, vol. 23, no. 4, pp. 261–277, 1989.
- [27] A. Serafini-Fracassini and J. W. Smith, *The Structure and Biochemistry of Cartilage*. Edinburgh: Churchill Livingstone, 1974.

- [28] A. Poole, T. Kojima, T. Yasuda, F. Mwale, M. Kobayashi, and S. Laverty, "Composition and structure of articular cartilage: a template for tissue repair.," *Clin. Orthop. Relat. Res.*, vol. 391, pp. S26-33, 2001.
- [29] D. R. Eyre, S. Apon, J. J. Wu, L. H. Ericsson, and K. A. Walsh, "Collagen type IX: Evidence for covalent linkages to type II collagen in cartilage," *FEBS Lett.*, vol. 220, no. 2, pp. 337–341, 1987.
- [30] J.-J. Wu, P. E. Woods, and D. R. Eyre, "Identification of Cross-linking Sites in Bovine Cartilage Type IX Collagen Reveals an Antiparallel Type II-Type IX Molecular Relationship and Type IX to Type IX Bonding," *J. Biol. Chem.*, vol. 267, no. 32, pp. 23007–23014, 1992.
- [31] S. Ichimura, J.-J. Wu, and D. R. Eyre, "Two-Dimensional Peptide Mapping of Cross-Linked Type IX Collagen in Human Cartilage," *Arch. Biochem. Biophys.*, vol. 378, no. 1, pp. 33–39, 2000.
- [32] M. Diab, J. Wu, and D. R. Eyre, "Collagen type IX from human cartilage: a structural profile of intermolecular cross-linking sites," *Biochem. J.*, vol. 332, pp. 327–332, 1996.
- [33] J. Smith, G.N. and K. D. Brandt, "Hypothesis: can type IX collagen 'glue' together intersecting type II fibers in articular cartilage matrix? A proposed mechanism.," *J. Rheumatol.*, vol. 19, no. 1, pp. 14–17, 1992.
- [34] T. Aigner, W. Bertling, H. Stoss, G. Weseloh, and K. Von Der Mark, "Independent Expression of Fibril-forming Collagens 1, 11, and in Chondrocytes of Human Osteoarthritic Cartilage," *J. Clin. Invest.*, vol. 91, no. March, pp. 829–837, 1993.
- [35] M. Wong and D. R. Carter, "Articular cartilage functional histomorphology and mechanobiology : a research perspective," *Bone*, vol. 33, pp. 1–13, 2003.
- [36] J. Chang and C. A. Poole, "Sequestration of type VI collagen in the pericellular microenvironment of adult chondrocytes cultured in agarose.," *Osteoarthr. Cartil.*, vol. 4, no. 4, pp. 275–285, 1996.
- [37] S. L. Watt, G. P. Lunstrums, A. M. McDonough, D. R. Keene, R. E. Burgesons, and N. P. Morrissll, "Characterization of Collagen Types XII and XIV from Fetal Bovine Cartilage \*," *J. Biol. Chem.*, vol. 267, no. 28, pp. 20093–20099, 1992.
- [38] K. E. Gregory, D. R. Keene, S. F. Tufa, G. P. Lunstrum, N. P. Morris, and G. E. T. Al, "Developmental Distribution of Collagen Type XII in Cartilage : Association with Articular Cartilage and the Growth Plate," *J. Bone Miner. Res.*, vol. 16, no. 11, 2005.
- [39] C. Kiani, L. Chen, Y. J. Wu, A. J. Yee, and B. B. Yang, "Structure and function of

- aggrecan.," *Cell Res.*, vol. 12, no. 1, pp. 19–32, Mar. 2002.
- [40] J. Buckwalter and H. Mankin, "Articular cartilage: tissue design and chondrocyte-matrix interactions.," *J. Bone Jt. Surg. Bone Jt. Surg.*, vol. 79, pp. 600–611, 1997.
- [41] T. E. Hardingham and H. Muir, "Hyaluronic acid in cartilage and proteoglycan aggregation," *Biochem. J.*, vol. 139, no. 3, pp. 565–581, 1974.
- [42] T. E. Hardingham and H. Muir, "The specific interaction of hyaluronic acid with cartilage proteoglycans," *BBA - Gen. Subj.*, vol. 279, no. 2, pp. 401–405, 1972.
- [43] T. E. Hardingham, "The role of link-protein in the structure of cartilage proteoglycan aggregates," *Biochem. J.*, vol. 177, no. 1, pp. 237–247, 1979.
- [44] W. M. Lai, J. S. Hou, and V. C. Mow, "A Triphasic Theory for the Swelling and Deformation Behaviors of Articular Cartilage," *J. Biomech. Eng.*, vol. 1, no. August 1991, pp. 245–257, 2016.
- [45] A. Grodzinsky, V. Roth, E. Myers, W. Grossman, and V. Mow, "The significance of electromechanical and osmotic forces in the nonequilibrium swelling behavior of articular cartilage in tension," *J. Biomech. Eng.*, vol. 103, no. 4, pp. 221–231, 1981.
- [46] V. Sahni, S. Tibrewal, L. Bissell, and W. S. Khan, "The Role of Tissue Engineering in Achilles Tendon Repair : A Review," *Curr. Stem Cell Res. Ther.*, vol. 10, pp. 31–36, 2015.
- [47] L. W. Fisher, J. D. Termine, and F. Young, "Deduced Protein Sequence of Bone Small Proteoglycan I ( Biglycan ) Shows Homology with Proteoglycan II ( Decorin ) and Several Nonconnective Tissue Proteins in a Variety of Species \*," *J. Biol. Chem.*, vol. 264, no. 8, 1989.
- [48] H. C. Bock *et al.*, "The small proteoglycans decorin and biglycan in human articular cartilage of late-stage osteoarthritis," *J. Osteoarthr. Res. Soc. Int.*, vol. 9, pp. 654–663, 2001.
- [49] N. Miosge, K. Flachsbarth, W. Goetz, W. Schultz, H. Kresse, and R. Herken, "Light and electron microscopical immunohistochemical localization of the small proteoglycan core proteins decorin and biglycan in human knee joint cartilage," *Histochem. J.*, vol. 26, no. 12, 1994.
- [50] J. Gallegher, "The extended family of proteoglycans: social residents of the pericellular zone," *Curr. Opin. Cell Biol.*, vol. 1, no. 6, pp. 1201–1218, 1989.
- [51] J. C. Mansfield, J. S. Bell, and C. P. Winlove, "The micromechanics of the superficial zone of articular cartilage," *Osteoarthr. Cartil.*, vol. 23, pp. 1806–1816, 2015.

- [52] K. Y. Tsang, D. Chan, and K. S. E. Cheah, "Fate of growth plate hypertrophic chondrocytes: Death or lineage extension?," *Dev. Growth Differ.*, vol. 57, pp. 179–192, 2015.
- [53] P. Lu, K. Takai, V. M. Weaver, and Z. Werb, "Extracellular Matrix degradation and remodeling in development and disease," *Cold Spring Harb. Perspect. Biol.*, vol. 3, no. 12, pp. 1–24, 2011.
- [54] W. H. Simon, "Scale effects in animal joints. II. Thickness and elasticity in the deformability of articular cartilage," *Arthritis Rheum.*, vol. 14, no. 4, pp. 493–502, 1971.
- [55] W. H. Simon, "Wear properties of articular cartilage in vitro," *J. Biomech.*, vol. 4, no. 5, pp. 379–389, 1971.
- [56] E. S. Jones, "Joint lubrication," *Lancet*, vol. 1, pp. 1043–1045, 1934.
- [57] V. C. Mow and G. A. Ateshian, "Lubrication and wear of diarthrodial joints," in *Basic Biomechanics*, 2nd Editio., Philadelphia: Lippincott-Raven Publishers, 1997, pp. 275–315.
- [58] T. A. Schmidt, N. S. Gastelum, Q. T. Nguyen, B. L. Schumacher, and R. L. Sah, "Boundary lubrication of articular cartilage: Role of synovial fluid constituents," *Arthritis Rheum.*, vol. 56, no. 3, pp. 882–891, 2007.
- [59] S. R. Roberts, M. M. Knight, D. A. Lee, and D. L. Bader, "Mechanical compression influences intracellular Ca<sup>2+</sup> signaling in chondrocytes seeded in agarose constructs," *J. Appl. Physiol.*, vol. 90, pp. 1385–1391, 2001.
- [60] R. Flachsmann, N. D. Broom, and A. E. Hardy, "Deformation and rupture of the articular surface under dynamic and static compression," *J. Orthop. Res.*, vol. 19, pp. 1131–1139, 2001.
- [61] M. Christine Zink and J. B. Van Dyke, *Canine Sports Medicine and Rehabilitation*. John Wiley & Sons, 2013.
- [62] T. D. Brown and D. T. Shaw, "In vitro contact stress distribution on the femoral condyles," *J. Orthop. Res.*, vol. 2, no. 2, pp. 190–199, 1984.
- [63] T. D. Brown and D. T. Shaw, "In vitro contact stress distributions in the natural human hip," *J. Biomech.*, vol. 16, no. 6, pp. 373–384, 1983.
- [64] C. J. Little, N. K. Bawolin, and X. Chen, "Mechanical Properties of Natural Cartilage and Tissue-Engineered Constructs," *Tissue Eng.*, vol. 17, no. 4, pp. 213–227, 2011.
- [65] T. Ohashi, M. Hagiwara, D. L. Bader, and M. M. Knight, "Intracellular mechanics and mechanotransduction associated with chondrocyte deformation during pipette

- aspiration,” *Biorheology*, vol. 43, pp. 201–214, 2006.
- [66] F. Guilak, W. Jones, H. Ting-Beall, and G. Lee, “The deformation behavior and mechanical properties of chondrocytes in articular cartilage,” *Osteoarthr. Cartil.*, vol. 7, pp. 59–70, 1999.
- [67] W. Hodge, R. Fijan, K. Carlson, R. Burgess, W. Harris, and R. Mann, “Contact pressures in the human hip joint measured in vivo,” *Proc. Natl. Acad. Sci.*, vol. 83, no. 9, pp. 2879–2883, 1986.
- [68] M. Kuster, G. Wood, G. Stachowiak, and A. Gächter, “Joint load considerations in total knee replacement.,” *Bone Jt. J.*, vol. 79, no. 1, pp. 109–113, 1997.
- [69] D. Adams and S. A. Swanson, “Direct measurement of local pressures in the cadaveric human hip joint during simulated level walking,” *Annu. Rheum. Dis.*, vol. 44, no. 10, pp. 658–666, 1985.
- [70] T. Fukubayashi and H. Kurosawa, “The contact area and pressure distribution pattern of the knee. A study of normal and osteoarthrotic knee joints.,” *Acta Orthop. Scand.*, vol. 51, no. 6, pp. 871–879, 1980.
- [71] P. S. Walker and J. V. Hajek, “The load-bearing area in the knee joint,” *J. Biomech.*, vol. 5, no. 6, pp. 581–584, 1972.
- [72] J. Q. Yao and B. B. Seedhom, “A new technique for measuring contact areas in human joints--the ‘3S technique,’” *Proc Inst Mech Eng H*, vol. 205, no. 2, pp. 69–72, 1991.
- [73] B. B. Seedhom and D. J. Hargreaves, “Transmission of the Load in the Knee Joint with Special Reference to the Role of the Menisci,” *Eng. Med.*, vol. 8, no. 4, pp. 220–228, 1979.
- [74] A. S. Greenwald and D. W. Haynes, “Weight-bearing areas in the human hip joint,” *J Bone Jt. Surg Br*, vol. 54, no. 1, pp. 157–163, 1972.
- [75] C. Lee, S. Grad, M. Wimmer, and M. Alini, “The influence of mechanical stimuli on articular cartilage tissue engineering,” in *Topics in Tissue Engineering*, vol. 2, E. N. Ashammakhi and R. L. Reis, Eds. 2005, pp. 1–32.
- [76] J. Nilsson and A. Torstensson, “Adaptability in frequency and amplitude of leg movements during human locomotion at different speeds,” *Acta Physiol Scand*, vol. 129, no. 1, pp. 107–114, 1987.
- [77] B. . Seedhom and N. . Wallbridge, “Walking activities and wear of prostheses,” *Annu. rheum dis*, vol. 44, no. 12, pp. 838–843, 1985.
- [78] R. . Mann and J. Hagy, “Biomechanics of walking, running and sprinting,” *Am J Sport*.

- Med*, vol. 8, no. 5, pp. 345–350, 1980.
- [79] P. Rosenrot, J. C. Wall, and J. Charteris, “The relationship between velocity, stride time, support time and swing time during normal walking,” *J. Hum. Stud.*, vol. 6, pp. 323–335, 1980.
- [80] X. L. Lu and V. C. Mow, “Biomechanics of Articular Cartilage and Determination of Material Properties,” *J. Am. Coll. Sport. Med.*, no. 18, pp. 193–199, 2007.
- [81] H. Mankin and A. Thrasher, “Water Content Osteoarthritic and Binding in Normal Cartilage \*,” *J. Bone Jt. Surg.*, vol. 57, no. 1, pp. 76–80, 1975.
- [82] E. Kim, F. Guilak, and M. A. Haider, “The dynamic mechanical environment of the chondrocyte: A biphasic finite element model of cell-matrix interactions under cyclic compressive loading,” *Natl. Institutes Heal.*, vol. 130, no. 6, pp. 1–22, 2009.
- [83] F. Guilak and V. C. Mow, “The mechanical environment of the chondrocyte : a biphasic finite element model of cell-matrix interactions in articular cartilage,” *J. Biomech.*, vol. 33, pp. 1663–1673, 2000.
- [84] J. D. Humphrey, E. R. Dufresne, and M. A. Schwartz, “Mechanotransduction and extracellular matrix homeostasis,” *Nat. Rev. Mol. Cell Biol.*, vol. 8827, no. 12, pp. 572–579, 2014.
- [85] R. Madden, S. K. Han, and W. Herzog, “Chondrocyte deformation under extreme tissue strain in two regions of the rabbit knee joint,” *J. Biomech.*, vol. 46, no. 3, pp. 554–560, 2013.
- [86] F. Guilak *et al.*, “Mechanically induced calcium waves in articular chondrocytes are inhibited by gadolinium and amiloride,” *J. Bone Jt. Surg.*, vol. 17, pp. 421–429, 1999.
- [87] F. Guilak, A. Ratcliffe, and V. C. Mow, “Chondrocyte deformation and local tissue strain in articular cartilage : a confocal microscopy study,” *J. Orthop. Res.*, vol. 13, pp. 410–421, 1995.
- [88] D. A. Lee, M. M. Knight, J. F. Bolton, B. D. Idowu, M. V Kayser, and D. L. Bader, “Chondrocyte deformation within compressed agarose constructs at the cellular and sub-cellular levels,” *J. Biomech.*, vol. 33, pp. 81–95, 2000.
- [89] Z. Sun, S. S. Guo, and R. Fässler, “Integrin-mediated mechanotransduction,” *J. Cell Biol.*, vol. 215, no. 4, pp. 445–456, 2016.
- [90] T. T. Chowdhury, D. M. Salter, D. L. Bader, and D. A. Lee, “Integrin-mediated mechanotransduction processes in TGF $\beta$ -stimulated monolayer-expanded chondrocytes,” *Biochem. Biophys. Res. Commun.*, vol. 318, no. 4, pp. 873–881, 2004.

- [91] L. Ramage, "Integrins and extracellular matrix in mechanotransduction," *Cell Health Cytoskelet.*, vol. 4, pp. 1–9, 2012.
- [92] S. J. Millward-Sadler and D. M. Salter, "Integrin-Dependent Signal Cascades in Chondrocyte Mechanotransduction," *Ann. Biomed. Eng.*, vol. 32, no. 3, pp. 435–446, 2004.
- [93] B. B. Seedhom, "Conditioning of cartilage during normal activities is an important factor in the development of osteoarthritis," *Rheumatology*, vol. 45, pp. 146–149, 2006.
- [94] M. M. Knight, Z. Bomzon, E. Kimmel, A. M. Sharma, D. L. Bader, and D. A. Lee, "Chondrocyte deformation induces mitochondrial distortion and heterogeneous intracellular strain fields," *Biomechan Model Mechanobiol*, vol. 5, pp. 180–191, 2006.
- [95] M. Likhitpanichkul, X. E. Guo, and V. C. Mow, "The effect of matrix tension-compression nonlinearity and fixed negative charges on chondrocyte responses in cartilage," *Tech Sci. Press*, vol. 2, no. 4, pp. 191–204, 2005.
- [96] D. L. Bader and M. M. Knight, "Biomechanical analysis of structural deformation in living cells," *Med. Biol. Eng. Comput.*, pp. 951–963, 2008.
- [97] Y. Gao *et al.*, "The ECM-cell interaction of cartilage extracellular matrix on chondrocytes," *Biomed Res. Int.*, vol. 2014, 2014.
- [98] M. O. Wright, L. W. Davies, G. Nuki, D. M. Salter, and M. E. T. Al, "Mechanotransduction via integrins and interleukin-4 results in altered aggrecan and matrix metalloproteinase 3 gene expression in normal, but not osteoarthritic, human articular chondrocytes," *Arthritis Rheum.*, vol. 43, no. 9, pp. 2091–2099, 2000.
- [99] N. O. Deakin and C. E. Turner, "Paxillin comes of age," *J. Cell Sci.*, vol. 121, pp. 2435–2444, 2008.
- [100] K. A. Athanasiou, E. M. Darling, J. C. Hu, G. D. DuRaine, and A. H. Reddi, *Articular Cartilage*. CRC Press, 2013.
- [101] P. M. Tsimbouri, "Adult Stem Cell Responses to Nanostimuli," *J. Funct. Biomater.*, vol. 6, pp. 598–622, 2015.
- [102] A. Mobasheri, R. Lewis, J. E. J. Maxwell, C. Hill, M. Womack, and R. Barrett-jolley, "Characterization of a Stretch-Activated Potassium Channel in Chondrocytes," *J. Cell. Physiol.*, vol. 223, pp. 511–518, 2010.
- [103] D. E. Ingber, "Cellular mechanotransduction : putting all the pieces together again," *FASEB J.*, vol. 20, no. 7, pp. 811–827, 2006.
- [104] E. J. Blain, "Involvement of the cytoskeletal elements in articular cartilage homeostasis

- and pathology,” *Int. J. Exp. Pathol.*, vol. 90, pp. 1–15, 2009.
- [105] D. A. Fletcher and R. D. Mullins, “Cell mechanics and the cytoskeleton,” *Nature*, vol. 463, pp. 485–492, 2010.
- [106] M. Benjamin, C. . Archer, and J. . Ralphs, “Cytoskeleton of cartilage cells,” *Microsc. Res. Tech.*, vol. 28, pp. 372–377, 1994.
- [107] L. A. Durrant, C. W. Archer, M. Benjamin, and J. R. Ralphs, “Organisation of the chondrocyte cytoskeleton and its response to changing mechanical conditions in organ culture,” *J. Anat.*, vol. 194, pp. 343–353, 1999.
- [108] E. Langelier, R. Suetterlin, C. D. Hoemann, U. Aebi, and M. D. Buschmann, “The chondrocyte cytoskeleton in mature articular cartilage: structure and distribution of actin, tubulin, and vimentin filaments,” *J. Histochem. Cytochem.*, vol. 48, pp. 1307–1320, 2000.
- [109] B. D. Idowu, M. M. Knight, D. L. Bader, and D. A. Lee, “Confocal analysis of cytoskeletal organisation within isolated chondrocyte sub-populations cultured in agarose,” *J. Histochem. Cytochem.*, vol. 32, no. 3, pp. 165–174, 2000.
- [110] M. M. Knight, B. D. Idowu, D. A. Lee, and D. L. Bader, “Temporal changes in cytoskeletal organisation within isolated chondrocytes quantified using a novel image analysis technique,” *Med. Biol. Eng. Comput.*, vol. 39, no. 3, pp. 397–404, 2001.
- [111] W. R. Trickey, T. Parker Vail, and F. Guilak, “The role of the cytoskeleton in the viscoelastic properties of human articular chondrocytes,” *J. Orthop. Res.*, vol. 22, no. 1, pp. 131–139, 2004.
- [112] E. Blain, S. Gilbert, A. Hayes, and V. Duance, “Disassembly of the vimentin cytoskeleton disrupts articular cartilage chondrocyte homeostasis,” *Matrix Biol.*, vol. 25, no. 7, pp. 398–408, 2006.
- [113] M. Jortikka *et al.*, “The role of microtubules in the regulation of proteoglycan synthesis in chondrocytes under hydrostatic pressure,” *Arch. Biochem. Biophys.*, vol. 374, no. 2, pp. 172–180, 2000.
- [114] J. R. Sims, S. Karp, and D. E. Ingber, “Altering the cellular mechanical force balance results in integrated changes in cell, cytoskeletal and nuclear shape,” *J. Cell Sci.*, vol. 103, pp. 1215– 1222, 1992.
- [115] D. R. Haudenschild, J. Chen, N. Steklov, M. K. Lotz, and D. D. D’Lima, “Characterisation of the chondrocyte actin cytoskeleton in living three-dimensional culture: response to anabolic and catabolic Stimuli,” *Mol Cell Biomech*, vol. 6, no. 3, pp.

- 135–144, 2010.
- [116] V. Simon and L. Pon, “Actin-based organelle movement.,” *Experientia*, vol. 52, no. 12, pp. 1117–1122, 1996.
- [117] P. Traub, “Intermediate filaments and gene regulation.,” *Physiol. Chem. Phys. Med. NMR*, vol. 27, no. 4, pp. 377–400, 1995.
- [118] N. Wang, J. Butler, and D. Ingber, “Mechanotransduction across the cell surface and through the cytoskeleton,” *Science (80-. )*, vol. 260, no. 5111, pp. 1124–1127, 1993.
- [119] E. Lazarides, “Intermediate filaments as mechanical integrators of cellular space,” *Nature*, vol. 283, pp. 249–255, 1980.
- [120] J. D. Szafranski, A. J. Grodzinsky, E. Burger, V. Gaschen, H. Hung, and E. B. Hunziker, “Chondrocyte mechanotransduction : effects of compression on deformation of intracellular organelles and relevance to cellular biosynthesis,” *Osteoarthr. Cartil.*, vol. 12, pp. 937–946, 2004.
- [121] L. Setton, V. Mow, and D. Howell, “Mechanical behavior of articular cartilage in shear is altered by transection of the anterior cruciate ligament,” *J. Orthop. Res.*, vol. 13, pp. 473–482, 1995.
- [122] M. Palmoski, E. Perricone, and K. Brandt, “Development and reversal of a proteoglycan aggregation defect in normal canine knee cartilage after immobilization,” *Arthritis Rheumatol.*, vol. 22, pp. 508–517, 1979.
- [123] F. Guilak, B. C. Meyer, A. Ratcliffe, and V. C. Mow, “The effects of matrix compression on proteoglycan metabolism in articular cartilage explants,” *Osteoarthr. Cartil.*, vol. 2, pp. 91–101, 1994.
- [124] M. Buschmann, Y. Kim, M. Wong, E. Frank, E. Hunziker, and A. Grodzinsky, “Stimulation of aggrecan synthesis in cartilage explants by cyclic loading is localized to regions of high interstitial fluid flow,” *Arch. Biochem. Biophys.*, vol. 366, pp. 1–7, 1999.
- [125] M. Wong, M. Siegrist, and X. Cao, “Cyclic compression of articular cartilage explants is associated with progressive consolidation and altered expression pattern of extracellular matrix proteins,” *Matrix Biol.*, vol. 18, pp. 391–399, 1999.
- [126] W. Valhmu *et al.*, “Load-controlled compression of articular cartilage induces a transient stimulation of aggrecan gene expression,” *Arch. Biochem. Biophys.*, vol. 353, pp. 29–36, 1998.
- [127] R. Sah, Y. Kim, J. Doong, A. Grodzinsky, A. Plaas, and S. Sandy, “Effects of compression on the loss of newly synthesized proteoglycans and proteins from cartilage

- explants,” *Arch. Biochem. Biophys.*, vol. 286, pp. 20–29, 1991.
- [128] R. Sah, Y. Kim, J. Doong, A. Grodzinsky, A. Plaas, and S. Sandy, “Biosynthetic response of cartilage explants to dynamic compression,” *J. Orthop. Res.*, vol. 7, pp. 619–636, 1989.
- [129] Y. Kim, R. Sah, A. Grodzinsky, A. H. Plaas, and J. D. Sandy, “Mechanical regulation of cartilage biosynthetic behavior: physical stimuli,” *Arch. Biochem. ...*, vol. 311, no. 1, pp. 1–12, 1994.
- [130] D. A. Lee and D. L. Bader, “Compressive strains at physiological frequencies influence the metabolism of chondrocytes seeded in agarose,” *J. Orthop. Res.*, vol. 15, no. 2, pp. 181–188, 1997.
- [131] M. J. Palmoski and K. D. Brandt, “Effects of static and cyclic compressive loading on articular cartilage plugs in vitro,” *Arthritis Rheum.*, vol. 27, no. 6, pp. 675–681, 1984.
- [132] J. Deschner, C. R. Hofman, N. P. Piesco, and S. Agarwal, “Signal transduction by mechanical strain in chondrocytes,” *Curr. Opin. Clin. Nutr. Metab. Care*, vol. 6, pp. 289–293, 2003.
- [133] R. M. Schinagl, D. Gurskis, A. C. Chen, and R. L. Sah, “Depth-dependent confined compression modulus of full-thickness bovine articular cartilage,” *J. Orthop. Res.*, vol. 15, pp. 499–506, 1997.
- [134] R. M. Schinagl, M. K. Ting, J. H. Price, and R. L. Sah, “Video microscopy to quantitate the inhomogeneous Equilibrium strain within articular cartilage during confined compression,” *Ann. Biomed. Eng.*, vol. 24, no. 20, pp. 500–512, 1996.
- [135] S. S. Chen, Y. H. Falcovitz, R. Schneiderman, A. Maroudas, and R. L. Sah, “Depth-dependent compressive properties of normal aged human femoral head articular cartilage : relationship to fixed charge density,” *Osteoarthr. Cartil.*, vol. 9, pp. 561–569, 2001.
- [136] J. P. Wu, T. B. Kirk, and N. Milne, “A study of the shape change of sheep chondrocytes with application of compression to cartilage,” *Proc. 7th Aust. New Zeal. Intell. Inf. Syst. Conf.*, pp. 95–99, 2001.
- [137] J. B. Choi *et al.*, “Zonal changes in the three-dimensional morphology of the chondron under compression : The relationship among cellular , pericellular , and extracellular deformation in articular cartilage,” *J. Biomech.*, vol. 40, pp. 2596–2603, 2007.
- [138] A. L. Clark, L. D. Barclay, J. R. Matyas, and W. Herzog, “In situ chondrocyte deformation with physiological compression of the feline patellofemoral joint,” *J.*

- Biomech.*, vol. 36, no. 4, pp. 553–568, 2003.
- [139] N. O. Chahine, C. T. Hung, and G. A. Ateshian, “In-situ measurements of chondroncyte deformation under transient loading,” *Eur. Cells Mater.*, vol. 13, pp. 100–111, 2007.
- [140] Y. Sawae, J. U. C. Shelton, D. L. Bader, and M. M. Knight, “Confocal analysis of local and cellular strains in chondrocyte-agarose constructs subjected to mechanical shear,” *Ann. Biomed. Eng.*, vol. 32, no. 6, pp. 860–870, 2004.
- [141] M. M. Knight, S. A. Ghori, D. A. Lee, and D. L. Bader, “Measurement of the deformation of isolated chondrocytes in agarose subjected to cyclic compression,” *Med. Eng. Phys.*, vol. 20, no. 1998, pp. 684–688, 1998.
- [142] D. A. Lee and D. L. Bader, “The development and charaterisation of an in vitro system to study strain-induced cell deformation in isloated chondrocytes,” *Vtiro Cell*, vol. 31, pp. 828–835, 1995.
- [143] M. M. Knight, D. A. Lee, and D. L. Bader, “The influence of elaborated pericellular matrix on the deformation of isolated articular chondrocytes cultured in agarose,” *Biochim. Biophys. Acta*, vol. 1405, pp. 67–77, 1998.
- [144] P. M. Freeman, R. N. Natarajan, J. H. Kimura, and T. P. Andriacchi, “Chondrocyte cells respond mechanically to compressive loads,” *J. Orthop. Res.*, no. 12, pp. 311–320, 1994.
- [145] S. Han, R. Seerattan, and W. Herzog, “Mechanical loading of in situ chondrocytes in lapine retropatellar cartilage after anterior cruciate ligament transection,” *J. R. Soc. Interface*, vol. 7, no. November 2009, pp. 895–903, 2010.
- [146] L. G. Alexopoulos, L. A. Setton, and F. Guilak, “The biomechanical role of the chondrocyte pericellular matrix in articular cartilage,” *Acta Biomater.*, vol. 1, pp. 317–325, 2005.
- [147] R. K. Korhonen and W. Herzog, “Depth-dependent analysis of the role of collagen fibrils , fixed charges and fluid in the pericellular matrix of articular cartilage on chondrocyte mechanics,” *J. Biomech.*, vol. 41, pp. 480–485, 2008.
- [148] R. K. Korhonen, P. Julkunen, W. Wilson, and W. Herzog, “Importance of collagen orientation and depth-dependent fixed charge densities of cartilage on mechanical behavior of chondrocytes,” *J. Biomech. Eng.*, vol. 130, pp. 1–11, 2008.
- [149] G. Merkely, J. Ackermann, and C. Lattermann, “Articular cartilage defects: incidence, diagnosis, and natural history,” *Oper. Tech. Sports Med.*, vol. 26, no. 3, pp. 156–161, 2018.
- [150] J. A. Martin and J. A. Buckwalter, “Roles of Articular Cartilage Aging and Chondrocyte

- Senescence In The Pathogenesis of Osteoarthritis,” *Iowa Orthop. J.*, vol. 21, no. 319, pp. 1–7, 2001.
- [151] Arthritis Research UK, “Osteoarthritis in general practice,” 2013.
- [152] (NICE) The National Institute for Health and Clinical Excellence, “Osteoarthritis,” 2015.
- [153] W. W. Ang, “The Role of Telomeres in Musculoskeletal Diseases,” *J. Int. Med. Res.*, vol. 40, no. 4, pp. 1242–1250, 2012.
- [154] J. A. Buckwalter, K. E. Kuettner, and E. J. Thonar, “Age-related Changes in Articular Cartilage Proteoglycans: Electron Microscopic Studies,” *J. Orthop. Res.*, vol. 3, pp. 251–257, 1985.
- [155] V. C. Mow, L. A. Setton, F. Guilak, and A. Ratcliffe, “Mechanical Factors in Articular Cartilage and Their Role in Osteoarthritis,” in *Osteoarthritic Disorders*, K. E. Kuettner and V. M. Goldberg, Eds. American Academy of Orthopaedic Surgeons: Rosemont, 1995, pp. 147–171.
- [156] A. Verteramo and B. B. Å. Seedhom, “Effect of a single impact loading on the structure and mechanical properties of articular cartilage,” *J. Biomech.*, vol. 40, pp. 3580–3589, 2007.
- [157] B. O. Weightman, M. A. R. Freeman, and S. A. V. Swanson, “Fatigue of articular cartilage,” *Nature*, vol. 244, pp. 303–304, 1973.
- [158] B. Weightman, “Tensile fatigue of human articular cartilage,” *J. Biomech.*, vol. 9, no. 4, pp. 193–200, 1976.
- [159] M. Cross *et al.*, “The global burden of hip and knee osteoarthritis: estimates from the global burden of disease 2010 study,” *Ann. Rheum. Dis.*, vol. 73, no. 7, pp. 1323–30, Jul. 2014.
- [160] K. A. Lee, H. Y. Ng, L. Wei, and Y. Shen, “3D functional scaffolds for cartilage tissue engineering,” in *Functional 3D Tissue Engineering Scaffolds*, Elsevier Ltd, 2018, pp. 391–422.
- [161] J. C. Y. Chow, M. E. Hantes, J. B. Houle, and C. G. Zalavras, “Arthroscopic autogenous osteochondral transplantation for treating knee cartilage defects: a 2- to 5-year follow-up study,” *Arthroscopy*, vol. 20, no. 7, pp. 681–90, Sep. 2004.
- [162] G. Knutsen, L. Engeretsen, and T. C. Ludvigsen, “Autologous Chondrocyte Implantation Compared with Microfracture in the Knee,” *J. bone Jt. Surg.*, vol. 84, pp. 455–464, 2004.
- [163] J. Espregueira-Mendes *et al.*, “Osteochondral transplantation using autografts from the

- upper tibio-fibular joint for the treatment of knee cartilage lesions.,” *Knee Surg. Sports Traumatol. Arthrosc.*, vol. 20, no. 6, pp. 1136–42, Jun. 2012.
- [164] G. Filardo, E. Kon, F. Perdisa, F. Balboni, and M. Marcacci, “Autologous osteochondral transplantation for the treatment of knee lesions: results and limitations at two years’ follow-up.,” *Int. Orthop.*, vol. 38, no. 9, pp. 1905–12, Sep. 2014.
- [165] J. P. Petersen *et al.*, “Present and Future Therapies of Articular Cartilage Defects,” *Eur. J. Trauma*, vol. 29, no. 1, pp. 1–10, Feb. 2003.
- [166] S. L. Francis, C. Di Bella, G. G. Wallace, P. F. M. Choong, and S. L. Francis, “Cartilage tissue engineering using stem cells and bioprinting technology - barriers to clinical translation,” *Front. Surg.*, vol. 5, pp. 1–12, 2018.
- [167] A. Ozmeriç, K. B. Alemdaroğlu, and N. H. Aydoğan, “Treatment for cartilage injuries of the knee with a new treatment algorithm,” *World J. Orthop.*, vol. 5, no. 5, pp. 677–84, Nov. 2014.
- [168] M. T. Rodrigues, M. E. Gomes, and R. L. Reis, “Current strategies for osteochondral regeneration: from stem cells to pre-clinical approaches.,” *Curr. Opin. Biotechnol.*, vol. 22, no. 5, pp. 726–33, Oct. 2011.
- [169] B. R. Manual, “Osteochondral Injury of the Knee,” *Hosp. Physician Orthop. Sport. Med. Board Rev. Man.*, vol. 2, 2005.
- [170] K. Mithoefer, T. Mcadams, R. J. Williams, P. C. Kreuz, and B. R. Mandelbaum, “Clinical efficacy of the microfracture technique for articular cartilage repair in the knee: an evidence-based systematic analysis,” *Am. J. Sports Med.*, vol. 37, no. 10, pp. 2053–2063, 2009.
- [171] E. B. Hunziker, “Articular cartilage repair: basic science and clinical progress. A review of the current status and prospects,” *Osteoarthr. Cartil.*, vol. 10, no. 6, pp. 432–463, 2002.
- [172] S. L. Sherman, E. Thyssen, and C. W. Nuelle, “Osteochondral Autologous Transplantation,” *Clin. Sports Med.*, vol. 36, no. 3, pp. 489–500, 2017.
- [173] M. Brittberg, A. Lindahl, A. Nilsson, C. Ohlsson, O. Isaksson, and L. Peterson, “Treatment of deep cartilage defects in the knee with autologous chondrocyte transplantation,” *N. Engl. J. Med.*, vol. 331, no. 14, pp. 889–895, 1994.
- [174] J. D. Harris, R. A. Siston, X. Pan, and D. C. Flanigan, “Autologous chondrocyte implantation: a systematic review,” *J. BONE Jt. Surg.*, vol. 92, no. 12, pp. 2220–2233, 2010.

- [175] Y. Liu, G. Zhou, and Y. Cao, "Recent progress in cartilage tissue engineering — our experience and future directions," *Engineering*, vol. 3, no. 1, pp. 28–35, 2017.
- [176] C. Vinatier and J. Guicheux, "Cartilage tissue engineering : from biomaterials and stem cells to osteoarthritis treatments," *Ann. Phys. Rehabil. Med.*, vol. 59, no. 3, pp. 139–144, 2016.
- [177] Y. Wang, U.-J. Kim, D. J. Blasioli, H.-J. Kim, and D. L. Kaplan, "In vitro cartilage tissue engineering with 3D porous aqueous-derived silk scaffolds and mesenchymal stem cells.," *Biomaterials*, vol. 26, no. 34, pp. 7082–94, Dec. 2005.
- [178] R. S. Tuan, G. Boland, and R. Tuli, "Adult mesenchymal stem cells and cell-based tissue engineering," *Arthritis Res. Ther.*, vol. 5, no. 1, pp. 32–45, 2003.
- [179] H. Huang, H. Xu, and J. Zhang, "Current Tissue Engineering Approaches for Cartilage Regeneration," in *Cartilage tissue engineering and regeneration techniques*, 2019, pp. 1–20.
- [180] J. Gao, J. Q. Yao, and A. Caplan, "stem cells for tissue engineering of articular cartilage," *Proc. Inst. Mech. Eng.*, vol. 221, no. 15, pp. 441–450, 2007.
- [181] C. Vacanti, R. Langer, B. Schloo, and J. Vacanti, "Synthetic polymers seeded with chondrocytes provide a template for new cartilage formation," *Plast. Reconstr. Surg.*, vol. 88, no. 5, pp. 753–759, 1991.
- [182] R. MM, M. Kallioinen, O. Kaarela, J. Laiho, P. Törmälä, and T. Waris, "The role of polyglycolic acid rods in the regeneration of cartilage from perichondrium in rabbits," *J. Plast. Surg. Hand Surg.*, vol. 25, no. 1, pp. 15–18, 1991.
- [183] L. Wang, C. Ko, E. E. Meyers, B. S. Pedroja, N. Pelaez, and A. M. Bernstein, "Concentration-dependent effects of transforming growth factor  $\beta$ 1 on corneal wound healing," *Mol. Vis.*, vol. 17, pp. 2835–2846, 2011.
- [184] A. H. Huang, A. Stein, R. S. Tuan, D. Ph, R. L. Mauck, and D. Ph, "Transient Exposure to Transforming Growth Factor Beta 3 Improves the Mechanical Properties of Mesenchymal Stem Cell – Laden Cartilage Constructs in a Density-Dependent Manner," *Tissue Eng. Part A*, vol. 15, no. 11, pp. 3461–3472, 2009.
- [185] J. S. Park, J. S. Chu, A. D. Tsou, R. Diop, A. Wang, and S. Li, "The Effect of Matrix Stiffness on the Differentiation of Mesenchymal Stem Cells in Response to TGF- $\beta$ ," *NIH Public Access*, vol. 32, no. 16, pp. 3921–3930, 2012.
- [186] A. M. Mackay, S. C. Beck, J. M. Murphy, F. P. Barry, C. O. Chichester, and M. F. Pittenger, "Chondrogenic differentiation of cultured human mesenchymal stem cells

- from marrow,” *Tissue Eng.*, vol. 4, no. 4, pp. 415–428, 1998.
- [187] E. M. Darling and K. A. Athanasiou, “Articular Cartilage Bioreactors and Bioprocesses,” *Tissue Eng.*, vol. 9, no. 1, pp. 9–25, 2003.
- [188] R. L. Mauck *et al.*, “Functional tissue engineering of articular cartilage through dynamic loading of chondrocyte-seeded agarose gels,” *J. Biomech. Eng.*, vol. 122, no. 3, pp. 252–260, 2000.
- [189] M. Buschmann, Y. Gluzband, A. Grodzinsky, and E. Hunziker, “Mechanical compression modulates matrix biosynthesis in chondrocyte /agarose culture,” *J. Cell Sci.*, vol. 108, pp. 1497–1508, 1995.
- [190] S. E. Carver and C. A. Heath, “Increasing extracellular matrix production in regenerating cartilage with intermittent physiological pressure,” *Biotechnol. Bioeng.*, vol. 62, no. 2, pp. 166–174, 1999.
- [191] S. D. Waldman, C. G. Spiteri, M. D. Gryn timer, R. M. Pilliar, and R. A. Kandel, “Long-term intermittent shear deformation improves the quality of cartilaginous tissue formed in vitro,” *J. Orthop. Res.*, vol. 21, no. 4, pp. 590–596, 2003.
- [192] K. Shahin and P. M. Doran, “Tissue engineering of cartilage using a mechanobioreactor exerting simultaneous mechanical shear and compression to simulate the rolling action of articular joints,” *Biotechnol. Bioeng.*, vol. 109, no. 4, pp. 1060–1073, 2012.
- [193] S. D. Waldman, D. C. Couto, M. D. Gryn timer, R. M. Pilliar, and R. A. Kandel, “Multi-axial mechanical stimulation of tissue engineered cartilage: review,” *Eur. Cells Mater.*, vol. 13, pp. 66–73, 2007.
- [194] T. Davisson, S. Kunig, A. Chen, R. Sah, and A. Ratcliffe, “Static and dynamic compression modulate matrix metabolism in tissue engineered cartilage,” *J. Orthop. Res.*, vol. 20, pp. 842–848, 2002.
- [195] D. Lee, T. Noguchi, S. Frean, P. Lees, and D. Bader, “The influence of mechanical loading on isolated chondrocytes seeded in agarose constructs,” *Biorheology*, vol. 37, pp. 149–161, 2000.
- [196] R. L. Mauck, C. C. Wang, E. S. Oswald, G. A. Ateshian, and C. T. Hung, “The role of cell seeding density and nutrient supply for articular cartilage tissue engineering with deformational loading,” *Osteoarthr. Cartil.*, vol. 11, pp. 879–890, 2003.
- [197] S. Mizuno, T. Tateishi, T. Ushida, and J. Glowacki, “Hydrostatic Fluid Pressure Enhances Matrix Synthesis and Accumulation by Bovine Chondrocytes in Three-Dimensional Culture,” vol. 327, no. January 2001, pp. 319–327, 2002.

- [198] V. Rai, M. F. Dilisio, N. E. Dietz, and D. K. Agrawa, "Recent strategies in cartilage repair: a systemic review of the scaffold development and tissue engineering," *J. Biomed. Mater. Res. Part A*, vol. 105, no. 8, pp. 2343–2354, 2017.
- [199] S. G. Walter, R. Ossendorff, and F. A. Schildberg, "Articular cartilage regeneration and tissue engineering models : a systematic review," *Arch. Orthop. Trauma Surg.*, vol. 0, no. 0, p. 0, 2018.
- [200] E. G. Lima *et al.*, "The beneficial effect of delayed compressive loading on tissue-engineered cartilage constructs cultured with TGF-beta3," *NIH Public Access*, vol. 15, no. 9, pp. 1025–1033, 2009.
- [201] R. Levato *et al.*, "The bio in the ink : cartilage regeneration with bioprintable hydrogels and articular cartilage-derived progenitor cells," *Acta Biomater.*, vol. 61, pp. 41–53, 2017.
- [202] S. Waldman, C. Spiteri, M. Gryn timer, R. Pilliar, and R. Kandel, "Long-term intermittent compressive stimulation improves the composition and mechanical properties of tissue-engineered cartilage," *Tissue Eng.*, vol. 10, pp. 1323–1331, 2004.
- [203] P. Valonen, F. Moutos, and A. Kusanagi, "In vitro generation of mechanically functional cartilage grafts based on adult human stem cells and 3D-woven poly ( $\epsilon$ -caprolactone) scaffolds," *Biomaterials*, vol. 31, no. 8, pp. 2193–2200, 2010.
- [204] F. Guilak, D. L. Butler, S. A. Goldstein, and D. Mooney, *Functional Tissue Engineering*. Springer Science & Business Media, 2006.
- [205] W. Madej, A. Van Caam, E. N. B. Davidson, P. M. Van Der Kraan, and P. Buma, "Physiological and excessive mechanical compression of articular cartilage activates Smad2 / 3P signaling," *Osteoarthr. Cartil.*, vol. 22, no. 7, pp. 1018–1025, 2014.
- [206] S. O'Driscoll and R. Salter, "The induction of neochondrogenesis in free intra-articular periosteal autografts under the influence of continuous passive motion. An experimental investigation in the rabbit," *J. Bone Jt. Surg.*, vol. 66, no. 8, pp. 1248–1257, 1984.
- [207] E. B. Hunziker and T. M. Quinn, "Surgical removal of articular cartilage leads to loss of chondrocytes from cartilage bordering the wound edge," *J. Bone Jt. Surg.*, vol. 85, no. 2, pp. 85–92, 2003.
- [208] A. C. Hall, "The Role of Chondrocyte Morphology and Volume in Controlling Phenotype—Implications for Osteoarthritis, Cartilage Repair, and Cartilage Engineering," *Curr. Rheumatol. Rep.*, vol. 21, no. 8, 2019.
- [209] A. Qusous and M. J. P. Kerrigan, "Quantification of Changes in Morphology,

- Mechanotransduction, and Gene Expression in Bovine Articular Chondrocytes in Response to 2-Dimensional Culture Indicates the Existence of a Novel Phenotype,” *Cartilage*, vol. 3, no. 3, pp. 222–234, 2012.
- [210] F. Guilak, “Compression-induced changes in the shape and volume of the chondrocyte nucleus,” *J. Biomech.*, vol. 28, no. 12, 1995.
- [211] J. Z. Wu and W. Herzog, “Analysis of the mechanical behavior of chondrocytes in unconfined compression tests for cyclic loading,” *J. Biomech.*, vol. 39, pp. 603–616, 2006.
- [212] DuPont, “Delrin product and properties guide,” 2000.
- [213] J. Jonkman, C. M. Brown, G. D. Wright, K. I. Anderson, and A. J. North, “Tutorial: guidance for quantitative confocal microscopy,” *Nat. Protoc.*, pp. 1–26, 2020.
- [214] Mi. F. Ashby and D. R. H. Jones, *Engineering Materials 2: An introduction to microstructures, processing and design*, 3rd Editio. Butterworth Heinemann, 2006.
- [215] M. Minsky, “Microscopy Apparatus,” Patent #301467, 1957.
- [216] J. A. M. Beliën and F. G. Wouterlood, “Confocal laser scanning: of instrument, computer processing, and men,” in *Cellular Imaging Techniques for Neuroscience and Beyond*, First Edit., Elsevier Inc., 2012, pp. 1–34.
- [217] B. Herman, “Fluorescence Microscopy,” in *Current Protocols in Cell Biology*, 1998.
- [218] J. Jonkman, C. M. Brown, and R. W. Cole, “Quantitative confocal microscopy. Beyond a pretty picture,” in *Quantitative Imaging in Cell Biology*, 1st ed., vol. 123, Elsevier Inc., 2014, pp. 113–134.
- [219] S. P. Sepúlveda-Ramírez *et al.*, “Live-cell fluorescence imaging of echinoderm embryos,” in *Echinoderms, Part B*, 2019, pp. 79–397.
- [220] A. R. Hibbs, “What is confocal microscopy?,” in *Confocal Microscopy for Biologists*, New York: Springer, 2004, pp. 1–29.
- [221] J. Pawley, *Handbook of biological confocal microscopy*. New York: Springer, 2006.
- [222] J. C. Waters, “Live-cell fluorescence imaging,” in *Digital Microscopy*, 4th ed., vol. 114, Elsevier Inc., 2013, pp. 125–150.
- [223] A. Ettinger and T. Wittmann, “Fluorescence live cell imaging,” in *Quantitative Imaging in Cell Biology*, 1st ed., vol. 123, Elsevier Inc., 2014, pp. 77–94.
- [224] J. C. Waters and T. Wittmann, “Concepts in quantitative fluorescence microscopy,” in *Quantitative Imaging in Cell Biology*, 1st ed., vol. 123, Elsevier Inc., 2014, pp. 1–18.

- [225] D. Cerra, M. Rupert, and P. Reinartz, "Noise reduction in hyperspectral images through spectral unmixing," *IEEE Geosci. Remote Sens. Lett.*, vol. 11, no. 1, pp. 109–113, 2014.
- [226] R. S. Kathayat, P. D. Elvira, and B. C. Dickinson, "A fluorescent probe for cysteine depalmitoylation reveals dynamic APT signaling," *Nat. Chem. Biol.*, vol. 13, pp. 150–152, 2017.
- [227] S. Wang and I. V. Larina, "High-resolution imaging techniques in tissue engineering," in *Monitoring and Evaluation of Biomaterials and their Performance In Vivo*, Elsevier Ltd, 2017, pp. 151–180.
- [228] B. W. Graf and S. A. Boppart, "Imaging and Analysis of Three-Dimensional Cell Culture Models Microscopy," *Methods Mol Biol*, vol. 591, pp. 211–227, 2010.
- [229] P. Ariel, "A beginner's guide to tissue clearing," *Int. J. Biochem. Cell Biol.*, vol. 84, pp. 35–39, 2017.
- [230] J. M. Girkin, "Multiphoton Microscopy; in depth, in vivo sub cellular resolution imaging," *Opt. Technol. Biophys. Med.*, vol. 6163, 2006.
- [231] L. Song, E. J. Hennink, T. Young, and H. J. Tanke, "Photobleaching kinetics of fluorescein in quantitative fluorescence microscopy," *Biophys. J.*, vol. 68, pp. 2588–2600, 1995.
- [232] H. Giloh and J. W. Sedat, "Fluorescence microscopy : reduced photobleaching of rhodamine and fluorescein protein conjugates by n-Propyl Gallate," *Science (80-. )*, vol. 217, pp. 1252–1255, 1982.
- [233] A. Diaspro, G. Chirico, C. Usai, and P. Ramoino, "Photobleaching," in *Handbook Of Biological Confocal Microscopy*, Third., 2010, pp. 690–702.
- [234] M. Melak, M. Plessner, and R. Grosse, "Actin visualisation at a glance," *J. Cell Sci.*, pp. 1–6, 2017.
- [235] E. Wulf, A. Deboben, F. A. Bautz, H. Faulstich, and T. Wieland, "Fluorescent phallotoxin, a tool for the visualization of cellular actin (microfilaments/rat kangaroo PtK1 cells/bovine kidney MDBK cells)," *Cell Biol.*, vol. 76, no. 9, pp. 4498–4502, 1979.
- [236] B. J. Belin, L. M. Goins, and R. D. Mullins, "Comparative analysis of tools for live cell imaging of actin network architecture," *Bioarchitecture*, vol. 4, no. 6, pp. 189–202, 2014.
- [237] L.-G. Milroy *et al.*, "Selective Chemical Imaging of Static Actin in Live Cells," *J. Am. Chem. Soc.*, vol. 134, no. 20, pp. 8480–8486, 2012.
- [238] G. Lukinavičius *et al.*, "Fluorogenic probes for live-cell imaging of the cytoskeleton,"

*Nat. Methods*, vol. 11, no. 7, pp. 731–733, 2014.

- [239] B. M. Burkel, G. Von Dassow, and W. M. Bement, “Versatile fluorescent probes for actin filaments based on the actin-binding domain of utrophin,” *Cell Motil. Cytoskeleton*, vol. 64, no. 11, pp. 822–832, 2015.
- [240] K. Sliogeryte, S. D. Thorpe, Z. Wang, C. L. Thompson, N. Gavara, and M. M. Knight, “Differential effects of LifeAct-GFP and actin-GFP on cell mechanics assessed using micropipette aspiration,” *J. Biomech.*, vol. 49, no. 2, pp. 310–317, 2016.
- [241] H. Aizawa, M. Sameshima, and I. Yahara, “A green fluorescent protein-actin fusion protein dominantly inhibits cytokinesis, cell spreading, and locomotion in dictyostelium,” *Cell Struct. Funct.*, vol. 22, pp. 335–345, 1997.
- [242] M. Deibler, J. P. Spatz, and R. Kemkemer, “Actin fusion proteins alter the dynamics of mechanically induced cytoskeleton rearrangement,” *PLoS One*, vol. 6, no. 8, pp. 2–6, 2011.
- [243] P. Pravin Kumar, D. L. Bader, and M. M. Knight, “Viscoelastic cell mechanics and actin remodelling are dependent on the rate of applied pressure,” *PLoS One*, vol. 7, no. 9, 2012.
- [244] Z. Feng, W. N. Chen, P. V. S. Lee, K. Liao, and V. Chan, “The influence of GFP-actin expression on the adhesion dynamics of HepG2 cells on a model extracellular matrix,” *Biomaterials*, vol. 26, pp. 5348–5358, 2005.
- [245] J. Riedl *et al.*, “Lifeact: a versatile marker to visualize F-actin,” *Nat. Methods*, vol. 5, no. 7, pp. 605–608, 2008.
- [246] E. D. Este, D. Kamin, C. Velte, F. Göttfert, M. Simons, and S. W. Hell, “Subcortical cytoskeleton periodicity throughout the nervous system,” *Nature*, pp. 1–8, 2016.
- [247] E. D’Este, D. Kamin, F. Göttfert, A. El-Hady, and S. W. Hell, “STED nanoscopy reveals the ubiquity of subcortical cytoskeleton periodicity in living neurons,” *Cell Rep.*, vol. 10, pp. 1246–1251, 2015.
- [248] C. S. Thiel *et al.*, “Rapid morphological and cytoskeletal response to microgravity in human primary macrophages,” *Int. J. Mol. Sci.*, vol. 20, pp. 1–21, 2019.
- [249] A. Romarowski *et al.*, “Super-resolution imaging of live sperm reveals dynamic changes of the actin cytoskeleton during acrosomal exocytosis,” *J. Cell Sci.*, 2018.
- [250] V. Magliocca *et al.*, “Identifying the dynamics of actin and tubulin polymerization in iPSCs and in iPSC-derived neurons,” *Impact Journals*, vol. 8, no. 67, pp. 111096–111109, 2017.

- [251] N. V. Klementieva *et al.*, “Fluorescence imaging of actin fine structure in tumor tissues using SiR-actin staining,” *Anticancer Res.*, vol. 36, pp. 5287–5294, 2016.
- [252] T. D. Pollard, W. C. Earnshaw, J. Lippincott-Schwartz, and G. Johnson, “Actin and Actin-Binding Proteins,” in *Cell Biology*, 3rd ed., 2017, pp. 575–591.
- [253] A. I. Bachir, A. R. Horwitz, W. J. Nelson, and J. M. Bianchini, “Actin-based adhesion modules mediate cell interactions with the extracellular matrix and neighboring cells,” *Cold Spring Harb. Perspectives Biol.*, vol. 9, 2017.
- [254] G. Cooper, *The Cell: A Molecular Approach*, 2nd ed. American Society for Microbiology, 2000.
- [255] W. T. Bellamy, “P-GLYCOPROTEINS AND MULTIDRUG RESISTANCE,” *Annu. Rev. Pharmacol. Toxicol.*, vol. 36, pp. 161–183, 1996.
- [256] P. Mishra, D. C. Martin, I. P. Androulakis, and P. V Moghe, “Fluorescence imaging of actin turnover parses early stem cell lineage divergence and senescence,” *Nature*, vol. 9, pp. 1–12, 2019.
- [257] Y. Li, Y. Song, L. Zhao, G. Gaidosh, A. M. Laties, and R. Wen, “Direct labeling and visualization of blood vessels with lipophilic carbocyanine dye DiI,” *Nat. Protoc.*, vol. 3, no. 11, pp. 1703–1708, 2008.
- [258] B. Chazotte, “Labeling membrane glycoproteins or glycolipids with fluorescent wheat germ agglutinin,” *Cold Spring Harb. Protoc.*, vol. 6, no. 5, 2011.
- [259] J. E. N. Jonkman, J. Swoger, H. Kress, A. Rohrbach, and E. H. K. Stelzer, “Resolution in optical microscopy,” *Biophotonics*, vol. 360, pp. 416–446, 2003.
- [260] M. Abramowitz, K. R. Spring, H. E. Keller, and M. W. Davidson, “Basic principles of microscope objectives,” *Bioimaging*, vol. 33, no. 4, pp. 772–781, 2002.
- [261] A. White, “Application Note: A1R HD25: the latest in resonant scanning technology allows new live-cell imaging approaches,” *Nat. Methods*, vol. 16, no. 1, 2019.
- [262] M. M. Frigault, J. Lacoste, J. L. Swift, and C. M. Brown, “Live-cell microscopy - tips and tools,” *J. Cell Sci.*, vol. 122, no. 6, pp. 753–767, 2009.
- [263] F. Guilak *et al.*, “The pericellular matrix as a transducer of biomechanical and biochemical signals in articular cartilage,” *Ann. N. Y. Acad. Sci.*, vol. 1068, no. 1, pp. 498–512, 2006.
- [264] F. Guilak, “Volume and surface area measurement of viable chondrocytes in situ using geometric modelling of serial confocal sections,” *J. Microsc.*, vol. 173, pp. 245–256, 1994.

- [265] S. M. Turunen, M. J. Lammi, S. Saarakkala, A. Koistinen, and R. K. Korhonen, "Hypotonic challenge modulates cell volumes differently in the superficial zone of intact articular cartilage and cartilage explant," *Biomech. Model. Mechanobiol.*, vol. 11, pp. 665–675, 2012.
- [266] J. S. Jurvelin, M. D. Buschmann, and E. B. Hunziker, "Optical and mechanical determination of Poisson's ratio of adult bovine humeral articular cartilage," *J. Biomech.*, vol. 30, no. 3, pp. 235–241, 1997.
- [267] N. W. Roehm, G. H. Rodgers, S. M. Hatfield, and A. L. Glasebrook, "An improved colorimetric assay for cell proliferation and viability utilizing the tetrazolium salt XTT," *J. Immunol. Methods*, vol. 142, no. 2, pp. 257–265, 1991.
- [268] T. Mosmann, "Rapid colorimetric assay for cellular growth and survival: Application to proliferation and cytotoxicity assays," *J. Immunol. Methods*, vol. 65, no. 1–2, pp. 55–63, 1983.
- [269] K. Elson *et al.*, "Non-destructive monitoring of viability in an ex vivo organ culture model of osteochondral tissue," *Eur. Cells Mater.*, vol. 29, pp. 356–369, 2015.
- [270] M. V. Berridge, P. M. Herst, and A. S. Tan, "Tetrazolium dyes as tools in cell biology: New insights into their cellular reduction," *Biotechnol. Annu. Rev.*, vol. 11, no. SUPPL., pp. 127–152, 2005.
- [271] M. G. Stevens and S. C. Olsen, "Comparative analysis of using MTT and XTT in colorimetric assays for quantitating bovine neutrophil bactericidal activity," *J. Immunol. Methods*, vol. 157, pp. 225–231, 1993.
- [272] M. R. Correro-Shahgaldian, C. Ghayor, N. D. Spencer, F. E. Weber, and L. M. Gallo, "A model system of the dynamic loading occurring in synovial joints: The biological effect of plowing on pristine cartilage," *Cells Tissues Organs*, vol. 199, no. 5–6, pp. 364–372, 2014.
- [273] L. Bian *et al.*, "Mechanical and biochemical characterisation of cartilage explants in serum-free culture," *J. Biomech.*, vol. 41, no. 6, pp. 1153–1159, 2008.
- [274] A. K. T. Wann, J. Mistry, E. J. Blain, A. T. Michael-Titus, and M. M. Knight, "Eicosapentaenoic acid and docosahexaenoic acid reduce interleukin-1 $\beta$ -mediated cartilage degradation," *Arthritis Res. Ther.*, vol. 12, no. 6, pp. 207–215, 2010.
- [275] E. K. Moo, N. A. A. Osman, and B. Pinguan-Murphy, "The metabolic dynamics of cartilage explants over a long-term culture period," *Clinics*, vol. 66, no. 8, pp. 1431–1436, 2011.

- [276] D. M. Allen and J. J. Mao, "Heterogeneous nanostructural and nanoelastic properties of pericellular and interterritorial matrices of chondrocytes by atomic force microscopy," *J. Struct. Biol.*, vol. 145, pp. 196–204, 2004.
- [277] J. K. Loudon, "BIOMECHANICS AND PATHOMECHANICS OF THE PATELLOFEMORAL JOINT," *Int. J. Sports Phys. Ther.*, vol. 11, no. 1, pp. 820–830, 2016.
- [278] B. B. Seedhom, T. Takeda, M. Tsubuku, and V. Wright, "Mechanical factors and patellofemoral osteoarthritis," *Ann. Rheum. Dis.*, vol. 38, no. 4, pp. 307–316, 1979.
- [279] T. W. Flynn and R. W. Soutas-Little, "Patellofemoral joint compressive forces in forward and backward running," *J. Orthop. Sports Phys. Ther.*, vol. 21, pp. 1–6, 1995.
- [280] K. A. Athanasiou, M. P. Rosenwasser, A. Buckwalter, S. T. I. Malinin, and V. C. Mow, "Interspecies comparisons of in situ intrinsic mechanical properties of distal femoral cartilage," *J. Orthop. Res.*, pp. 330–340, 1991.
- [281] S. K. Han, P. Colarusso, and W. Herzog, "Confocal microscopy indentation system for studying in situ chondrocyte mechanics," *Med. Eng. Phys.*, vol. 31, no. 8, pp. 1038–1042, 2009.
- [282] M. I. Froimson, A. Ratcliffe, T. R. Gardner, and V. C. Mow, "Differences in patellofemoral joint cartilage material properties and their significance to the etiology of cartilage surface fibrillation," *Osteoarthr. Cartil.*, vol. 5, pp. 377–386, 1997.
- [283] W. E. Horton, P. Bennion, and L. Yang, "Cellular, molecular, and matrix changes in cartilage during aging and osteoarthritis," *J. Musculoskelet. Neuronal Interact.*, vol. 6, no. 4, pp. 379–381, 2006.
- [284] J. Q. Yao and B. B. Seedhom, "Mechanical conditioning of articular cartilage to prevalent stresses," *Br. J. Rheumatol.*, vol. 32, pp. 956–965, 1993.
- [285] V. c. Mow and R. Huiskes, "Structure and function of articular cartilage and meniscus," in *Basic orthopaedic biomechanics and mechano-biology*, Third., 2005, pp. 182–258.
- [286] Y. Xia, E. M. Darling, and W. Herzog, "Functional properties of chondrocytes and articular cartilage using optical imaging to scanning probe Mmroscopy," *J. Orthop. Res.*, pp. 620–631, 2017.
- [287] S. Finlay, "Towards Acellular Constructs for Cartilage Repair," University of Leeds, 2012.
- [288] C. D. Hoemann, J. Sun, V. Chrzanowski, and M. D. Buschmann, "A multivalent assay to detect glycosaminoglycan , protein , collagen , RNA , and DNA content in milligram

- samples of cartilage or hydrogel-based repair cartilage,” *Analytical Biochem.*, vol. 300, pp. 1–10, 2002.
- [289] I. Stoilov, B. C. Starcher, R. P. Mecham, and T. J. Broekelmann, “Measurement of elastin, collagen, and total protein levels in tissues,” in *Methods in Cell Biology*, 1st ed., vol. 143, Elsevier Inc., 2018, pp. 133–146.
- [290] H. Stegemann and K. Stalder, “Clinica Chimica Acta Determination of Hydroxyproline,” *Clin. Chim. Acta*, vol. 18, pp. 267–273, 1967.
- [291] D. D. Cissell, J. M. Link, J. C. Hu, and K. A. Athanasiou, “A Modified Hydroxyproline Assay Based on Hydrochloric Acid in Ehrlich’s Solution Accurately Measures Tissue Collagen Content,” *Tissue Eng. - Part C Methods*, vol. 23, no. 4, pp. 243–250, 2017.
- [292] N. Radhakrishnan, S. Kanagesan, A. Pandurangan, and P. Padmanabhan, “Basics to different imaging techniques, different nanobiomaterials for image enhancement,” in *Nanobiomaterials in Medical Imaging: Applications of Nanobiomaterials*, Elsevier Inc., 2016, pp. 101–129.
- [293] R. W. Farndale, D. J. Buttle, and A. J. Barrett, “Improved quantitation and discrimination of sulphated glycosaminoglycans by use of dimethylmethylene blue,” *Biochim. Biophys. Acta*, vol. 883, no. 2, pp. 173–177, 1986.
- [294] S. Chandrasekhar, M. A. Esterman, and H. A. Hoffman, “Microdetermination of proteoglycans and glycosaminoglycans in the presence of guanidine hydrochloride,” *Anal. Biochem.*, vol. 161, no. 1, pp. 103–108, 1987.
- [295] A. I. Dragan, J. R. Casas-Finet, E. S. Bishop, R. J. Strouse, M. A. Schenerman, and C. D. Geddes, “Characterization of PicoGreen interaction with dsDNA and the origin of its fluorescence enhancement upon binding,” *Biophys. J.*, vol. 99, no. 9, pp. 3010–3019, 2010.
- [296] S. Park, C. T. Hung, and G. A. Ateshian, “Mechanical response of bovine articular cartilage under dynamic unconfined compression loading at physiological stress levels,” *Osteoarthr. Cartil.*, vol. 12, no. 1, pp. 65–73, 2004.
- [297] H. A. Alturkistani, F. M. Tashkandi, and Z. M. Mohammedsaleh, “Histological Stains: A Literature Review and Case Study,” *Glob. J. Health Sci.*, vol. 8, no. 3, pp. 72–79, 2015.
- [298] J. A. Ramos-Vara, “Technical Aspects of Immunohistochemistry,” *Vet. Pathol.*, vol. 42, pp. 405–426, 2005.
- [299] H. J. Yoon *et al.*, “Type II collagen and glycosaminoglycan expression induction in primary human chondrocyte by TGF- $\beta$ 1,” *BMC Musculoskelet. Disord.*, vol. 16, no. 1,

2015.

- [300] S. B. Mahbub *et al.*, “Non-Invasive Monitoring of Functional State of Articular Cartilage Tissue with Label-Free Unsupervised Hyperspectral Imaging,” *Sci. Rep.*, vol. 9, no. 1, pp. 1–10, 2019.
- [301] Q. Q. Wu and Q. Chen, “Mechanoregulation of chondrocyte proliferation, maturation, and hypertrophy: Ion-channel dependent transduction of matrix deformation signals,” *Exp. Cell Res.*, vol. 256, no. 2, pp. 383–391, 2000.
- [302] J. C. Shelton, D. L. Bader, and D. A. Lee, “Mechanical conditioning influences the metabolic response of cell-seeded constructs,” *Cells Tissues Organs*, vol. 175, no. 3, pp. 140–150, 2003.
- [303] J. A. Kaupp and S. D. Waldman, “Mechanical vibrations increase the proliferation of articular chondrocytes in high-density culture,” *J. Eng. Med.*, vol. 222, no. 5, pp. 695–703, 2008.
- [304] R. H. J. Das, H. Jahr, J. A. N. Verhaar, J. C. van der Linden, G. J. V. M. van Osch, and H. Weinans, “In vitro expansion affects the response of chondrocytes to mechanical stimulation,” *Osteoarthr. Cartil.*, vol. 16, no. 3, pp. 385–391, 2008.
- [305] P. Catistagnola, B. Dozin, G. Moro, and R. Cancedda, “Changes in the expression of collagen genes show two stages in chondrocyte differentiation in vitro,” *J. Cell Biol.*, vol. 106, no. 2, pp. 461–467, 1988.
- [306] Q. Chen, D. M. Johnson, D. R. Haudenschild, and P. F. Goetinck, “Progression and recapitulation of the chondrocyte differentiation program: cartilage matrix protein is a marker for cartilage maturation,” *Dev. Biol.*, vol. 172, no. 1, pp. 293–306, 1995.
- [307] A. Oohira, K. Kimata, S. Suzuki, K. Takata, and I. Suzuki, “A correlation between synthetic activities for matrix macromolecules and specific stages of cytodifferentiation in developing cartilage,” *J. Biol. Chem.*, vol. 249, no. 5, pp. 1637–1645, 1974.
- [308] M. de Haart, W. J. C. M. Marijnissen, G. J. V. M. van Osch, and J. A. N. Verhaar, “Optimization of chondrocyte expansion in culture: Effect of TGFB-2, bFGF and L-ascorbic acid on bovine articular chondrocytes,” *Acta Orthop. Scand.*, vol. 70, no. 1, pp. 55–61, 1999.
- [309] M. Jakob *et al.*, “Specific growth factors during the expansion and redifferentiation of adult human articular chondrocytes enhance chondrogenesis and cartilaginous tissue formation in vitro,” *J. Cell. Biochem.*, vol. 81, no. 2, pp. 368–377, 2001.
- [310] P. C. Yaeger, T. L. Masi, J. L. B. De Ortiz, F. Binette, R. Tubo, and J. M. McPherson,

- “Synergistic action of transforming growth factor- $\beta$  and insulin-like growth factor-I induces expression of type II collagen and aggrecan genes in adult human articular chondrocytes,” *Exp. Cell Res.*, vol. 237, no. 2, pp. 318–325, 1997.
- [311] F. Lemare, N. Steimberg, C. Le Griel, S. Demignot, and M. Adolphe, “Dedifferentiated chondrocytes cultured in alginate beads: Restoration of the differentiated phenotype and of the metabolic responses to interleukin- $1\beta$ ,” *J. Cell. Physiol.*, vol. 176, no. 2, pp. 303–313, 1998.
- [312] J. Rouwkema, B. F. J. M. Koopman, C. A. V. Blitterswijk, W. J. A. Dhert, and J. Malda, “Supply of nutrients to cells in engineered tissues,” *Biotechnol. Genet. Eng. Rev.*, vol. 26, no. 1, pp. 163–178, 2009.
- [313] L. Zhang, J. Hu, and K. A. Athanasiou, “The role of tissue engineering in articular cartilage repair and regeneration,” *Crit. Rev. Biomed. Eng.*, vol. 37, no. 1–2, pp. 1–57, 2009.
- [314] I. Kii, N. Amizuka, J. Shimomura, Y. Saga, and A. Kudo, “Cell-cell interaction mediated by cadherin-11 directly regulates the differentiation of mesenchymal cells into the cells of the osteo-lineage and the chondro-lineage,” *J. Bone Miner. Res.*, vol. 19, no. 11, pp. 1840–1849, 2004.
- [315] F. Djouad *et al.*, “Microenvironmental changes during differentiation of mesenchymal stem cells towards chondrocytes,” *Arthritis Res. Ther.*, vol. 9, no. 2, pp. 1–12, 2007.
- [316] J. Feher, “Cell Signaling,” in *Quantitative Human Physiology*, 2017, pp. 205–217.
- [317] K. L. Collins, E. M. Gates, C. L. Gilchrist, and B. D. Hoffman, *Bio-Instructive Cues in Scaffolds for Musculoskeletal Tissue Engineering and Regenerative Medicine*. 2017.
- [318] R. Kamada *et al.*, “Effective cellular morphology analysis for differentiation processes by a fluorescent 1,3a,6a-Triazapentalene derivative probe in live cells,” *PLoS One*, vol. 11, no. 8, pp. 1–13, 2016.
- [319] P. D. Benya and J. D. Shaffer, “Dedifferentiated chondrocytes reexpress the differentiated collagen phenotype when cultured in agarose gels,” *Cell*, vol. 30, no. 1, pp. 215–224, 1982.
- [320] D. G. Stokes, G. Liu, R. Dharmavaram, D. Hawkins, S. Piera-Velazquez, and S. A. Jimenez, “Regulation of type-II collagen gene expression during human chondrocyte dedifferentiation and recovery of chondrocyte-specific phenotype in culture involves Sry-type high-mobility-group box (SOX) transcription factors,” *Biochem. J.*, vol. 360, no. 2, pp. 461–470, 2001.

- [321] P. M. Van Der Kraan, "The changing role of TGF $\beta$  in healthy, ageing and osteoarthritic joints," *Nat. Rev. Rheumatol.*, vol. 13, no. 3, pp. 155–163, 2017.
- [322] G. Plopper, E. Sikorski, and D. Sharp, "The extracellular matrix and cell adhesion," in *Lewin's Cells*, 3rd Editio., 2014.
- [323] M. L. Gray, A. M. Pizzanelli, A. J. Grodzinsky, and R. C. Lee, "Mechanical and physicochemical determinants of the chondrocyte biosynthetic response," *J. Orthop. Res.*, vol. 6, no. 6, pp. 777–792, 1988.
- [324] Y. O. S. Awae, J. U. C. S. Helton, D. A. N. L. B. Ader, and M. A. M. K. Night, "Confocal analysis of local and cellular strains in chondrocyte-agarose constructs subjected to mechanical shear," *Ann. Biomed. Eng.*, vol. 32, no. 6, pp. 860–870, 2004.
- [325] M. M. Knight, J. M. Ross, A. F. Sherwin, D. A. Lee, D. L. Bader, and C. A. Poole, "Chondrocyte deformation within mechanically and enzymatically extracted chondrons compressed in agarose," *Biochim. Biophys. Acta - Gen. Subj.*, vol. 1526, no. 2, pp. 141–146, 2001.
- [326] K. S. McDorman, C. Chan, J. Rojko, C. M. Satterwhite, and J. P. Morrison, "Special techniques in toxicologic pathology," in *Haschek and Rousseaux's Handbook of Toxicologic Pathology*, 3rd Editio., 2013, pp. 175–214.
- [327] M. Thurston, D. Maida, and C. Gannon, "Oxyrase Cell-Membrane Preparations Simplify Cultivation of Anaerobic Bacteria," *Microbiology*, vol. 31, no. 9, pp. 509–512, 2000.
- [328] S. M. Turunen, S. K. Han, W. Herzog, and R. K. Korhonen, "Cell deformation behavior in mechanically loaded rabbit articular cartilage 4 weeks after anterior cruciate ligament transection," *Osteoarthr. Cartil.*, vol. 21, no. 3, pp. 505–513, 2013.
- [329] E. H. K. Stelzer, "Contrast, resolution, pixelation, dynamic range and signal-to-noise ratio: Fundamental limits to resolution in fluorescence light microscopy," *J. Microsc.*, vol. 189, no. 1, pp. 15–24, 1998.
- [330] H. H. Hopkins, "The airy disc formula for systems of high relative aperture," *Proc. Phys. Soc.*, vol. 55, no. 2, pp. 116–128, 1943.
- [331] M. Abramowitz and M. W. Davidson, "Numerical aperture and resolution," *Molecular Expressions*, 2018. .
- [332] R. Hoffman and M. W. Davidson, "Contrast in optical microscopy," *Molecular Expressions*, 2018. .
- [333] R. T. Borlinghaus, "Pinhole effect in confocal microscopes," *Leica Microsystems*, 2017.

- [334] L. E. Smith, R. Smallwood, and S. Macneil, "A comparison of imaging methodologies for 3D tissue engineering," *Microsc. Res. Tech.*, vol. 73, no. 12, pp. 1123–1133, 2010.
- [335] E. A. Calle *et al.*, "The use of optical clearing and multiphoton microscopy for investigation of three-dimensional tissue-engineered constructs," *Tissue Eng. - Part C Methods*, vol. 20, no. 7, pp. 570–577, 2014.
- [336] E. Olson, M. J. Levene, and R. Torres, "Multiphoton microscopy with clearing for three dimensional histology of kidney biopsies," *Biomed. Opt. Express*, vol. 7, no. 8, p. 3089, 2016.
- [337] A. E. Carpenter *et al.*, "CellProfiler: image analysis software for identifying and quantifying cell phenotypes," *Genome Biol.*, vol. 7, no. 10, 2002.
- [338] C. L. Haass-Koffler, M. Naemuddin, and S. E. Bartlett, "An analytical tool that quantifies cellular morphology changes from three-dimensional fluorescence images," *J. Vis. Exp.*, vol. 2, no. 66, pp. 1–6, 2012.
- [339] I. Youn, J. B. Choi, L. Cao, L. A. Setton, and F. Guilak, "Zonal variations in the three-dimensional morphology of the chondron measured in situ using confocal microscopy," *Osteoarthr. Cartil.*, vol. 14, no. 9, pp. 889–897, 2006.
- [340] D. Stalling, M. Westerhoff, and H. C. Hege, "Amira: A highly interactive system for visual data analysis," *Vis. Handb.*, vol. 1, pp. 749–767, 2005.
- [341] H. Akhondzadeh *et al.*, "Pore-scale analysis of coal cleat network evolution through liquid nitrogen treatment: A Micro-Computed Tomography investigation," *Int. J. Coal Geol.*, vol. 219, 2020.
- [342] M. Arshadi, M. Gesho, T. Qin, L. Goual, and M. Piri, "Impact of mineralogy and wettability on pore-scale displacement of NAPLs in heterogeneous porous media," *J. Contam. Hydrol.*, vol. 230, 2020.
- [343] T. Wejrzanowski, J. Gluch, S. H. Ibrahim, K. Cwieka, and E. Zschech, "Characterisation of spatial distribution of electrolyte in molten carbonate fuel cell cathodes," *Adv. Eng. Mater.*, pp. 1–6, 2018.
- [344] J. M. Bueno, F. J. Avila, and P. Artal, "Second Harmonic Generation Microscopy: A Tool for Quantitative Analysis of Tissues," *IntechOpen*, pp. 100–119, 2016.
- [345] R. Kumar and A. Kumar, "Assessment of Articular Cartilage by Second Harmonic Microscopy : Challenges and Opportunities," *Front. Phys.*, vol. 7, pp. 1–9, 2019.
- [346] J. C. Mansfield, V. Mandalia, A. Toms, C. P. Winlove, and S. Brasselet, "Collagen reorganization in cartilage under strain probed by polarization sensitive second harmonic

generation microscopy,” *R. Soc. Publ.*, 2019.

- [347] R. Chaudhary *et al.*, “Articular Cartilage Zonal Differentiation via 3D Second Harmonic Generation Imaging Microscopy,” *Connect Tissue Res.*, vol. 56, no. 2, pp. 76–86, 2015.
- [348] D. A. Reed, M. Yotsuya, P. Gubareva, P. T. Toth, and A. Bertagna, “Two-photon fluorescence and second harmonic generation characterization of extracellular matrix remodeling in post-injury murine temporomandibular joint osteoarthritis,” *PLoS One*, vol. 14, no. 3, pp. 1–17, 2019.
- [349] T. Saitou, H. Kiyomatsu, and T. Imamura, “Quantitative Morphometry for Osteochondral Tissues Using Second Harmonic Generation Microscopy and Image Texture Information,” *Sci. Rep.*, no. September 2017, pp. 1–14, 2018.